DEVELOPMENT AND EVALUATION OF A MULTIMODALITY TRACKING AND NAVIGATION ASSISTED ROBOTIC FETAL SURGERY SYSTEM

Hariprashanth Elangovan

This thesis is submitted in partial fulfilment of the requirements

for the degree Doctor of Philosophy in Biomedical Engineering

University of Strathclyde

Glasgow, UK

Supervisor: Dr. Wei Yao

September 2017

Declaration

Signed:

Date:

Acknowledgements

First, I would like to thank my supervisor, Dr. Wei Yao, for his time and valuable guidance for these years. I also would like to thank Dr. Chi Hsu for his insight and help and all subjects participating the experiments and people who helped me through this study. Finally, I want to thank my families for their support and encouragement.

Abstract

Minimally Invasive Surgeries have been on the rise since the early 1980s and have developed into several forms of Minimal Access Surgeries. Since the amount of anatomical impact is considerably less than open procedures, the principles of such Minimal Access Surgeries have recently been used in intra-uterine fetal procedures.

However, these procedures are associated with several difficulties that arise from minimal access, such as decreased visualization, anatomical orientation, precision and force transmission. A combination of micro endoscopy and ultrasound has been widely used to aid the surgeon's perception of anatomical orientation. But the inaccuracies due to the inherent principles of ultrasound and the narrow field of view limit the orientation, perception and anatomical relationship and therefore, can impact the surgical outcome. While handling fragile anatomical structures, the perception of force can be of prime importance which can be limited by the narrow size of the instruments used. Also, the lack of feedback from the instruments used could result in un-noticed overshoot.

This project proposed a new robotic surgery system to solve the problems in Minimal Access Fetal Surgeries by improving the perception of visualization, orientation and force feedback. The proposed system is comprised of, a new robotic fetoscope with haptic feedback, integrated with a tracking and navigation system and a complete software environment.

Five experiments were performed to evaluate the efficacy of the proposed robotic surgery system in terms of orientation accuracy, dexterity, the time taken for the procedure, force feedback and the effectiveness and implementation of safety parameters of overshoot protection in surgical assistance. The results of the experiments demonstrated a better efficacy can be achieved by using the proposed tracking and navigation system in combination with the robotic equipment

As the proposed system can give the surgeon the positional orientation, precise controls and a better perception of the entire surgery, it is hoped that further improvements in hardware and software user interface can lead to a surgeon friendly system which can save numerous lives in the near future.

List of Abbreviations

Complementary Metal Oxide Semiconductor (CMOS) – A production technology used mostly to manufacture camera sensor chips, RAMs etc.

Congenital cystic adenomatoid malformation (CCAM) —A condition in which one or more parts of the fetal lungs develop into fluid-filled sacs called cysts.

Congenital diaphragmatic hernia (CDH) —A condition in which the fetal diaphragm (the muscle dividing the chest and abdominal cavity) does not close completely.

Ex utero intrapartum treatment (EXIT) —A caesarean section in which the infant is removed from the uterus, but the umbilical cord is not cut until after surgery for a congenital defect that blocks the air passage.

Fetal Endoscopy (FETENDO) – Fetendo is a form of fetal intervention in the treatment of birth defects and other fetal problems. The procedure uses real-time video imagery from fetoscopy and ultrasonography to guide very small surgical instruments into the uterus in order to surgically help the fetus.

Minimally Invasive Surgery (MIS) - A surgery minimizing surgical incisions to reduce trauma to the body. This type of surgery is usually performed using thin-needles and an endoscope to guide the surgery visually.

Minimal Access Surgery (MAS) – A form of MIS where the amount of access to the surgeon is either limited by the space, approach, visualization and perception or a combination of all the above.

Pulse Width Modulation (PWM) – Electrical pulse width (time) modulated to a specific input which is usually an amplitude

Radiofrequency ablation (RFA) —A procedure in which radiofrequency waves are used to destroy blood vessels and tissues.

Sacrococcygeal teratoma (SCT) —A tumour occurring at the base of the tailbone in a fetus.

Spina bifida (SB) —A birth defect (a congenital malformation) in which part of the vertebrae fail to develop entirely so that a portion of the spinal cord, which is normally protected within the vertebral column, is exposed. People with spina bifida can suffer from bladder and bowel incontinence, cognitive (learning) problems, and limited mobility.

Twin-twin transfusion syndrome (TTTS) —A condition in identical monochorionic twins in which there are connections between the two circulatory systems so that the donor twin pumps blood to the recipient twin without a return of blood to the donor.

Twin:twin reverse arterial perfusion (TRAP) sequence —A condition in which one fetus lacks a heart, and the other fetus pumps the blood for both.

LASER - Light Amplification by Stimulated Emission of Radiation

Contents

List of Figures

List of Tables

Chapter 1

Introduction

The advent of the Minimally Invasive Surgeries (MIS) has changed the way that conventional surgeries are being practiced. With the advancement in surgical instrument design and discovery of new operating techniques in the late 1970s, the size of the surgical incision and the rate of open surgeries have been reducing consistently. MIS could benefit patients in terms of shorter hospital stay and lower risk of surgical complications.

More than 75% of all the procedures with a minimally invasive approach is appendectomy (Cooper et al., 2014) and more than one in four surgeries are performed using MIS. The trend is growing every year, in favour of MIS. The utilisation rates of other procedures for colectomy and hysterectomy are 0.7% and 1.6% respectively. Compound Annual Growth Rate (CAGR) for other procedures is estimated at 10.5% per annum between 2013 and 2019 (Tsui et al., 2013).

The overall complication rates have been significantly reduced among patients who underwent MIS when compared to open surgery. Randomised controlled trials of 863 patients have showed a reduction in postoperative pain, postoperative analgesic requirements, and hospital length of stay (Group, 2004). For example, in appendectomy, the MIS complications were at 3.94% vs 7.90% for the open procedures; 13.8% vs 35.8% for colectomy 4.69% vs 6.64% for hysterectomy and 17.1% vs 25.4% for lobectomy (Cooper et al., 2014).

One of the challenges in MIS technology is to reduce the incision size smaller than the size of a keyhole. The reduction of incision size to this extent would mean the patients can have less scarring and lesser number of sutures applied in surgeries with a reduced recovery time, and a lower rate of infection (Group, 2004). This would also mean that the rate of wound dehiscence can be virtually non-existent.

Such a reduction in the size comes at a great cost to visual and proprioceptive perceptions of the surgeon. During the process of surgery, the perceptions of the surgeon are mostly limited to reduced field of vision, altered force feedback from surgical tools, a mental image of the anatomy and physical correlation to the specific surgical site, which gives the surgeon the ability to make a judgement (Kwok, 2012). When any of the above is compromised as in laparoscopic procedures, it imposes a mental strain on the surgeon, resulting in reduced confidence (Gofrit et al., 2008) and the accuracy of the surgical procedure to a great extent, raising the difficulty of the procedure to the extent of a challenge.

The surgeon, in most cases, compensates for the loss in perception using a refinement of surgical skills by way of practice and reprogramming his mental orientation (Farmer, 1998). Hence, by reducing the size of the surgeries to an extent that the procedures would not require suturing, the surgeon would require assistance from technology to carry out the surgeries successfully due to the loss of the perceptions (Yao et al., 2014) (Yao W., Hariprashanth E. &Kypros N., 2014).

The above is the scenario for fetal surgeries, where the surgeon performs procedures with the assistance of ultrasound guidance and video guidance. There are procedures which can be explained easily in theory. But to actually accomplish a successful surgical procedure has always proven to be a challenge (Cass, 2005) (Yao W., Hariprashanth E. &Kypros N., 2014). The very fact that we have hardly limited numbers of accomplished fetal surgeons around the world is an evidence of this.

This project will develop a general tracking, navigation and guidance system for all Minimal Access Surgeries (MAS), but will mainly focus on developing instruments for use in fetal surgery. Such devices would be embedded with passive artificial intelligence, tele-control capabilities, sense of orientation and force and integrated with computerised imaging software. The software merges the 3D model of the device itself, with the ultrasound images, giving the perspective orientation of the surgeon's hands with the data from the active tool tips inside the abdomen of the mother.

1.1 Aims of the project

Navigated robotic surgeries have been consistently in use since 1985 in the field of orthopaedics and have since found wide acceptance in the fields of urology, intra-abdominal, cardiothoracic, gynaecology and neurosurgery. In spite of great acceptance of these systems, they are very expensive and require extensive training for the surgeon to become proficient (Ho et al., 2012). Further, the navigating systems which have been designed for specific surgeries cannot be easily adapted to fulfil the requirements of other surgeries.

Though CT guided surgeries have been widely practiced, CT guidance is not suitable for biopsies near any moving structures or the surguries in dynamic structures. Such procedures may require multiple exposures to X-Rays or a real-time imaging modality like medical ultrasound. However, ultrasound guided robotic navigation is still experimental due to image noise, and positional variation errors resulting from sound velocity change in harder objects (Hong et al., 2004).

Fetal surgery is a highly complex surgical intervention to repair birth defects in the womb that requires the most expert care for both mother and unborn baby. This is an emerging field of minimally invasive surgery heavily limited by the lack of perception of orientation and feedback. Therefore, improvements in technology is expected to aid the surgery. Since these procedures are very recently on the rise, they do not yet have a dedicated robotic platform adaptable to the set of procedures. (Farmer, 1998). Further, such ultrasound guided MAS procedures require extensive experience in coordination of hand – eye – ultrasound - equipment and assessment of relative anatomy. As a result, such surgeries require skills that can only be acquired over long periods of training (Yao et al., 2014).

Therefore, there is a need to fill the gap between fetal surgery and the robotic surgical system. With this taken into consideration, this project aims at:

1. Identifying the difficulties in Minimal Access fetal Surgeries.
2. Identifying the challenges in available tracking technology within a MAS environment and to propose the solutions specific to such procedures.
3. To explore a method of reliable cross calibration of ultrasound with tracking modality and registration.
4. Development of a robotic surgical system for MAS, and the software to improve the surgeon's physical and mental perception (Howe and Matsuoka, 1999).
5. Integration of the surgical system with multiple modalities of tracking, navigation, sensors, hardware actuators and the software to assist the surgeon.
6. Development of an evaluation environment of the system for testing and evaluation of the above system.

A surgical assistance system is to be developed which delivers:

a) Improvisation of the surgeon's perception by:

    1. Improving physical and anatomical orientation by integration of multiple imaging systems
    2. Providing better haptic feedback
    3. Giving a navigation interface with 6DoF tracking for improving accuracy
    4. Increasing the field of view of the camera by using micro manipulators
    5. Better feedback using sensors and integrated robotics

b) Increases the accuracy using:

    1. Software guided surgical planning and execution
    2. Robotics for precise movements

3. Optical 6DoF tracking and ToF 1D tracking

c) Offers safety options:

1. Navigation interface with guidance and overshoot indication
2. Automatic robotic correction options when the target is set
3. Automatic control of high power devices

1.2 Requirements of this project

The primary goal of this project is to design, develop and evaluate a multi-modality navigated robotic system for fetal surgery. The following requirements have been identified:

1. A tracking and navigation system for the surgical guidance.
2. Image registration methods and rapid on-table registration.
3. A portable robotic system capable of MAS for use in fetal surgery - imaging, suction, insufflation, LASER ablation functions.
4. Software with the integration of the above, target setting and guidance abilities.
5. Warning and error notification for human errors.
6. Evaluation of different aspects of the system using multiple phantom environments designed to test them respectively.
7. Software environment to support the above evaluation environment.

1.3 Achievements and contributions of this project

The following have been developed, implemented and evaluated:

1. A novel optical tracking system specifically designed to reduce the number of optical markers to 2 which occupy lower space than the currently used 5 marker systems and avoid marker confusion.

2. A real-time ultrasound imaging/tracking system and method of cross calibration of one imaging modality to the other.
3. Multi-modality tracking system achieved by merging optical tracking guidance and ultrasound tracking.
4. A passive, surgeon controlled portable hand held Robotic catheter unit with multiple forms of sensors and actuators to provide haptic feedback, motion and kinematic assistance.
5. Software environment development with Virtual Reality software guidance integrating the above systems in real-time using communication methods.
6. A smart one-click 3D registration method for cross calibration across multiple imaging platforms.
7. Development of a phantom environment for surgical testing, evaluation and training.

1.4 Organization of the thesis

The rest of the thesis is organised as follows:

Chapter 2 presents an overview of Minimally Invasive surgeries (MIS) and fetal surgeries. Firstly, this chapter will focus on the advantages of MIS and the current challenges of MAS using based ultrasound guided fetal surgeries. The embryology of fetal development and the pathology behind certain fetal disorders will be briefly explained, followed by a discussion of the challenges of MIS surgical procedures.

This chapter also compares state-of-the-art technology instruments and their limitations. This chapter also provides an overview on the foundation for the design of the fetal surgery system and outlines the principles in medical ultrasound imaging and optical tracking which were used for development of the robotic hardware and software. This chapter also describes the methodologies for the validation of reliability of such devices. Based on these existing gold standard methods, the hardware and software developed for assessment of the robotic device have been performed.

Finally, the literature review summaries the technological aspects used in state-of-the-art robotic MIS, which are relevant to MAS and how they can be modified to overcome the challenges faced in Minimal Access fetal Surgeries. These technologies are used to develop the proposed fetal surgery system in the later chapters.

Chapter 3 focuses on the principles and the limitation of Optical tracking when used with ultrasound in Minimal Access surgeries. This chapter also discusses a novel tracking architecture and merging this tracking modality with ultrasound to surpass some of the limitations in conventional optical tracking system.

This chapter further discusses the evaluation of the novel optical tracking system.

Chapter 4 describes the use of ultrasound hardware in Minimal Access Surgeries and evaluates the limitations of accuracy of plain ultrasound guidance. Further, this chapter investigates the specificity of real time object detection and orientation by using the alternate tracking system and merging different tracking modalities. The effectiveness of such a system is compared with human perceptions and the sensitivity and specificity are evaluated.

Chapter 5 details the design of a robotic fetoscope from development to evaluation. The software and hardware used for construction and evaluation of the fetoscope are elaborated.

Chapter 6 This chapter focuses on the development of surgical navigation interface and the algorithms. The fetoscope, developed in Chapter 5, is combined with the tracking system discussed earlier to form a complete unit. This complete system is integrated into the surgical environment.

Chapter 7 describes the principle of a test platform for the fetoscope and the navigation system.

The chapter also explains the experiments for evaluation of the robotic surgery devices with the navigation interface in Chapter 6, within the artificial surgical environment.

Chapter 8 critically discusses the experimental results and findings reported in Chapter 7. Clinical implications are also discussed.

Chapter 9 concludes the thesis and outlines potential further studies

In Figure1.1, the outline of the process flow for this project is shown. This involves the following:

1. Selecting a group of congenital malformations for which Minimal Access Surgeries are already available.
2. Classifying the types of management available
3. Identifying the significant challenges faced in the available methods of management.
4. Technological solutions are proposed to the challenges identified.
5. Proposing hardware and software approach to the solutions where required. Target specifications are then identified for every respective solution proposed.
6. Hardware – software integration.
7. Evaluation of the proposed solutions in phantom environments.
8. Discussion and analysis of the results from evaluating the proposed solutions.
9. Conclusion and future work.

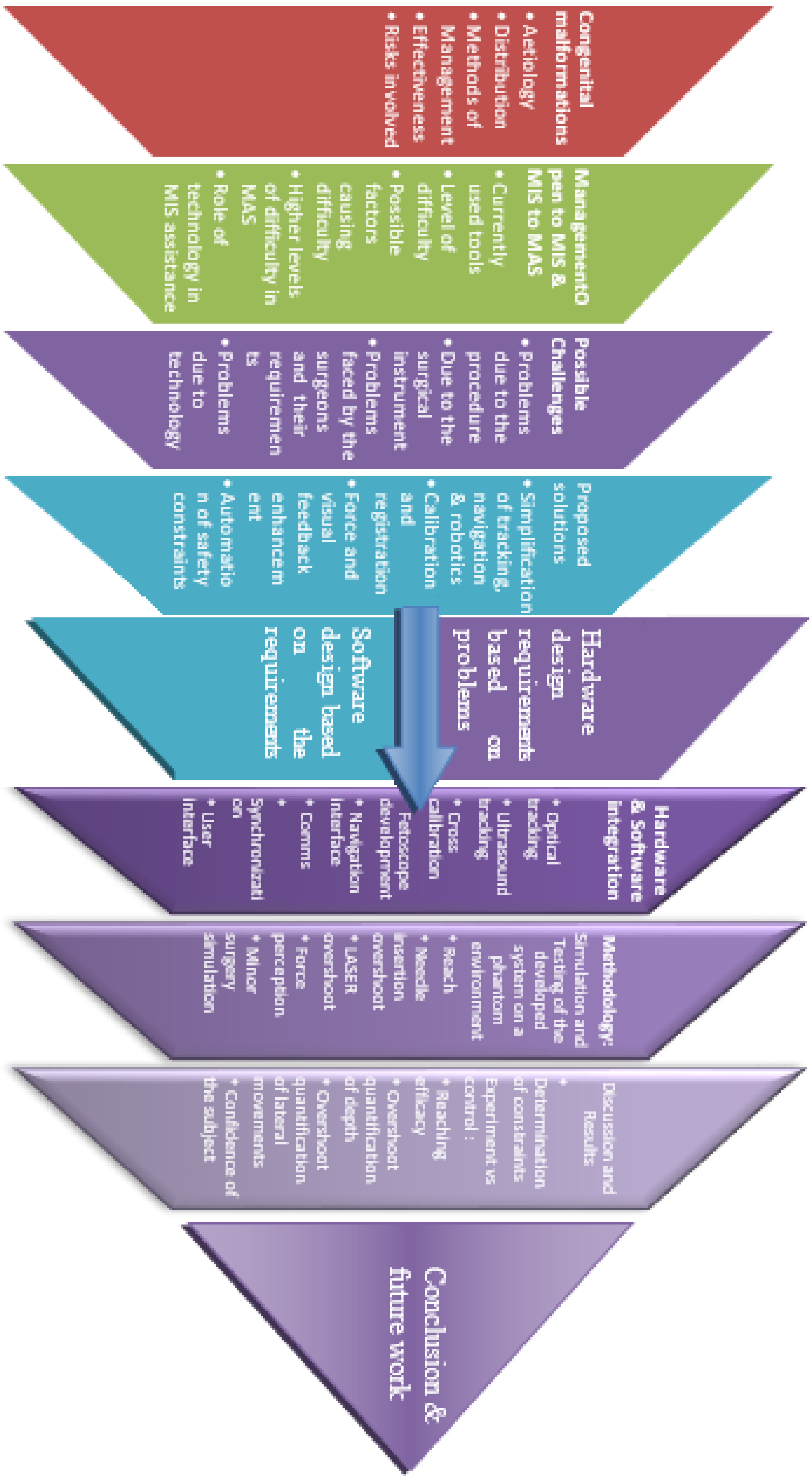

Figure 1-1 Flowchart showing the outline of the project

Research overview in this project is as follows:

1. Congenital malformations which have existing methods of management are found.
2. The problems faced during the management methods identified in step 3 of Figure 1.1 and their possible solutions are first identified as seen in Figure 1.2.
3. The challenges faced are classified based on whether they require software or hardware solutions.
4. Specific hardware and software solutions are then proposed.
5. Target specifications are then identified for the proposed solutions.

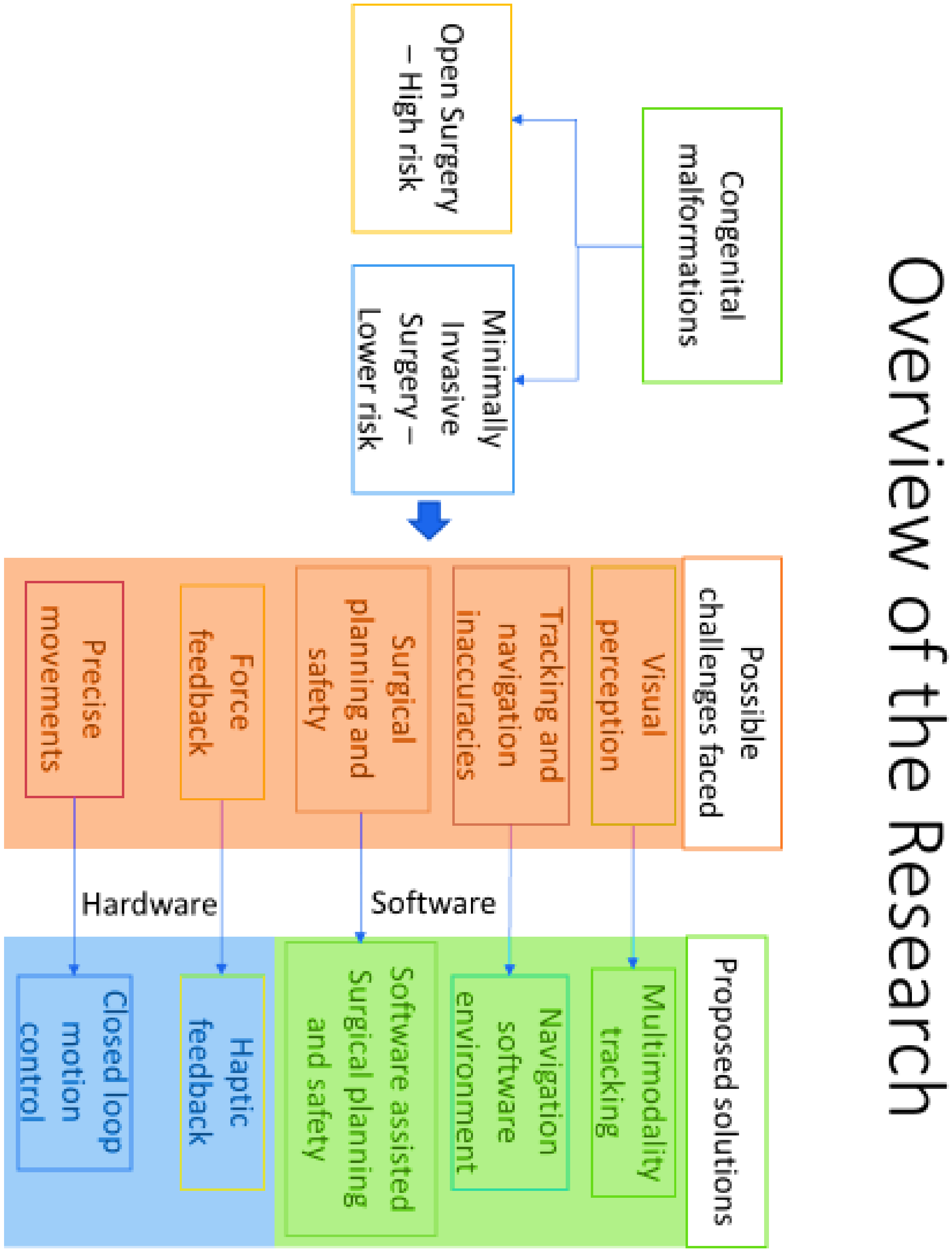

Figure 1-2 Research overview

The hardware and software solutions proposed in Figure 1.2 have inherent challenges in implementation. Solutions are proposed to solve or alter the outcomes of the proposed solutions are given in Figure 1.3 as follows:

1. Expanding the proposed solutions in relation to the problems faced.
2. Identifying the problems faced for every respective solution proposed.
3. Proposing solutions or alteration in methodology for making the primary solutions proposed viable.

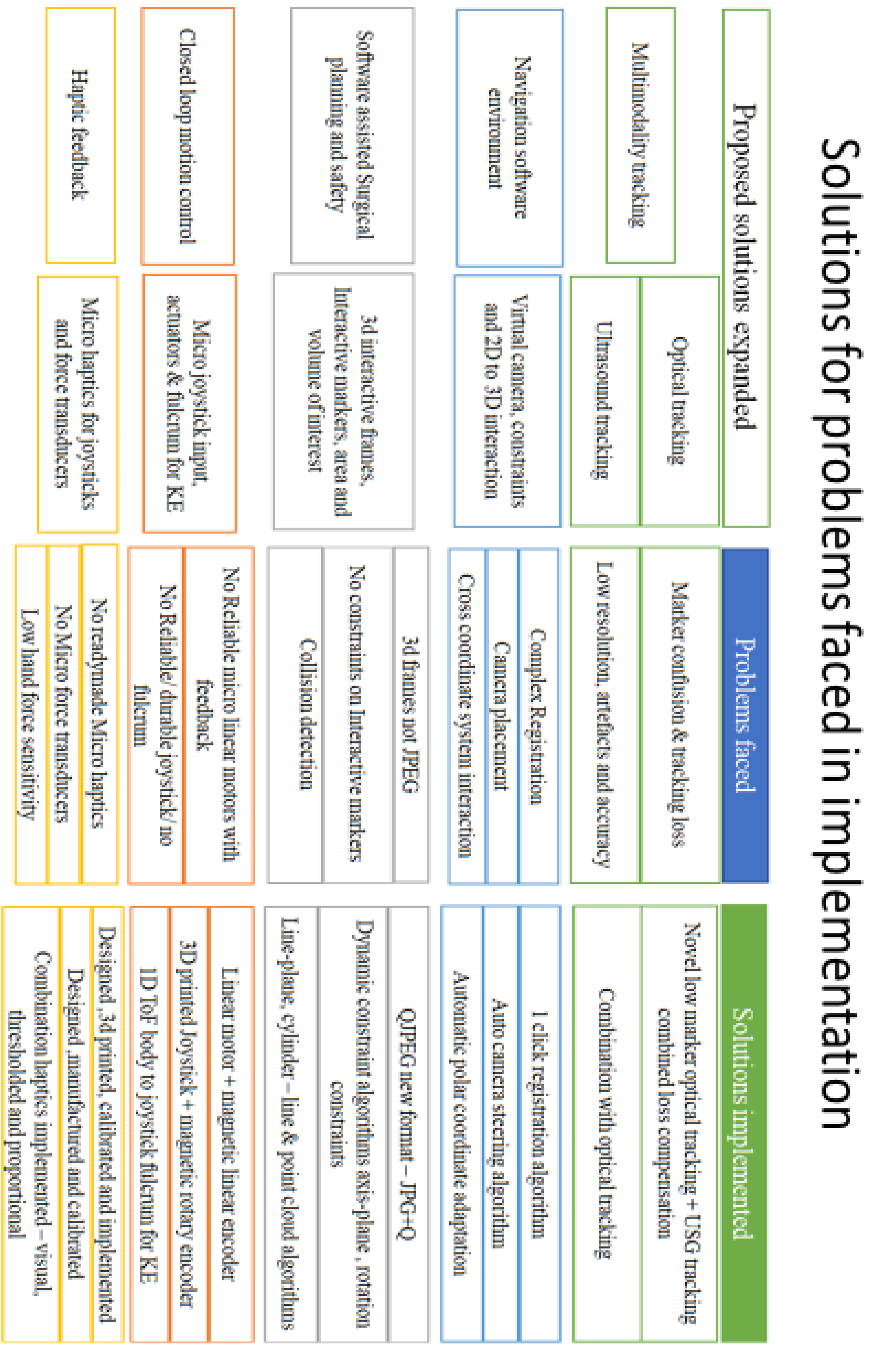

Figure 1-3 Overview of solutions offered to problems faced in the project implementation

Later the challenges of such solutions and the possibility of alteration of these solutions are investigated, as shown in Figure 1.3. These modified solutions are used as a basis for the development of hardware and software combination. The hardware-software combination with aspects of the surgeon's perception of orientation, force, safety and performance in a phantom environment are is evaluated using specific experiments as seen in Figure 1.4. Finally, the conclusions from the evaluation are drawn and the possible future work is discussed.

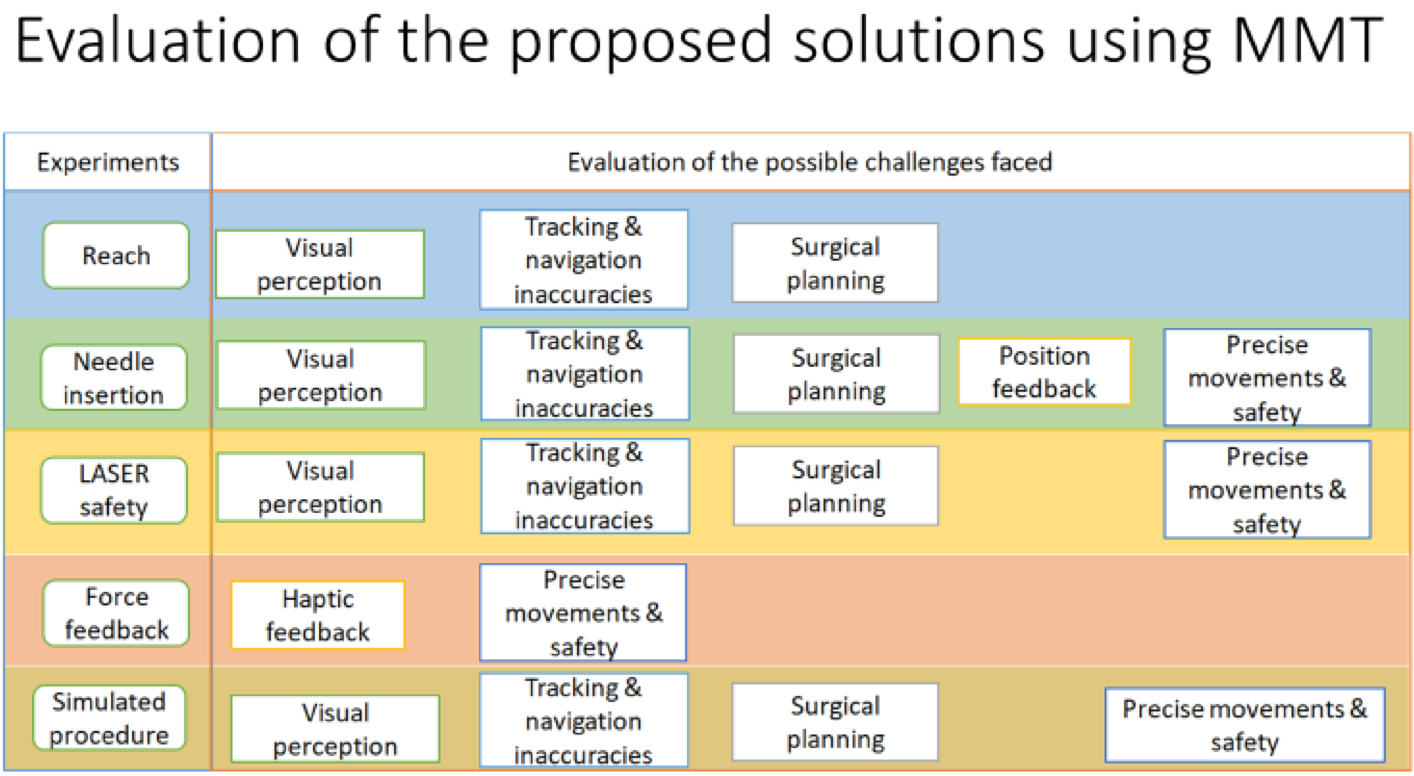

Figure 1-4 Evaluation plan for the Multimodality tracking and navigation with haptic feedback

Chapter 2

Fetal surgery & tracking - Literature review & fundamentals

The project centres around the understanding of difficulties faced during Minimal Access fetal surgery and development of technology for use in such surgeries. Hence, the initial review will briefly discuss fetal development and problems during such development leading to congenital conditions. The understanding of the problems encountered during management of such conditions requires understanding the background of Minimally invasive surgeries, the instruments used, and the challenges faced during the same. Therefore, minimally invasive surgeries are reviewed in relation to fetal surgeries in the later sections. To be able to design technological equipment for surgery, currently available technology needs to be reviewed. Based on the review, the technological requirements will be narrowed down, and the fundamentals of the underlying technologies used will be established in the final part of the literature review to provide a better understanding of device development featured in the rest of the chapters.

2.1 Overview of fetal development & congenital malformations

From the phase of fertilization to the end of the second week, the human organism is a collection of replicating cells. After this phase, it is referred to as an embryo till 8 weeks. Organogenesis starts after the 8th week and in this phase, is it known as fetus till the 36 weeks period of gestation. Between 37 to 39 weeks, the fetus matures and can survive if there are no associated abnormalities. The development of a fetus is by any standards of comparison the most sophisticated and complex form of engineering known to mankind. A better understanding of the developmental stages can help us understand the problems during development and the causes of such problems.

2.1.1 Growth and development of a fetus

In terms of engineering, manufacturing processes, the methods of production are usually additive or subtractive. Whereas in the case of biological formation, it is a combination of additive and subtractive processes guided by very complex chemotactic processes which are not yet understood but are quite commonly referred to as processes of tubulation which form most structures as chords, which undergo central cellular apoptosis (Brill et al., 1999) resulting in tube formation. There are several stages of fetal development which have been identified and several substages which are still under research. The main stages of fetal development are outlined in Table 2.1.

Table 2-1 Fetal Development (Weeks 9–38). Organ development is completed, and body size increases dramatically during weeks 9–38.

Time of development	Fetal development
Weeks 9-15	Reproductive organs form Tooth buds appear Eyelids form The fetus is very active Brain activity can be detected
Weeks 16-26 (Fetal surgeries done)	Brain develops rapidly Alveoli form in lungs Internal parts of the eyes and ears form Eyebrows, eyelashes and nails appear Muscles develop
Weeks 27-38	Body fat increases rapidly Bones complete their development Head hair gets coarser and thicker Brain is continuously active

2.1.2 Congenital malformations and available methods of surgical management(Brill et al., 1999)

Congenital malformations account for one of the major causes of perinatal mortality and morbidity. Single major birth defects, affect 3% of new-borns and multiple defects, affect 0.7% of babies (Canfield et al., 2006). The hidden prenatal mortality is higher since the majority with considerable defects undergo a spontaneous abortion (Larsen et al., 2013) as mentioned earlier in this review. In the BINOCAR data from 2012, 23% of malformations had a spontaneous abortion (BINOCAR report 2012). Despite improvements in perinatal care, serious birth defects still account for 20% of all deaths in the neonatal period and an even greater percentage of serious morbidity later in infancy and childhood. Yet, the major causes of congenital malformation are chromosomal abnormalities, mutant genes, multifactorial disorders and teratogenic agents.

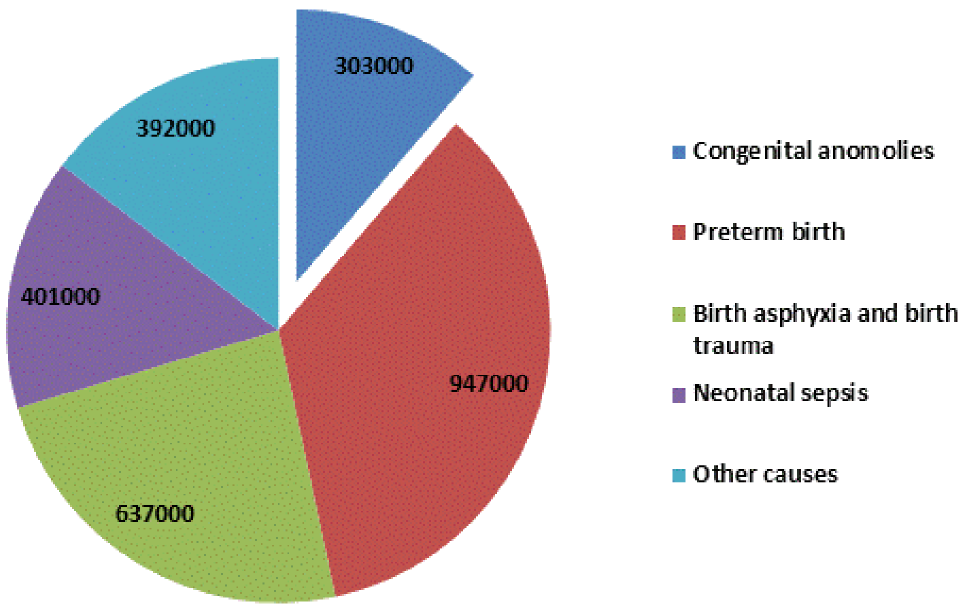

Figure 2-1 WHO 2000 to 2015 causes of neonatal (WHO 2000-2015 child causes of death)(Liu et al., 2015)

From Figure 2.1, it can be observed that 30300 newborns die due to congenital malformations between 2000 and 2015 according to WHO reports. About 3% of fetuses and newborns are diagnosed with a congenital anomaly in the UK each year, either before or soon after birth; this includes fetuses which are terminated because of the presence of a congenital anomaly (TOPFA). This means that in 2008 when there were 712, 328 births in England and Wales over 21,000 were affected by a congenital anomaly diagnosed before or around birth (Graya et al., 2009). When these malformations do not result in death, the result can be long term disability, which can have a significant impact on families, society and the world. The birth prevalence of congenital anomalies decreased from 265 per 10,000 total births in 2007 to 250 per 10,000 total births in 2011. Between 2007 and 2011, significantly increasing trends can be seen in neural tube defects (5% per year) and respiratory anomalies (7%). The increasing trend in neural tube defects is of concern in the West of Scotland and Northern Ireland (BINOCAR report 2012). Folic acid supplementation preconceptionally and in the first trimester is shown to reduce the incidence of Neural tube defects. A significantly decreasing trend was seen in limb reduction anomalies (6% per year) and oro-facial clefts (4%). There are a number of other anomalies, including other limb anomalies, which also showed significantly decreasing trends, however these are mainly due to issues around the ascertainment of the less severe forms of these anomalies (BINOCAR report 2012).

The danger of structural defects caused by teratogens is the greatest in early pregnancy because the initial cells, which form the different tubes can replicate the genetic defects at a very high rate which get carried on to the parts destined to be formed. Malformations can be as common as 14% of newborns and are of mostly very less significance, for example, ear tags, simian crease or major problems such as congenital cardiac defects (Marden et al., 1964). It has been observed that the greater the number of minor malformations, the greater is the likelihood of major malformation. For example, in a study conducted by Leppig and his team, 4305 white newborns were examined for 114 minor physical abnormalities to evaluate the association with major abnormalities and the risk was found to be 19.6% in babies with 3 or more minor anomalies (Leppig et al., 1987). With the increase in the severity of the malformations, the incidence of miscarriage is very high, probably a process of complicated natural selection. In certain cases where a baby with severe structural malformations is born due to chromosomal defects, the survival rates are usually quite low. For example, in a study conducted by Dastgiri and team based on Glasgow Register of Congenital Anomalies, (Dastgiri et al., 2003) the proportions of all live born infants with congenital anomalies surviving till the end of the first week, and first and fifth year were 94%, 89%, and 88%, respectively. Survival to age 5, the end point of follow up, was significantly poorer for infants with chromosomal anomalies (48%) compared to neural tube defects (72%), respiratory system anomalies (74%), congenital heart disease (75%), nervous system anomalies (77%), and Down's syndrome (84%). Although almost 90% of all live born infants with congenital anomalies survive to 5 years, there are notable variations in survival between anomaly types. Our findings should be useful for both clinicians and geneticists to assess the prognosis of congenital anomalies. The main causes of congenital malformation and the rate at which they are observed to cause such problems is shown in Figure 2.2(Killeen, 2006). From the Figure 2.2, it can also be seen that nearly 70% of the causes are usually not defined. Figure 2.2 demonstrates the main causes of congenital malformation and the percentage attributable to each of the different groups.

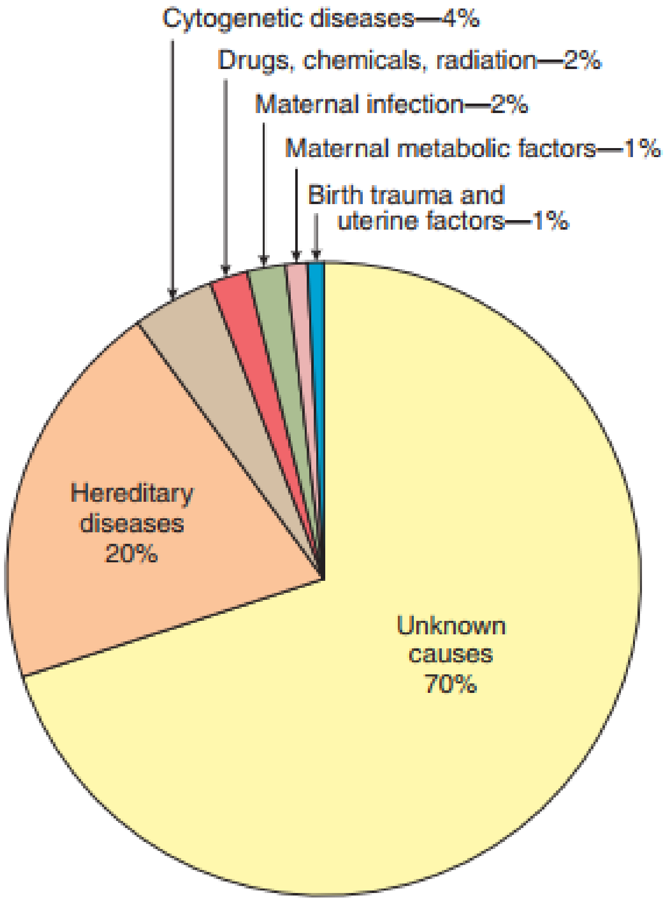

Figure 2-2 Causes of birth defects in humans. Most birth defects have unknown causes(Anthony A. Killeen, 2006)

In Figure 2.3, the period of organogenesis is given in red colour and lasts about six weeks. Later, assaults by teratogens, shown in 'blue colour' mainly occur in the fetal period and are more likely to result in stunting overall of growth or organ(Moore et al., 2015) malfunction. In Table 2.2, the congenital malformation with respect to the time of occurrence is elaborated. The initial two weeks of gestation from the time of conception to the formation of the embryo, though do not seem to be very sensitive to teratogens, can lead to killing of the embryo instead of congenital problems. During this period, the risk of congenital malformations due to chromosomal or genetic mutation is high as this is the period where cell division occurs. This is known as the "all-or-nothing" period, but even during this period some exposures can adversely affect the development of surviving embryos (Rutledge, 1997).

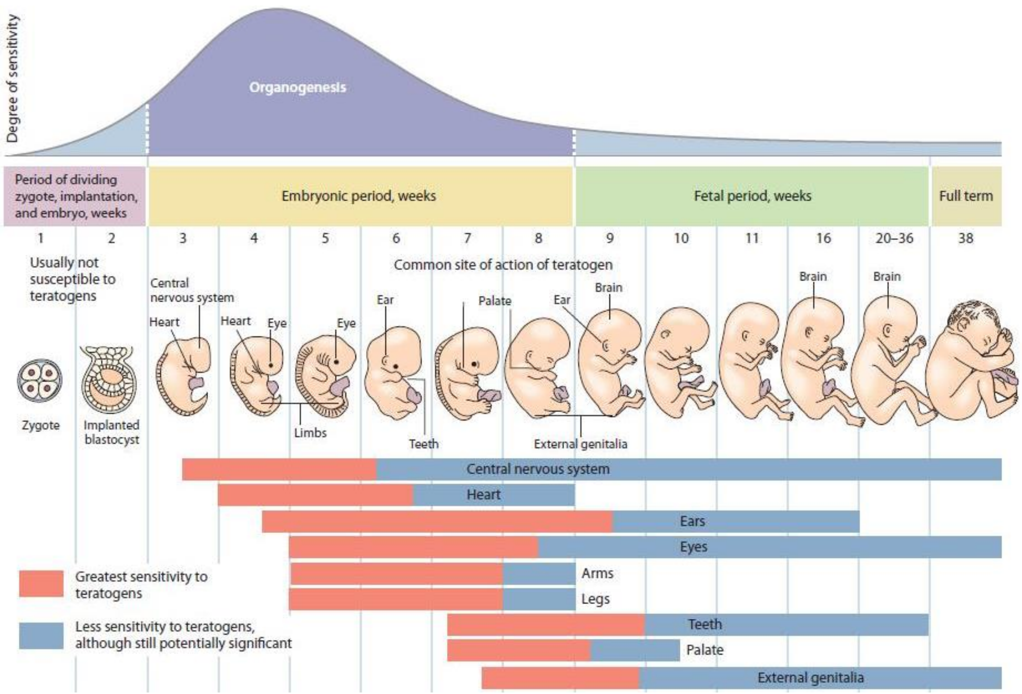

Figure 2-3 Teratogens and the timing of their effects on prenatal development(Moore et al., 2015).

From Figure 2.3 it can also be observed that the effect of the teratogens on prenatal development is variable. Therefore, provided every important development phase is screened using well-known ultrasound markers, corresponding to the development stages, progression of malformations can be prevented by either termination of pregnancy or active intervention methods which can be either an open fetal surgery or minimally invasive intra-uterine surgery (Moore et al.,2015).

Table 2-2 Congenital malformations at the time of occurrence(Moore et al., 2015)

Tissue	Malformation	Defect	Timing of the cause	Additional information
Central Nervous system	Holoprosencephaly	Prechordal mesoderm	23 days	Associated fetal defects
	Anencephaly	Closure of anterior neural tube	26 days	Subsequent degeneration of forebrain
	Meningomyelocele	Closure in portion of posterior neural tube	28 days	80% lumbo sacral
Face	Cleft lip	Closure of the lip	36 days	42% associated with cleft palate
	Branchial sinus or cyst	Resolution of branchial cyst	8 weeks	Preauricular & along line anterior to sternocleidomastoid
	Robin sequence	Early mandibular hypoplasia	9 weeks	U- shaped posterior cleft palate
	Cleft maxillary palate	Fusion of maxillary palatal shelves	10 weeks	Cleft palate
Neck	Oesophageal atresia and tracheoesophageal fistula	Fusion of maxillary palatal shelves	30 days	More common in XO- Turners syndrome
	Posterior nuchal cystic hygroma	Lateral septation of foregut into the trachea and foregut	40 days	
Abdomen	Rectal atresia with fistula	Lateral septation of cloaca into rectum and urogenital sinus	6 weeks	Associated incomplete or aberrant mesenteric attachments
	Diaphragmatic hernia	Closure of pleuroperitoneal canal	6 weeks	May contain gastric or pancreatic tissue
	Ductal atresia	Recanalization of duodenum		
	Malrotation of gut	Rotation of the intestinal loop so that cecum lies to right	7-8 weeks	
	Omphalocele	Return of midgut from yolk sac to abdomen obliteration of vitelline duct	10 weeks	
	Meckel's diverticulum		30 days	
Genitourinary system	Extroversion of bladder	Migration of infra umbilical mesenchyme	30 days	Associated Mullerian and wolfian duct defects
	Urethral obstruction sequence	Usually prostatic urethral valves	9 weeks	More common in males
	Bicornuate uterus	Fusion of lower portion of Mullerian ducts	10 weeks	
	Hypospadias	Fusion of urethral folds (labia minora)	12 weeks	
	Cryptorchidism	Descent of testicle into scrotum	7-9 months	
Heart	O-transportation of great vessels	Directional development of bulbus cordis septum	14 days	
	Ventricular septal defect	Closure of ventricular septum	6 weeks	
	Patent ductus arteriosus	Closure of ductus arteriosus	9-10 months	
Limb	Aplasia of radius	Genesis of radial bone	36 days	Often accompanied by other defects of the radial side of distal limb
	Severe syndactyly	Separation of digital rays	6 weeks	

With the advent of medical ultrasound usage, many of the abnormalities associated with the developmental problems seen in Table 2.2 can be observed within the womb of the mother (Carrera et al., 1995). Hence, regular screening has been commonly advised to monitor fetal growth and development initially between 11 to 14 weeks of gestation (UKNSC and National Institute for Health and Clinical Excellence (NICE) (Press, 2008 Mar) guidelines)and later at 20 weeks of gestation using ultrasound scan and biochemical screening (Dane et al., 2007). Growth is later monitored using serial scans from 24 weeks. However, many abnormalities such as cleft palate, branchial cyst, rectal atresia, gut malrotation, meckel's diverticulum, bicornuate uterus, hypospadias, cryptorchidism and many other such cases cannot be diagnosed. UK FASP programme offers screening for Down's (trisomy 21), Edwards' (trisomy 18) or Patau's (trisomy 13) syndromes; and to offer screening for 11 specific fetal structural anomalies via ultrasound scan between 18+0 to 20+6 weeks (NHS fetal anomaly screening programme (FASP).

The NHS FASP has developed many interactive resources, created to support decision making and informed choice regarding Down's, Edwards' and Patau's syndrome screening and the 18+0 to 20+6 weeks fetal anomaly scan. If such abnormalities are found, the mothers are given an option to abort only when the structural abnormality is serious enough to merit the abortion as defined by the Abortion act (RCOG, 2010 May). When most non-invasive forms of management fail, fetal surgeries are attempted.

2.2 Basis of fetal surgeries and types of procedures attempted

The entire concept of fetal surgeries is based on the ability of the fetal tissue to regenerate and helping the embryological processes when required at the specific period of development (Larson et al., 2010). Table 2.3 shows the indications for fetal surgery and the altered physiology which requires reversal with the help of the surgery. It should be noted that the process of fetal healing is very efficient and is not yet clearly understood. However, there can be a number of ethical considerations for such procedures (Flake, 2001).

Table 2-3 Indications for Fetal surgery (Deprest et al., 2008)

Surgery on the fetus	Rationale for in utero therapy
Congenital diaphragmatic hernia	Reversal of pulmonary hypoplasia and prevention of pulmonary hypertension
Sacrococcygeal teratoma	Cessation of steal phenomenon, reversal of cardiac failure and prevention of polyhydramnios
Thoracic space-occupying lesions	Prevention of pulmonary hypoplasia and/or reversal of cardiac failure
Lower urinary tract obstruction	Prevention of renal failure and pulmonary hypoplasia
Myelomeningocele	Covering of exposed spinal cord, cessation of cerebrospinal fluid leakage to prevent/reverse hydrocephalus and hindbrain herniation
Surgery on the placenta, cord or membranes Complicated monochorionic pregnancies	Arrest of feto-fetal transfusion and its consequences
Twin–twin transfusion syndrome (TTTS)	Preventing preterm delivery
Twin-reversed-arterial-perfusion sequence (TRAP) and other discordant anomalies	Prevention of potential damage to co-twin
Twin-anaemia polycythaemia sequence	In some conditions (TTTS/TRAP) reversal of cardiac failure and Polyhydramnios
Chorioangioma	Prevention/reversal of cardiac failure, hydrops fetoplacentalis and polyhydramnios
Selective intrauterine growth restriction	In some conditions, selective feticide is a goal in itself
Amniotic band syndrome	Prevention of deformities and functional loss
Cardiac malformations	Prevention of hypoplasia or the arrest of progressing damage to developing heart

Pain perception in fetuses is not developed until the end of 25 weeks, and therefore specific administration of anaesthesia to the fetus may not be required but recently fetal stress has been attributed to some fetal surgical procedures and direct analgesic administration in experiments done by Fisk and his group (Fisk et al., 2001), (Deprest et al., 2008).

2.2.1 Types of fetal surgical interventions

There are three types of fetal surgical interventions depending on the complexity of the procedure and the stage of pregnancy (Adzick, 2013). The fetal surgical interventions are: 1. Ex-utero intrapartum treatment(EXIT), 2. Mid-gestation open procedures, 3. Minimally invasive mid-gestation procedures. These procedures require many manipulations and monitoring in both the mother and the unborn fetus, some of which will be described in the later part of this chapter. Table 2.2 describes congenital malformations clinically observed in relation to the time of occurrence.

2.2.1.1 Ex utero intrapartum treatment(EXIT)

EXIT type interventions are performed on vaginal delivery or caesarean section, where only a part of the fetus is delivered (Hirose and Harrison, 2003). The procedures done are usually basic and done while the placenta is still connected, and therefore the procedures are generally short, <10 minutes and involve incubation and examination of fetal abnormalities. However, EXIT procedures can facilitate surgery up to 2.5 hours.(Yaneza et al., 2015)The considerations and outcomes during such procedures are discussed in (Marwan and Crombleholme, 2006) and (Bouchard et al., 2002). In cases such as cystic hygroma, air way securing is important for fetal survival. The procedures described in Table 2.4 are done as EXIT procedures. Short-term maternal outcomes that are associated with the EXIT procedure, as compared with caesarean delivery are discussed in (Noah et al., 2002). These procedures can also have adverse effects as described in (Zamora et al., 2013).

Table 2-4 EXIT procedures performed(Cruz-Martinez et al., 2015)

Anatomical malformation	Procedure
Congenital Diaphragmatic at Hernia	Removal of a tracheal balloon inserted 22–27 weeks with the mid-gestation procedure.
ECMO cannulation for severe pulmonary hypoplasia	Congenital high airway obstruction Syndrome(CHAOS)Perform tracheostomy
Giant cervical neck mass	Resection of mass
Anticipated difficult intubation	Laryngoscopy, bronchoscopy, tracheostomy

2.2.1.2 Mid-gestation open procedures

As mentioned in the previous section, recognition of fetal abnormalities in early fetal life is very important, as it allows intervention in mid-gestation, while reversal is still possible using fetal surgical procedures. Such procedures require a low transverse abdominal incision after ultrasound visualization of the placental position. The incision is widened, and absorbable staplers are used to achieve haemostasis – bloodless Hysterotomy. The fetal part is exteriorised and the surgery is performed and placed back into the uterus.

Post procedural intervention, the fetus grows with the reversal of the disease process. A typical example is meningomyelocele intervention done at 22 weeks, to prevent exposure of fetal neural tissue to amniotic fluid. Some bladder, bowel dysfunction and club feet can be prevented. Some of the indications are given in Table 2.5

Table 2-5 Mid-gestation open surgical procedural indications (Fowler et al., 2002)

Anatomical malformation	Surgical procedure
Meningomyelocele	Surgical repair of meningomyelocele
Sacrococcygeal teratoma	Surgical resection of teratoma
Intrathoracic masses	Resection of mass
Congenital Diaphragmatic Hernia	Temporary tracheal occlusion with intrathoracic liver
Congenital Cystic Adenoid Malformation	Lobectomy, pneumonectomy

2.2.1.3 Minimally invasive mid-gestation procedures

Fetoscopes have given fetal surgeons excellent visualization of fetal and placental structures. With maintenance of uterine distension using fluid irrigation, fetal surgical intervention can be performed over a period of time and can be of two types:

(a) FETENDO procedures- Fetendo is a form of fetal intervention in the treatment of birth defects and other fetal problems. The procedure uses real-time video imagery from fetoscopy and ultrasonography to guide very small surgical instruments into the uterus in order to surgically help the fetus. Examples include - Ablation using LASERS, RFA (Milner et al., 2000) or ligation of aberrant placental vessels to manage twin to twin transfusion syndrome(TTTS), coagulation of the umbilical artery of non-viable twin to prevent Twin Reversed Arterial Perfusion(TRAP), severing the amniotic bands in Amniotic band syndrome(ABS), LASER ablation of posterior urethral valves in Urinary Obstruction Syndrome.

(b) FIGS-IT- Fetal Image Guided Surgery for Intervention or Therapy (FIGS-IT) is a procedure where the fetus is manipulated without an incision in the uterus or an endoscopic view inside the uterus. Ultrasound guidance is used to help real-time fetal manipulation from outside the uterus. This procedure is mostly diagnostic or to guide instruments and surgical planning.

Many of the above procedures can be performed as Minimal Access Surgery(MAS) for fetal surgeries. The procedures are done under epidural or spinal anaesthesia or even under local anaesthesia. These forms of fetal surgery are the least invasive and cause the least discomfort to the mother in terms of hospitalization. In the next section, Minimally Invasive surgeries are compared to MAS, to find the scope for improvements which can be made in fetal surgery assistance.

2.3 Minimally Invasive Surgeries (MIS) & Fetal surgeries

The field of Minimally Invasive Surgeries has come a long way and has branched out into many different areas including but not limited to, general surgery, urology, gynaecology, orthopaedics, neurology, ophthalmology and more recently, in fetal surgery (Deka et al., 2012). While every other form of MIS has been progressing with advancement in technology, the field of fetal surgery has been in its infancy. With progression in technology, certain forms of surgery such as Ophthalmological and spinal procedures in specific, have been consistently reducing the size of the surgery, giving rise to Micro-Invasive Surgeries; fetal surgeries became Minimal Access Surgeries (Danzer et al., 2003). Since this project aims at providing features specific to fetal surgery and can easily be extended for use in other forms of surgeries, it becomes essential to discuss the current state of MIS and the different technologies available to facilitate these forms of surgeries. The discussion of the MIS is done in the following sections:

a) The first section describes the most common difficulties faced in Minimally Invasive Surgeries and how these difficulties get magnified in a Minimal Access Procedures. The section also covers problems specific to Minimal Access Surgeries and some of the available solutions for these problems.
b) In the next section, the current state of different fetal surgeries, the type of procedures performed, their importance, scope and how technology is currently used in such surgeries is elaborated.
c) In the penultimate section, how technology assists MIS procedures and how some of these methods of assistance from technology can be of potential use in Minimal Access Surgeries for fetal procedures as described previously.
d) The last section acquires the most suitable technologies from the previous sections, and these will be developed as a part of the fetal surgery system along with safety measures implemented in the later chapters.

Table 2-6 Differences between Open surgeries, MIS, and Minimal Access Surgeries

Sno	Open surgeries	Minimally invasive surgeries	Micro invasive surgeries and Minimal Access surgeries
1	Procedures are done since		
	Since 3000BC	1929	2000
2	Surgeon's Orientation		
		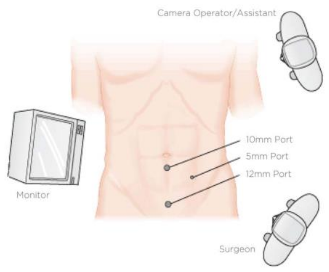	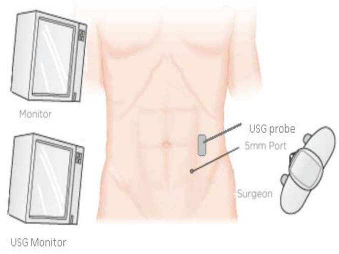
3	Field of View		
	Depends on size of the incision and is usually very wide	Depends on the FOV of the endoscopic camera (about 70 degrees maximum). Frame size is relatively large, and the focal length is about 10 cm	Depends on the FOV of the endoscope (about 40 degrees). FOV of the camera is very small, and the focal length is low (2 cm) reducing the area viewed.
4	Size of incision		
	Up to +/-25cm depending on the procedure	15to 20cm, single port access < 1inch depending on the surgery	Entry via skin piercing and expansion size <3mm
5	The risk of acquiring infection		
			
	Appendectomy 7.90% Colectomy 35.8% Lobectomy 25.4% Hysterectomy 6.64%	3.94% 17.1% 13.8% 4.69%	Yet to be evaluated. Only procedures like fetal surgeries and forms of biopsies have been tried successfully.
6	Complexity of the procedure		
	Procedures are straightforward, and surgeons can be trained relatively easily	Procedures are challenging even to most skilled hands. Requires extensive training	Extremely challenging. Only a few gifted surgeons have been able to do the procedures successfully.

In this section, the background of the Minimally Invasive Surgeries, improvements in technology leading to reduced invasiveness of the surgeries and how they have led to the development of fetal surgeries have been discussed. The overview of certain differences between laparotomy, MIS and MAS are given in Table 2.6.

The challenges faced by the surgeon during the process of such surgeries and the currently available technological solutions, their advantages, and disadvantages are elaborated, and the relevant literature is being reported. Fetal surgery is a form of minimally invasive surgery, where, unlike most other MIS, the procedure is highly restricted in terms of Field of View, dexterity, force perception and orientation, leading to limitations in the number and type of procedures done. Hence such surgeries are referred to as Minimal Access Surgeries (MAS).

Specifications generally considered standard for a MIS system are as follows:

a) Sub millimetre accuracy
b) Line of sight tracking for many orthopaedic procedures and non-line of sight tracking for some ultrasound guided procedures.
c) Tracking frame rate is normally about 60 to 120 FPS in most systems.
d) Tracking volume is normally less than 3 x 3 x 6 m
e) If multiple instruments are used, the distance between the instruments should be larger than the largest distance within the rigid body marker used.
f) Markers cannot be covered by dust or fluids during the procedure in the case of optical tracking and markers cannot be near ferromagnetic substances, in the case of electromagnetic tracking.

2.3.1 Minimal Access fetal surgeries and their importance

Fetal surgeries are performed as a final resort to save the life of a fetus, especially when the postnatal prognosis for the condition is poor. Earlier, some of these procedures were done by open surgery, a form of cesarean section, but fetal mortality and maternal distress are very high (Adzick, 2010), (Zamora et al., 2013). Indications for intrauterine fetal surgery are given in Table 2.7. Though these surgeries are been performed, they may not all have favourable outcomes. For example, in the case of

Lower Urinary Tract Obstruction(LUTO), most recent studies have not shown an improvement in outcomes with intervention(Morris et al., 2013).

Table 2-7 Intrauterine fetal surgery is proven and medically necessary for the following indications (Walsh WF, 2011)

Congenital malformation	Procedure
Congenital cystic adenomatoid malformation (CCAM)	Fetal lobectomy or Thoraco amniotic shunt placement for CCAM and Thoraco amniotic shunt placement for EPS
Extralobar pulmonary sequestration (EPS)	Fetal lobectomy or Thoraco amniotic shunt placement for CCAM and Thoraco amniotic shunt placement for EPS
Sacrococcygeal teratoma (SCT)	SCT resection
Urinary tract obstruction (UTO)	Urinary decompression via vesica amniotic shunt placement
Twin-twin transfusion syndrome	Fetoscopic laser surgery
Twin reversed arterial perfusion (TRAP):	Ablation or occlusion of anastomotic vessels
Myelomeningocele (MMC)	Repair
Congenital diaphragmatic hernia (CDH)	Fetoscopic endoluminal tracheal occlusion (FETO) for severe CDH

2.3.1.1 Role of Fetal surgery in Congenital diaphragmatic hernia and few other fetal conditions

Congenital diaphragmatic hernia is described in more detail in the literature review, as in later chapters demonstration of the surgical procedure is performed with CDH as an example.

2.3.1.1.a Congenital Diaphragmatic hernia treatment using Fetendo

Congenital Diaphragmatic Hernia accounts for 1 in 3,000 live births and challenges the neonatologist and pediatric surgeons in the management of this high-risk condition. Mortality remains high (more than 60%) when the “hidden” mortality of in utero death and termination of pregnancy is considered. Lung hypoplasia and pulmonary hypertension account for most deaths in isolated CDH newborns. Associated anomalies (30–40%) signify a grave prognosis with a survival rate of less than 10%. In the UK, most CDHs are diagnosed at the 20-week anomaly scan with a detection rate approaching 60%, although as early as 11 weeks gestation has been reported. Magnetic resonance imaging (MRI) has a useful role in accurately differentiating CDH from cystic lung lesions and may be useful in measuring fetal lung volumes as a predictor of outcome (Coakley, 2001). Cardiac anomalies (20%), chromosomal anomalies of trisomy 13 and 18 (20%) and urinary, gastrointestinal and neurological (33%) anomalies can coexist with CDH and should be ruled out by offering the patient fetal echocardiogram, amniocentesis, and detailed anomaly scans. Lung to Hear Ratio (LHR) is one of the very important measurements, as it impacts the prognosis. MRI or ultrasound measurements of lung volumes have not been shown to be definitively better. The main benefit of MRI is to determine if liver is in the fetal chest, as it significantly impacts on the prognosis.

Congenital diaphragmatic hernia (CDH) results from abnormal development of the diaphragm, which allows abdominal organs like the bowel, stomach, and liver to protrude into the chest cavity as seen in Figure 2.4. Fetuses diagnosed in utero because of maternal symptoms have a high mortality risk. Methods used for lung lesion management in fetuses has been discussed by Adzick and group. (Adzick et al., 1998). Less invasive fetal procedures are being developed that focus on methods to accomplish tracheal occlusion (Walsh et al., 2011), (Harrison et al., 2001). Different sonographic predictors have been suggested by Metkus and his group (Metkus et al., 1996).

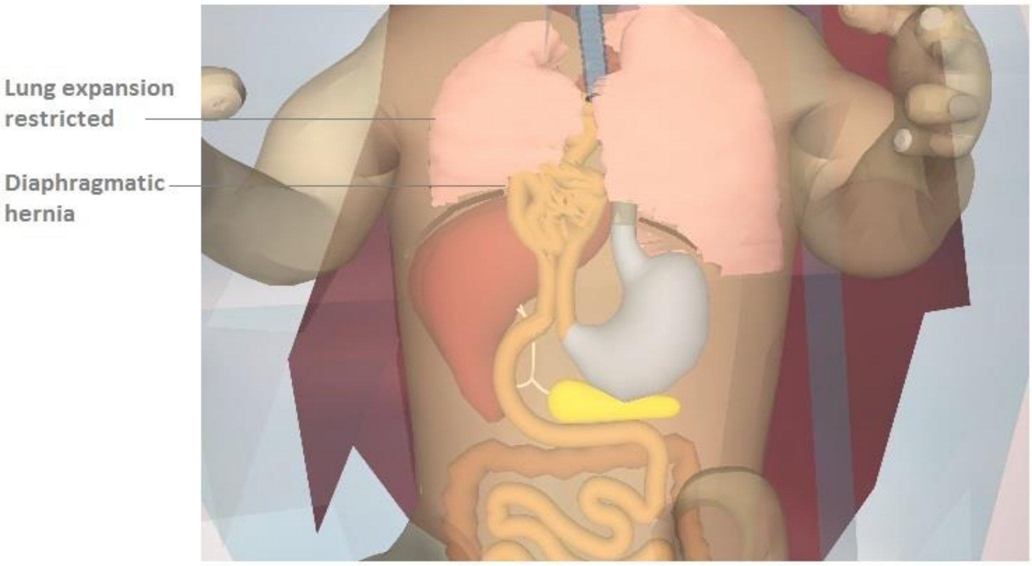

Figure 2-4 Fetus with Congenital diaphragmatic hernia with abdominal contents herniating into the thoracic cavity(Yao et al., 2014)

In Figure 2.5, it can be observed that when the lungs are in a canalicular phase of development, where they still produce fluid, therefore occlusion of trachea will result in back pressure leading to the expansion of the lungs. The procedure is done in about 24 weeks of gestation under ultrasound guidance. Figure 2.6 gives a graphic representation of usage of fetendo for tracheal occlusion using a fetendo. After the inflation, the balloon stays inside, increasing the pressure within the lung tissue, thereby expanding and maturing it as seen in Figure 2.7 and Figure 2.8.

The balloon is removed by Ex-utero intrapartum treatment (EXIT) procedure, as mentioned earlier. However, the success of the procedure entirely depends on whether the fetus has additional malformations. In these CDH patients, early detection, liver in the chest, polyhydramnios and the fetal lung-head ratio (LHR) of less than 1 are implicated as poor predictors of outcome. In these patients with poor prognostic signs, fetal surgery for CDH over the last 2 decades has been disappointing; however, benefit from fetal intervention with tracheal occlusion (FETO) awaits more randomized studies. A favourable outcome in CDH with the use of antenatal steroids has not been resolved in the clinical settings (Lally et al., 2006). Elective delivery at a specialized centre is recommended where there can be no benefit from a caesarean section (Wilson et al., 2003).

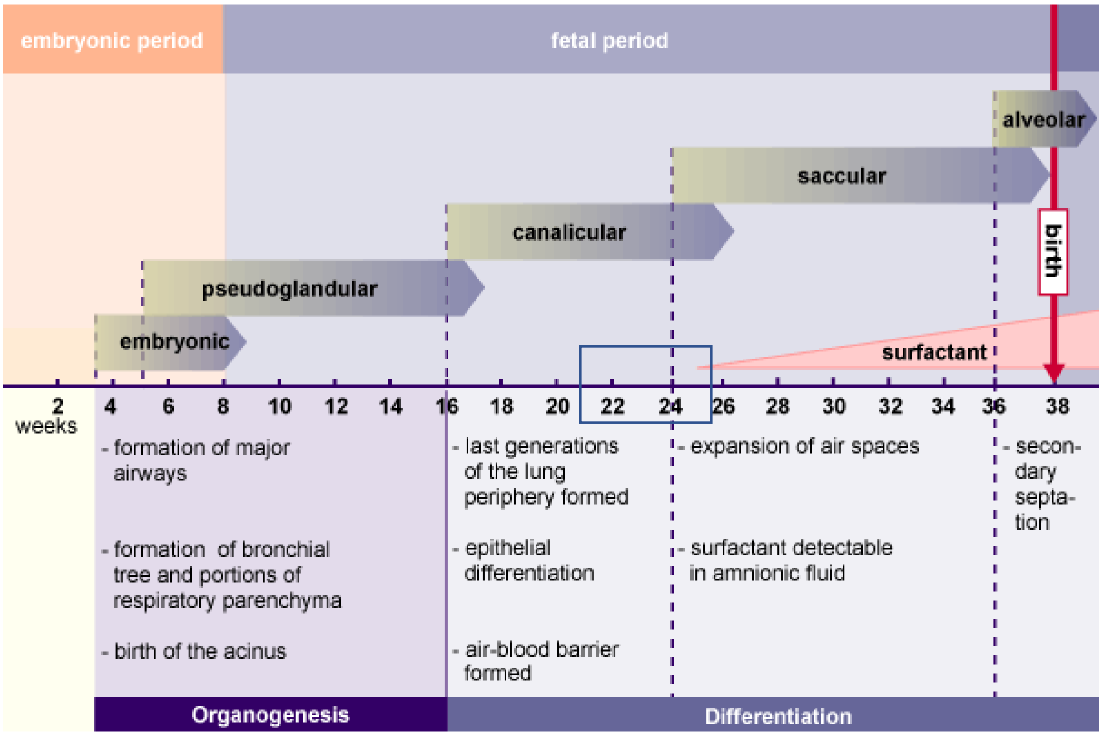

Figure 2-5 Phases of intrauterine development. 20 to 26 weeks is the most important time for fetal surgery (Moore et al., 2015)

The technique of tracheal balloon inflation is shown in Figure 2.6, and it can have the following effects:

- is being carried out as an outpatient procedure and can result in severe injury and discomfort to fetal tissues.
- requires a series of manipulations by experienced hands and extensive sense of orientation and positioning under USG.

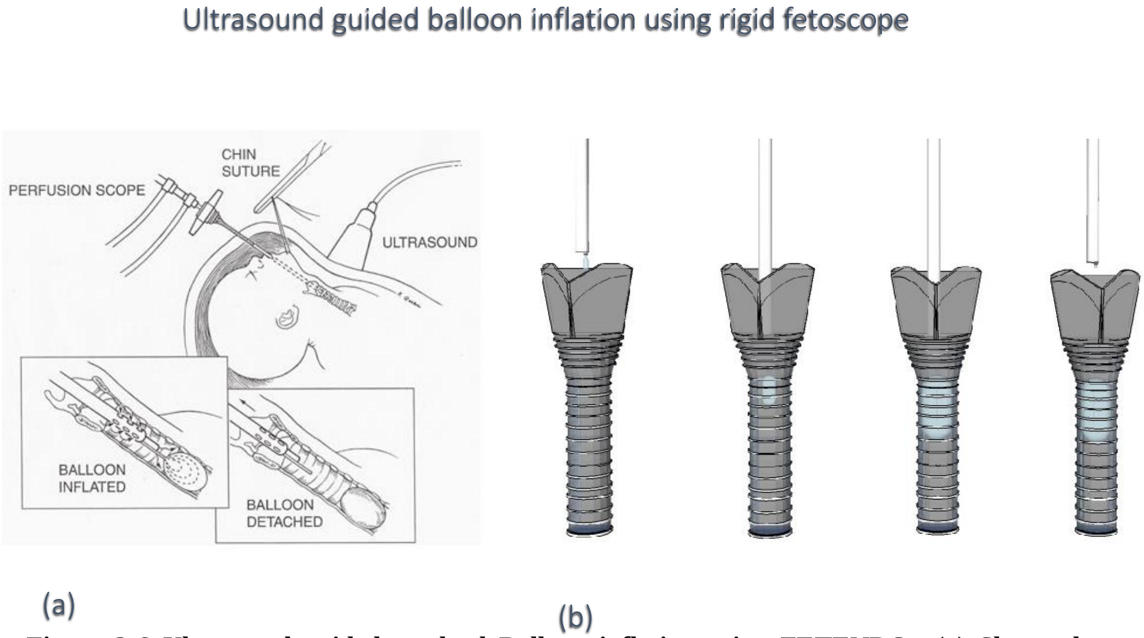

Figure 2-6 Ultrasound guided tracheal Balloon inflation using FETENDO (a) Shows the technique of tracheal balloon inflation (b) Shows the different stages of tracheal insertion and balloon detachment (Yao et al., 2014)

There is insufficient evidence that in utero correction of CDH improves health outcomes for fetuses with CDH compared with standard postnatal surgery. Consistent improvements in survival following in utero fetal surgery have not been observed. A systematic review and meta-analysis by Grivell (Grivell et al., 2015) compared the effects of prenatal versus postnatal interventions for CDH on perinatal mortality and morbidity, longer-term infant outcomes and maternal morbidity. The review also includes comparison of the effects of different prenatal interventions with each other. Three studies were included involving 97 women. Two trials examined in-utero fetal tracheal occlusion with standard (postnatal) care in fetuses with a severe diaphragmatic hernia. The results from Grivell et al. showed insufficient evidence to recommend in-utero intervention for fetuses as a part of routine clinical practice.

In Figure 2.7 (a) and (b), the process of tracheal blockage resulting in the increased pulmonary pressure is illustrated. This pressure then leads to expansion of the lungs, growth and maturity as seen in Figure 2.8, after which the balloon can be removed physically. The outcomes of CDH procedures are discussed in (Langham et al., 1996) and (Harrison et al., 2003). The randomized trials conducted by Harrison and his group have not suggested any significant difference in terms of fetal mortality or morbidity in fetuses having a lung to head ratio of less than 0.9.

LHR and gestational age offer significant prediction of survival. Fetuses with left CDH treated with FETO had an increased survival rate from 24.1% to 49.1% and in the right, the CDH survival rate increased from 0 to 35.3%. FETO in severe CDH has a high association with PROM (Jani et al., 2009).

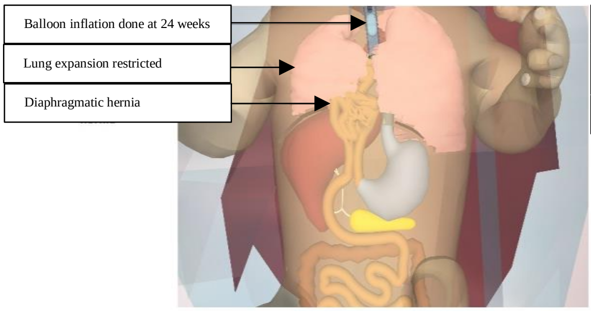

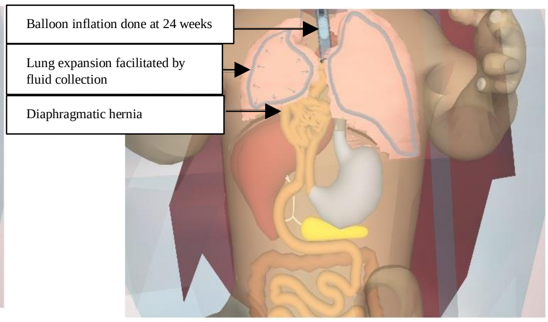

Figure 2-7 Tracheal balloon inflation – principle (a) Block created in the trachea leads to the fluid build-up inside the lungs, causing an increase in pressure shown in(b)(Yao et al., 2014)

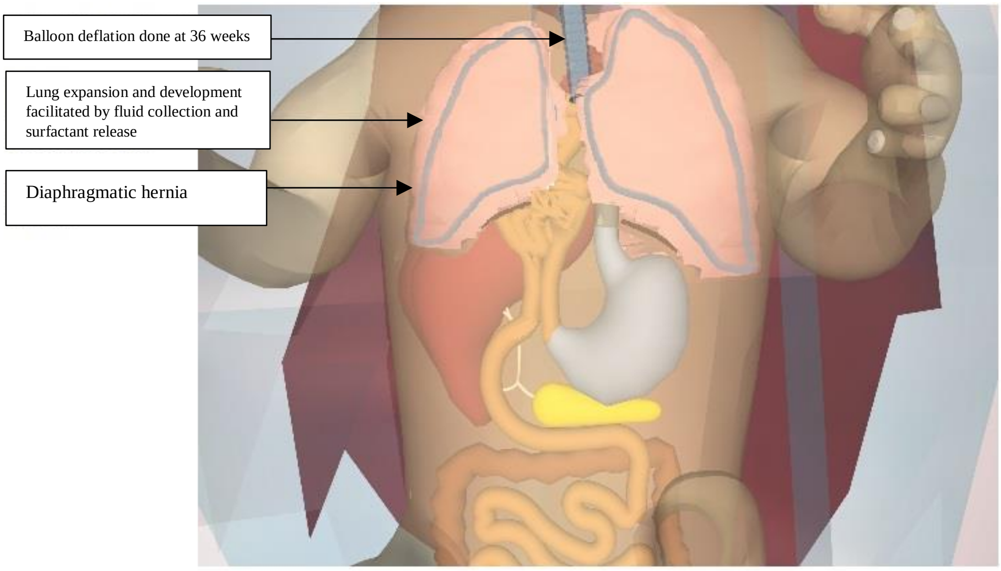

Figure 2-8 Block created in the trachea leads to the fluid build-up inside the lungs, causing an increase in pressure, which expands the lungs.(Yao et al., 2014)

Ruano and his team (Ruano et al., 2012) conducted an RCT to determine whether fetal endoscopic tracheal occlusion (FETO) improved survival in cases of congenital diaphragmatic hernia (CDH). Patients whose fetuses had severely isolated CDH (lung-to-head ratio < 1.0, liver herniation into the thoracic cavity and no other detectable anomalies) (Straňák et al., 2017) 20 patients were randomly assigned to FETO and 21 to standard postnatal management. Ruano's team conducted tracheal balloon placement with ultrasound guidance and fetoscopy between 26 and 30 weeks of gestation. Though postnatal therapy was the same for both treated fetuses and controls, the primary outcome was survival to 6 months of age. Delivery occurred at 35.6 ± 2.4 weeks in the FETO group and at 37.4 ± 1.9 weeks in the control group. In the intention-to-treat analysis, 10/20 (50.0%) infants in the FETO group survived, while 1/21 (4.8%) controls survived. In the received-treatment analysis, 10/19 (52.6%) infants in the FETO group and 1/19 (5.3%) controls survived. The authors concluded that FETO improved infant survival in isolated severe CDH; however, the risk of prematurity and preterm premature rupture of membranes was high.(Ruano et al., 2011) treated 16 fetuses with a severe congenital diaphragmatic hernia (CDH) with fetal endoscopic tracheal occlusion (FETO) and compared their outcome to 18 similar cases treated with standard neonatal therapy. The primary outcome was neonatal survival (up to 28 days after birth). Survival in the FETO group was 53% compared to 6% in the standard therapy group. This study is limited by small sample size and lack of randomization.

2.3.1.2 Meningomyelocele:

Myelomeningocele (MMC) is a type of neural tube defect in which the spinal cord forms but remains open. Although MMC is rarely fatal, individuals affected by it have a range of disabilities, including paraplegia, hydrocephalus, skeletal deformities, bowel and bladder incontinence and cognitive impairment. Standard therapy is the postnatal surgical closure of the MMC followed by shunting for hydrocephalus if needed (Belfort et al., 2015). The procedure using endoscopic methods have been described in Pedreira et.al. , 2016 (Pedreira et al., 2016).The effectiveness of MMC management using fetal surgery and the clinical outcomes needed to achieve is discussed by Cochrane, Irwin et al. (Cochrane et al., 2001). Consecutive MRI imaging has shown reduction of hindbrain herniation and the findings have been in favour of fetal surgery for MMC management (Sutton et al., 1999), (Meuli et al., 1996). It was proven in a study by Bruner et al. that intrauterine repair of MMC resulted in lower incidence of hind brain herniation and shunt dependant hydrocephalus in infants with spina bifida, but increases the incidence of premature rupture of membranes which can be as high as 46% (Bruner et al., 1999). Johnson and his team followed neurodevelopmental outcomes of these procedures up to 30 months and confirmed the improved outcomes (Johnson et al., 2006). MOM trial showed that these procedures decreased the risk of death or need for shunting by the age of 12 months and also improved scores on a composite measure of mental and motor function, with adjustment for lesion level, at 30 months of age. Though there can be considerable improvements, these do not imply cure.

2.3.1.3 Congenital cystic adenomatoid Malformation CCAM:

Thoracic Lesions Congenital cystic adenomatoid malformation (CCAM) and bronchopulmonary sequestration (BPS) are congenital anomalies of the lung. Appropriate candidates for in utero treatment include a small subset of patients with congenital pulmonary airway malformations. In this subset, the fetal mediastinum is compressed, leading to impaired venous return with resulting fetal hydrops, secondary to cardiac failure (Walsh et al., 2011).

2.3.1.4 Sacrococcygeal Teratoma (SCT):

Sacrococcygeal Teratoma Fetuses with large, vascular sacrococcygeal teratomas (SCT) have a high incidence of prenatal mortality from high output cardiac failure or spontaneous haemorrhage of a growing tumour. Fetal surgical procedures for SCT have focused on the small subgroup of fetuses with SCT and hydrops because untreated cases are expected to die in utero or at birth. In severe cases, SCT with hydrops is associated with a maternal risk of developing Mirror syndrome, a severe form of preeclampsia (Walsh et al., 2011). The use of Radio Frequency Ablation has been described by Paek, Jennings and team (Paek et al., 2001). Hedrick and his team conducted Prenatal diagnostic studies including ultrasound scan, magnetic resonance imaging (MRI), echocardiography and pre- and postnatal outcomes were reviewed in 30 cases of SCT that presented between September 1995 and January 2003. In the above stated study, the mean gestational age (GA) at presentation was 23.9 weeks (range, 19 to 38.5) with 3 sets of twins (10%). Overall outcomes included 4 terminations, 5 fetal demises, 7 neonatal deaths, and 14 survivors (Hedrick et al., 2004).

2.3.1.5 Urinary Tract Obstruction:

Fetal urinary tract obstruction (UTO) interferes with normal development of the kidneys and lungs, particularly when involving the lower urinary tract (LUTO). Goals of fetal surgery have emphasized decompression procedures, such as percutaneous shunting, rather than repair of the specific lesion (Walsh and Johnson, 1999). The goal of decompression of the distended portion of the urinary tract is to protect the function of the remaining kidney and to promote lung development (Walsh et al., 2011). The results of the PLUTO randomised controlled trial are consistent with the findings of the observational evidence for perinatal survival, but the chance of newborn babies surviving with normal renal function is very low irrespective of whether or not vesico-amniotic shunting was done. (Morris et al., 2013).

2.3.1.6 Twin-Twin Transfusion Syndrome (TTTS):

In twin-twin transfusion syndrome (TTTS), twins share a single chorionic membrane and a single placenta but have separate amniotic sacs. Women with severe TTTS, who have not undergone treatment before 26 weeks, will usually experience loss of both fetuses. However, if both twins survive, they often experience severe neurologic compromise and organ failure. Treatment options include amnioreduction to relieve pressure and uterine size, termination of the sicker twin, or fetoscopic laser ablation of the communicating vessels (Senat et al., 2004). In non-selective ablation, all vessels crossing the dividing membrane are ablated, whereas selective ablation is limited to certain vessels connecting the two fetuses (Walsh et al., 2011). Apart from the fetal aspect of the surgery, these procedures can have an impact on maternal health (Mari et al., 2001).

In a study conducted by Ierullo and team, a total of 77 women underwent the procedure. The mean gestational age at treatment was 20 (range 16-26) weeks. On average, four vessels were ablated during each procedure, with a mean operative time of 15 (range 5-25) minutes. None of the women required a repeat fetoscopic laser treatment for recurrence of the TTTS. There was at least one survivor in 74% (57/77) of pregnancies, and the overall survival rate was 57% (88/154) (Ierullo et al., 2007).

2.3.1.7 Twin Reversed Arterial Perfusion (TRAP):

Twin reversed arterial perfusion (TRAP) sequence is a condition in which an acardiac/acephalic twin receives all of its blood supply from a normal twin, the so-called "pump" twin. Blood enters the acardiac twin through a retrograde flow via the umbilical artery and exits via the umbilical vein. The extra work places an increased demand on the heart of the pump twin, resulting in cardiac failure. Twin death occurs more frequently when the size of the acardiac twin is greater than half that of the pump twin (Peiró et al., 2009). The goal of fetal surgery is to interrupt blood supply to the nonviable twin. The outcome is worse if the birth weight ratio of the pump twin to the acardiac twin is > 70% (Oliver et al., 2013).

2.3.1.8 Congenital Heart Disease (CHD):

In-utero procedures are performed for cardiac conditions such as pulmonary atresia with intact ventricular septum, critical aortic stenosis with impending hypoplastic left heart syndrome, and hypoplastic left heart syndrome with an intact atrial septum. All of these conditions, if untreated either in-utero or soon after birth, are fatal (Kohl et al., 2006b), (Walsh et al., 2011). Kohl and his team have been working on percutaneous fetoscopic surgical techniques for upcoming minimally invasive fetal cardiac interventions. The extent of these procedures greatly depends on the kind of instrument available and solving the common MAS problems.

A common risk for all the intrauterine procedures apart from problems to the fetus itself is maternal morbidity after these procedures. Minimal Access Surgeries have resulted in a considerable reduction in maternal morbidity when compared to the open surgical procedures (Golombeck et al., 2006).

2.3.2 Overall state of Fetal surgery and how technology plays a role

Fetal surgeries started taking shape when the surgeons were given a peek inside the uterus using micro optics. Therefore, in other words, the revolution in imaging has lead to fetal surgery, just like it has enabled Minimally Invasive surgeries. Deprest and his team have for long been involved in fetal surgery research and in every publication of theirs' have mentioned the use of technology and that they have had limitations which had to be overcome with extensive clinical expertise (Deprest et al., 2006).

Further advancement in technology for clinical assistance is expected to help fetal surgeons perform more challenging and extensive surgeries with lesser challenges.

2.4 Difficulties faced in MIS and how they affect fetal surgery

When compared to the open surgeries, MIS is much more challenging and require extensive practice and training. Even simple processes such as grasping, suturing and cauterisation can be daunting. Also, the smaller the surgical instrument is, the harder the manipulation and positioning become. Fetal surgeries from this perspective raise the bar for the challenge. In this section, how difficulties in MIS can become even more challenging in terms of MAS for use in fetal surgery is being discussed.

2.4.1 Imaging in MIS

Minimally invasive surgeons greatly benefit from optical imaging but are heavily limited by the field of view, and there is a requirement for high clarity optics and illumination. The illumination is often used Xenon light source with infrared filters to avoid overheating of the optics or light emitting diodes directly on the tip of the respective endoscope. Until the advent of Charge Coupled Device CCD, fibre optic patch cables had been used for image transmission and hence the resolution of the image heavily depended on the number of fibres in the optic fibre patch cable and the quality of the coupling. Also, the output of the camera was analog, and the screens operated with analog reception as well. Recently, with the introduction of CCD modules, the cameras are placed at the tip, and the lenses mounted on top of the stem of the endoscope are usually replaceable with varying angle of view, the field of view and anti-fogging capabilities. Multi-camera versions, such as the one shown in Figure 2.9 have also been used more recently for better visualization but come at the cost of increased diameters and limited field of view.

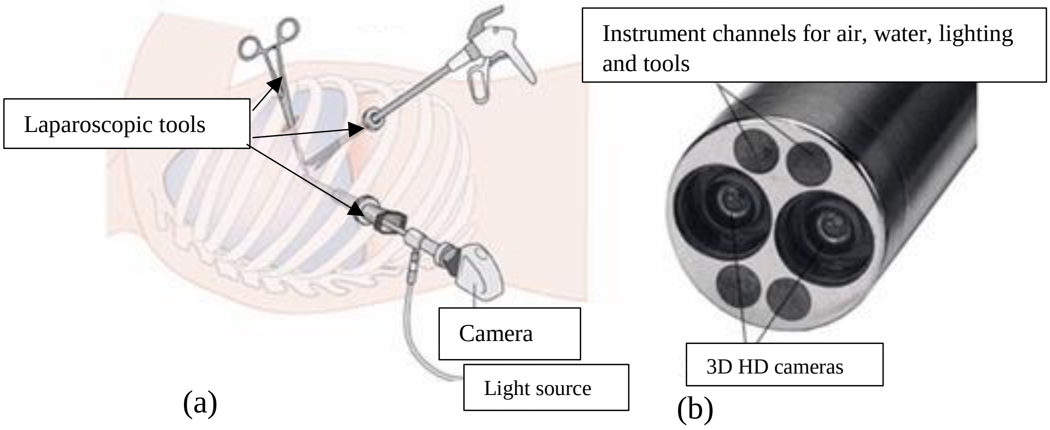

Figure 2-9 Laparoscopic camera and tools (a) Diagram showing a setup for video-assisted laparoscopy. (b) Dual camera laparoscope. The surgeon holds the tools, while the camera is usually held by an assistant. The instruments are inserted into the body via a trocar—a hollow tube which pierces the abdomen and provides a point of access to the target. The abdominal cavity is filled with gas (usually CO2) to create more space to operate. Picture by Cancer Research UK (Wikimedia Commons) distributed under a CC-BY-SA 4.0 license. Right: a flexible endoscope, which can be equipped with three-dimensional high-definition cameras, light guides, instrument channels as well as pipes for water and air. 2016 Intuitive Surgical.

2.4.2 Imaging in fetal surgery

Imaging in fetal surgery can basically be classified into non-invasive and invasive methods. The non-invasive methods are used for surgical planning, to place the incision and see the anatomical orientation, while the invasive methods usually provide a visual port into the scene, post-incision.

2.4.2.1 Non-invasive imaging:

Diagnostic modalities such as CT, X-Ray, PET and most others which are based on high energy radiations are considered unsafe for use in pregnant women, as these can result in fetal abnormalities (Sreetharan et al., 2017). MRI has been approved for use in pregnant women, but its effects on embryology are yet to be clearly understood (Bekiesińska-Figatowska et al., 2017) and therefore is avoided unless is an absolute requirement, mostly to replace having to take a CT scan. Therefore, the only proven and safest known noninvasive imaging modality which can be used with the least effects on fetal development has been a medical ultrasound (Bekiesińska-

Figatowska et al., 2017). While Ultrasound provides cross-sectional images, the resolution of the images is restricted by the frequency of the ultrasound, the type of material, transmission, reflection, refraction and dispersion characteristics of the medium these will be discussed in further detail in the Ultrasound fundamentals section.

2.4.2.2 Invasive imaging

With the advent of miniaturization of CCD cameras and optics, video fetoscopy has become possible (Curtiss, 1976). This has given the fetal surgeons a port for visualizing the state of the fetus inside the uterus (Macdonald et al., 2005). Figure 2.10 is a photograph of a typical fetoscope with balloon and camera optics at the tip of the fetoscope.

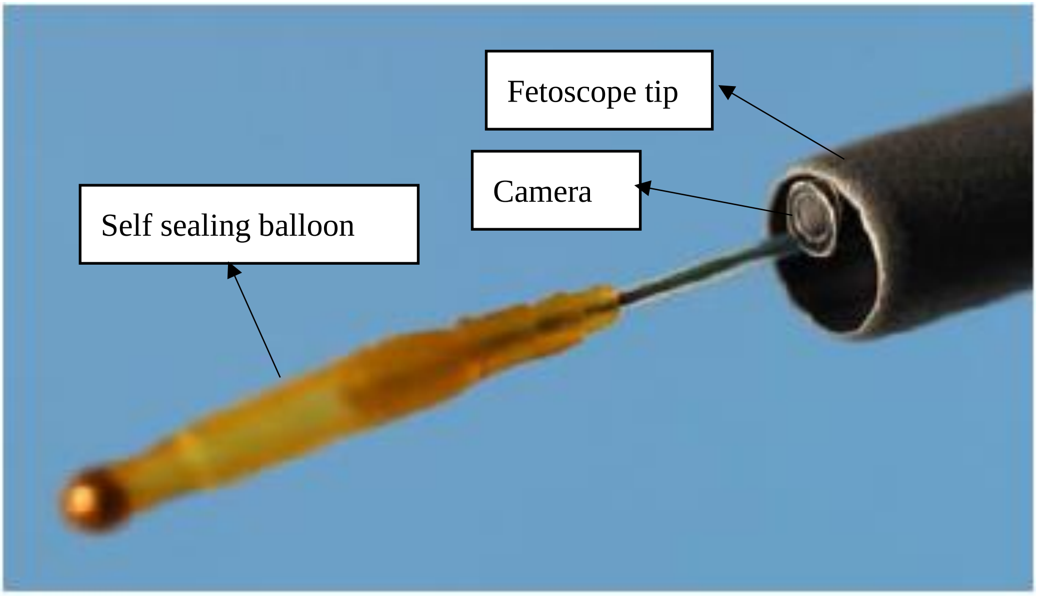

Figure 2-10 Shows fetoscope camera (Deprest et al., 2011)

The optics used in Minimal Access Fetal Surgeries have a limited field of view because of the size of the optics and suffer from problems due to reduced focal length as well. Camera fetoscope and hysteroscopy are few of the most recent innovations in the area of fetal surgical equipment. The camera output as seen on the display screen by the surgeons is 2D, and hence the perception of depth is highly limited. The surgeon usually estimates the depth by moving the tools are reaching for the specific anatomy (Fuchs and Livingston, 2006).

2.4.3 Coordination in MIS vs MAS for fetal procedures

Acquiring skills for MIS is much more difficult when compared to open surgical procedures in general. MIS is entirely dependent on spatial positioning and orientation capabilities of the surgeon. Direct, a line of sight visualization, in the case of open surgeries is replaced by 2D displays in the case of laparoscopic surgery. Direct access, as in open surgery is replaced by a minimal access due to the miniature incision. Hence Minimally Invasive Surgery also becomes a minimal access surgery. Complicated visuospatial perception of the surgeon is an absolute necessity. In Figure 2.11, a typical method of hand to screen coordination.

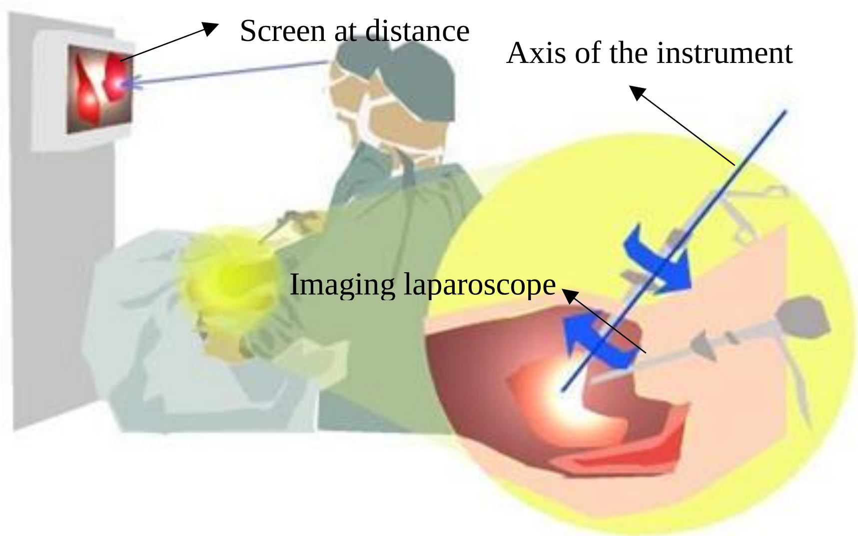

Figure 2-11 Surgeon's method of hand to screen coordination in laparoscopic surgery

Apart from the orientation skills and surgeon's understanding of anatomy, the surgery also suffers from the fulcrum effect and force transmission. Perceptual-motor skills, also known as psychomotor skills, include the following main elements, as illustrated in Table 2.8 (Magill, 1998)

Table 2-8 Common terms for psychomotor skills with relevance to surgery

Psychomotor Skills	Description
Multi-limb coordination	Coordinate the movements of limbs simultaneously
Control precision	Make highly controlled and precise muscular adjustments
Response orientation	Select rapidly where a response should be made
Reaction time	Respond rapidly to a stimulus when it appears
Speed of arm movement	Make a gross rapid arm movement
Rate control	Change speed and direction of responses with precise timing
Manual dexterity	Make skilful, well-directed arm-hand movements that are involved in manipulating objects under speed conditions
Finger dexterity	Perform skilful, controlled manipulations of tiny objects involving primarily the fingers
Arm-hand steadiness	Make precise arm-hand positioning movements where strength and speed are minimally involved
Wrist and finger speed	Move the wrist and fingers rapidly
Aiming	Aim precisely at a small object in space
Visual acuity	See clearly and precisely
Visual tracking	Follow a moving object visually hands
Hand-eye coordination	Perform skills requiring vision and the precise use of the hands

In fetal surgery, however, there is a requirement of multi perspective viewing - hand to eye to ultrasound - eye - hand and Video – eye – hand. After which there is a process of assimilation of images into surgeon’s anatomical orientation, making the process more difficult.

2.4.3.1 Difficulties in Perception and orientation of anatomy

Laparoscopic surgery (LS) has become the standard in many abdominal procedures such as cholecystectomy and splenectomy, and other forms of MIS have been introduced in orthopaedics, cardiology, urology etc. However, LS imposes severe limitations in visual and haptic perceptions, and create challenges unique to this type of surgery: reduced depth perception of the operative field caused by the use of 2D monitors; poor hand-eye coordination as a result of the location of the monitor, variable amplification, mirrored movement, and misorientation; motion limitations due to tracer-induced invariant points and reduced haptic feedback from the use of long and slender surgical instruments.

Orientation in 3D space can be very difficult in MIS procedures even to the most trained eyes. In a simulated laparoscopic cholecystectomy environment, 22% of spatial orientation errors have been estimated by well-trained surgeons (Sodergren et al., 2010). While this is the case with MIS, these problems become enhanced with thinner instruments with lower field of view and very minimal perception of forces, especially in a fragile tissue environment, as in the case of MAS for fetal surgery.

2.4.4 Difficulties in force transmission and force perception

In laparoscopic surgery, the surgeon receives limited haptic feedback and relies on visual feedback to judge the amount of force applied to the tissues. It has been shown that friction forces inherent in the instrumentation increased the haptic perception threshold of naïve subjects. One of the major concerns with laparoscopic surgery is potential for tissue damage, possibly caused by inappropriate use of force, as observed by Lamata. Providing force feedback, either direct or augmented by visual/audio means, has the potential to improve laparoscopic surgical performance by reducing the peak force used during LS, and in turn, reduce intra-operative injury to patients. (Lamata et al., 2008)

A controlled experiment was conducted by Tholey and his group to examine the effects of experience on the force perception threshold in a simulated tissue-probing task. Fourteen subjects participated in a mixed design experiment, with friction, vision, and tissue softness as independent within-subject factors, experience as an independent between-subjects factor, and applied force and the detection time as dependent measures. Higher thresholds and longer detection times were observed when friction was present. Experienced surgeons applied a greater force than novices, but were quicker to detect contact with tissue, suggesting that experience allowed surgeons to perform more efficiently while keeping within the limits of safety. (Tholey et al., 2005)

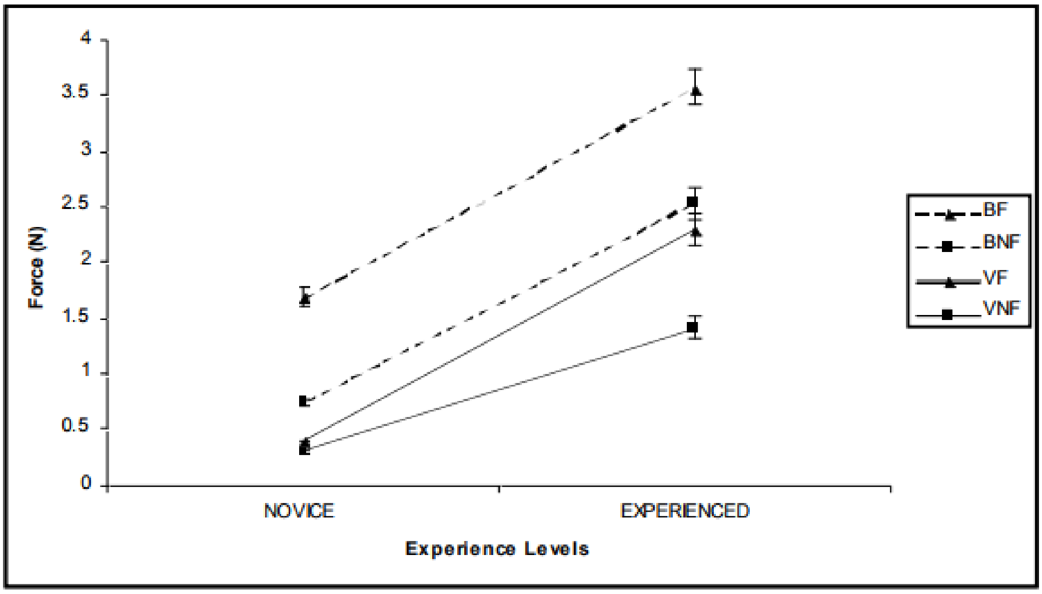

Figure 2-12 Applied force of novice and experienced participants under different Vision and Friction conditions. Error bars showed the standard error. (Zhou, 2007). BF – Blind friction, BNF – Blind no friction, VF – Vision friction, VNF – Vision no friction

Most surgical tools are made of carbon steel or surgical quality steel, which are very hard when compared to the soft structures. Such soft structures can be injured because of such surgical tools. The surgeon is expected to refine his skills to avoid injuring the soft structures, especially which handling the intestines and similar soft structures as in the case of fetal surgery. Shifts in force perception of different people with experience have been studied and have been proven to occur with a significant margin of difference (Zhou, 2007).

Zhou and his team conducted experiments regarding force perception differences. The variations include estimation of friction perception when the surgeons were unaware of where the resulting force is applied, when the surgeons knew where the force was applied using the instrument. From Zhou's experiments, it has been found that paired sample t-tests of the vision and friction conditions across experience levels showed a significant difference between each of the four pairs of means that were considered - extreme conditions:

(a) blind-friction (BF) and vision-no friction (VNF), $t(419) = 21.3$, $p<.001$

(b) BF and blind no friction(BNF), $t(419) = 14.4$, $p<.001$

(c) vision-friction(VF) and vision – no friction VNF, $t(419) = 7.1$, $p<.001$

(d) VF, $t(419) = 4.9$, $p<0.001$

Paired-sample t-tests showed a significant difference between novice and experienced surgeons in each of the Vision × Friction conditions. Figure 2.12 shows the experimental results from Zhou's experiments which indicate a significant difference in perception of forces with the experience of the surgeons. This can be important, as though force-based haptics result in reflection of end effector forces at the operating handle, they may be perceived differently. From Figure 2.12, it can be observed that the perception of forces in experienced surgeons is much higher mostly because of the fact that training increases sensitivity to the force stimulus. In such cases, vibrational haptics has an advantage, as they provide a better sense of perception. Something which should be noted from Figure 2.12 is the fact that even with very high experience levels, forces below 0.5 Newtons do not make any difference to the perception of surgeons. In the cases of procedures such as fetal surgeries, the forces applied can be lower than in conventional surgeries.

2.4.5 Surgical tools and features in MIS and fetal surgery

Surgical tool development within the constraints of MIS is always a challenge to develop. Several open surgery instruments have been developed into instruments for minimally invasive surgeries. Several companies such as Medtronic, Dublin, Ireland, do specialized products such as Endo-Stich. Graspers are manufactured by a number of companies like Metroid Healthcare, Taiwan. Needle drivers LiV instruments, California USA. More recently staplers, for example, MicroCutter - XCHANGE, New York has replaced sutures in certain cases such as gastrotomy closure and prevent anastomoses.

Hemostasis can be either achieved by suturing, electrocauterization, suture knots, are regularly used, whereas radiofrequency ablation, ultrasonic coagulation and LASERS are used either rarely or in very specific applications like prostatectomy. Whereas in the case of MAS for fetal surgery, LASERS, and RFA are commonly used, and electrocautery has been used with care, Suturing is still under research. Stenting, ballooning, needle insertion, drainage and ablation are the methods consistently used in fetal surgeries.

2.4.6 Challenges specific to Fetal MAS and available solutions

There are certain difficulties and risks specifically associated with fetal surgeries, which are not a concern in other forms of Minimally Invasive surgeries. Table 2.9 describes some of the main problems which already have solutions for use with fetal surgeries.

Table 2-9 Obstacles to be overcome for successful minimal access fetal surgery (Danzer et al., 2003)

S.No	Problem	Solution
1	Poor visualization in turbid amniotic fluid	Pump-driven fluid exchanger replaces amniotic fluid with saline during operation
2	Tenting and separation of chorioamnionitis membranes with trocar insertion	Specifically, designed diamond tipped needle that precisely cuts through membranes on the entry
3	Fetal hypothermia with fluid exchange	Exchanged fluid kept at physiologic temperature
4	Lack of fetal monitoring	Ultrasonographic monitoring
5	Lack of fetal analgesia	Intramuscular fetal needle punctures with an analgesic
6	Anterior placental location	Elevation of uterus for anterior placenta with fundic or posterior uterine entry
7	Mobile fetus	Fetal suture fixation techniques, ultrasound-directed trocar entry when fetal position is known
8	Uterine wall compliance	Effective tocolysis
9	Cramped intraamniotic operating space	Modify operative techniques and accessories to design single-port procedures, ultrasound guidance of operating instruments
10	Uterine bleeding during trocar insertion	Radially expanding access devices outwardly compress uterine vessels and secure trocar in place

2.5 Solutions available to problems in MIS

Technological assistance has provided solutions to many major problems faced during the process of a MIS. In this section, some of these problems are discussed.

2.5.1 Problems in guidance - Navigation in Surgery

Navigation, in general, is the process or activity of accurately ascertaining one's position and planning and following a route. In Surgery, navigation is the process of helping direct a surgeon with respect to the surgical environment. Navigation in surgery was first discovered in 1986 by an American doctor, Roberts in the year 1986 and has undergone rapid development and the process of surgical navigation using technology has been adopted in several areas since then since then (Solberg et al., 2007). Surgical navigation can either be image guided or guided by tracking guided virtual reality-based navigation. For achieving VR-based surgical navigation within a surgical environment, the surgeon either has access to the CT or MRI images which have been taken earlier and registered on the table, forming a reference for the image processing algorithms used for orientation. However, for procedures such as fetal surgeries, fetuses are mostly independent and moving, therefore, require an acquisition of real-time data from a modality such as ultrasound, which is assimilated by the surgeon for surgical planning and has been done by manual intraoperative navigation (Yao et al., 2014).

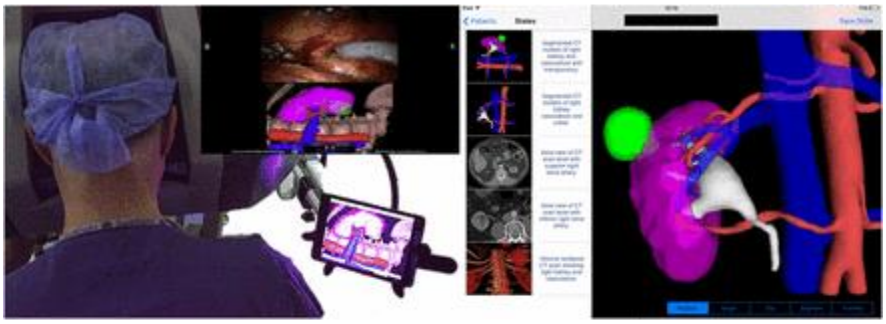

Figure 2-13 A navigation setup based on augmented reality, in use with a DA Vinci SP console. Left: the real scene is augmented with virtual images showing a reconstruction of the target's anatomy. The same scene, or a different one, can be seen on a tablet positioned next to the console. Image adapted with permission from Hughes-Hallett et al. 2014 Elsevier. Right: Examples of navigation images available on the tablet. The surgeon can choose to view the raw scans (such as MRI or CT), or the three-dimensional reconstructions. Registration software makes sure that the position of the tools relative to the anatomy is always known. Image courtesy of Philip Pratt, Imperial College London.

An example of navigation interface using augmented reality for use in surgery can be seen in Figure 2.13. One of the main reasons why most real-time procedures have less navigation guidance is because of time required for registration and pre-processing. (Zheng and Nolte, 2015). Statistical evidence suggests that there is an improvement in resection rate of 86.7% and reduction in complications by 12.1% and mortality by 0.8% (Zhou, 2009). Navigation, in general, allows a good opportunity for pre-operative planning, especially in cases where the relation to the anatomy is complex, as in the case of neuro surgeries(Mezger et al., 2013). However, this is not applicable for moving structures, as in the case of fetal surgery and motion compensation is required (Pratt et al., 2015). It has been proven that Laparoscopic Ultrasound (LUS), increases surgical safety in resection by visualizing vascular structures and the structures underneath (Våpenstad et al., 2010). In most cases, the navigation environment is rather static and does not change with the change in the environment. Therefore, it is clear that a different approach to real-time registration and capability of changing the registration on the fly becomes essential.

2.5.2 Fulcrum effects and tremors – Robotics for use in surgery

Robotics has been one of the most adopted solutions in MIS, as in a robotic-assisted surgery, the instruments in many cases are not moved directly by the surgeon, with the help of ad-hoc instruments which act as controllers and are accompanied by software. The tools have been made available with a varying number of degrees of freedom, 6 degrees being the maximum. These instruments filter and limit tremors and simulate tactile sensations, thereby increasing the surgeon's dexterity and eye-hand coordination improvements (Tonutti et al., 2016).

2.5.3 Unregistered robotic systems

DA Vinci SP has been the most successful of robotic surgical systems and is teleoperated and the only system with FDA approval so far. Also, since the interface is quite flexible, it has been used in a wide range of areas from general abdominal, urology to cardiac surgeries. The master console of this unit is composed of controllers which are self -intuitive to the surgeon so that it can be readily taken up by surgeons with less training. Since the arms of the robot are also equipped with a variety of instrument handling capabilities, the unit is capable of doing procedures such as stent grafting, transurethral or abdominal prostatectomy (Tonutti et al., 2016). Different segments of the Da Vinci surgical robotic platform are shown in Figure 2.14.

Figure 2-14 The DA Vinci surgical robotic platform. (1) The surgeon console. The surgeon operates through master controls and is supplied with a high-definition, three-dimensional (3D) view of the operating space. Hand, wrist and finger movements control the tools accurately and in real time. (2) The patient-side cart, consisting of three or four robotic arms which carry the camera (usually a flexible HD 3D endoscope) and the instruments. The tools are controlled directly by the surgeon, with safety mechanisms preventing independent movements. The tip of the tools is articulated to simulate the 7° of freedom of the human wrist and fingers. (3) The vision system. Dedicated hardware and software for image processing provide detailed images of the patient's anatomy; the screen provides a view of the operating field to the whole surgical team. 2016 Intuitive Surgical. (Tonutti et al., 2016)

2.5.4 Registration of anatomy in navigated surgeries

Registration is a process of assigning a set of coordinate points to another set of coordinate points and finding the best fit. For example, the CT scan image of a joint can be registered to the actual bone during the surgery by locating the 3D coordinates of the bony prominences, or by painting on the surfaces while the painting instrument is optically tracked.

In surgeries unlike DA Vinci SP assisted forms, which require a constant registration system, such as orthopaedic surgeries which require 3D milling and implantation, registration is of primary importance. However, for the registration to be valid, the structures are required to be solid and to be mounted to metal plates or rods to a steady base. Normally the process is cumbersome and time taking.

Orthopedic surgical robots have the best human-robot interaction known. They achieve this by providing a friendly CT/MRI import and on- table registration, and tracking using optical tracking system, while the navigation interface provides a complete guidance of details such as implant size, placement and best fit for specific dimensions of the bone. They also offer procedural verification methods and post surgical implant fit identification.Also, human robot interactions can be made smooth with several methods of cooperative control algorithms. Typical examples include orthopaedic robots seen in Table 2.10, where ROBODOC, Arthrobot are active robotic systems. Acrobat is Semi Active and robots such as MAKO, and more recently Blue-belt is entirely passive.

The best of these aspects being the applied image registration techniques, passive and semi-active robotics. If these can be applied in Minimal Access Surgeries, the amount of complexity of the surgeries can be reduced by several folds.

Table 2-10 Orthopedic robots, interaction types and registration

Sno	**Robotic Systems**	**Institution**	**Procedures**	**System types**	**Imaging/registration types**
1	ROBODOC	IBM/U. C. Davis	THA, TKA	Ex-mounted, SCARA	Preoperative CT
2	Acrobot	ImperialC	UKA	Semi-active	Preoperative CT
3	MBARS	Carnegie MU	TKA	Bone - mounted,parallel	X-ray imaging
4	CASPAR	Orto Maquet	TKA	Active	Preoperative CT
5	Praxiteles	Praxim-Medivision	TKA	Passive	Manual orientation
6	MARS	Mazor	PFA	Active with parallel	Surface painting image registration
7	PFS	Carnegie MU	TKA	Semi-active	Surface painting image registration
8	BRIGIT	Zimmer	HTO	Passive	Sensor – surface paint
9	ARTHROBOT	KAIST, Korea.	TKA	Active	Sensor – surface paint
10	MAKO RIO	MAKO Surgical	MAKOplasty	Passive	Preoperative CT

2.5.5 Problems of orientation - Tracking for use in MIS

Every navigation interface requires a tracking system for providing reference and guidance. There are two main methods available for tracking which is consistently used in surgeries- Optical tracking and Magnetic tracking. While Magnetic tracking is used mostly in ultrasound tracking, Magnetic tracking is used mostly in forms of navigated robotic surgeries and has been consistently in use for the past 2 decades, especially in the area of orthopaedics and hence has been time tested.

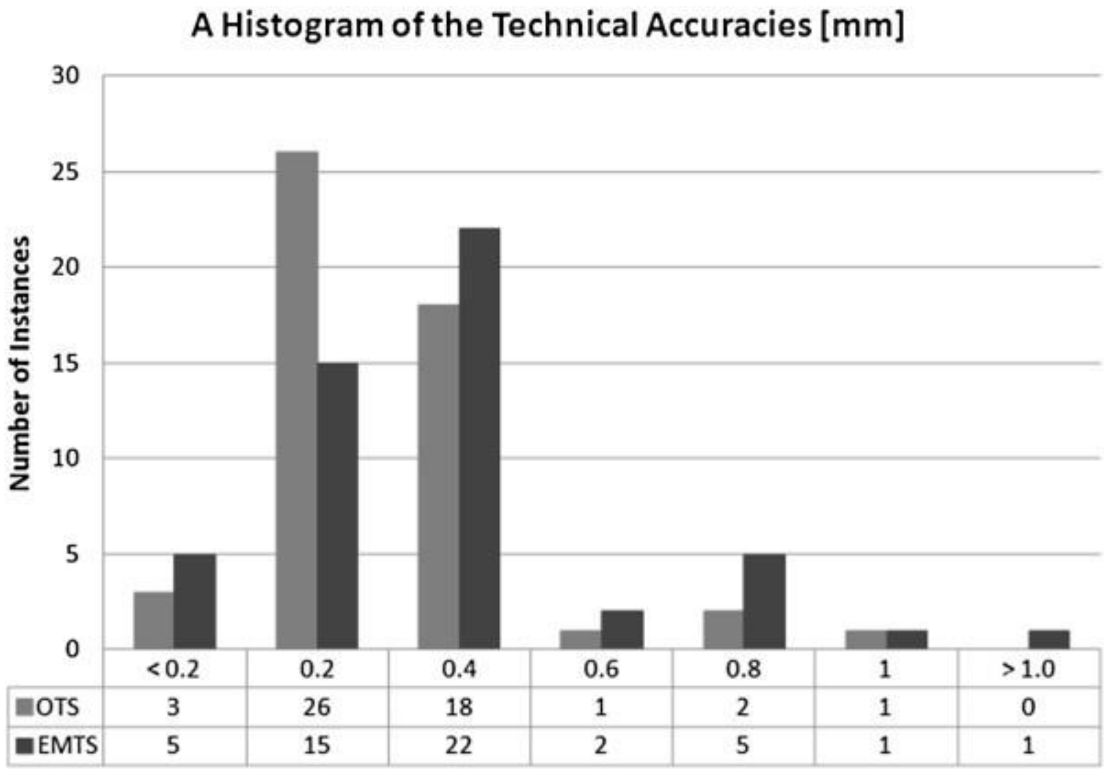

Figure 2-15 A histogram of comparison between Optical tracking system 'OTS' and Elactro Magnetic Tracking System 'EMTS'the accuracy of the tracking modalities. (Koivukangas et al., 2013)

Figure 2.15 shows a comparison of errors between optical and magnetic tracking systems at a distance of 2 metres from the tracking base, under ideal conditions. It can be seen that the overall errors are less than 1 millimetre in both systems. However, this may not be the case in actual surgeries. Dust coverage of cameras or markers covered in bone dust or surgical debris can affect the tracking accuracy of optical tracking and may even cause complete loss of tracking.

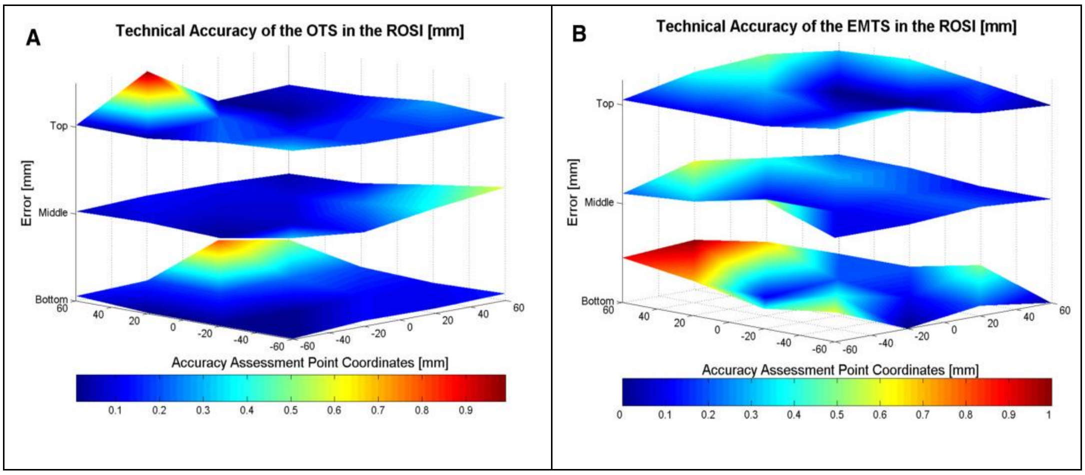

Figure 2-16 ***The 3D error surfaces of the OTS (A) and the EMTS (B).*** **The trend of error for both modalities is seen with the changes of the shading within the surfaces. The dark blue colour represents 0 mm error and dark red the highest error. The orientation of the phantom with respect to the navigator is such that the optical camera pair of the OTS (A) is located perpendicular to the right front edge and the EM field generator of the EMTS (B) perpendicular to the right front edge, in both cases at the middle level. (Koivukangas et al., 2013)**

In the Figure 2.16 (a) the optical tracking peripheral errors can be seen on the top and bottom limits of the vertical field of view of the optical tracking system. Figure 2.16 (b), the same is repeated with the magnetic tracking system and the error distribution can be seen. From the Figure 2.15 and 2.16, Optical tracking provides higher accuracy while magnetic tracking is a non-line-of-sight system. However, magnetic tracking suffers from electromagnetic interference and hard iron interference. Since robotics, actuators and RFA cause heavy electromagnetic disturbances, magnetic tracking may not be favoured in many surgeries. Also, it has to be noted that optical tracking has a higher tracking volume than magnetic tracking. Hence Optical tracking is better suited for most navigated surgeries and used as a standard for most navigated surgeries. But because of the limitations, it is used with caution to have the markers in the line of sight of the tracking cameras. Optical tracking fundamentals, problems during usage and solutions will be further elaborated in the upcoming sections.

2.5.6 Problems of real time imaging in MIS – Laparoscopic ultrasound

MIS and MAS though closely related in many principles, the type of skills and the difference in the amount of perception required are vastly higher in MAS.

Preoperative planning and static non-invasive 3-dimensional imaging such as CT and MRI can be extremely helpful in terms of having a successful outcome, more so in a navigated MIS (Pugash et al., 2008). Whereas in the case of MAS, it is not crucial to have a static image but is highly indispensable to have a non-invasive real-time dynamic imaging technique such as ultrasound, though the importance of MRI imaging because of the resolution and detail cannot be undermined (Coakley, 2001). The decision for open surgery in the case of an MIS can be made well ahead based on the non-invasive imaging techniques or on the table when the procedure suffers problems (Dolkart et al., 2005). In the case of MAS, the decisions are made mostly on Ultrasound observations (Yagel et al., 2007) and very rarely on MRI. The workflow in the case of ultrasound guided surgeries is given in Figure 2.17.

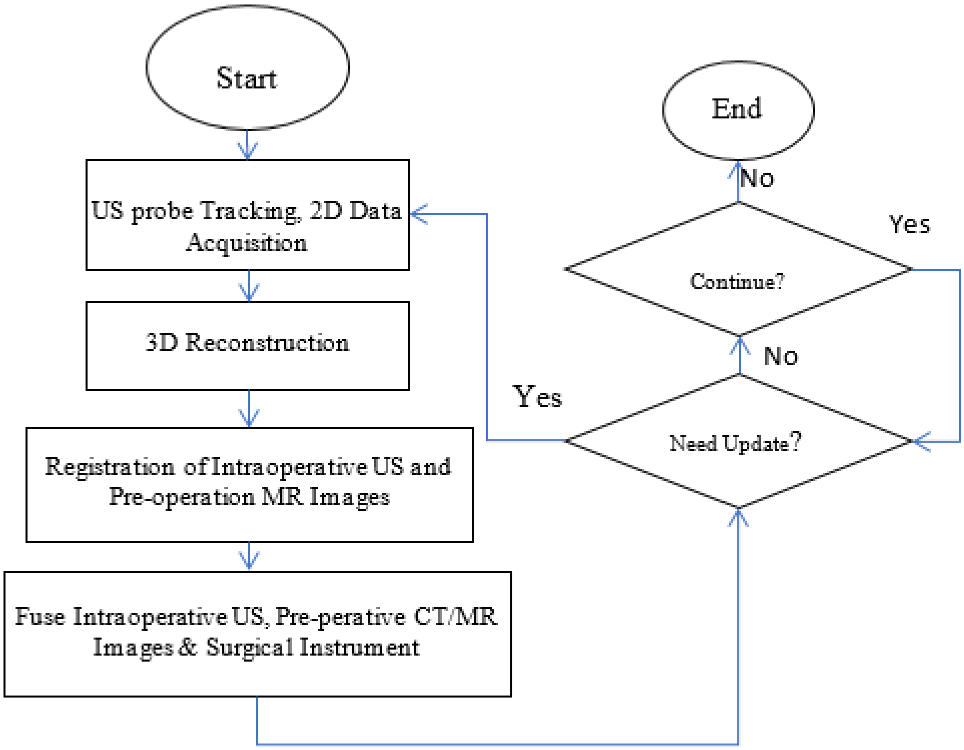

Figure 2-17 Intraoperative 3D ultrasound navigation flow chart (Chen and Bao, 2012)

Navigation and surgical planning in the case of Medical ultrasound guided MAS follow the pattern shown in Figure 2.17. This process mainly involves preoperative USG imaging mental reconstruction of the anatomical imagery (Pratt et al., 2015). The surgery depends on dynamic structures which require exploration. Therefore, the use of intraoperative ultrasound imaging becomes mandatory. More recently 3D ultrasound has been considered for usage in ultrasound guided surgery

(Kurjak et al., 2007) but the usage has been debatable because of the heating effects of 3D ultrasound. Due to the fact that the reverberations observed with rigid instruments can result in false anatomical artefacts, this problems have been under research for image processing optimization (Linguraru et al., 2007). Therefore, usage of a tracking system and tip tracking technology can turn out to be more straightforward and accurate.

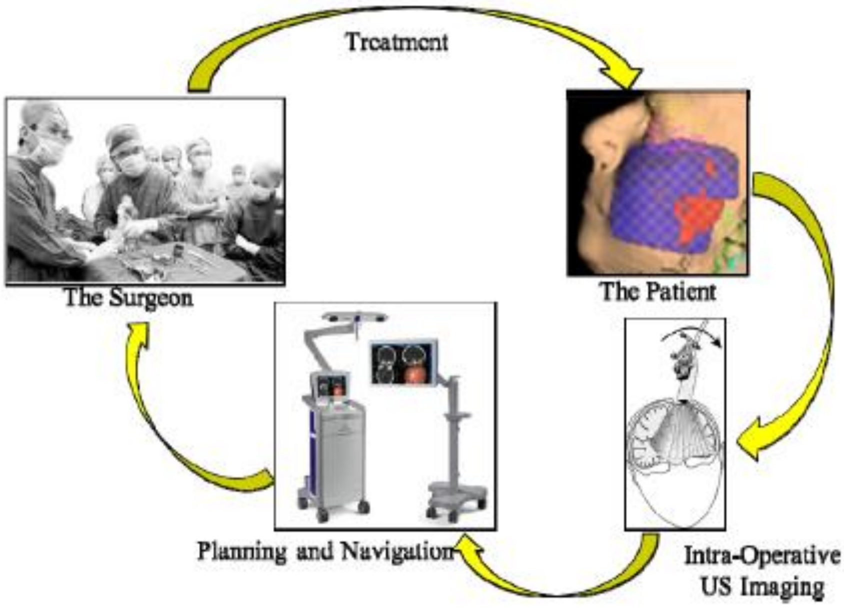

Figure 2-18 Surgery navigation guided by intraoperative US images, correcting pre-operative images (Chen and Bao, 2012)

The workflow of ultrasound-guided surgery is shown in Figure 2.18. However, it should be noted that ultrasound imaging is limited by its lower accuracy and change in speed of sound and its interaction with highly dissimilar tissue consistencies. Such problems will be described in the fundamentals of ultrasound imaging in the later chapters.

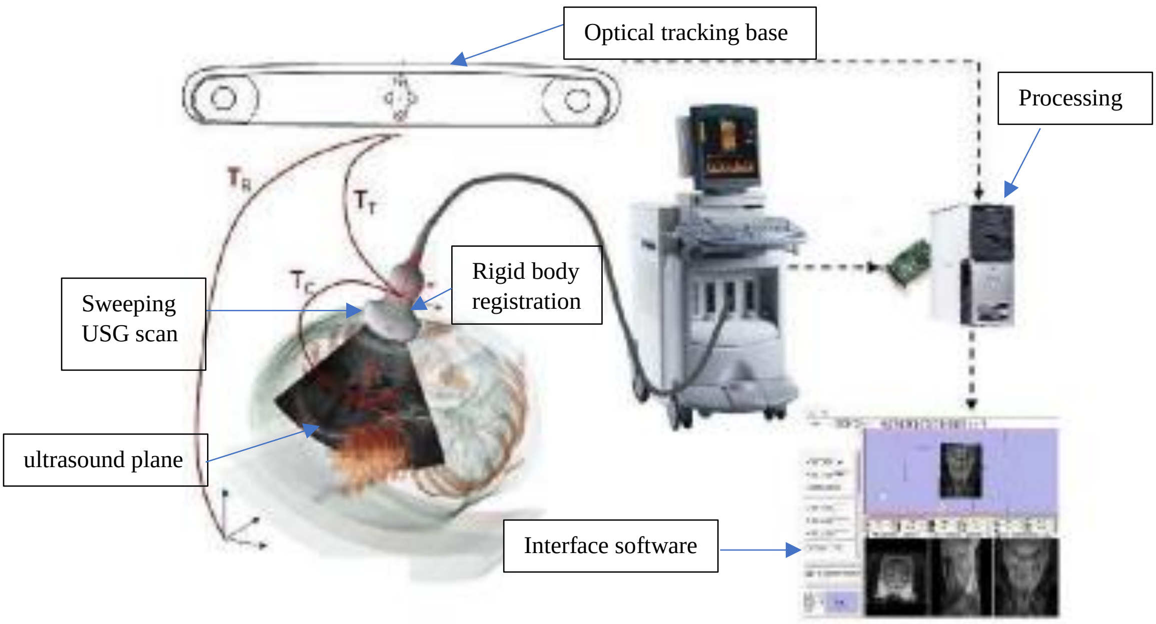

Figure 2-19 Intraoperative 3D ultrasound-guided navigation system structure (Chen and Bao, 2012)

An example of multimodality 3D optical tracking navigation is shown in Figure 2.19. The equipment available for such navigation is known as a ‘Laparoscopic Ultrasound system’. However, MAS, especially fetal surgeries have not been using this system because of the amount of sophistication involved and unavailability of the right software, including complicated registration processes.

2.5.7 Force feedback – haptics

In the recent years, haptics has been a major area of focus in surgical robotic platform research. Though haptics is normally considered to include pressure and vibration perception, it includes texture and temperature. Most professional surgical robots like DA Vinci do not include haptics, but a lot of effort has gone into the development of haptics to be made into these devices and are still under experimentation. Surgeons repeatedly favoured having vibrational haptics, which proves that this modality of force feedback is quite essential (Koehn and Kuchenbecker, 2015). Especially suture manipulation can be very crucial in terms of force management or can result in ripping off or injury to the soft tissue, without the perception of the surgeon. There has been a lot of evidence that haptics has achieved a good feedback from surgeons for suturing applications (Kitagawa et al., 2005).

From experiments conducted by Zhou et al., it can be observed that the forces lower than 0.5 N are not even considered significant, as surgeons, even the more experienced of the group were less sensitive to these levels of forces (Zhou, 2007). With the above in mind, it has to be noted that the more delicate the structures are lower the force perception becomes, and this is the case for fetal structures and the intra-uterine environment. Therefore, the use of plain force feedback cannot be justified in a fetal surgery environment.

Though on the one hand, MIS robots have had no haptics in their product version of the hardware, on the other hand, with endoscopy, handheld haptics has been quite successful (Payne et al., 2015). Although fetoscopic procedures use an endoscope, force measurements and feedback have not yet been implemented, leading to the nearly complete absence of tactile sensations on the end of the surgeon.

2.5.8 Applying available technologies for MIS to MAS fetal surgeries

Based on the above discussion about the available technologies for MIS, the following are relevant to the development of a fetal surgery system:

(a) Optical tracking - for tracking of surgical tools in 6 Degrees of freedom,

(b) Ultrasound image processing - for tracking of tools and objects in 2D within the USG frame

(c) Navigation with CT and MRI registration and Augmented reality - For displaying surgical tools in 3D to give a better understanding of orientation with the surrounding structures

(d) Robotics for improving movement accuracy

(e) Haptics with a combination of force and vibrations for force feedback

With the combination of the above in place, the surgical system would be capable of causing inadvertent injury to the surrounding structures in the absence of safety constraints. Therefore, for an endoscopic system such as fetal surgery, a combination of passive control in normal conditions and negative feedback in a safety control mode would make the system more reliable.

2.6 Target specifications of ultrasound system for use in fetal surgeries

Fetal surgeries are performed using obstetric ultrasound at 3.5MHz frequency. Since ultrasound does not have sub millimetre accuracy, several procedures which require high accuracy of movement cannot be proposed or performed. Also, when rigid instruments are used, there can be multiple reflections within the ultrasound image. Therefore, the surgeon assumes the most probable position by hand – eye – tool coordination. Also having multiple instruments under one ultrasound field will result in multiple shadows of one on the other and estimation of position becomes nearly impossible. Having the above stated in mind the following are the target specifications considered:

a) Sub millimetre resolution
b) Ability to use multiple instruments without confusion by superimposing the images with virtual tools
c) Ultrasound cross referencing for object positions with another modality
d) Ability locating the tip accurately

2.7 Background of ultrasound tracking

A B mode ultrasound is an imaging modality which uses inaudible sound waves to create a picture of a person's internal organs, muscles, bones, and other body parts. The process of tracking an object within the ultrasound image frame is referred to as ‘Ultrasound object tracking’.

2.7.1 Ultrasound object tracking

Ultrasound object tracking suffers from various issues due to image noise, properties of the sound like the variation in the velocity in different media, reflection, refraction, scattering etc. So, to proceed to ultrasound tracking, some introduction to the principles used in ultrasound imaging are discussed briefly, followed by sections of calculations used to estimate parameters used in ultrasound. In the later sections, image processing usage and outputs are discussed.

The errors due to image processing of ultrasound are then compared to errors by manual observation. Further, the basis for merging multiple tracking systems to achieve a higher accuracy is explained with experiments.

2.7.2 Principle of a B-Mode ultrasound

The medical ultrasound works by first emitting an ultrasonic wave from a piezo electric transducer and using an array of ultrasonic receivers to measure Time of Fight and return of the sound waves. The timing of return is then reconstructed into a rasterized pixel array on a cathode ray screen or other display systems, which is then available to view as an image.

Since the image is obtained from a penetrated back to scatter the images provided to us from the ultrasound device are in XZ plane, it can be called a depth image or a cross sectional image. A normal 2D ultrasound image without Doppler contains monochromatic pixels with shades of white to black(greyscale), depending on the intensity of reflection, refraction and velocity of sound in the specific medium. The system of ultrasound scanning assumes the velocity of sound to be the velocity of sound in the Human tissues, which is mostly composed of water and therefore is in line with the velocity of sound propagation in water. However, not all human tissues are uniform, as there are areas of higher density such as bones, teeth etc. and other areas which are relatively soft and containing dissimilar media such as lungs. Hence, the sound wave propagation cannot be uniform in such areas. Table 2.11 shows the different densities of bodily tissues, the speed of sound in these tissues and the impedance of sound of the corresponding medium. It can be observed that the velocities in the bone are the highest and the lungs are the lowest, whereas the impedance characteristic is the direct opposite.

Table 2-11 Densities of tissues in the human body, the corresponding velocities and impedance values. The rows with missing velocities have varying densities with wide ranges.

Material	Density ρ[Kg/m^3]	Speed c [m/s]	Characteristic Impedance Z [Kg/m^{2}s](x10^6)
Blood	1060	1570	1.62
Bone	1380 – 1810	4080	3.75-7.38
Brain	1030	1541	1.55-1.66
Fat	920	1450	1.35
Kidney	1040	1560	1.62
Liver	1060	1570	1.64-1.68
Lung	400	>343	0.26
Muscle	1070	1585	1.65-1.74
Spleen	1060	1561	1.65-1.67
Water	1000	1484	1.52

2.7.3 Determination of ultrasound resolution parameters

It is essential to establish the ultrasound parameters used in medical ultrasound to understand the implications of physical objects within the ultrasound scanning plane. The ability of an ultrasound system to distinguish between two points at a particular depth in tissue, that is to say, axial resolution and lateral resolution, is determined predominantly by the transducer (Ng and Swanevelder, 2011). The parameters of the ultrasound are to be known to know the limits of an ultrasound image-processing based object tracking. Though there are many parameters in ultrasound imaging, the most important ones of concern include axial resolution, lateral resolution and the depth of penetration.

2.7.3.1 Axial Resolution

The ability to recognise two different objects at slightly different depths from the transducer along the axis of the ultrasound beam depends on the wavelength of the sound wave within the specific medium. The Spatial Pulse (SPL) Length depends on the wavelength. A comparison between the different SPL values is shown in Figure 2.20(a) showing low frequency transducer output and (b) showing a high frequency transducer.

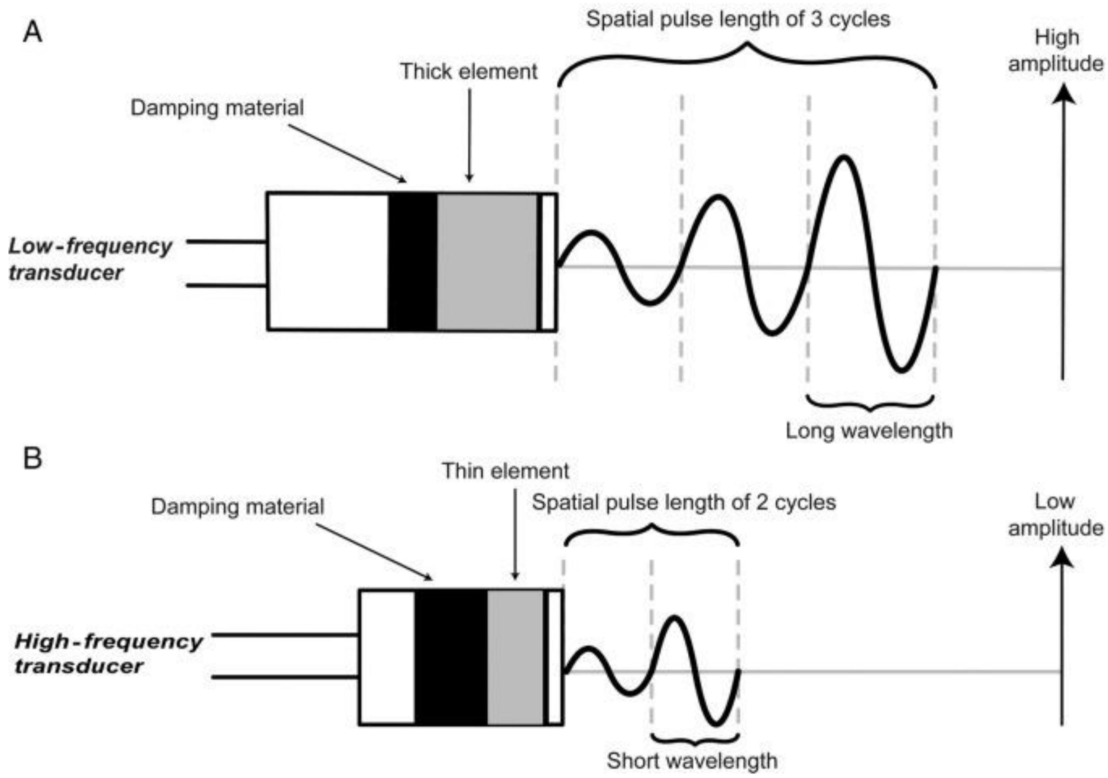

Figure 2-20 Spatial pulse length –(a) Low-frequency transducer with long spatial pulse length and low axial resolution. (b) High-frequency transducer with short pulse length and high axial resolution.

The wavelength of 3MHz ultrasound in water, $'\lambda'$ is 0.457 mm. Therefore, SPL is given as:

$$SPL = \lambda * (number\ of\ cycles) \qquad 2.1$$

2.2

$$Axial\ resolution = SPL/2$$

From the above Equations (2.1) and (2.2), we get the axial resolution of 3MHz ultrasound as,

$$Axial\ resolution = 3 * \frac{0.457}{2} = 0.6855\ mm$$

2.7.3.2 Lateral resolution of ultrasound

With respect to an image containing pulses of ultrasound scanned across a plane of tissue, lateral resolution is the minimum distance that can be distinguished between two reflectors located perpendicular to the direction of the ultrasound beam. Lateral resolution is high when the width of the beam of ultrasound is narrow or the distance from the source 'S', 'F' is minimal and decreases with beam divergence 'D', as shown in Figure 2.21. φ is half the angle of divergence and W_f is the Lateral resolution in Figure 2.21.

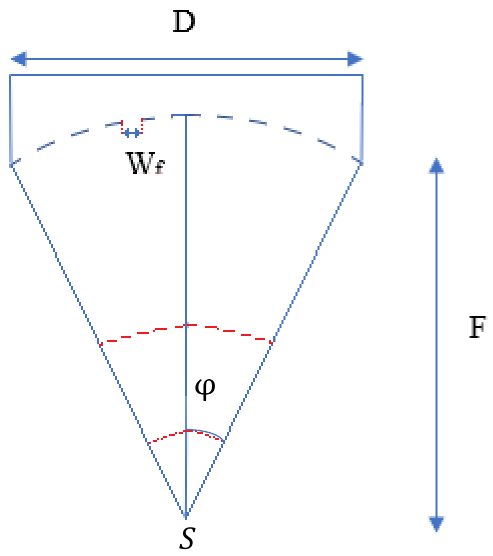

Figure 2-21 Shows an ultrasound beam with divergence D, distance from source F and angle of divergence 2 φ

$$\text{If } \varphi < 50^\circ$$

Lateral resolution W_f is given as:

$$W_f = \frac{\lambda F}{D} \tag{2.3}$$

From the Equation (2.3), it can be observed that the resolution of an obstetric ultrasound decreases with an increase in depth and at 1mm distance from the ultrasound probe when the divergence is 1mm, and the depth is 1mm, the lateral resolution is

$$W_f = 0.457 * \frac{F}{D} \approx 0.5\text{mm}$$

The lateral imaging resolution also depends on the number of ultrasound elements observing the reflected ultrasound beam.

2.7.3.3 Maximum depth of penetration:

The depth of penetration of the ultrasound wave depends on the density of the medium, impedance and the amount of the ultrasound energy emitted by the transducer. Table 2.12 shows the depth of penetration of different frequencies of sound with the amplitude fixed at 75dB.

Table 2-12 Depth of penetration of sound frequencies based on the frequency with amplitude as a constant at about 75 dB.

Frequency (MHz)	Depth of penetration
1	40
2	20
3	13
5	8
10	4
20	2

The output of the ultrasound probe is 65 - 90 dB , hence the maximum depth of penetration at 3.5MHz can be given by

$$D_{max} = \frac{65}{st * f * 2} \tag{2.4}$$

Where,

D_{max} = Maximum depth of penetration

st = Decibels/cm/MHz

f = frequency of the ultrasound probe

Therefore,

D_{max} = 65/1(dB/cm/MHz) x 3.5 (MHz) x 2

D_{max} = 12.85 cm

Though the penetration depth can be raised significantly by increasing the decibel gain in the ultrasound machine, with higher intensities of ultrasound, heat can be induced in hard and soft tissues, depending on the frequency ultrasound used. Smaller wavelengths get absorbed at shallower depths, while longer wavelengths can propagate deeper while offering a lowered resolution of the image.

2.7.4 Materials and ultrasound characteristics

Sound propagation properties in different biological media have been described in the earlier sections. Depending on these characteristics the ultrasound imaging can be affected and further, at the interface of dissimilar objects, depending on the combination of material properties the sound wave can be scattered, absorbed, transmitted or reflected as seen in Figure 2.22. The quality of the image obtained using a B- mode ultrasound system is therefore limited by the factors of ultrasound interaction with dissimilar materials. Such interactions being variable, can lead to differences in the observed shape, reflections. Therefore, the true shape of cross-section of the rigid tool may not be observed in the ultrasound image. The equations in this section govern the quality of the image observed in ultrasound images.

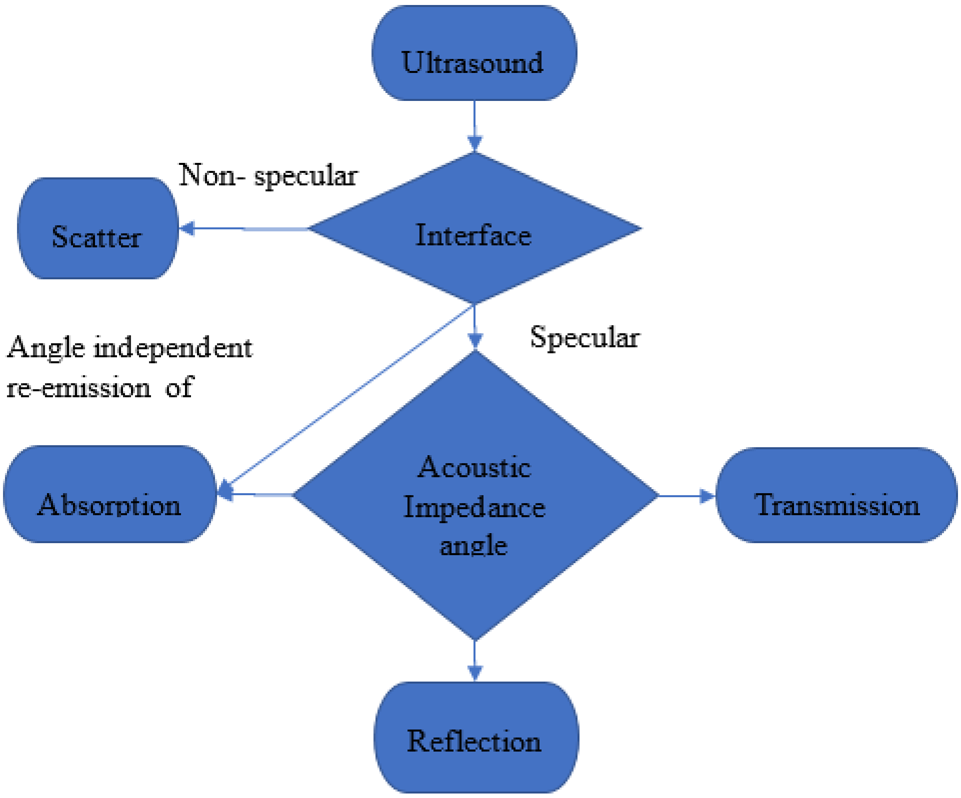

Figure 2-22 Ultrasound interactions at boundaries of materials

The phenomena shown in Figure 2.22 depends directly on the velocity of sound in materials ‘*c*', compressibility ‘*κ*’ and the density of the medium. Therefore, the relationship of ‘*c*‘ is given in relation to the compressibility ‘*κ*’ and density ‘*ρ*’, by:

$$c = \sqrt{\frac{1}{\kappa\rho}} \qquad 2.5$$

In most human soft tissues, ***c*** is 1540 m/s, mainly because it is mostly water and a frequency ‘*f*’ of 3.5MHz corresponds to a wavelength of 0.44mm. Hence, when the medium changes the velocity ‘***c’*** tends to change. Therefore, the relationship between the wavelength ‘λ’ and frequency ‘*f*’ can be given as:

$$\lambda = \frac{c}{f} \qquad 2.6$$

Reflection of sound waves can happen while the sound travels in one medium and interacts with another medium within which there is difference in sound wave velocity. As shown in Figure 2.22, it can impact image quality when there are too many reflections or when there is a gross difference in sound velocity between two media, can lead to total internal reflection or absorption. The effect on sound reflections or transmission within two media with impedance to sound waves '*Z1*' and '*Z2*' respectively will have a reflection coefficient 'R' and a Transmission coefficient 'T' which can be given by the calculation:

$$R = \left[\frac{Z_2 - Z_1}{Z_2 + Z_1}\right]^2 \tag{2.7}$$

Transmission coefficient calculation:

$$T = \left[\frac{4 * \mathrm{Z}_1 * Z_2}{(Z_2 + Z_1)^2}\right] \tag{2.8}$$

2.7.5 Ultrasound tracking - Discussion

From the equations in the previous section, it can be seen that when materials with gross dissimilarity in sound propagation speed are used within an ultrasound imaging setup, it can either result in high amount of reflections or artefacts which cannot be corrected by any amount of image processing. Also, the tip position tracking of rigid instruments under ultrasound imaging can provide unreliable or completely wrong results due to a combination of the factors suggested above. Therefore, using image processing alone or even plain visualization by the eye as a method for instruments to be tracked under ultrasound is not reliable and therefore merging this imaging modality with another system which has a higher accuracy and is not affected by the problems induced by the medium of ultrasound propagation and the material being used is ideal. Hence merging ultrasound tracking using image processing with Optical tracking or Electromagnetic tracking methods is be recommended.

2.7.6 Surgical Instruments under ultrasound observation

The consistency of most of the material in the human body is either elastic solids, fluids or gases but not materials of high density. Hence it is assumed to be penetrative to ultrasound energy. Since the principle behind ultrasound depends on velocity of sound in a specific medium 'c' and its reflection after a specific amount of time (Time of Flight measurements), the medical ultrasound as an imaging modality can receive proper images only when there are only fewer dissimilarities in the consistency (less impedance Z) in the type of medium present.

$$Z = \rho c \tag{2.9}$$

'ρ' and 'c' can be defined as the local density and speed of sound, respectively. When there is a discontinuity, there is a change in the impedance. Different materials, the respective velocity of sound and the impedance are given in Table 2.13

Table 2-13 Density, speed of sound, and impedance values for biological materials compared to engineering materials (at 37C)(Kline, 2012)

Material	Density [kg /m^3]	Speed of Sound [m/s]	Impedance[kg/m^{2}s ×10^6]
Air	1.14	353	0.000402
Water	993	1527	1.52
Blood	1060	1530	1.62
Fat	950	1460	1.39
Muscle	1080	1590	1.72
Bone	1200-1800	2700-4100	3.2-7.4
Aluminium	2700	6420	17.3
Steel	7900	5800	45.8

The percentage of reflection of ultrasound between two different media according to equation (2.7) is given in Table 2.14. The percentage of reflection increases with the amount of dissimilarity between the two media. In any case of gas – metal interface the amount of reflection is literally 100%. In the case of liquid metal interface, provided the metal is not a very dense material, the amount of sound waves entering the medium of the metal is less and not entirely reflected. Therefore, most surgical instruments do let reduced intensity of ultrasonic waves through their body.

Table 2-14 Percentage reflection of ultrasound between two dissimilar media(Kline, 2012)

Material	Aluminium	Steel	Glass	Water	Oil	Air
Aluminium	0%	21%	2%	72%	74%	100%
Steel	-	0%	31%	88%	89%	100%
Glass	-	-	0%	65%	67%	100%
Water	-	-	-	0%	0%	100%
Oil	-	-	-	-	0%	100%
Air	-	-	-	-	-	0%

Using Equation (2.8) the amount of transmission and reflection have been calculated in Table 2.15.

Table 2-15 Calculated values for transmission and reflection coefficients of different material combinations

Material1 and Material2	Reflection Coefficient	Reflection dB	Transmission Coefficient	Transmission dB
Water and tissue	0.003	-50.458	0.997	-0.026
Water and Steel	0.877	-1.140	0.123	-18.202
Tissue and steel	0.863	-1.280	0.137	-17.266
Tissue and silicone	0.003	-50.458	0.997	-0.026
Water and silicone	0.015	-36.458	0.985	-0.131

From the calculation results in Table 2.15, it can be noted that in many biological tissues the transmission T occurs, as R is low T is high. In cases where the media are grossly dissimilar, the reflected energy R becomes higher than T. Hence, further transmission of ultrasound energy cannot happen.

Refraction is a process that takes place at an interface between two materials having different material properties such as elastic modulus and density. The phenomenon is since sound velocity depends on the properties of the medium. Therefore, when the sound wave encounters the interface between two materials, the portion of the wave in the second material is either moving faster or slower than the one in the previous material, resulting in the bend of the wave inside the second medium. From observation, it should also be seen that, in a B-Mode ultrasound, the shadow (imaginary ray) follows the direction of the sound waves (incident ray) and can be given by Snell's law:

$$\frac{sin\theta 1}{VL1} = \frac{sin\theta 2}{VL2} = \frac{sin\theta 3}{VS1} = \frac{sin\theta 4}{VS2} \qquad 2.10$$

Where, VL1, VL2, VS1 and VS2 are longitudinal and shear wave velocities of material 1 and material 2 respectively.

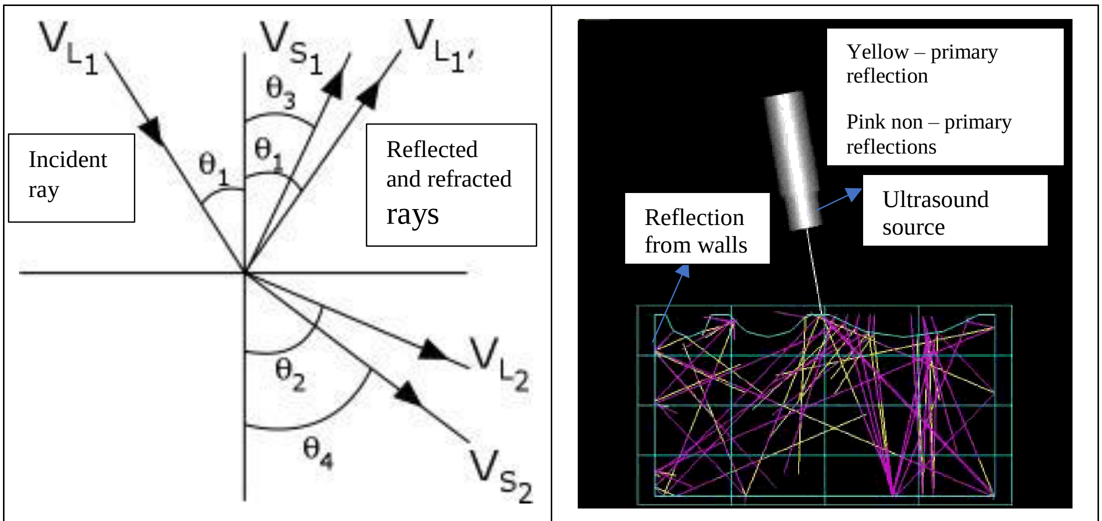

(a)Snell's law

(b)Snell's law and reflections

Figure 2-23 Snell's law and its effects.(a) VL1 and VL2 are different longitudinal velocities, and VS1 and VS2 are shear velocities in respective material 1 and material 2. (b) shows the simulated combined effects of Snell's law and reflections from the internal surfaces of the box

From Figure 2.23 (a), VL1 is reflected at the same angle as the angle of incidence, while VL2 is refracted into the second medium. The reflected part obeys Snell's Law. It should be noted that there is a loss of energy at the interface between two different media. In Figure 2.23(a), it can be seen how there is an initial reflection at the interface and then refraction of the ultrasound beam inside the second medium from the ultrasound probe, and there is a reflection of the sound waves from the sides of the container. This can, in turn, induce noise in the final image received. In Figure 2.23(b), the secondary reflections from the wall and the top surface are shown as yellow lines and the pink lines depict all reflections above the second time.

When the longitudinal wave gets transferred from a medium where its velocity is low to a medium where the velocity is high, there is an incident angle which makes the angle of refraction 90 degrees, which is known as the first critical angle. This angle can be calculated from Snell's law by putting 90 degrees for the angle of the refracted ray. At this angle of incidence, much of the acoustic energy is in the form of an inhomogeneous compression wave, which travels along the interface between the two-dissimilar media and decays exponentially with the depth from the interface. This wave is known as the creep wave.

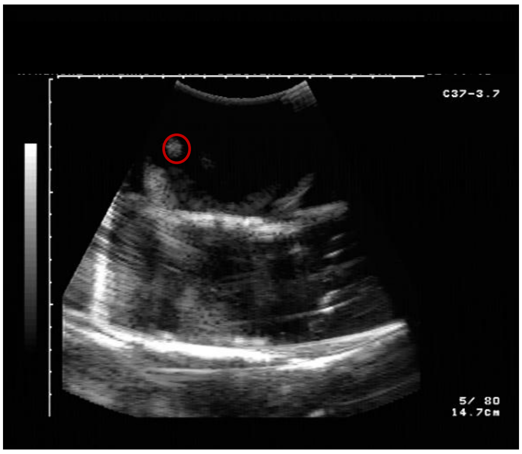

(a) Silicone tube in water

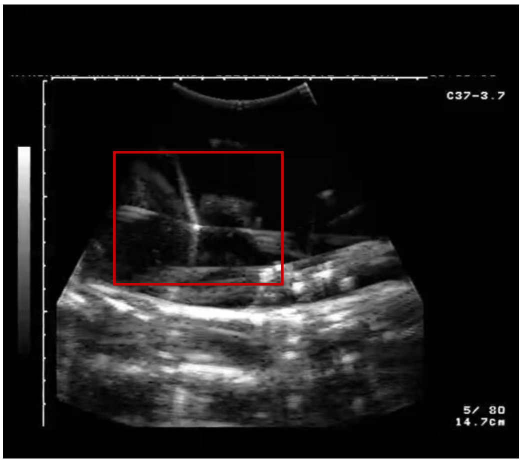

(b) Stainless steel catheter in water

Figure 2-24 Materials and visibility under ultrasound.(a) Silicone tube is seen as a clear circle(b) Metal catheter showing multiple reflections and shadows

Figure 2.24 are observations from ultrasound imaging when different surgical instruments such as needles, catheters etc. are inserted in water, which follows Snell's law of refraction and reflective principles of sound.

2.7.7 Discussion – Ultrasound

(a) In Figure 2.23(b), the incident ray gets refracted by the second medium and further reflects off from the container if the container is made of a hard material shown as yellow for primary internal reflections and above the primary reflections are shown as pink, according to the calculation results in Table 2.15. Hence, the container needs to be lined with a softer material, to reduce such reflections.

(b) Figure 2.24(a) B-Mode ultrasound, the silicone tube is seen as a reasonably well-defined circle and the amount of noise produced, as seen in Table 2.15 is very low.

(c) The metal catheter on the other hand, as seen in Figure 2.24(b) because of refraction, given in equation 2.8 and as seen in Table 2.15, the image shows shadows with varying angles based on the angle of incidence, radial to the curvature of the source. Such artefacts with varying sizes and shapes can be missed out by image processing resulting in the accuracy being further reduced. Hence simple image processing techniques blob detection and centroid approximations cannot estimate the actual position of the cross section of the instrument.

(d) Surgical instruments, generally made of hard materials are likely to cause noise in the ultrasound images. Hence registration and tracking become less accurate. The amount of inaccuracy is highly variable depending on the material type, location, angle of beam incidence, reflection and refraction properties. Hence, any characterization done using any number of samples can become erroneous.

2.7.8 Ultrasound tracking conclusions based on the above discussion

From the calculations in the previous section, the ultrasound equipment used falls within the accuracy limits of MIS procedures, as the axial resolution is about 0.7mm and the lateral resolution is approximately 0.5mm. Also, the materials used affect the outcome of using ultrasound imaging as a sole method of tracking instruments. Some of the observations are listed below:

(a) Image registration of hard surgical instruments is better done using a soft material sleeve, like silicone, polyurethane etc.

(b) The lining of containers for experiments to be done with a soft material to reduce reflections.

(c) Though the resolution of the B-Mode ultrasound is ≈0.7mm, the effects of reflection, refraction and scattering of ultrasound can lead to a reduced accuracy of measurements.

(d) If combined with another, more accurate mode of tracking, something which is not affected by tissue interactions and artefacts, tracking surgical instruments in an ultrasound image can be achieved with sub-millimetre accuracy.

2.8 Ultrasound Image processing principles

The ultrasound image obtained in a B-Mode scan without Doppler is a greyscale image. Materials with densities different to that of water, show up on the ultrasound image as regions with different intensities. Such regions of different intensities, forming a set of pixels each, is referred to as a blob. For detecting blobs in a given image, they should be made more distinct and identifiable. For example, in the case of fetal surgeries, surgical instruments are to be tracked on the ultrasound frame at all times. This section describes the principles used to identify blobs. Many of the principles for image pre-processing and processing have been described by Lizzi and Feleppa in their publication (Lizzi and Feleppa, 2000).

The following preparation steps are followed before blob detection is done:

(a) **Intensity normalization:**

The ultrasound image, though in most cases has intensity values between 0 and 255. There are cases with 16-bit or 24-bit intensity values where intensity normalization needs to be done. The acquired greyscale image '*I(x)*' is obtained intensity normalized '*In(x)*' into the interval (0,255) using the following equation:

$$In(x) = W.(I(x) - Gl)\left\{\frac{255}{Gy - Gl}\right\} \qquad 2.11$$

Where '*Gv*' and '*Gl*' are the upper and lower limits of pixel intensities in the grey level histogram of I(x) and '*W*' is a manual factor of intensity adjustment with values between 0 and 1.

(b) Median filtering:

The obtained image can have extremes of brightness values. Hence blob tracking may not work well. So, the image is smoothened by median filtering, the brightness is adjusted, and the contrast of the image is increased initially. The pixel brightness (β) and contrast (α) are given by:

$$g(x) = \alpha f(x) + \beta \qquad 2.12$$

where f(x) is the source of the pixels, in 8-bit grayscale (0-255) and g(x) is the result. 'x' can have i and j pixel locations. Hence the equation can be given by:

$$g(i, j) = \alpha . f(i, j) + \beta \qquad 2.13$$

The output of the above equation is constrained to 255. The above equation loops through every pixel in the entire frame in real-time.

(c) Calculation of global brightness thresholding:

The next step is to automatically calculate constraints global brightness threshold 'T' (between 0 - 255), and then a binary image is formed, for every level of brightness required.

(d) Selection of blob weight and size:

A size threshold '*St'* is chosen by observation of the size of the catheter under ultrasound and by drawing a rectangle around the specific blob.

(e) Area of Interest selection:

Since the blob detection is a processing intensive solution, a larger region of interest can have a higher number of pixels, increasing the latency of the output. Hence, the area of interest is combined with the blob detection functions.

2.8.1 Graphical blob detection principle:

The most commonly used method for blob detection is Connected-component labelling(CCL)(Hinz, 2005) or connected component analysis, which is an algorithmic approach to the Laplacian of the Gaussian methods of graphical blob detection. The graphical blob detection is performed by applying the kernel given below:

$$g(x,y,t) = \frac{1}{2 * \pi * t} e^{-\frac{x^2+y^2}{2*t}} \qquad 2.14$$

Where, '*g(x,y)*' is an image source, and '*t*' is the scaling operator. The scale space representation is given as

$$L(x,y;t) = g(x,y,t) * f(x,y)$$

The result of applying the Laplacian operator is

$$\nabla^2_{norm} L = t(L_{xx} + L_{yy})$$

A scale normalized Laplacian operator (Lindeberg, 2013) is given as:

$$\nabla^2_{norm} L = t(Lxx + Lyy) \qquad 2.15$$

Thus, for the selection of interest points **(xi, yi)** and scale '**ti'** , the blob is found according to:

$$(xi, yi; ti) = argmaxminlocal(x,y,t)\{(\nabla^2_{norm} * L)(x,y;t)\} \qquad 2.16$$

2.8.2 Algorithmic method of blob detection

A blob B[n], (where 'n' is the number of blobs), is detected every time the brightness of a set of pixels (m) in the image source *g(x)* is greater than threshold 'T' (m.*p(x)>T)* and the size threshold *St* is reached. The CCL equivalent used in image processing blob detection is done by applying subsets of connected components, unique labels based on their relationship with the neighbours. The kernel to be applied is given in Figure 2.25.

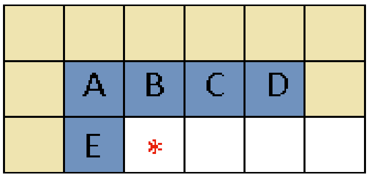

Figure 2-25 Kernel for CCL blob detection

The CCL process is done in a binary image after the thresholding step. If the thresholding step is not done, the latency can be remarkably higher.

2.8.2.1 Principle of blob detection

The simplified algorithmic process used in blob detection is shown in Figure 2.26.

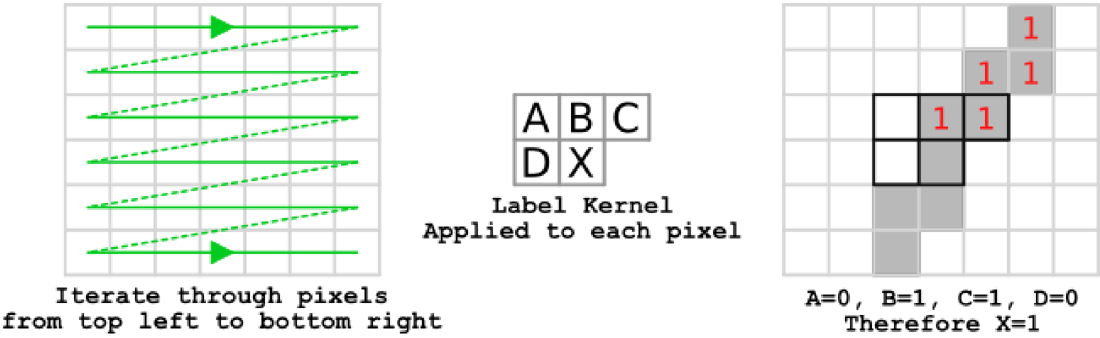

Figure 2-26 Blob detection process explained – rastering, application of kernel and labelling

1. Labelling the blobs by creating a sawtooth raster of all the available pixels in the frame In(x) and find the pixels with an intensity threshold T. the label number of the neighbouring pixels is checked as the raster progresses and a kernel is applied as shown in Figure 2.25.

2. A buffer of the frame size of null pixels or unlabelled, equal to that of the original frame is initialized and is used to store the labels. The scanning is done from left- upper pixel to right- bottom pixel. The labelling kernel is applied to every pixel (pixel position X). This labelling method is used so that the labels of neighbouring pixel already labelled (pixels A, B, C, D) are checked.

3. The earlier process described results in multiple labels within the same blobs. This problem is addressed by using a table array which links all labels within the same blob. Subsequently, the label array is updated with the minimum label value.

4. The minimum label value becomes the name of the respective blob.

2.8.3 Blob identification

Figure 2.27 shows ultrasound image acquired, thresholding (Otsu, 1979) applied and specific blobs identified and coloured with distinct colours with respect to the labels. Though blobs until now are detected using blob detection techniques, it may not result in the identification of the blobs. Blob characteristics can include size, shape and can also be described in relation to adjacent structures (Minor and Sklansky, 1981). Determination of basic blob characteristics which form the foundation of complicated forms of blob identification is essential and are discussed in this section.

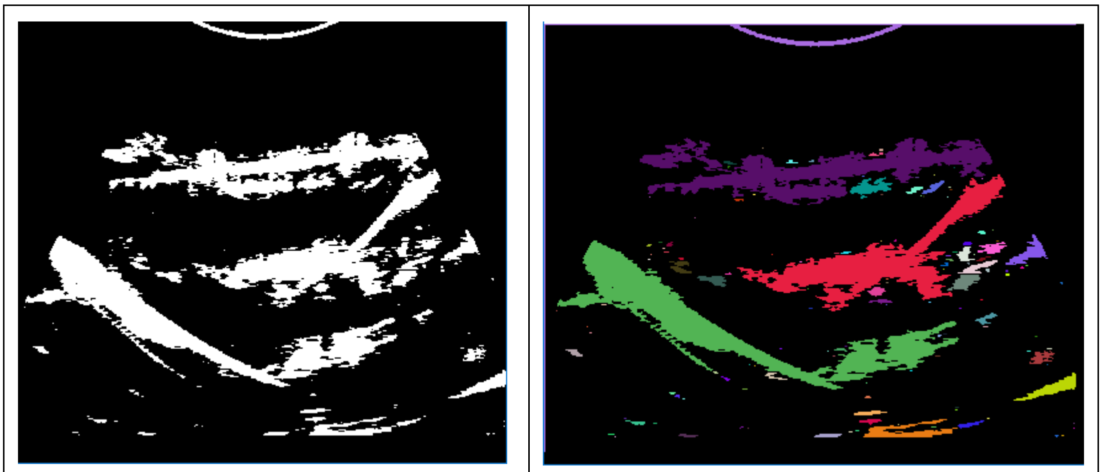

(a) Noisy image to binary colouring

(b) Blob identification and random colouring

Figure 2-27 Input ultrasound image was thresholding applied(a) vs output with blob coloured ultrasound image (b) observed latency was 52 mS for the blob detection with 105 blobs in the above case

Some of the blob detection and identification methods are shown in Table 2.16. For higher accuracy of blob detection, techniques such as subpixel interpolation of several orders are commonly used in ultrasound and Optical tracking systems. However, such processing intensive techniques raise the bar of technological requirements for real-time usage. From the table, it can be observed that the more sophisticated blob identification techniques usually consume more time than simpler ones. Hence most newer image processing techniques try to strike a balance between the level of complexity and the accuracy of blob detection to achieve an optimum efficiency for the specific application.

Most of the speed limitations are caused by the capability of affordable hardware technology at the point of time of this research. However, in future, with better processors having more memory and higher rates of execution, complicated algorithms can be executed in real-time. Though there are available technologies such as FPGAs which can be used at very high speeds with parallel processing capabilities, the amount of time required for development of algorithms within such platforms can be very high and require technical solutions and software which are beyond the scope of this project.

Table 2-16 Comparison of blob detection methods(Kaspers, Hinz, 2005)

Method	Pros	Cons
Template matching	Exact blob matching possible Very fast Easy to implement	Restricted blob definition Manual template design Single-scale Translation, rotation and scaling only possible by designing extra templates
Watershed detection	Works good for blobs with homogenous contract and a clear edge Near real-time performance Automatic Can extract bright and dark blobs	Very sensitive to noise, which leads to over segmented results Single-scale No shape and size information available
Spoke filter	Works good for blobs of all sizes with clear consistently oriented edges Extension to multi-scale possible Extension works well for blobs with non-homogeneous background Fast Automatic Single-scale is easy to implement	Very dependent on blob boundary orientation; works only for perfect boundaries with edge directions crossing in the middle of the blob Only perfect circular blobs are detected
Automatic scale selection	Works well for blobs of all sizes Invariant under scaling, translation and rotation Insensitive to noise because of significant measurement and scale-space lifetime threshold Size measurement possible Automatic	Works not well for blobs with unsharp boundaries No accurate extraction of the blob position and size Rather slow because multiple scales are analysed Only circular blobs are recognized
Sub-pixel precise blob detection	Works well for circular and elliptic blobs Sub-pixel precise detection Extraction of several useful blob attributes possible Blob classification possible	Scale-space parameter needs to be manually adjusted for detecting blobs of different sizes Works not well on blobs with lots of different sizes Difficult to implement Slow when blobs with lots of sizes need to be detected
Effective maxima line detection	Works well for blobs of all sizes Invariant under scaling, translation and rotation Extraction of blob size computation possible Robust to noise	Same as for automatic scale selection
Confidence measurement	Works well for homogenous blobs of all sizes Overlapping blobs and blobs within blobs can also be detected Proven noise insensitiveness for salt and pepper noise, white rectangular noise and 1/f noise	Works not well for inhomogeneous blobs Not fully evaluated Hard to implement Detects a lot of small blobs within bigger blobs

2.8.3.1 Calculation of Blob parameters

Blob parameters are required to identify and refer to a specific blob in a complete frame of blobs. Such parameters are specific to specific blobs in an ultrasound frame. The following are some of the blob features used for referring to specific blobs:

(a) Blob weight calculation:

The blob weight of a blob ‘$\boldsymbol{W}$ ‘, pixels ‘p’, with a number of pixels ***n*** can be given by:

$$W(n) = \sum_{k=1}^{n} p(i,j) \qquad 2.17$$

(b) Centroid calculation

The blob position when required is always given as its centroid, as usually, blobs are irregular objects. The centroid ***(Xc, Yc)*** of the blob with a number of pixels **n** forming an area and is given by:

$$X_c = \frac{1}{n}\sum_{k=1}^{n} x_k \qquad 2.18$$

$$Y_c = \frac{1}{n}\sum_{k=1}^{n} y_k \qquad 2.19$$

(c) Blob shape detection

In areas such as camera, optical tracking and ultrasound tracking, blob shape monitoring to identify a specific object is commonly used and can be obtained by using a variety of methods. The simplest being the application of spoke filter.

(d) Blob edge detection

If blob edge is required, the edge detection kernel is used and is of the form:

$$\begin{vmatrix} -1 & -1 & -1 \\ -1 & 9 & -1 \\ -1 & -1 & -1 \end{vmatrix} \qquad 2.20$$

In the image frame, the adjacent pixels to the pixel X are multiplied by the kernel.

$$sum \mathrel{+}= kernel[ky+1][kx+1] * X \qquad 2.21$$

In the above equation, 'kx' and 'ky' are between -1 and +1. The same is repeated for all the pixels to get the edges.

(a) Noisy ultrasound image

(b) Edge detection applied

Figure 2-28 Edge detection applied in ultrasound frame (a) Raw ultrasound image with multiple reflections (b) Edge detection application white outline for the edges and pink infill

We can see in Figure 2.28 that white edges are applied to all the blobs identified. The common problems in ultrasound image processing when it comes to blob detection are illustrated with blob detection applied on real-time Ultrasound images in Figure 2.29. These mainly include blob evolution, due to multiple reflections of the rigid object or merging of blobs into other adjacent blobs. Loss of tracking due to rapid movement resulting in rolling shutter effects can happen when the movement velocity of the surgical instrument is considerably high when compared to the respective frame rate of the ultrasound scanning system.

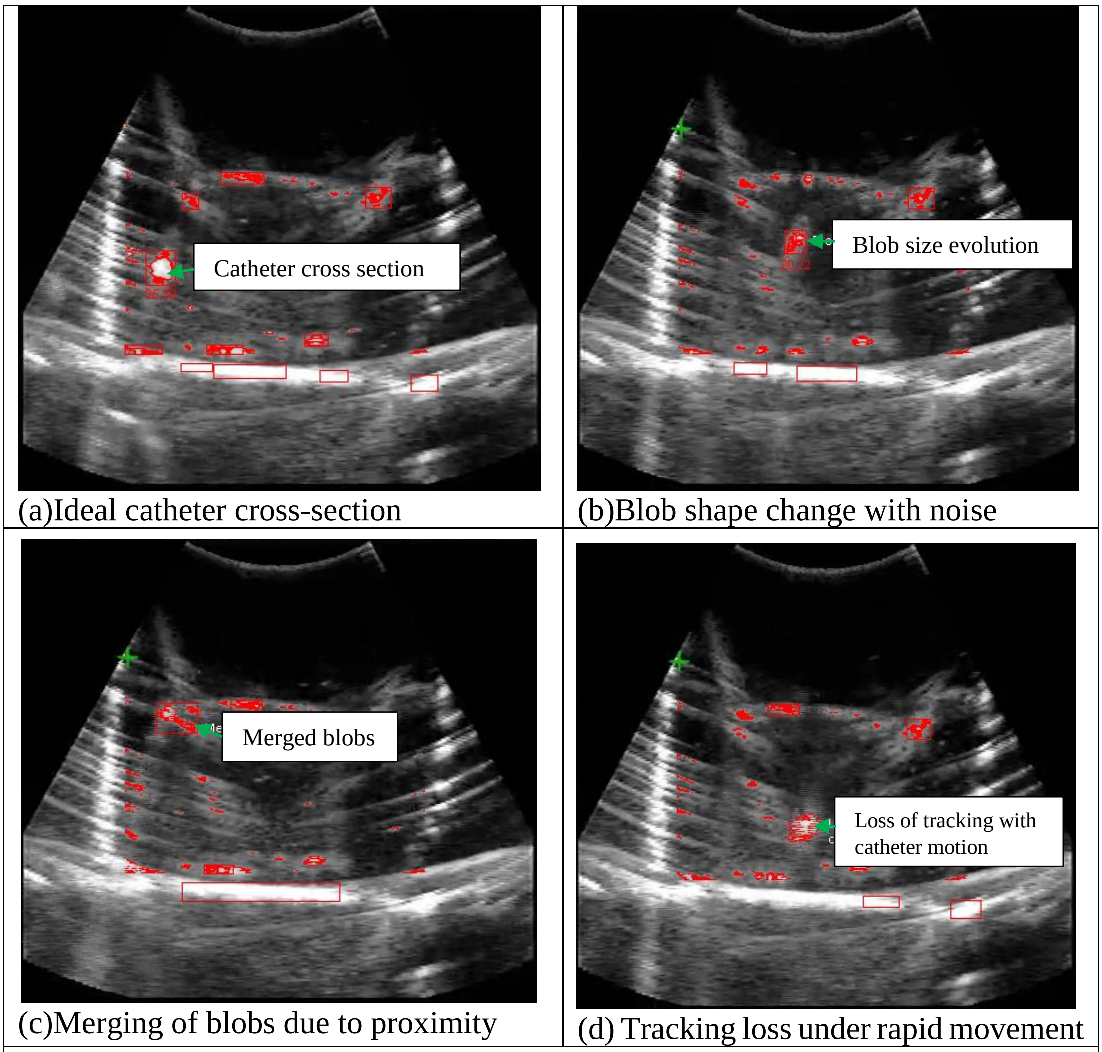

(a)Ideal catheter cross-section
(b)Blob shape change with noise
(c)Merging of blobs due to proximity
(d) Tracking loss under rapid movement

Figure 2-29 Common problems in ultrasound image processing with the conventional real-time image processing methods

In Figure 2.29, the image processing methods described earlier have been applied for blob tracking. The following observations can be made:

(a) image processing output showing ideal section, with fewer shadows of the catheter after encapsulated in polyurethane, when the catheter is held stationary

(b)shows blob size evolving to a smaller size (20,22) when the catheter is held static, closer to the ultrasound probe

(c) Shows 2 blobs merged together. Hence the blob is not identified with the set characteristic.

(d) Image processing output shows a section of the catheter in motion at 5mm/sec, resulting in a change of blob characteristic.

2.8.4 Summary and conclusion

Different commonly used techniques for blob detection of ultrasound images have been discussed and application of these algorithms are illustrated with real image processing output of ultrasound images. Since ultrasound is a real-time and dynamic imaging system, the images can have a lot of noise. Several features can be merged and may require complicated image processing algorithms if used for tip tracking. To reduce the amount of processing time, area of interest can be reduced. However, depending on the medium of imaging, rate of movement and several other parameters, sub millimetre accuracy is not possible in all cases. The area of interest can be determined manually or by merging with an alternative imaging or tracking system.

2.9 Optical tracking

Optical tracking is the process of identification of features in a video stream composed of an array of images. In terms of Infrared Optical tracking of retro-reflective markers, the marker locations are identified in 3D space and streamed across as coordinate positions. The initial technique involves tracking of blob centroids and application of noise filters to get resultant positions in cameras having pixel resolutions well above 640 x 480 per frame, combined with several levels of subpixel interpolation(Koivukangas et al., 2013). The observations are done from different perspectives, determined by the camera positions. The observations are later used in trigonometric calculations, resulting in X, Y and Z positions of the marker arrays. The process involved in optical tracking is described in Figure 2.30.

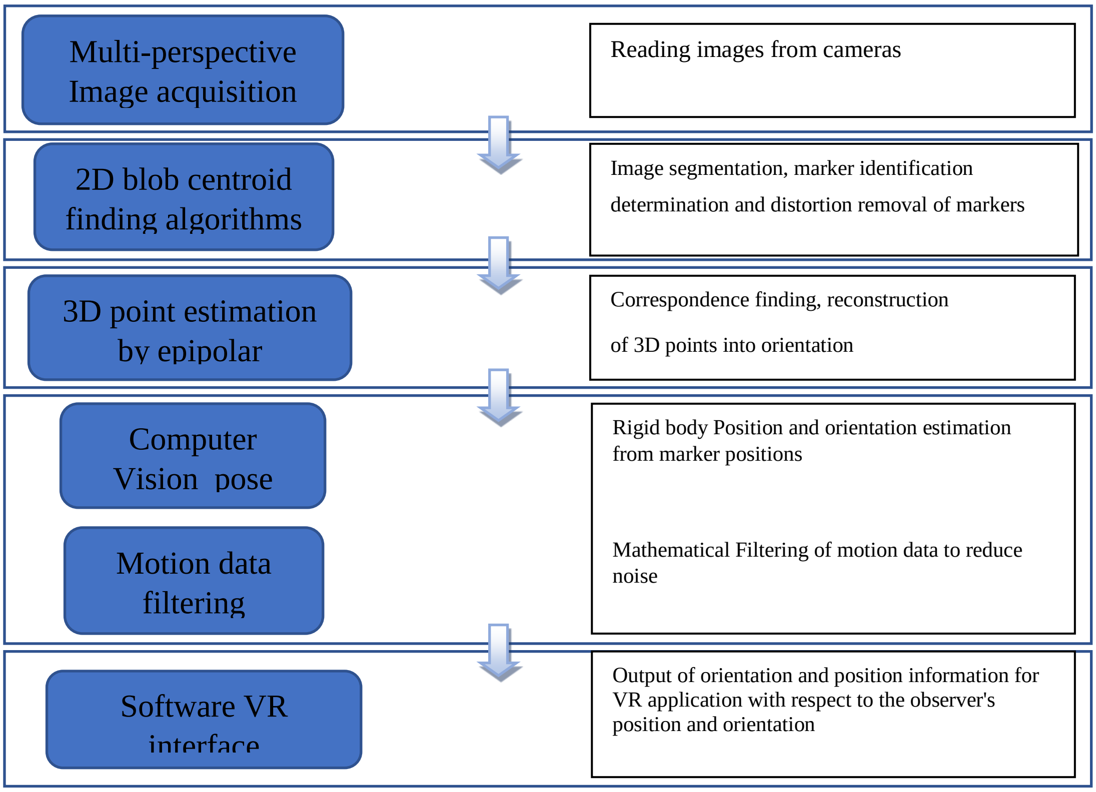

Figure 2-30 Overview of Optical tracking using multiple cameras

Marker combinations of 4 or more can be used to form rigid bodies, therefore would have a position and orientation in 3D space. Usually, a plane of reference is considered, and a minimum of 3 markers are placed on the plane. The coordinate positions are calculated with reference to the plane reference, instead of the actual camera itself.

2.9.1 Optical tracking marker localization

Post image processing algorithms to find the centroid of the blobs, the markers have to be localised from different camera perspectives from two calibrated cameras C1 and **C2** at known distance ‘***d***’. Consider a marker located at P***(x,y,z)***. It will be viewed by camera **C1** as P(x1, y1,z1) and camera **C2** as P(x2,y2,z2) as seen in Figure 2.31.

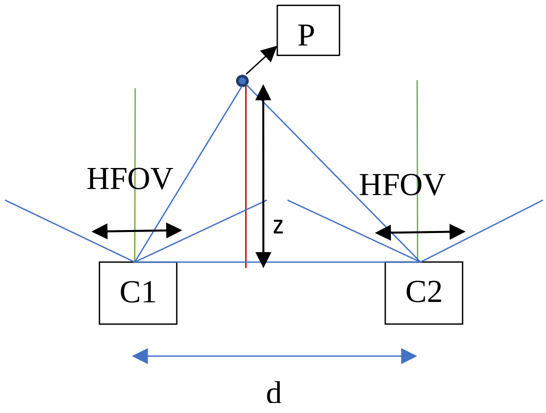

Figure 2-31 Two Cameras C1 and C2 at distance 'd' optically tracking a marker 'M.'

The horizontal field of view as seen in Figure 2.31, '*HFOV*' is the maximum extent of visibility in the horizontal direction. Field of view per pixel in the horizontal direction given as '*HFOVp*', per pixel in the vertical direction is '*VFOVp*' and the angular observations $'\theta x'$ and $'\theta y'$ by both the cameras is given in the below equations

$$HFOVp = \frac{HFOV}{(horizontal\ pixels)} \tag{2.21}$$

$$\theta x1 = 90 - HFOV1p \cdot x1 \tag{2.22}$$

$$\theta x2 = 90 - HFOV2p \cdot x2 \tag{2.23}$$

$$VFOVp = \frac{VFOV}{(vertical\ pixels)} \tag{2.24}$$

$$\theta y1 = 90 - VFOV1p \cdot y1 \tag{2.25}$$

$$\theta y2 = 90 - VFOV2p \cdot y2 \tag{2.26}$$

From (2.25) and (2.26), (x,y) coordinate point at distance z can be given by the following equations

$$Zx = \frac{d}{\cot(\theta x1) + \cot(\theta x2)} \quad 2.27$$

$$Zy = \frac{d}{\cot(\theta y1) + \cot(\theta y2)} \quad 2.28$$

For a point M seen by the camera C1 and C2, the 3D coordinate of position M(x,y,z) can be got from the following equations

$$Mz = \sqrt{(Zx^2 + Zy^2)} \quad 2.29$$

$$Mx = Mz/\tan(\Delta\theta x) \quad 2.30$$

$$My = Mz/\tan(\Delta\theta y) \quad 2.31$$

The output of the optical tracking systems for rigid markers, as suggested earlier is in terms of coordinate position and orientation of the centroid based on pose estimation calculations (Wu et al., 2016), which involve knowing the initial position of all the individual markers of the specific rigid body and calculation of the distance of the rigid body by using the average distance of the markers from the camera and the rotations from the relative orientation of the other markers to the centroid, with reference to the initial positions of registration (Wu et al., 2016).

2.9.2 Optical tracking problems

Optical tracking systems are well-established standards for surgical guidance in robotic and manual assisted surgeries (Ungi et al., 2016). Surgical optical tracking systems usually have 3 or less than 3 cameras as one unit, facing the targets from the front of the retroreflective or active (LED based) markers. Therefore, these systems do have their problems as stated below:

- Line of sight of the retro reflective or active optical markers should be maintained at any cost (Ungi et al., 2016)

- Markers are to appear the same (not covered with particles during the surgery)
- Two sets of optical markers, when seen by the tracking camera cannot be present too close(Ungi et al., 2016). More the distance of the 5 markers, better the accuracy. This can also result in marker confusion because of similarity between the markers.
- Angle of rotation of Yaw and pitch cannot exceed 90 degrees
- When the position or rotation changes to have two rigid bodies, very close to each other, closer than the minimum distance between the markers, marker confusion can occur.
- Calibration processes can be long depending on the procedure that was performed

2.9.3 Optical tracking for ultrasound problems and solutions

Problems due to optical tracking that are significant for ultrasound navigated surgery:

- Maintenance of line of sight
- Markers being covered by dirt
- 5 markers for every instrument can lead to blocking out of the other instrument
- Marker confusion can easily happen as the markers are close
- Principles of optical tracking and problems

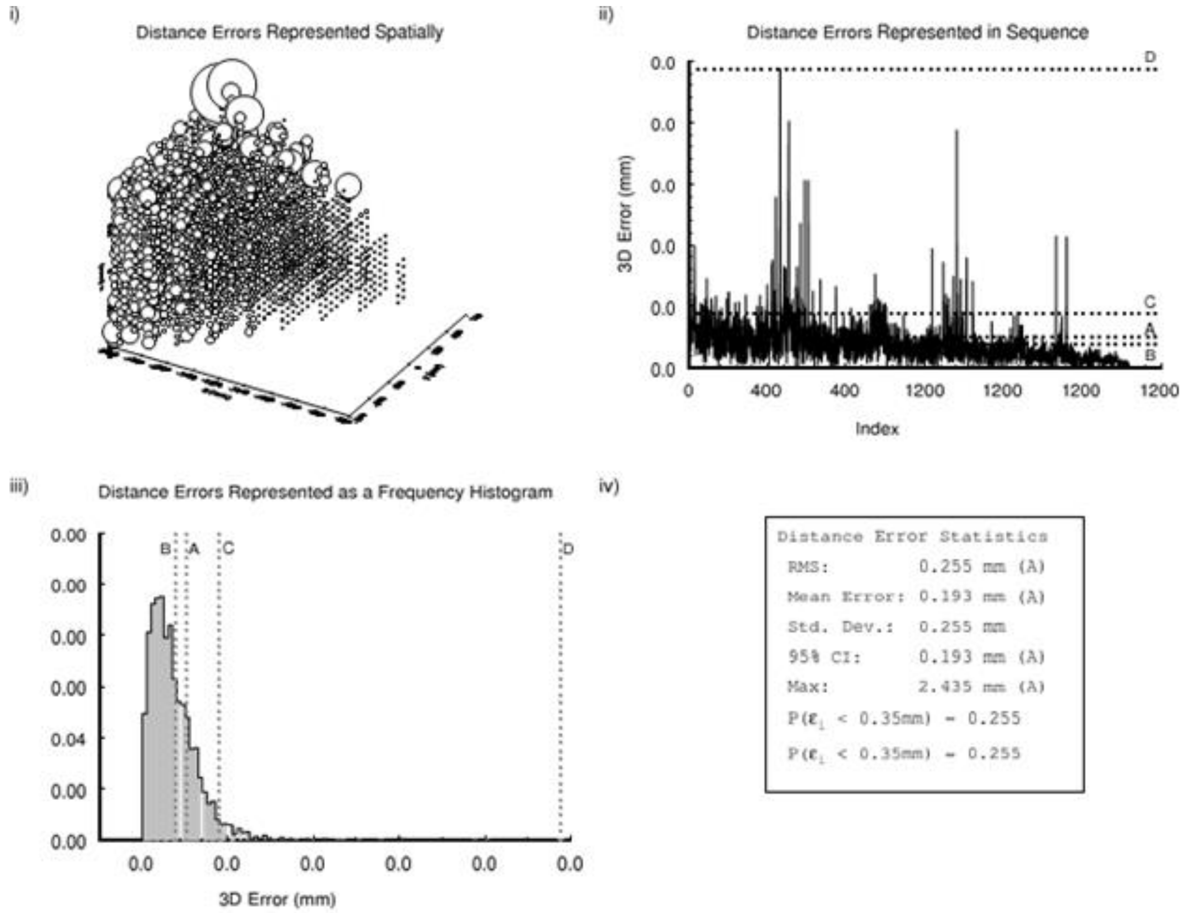

Figure 2-32 Accuracy of Optical tracking system from Naturalpoint Optitrack and the variation of accuracy with an increase in distance from the tracking base(Wiles et al., 2004).

In Figure 2.32, the loss of accuracy with an increase in distance of Optical markers in an optical tracking system is seen and can be up to 2.435mm when the Z axis distance from the tracking system is over two meters. Hence most optically tracked surgeries are performed are done within three meters distance from the tracking system. The same case will apply to Ultrasound guided minimal access surgeries. Table 2.17 compares the different commercially available optical tracking systems and their capabilities.

Table 2-17 Comparison of different commercially available Motion tracking systems (Koivukangas et al., 2013, Rahimian and Kearney, 2016, Song and Godøy, 2016, Stoll et al., 2012, Wiles et al., 2004)

Company name:	**Advanced Realtime Tracking GmbH**		**Motion Analysis Corp.**		**Northern Digital Inc.**		**Origin Instruments Corp.**	**Performance Technologies Inc**	**Qualisys Inc.**	**Vicon Motion Systems Limited**
Internet address:	www.ar-tracking.de		www.motionanalysis.com		www.ndigital.com		www.orin.com	www.peakperform.com	www.qualisys.com	www.vicon.com
Product name:	ARTtrack1	ARTtrack2	Eagle Digital System	Falcon Analog System	Optotrack 3020	Polaris	DynaSight Sensor	Peak Motus	ProReflex	Vicon 8i
RMS accuracy:	0.5 mm (at 1.5 m)	0.6 mm (at 1.5 m)	*	*	0.1mm (at 2.25 m)	0.35 mm (at 2-2.5 m)	0.1 mm (at 80 cm)	*	*	*
Number of cameras:	4	4	64	32	3	2	2	2 to 12	up to 32	up to 24
Frame rate:	60 Hz	60Hz	up to 480 Hz	up to 120 Hz	up to 750 Hz	up to 60 Hz	up to 65 Hz	60 Hz	up to 1000 Hz	up to 120 Hz
Maximum number of tracked markers:	60	15	*	*	256	6 tools per 6 markers	4	*	150 (at 60 Hz)	200
Field of view:	60° Azimuth, 45° Elevation	69.6° Azimuth, 55.3° Elevation	*	*	*	*	75° Azimuth, 75° Elevation	*	*	*

2.9.4 Conservative solutions to problems faced due to optical tracking

Optical tracking is one of the most accurate system for medium range motion tracking and therefore cannot be eliminated altogether because of its problems with line of sight associated problems.

2.9.4.1 Line of sight

The line of sight maintenance can be accomplished by planning the surgery in such a way that the perspective of the markers to the camera is always clear and there is no combination of the movements resulting in the markers being covered.

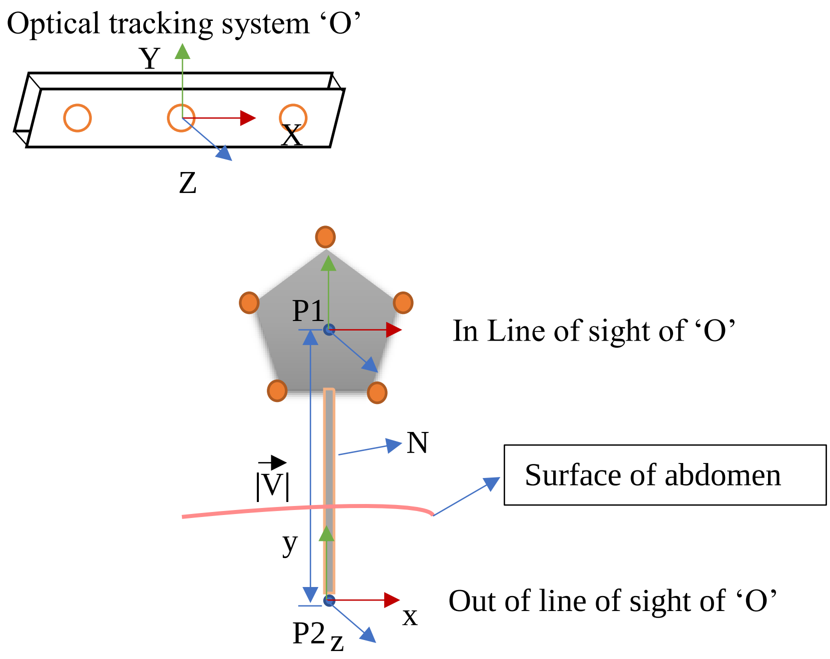

Figure 2-33 Proposed dual marker system with 2 IR leds, one IR camera with image processing integrated on a cortex M4 processor

In cases where the tip of a catheter or a needle needs to be identified, the base of the needle needs to be optically tracked in 6 DoF using a set of markers, which are in view of the tracking system. For example, the setup shown in Figure 2.33 has an optically tracked base with centroid '***P1***' for a needle '***N***' with a needle tip '***P2***'. Since the tip will always maintain its distance '|***V***|' which when represented as a vector '***V***' has x,y and z components. The positional and orientation relationship between the base and its optical centroid '***P1***', the tip can further be calibrated by placing a temporary optical marker on the tip, which can be removed later. The relationship between the tip '***P2***' and the optically tracked centroid can be given as:

$$\mathbf{P2(x,y,z)} = \begin{vmatrix} \mathbf{1} & \mathbf{0} & \mathbf{0} & \boldsymbol{P1x} \\ \mathbf{0} & \mathbf{1} & \mathbf{0} & \boldsymbol{P1y} \\ \mathbf{0} & \mathbf{0} & \mathbf{1} & \boldsymbol{P1z} \\ \mathbf{0} & \mathbf{0} & \mathbf{0} & \mathbf{1} \end{vmatrix} . \begin{vmatrix} \boldsymbol{Vx} \\ \boldsymbol{Vy} \\ \boldsymbol{Vz} \\ \mathbf{1} \end{vmatrix} \qquad \mathbf{2.32}$$

$$P2 = P1 + V$$

The distance of the marker from the tip |V| remains a constant irrespective of the orientation of the fetoscope. But, since the orientation of the tip changes with rotation about P1(x,y,z) as the centre, the sub components of the vector V(x,y,z) change. Therefore the rotated P2(x,y,z) by an orientation value '***R***' can be given by:

$$P2(x,y,z) = P1 + V.R \qquad 2.33$$

The rotation '*R*', when represented in quaternion form has 4 components '*qx*', '*qy*', '*qz*', '*qw*' and can be represented by:

$$\mathbf{R} = \begin{vmatrix} 1-2qy^2-2qz^2 & 2qxqy-2qzqw & 2qxqz+2qyqw \\ 2qxqy+2qzqw & 1-2qx^2-2qz^2 & 2qyqz-2qxqw \\ 2qxqz-2qyqw & 2qyqz+2qxqw & 1-2qx^2-2qy^2 \end{vmatrix} \quad 2.34$$

2.9.4.2 Markers being covered by matter

Passive markers like retro-reflective markers can get covered with matter, which can result in the loss of tracking and change in marker shape, thereby resulting in lowered accuracy. However, with active markers like IR LED markers, the incidence of marker loss can be reduced, though not eliminated altogether. A typical active marker based tracking is used in OPTOTRACK 3020 (Northern Digital) resulting in a reported accuracy of 0.1 in the X and Y axes and 0.15 in the Z axis, while POLARIS (Northern Digital) tracking system using spherical retro-reflective markers is reported to have an accuracy of 0.35mm (Sugano, 2003) Also, the wavelengths of IR in the order of 800 to 940 nm can easily penetrate most organic matter especially subchondral bone (Padalkar and Pleshko, 2015). Table 2.18 describes the types of markers used commonly in surgery and biomechanics.

Table 2-18 Types of markers and comparison of their characteristics

Marker type	Visibility	IR range	Description	Switching	Disadvantages
Passive spherical	All sides	4 to 10m	Retroreflective ball	Not possible	Needs IR source
Passive flat	Limited 45 degrees	4 to 10m	Retroreflective surface	Not possible	Needs IR source
Active single LED	Limited to LED FOV	<10m based on intensity	LED with linear power supply	Possible	Powered actively
Active single LED with diffuser	Almost all sides with uneven beam intensity	Depends on intensity but range is lower than without diffuser	LED with linear power supply	Possible	Powered actively, quality of diffuser

2.9.5 Problems without simple solutions

Problems induced by large number of markers, marker over riding and inter marker confusion within a rigid body, do not have any simple solutions. Therefore, newer or alternative methods of tracking maybe required.

2.9.5.1 Number of markers

The number of markers used in optical tracking results in occupation of a larger volume, which in-turn can result in one set of markers blocking the other. The chances of markers overriding increases with the increase in the number of markers. The currently available optical tracking systems require at least 4 four markers to give an almost constant 6 DoF tracking. But using 5 Markers ensures more reliability and avoids the occasional cases of 180 degrees flipping of marker orientation when the rotation angles become close to 90 degrees (Pintaric and Kaufmann, 2008).

Also, usage of smaller markers or close placement of individual markers can lead to higher orientation errors (Yoon et al., 2006). Hence there is no simple solution to this problem. Table 2.19 shows a comparison between different commonly used optical tracking systems. Though the accuracy of such systems can be sub millimetre, the distance of the tracked object from the tracking system and the angle at which the markers are present or the distance between different rigid bodies can cause confusions. Therefore, the accuracy of these systems is valid only under specific conditions of distance and orientation with respect to the tracking base.

Table 2-19 Comparison of different commercially available optical tracking systems (Andrew D. Wiles et al.)

Company name	Markers	Sampling Rate (frames/sec)	System Resolution(mm)	Precision(mm)	System Accuracy (%)
Optitrack	Passive	50-100	0.63	-	94.82
Vicon	Passive	120-250	1.49	-	98.30
Optotrack	Active	50	-	0.03	98.44
Cortex(MAC)	Passive	200	-	-	-

2.9.5.2 Marker overriding

The incidence of marker overriding can increase with the increase in the number of markers and the increase in size/ distance of the markers. But the accuracy of the optical tracking pose estimation equations entirely depends on the distance between the markers as the primary reference and the performance degrades with a decrease in the distance of markers. We find that the rotational errors increase with a decrease in distance between the markers from the design considerations for markers suggested by Pintaric et.al (Pintaric and Kaufmann, 2008). Therefore, there is no simple solution for this problem.

2.9.5.3 Marker confusion

Marker confusion can happen due to one set of markers being in close proximity to the other set of markers. The problems with marker confusion require novel designs for marker placements to avoid confusion and spacing (Pintaric and Kaufmann, 2008). Another reason for marker confusion can occur because of change in marker ordering, which can occur when the markers rotate quickly. One proposed method of avoiding marker confusion is by using active markers, as they are switchable and hence can be switched to a passive state when the confusion occurs for a period of time, after which it can be turned on for regular tracking.

Though this technique is doable, the complexity to achieve this is quite high. This is because it involves a 2-way radio communication link between the tracking base computer and every active marker. This can also result in a period of latency, as the solution involves turning the LEDs off momentarily and turning them back on to ensure that the rigid bodies tracked are identified correctly. However, since the optical tracking frame rate in most systems are more than 100 Hz, the systems can get away with the latency created by the information transfer between the computer and the respective active elements.

2.9.6 Summary and conclusions for optical tracking

In this section, it can be observed that, though commercial optical tracking systems are consistently used in surgeries, there are problems like marker overriding, marker spacing and line of sight which can greatly reduce the usability of the optical tracking system in ultrasound navigation. Further, the problem of marker confusion cannot be solved without making active modifications to the currently existing optical tracking system. Hence, a different approach to conventional optical tracking is necessary to reduce the number of markers and the incidence of marker confusion.

2.10 Conclusions- Fetal surgery: encouraged by clinical experience and boosted by innovation

This review briefly introduces fetal development, some developmental anomalies in fetuses and their current modes of management. The review then discusses the different procedures performed and their effectiveness. It also delved into the differences between MIS and MAS; the difficulties faced during the procedures; the importance of navigation guidance, force perception, and robotics in surgery to tide across the aforesaid difficulties have also been discussed. Further, it has been evidently proven that technological improvements in navigation and robotics with respect to MIS are far ahead of the ones used in MAS and that if a different approach is used to make a custom hardware and software interface, with less time consuming for registration processes, more fetal surgeons may adopt MAS for fetal surgeries, as in the case of Orthopaedic surgeries.

Use of tracking and navigation for minimal access surgeries has been suggested as a solution to problems with tracking and orientation in ultrasound guidance. Image processing for ultrasound, currently available technologies for tracking and navigation and dexterity have been discussed. From the comparison between tracking systems, it can be found that despite the disadvantages of optical tracking, it is more reliable for use in Minimal Access procedures because of the accuracy, insensitiveness to ferromagnetic materials used in surgical instruments and robotics. Since marker crossing over can be a major problem in ultrasound guided procedures, it demands special methods of resolution.

Experienced fetal surgeons such as Prof. Kypros Nicolaides, Prof. Jan Deprest and many others have suggested in their publications that advancement in technology can lead to further success in fetal surgical procedures and can also lead to wider acceptance (Danzer et al., 2003, Deka et al., 2012, Deprest et al., 1997, Deprest et al., 2006, Deprest et al., 2011, Farmer, 1998, Fowler et al., 2002). From the afore said literature, the need for smart handheld instruments compatible with real-time imaging and inbuilt robotics for surgical safety and overshoot prevention with force-feedback can be realized. Lastly, the optimal modalities of real-time imaging and tracking have been narrowed down based on the data available from the literature.

The considerations of the literature reviewed are made the aims of the thesis outlined.

Chapter 3

Design and development of optical tracking system for ultrasound navigation

3.1 Introduction

From the previous section, it is evident that conventional optical tracking system, though very accurate has problems such as marker spacing, number of markers, marker overriding, 'marker confusion' and a combination of the factors discussed in the literature review. This chapter discusses a possible solution to the problems faced during rigid body tracking processes in conventional optical tracking system. The above stated the problems along with the volume occupied by the markers can lead to problems such as tracking loss and errors in tracking especially in a surgery where equipment and instruments are close (as in fetal surgery- ultrasound probe and fetoscope).

3.2 Aims

This chapter aims at solving the problems caused by using over 4 markers, marker confusion and reduction of the marker volume by design and development of a novel optical tracking system. Such a system will have lesser number of markers and thereby reducing confusion.

3.2.1 Optical tracking system target specifications

Optical tracking systems with the following characteristics are desired:

1. Sub-millimetre tracking accuracy
2. Large volume of tracking usually > $4m^3$
3. No incidence of marker confusions
4. Low volume of markers/ less interference of markers with the surgical procedures
5. Ability to work I proximity with other optical tracking markers, or eliminate crossing over problems entirely
6. High frame rates minimum 30 usually >100 in commercial systems

3.3 Methods

The dual marker based active tracking system is composed of a base camera and a mobile camera with markers. Therefore, has lower number of markers compared to the conventional optical tracking methods, has reduced probability of confusion and wider-angle range which will be discussed later in this chapter.

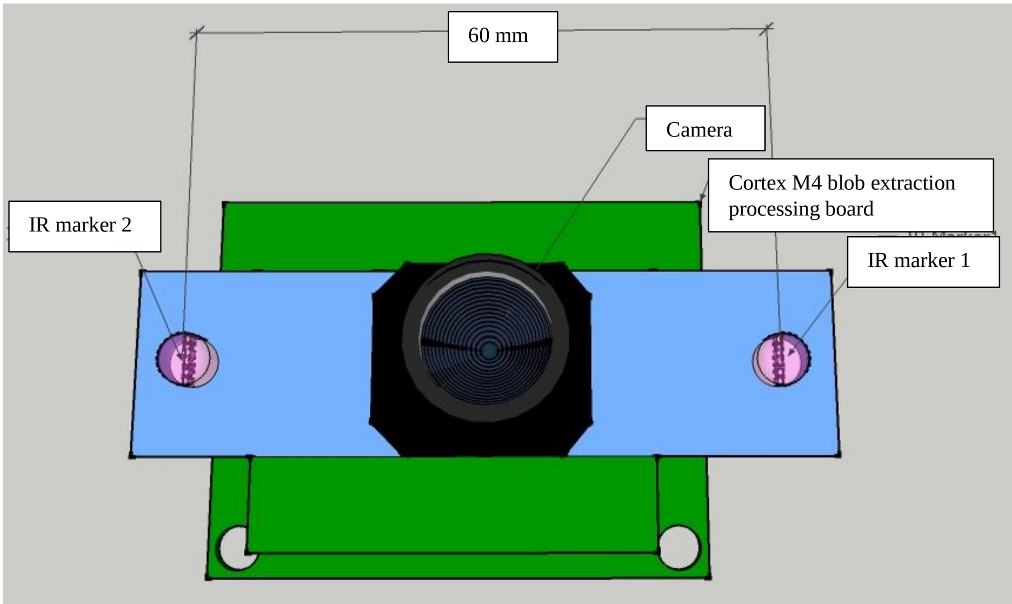

Figure 3-1 Proposed dual marker system with 2 IR leds, one IR camera with image processing integrated on a cortex M4 processor

Figure 3.1 shows the proposed dual active IR marker system with IR camera and on-board blob extraction algorithm implemented in the cortex M4 processor. The system has the following specifications:

1. 2 800nm IR LEDs with duty cycle control

2. 640 × 480 pixels camera at the centre of the IR markers

3. On board image processing capable of 30 FPS from OPENMV

Geometric parameters of the dual marker system

1. The IR LEDs ae placed at 60mm and can come inline only when there is extreme pitch rotation ≈ 90 degrees.

2. Yaw rotation does not affect the marker visibility

3. Roll rotation does not affect the marker visibility

4. Camera ‘s image frame centre is at the centre of the LED markers

Table 3.1 shows how a rigid body marker unit containing about 5 markers can occupy more volume than a dual-marker based system, which only has a length dimension. Also, the probability of distance confusion when there is more than one similar distance within the rigid body. For example, when the rigid body is rotation is very high, when compared to a dual-marker system which has only the possibility of crossing of markers with extreme rotation. Inter marker distances can be crucial in the case of navigation guided surgeries because markers can come into close proximity, increasing the probability of tracking loss because of mathematical uncertainty in pose estimation calculation. Whereas, inter-marker distance problem can be dealt using active control of the markers. For example, in a two-active marker system by turning of the active markers either periodically or as a closed loop in synchronization with the tracking base. Thus, overriding problems can be avoided in two-marker system.

Table 3-1 Comparison between the marker placement configuration in a conventional optical tracking system and the proposed optical tracking system

Conventional rigid body markers for 6DoF tracking	**Novel optical tracking system with active markers**
Volume occupied is high 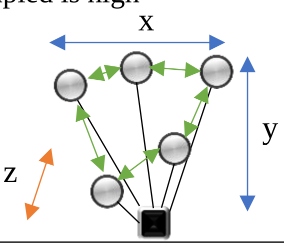	Only planar distances used 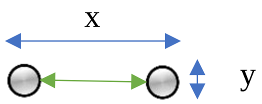
High probability of Inter marker similar-distance confusion 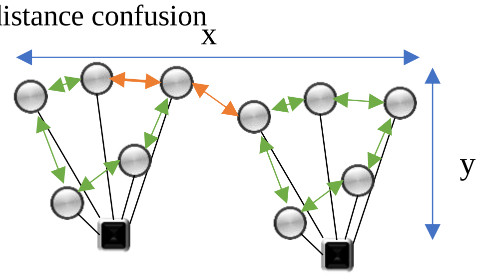	Low probability of Inter marker similar-distance confusion and elimination possible using active markers 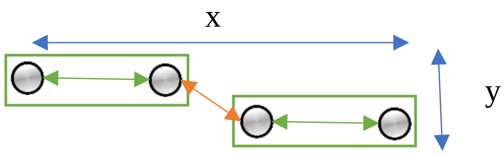
High probability of Intra marker similar-distance confusion 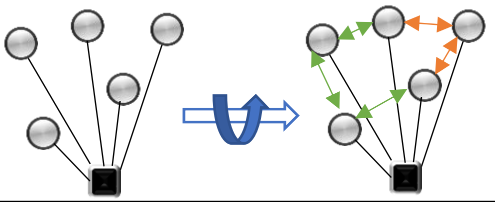	Intra marker similar-distance confusion can occur only when the two single markers cross over 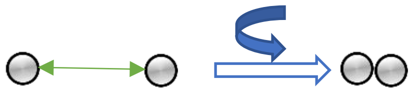
High probability of Intra marker crossing over 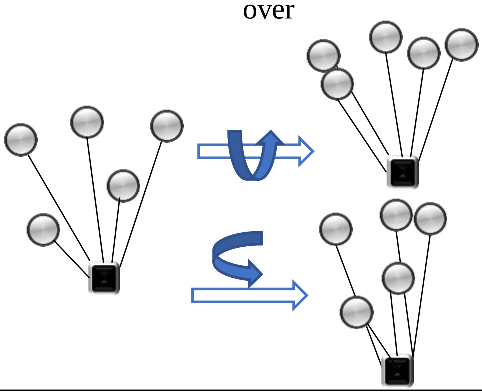	Intra marker similar-distance confusion can occur only when the two single markers cross over 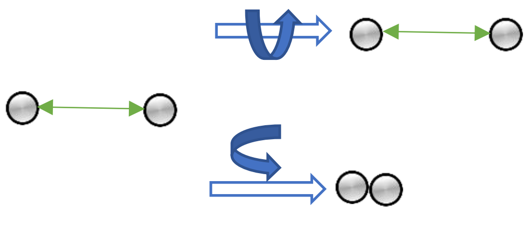

.

3.4 Requirements for ultrasound guidance assisted by 6 DoF tracking

From the conclusions of the literature review on Minimal Access Surgery requirements in dexterity and navigation, we can infer the following as requirements for optical tracking to be usable in ultrasound guided surgeries:

1. An accurate and precise reference for refining ultrasound tracking.
2. Frame rates much higher than that of ultrasound, to compensate for the delays in multimodality tracking calculations.
3. Multiple closely placed instruments to be tracked reliably without loss of tracking or rigid body confusion
4. Maximum intra -marker spacing should not interfere with other medical instruments during surgery.
5. Active markers, to avoid inter-marker confusion and the chance of being covered by matter.

3.5 Primary requisites of an accurate optical tracking system

For any system to be accurate, the measurement transducer is required to have a reasonably high resolution. In this case, the transducer is a CCD camera and the maximum measurement distance is 2.5 metres. with 640 x 480 pixels resolution.

3.5.1 Calculation of resolution

The resolution of a camera tracking system is dependent on the Field Of View of the camera and the pixel resolution in the horizontal and vertical directions. This can be given by:

Horizontal Field Of View ‘HFOV’ = 115 degrees

Vertical Field Of View ‘VFOV’ = 115 degrees

3.5.1.1 X Axis resolution calculation

The resolution on the X- Axis is usually higher than that of Y- Axis because of the higher number of pixels along the X axis. At 1 m distance, the resolution is 3.13mm.

Maximum attainable (X-Axis) 1-point resolution in mm at 2.5m distance is 7.83 mm.

Maximum attainable (X-Axis) 2-point resolution = single point distance / 2 = 3.91mm.

3.5.1.2 Y Axis resolution calculation

Y- Axis can have the same Field Of View but the number of pixels along the Y- direction can be lower than in the horizontal direction. This is because of the way the CCD chips in the camera are constructed. So, Y Axis resolution is usually lower than X axis resolution.

VFOV = 115 degrees

VFOV per pixel = 115/480 = 0.23 degrees or 0.0041 radians

At 2.5 meters distance,

Maximum attainable (Y-Axis) 1-point resolution in mm at 2.5m distance is 10.45mm.
Maximum 2-point Y axis resolution at 2.5 m is 5.22 mm.

Therefore, without advanced forms of sub- pixel interpolation, optical tracking systems cannot attain sub-millimetre accuracy.

3.5.2 Bicubic Interpolation:

In the previous section, it has been discussed that better tracking accuracy can be achieved only using sub-pixel interpolation. Bicubic interpolation is a commonly used technique for optical tracking applications. In order to achieve bi-cubic interpolation, let us consider an image $I = f(x_1, x_2)$, as a two-dimensional array of pixels from a camera. Bicubic interpolation was described for digital image processing in 1981 and has been common knowledge since then. (Keys, 1981, Hinz, 2005) ../

Onboard processing of sub-pixel interpolations has a very high processing load, require large frame buffers, multiple floating-point precision and doable, mostly in a high-end FPGA environment or dedicated processors. All the above can be implemented in a dedicated project. However, since they are out of the scope of the current project, the feasibility of the system without sub-pixel interpolation will be demonstrated and evaluated at a one-meter distance.

3.6 Requirements Optical tracking system in navigated ultrasound surgery

Ultrasound guided Minimally Invasive Surgeries, unlike laparoscopic surgeries, make use of only one operator- the surgeon. Therefore, the fetoscope and the ultrasound scanning probe are in full control of the surgeon(Klaritsch P and surgery., 2009). Depending on the choice of handedness for handling the ultrasound probe and the hand tool, and the convenience, the ultrasound machine is placed, as shown in Figure 3.2. The optical tracking base location depends on the type of procedure performed, as optical tracking is a line of sight system and requires all the markers to be seen in their entirety throughout the procedure.

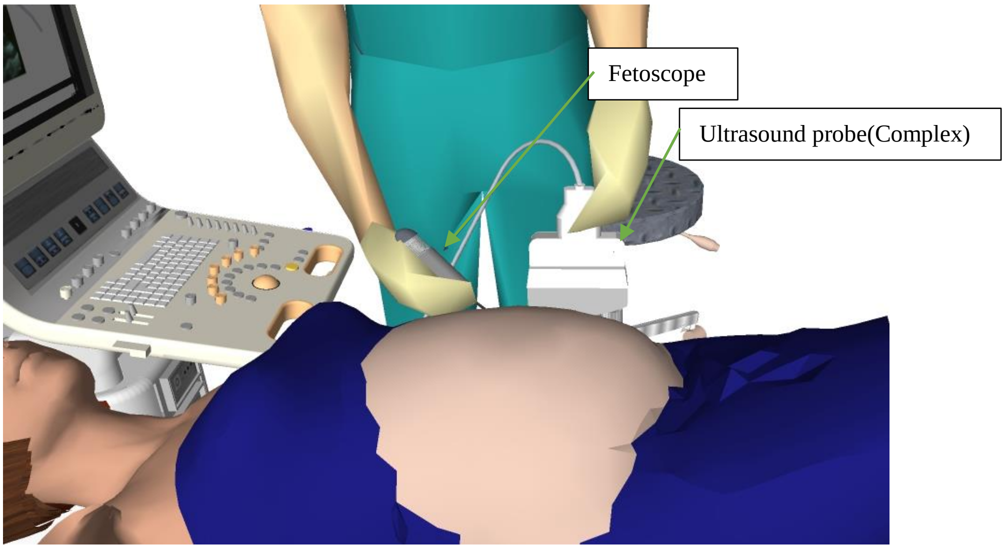

Figure 3-2 Orientation of surgeon with respect to the patient and the fetoscope

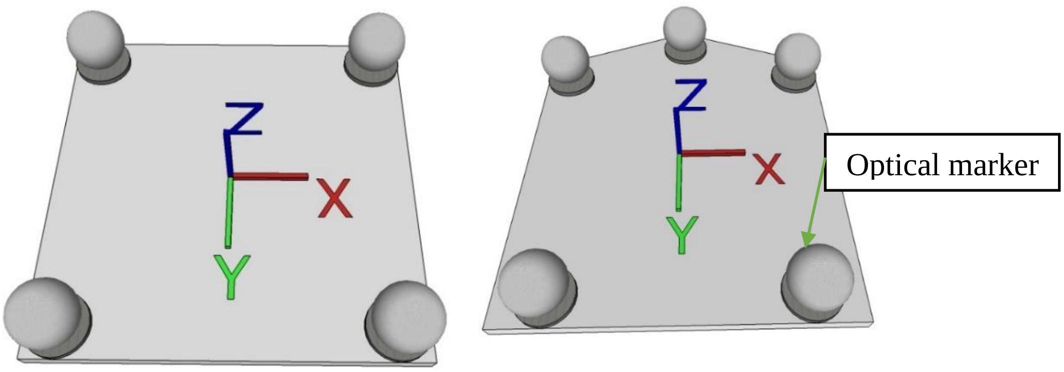

(a) 4 optical trackers forming a rigid body

(b) 5 optical trackers forming a rigid body

Figure 3-3 Configurations of optical markers. Symmetric configuration (a) is unstable, and rotations can be switched to the negative direction. Configuration(b), the 5th marker leads to consistent asymmetry(Yoon et al., 2006)

In principle for optical tracking, we require at least 4 markers to get all 6 DoF. The 4-marker configuration seen in Figure 3.3 (a) is symmetrical and hence pose estimation can result in more than one mathematical solution. The 5-marker configuration in Figure 3.3 (b) is more accurate and directionally stable, as pose estimation requires at least one asymmetry to be reliable. Also, marker ordering is highly essential for the pose estimation algorithms to be applied. Symmetric markers can cause confusion in marker order, thereby resulting in orientation problems.

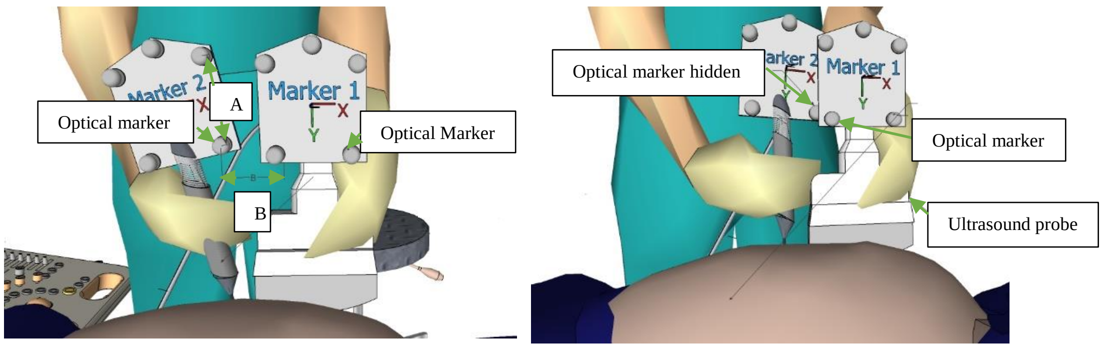

(a) Rigid bodies in proximity

(b) Rigid body loss of tracking

Figure 3-4 Marker confusion due to cross-over Intra-marker distance is A, and inter-rigid body(Marker1 to Marker2) distance is B. When B<A there is a complete loss of tracking.(b) Marker overriding resulting in loss of tracking(Yoon et al., 2006)

Figure 3.4 (a) shows a case where there can be a loss of rigid-body tracking because of proximity, where the intra marker distance ‘A’ is higher than the inter-rigid body distance ‘B’, thereby resulting in confusion in pose estimation calculations. Figure3.4(b) illustrates a condition where there is overriding of optical tracking markers, resulting in complete loss of tracking of the ‘Marker2’ and confusion in tracking ‘Marker1’. Both the scenarios can be avoided, provided the number of markers is reduced to minimum and marker ordering confusion can be avoided by using active markers and controlling them from the base unit actively when the base unit recognises a confusion of individual marker ordering(Pintaric and Kaufmann, 2008).

In the case of fetal surgeries, the position of the tracked instruments can be in close proximity to the ultrasound probe. Hence there can be easy overriding of markers, leading to ‘marker confusion’ and errors(Pintaric and Kaufmann, 2008). Hence, an alternative approach to the tracking system with a lesser number of markers becomes necessary.

3.7 Development of a low marker count active optical tracking system

From the previous section, the following design considerations for the new optical tracking system are recognised:

(1) Only 2 markers required
(2) Preserving 6 Degrees of freedom
(3) Reducing marker confusion

The tracking system has been designed with two active markers and a camera on the ‘Mobile’ handheld equipment’ and the same configuration for the ‘Base’, ‘B’, offering a stationary perspective of the mobile unit and a mobile perspective of the stationary unit. The stationary perspective of the mobile unit can be used for translation calculations of the mobile unit, and the mobile perspective of the stationary unit can be used to find the orientation of the mobile unit with respect to the stationary unit’s principal axis, after tilt correction due to translation effects. Thereby, yielding 6 Degrees of Freedom based on perspective geometry.

Multiple mobile equipment tracking can be done with the same principle, and the Marker confusion can be avoided by temporarily turning off the active markers on the respective unit, whenever confusion due to marker ordering happens, and the corresponding labels are applied.

3.7.1 Perspective observations during the process of transformation

Perspective geometry calculations applied to tracking environments require a minimum of 2 perspectives of view to determine the 3-Dimensional location of the optical markers. In the case of the current tracking system, we have the perspective of a pair of markers from a stationary camera and another perspective of the other pair of markers from the mobile camera, thereby satisfying the requirements of 6 DoF tracking.

3.7.1.1 Perspective observations of the stationary unit by the mobile unit

The perspective observations of the stationary unit by the mobile unit and vice versa result in unique observations for every set of translations and rotations. Though the above is the case, to separate the translational effects of rotation and the rotational effects of translation and to also isolate every rotation without the influence of other rotations is essential for successful tracking.

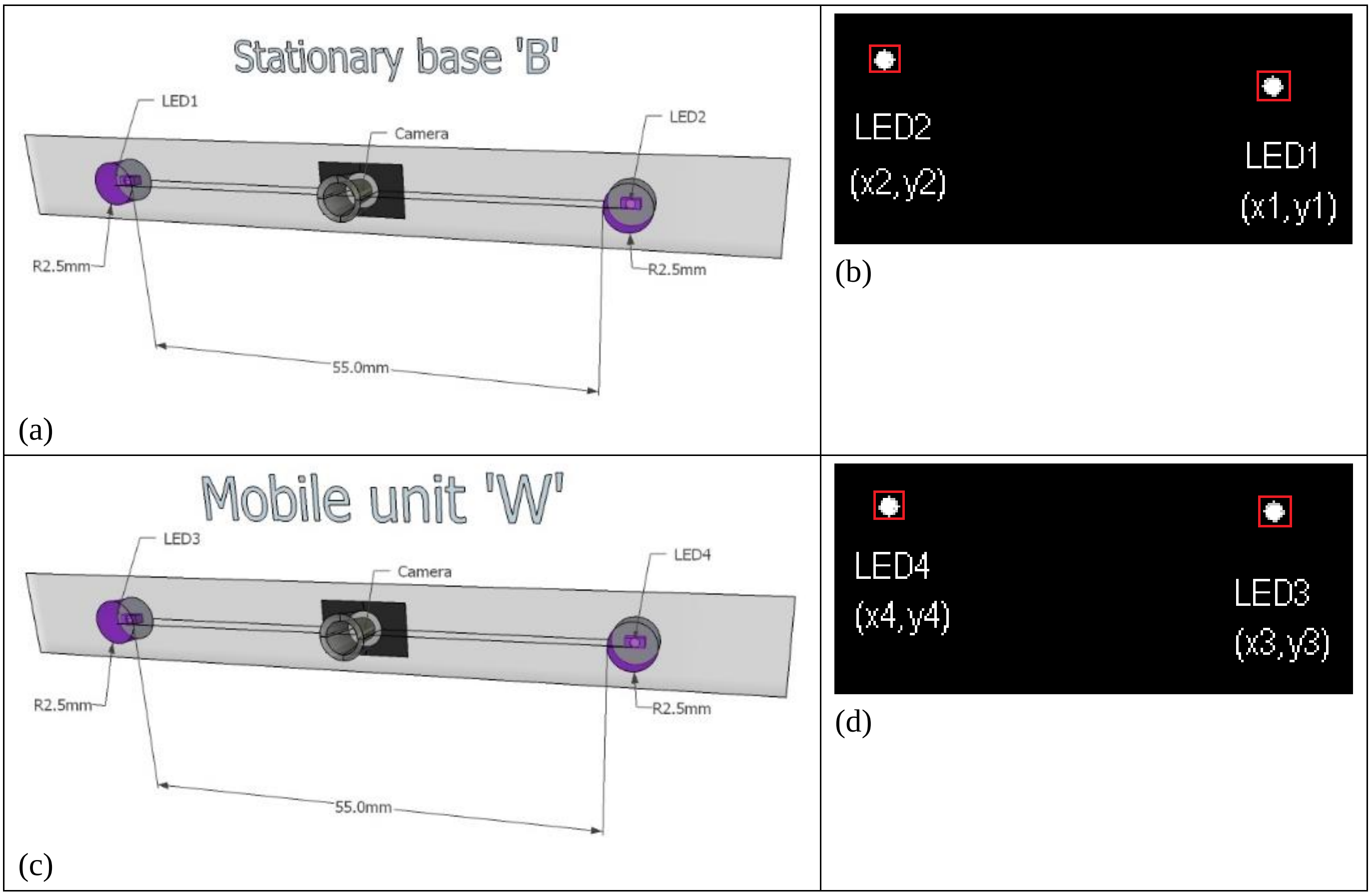

Figure 3-5 Stationary unit perspective 1 (a)Stationary base and (c) mobile unit with 2 LEDs at 60 mm distance between each other with a camera placed in the centre. (b) and (d) showing LEDs seen by an IR camera

As seen in Figure 3.5(a), the stationary unit has 2 IR LEDs at 60mm from each other and a camera at its centre. To an IR camera viewer, only the LEDs are visible as two bright spots, as seen in Figure 3.5(b). Figure 3.5(c) mobile unit has the same configuration of LEDs and camera. Figure 3.5(d) shows the LED output as visualised by an IR camera as before.

When the above two units are placed in front of each other, in such a way that the LED markers on one unit are visible to the camera of the other unit, two perspectives for the location of the LED pairs are obtained, as seen in Figure 3.6. The centre of the stationary camera in the given case forms the origin of the coordinate system. When there is no rotation of the mobile unit '*W*' with respect to the stationary base '*B*', the centroid of the LEDs 1,2,3,4, as observed by the respective cameras is equidistant from the corresponding origins in the image plane.

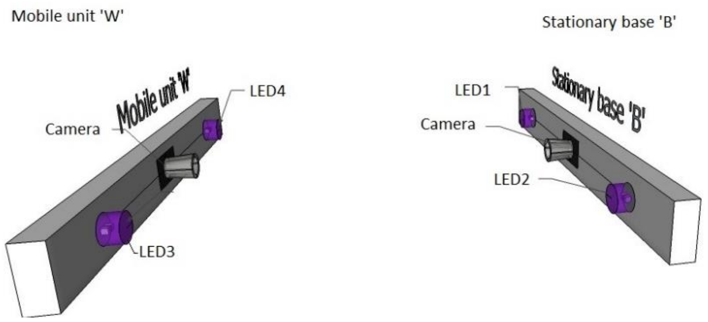

Figure 3-6 Stationary unit perspective 2. Stationary unit and Mobile unit facing each other. LED1&2 are visible to Mobile unit camera '*W*', and LED3&4 are within the Field of View of the Stationary base camera '*B*'.

3.7.1.2 Mobile unit perspectives with rotation

In the figures given in this section, observations of the mobile unit camera 'M' with respect to the static unit 'B' markers are illustrated for every possible case of rotation.

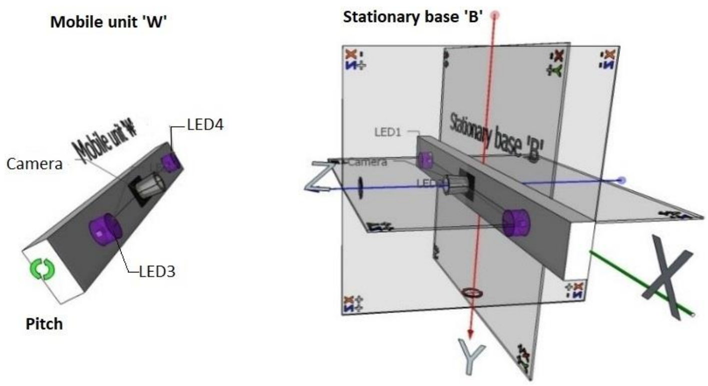

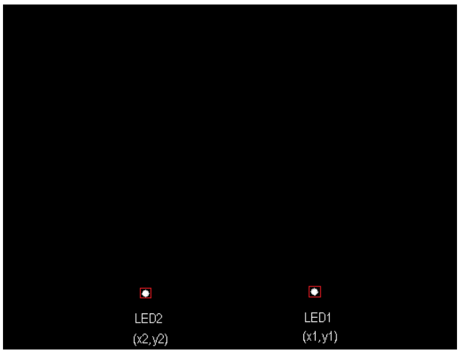

(b) Mobile camera image plane

(a) Rotation of mobile unit along X axis

Figure 3-7 Mobile unit perspective 1 (a) Mobile unit '*W*' is rotating along its X-axis respect to the Stationary base '*B*'. (b)The stationary unit '*B*' LEDs as seen by the mobile unit camera move down when the pitch increases and vice versa

Figure 3.7 shows a case where the mobile unit rotates about its X axis (Pitch) with respect to the stationary base '*B*'. The observed marker centroids from the perspective of the mobile unit shift up and down and is inversely related to the angle of rotation.

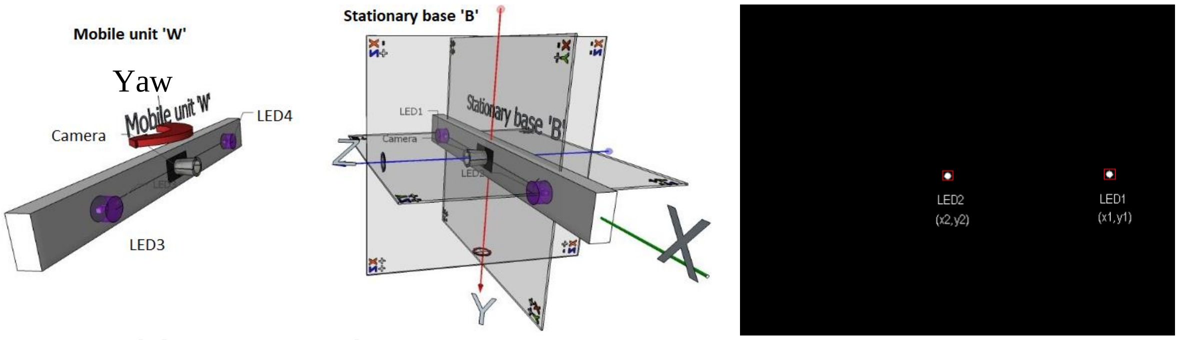

(a) Mobile unit rotation about Y axis (b) Mobile camera image plane

Figure 3-8 Mobile unit perspective 2. Mobile unit rotates about its Y-axis or Yaw with respect to the stationary base B. The stationary unit B LEDs when observed by the mobile unit seem to move from left to right when the pitch increases

Figure 3.8 shows a condition where the mobile unit is rotated along the Y-Axis with respect to the stationary base. The angle of rotation is inversely related to the centroids of the marker blobs seen by the mobile camera and the movement is in the transverse direction.

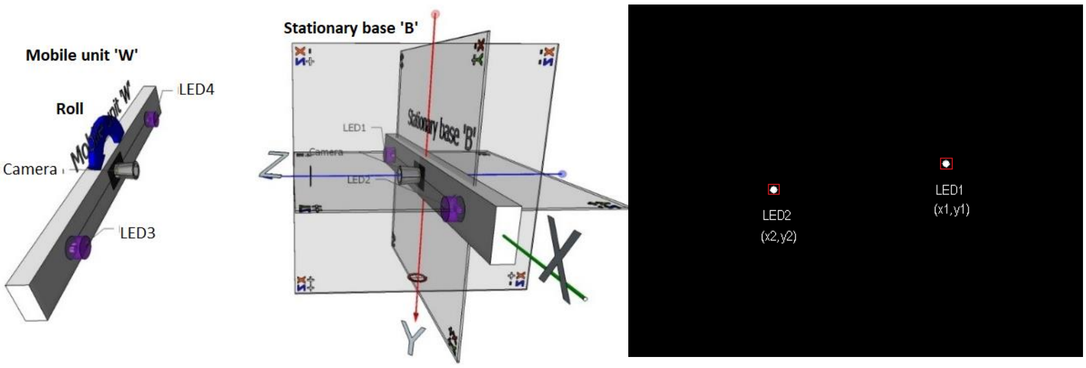

(a) Mobile unit rotation about its Z axis (b) Mobile unit image plane

Figure 3-9 Mobile unit perspective 3. Mobile unit rotates about its Z-axis with respect to the Stationary base. The line drawn between the LEDs is observed to tilt proportional to the Roll of the Mobile unit - Stationary unit perspective with translation of the Mobile unit

In Figure 3.9, The mobile unit rotates about the Z-Axis performing Roll and the centroid of the marker blobs observed by the mobile unit camera perform a twisting movement about the principal axis of the camera.

3.7.1.3 Stationary unit perception with motion

In this section, the observations from the perspective of the stationary unit camera '*S*' with respect to the LED markers on the mobile unit '*M*' are illustrated.

Figure 3.10 illustrates a case where Stationary unit '*B*' and mobile unit '*M*' are fixed at a distance of 25cm, facing each other. In this case, the distance between the centroids of the blobs seen by the stationary base camera move closer when the mobile unit markers move further away. For example, an increase in the Z translation for instance by about 2.5 meters, results in the LEDs being observed by the camera '*B*' to come closer, as seen in Figure 3.10.

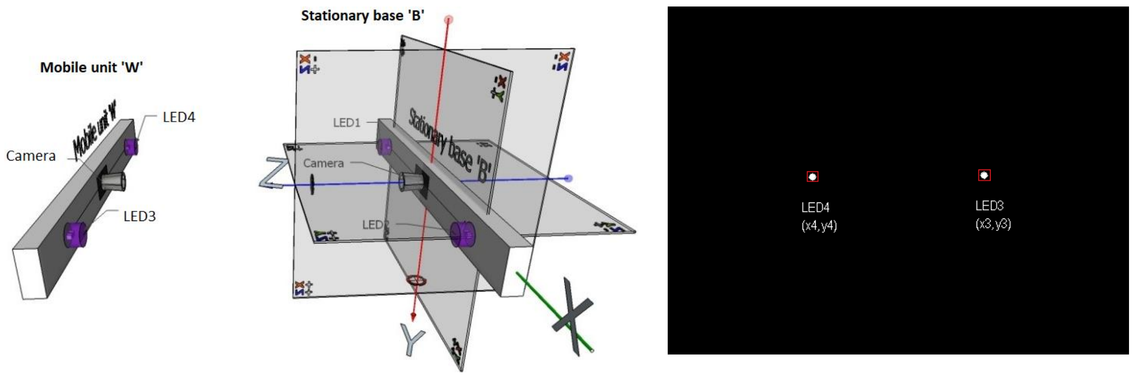

(a)Mobile unit at fixed Z distance from stationary unit

(b) Mobile unit LEDs as seen by the stationary camera

Figure 3-10 Mobile unit perspective 4 (a)The mobile unit is at a starting distance of 25 cm from the centre of the Stationary base B. (b)Observations in the image plane of stationary camera 'B.'

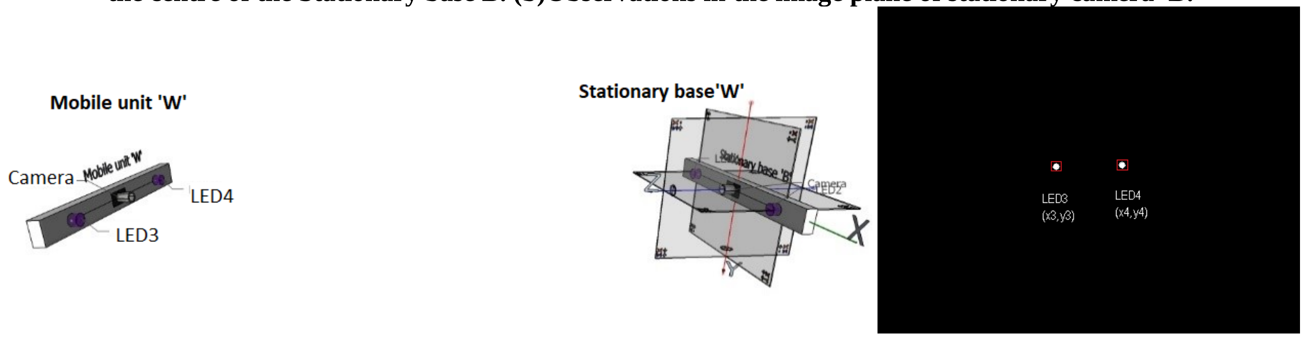

(a) Z translation of mobile unit from the stationary unit

(b) Stationary camera output

Figure 3-11 Mobile unit perspective 4 (a) Mobile unit undergoes a Z translation of 2.5 metres from the centre of the Stationary base '*B*'. (b)The LEDs are observed on the image plane of '*B*' come closer with increase in Z distance

When there is a translation of the mobile unit along with its' markers along the X-Axis, the camera '*B*' shows that the centroid of the blobs seen by the stationary camera markers move to the opposite direction of translation on the image plane, as seen in Figure 3.11.

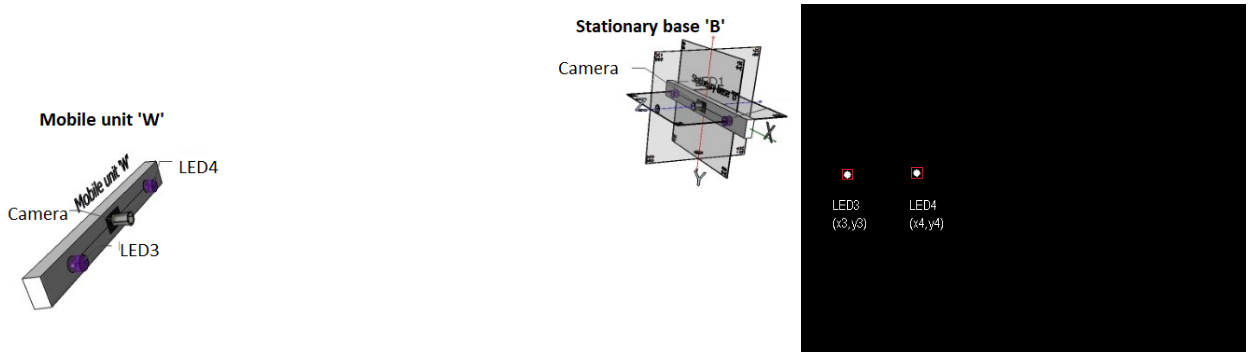

(a) X and Z translation of mobile unit

(b) Stationary camera output

Figure 3-12 Mobile unit perspective 5 (a) The mobile unit is translated by 2.5 metres along the Z axis and 25 cm along the X axis. (b) shows the output from the stationary camera. LEDs appeared closer and shifted to the left

A Y axis translation similarly results in an opposite direction of movement on the image plane shown in Figure 3.12.

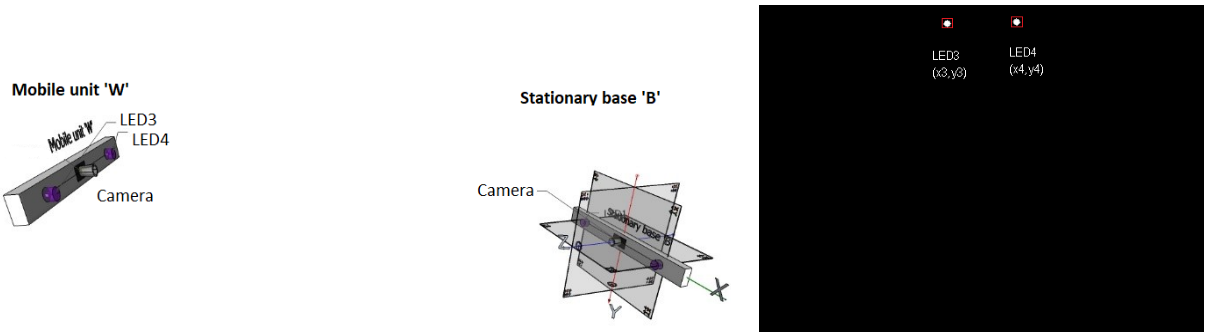

(a) Y and Z translation of mobile unit

(b) Stationary camera output

Figure 3-13 Mobile unit perspective 6 (a) Mobile unit is translated by 2.5 metres along the Z axis, and 25cm along the Y axis (b) Stationary camera output showing the distance between LEDs smaller and shifted up with Y translation

Figure 3.13 illustrates a condition where the mobile unit markers move along the Y and the Z direction. In this case, the blob centroids move closer and move up when the Y axis is incrementing.

The above outcomes of translation from the stationary unit are only possible when there is no rotation of the mobile unit with respect to the stationary unit. When rotations happen, the mobile unit perceives the stationary unit LEDs to have a distance that depends on the distance between the stationary and the mobile unit and also the angle of tilt of the observing camera (twist axis distance). When the tilt angle of observation increases in any direction beyond the field of view of the observing camera, tracking loss is inevitable. Therefore, a combination of tracking field of view of the stationary base camera and the mobile unit camera results in the net tracking volume.

3.8 Tracking system calculations for translation and rotation

Let us consider a system where the blob centroid coordinates obtained from Mobile unit '*W*' looking at stationary unit '*B*' are M1(MX1, MY1) and M2(MX2, MY2), as seen in Figure 3.14. (X4,Y4) is the midpoint of the line (M1,M2).

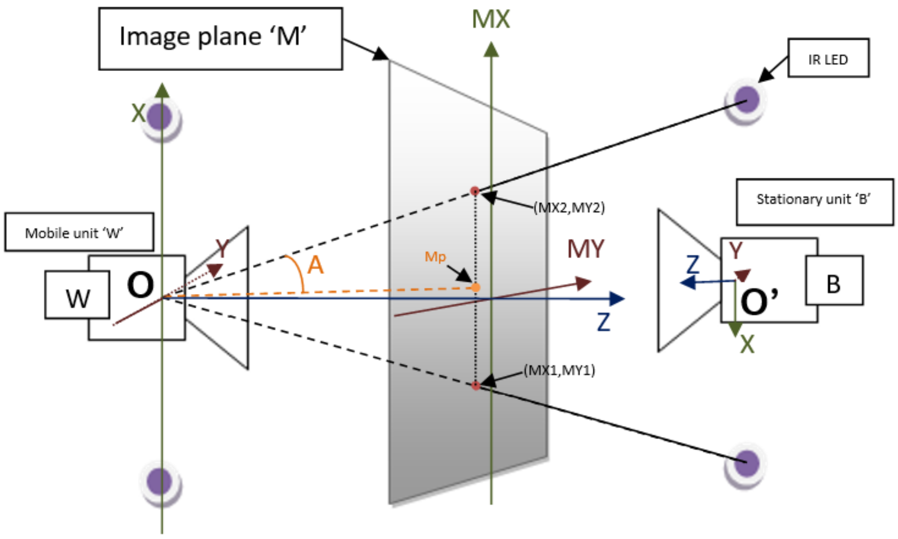

Figure 3-14 Mobile unit perspective Mobile unit observes the stationary unit LEDs, resulting in M1(MX1, MY1) & M2(MX2, MY2). Mp(X4, Y4) is the mid-point calculated and '*A*' is half the angle subtended between the points '*M1*' and '*M2*'

Midpoint of (M1,M2) is given by

$$X4 = \frac{MX1 + MX2}{2} \quad 3.5$$

$$Y4 = \frac{MY1 + MY2}{2} \quad 3.6$$

Mean pixel distance between (MX1, MY1) and (MX2, MY2) is

$$Mpd = \frac{\sqrt{(MX2 - MX1)^2 + (MY2 - MY1)^2}}{2} \quad 3.7$$

Angle per horizontal pixel of the camera 'α' can be given by

$$\alpha = \frac{HFOV}{number\ of\ horizontal\ pixels} \quad 3.8$$

Angle per vertical pixel of the camera 'β' can be given by

$$\beta = \frac{VFOV}{number\ of\ vertical\ pixels} \quad 3.9$$

Angle between (MX, MY) and (X4, Y4) , '*A*' can be given as

$$A = Mpd \cdot \alpha \quad 3.10$$

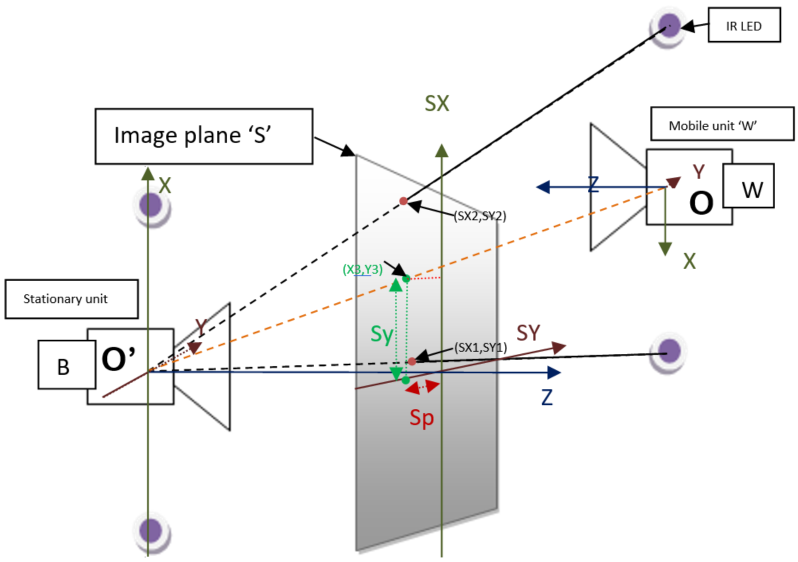

Figure 3-15 Stationary unit observes the mobile unit C (SX1, SY1) and D(SX2, SY2) are the points on the image plane (X3, Y3) is the calculated centre. '*Sy*' is the X- axis tilt and '*Sp*' is the Y-axis tilt from the Principal axis along Z

When the Mobile unit '*W*' moves about the X-axis and Y-axis with respect to the Stationary unit '*B*' as seen in Figure 3.15. Movement along the X- Axis is observed as a tilt angle when observed by the stationary unit '*B*' and can be given in the horizontal direction as '*Sy*' and the movement along Y direction as '*Sp*'. Since the tilts are always calculated from the principal axis, the angles are required to be calculated from the centre. Therefore, the total field of view is subtracted from the total angle from the image plane axes (XX' for '*Sy'* and '*Sp*' for YY').

$$Sy = -\alpha \cdot X3 - \frac{HFOV}{2} \qquad 3.11$$

$$Sp = \beta \cdot Y3 - \frac{VFOV}{2} \qquad 3.12$$

Calculating net tilt from (3.7) and (3.8) in '*Sy*' and '*Sp*' directions '*XYt'* given by:

$$XYt = \sqrt{Sy^2 + Sp^2} \qquad 3.13$$

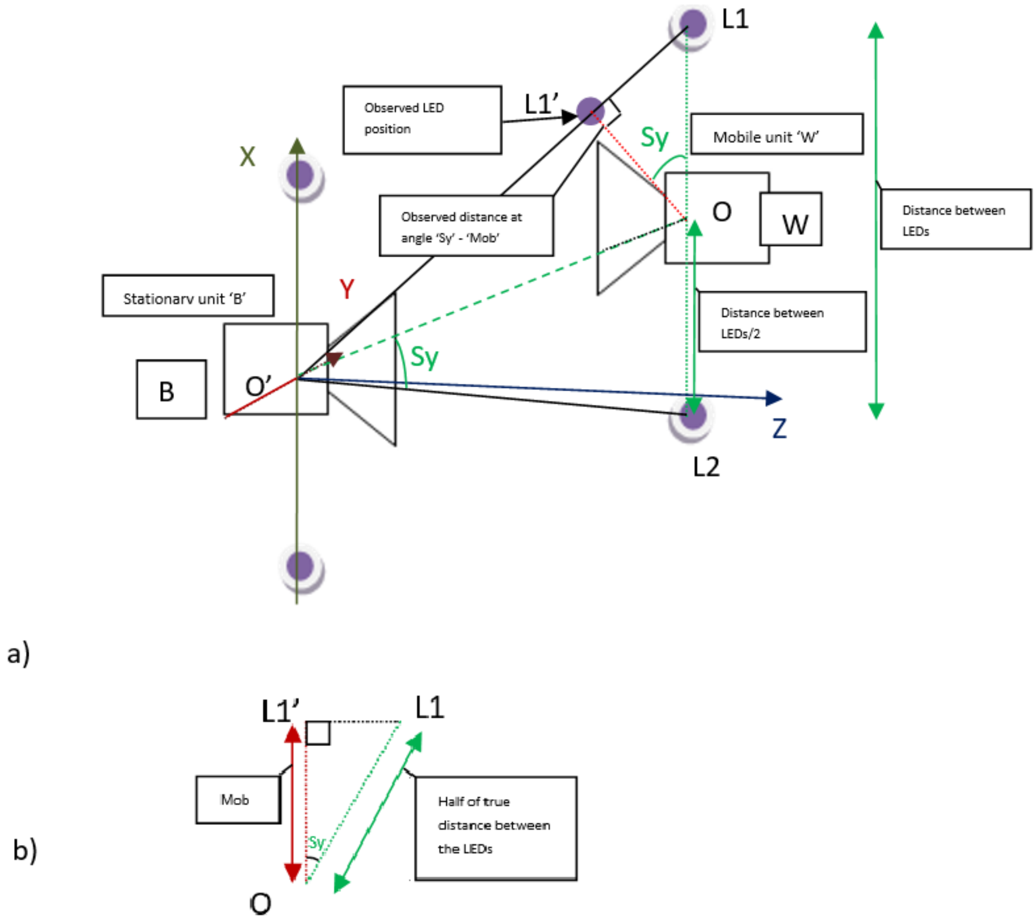

Figure 3-16 Stationary unit observed half the distance of the mobile unit LEDs L1-O reduces with lateral movement of the mobile unit to L1'-O. a)Observed distance L1'-O between the LEDs depends on the tilt 'Sy' in the plane formed by O,O',L1' b) O-L1' or 'Mob' is the observed distance when the half the real distance between the LEDs is O-L1

From the Figure 3.16 (a), we see that the observed distance between the LEDs on the mobile unit L1'-O varies with change in '*Sy*' angle. Therefore, this tilt needs to be corrected to get the observed length. It can be observed that when the LEDs on the mobile unit L1, L2 are collinear with the X- axis of the Stationary unit, ie. the tilt '*Sy*'= 90, the observed distance between the LEDs will become equal to zero eventually (Cosine dependence). This is because the observed distance between two points as observed by an observer, according to epi-polar geometry obeys the cosine of the angle of observation from the point of observation. When a triangle formed by O, L1' and L1 is considered, half mobile oblique observed distance, '*Mob*' as seen by Stationary camera '*B*' as shown in Figure 3.16 can be given by:

$$Mob = \left(\frac{actual\ distance\ between\ LEDS}{2}\right) \cdot \cos(Sy) \qquad 3.14$$

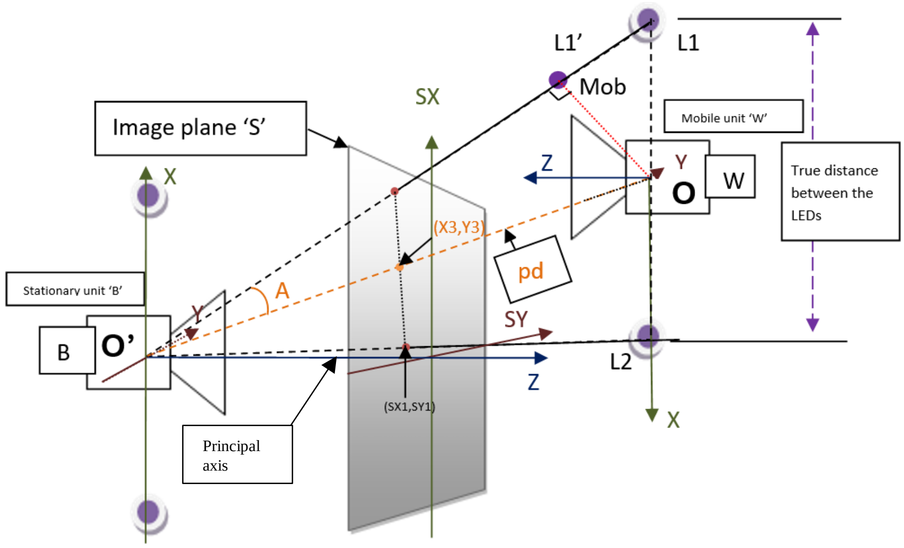

Figure 3-17 Planar distance calculation. Planar distance '*pd*' between '*O*' and '*O*'' along the plane formed by O', O and L1' in relation to the oblique distance '*Mob*' and angle '*A*' subtended by (Sx2, Sy2) and midpoint (X3, Y3)

From the Figure 3.17, Planar Distance '*pd'* of '*O*' to '*O*'' on the plane formed by O',O and L1' can be given as

$$pd = \frac{Mob}{\tan(A)} \qquad 3.15$$

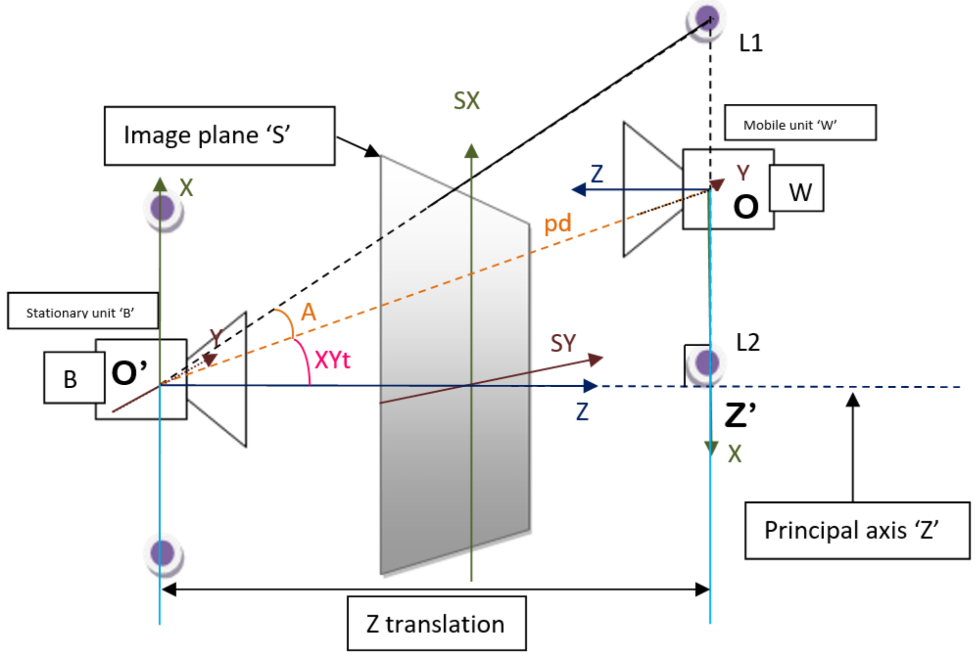

Figure 3-18 Z translation calculation. Z translation in relation to the Planar distance and the net tilt from the principal axis 'XYt.'

3.8.1 Calculation of *Z* translation with tilt correction

The true Z translation can now be obtained from the planar distance obtained in the XZ plane using the net angle of tilt from the principal axis 'Z', as seen in Figure 3.18, by using the following equation:

$$Ztranslation = pd \times \cos(XYt) \qquad 3.16$$

From the above equations, the calculation of Z translation can be summed up in a single step as

$$Z\ translation = \left(\frac{L}{2}\right)\left(\frac{\cos(Sy)}{\tan(\alpha * Mpd).\cos(XYt)}\right) \qquad 3.17$$

3.8.2 Calculation of X translation

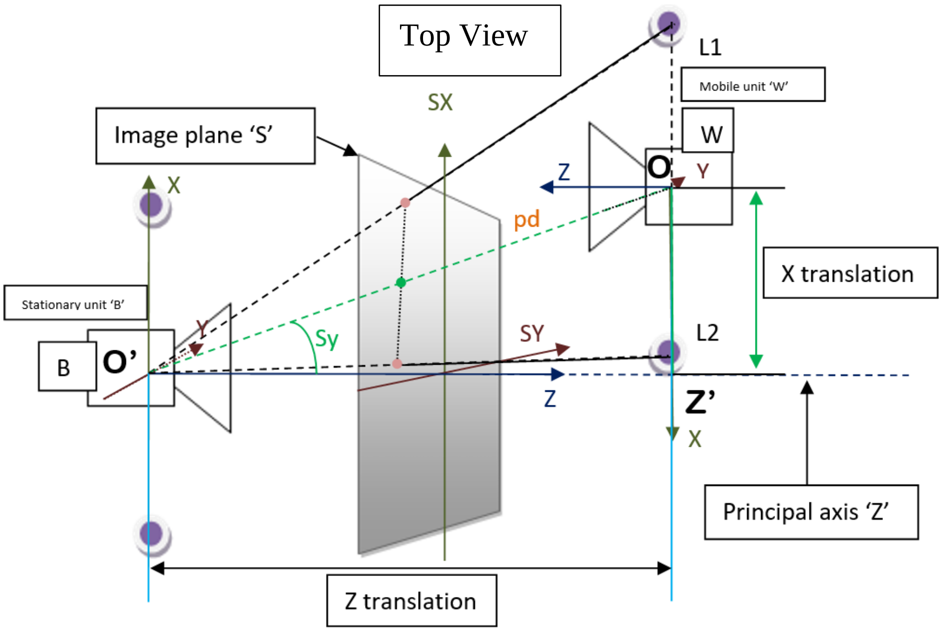

Figure 3-19 X translation calculation. X – axis translation due to tilt Sy along X axis in relation to the principal axis and Z translation

Z translation value has been estimated in equation 3.16 from the image plane distance. The triangulation calculation for the configuration seen in Figure 3.19, required for the X-translation uses the same image plane distance '*pd*' as the Z-translation calculation. The calculation of translation in the X-direction with '*Sy*' as the direction of tilt along the X-direction can be given as:

$$Xtranslation = Ztranslation \times \tan(Sy) \qquad 3.18$$

3.8.3 Calculation of Y translation

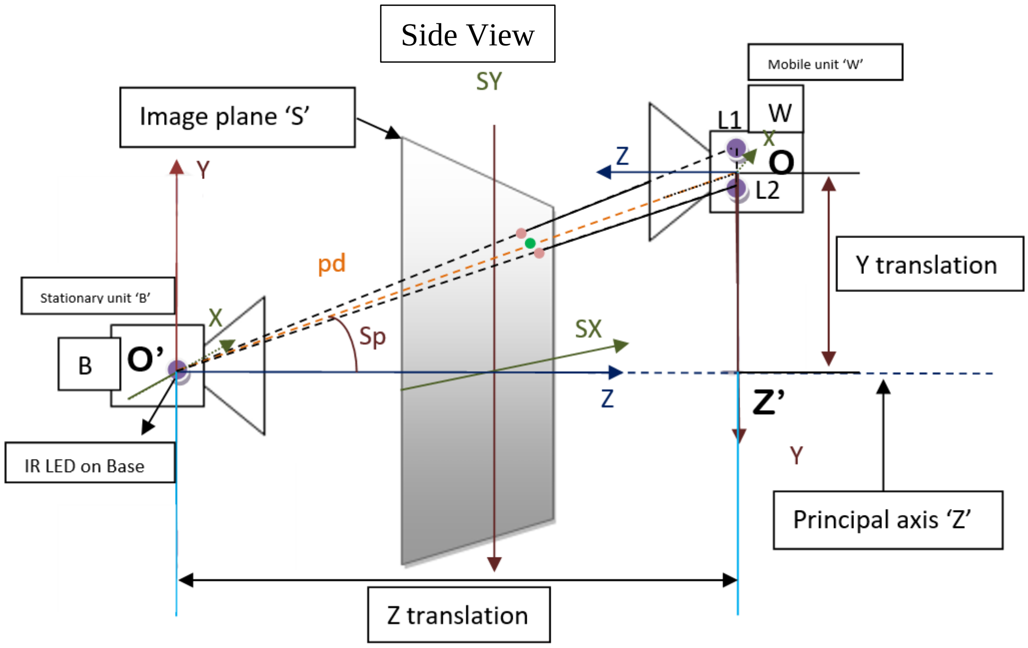

Figure 3-20 Ytranslation calculation. Y-Axis translation due to the angle subtended '*Sp'*, in relation to the principal axis and Z-translation

From the vertical tilt '*Sp*' and the image plane distance as seen in Figure 3.20, are known. Hence the translation in the Y-direction can be given as:

$$Ytranslation = Ztranslation \times \tan(Sp) \qquad 3.19$$

3.8.4 Calculation of Roll

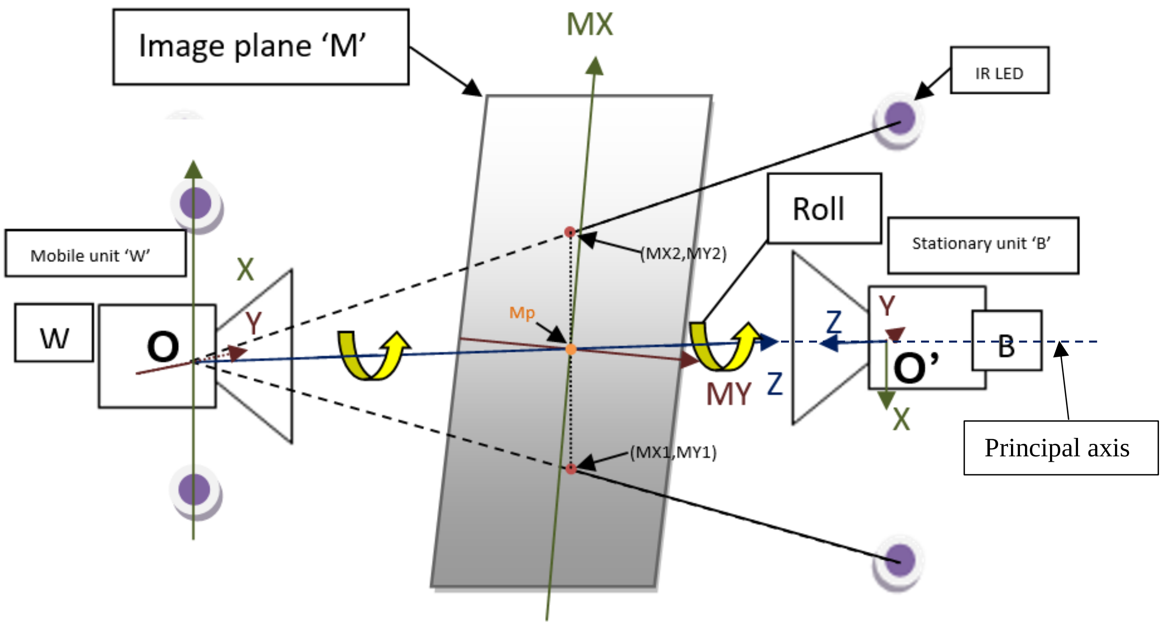

Figure 3-21 Roll calculation. Calculation of Roll in relation to the principal axis

Figure 3.21 shows mobile unit performing a rotation about Z- axis with respect to the stationary unit. Though it is possible to use the blob tracking output of the stationary unit to calculate roll, the output from the mobile unit camera is used because the accuracy of roll calculation depends on the distance between the LED markers as seen by the camera. When the mobile unit tilts along pitch or roll directions, the distance between the LEDs can get lower leading to inaccurate roll measurements. Therefore, roll calculations are performed using the observations and output of the mobile unit camera.

The roll calculation is relatively straight forward, as it involves the usage of the points(MX1,MY1) and (MX2,MY2) as observed by the mobile unit '*W*' of the stationary unit '*B*' as follows:

$$Roll = atan\left(\frac{MY2 - MY1}{MX2 - MX1}\right) \qquad 3.20$$

3.8.5 Roll correction of Pitch and Yaw

Roll rotation calculation can be straight forward as seen in equation 3.19 but it induces skewing in the simultaneous rotations along pitch and yaw directions. Therefore, '*My'* and '*Mp'* are orthogonal vectors and hence if '*My'* is denoted by '*a*' (X Axis) and '*Mp'* by '*b*'(Y Axis). When there is no rotation, for the resultant vector '*P'* vector addition is obeyed.

$$P = a + b \qquad 3.21$$

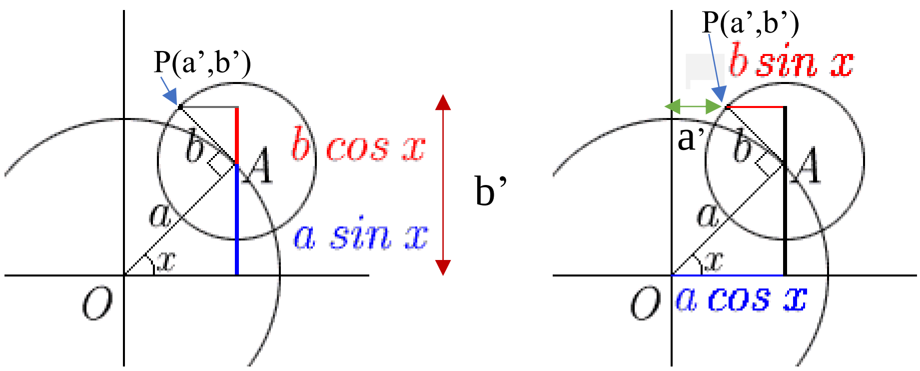

(a) Calculation of b'(Y -coordinate of P)

(b) Calculation of a'(X – coordinate of P)

Figure 3-22 Roll correction for pitch and yaw. '*a*' and yaw '*b*' rotate by an angle 'x' or roll, to a new point P(a', b') (a) calculation for shifted Y- coordinate of the point P (b) Geometric representation of shifted X- coordinate of the point P

Whereas, when '*a*' and '*b'* rotate by an angle '*x*' or roll, P(*a'*,*b'*) as seen in Figure 3.22 can be given as

$$b' = a\sin(x) + b\cos(x) \qquad 3.22$$

Using vector method of rotation of axis, if Mp = b(Y axis) and My = a (X axis) and a gets rotated to a new vector '*a*'' along '*n*' by an angle of 'Roll', '*x*', then '*a*' vector is given by

$$a' = a\cos(x) - b\sin(x) \qquad 3.23$$

3.8.5.1 Calculation of Pitch and Yaw

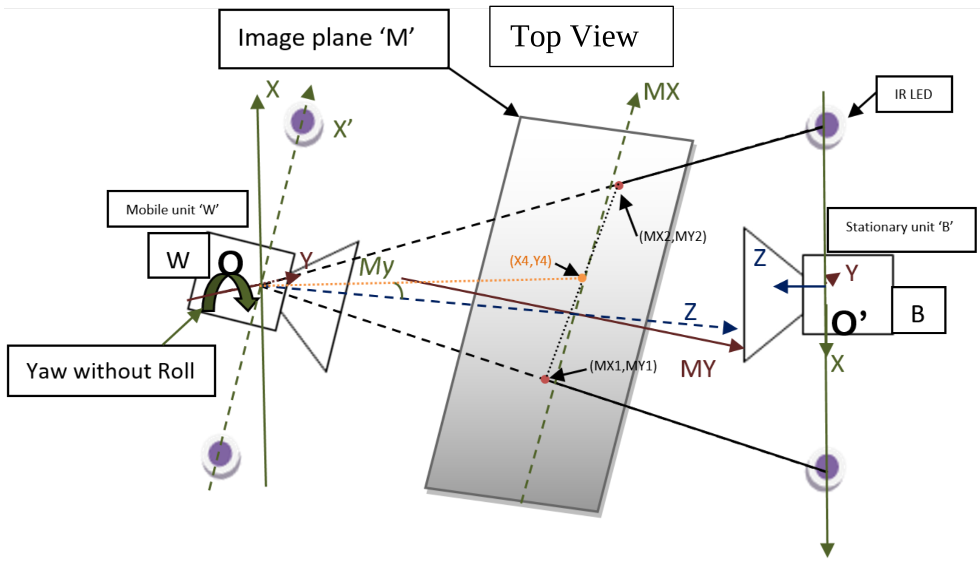

Figure 3-23 Yaw rotation calculation without Roll effects '*My*' about Y-Axis. (X4,Y4) is the mid point of the line M1-M2

In Figure 3.23, rotation along the X- direction of the mobile unit with reference to the principal axis 'MY', 'α' is angle per pixel in the Horizontal Field of View, is given by

$$My = X4 \cdot \alpha - HFOV/2 \qquad 3.24$$

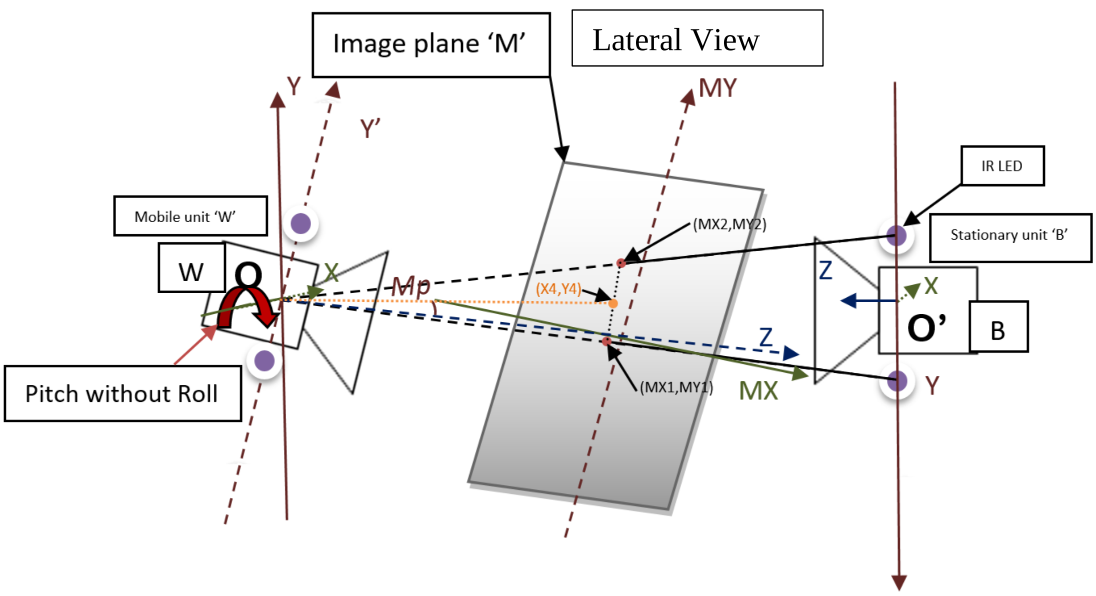

Figure 3-24 Pitch rotation calculation without roll effects '*Mp*' about X-Axis. (X4,Y4) is the mid point of the line M1-M2

In Figure 3.24, rotation along the Y- direction of the mobile unit with reference to the principal axis 'MP', 'β' is the angle per pixel in Vertical Field of View, is given by

$$Mp = Y4 \cdot \beta - \frac{VFOV}{2} \qquad 3.25$$

3.8.5.2 Roll correction applied to Pitch- Combination rotation

Yaw distortion due to roll is affected along the X – direction and the Y – direction and therefore the combined correction is required to be applied to get a resultant Yaw angle. Roll distortion of pitch rotation along the X – direction and Y – direction of the mobile unit combined, '*SRp*' from equation 3.23 is given by,

$$\mathrm{SRp} = \mathrm{My}[\sin(\mathrm{Roll})] + \mathrm{Mp}[\cos(\mathrm{Roll})] \qquad 3.26$$

Net pitch = movement along X – direction of static unit, observed by static base 'B'- Pitch obtained after roll correction

$$Pitch = Sy - SRp \qquad 3.27$$

3.8.5.3 Roll correction applied to Yaw

Yaw distortion due to roll is affected along the X – direction and the Y – direction and therefore the combined correction is required to be applied to get a resultant Yaw angle. Roll distortion of Yaw due to rotation along the X – direction and Y – direction of the mobile unit combined, '*SRy*' from equation 3.22 given by,

$$SRy = My[\cos(Roll)] - Mp[\sin(Roll)] \qquad 3.28$$

Corrected Yaw = Movement along Y direction of the stationary unit observed by static camera 'B'+ Yaw obtained from mobile camera after roll correction from equation 3.22.

$$yaw = Sp + SRy \qquad 3.29$$

3.9 Optical tracking evaluation

The described tracking system which implements blob tracking and centroid extraction was implemented on Open MV camera system, which is an open source embedded systems camera development system. The tracked coordinates are streamed serially to the tracking base and then into the computer for the calculations described earlier in this chapter,

3.9.1 Translation experiments

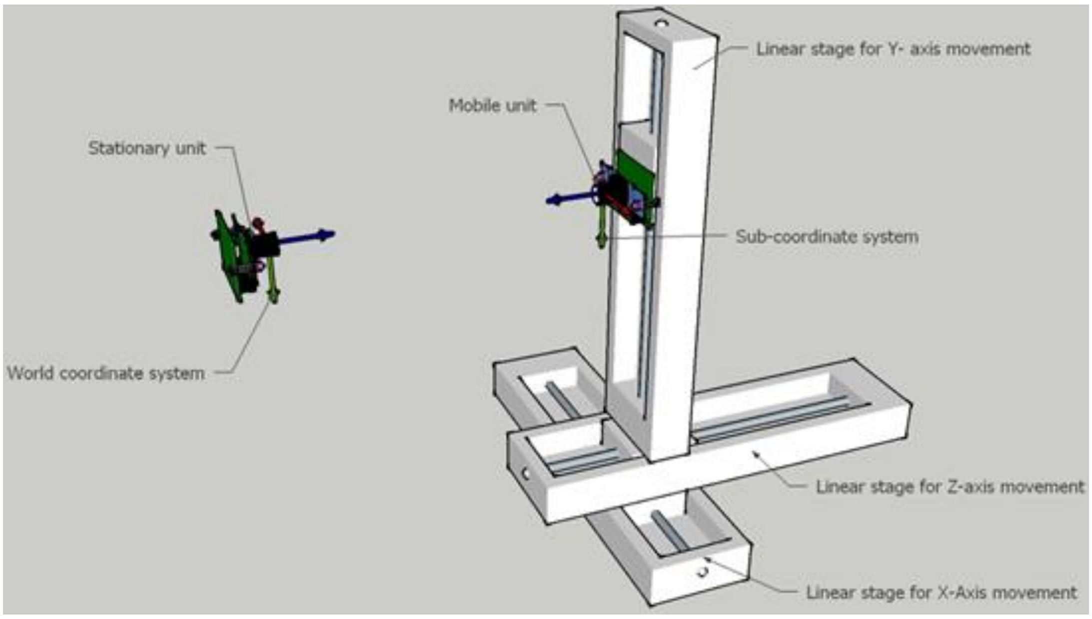

Figure 3-25 Compound translation stage evaluation setup.

The mobile unit as seen in Figure 3.25 is mounted to a 3 axis Zaber linear stages with 300mm travel on each axis and an automated 3D raster is done at 60mm intervals. The entire experiment is done without human intervention and the distance used is 1m. The results of the evaluation are given in this section. Figure 3.26 shows the actual setup used to evaluate translations.

Figure 3-26 Translation evaluation setup. 3 Axis Zaber stages with stationary unit on the stand and mobile unit on the linear stages

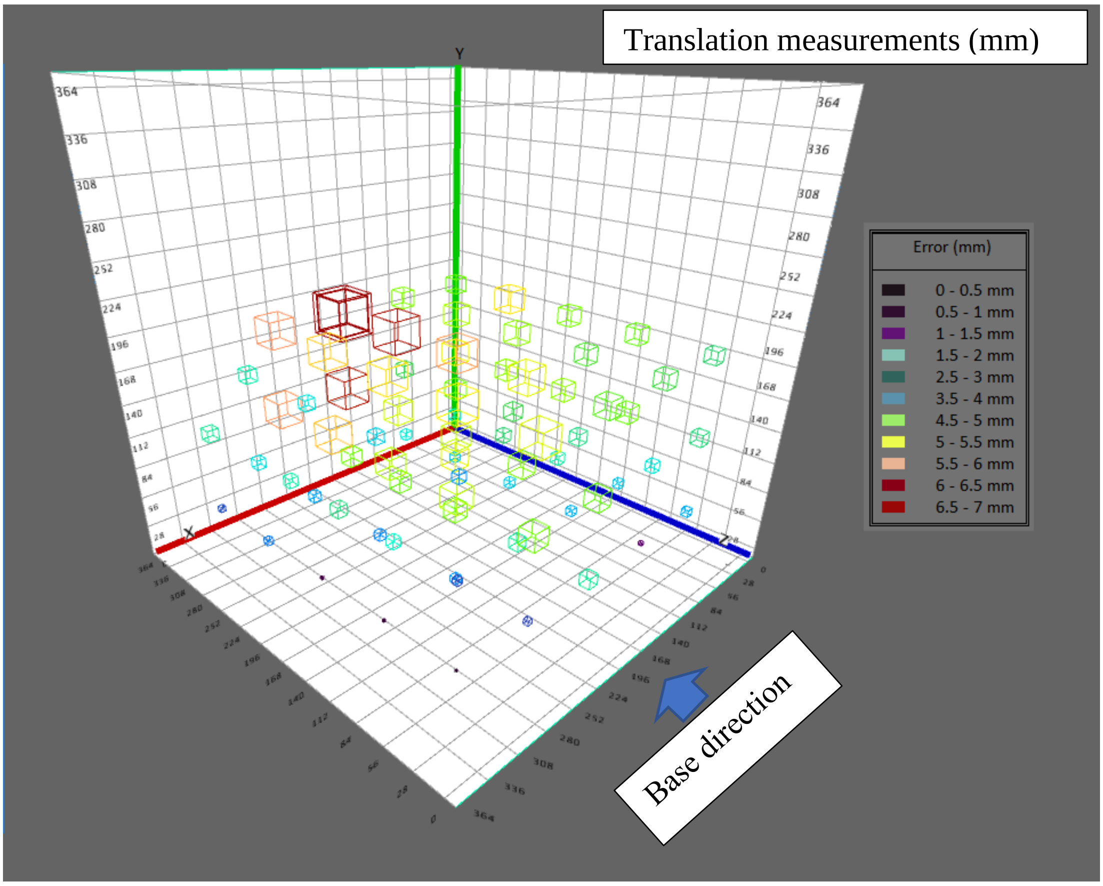

Figure 3-27 Translation experiments using Zaber linear stages showing errors along X, Y direction and Z direction with respect to the tracking base

To determine the translational accuracy of this system, three linear stages, each having a travel distance of 300 mm, aligned perpendicular to each other – from Zaber is used, as seen in Figure 3.26. The results of errors for the translation experiment can be seen in Figure 3.27. It can be observed that the errors increase from about less than 0.5 mm when the distance is less than 50mm and increases up to 7mm with an increase in movement along Z axis distance in reference to the base camera at 1 metre distance.

3.9.2 Rotation experiments

The software developed in JAVA acquired the detected blob centroids, works out the different angles based on calculations given above and exports the feedback readings from the servo to a CSV file. The process is completely automated except for changing the axis of rotation manually. The rotational observations at half a meter are documented in this section. The setup shown in Figure 3.26 is used for translation experiments.

The three rotations Pitch, Yaw and Roll, are evaluated one after the other with a precision servo from Robotis (Dynamixel MX-28) with a 0.088-degree resolution rotary encoder. The shaft of the servo is attached to a 3D printed structure which supports the mobile unit. The mobile unit is rotated with steady increments of 0.25 degree along Roll, Yaw and pitch direction as shown in Figure 3.28 till the time the observing unit loses identification of the pose and proceeds further to sweep till 360 degrees and back.

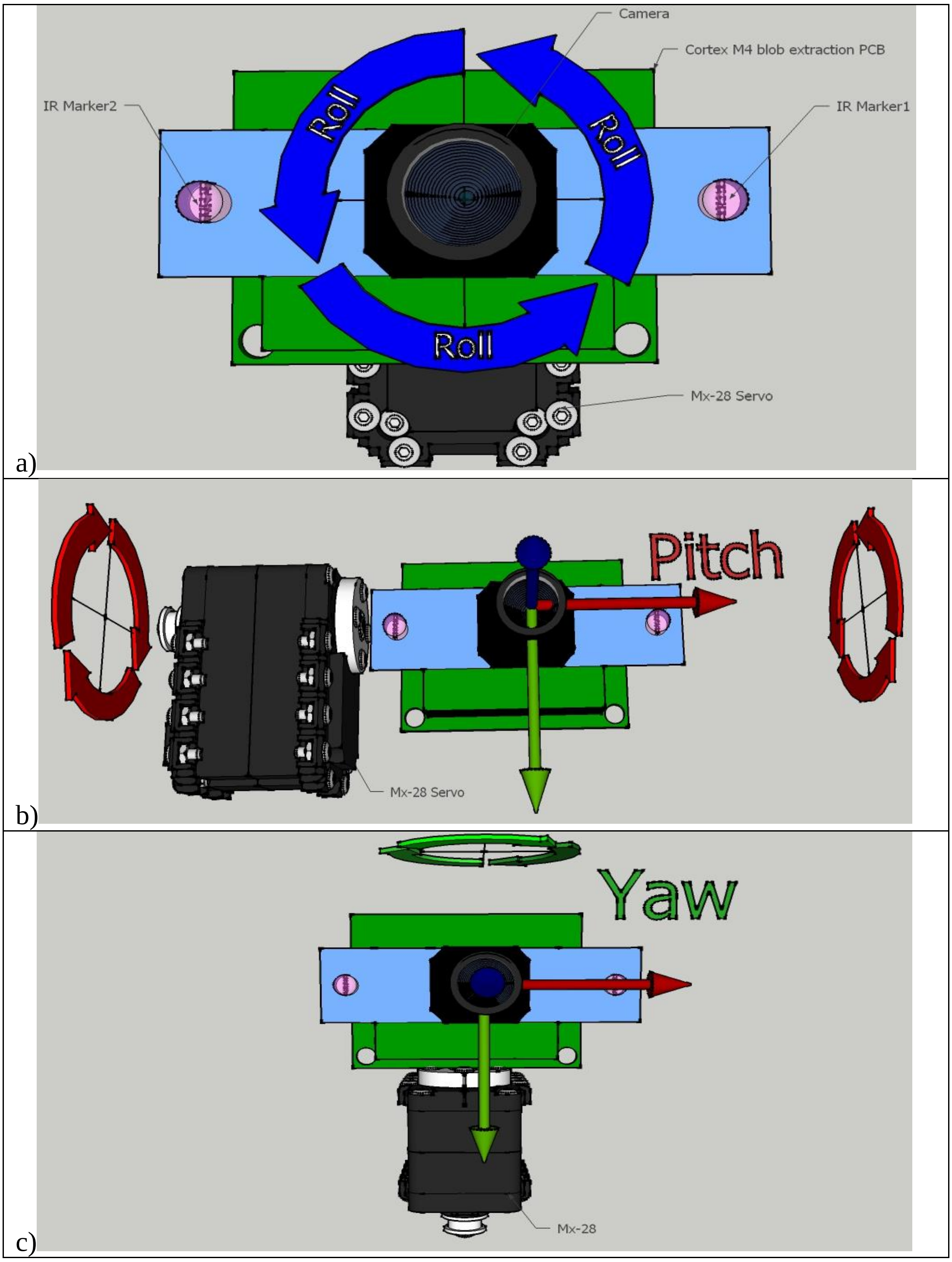

Figure 3-28 Rotation experiments using Mx28 servo incrementing angles along every axis a) roll direction b) pitch direction c) yaw direction. Mobile unit with 2 LED markers rotates with respect to the stationary unit

The actual setup used for evaluation of rotations can be seen in Figure 3.29. The linear stage is used to hold the stationary unit, in line with the mobile unit fixed on a camera stand attached to the servo.

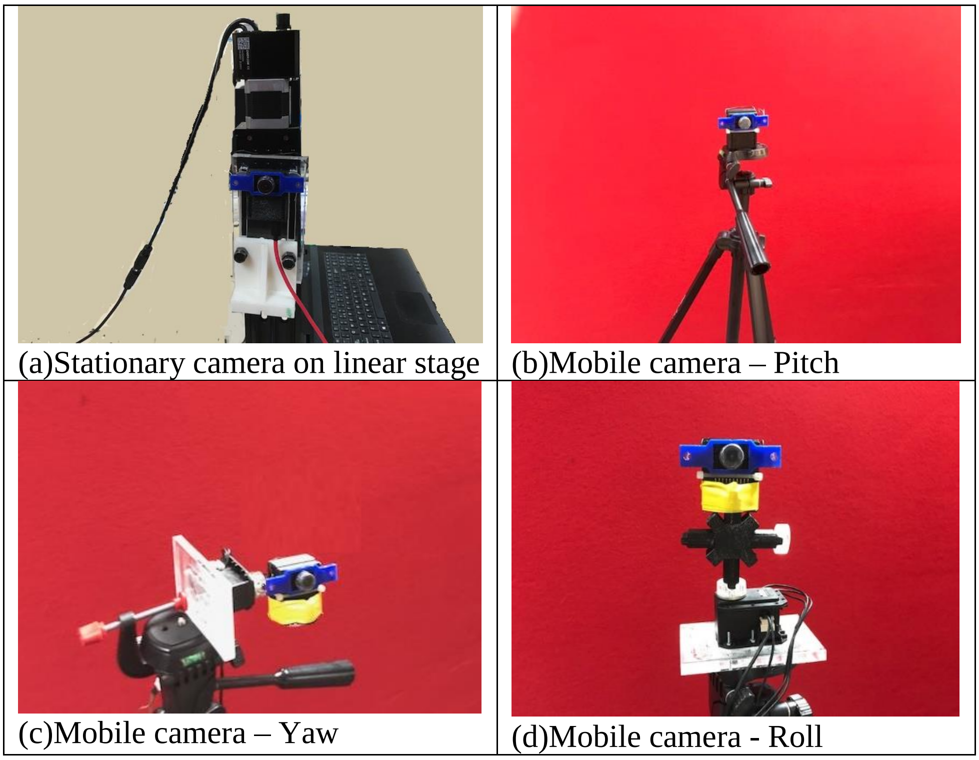

(a)Stationary camera on linear stage
(b)Mobile camera – Pitch
(c)Mobile camera – Yaw
(d)Mobile camera - Roll

Figure 3-29 Rotation experiment with camera attached to servo at different axis alignment (a) Stationary camera (b) Pitch evaluation (c) Yaw evaluation (d) Roll evaluation

3.9.2.1 Rotation in Yaw direction:

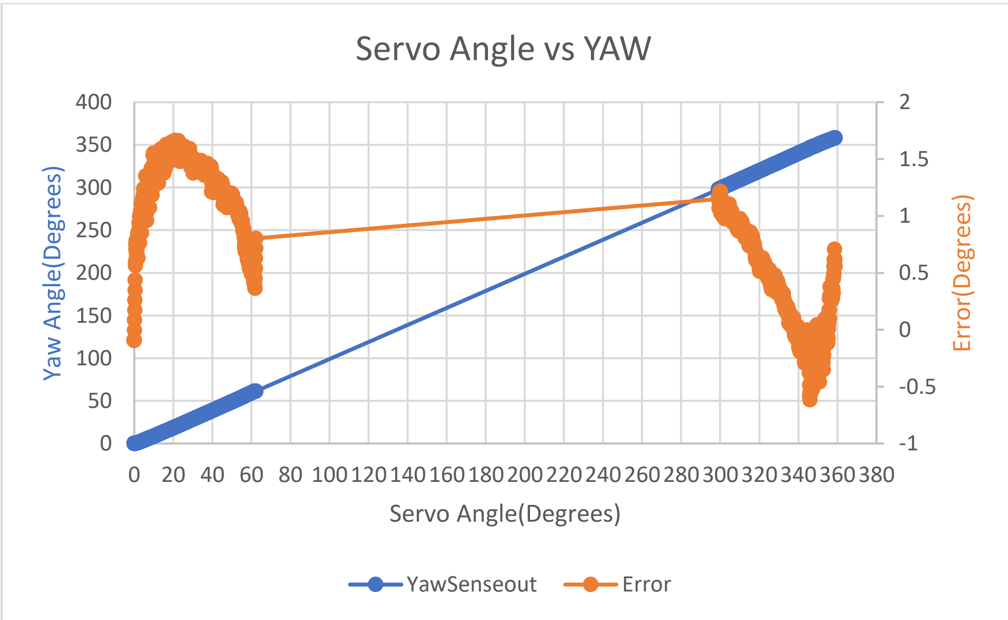

Figure 3-30 Rotational error in Yaw direction. The graph shows the Yaw variation compared to a servo angle encoder. The dynamic range of the measurement is between 0-65 and 290 – 360 after which there is a tracking loss

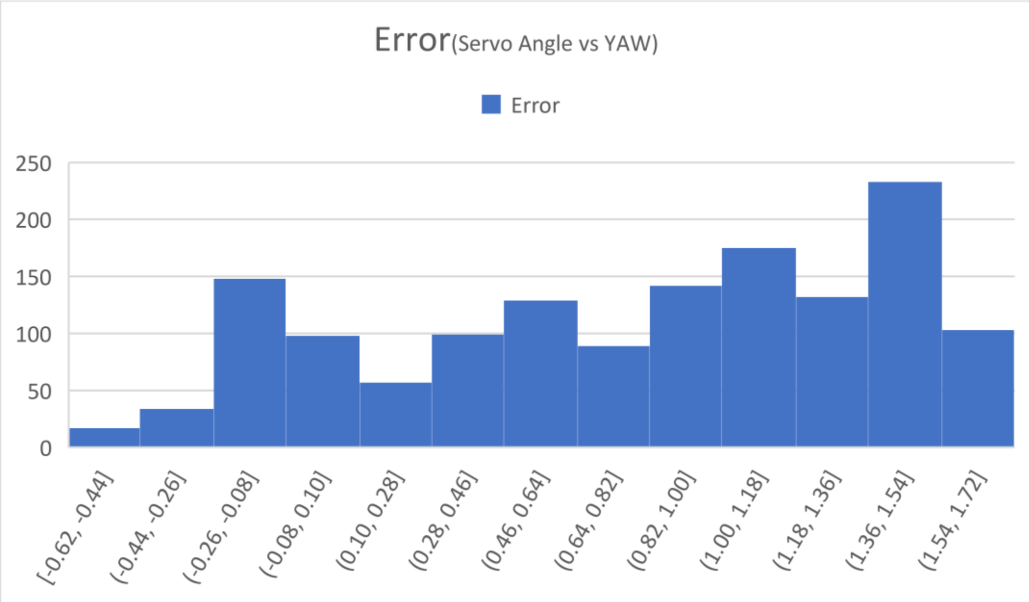

Figure 3-31 Yaw error is lower than Pitch because of a higher resolution of measurement along the Yaw direction.

Figure 3.30 shows that the system was sensitive between 0 and 65 degrees and 290 and 360 degrees in the Yaw-direction. In Figure 3.31 it can be seen that the errors were a maximum of 2 degrees.

3.9.2.2 Rotations in Pitch direction

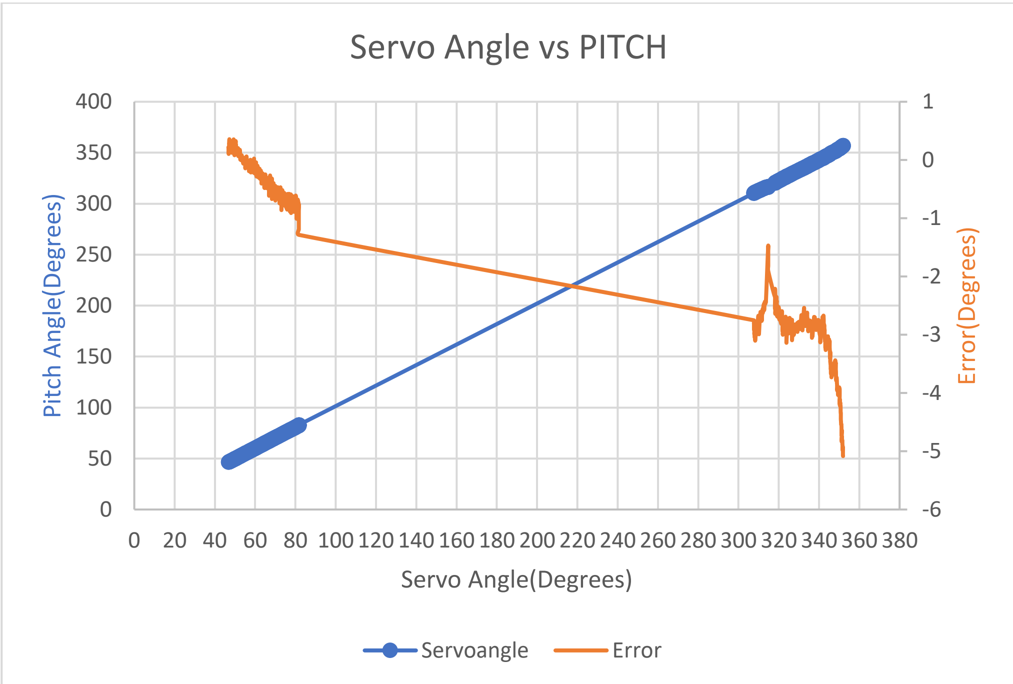

Figure 3-32 Rotational error in the Pitch direction. The graph shows the pitch variation compared to a servo angle encoder. The dynamic range of the measurement is between 50-85 and 308 – 355 after which there is a tracking loss

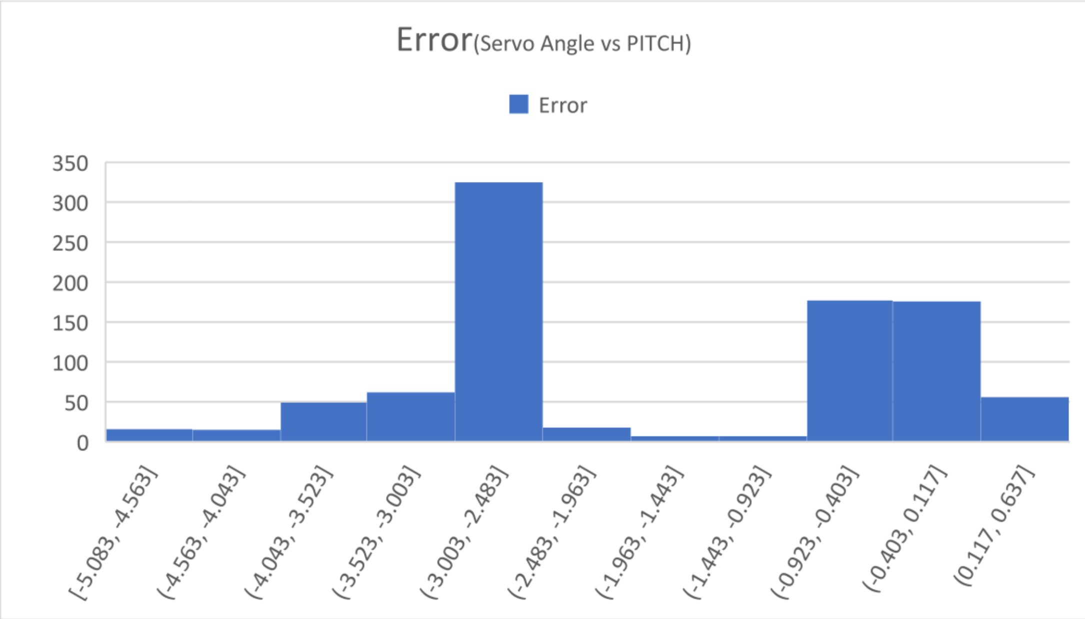

Figure 3-33 Pitch error is higher than Yaw error because of the reduced pixel resolution in the Pitch direction.

From Figure 3.32, the system works between 50 and 85 degrees and 308 – 355 degrees range, after which there is complete tracking loss. The range of the error is about 6 degrees and from Figure 3.33 and Figure 3.31(Page128), the error is higher in the Pitch-direction and this is because of the lower pixel resolution in the Pitch-direction.

3.9.2.3 Rotations in Roll direction

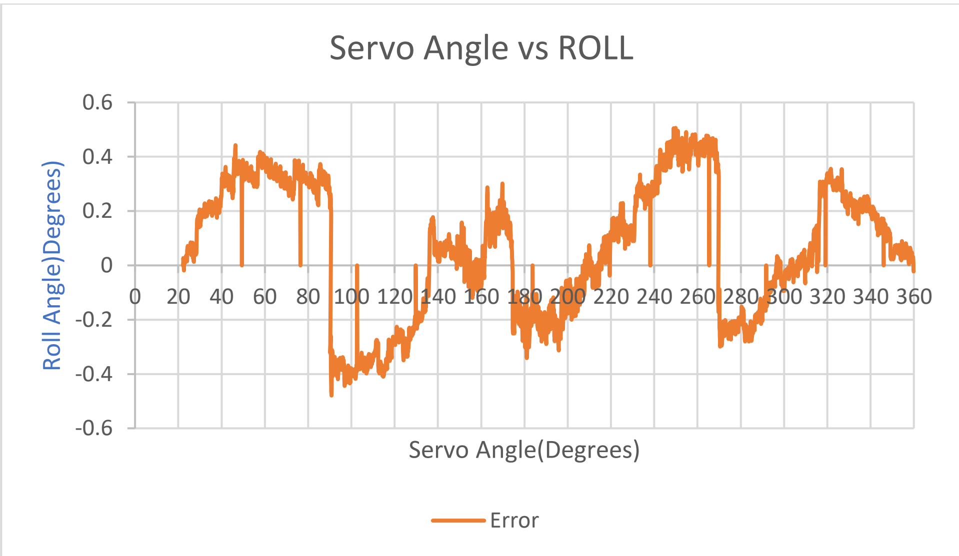

Figure 3-34 Rotational error in Roll direction. The graph shows the Roll variation compared to a servo angle encoder. The dynamic range of the measurement is between 0-360 there is no tracking loss, but sign correction of the angles has been used.

Figure 3-35 Histogram showing Roll – Axis errors. The Roll axis has the lowest amount of errors as the markers have the highest dynamic range within this axis of rotation and the visibility is very high.

From Figure 3.34, the error along the Roll- direction is the lowest and the range is about 0.8 degrees. Also, the Roll axis has the highest dynamic range within this axis of rotation and the visibility is very high.

3.10 Discussion and results

The translation and rotation data collected in this chapter indicate that the accuracy of the system diminishes towards the peripheral field of view of the cameras. During the translation experiment, it should be noted that translation as such can induce rotation errors because of reduced angular resolution with increasing distance. The translation experiments are performed at a 1-metre distance, and rotation experiments are conducted at 0.5m to compensate for the reduced camera resolution.

The following are the hardware parameters to be worked with:

(a) Camera has a pixel resolution of 640 x 480 in greyscale mode
(b) IR LEDs are used without illuminating diffusers
(c) Lower field of view lens was used to prevent fish eye and pin cushion effects and maintain high accuracy
(d) Camera frame rate is 25 and is limited by the processing capability of the controller.
(e) Only blob centroids are considered, no sub-pixel interpolation is done because of reduced onboard buffer memory
(f) IR filters were custom made from Floppy disk magnetic film
(g) The mobile unit is wireless and can communicate Blob data wirelessly to the computer through Bluetooth.
(h) Linear translation stages from Zaber have velocity limitations of 10mm/second, and MX28T servo has an angular velocity limitation of 97 RPM

The translation experiments showed a decrease in accuracy from 0.5mm at 1 metre distance to 7mm at 1.3 metres distance. The average rotational error along Roll of about +/-0.4 degrees +/- 0.8 in the direction of Yaw and +/-1.5 average error along the pitch direction.

3.11 Summary

In this chapter, a different approach to optical tracking is demonstrated for reducing the number of markers and reduce marker confusion in surgeries which are optically tracked. However, for the accurate working of such a system and to be functional in such surgeries, the cameras used are required to have a high resolution with a higher field of view and high frame rates. Further, they will also require subpixel image processing which simple processors cannot handle without significant modifications and additional resources. Therefore, only the concept has been demonstrated, and the main characteristics are evaluated.

Table 3-2 Technical summary of the hardware achievements in this section

Hardware	Status	Displacement accuracy	Angular accuracy	Tracking volume	Errors
Ideal requirements	Not implemented	Sub millimetre at 2 metres along all axis	Sub degree at 2 metres along all axis	4m × 4m × 4m	Active marker cross-over correction & low marker count
Optitrack	Commercially available	Sub millimetre at 2 metres along all axis	Sub degree at 2 metres along all axis	3m × 3m × 6m	Tracking loss + high marker count
Dual marker altered optical tracking system	Implemented, evaluated	Error range- X– direction 5mm Y- direction 5mm Z – direction 7mm	Error range Yaw- 2 degrees Pitch- 6 degrees Roll- 0.8 degree	300 mm × 300mm × 300mm	Cross over correction using 2 active markers

Table 3.2 shows the comparison between ideal requirements of the system, limitations of the commercially available Optitrack system, and the face that low marker count and marker confusion have been solved in the proposed system. Whereas, limitations of image processing power and limited frame rate <30 fps prevent the system from being used in fetal surgery system described in this project. Therefore, the actual experiments for the fetal surgery system, a commercial optical tracking system from Optitrack will be used with retro reflective markers.

3.11.1 Target specifications proposed vs specifications achieved

From Table 3.3, it can be seen that most of the target specifications have been achieved. Only specifications such as higher accuracy and higher frame rates were not achieved because of the limitations in cost, processing speed and time.

Table 3-3 Technical summary of the hardware achievements in this section

Parameter	Target specifications	Optitrack	Proposed optical tracking system
Interpolation and resolution	Microns resolution with advanced interpolation	640×480 for 2 or more cameras / advanced cubic interpolation Microns resolution	No interpolation /640×480/mm resolution
Tracking accuracy	Sub-mm	Sub mm under 2 metres	>2mm under 1 m distance
Tracking volume	> $4m^3$	4m × 4m × 4m	300mm × 300mm× 300mm
Frame ate	>100	120	24 - 30
Lowest market count	2	high marker count >4	marker count = 2
Tracking loss due to marker confusion	Marker confusion at specific angles and translation	Tracking loss	Tracking loss at extreme translations and rotations
Tracking loss due to cross over	No tracking loss when markers cross over	Uses trajectory tracking to help the case but fails mostly	Active marker cross-over correction by sequentially scanning the required LEDs for tracking

3.12 Conclusion

A novel optical tracking system using only 2 markers at the mobile unit has been developed and evaluated for use in Ultrasound guided surgeries, where space is an important constraint. However, due to the low resolution of the camera used, limited field of view and the limitations in processing and buffer memory of the microcontroller system used, sub-pixel interpolation could not be performed. However, the principle and feasibility have been clearly demonstrated in this section.

Chapter 4

Ultrasound object tracking

The process of tracking organs and surgical instruments in a ultrasound image output is known as ultrasound object tracking. The fact that the ultrasound image has a high amount of specular noise and has relatively low resolution, the amount of processing load on the computing system can become very high. This chapter discusses how positive aspects of Optical tracking can complement ultrasound object tracking for surgical instruments.

4.1 Introduction

From the literature review, it can be inferred that standalone ultrasound equipment has not been optimized for minimally invasive surgeries, as they require sub-millimetre accuracy. The key points of inference, when it comes to ultrasound can be listed as follows:

- Real – time ultrasound guided surgeries are on the rise but are more consistently in use for minor procedures.
- For surgeons to do complex procedures, image visualisation, tracking and orientation are very essential.
- A lot of work has been done on ultrasound image processing and accuracy testing, but many have not used very accurate controls, especially for real-time and dynamic tests;
- Simple calibration procedures and quicker learning curves encourage the uptake of new technologies;

- Though many image processing techniques are currently available, most are computationally intensive and will need hybrid tracking technologies to make the tracking process quicker.

Related to these outlined points, what emerges from the previous chapter is also:

- There has not been a reliable and expandable platform for special surgeries like fetal surgeries;
- The uncertainties and inaccuracies in tracking of surgical instruments can have adverse effects on the patient;
- Ultrasound tracking accuracy has been taken for granted in a lot of medical procedures and has evidence for the same in procedures such as Jugular Venous Puncturing.
- The necessity of ultrasound sub millimetre accuracy measurement has been over looked in many cases, especially in image processing systems.

The above put together, form the aims of the project. Hence, the initial step was to see the characteristics of the ultrasound machine with the different instruments and materials. The second step was to evaluate the accuracy of ultrasound image processing algorithms with a higher accuracy measurement standard. The third step was to see how the accuracy and the efficiency of ultrasound image processing can be improved. Finally, to compare the output from the automated, real-time ultrasound tracking to that of human abilities to track the equipment on multiple static frames of the ultrasound screen.

Further, in the sections that follow, the work done using ultrasound in this chapter will be tied up with optical tracking, robotics and a software navigation system forming a platform for fetal surgeries.

4.2 Aims

This chapter deals with the following:

1. Identification and evaluation of the problems in using medical ultrasound with surgical instruments
2. Problems with ultrasound image processing for surgical instrument tracking
3. Method of combination of optical tracking to ultrasound object tracking
4. Comparison of multimodality tracking with plain ultrasound and optical tracking

4.2.1 Ultrasound object tracking target specifications

Object detection and tracking accuracy depends entirely on the resolution of the image, the distinctiveness of the object to be tracked and the efficiency of the tracking algorithms. In the literature review it has been discussed that ultrasound image resolution, apart from the physical characteristics of the wave source, can also be affected by the type of medium used, intervening structures and noise in the environment. Since the highest of standards in ultrasound imaging-based object tracking, during the surgery, are always based on what the surgeon can perceive, the required target resolution cannot be set as a rule or have a numerical value unless universally agreed upon. However, the following can be considered as valid targets for the tracking system:

1. Object detection using tracking algorithms should be at par with human abilities to distinguish the object
2. The true centroid of the object cross-section should be in line with the centroid of the object tracked on the image.
3. Speed of tracking should be under the perceivable limits of human vision 12 to 15 Hz or more for real-time vision.

4.3 Materials

4.3.1 Ultrasound image acquisition

The Ultrasound equipment used for the experiments is a Toshiba F400 shown in Figure 4.2 (a), capable of B-Mode scanning, used for obstetric ultrasound adjustable between 2.5 MHz to 3.5 MHz depending on the depth of penetration.

There are different types of probes such as the ones shown in Figure 4.1(a) which can be used, but in most obstetric applications, a curved array probe as seen in Figure 4.1(b) has been used. The image produced by the device is in analog (PAL) format at 25 frames/second at 625 lines using an 'EasyCap' device shown in Figure 4.2 (b) device. Hence is acquired using a USB 2.0 digital conversion unit. The device acquires the image available in an H.264 encoded high definition format. The h.264 format is readily decoded by Video Communication library in Java, and USB Video Class and hence is usable as 720 x 576-pixel frames at 25 frames/second grayscale pixel frame, with no observable latency. Though the acquired image is constrained by the frame rate of the ultrasound machine output, the refresh rate of the image processing software can be much different based on the speed of the image processing algorithm used. However, for all practical reasons, 25 frames per second is considered the real time and has been considered as the target rate in most image processing algorithms.

(a)F400 machine

(b) EasyCap image digitizer

Figure 4-1 Ultrasound machine and image acquisition system (a) F400 B-Mode obstetric ultrasound machine from Toshiba, with convex piezo array of 128 elements operating at 3.5MHz to2.5MHz (b) EasyCap image digitizer converts NTSC/ PAL USG output to USB 2.0 Webcam inputs

In Figure 4.2(a) different types of available probes for various applications are shown. For most trans abdominal and Gynaecological procedures, the 3.5 MHz probe is widely used because of the wider field of view it produces and the depth of penetration is much higher than most other probes which have higher frequencies. Though the depth of penetration is higher, the lower frequency does reduce the vertical resolution and when an expanding beam is used, there is reduction of lateral resolution.

Linear array probes are used mainly for blood vessel imaging and normally have high frequencies to enable high imaging resolution but have less depth of penetration, therefore cannot be used in applications such as fetal surgery of other intra-abdominal surgeries.

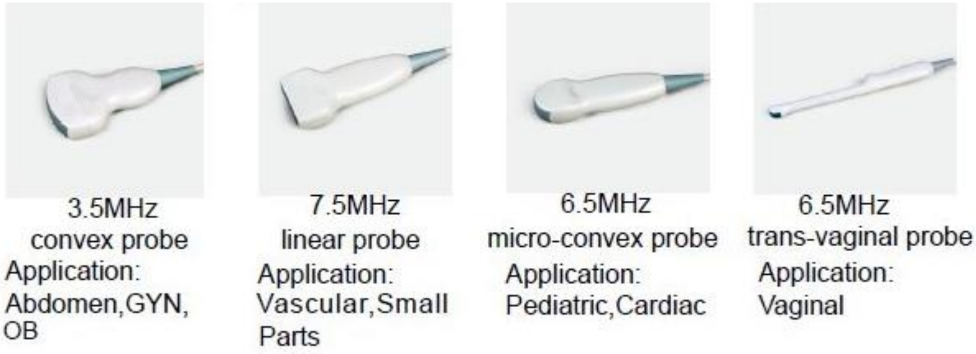

(a)

(b)

Figure 4-2 Types of ultrasound probes and the probe used for experiments (a)The different ultrasound probes are shown above. (b) The one which is used is a convex probe for Gynaecological examination.

In Figure 4.2(b), a convex probe used for obstetric and gynaecological procedures is shown. Figure 4.2(b) also shows optical trackers attached to the ultrasound probe, which enables the user to track the movements of the ultrasound probe in 6 DoF.

4.3.2 Optical tracking using Optitrack from Naturalpoint

Optitrack Trio, a commercially available optical tracking system with 3 cameras and sub-millimetre accuracy – 0.77% error for static errors (Thewlis, 2011) and within a tracking volume of 2 x 2 x 2 m is being used for the ultrasound static, dynamic experiments and to merge the output of optical tracking to form multimodality navigation in the further stages of development.

The tracking system comes with a visualization and interface software called '*Motive'* which can show the identified reflective markers. These markers can then be combined into rigid bodies with a minimum number of markers being three. For a set of 3 markers declared as a rigid body, the orientation at the instance of the declaration is taken as its starting rotational orientation. Therefore, a calibration unit is built which would provide a constant reference for the tracking system and serve as a base for the equipment.

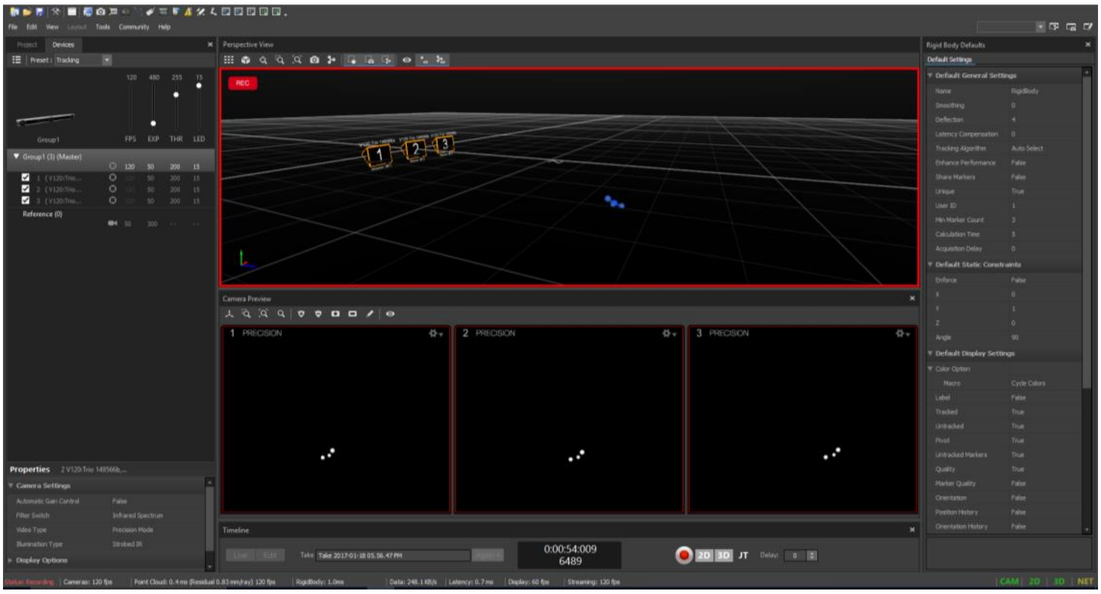

Figure 4-3   Motive software for optical tracking of markers using Optitrack cameras

The software is shown in Figure 4.8 also records the video of the marker movements and exports the marker positions and orientation into a comma delimited CSV format. The single and unlabelled markers are exported too, with marker positions (in metres) exported. Such unlabeled markers are always to be placed at a higher distance than the highest distance between the individual markers in the rigid body marker array. Sunlight and other sources like brightly lit lamps, especially IR sources are avoided, or masked with the help of the software, in order to prevent errors.

4.3.3 Optical tracking of a rigid metal catheter

Figure 4.9 shows a 3D printed joystick attached to a stainless-steel catheter. The length of the catheter, which is a tube of 3.0mm outer diameter and 2.2mm inner diameter is supported by a 3D printed handle custom made to fit into the hand. The 3D printed device has been printed in such a way that the optical markers can be attached to the device magnetically and each of their centroids is close to the plane of the metal catheter.

Figure 4-4 3D printed hand-held joystick with catheter and magnetic receptacles for optical trackers

The 4 markers are placed in such a way that the upper 2 markers are 9 cm from each other and the bottom two markers are 6 cm from each other. The markers are placed this way in order to avoid marker angle confusion when the set of markers are classified as a rigid body in 'Motive' software. Once declared as a rigid body, the software works out the marker set patterns and uses the perceived geometry into a specific translation (x, y, z values in metres) and rotation (x, y, z, w Quaternion form) are calculated and observed live on the software at about 120 frames per second.

Further, change in orientation can lead to the marker distances reduce more than the largest distance within the sensor array, there can be evident marker confusion in terms of pose estimation and can lose track of the rigid body as such.

4.3.4 Rigid body orientation calibration unit

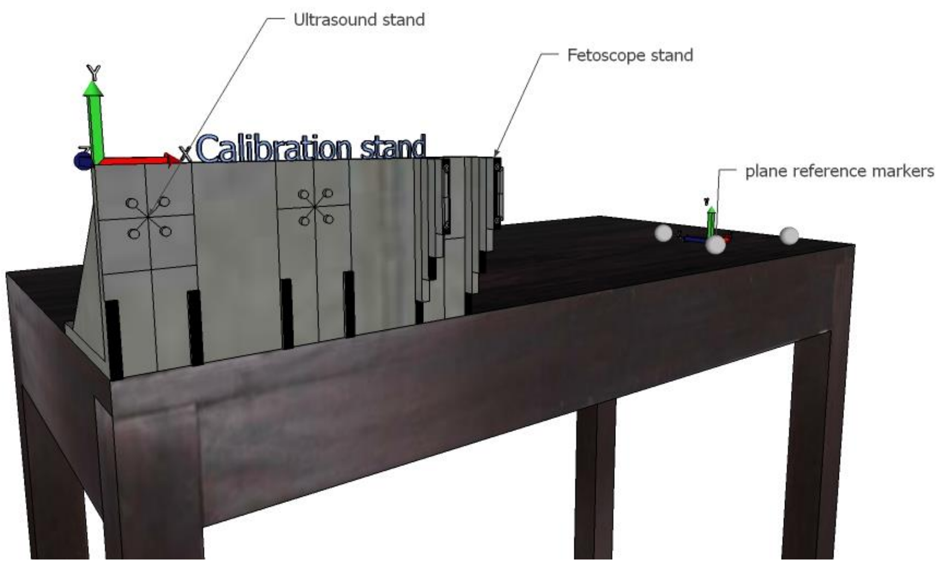

Figure 4-5 The calibration rigs with stand templates for fetoscope and ultrasound marker set patterns and set of 3 markers on the table for plane reference

In Figure 4.5, the calibration block setup on the corner of the table made in specific to hold the catheter unit vertically upright and with the table as the plane and origin reference, also forming the new world reference for position and orientation. It has been manufactured in such a way that the position and orientation calibration with reference to the table is repeatable and can hold the tools made for the surgery and non-reflective finish is used so that the Infrared reflection is minimized.

Though the rigid-body position and orientation are known, the location of the tip of the catheter in 3D is unknown. Also, though when the tip is present outside, it can be optically tracked by placing markers, in the case of surgeries, the line of sight is entirely lost. Hence, the tip calibration should be done for the tip to be identified in relation to the rigid body.

4.3.5 Phantom for ultrasound digital image scaling

Ultrasound images are unscaled and exist only as an array of pixels, post digitization. Whereas optical tracking system and the essential measurements are done in physical units of measurement – millimetres. Therefore, ultrasound image scaling experiments need to be done to convert pixel distances to real world distances.

To calibrate and scale ultrasound images to millimetres, scaling experiments are performed using an object with known dimensions. Hence, an accurately built phantom is visualized under ultrasound and a size comparison is performed on the digitised image. The phantom is made from fibreglass plate with perforations and glass beads coated with polyurethane paint as seen in Figure 4.6(a). Ultrasound imaging is performed with the phantom placed under water at different positions. Sample digitized image obtained can be seen in Figure 4.6(b).

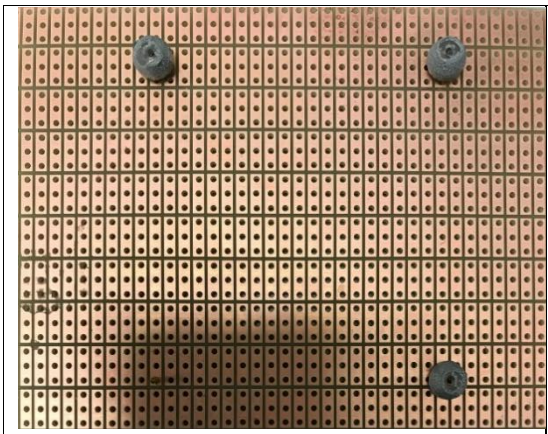

(a) Glass beads on FR4 PCB

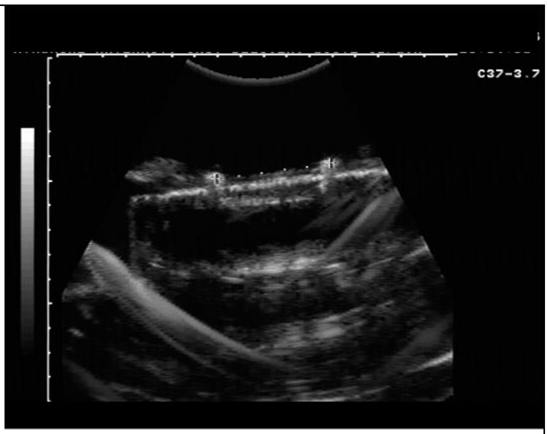

(b) Glass beads on FR4 PCB under Ultrasound

Figure 4-6 Ultrasound scaling phantom. (a) Shows the picture of the FR4 board with two glass beads at measured distance (b) FR4 board cross section and the glass beads seen.

In Figure 4.6(b), the shadows seen are due to a severe acoustic mismatch between the surrounding medium, water and the stainless-steel catheter. The differences in velocity of sound in different media have been discussed in detail in the literature review. In the above-stated case, almost all the sound energy is reflected, and no energy is further transmitted below. Such specific artefacts in an Ultrasonic field due to the introduction of rigid materials, especially metal needles or catheters, which look like comet's tail (Ziskin et al., 1982) can be seen.

4.3.6 Ultrasound image interface and image processing

A custom ultrasound image interface was developed in Java, as seen in Figure 4.7, for ease in real-time image display, calibration, manipulation, application of different algorithms, latency measurements and physical measurements. Some of the essential basic features implemented include:

- Mouse click tracking, distance between clicks, creating marks, recording click positions on the image
- Image source selection, recording frames and playback
- Region of Interest, static and dynamic selection for image processing application
- Real-time image processing with choice of different kernels in the same interface
- Frame rate, latency information and image controls to adjust brightness, contrast
- Support for CSV export and read CSV for use with a current image processing

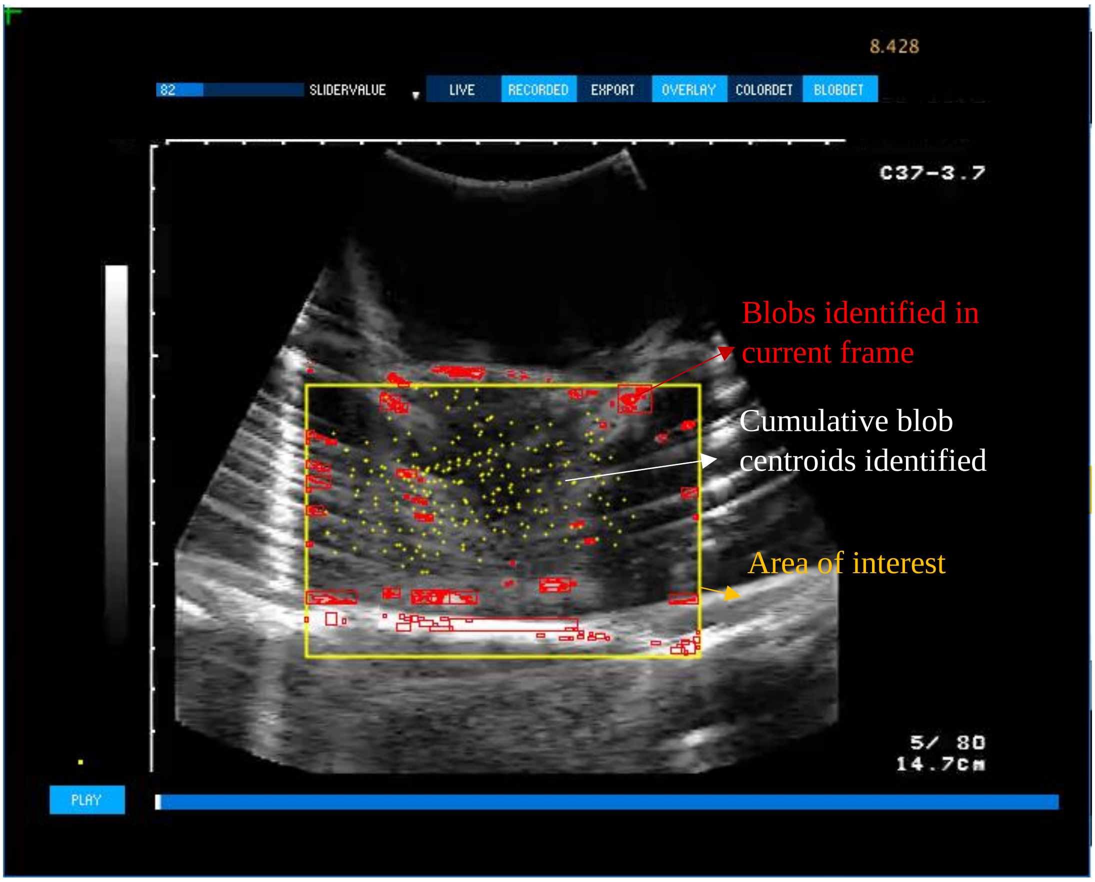

Figure 4-7 Sample image of ultrasound interface with image processing, export and import capabilities

4.3.7 Improving ultrasound visibility during dynamic tracking

Problems of monitoring instruments during ultrasound guided procedures have been elaborated in the literature review. The visibility becomes worse with an increase in dynamic movements. This can impose enormous problems in ultrasound image processing, as tracking loss is a common occurrence in a noise field, where trails of high brightness objects can be clearly seen respective to the direction of movement. Also, problems with visualising high-density materials in a highly dissimilar medium have been discussed in the literature review, with contributes further to the tracking problems.

Some of the problems observed during dynamic ultrasound tracking include:

1. Changing blob location and blob size, with rate of movement
2. Change in blob size with location of the object
3. A metal instrument created reverberation shadows at certain angles and locations.
4. The reverberation shadows and the shadow of the rigid object did vary in intensity and density based on the distance from the Ultrasound probe.
5. Structures of the rigid object suffered distortion due to the reverberation effects and appear to move or dislodge, with the movement of the rigid object

The following are some of the solutions applied to be able to visualize the objects better under ultrasound.

Solution 1:

Using a soft cover on the rigid catheter to match the density of the surrounding medium. The velocity of sound in silicone is 1485 m /sec and is the closest to the speed in water 1480 m/sec. When the soft silicone coating was applied, the lateral reverberation shadows have reduced which can be seen in Figure 4.20.

Solution 2:

Moving the catheter only in the operating range and not too close to the Ultrasound Imaging probe.

Solution 3:

The container used was lined with silicone to avoid reflections from the base.

Key:	Red box – catheter cross section Green ovals – Ultrasound lateral scattering Yellow lines – Total internal reflection and reverberation shadows	
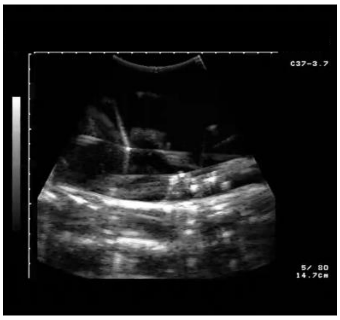 (a)Metal catheter	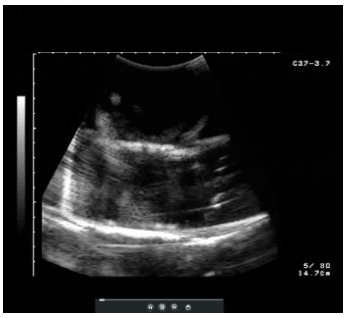 (b)Latex catheter	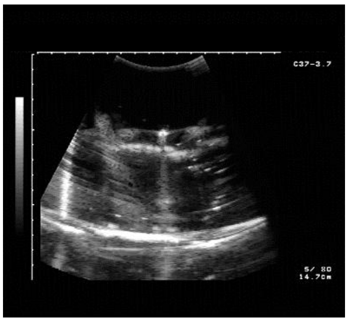 (c)encapsulated catheter
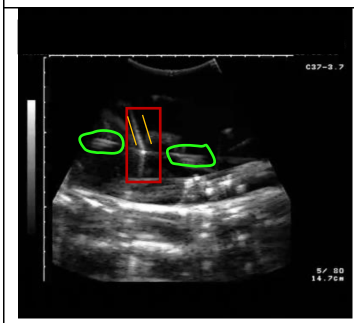 (d)Metal catheter shadows marked	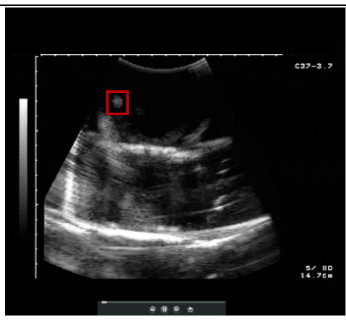 (e) Latex catheter no other shadows	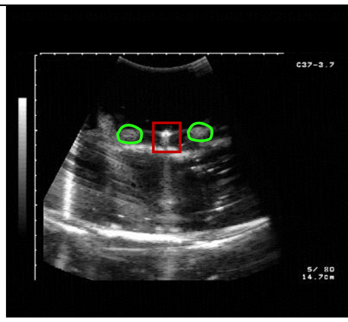 (f) Encapsulated catheter with reduced shadows

Figure 4-8 Ultrasound visibility of different materials (a) and (d) show a metal catheter under Ultrasound visualization with the different shadows. (b) and (e) shows a cross section of a plane silicone catheter under USG. (c) and (f) shows a metal catheter encapsulated in silicone showing reduced shadows than in (a) and (d)

Figure 4.8 (a) and (d) show how a metal catheter cross section produces shadows under ultrasound. Figure 4.8 (b) and (e) show a latex catheter under ultrasound. It can be seen that latex material has very less shadows observed in the ultrasound image. Figure 4.8 (c) and (f) show how the combination of soft material with the metal catheter reduces the amount of reflections and shadows as discussed earlier in the solutions offered.

4.4 Methodology

To be able to identify objects in the ultrasound image can be referred to as object tracking for Ultrasound. Such object tracking involves digitizing and acquiring the image initially, followed by scaling of the digitized images in millimeters and then the required features are extracted using image processing. In ideal cases, for example, ultrasound static images, the ultrasound image processing should be able to work without any loss of identification. Whereas, in a real-time varying image, since the objects are constantly evolving in shape and size, there can be a loss of tracking. This section will deal with experiments to identify static and dynamic ultrasound variations in surgical instrument tracking and effectiveness of human identification of objects in comparison with ultrasound image processing and ultrasound image processing, merged with optical tracking using the flowchart seen in Figure 4.9.

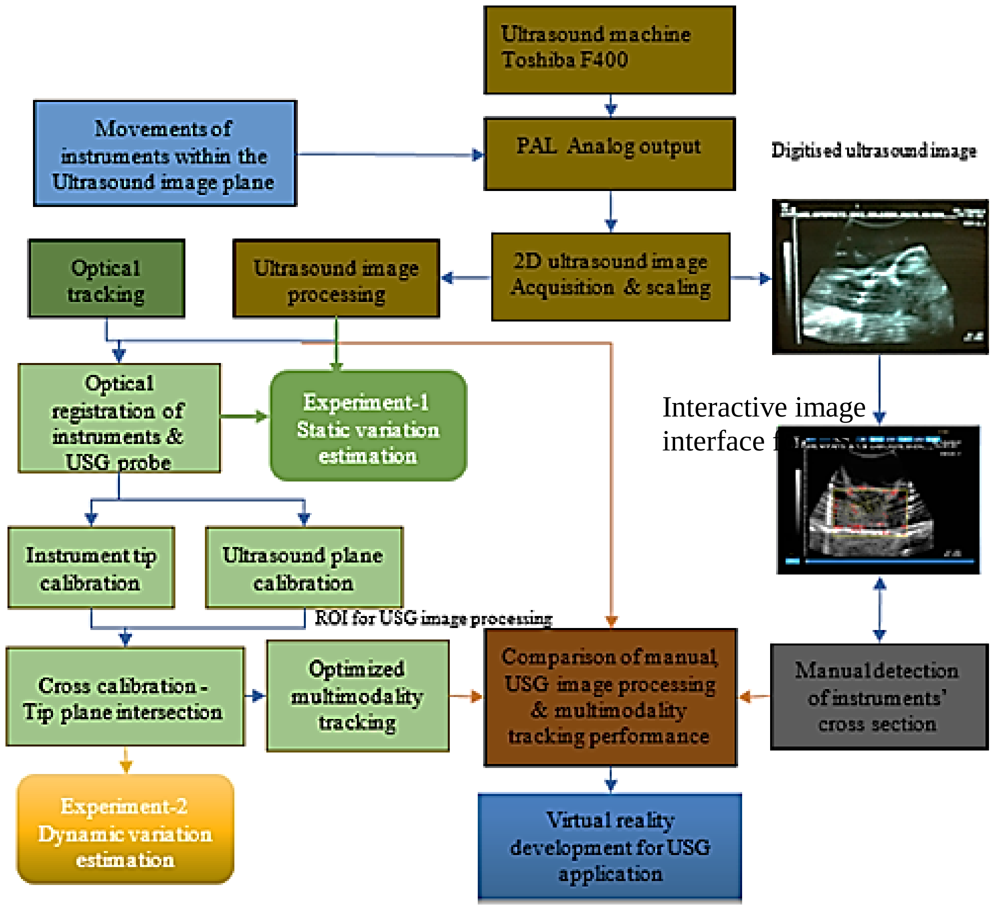

Figure 4-9 Simplified chart of manual and automatic ultrasound object tracking and comparison

In Figure 4.9, The flowchart shows a 2D ultrasound machine being used to acquire the image input initially. It should be noted that the real-world movements can have 3 dimensions, whereas the observation of the ultrasound probe is in 2 Dimensions and hence it gives us a cross-sectional view of the instrument on the image. When such an image is imported into a virtual environment, it is imported as an image texture for a given area and a given scale, which is referred to as the image plane. Since ultrasound image and the real world and the software environment have different coordinate systems and different scaling, initially the scaling has to be made universal. For this reason the ultrasound scaling experiment is done.

After the scaling process, the scaled image is used for the comparison of manual identification of a defined object moving in the image plane with image processed output to identify the same object.

Initially, to estimate the amount of static noise that can impact the ultrasound accuracy. A static variation experiment is done by confirming that the instrument viewed in the ultrasound plane, does not actually move in the real world using optical tracking. For the automated experiment to track the cross section of the moving instrument in the ultrasound plane, a dynamic tracking experiment is performed. Ultrasound scale calibrated output is merged with Optical tracking. Optical tracking has a resolution in microns but the accuracy falls within the sub millimetre range under 2 metres from the tracking system. Therefore, software environment was designed to have 1/10th of a millimeter spatial resolution and hence the calibration of the ultrasound plane needs to be done to match this scale.

4.4.1 Ultrasound calibration experiments

Ultrasound and optical tracking are two different system existing in the same coordinate space and hence one system needs to be registered to the other to unify the coordinate axis and then the displacements are required to be matched by scaling one to the other.

4.4.1.1 Ultrasound digital image scaling experiment

The ultrasound pixel image obtained is unscaled, though it can show measurements which the Toshiba F400 has been calibrated by the manufacturer. Hence scaling experiments were performed against the template with a known magnitude as shown in Figure 4.6 (a). The analog on screen scaling measurements are compared to pixel measurements done on the computer with on-screen measurements as seen in Figure 4.10 at different heights.

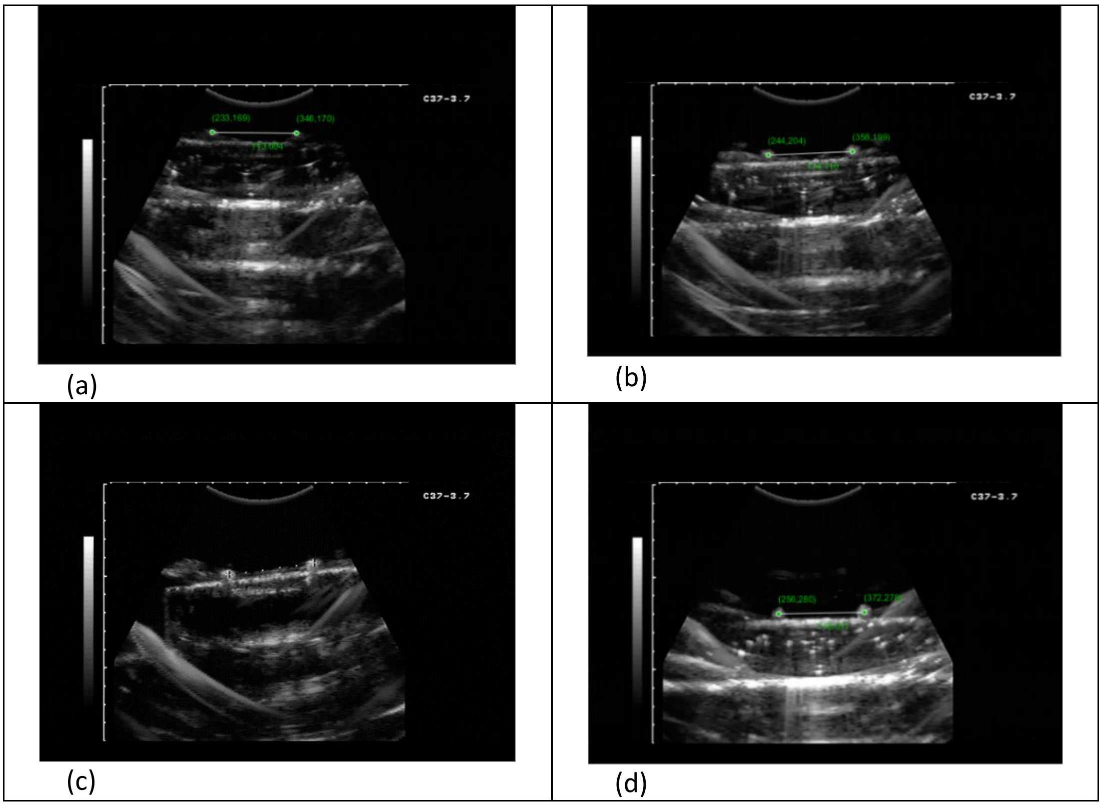

Figure 4-10 Scaling using the 'Ultrasound phantom'. (a), (b), (c) and (d) are ultrasound images of the phantom at different heights measured within the ultrasound machine interface and compared with measurements one on the digitized pixel image in the computer image interface to aid scaling.

The screen pixel measurements seen in Figure 4.10, *S(x,y)* in terms of millimetres *R(x,y)* are given by:

$$R(x, y) = S(s.x, s.y) \qquad 4.1$$

The *R(x,y)* gave the calibrated Cartesian coordinates of the ultrasound images in millimetres, which are used for further measurements.

4.4.1.2 Tip calibration of the catheter for optical tracking

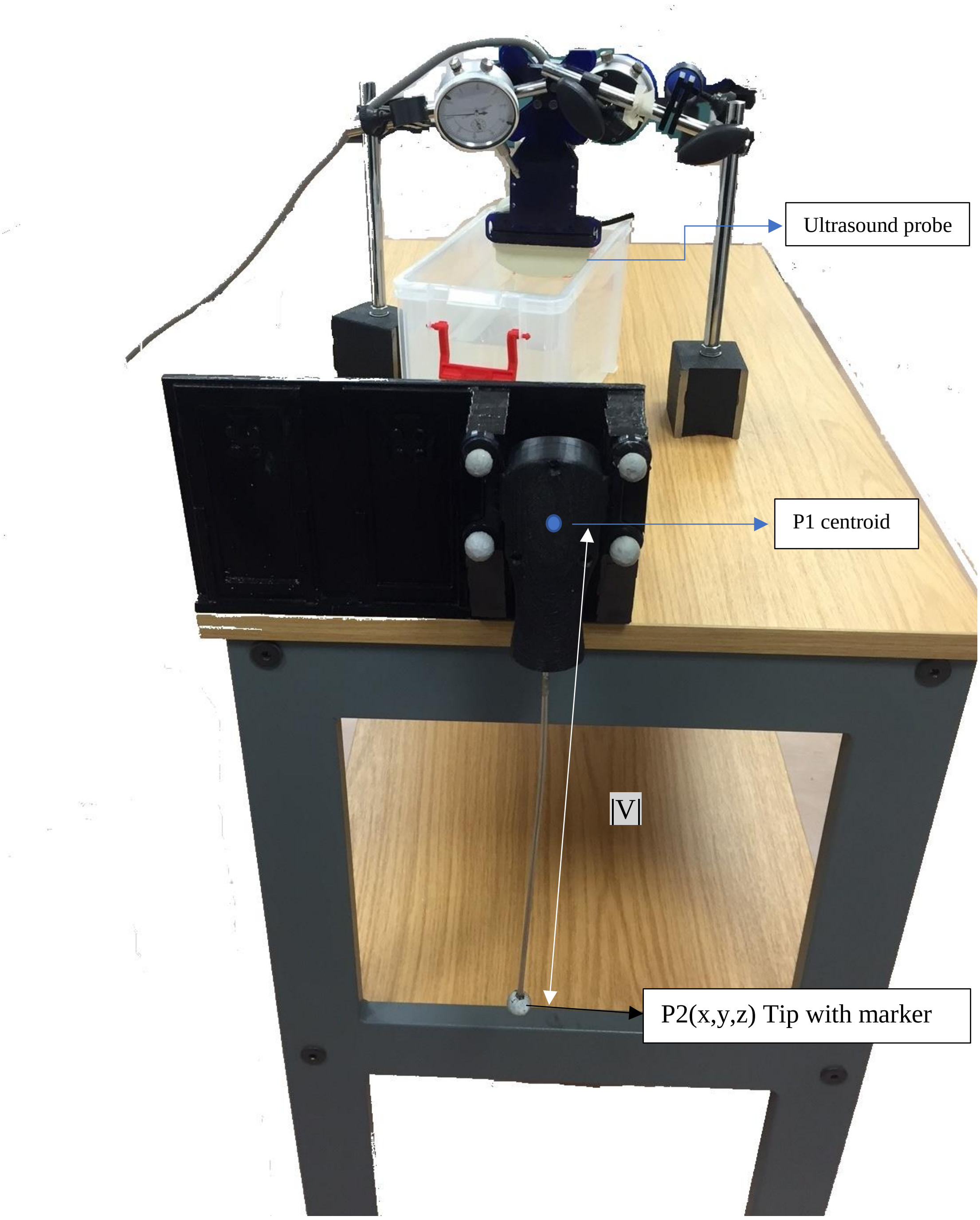

Figure 4-11 Fetoscope with detachable retro-reflective optical markers and a 15mm diameter detachable optical tracker placed at the tip, for tip calibration

As seen in Figure 4.11, the fetoscope model is mounted to the calibration block, and the rigid bodies are declared in '*motive*'. After which, a 15mm optical marker is drilled with the depth of 7.5mm and approximately 3mm diameter, in such a way that the catheter tip can be inserted with a snug fit. Irrespective of the position and the orientation of the rigid body, the marker at the tip of the catheter is theoretically going to remain the same as the tip dimensions are constant.

Since the tip dimensions are constant, when there is no rotation, the location of the marker placed at the tip P2(x,y,z) at a distance |V| can be given by:

$$\mathrm{P2(x,y,z)} = \begin{vmatrix} 1 & 0 & 0 & P1x \\ 0 & 1 & 0 & P1y \\ 0 & 0 & 1 & P1z \\ 0 & 0 & 0 & 1 \end{vmatrix} \cdot \begin{vmatrix} Vx \\ Vy \\ Vz \\ 1 \end{vmatrix} \qquad 4.2$$

Which can be expressed as:

$$P2 = P1 + V \qquad 4.3$$

The distance of the marker from the tip |V| remains a constant irrespective of the orientation of the fetoscope. But, since the orientation of the tip changes with rotation about P1(x,y,z) as the centre, the sub components of V(x,y,z) change. Therefore the rotated P2(x,y,z) by an orientation value R can be given by:

$$P2(x,y,z) = P1 + V.R \qquad 4.4$$

R, when represented in quaternion form has 4 components qx, qy, qz, qw and can be represented as:

$$\mathbf{R} = \begin{vmatrix} 1 - 2\mathrm{qy}^2 - 2\mathrm{qz}^2 & 2\mathrm{qxqy} - 2\mathrm{qzqw} & 2\mathrm{qxqz} + 2\mathrm{qyqw} \\ 2\mathrm{qxqy} + 2\mathrm{qzqw} & 1 - 2\mathrm{qx}^2 - 2\mathrm{qz}^2 & 2\mathrm{qyqz} - 2\mathrm{qxqw} \\ 2\mathrm{qxqz} - 2\mathrm{qyqw} & 2\mathrm{qyqz} + 2\mathrm{qxqw} & 1 - 2\mathrm{qx}^2 - 2\mathrm{qy}^2 \end{vmatrix} \qquad 4.5$$

$$\mathrm{P2(x,y,z)} = (P1 + V.R) \qquad 4.6$$

Hence the position of the tip P2(x,y,z) can be estimated and therefore, the optical tracker can be removed after calibration.

4.4.1.3 Finding the plane of the ultrasound image

Though the ultrasound probe can be tracked by optical tracking, the location of the image plane is not at the same plane or position as the probe. Therefore, experiments are required to find the plane and use the plane equation for calibration within the 3D interface for multimodality tracking which will be discussed in the next chapter.

The ultrasound probe is initially stabilised using clamps and magnetic bases. Location of the ultrasound probe is found by placing optical markers on the ultrasound probe, with the setup described in Figure 4.12. The virtual plane corresponding to the ultrasound plane of the probe is found by using the following steps:

1. Catheter tip calibration is done by fitting a 5mm temporary, insert-able retro reflective marker on the tip. The tip relationship with to the centroid of the rest of the markers is recorded.

2. Since the relationship between the tip and the other markers is known, it can be easily estimated without the actual marker present. Hence, now it is removed.

3. Optically tracked surgical catheter tip (with silicone cap) is adjusted till its tip is faintly seen on the ultrasound monitor.

4. The projected tip location of the catheter is found for every time the tip is seen on the screen.

5. The experiment is repeated till a minimum of 3 points are found furthest from each other.

6. The process is repeated 15 times, and the equation of the plane with these 3Dpoints is found.

7. Least square fit was done with the points obtained from the experiment, using the plane fitting algorithm in Java, as seen in Figure 4.13.

The plane formed by a triangle ABC containing all the points using the setup shown in Figure 4.12, collected by line plane intersection between the ultrasound plane and the axis of the fetoscope tip – stem is given by:

$$E(A,B,C) = \sum(Ax + By + C - z)^2 \quad 4.7$$

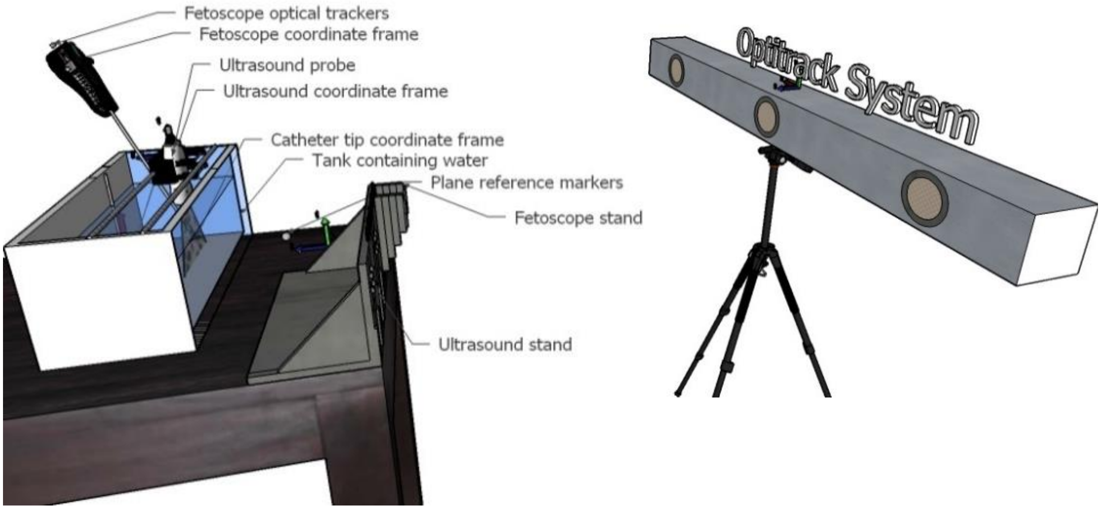

Figure 4-12 Setup for dynamic tracking. 3D printed handheld fetoscope, being optically tracked and intersecting the ultrasound plane. The plane of the table is the plane reference.

4.4.1.4 Single point Cross-calibration of ultrasound with optical tracking

After the optical tracking tip calibration shown in Figure 4.11, the tip is sleeved with a silicone cap to produce the image seen in Figure 4.8. From Figure 2.24 (a) in the Chapter 2 and Figure 4.8 (a), (b), and (c), it can be observed that the material used for the silicone cap is clearly visible as a relatively round object. Once the tip touches the ultrasound image plane, the image is frozen and captured. The interface has blob label return capability when the desired blob is clicked on with the mouse. Hence, with manual clicking, ultrasound blob detection can easily locate and return the specific blob and its centroid.

The green dot at the centre is the identified centroid of the object's cross section. The edges considered have dimensions of 36 x 34 pixels, and 8 significant edges have been identified. Hence the object's identified edges have been highlighted. In the case of similar objects, the system would highlight the object numbers with different serial number labels starting from '0'. Hence, more than one instrument can be identified in the USG image plane. Further developments have been planned to identify with greater accuracy using frame differencing techniques to make the calibration process completely automatic. But the manual method ensures safety and is relatively simple for the surgeon to identify and use.

Figure 4-13 Image processed USG frame highlighting the outline contour. Blob and edge detection of the catheter blob get indicated when indicated by the mouse pointer

4.4.1.5 Out-of-plane calibration

A sequence of positions of the fetoscope in ultrasound are adapted, and the centroid is found by mouse over blob centroid detection as described in the earlier section. The position sequence is shown in Figure 4.14. The position output from the scaled ultrasound image as described in the earlier sections and the plane equation of the points are then used to cross-calibrate the line plane intersection points to the actual ultrasound image plane. The calibration process is done with the soft tip for better visualization.

Once the tip registration is successfully done, the soft tip cap can be removed, and the true tip position follows the optical tracking registration, though there can be a discrepancy between the ultrasound blob centroid and the optical tracking tip position. Since the tip position always corresponded to the optical tracking calculations, the optical tracking output is considered as a gold standard for further comparison and merging ultrasound blob tracking outputs with optical tracking outputs for registering one system to the other. The linear transformation equation for the optical tracking output O(x, y) to the desired fetoscope cross section centroid Fc(x, y) and calibration offset C(x, y) can be given as.

$$Fc(x,y) = ([O(x) + P(x)], [O(y) + P(y)]) \qquad 4.8$$

The plane calibration is done using the fetoscope intersection on the ultrasound plane with catheter positions suggested in different quadrants as see in Figure 4.14. Though random positions can be used for calibration, the closer the positions are, the more will be the line plane intersection errors.

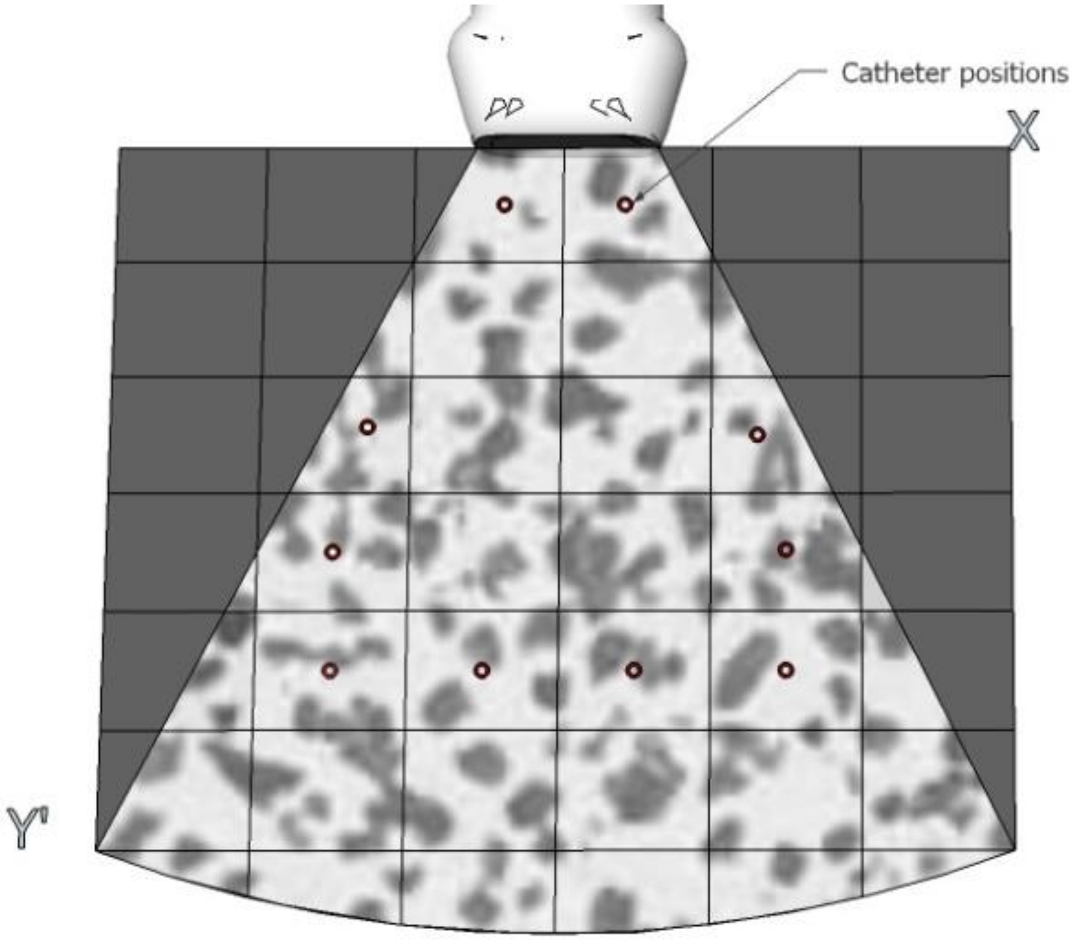

Figure 4-14 Catheter positions on Ultrasound plane for use in plane calibration

The output obtained from this section is used to translate and rotate the Ultrasound plane in with respect to the optically tracked position of the ultrasound probe.

4.4.1.1 Fetoscope – Ultrasound intersection in 3D

To find the respective blob in the Ultrasound plane in 3D, with a reference obtained from the optical tracking system, both the optical tracking system and the ultrasound plane should be in the same world coordinate system. Hence, a virtual plane with the plane equation obtained from the previous experiment is created in OpenGL Java 3D interface, and the locations of the fetoscope centroid and the calibrated tip are streamed from the optical tracking output to the interface. The output is as seen in Figure 4.15.

The ultrasound plane should ideally intersect the line drawn from the fetoscope centroid to the tip. The points of plane – line intersection should be the same when observed from the ultrasound and the optical tracking system alike. Since the optical tracking system has a 3D output, whereas the ultrasound output is 2 Dimensional, the corresponding 2D point in the ultrasound coordinate system is found for comparison with the ultrasound output.

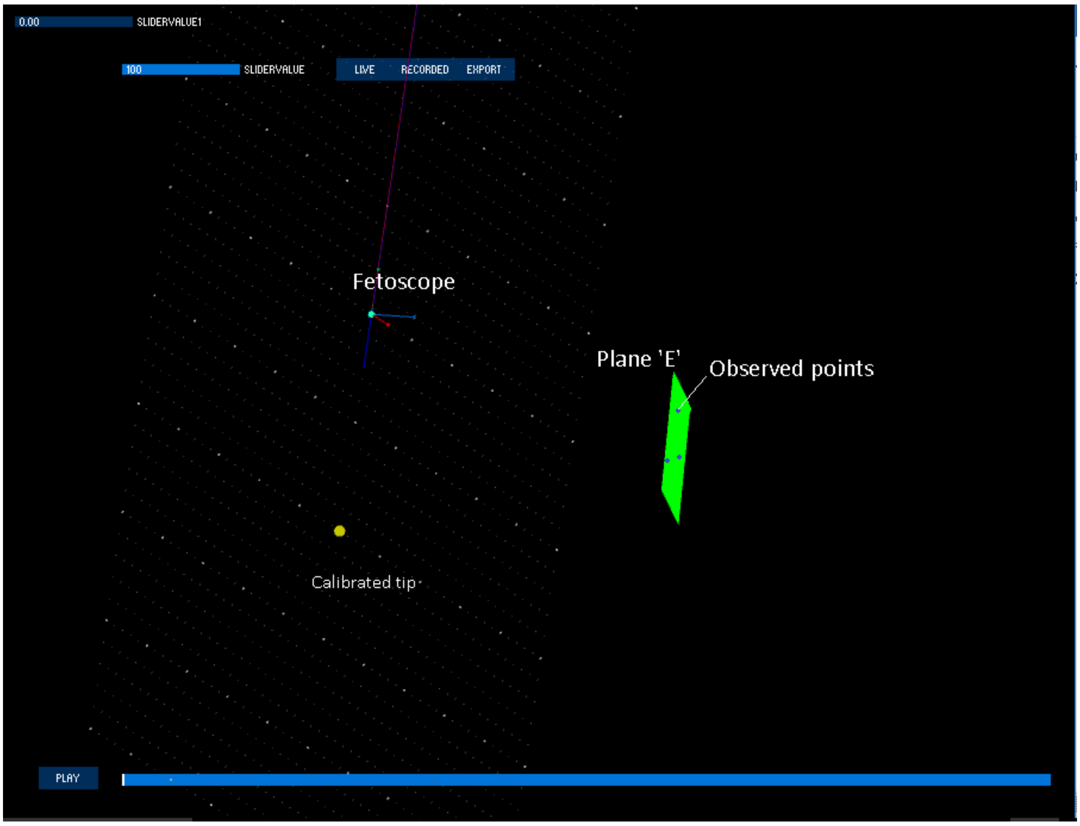

Figure 4-15 3D Navigation environment with the registered plane. The plane defined by the 3 best-fit points on the plane using plane equation are imported in 3D navigation interface developed in Java, as seen from a lateral perspective. Fetoscope is located in the calibration stand. The yellow sphere is the calibrated tip of the fetoscope.

4.4.1.2 Plane – line intersection calculation:

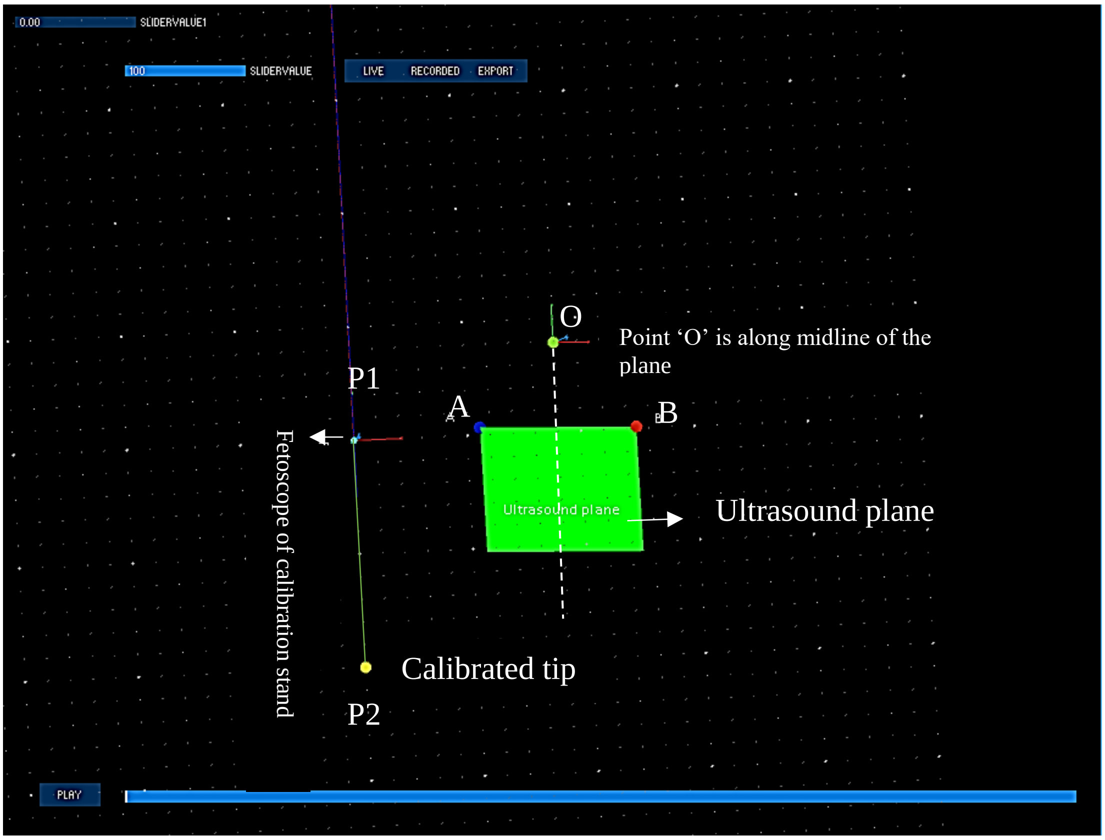

Figure 4-16 Ultrasound plane from a forward camera view, scaled to millimetres. Points A(x,y,z), B(x,y,z) and O(x,y,z) are points on the plane outside the image area, for better viewing, required for plane line intersection calculations.

In Figure 4.16, an ultrasound plane with 3 points A, B and O is considered. The triangular plane centroid C is given by:

$$C = (A + B + O)/3 \tag{4.9}$$

Normal N for this plane is given by:

$$N = (A - O) \times (A - B) \tag{4.10}$$

Let us consider a virtual line, joining the optical tracking centroid of the fetoscope P1 to the calibrated tip P2, as seen in Figure 4.16, changing position to intersect the plane, as seen in Figure 4.17, and P3 a point on the plane, when the ray from P1 and P2 intersects the ultrasound plane E.

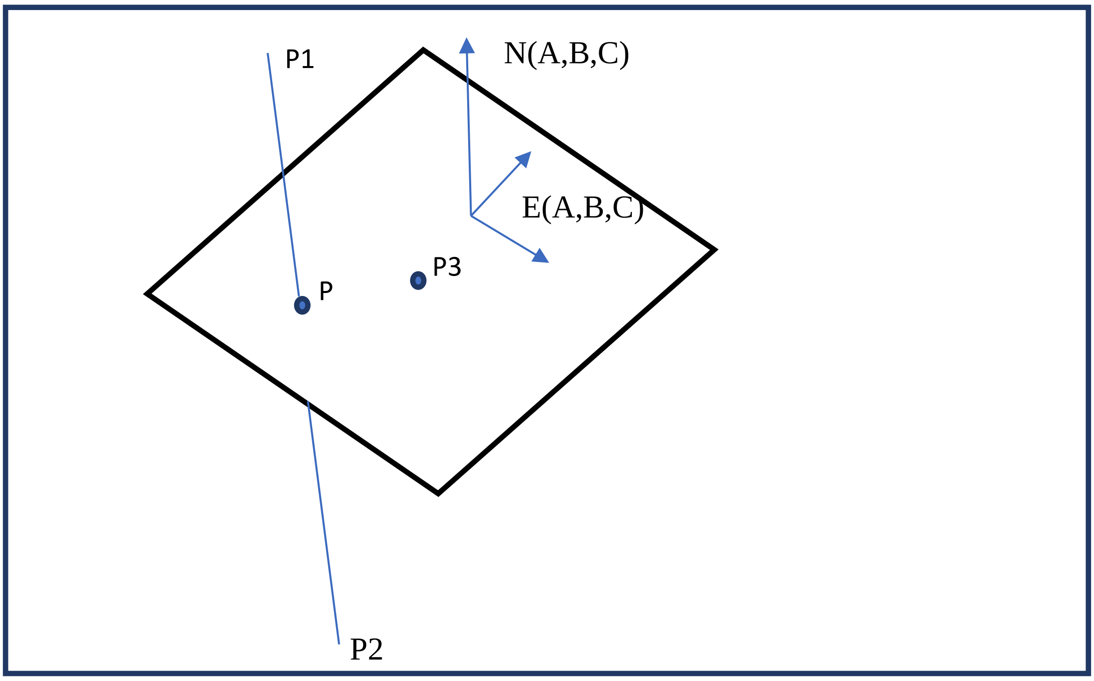

Figure 4-17 Plane line intersection. Plane E(ABC), with normal N(ABC) and P3, is a point on the plane. A line P1, P2 intersects with the plane at point P

The equation of the plane with normal N and points P and P3 on the plane can be given by:

$$N.(P - P3) = 0 \tag{4.11}$$

The equation of the line with an arbitrary point P on the line P1, P2 can be given as:

$$P = P1 + u(P2 - P1) \tag{4.12}$$

Line plane intersection occurs when:

$$N.\big(P1 + u(P2 - P1)\big) = N.P3 \tag{4.13}$$

The plane-line intersection point P in 3D can now be found real time using the following equation:

$$u = \frac{N.(P3 - P1)}{N.(P2 - P1)} \tag{4.14}$$

Therefore, point P can be given by,

$$P = P1 + u(P2 - P1) \tag{4.15}$$

4.4.1.1 Conversion of plane-line intersection points to 2D

Since the intersection points on the plane are calculated as 3D points, comparison with the ultrasound output in 2 dimensions is not very straightforward. Hence, the corresponding 2D points are found using point ‘A’ as the origin of the ultrasound image plane, ‘B’ as the image plane maximum in X - axis direction of the navigation volume and the 3D point to be converted which is ‘C’. Point ‘U’ is the center of the probe surface on the plane and is also the center of the image frame border AB, as seen in Figure 4.18.

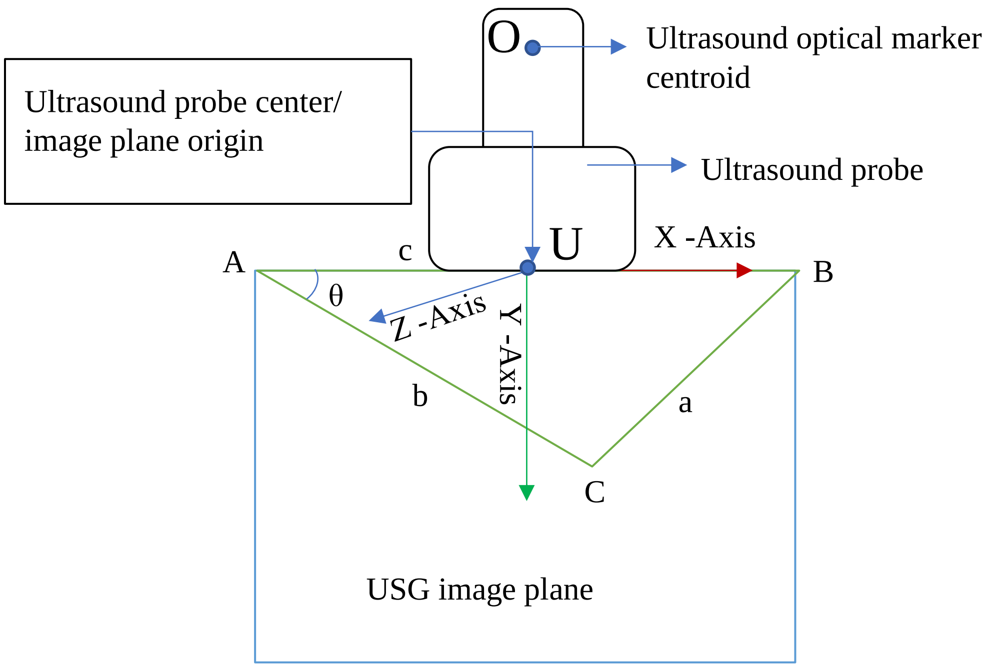

Figure 4-18 Ultrasound image plane with 3D line plane intersection ‘C’ A and be are the extents in the X direction

Consider a triangle ABC where distance between A, B and C points are AB- c, BC-a and AC- b respectively. The angle BAC (θ) can be given using the law of cosines:

$$\theta = cos^{-1}\left(\frac{-a^2 + b^2 + c^2}{2bc}\right) \tag{4.16}$$

From the above, b and **θ** are known and can therefore form a polar coordinate system in 2D on the given plane. Hence, the corresponding 2D point J(x,y) is given by:

$$J(x, y) = J(b\ cos\theta, b\ sin\theta) \tag{4.17}$$

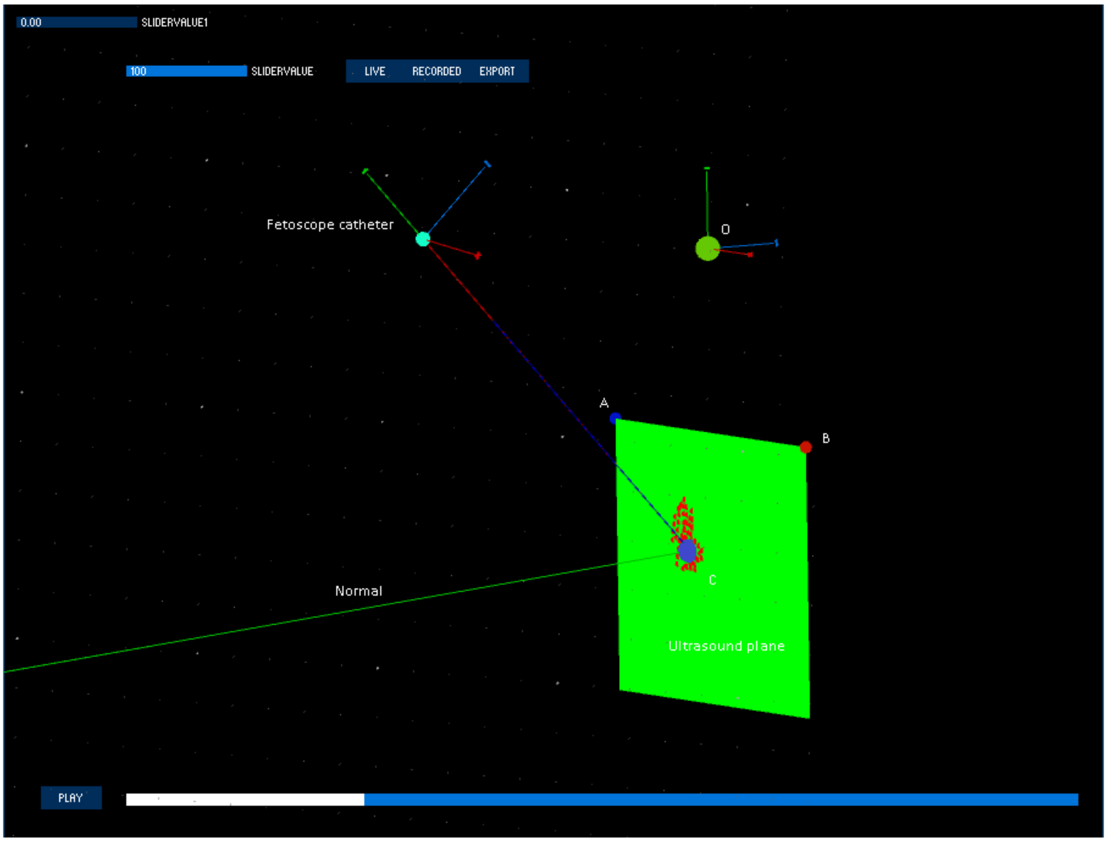

Figure 4-19 Calibrated tip is undergoing a ultrasound-fetoscope (plane-line) intersection. The yellow sphere changes colour to blue and creates a set of points P[i](x,y,z) on the plane, with minimum 1mm between each set of points to reduce overcrowding.

Figure 4.19, shows the intersection of the fetoscope axis line with the ultrasound image plane. The points of intersection in 2D f[i](x,y) are calculated from 3D intersection points P[i](x,y,z) using equations 4.11 to 4.17. The outcome of the calculations can be viewed in real-time using the interface seen in Figure 4.19.

4.4.2 Ultrasound experiment methodology

After the scaling of the digitised image is calibrated, experiments are done under ultrasound observation with optical tracking output as a reference to estimate the number of inaccuracies in ultrasound object tracking. The first experiment targets at estimating the amount of static variation in ultrasound imaging while observing a metal catheter and the second experiment is used to evaluate the dynamic tracking accuracy of the metal catheter.

4.4.2.1 Experiment 1 - Ultrasound static variation estimation

Ultrasound, being a real-time device, produces dynamic pixel images which change with time. By observation, the images obtained from a ultrasound machine in a nearly static medium was observed to be varying over time. Hence, the blob tracking algorithm, no matter how accurate will show consistent variation.

To prove that static noise in an ultrasound image can result in drastic variation in the centroid of the catheter cross section can be proved with a simple setup shown in Figure 4.20. A water tank containing a metal catheter of 3mm diameter, with 3 optical markers on the other end is used. The optical markers are tracked by the Optitrack tracking system. The ultrasound images are processed in real time using the simple blob detection algorithm described, with blob mass tracking and spoke filter were applied to the region of interest chosen. The centroid of the extracted blob is tracked over time and the change in position over time is found in relation to the output of the optical tracking over a period of an hour and the variations are documented.

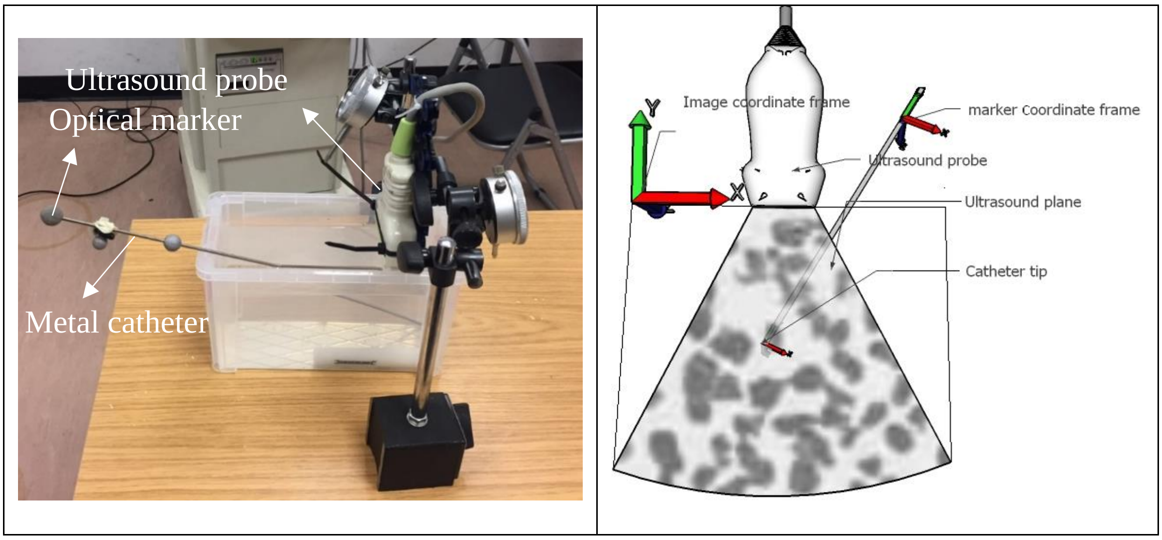

Figure 4-20 Metal tube with 3 mounted optical trackers and ultrasound probe is placed in such a way that the metal tube is in view of the ultrasound plane

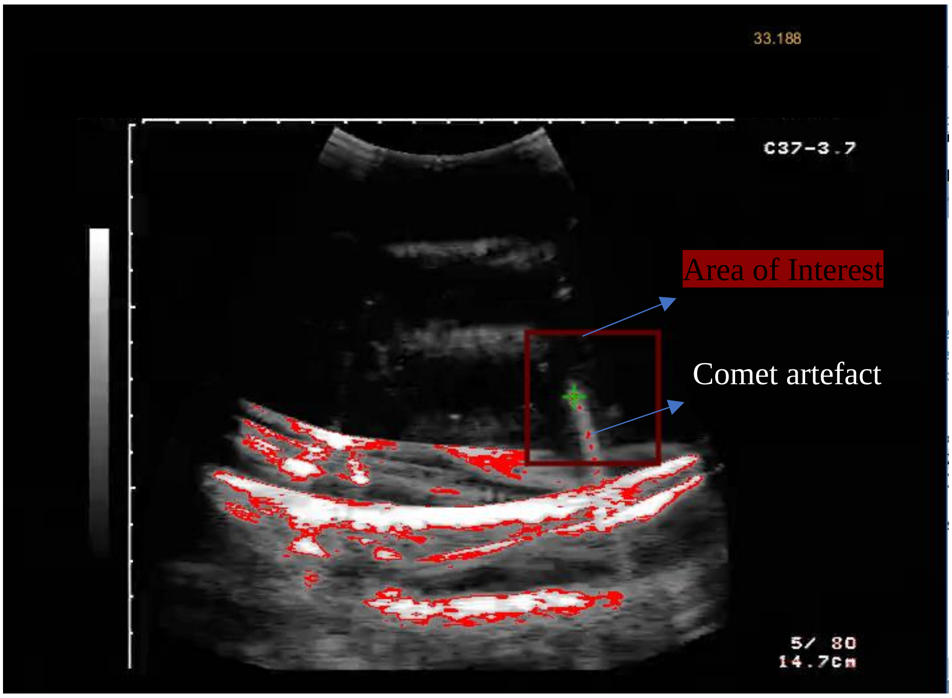

Figure 4-21 Result of blob tracking and centroid detected from the blob within the area of interest represented by the red rectangle

The cross seen in Figure 4.21 is the centroid of the blob observed in the ultrasound image. Ideally, the blob is not expected to move when the fetoscope stem is static, and the surrounding medium is relatively static.

4.4.2.2 Experiment 2 - Ultrasound & Optical dynamic movement tracking

The experiment started with the static setup is repeated with random movements of the metal catheter of the fetoscope under Ultrasound and optical tracking observation at an average movement velocity of about 20 mm/sec (Sánchez et al., 2014). The method used for covering the tip of the metal catheter to increase the visibility is used to reduce shadows.

If the ultrasound plane is scaling, the tip calibration and the plane orientation are accurately done, it was found that the line plane intersection P was invariably at the centre of the blob. The point of intersection +/- 2mm radius (maximum error from previous graphs) is taken as the region of interest. Which translates to a pixel area given by:

$$\mathrm{PA} = \pi\,(s \times \mathrm{BR})^2 \qquad 4.18$$

Where,

BR – Average blob radius found to be 2.086 mm

s- scaling factor found to be 2.178

PA – 64.184 mm^2

Hence, from a frame size of 720 × 576 = 414720 pixels or 640 × 480 = 307200 pixels to be scanned from, it has been reduced to the value of PA, which forms the Region Of Interest (ROI). Using the minimal size of ROI, the Ultrasound Image Processing can be fast and efficient.

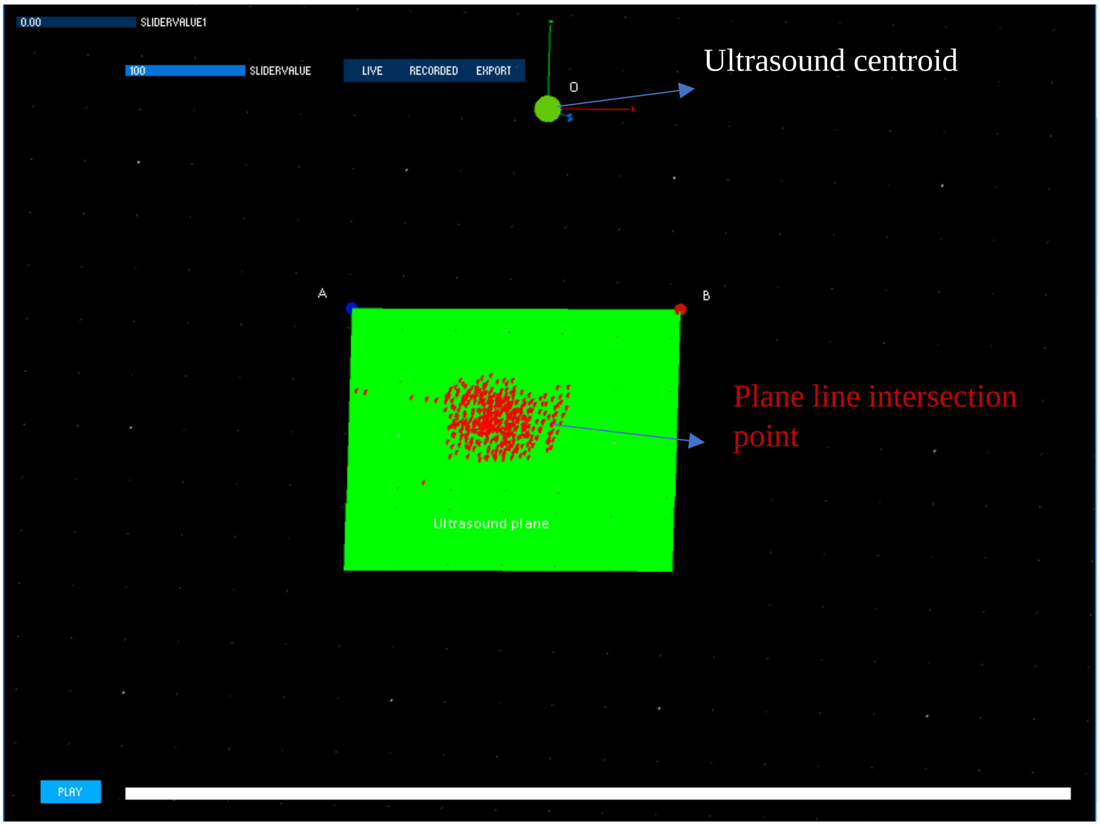

Figure 4-22 Shows the result of plane line intersection tracing.

In Figure 4.22, the result of plane line intersection tracing (Red spots) can be seen on the ultrasound plane (seen as green plane) in 3D when the experiment was complete. This output generates an area of interest for ultrasound image processing and is not the end result of this experiment. The green ball 'O' is the centroid of the rigid body optical tracker attached to the ultrasound probe. Points A and B form the corners of the ultrasound plane.

4.4.2.3 Experiment 3 - Manual Blob Detection Experiment

This experiment involves the use of the video recorded from Experiment2 and using subjects to observe the cross section of the fetoscope in the image frames. Though this seems straight forward due to the factors that are seen in the literature review (Ultrasound background), the effects of reflection, refraction and scattering can evidently result in the deformation of the metal catheter cross section to a variety of shapes making the process more challenging. Hence, the actual centroid of the catheter cannot be the same and is also not the equivalent of the centroid observed from ultrasound images. Though the above is the case, sonologists assume ultrasound to be reasonably accurate. An experiment involving finding catheter cross-sections was done to prove that the blob centroid may not be the true centroid of the object under ultrasound observation.

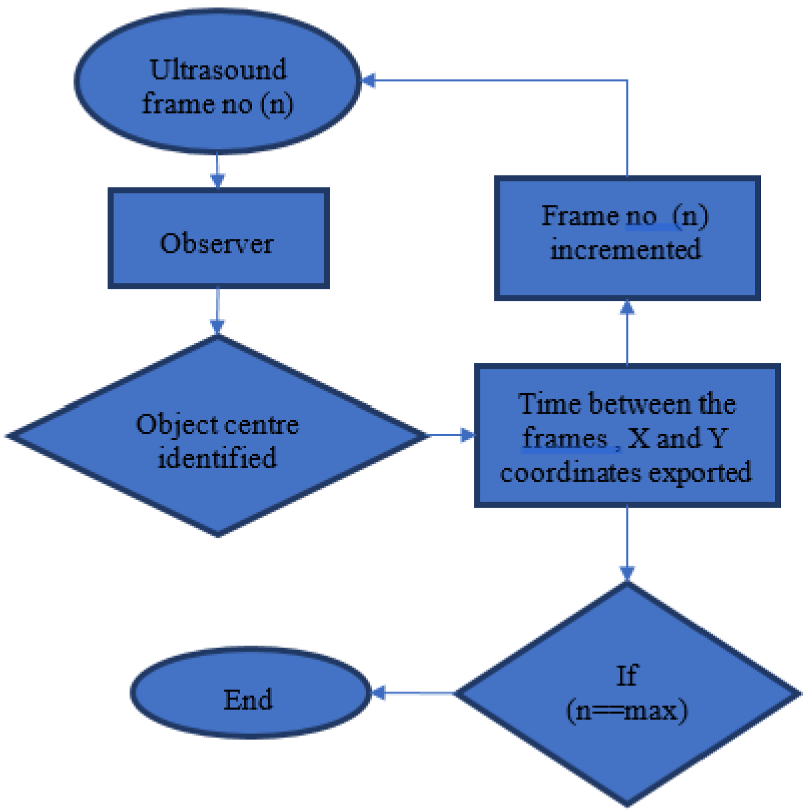

Figure 4-23 Ultrasound object centre identification, duration and coordinate data collection

Frames from the previously recorded ultrasound video of random movements are shown to 5 ultrasound trained professionals, with experience ranging from 3 to 15 years. All of the aforementioned candidates were able to recognise the region of a cross-section of the metal catheter in every single slide without any mistakes, within a fraction of a second. However, the experiment requires comparison with single points and hence, the experiment involved required the visual identification of what the subjects felt was the centroid of a cross section of the metal catheter, as seen on ultrasound. The ultrasound frames were programmed to switch to the next with every click on the image, and the timing between every frame is noted, as seen in the flowchart in Figure 4.23, using the interface seen in Figure 4.1

4.5 Results - Ultrasound calibration methods & experiments

The ultrasound experiments have two initial experiments to scale and calibrate the setup and two main experiments which will be used later to compare different methods of object tracking within the ultrasound plane.

4.5.1 Ultrasound scaling experiment

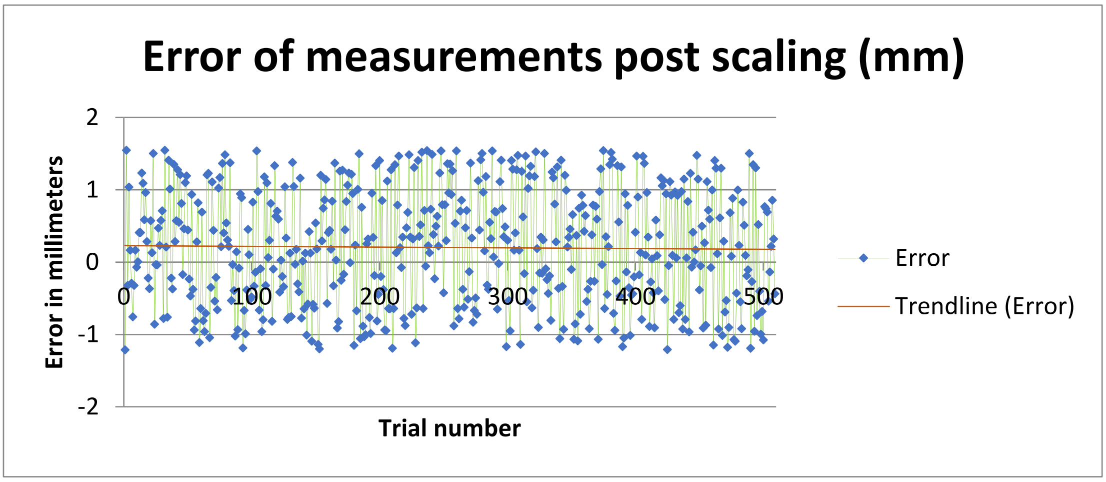

Figure 4-24 Error of measured measurements after scaling. Actual measurements when scaled with a calibration value of 2.17 pixels per millimetre

From the readings obtained from the scaling experiment, the scaling factor '*s*' is found to be 2.17 by 510 repetitions of manual measurements, from the ultrasound image. The errors seem to have a random magnitude as seen in Figure 4.24 with a mean error of 0.201 mm, the standard deviation of 0.801 mm and the error seems to have a normal distribution as seen in Figure 4.25. The highest error value happens to be in the mean.

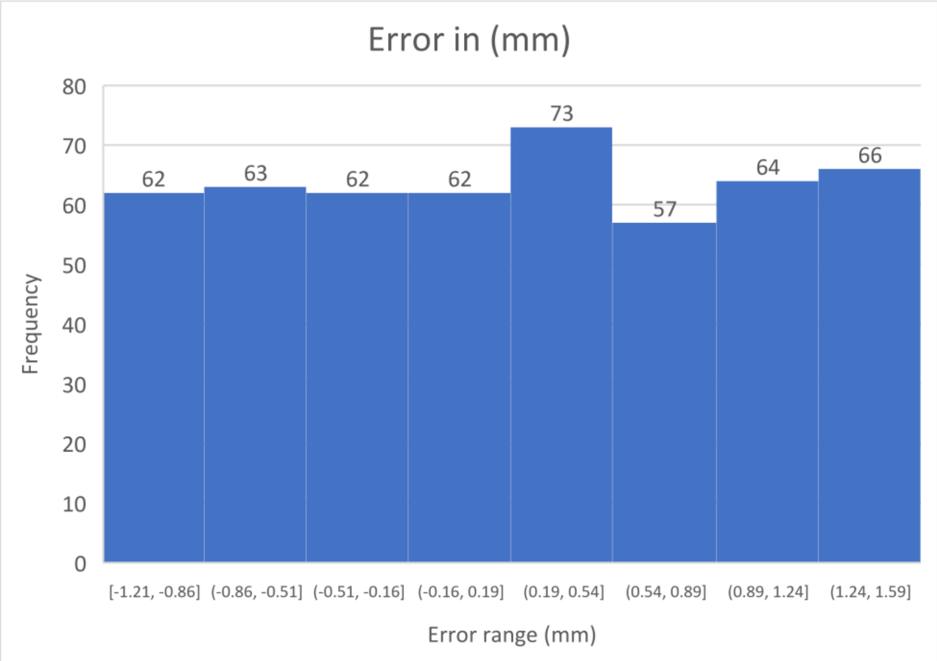

Figure 4-25 A histogram of the post scaling errors in millimetres showing a normal distribution

After the process of scaling, plane calibration, tip calibration, the said experiments are performed under Optical tracking and Ultrasound visualization. The line of sight is ensured in all cases, and the retro - reflective markers are magnetically attached to the catheter base and the ultrasound probe. The calibration rig is mounted on the edge of the table used for the experiments and this rig seats the 3D printed catheter and the ultrasound probe and holds them magnetically.

4.5.2 Ultrasound plane calibration

Ultrasound plane calibration is done by monitoring the 2D ultrasound while the fetoscope tip appears and the tip coordinates are recorded and the corresponding 2D coordinates of the ultrasound plane are noted and scaled. The tip coordinates recorded during this process are fit on to a plane with least squares regression fit method to get the 3D plane equation.

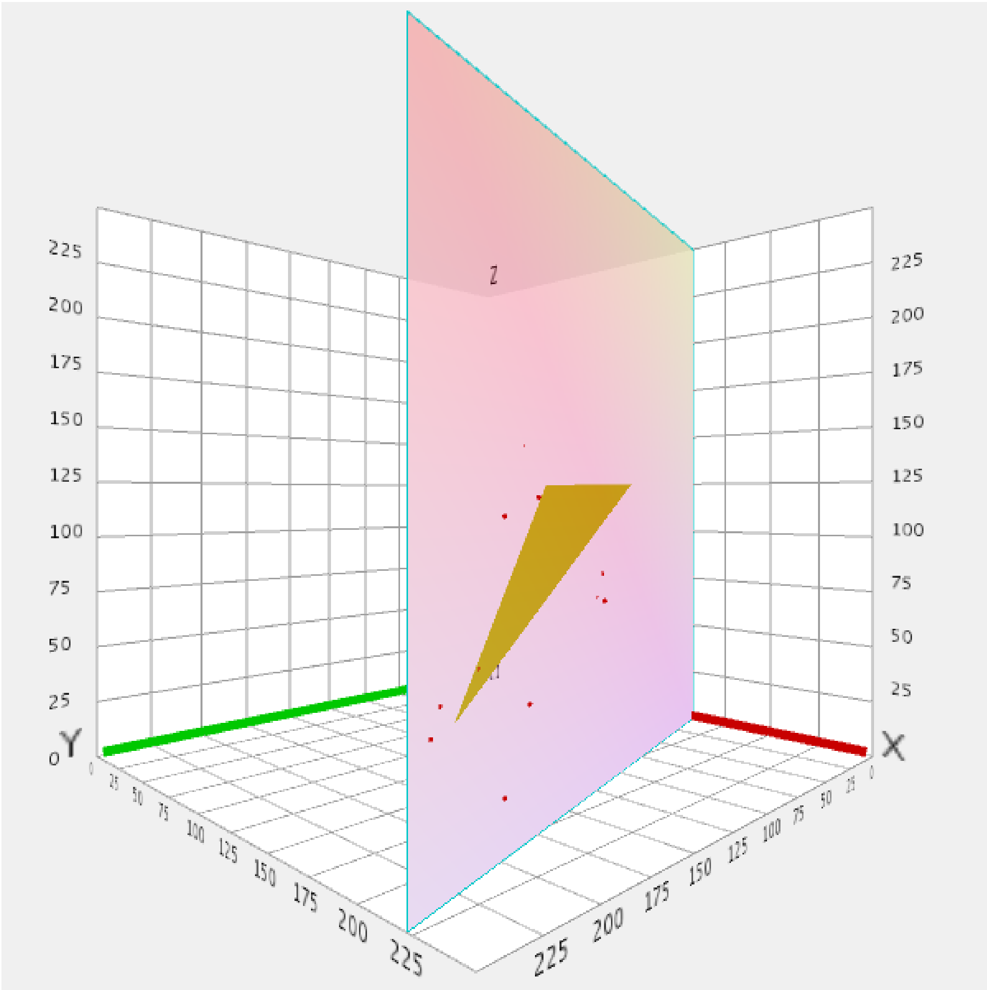

Figure 4-26 Plane fitting of the points obtained from Optical Tracking-Ultrasound image plane intersection.

The least squares regression plane fit is seen in Figure 4.26. The thus plane obtained in relation to the ultrasound probe when used with an optically tracked ultrasound probe will ideally not need any further 3-dimensional plane calibration. The plane equation obtained from least square regression fit (Shakarji, C.M., 1998) is of the form:

$$(1.575)x+(-0.007)y+(5.882)z+(-2669.472) = 0 \qquad 4.19$$

From equation 4.19, the slope of the plane is known. However, the image plane translation in relation to the ultrasound probe 'O' is still not known. Now that the orientation in the real-world reference coordinate system is known, the X and Y axis translation coefficients ('u' and 'v') of the ultrasound plane can be estimated by average distance between the scaled 2D points on the ultrasound image plane and the closest tip 2D coordinate position using equation 4.17. Equation 4.19 and the translation coefficients are used to create the virtual plane in the 3D interface used in the dynamic variation experiments. The position of the image plane top centre can be given by a translation coefficient

4.5.3 Experiment 1 - Static variation estimation for ultrasound images

The metal catheter placed under ultrasound is placed under water as described earlier and the variation of position of the blob over time is observed, and it can be seen in Figure 4.26, blob size and shape variation are evident, and also the position on the ultrasound plane can be seen to change consistently, though the actual metal catheter does not change in any respect. A measurement of the variation in the blob centroid can, in other words, reflect the observed position of the catheter, therefore resulting in a wrong assumed position, in ultrasound guided procedures.

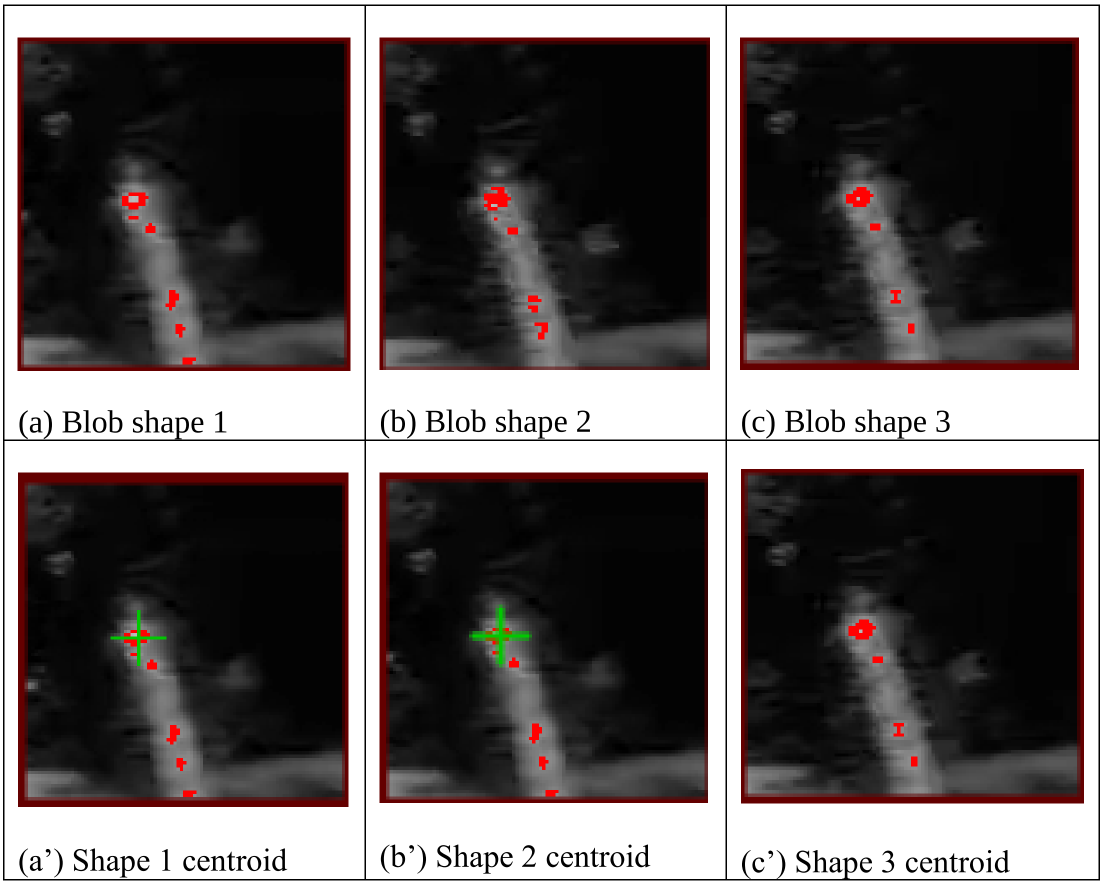

Figure 4-27 Blob centroid variation in a static Ultrasound field. The change in blob shape can be seen in a, b and c. The change in corresponding centroids is seen in a', b' and c.'

In Figure 4.27(a) and (a') a specific shape can be seen for the blob identified while the catheter remains static. It is to be noted that the line seen below is the comet tail shadow artefact. Figure 4.27(b) and (b') shows how the blob evolves over time with no actual movement of the metal catheter but the blob centre is still identified. Figure 4.27 (c) and (c') shows further blob evolution resulting in complete tracking loss.

The quantification of static variation in position when compared to that of optical tracking can be seen in Figure 4.26. Figure 4.27 represents variation over time of both the systems.

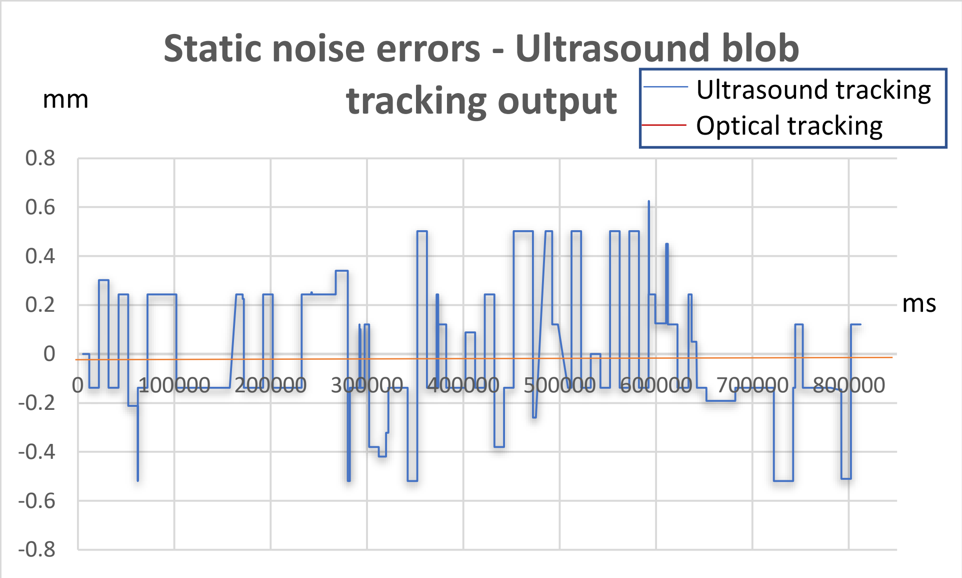

Figure 4-28 Blob centroid variation over time in milliseconds vs variation in displacement observed by optical tracking

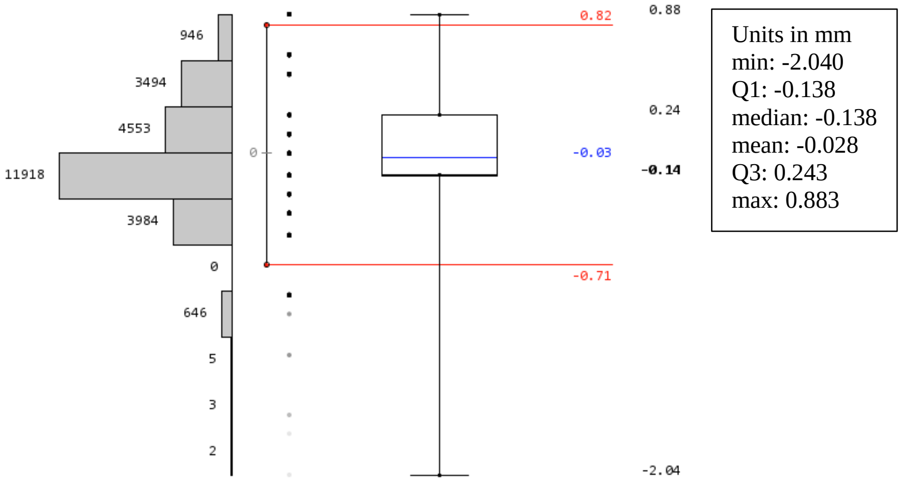

Figure 4-29 Histogram of ultrasound blob tracking inaccuracy of a static metal catheter. The catheter is observed for one hour and is found to be between -0.71 mm and 0.82 mm

In Figure 4.28 Ultrasound blob tracking inaccuracy is clearly observed. The mean is suggestive of fewer variations because the random variations occur almost equally in both positive and negative directions. The amount of variation is very significant and of the order of +/- 0.8mm and the distribution can be seen in Figure 4.29.

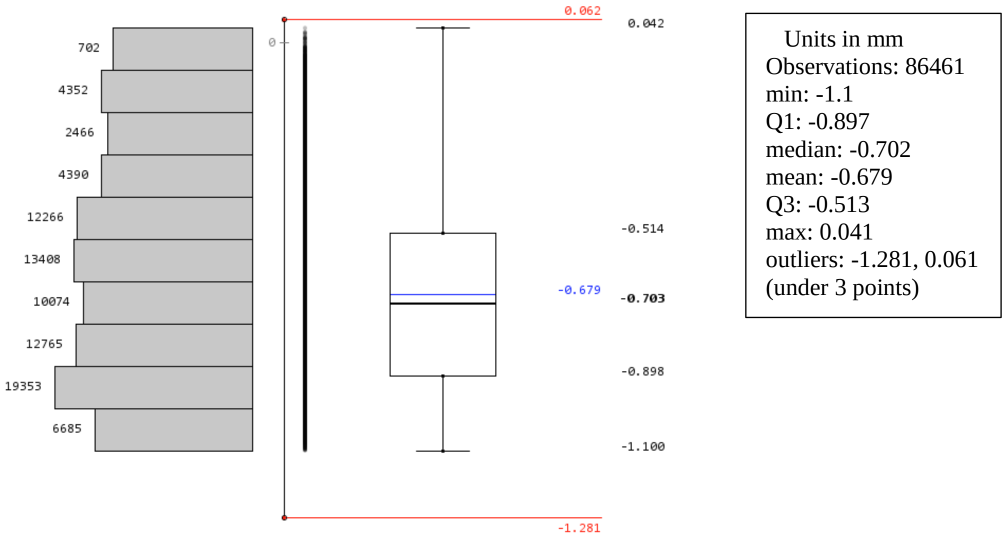

Figure 4-30 Optical tracking of the static metal catheter. The maximum displacement error as observed by the optical tracking system is approximately 1mm

In Figure 4.30, the optical tracking variations observed are used to indicate that the catheter movement has been under 0.8mm for the most part from 86461 observations and has been static, while the ultrasound blob shows a movement of up to +/- 0.8mm error for every 30 frames, indicative of high static noise. Therefore, ultrasound imaging as a tracking system with simple image processing techniques cannot have sub millimetre accuracy. Ultrasound guided procedures do not require high speeds of movement therefore, 30 frames is considered high enough.

4.5.4 Experiment 2 - Manual observation of object trajectory on ultrasound image

The experiment with about 318 slides for object identification as described in the section 4.3.6 and the blobs are manually extracted by the sonologists shown as yellow dots in Figure 4.7 (page 145). A comparison between the points extracted by the sonologists compared with optical tracking (catheter axis to ultrasound plane (line-plane) intersection) resulted in the graph Figure 4.31(a). In Figure 4.31(a), however, there are intersection points which are numerous because of the high refresh rate of the optical tracking system and points outside the image plane because of the lack of constraints. To find the corresponding points, the closest points between the manual tracking and the optical tracking are found and can be seen in Figure 4.31 (b).

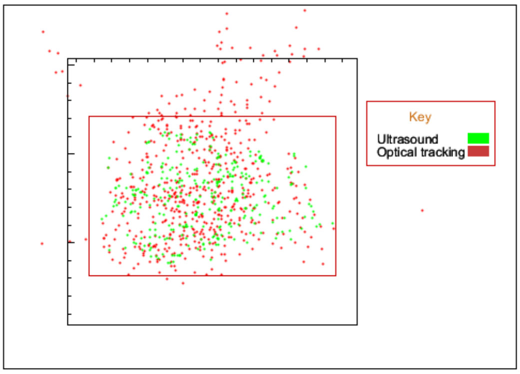

(a) Optical tracking and manual blobs coordinates

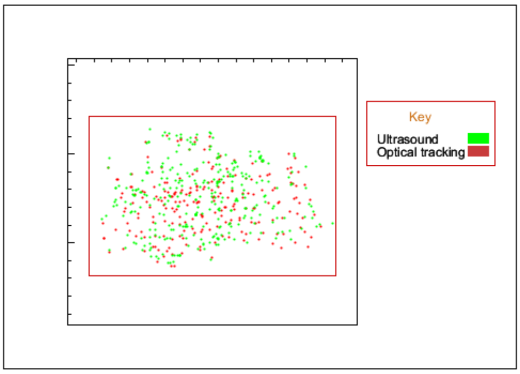

(b)Closest points from optical tracking to manual blob identification

Figure 4-31 Manual and Optical tracking comparison (a) Superimposed coordinates of manual and optical tracking (b) closest points between the two methods

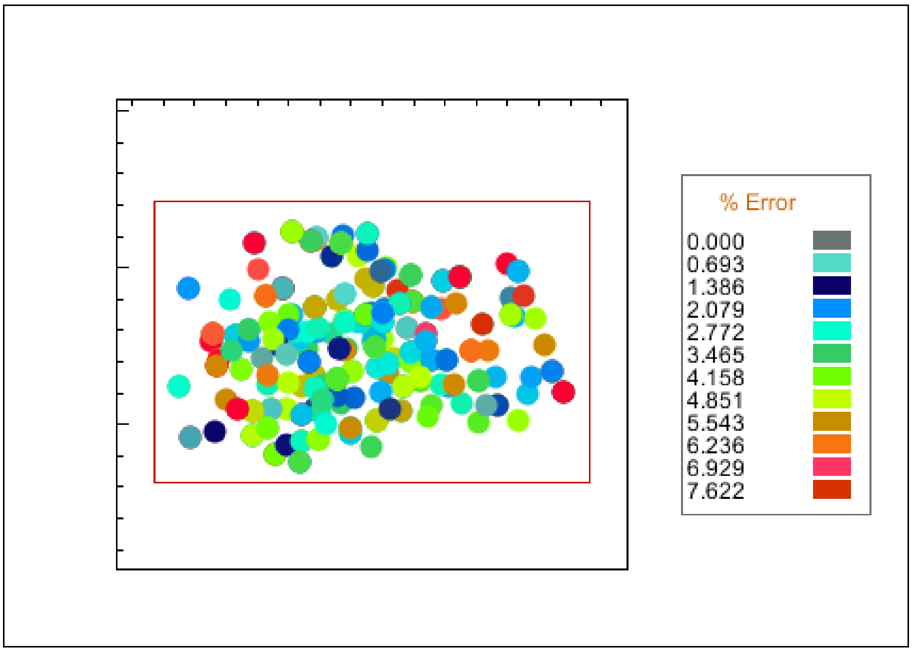

Figure 4-32 Chromatogram % variation of error from periphery to centre Variation of % identification error by manual observations from the periphery to the centre.

From Figure 4.33, it can be observed that the mean error is 3.869 mm approximately when compared to the optical tracking output. The time taken for identification of the successive slides is seen in Figure 4.34 and has a mean of 1.848 Seconds.

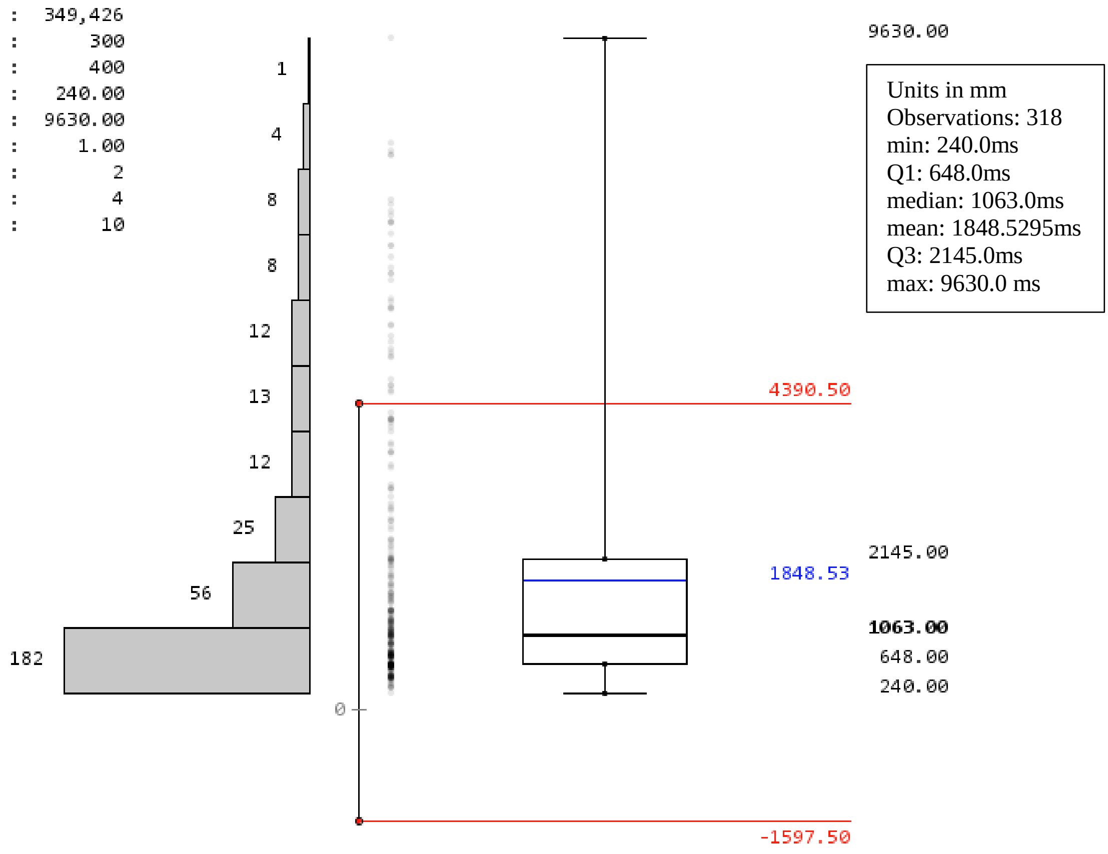

Figure 4-33 Histogram with milliseconds between identification of successive slides combined with Box plot

4.5.4.1 Automated object tracking using combined Optical tracking and image processing

Assuming that the maximum acceleration '*a'* during surgery is 0.08 m/s^2 from work done by Sánchez et al., (Sánchez et al., 2014) the maximum velocity of the hand 'v_1', with an initial velocity 'v_0' being 0 m/s can be given as:

$$v_1 = v_0 + a\,t \qquad 4.20$$

Assuming the time '*t'* as 1000 ms, v_1 is 0.8 m /s . Velocity per frame *fv* is given by:

$$fv = v_1 / 33 \qquad 4.21$$

From the above,' *fv'* is 0.0238m/frame or 23.8mm per frame.

4.5.4.2 Optical tracking on Ultrasound plane and correction of Optical tracking outliers

In this part of the experiment, optical tracking is used to track a 3D printed catheter stem, and the intersection between the ultrasound plane and the optical tracking system are found while the movements are recorded by the optical tracking interface '*motive*', as described earlier in this chapter.

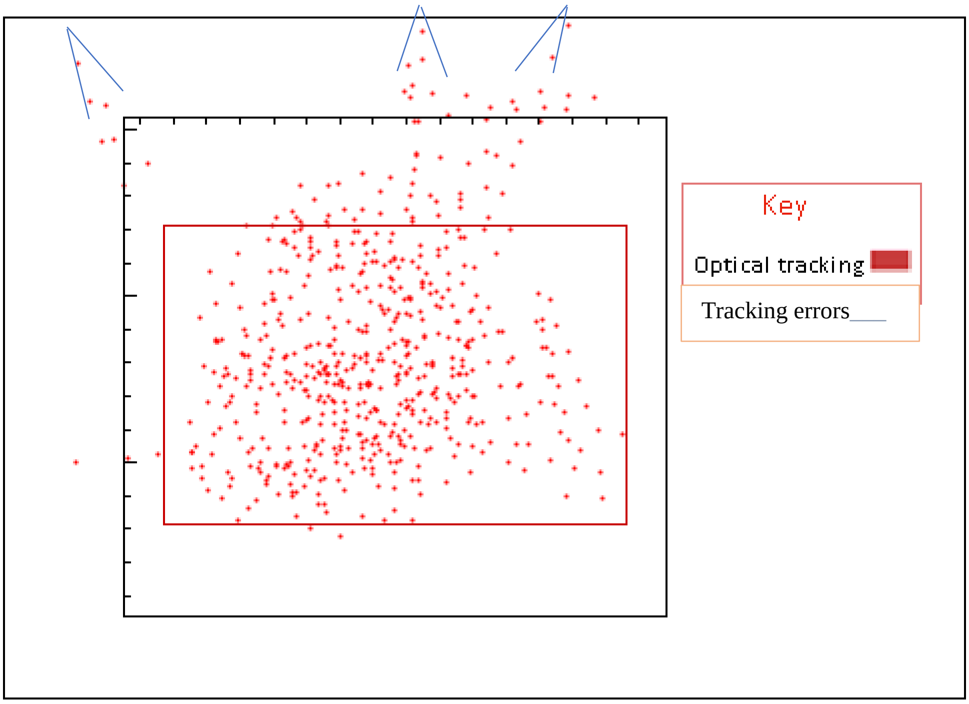

Figure 4-34 Output of optical tracking line- plane intersection points and the 2D points obtained from the 3D to 2D coordinate transformation equations

Figure 4.35 shows the resultant output of the optical tracking on the ultrasound plane. It should be noted that the optical tracking system resulted in 3 spikes, which is indicative of the loss of tracking or partial hiding of markers or combination with what may look like markers. Therefore, severe pose estimation error occurs as exact marker positions are essential for the inverse transformation matrices to work. These errors can be avoided using a velocity filter, knowing that rate of displacement of a specified tracker for every slide cannot be more than a specific value. Displacement s between the tracker in previous frame position $\boldsymbol{p}$ and current frame $\boldsymbol{i}$, given that $\boldsymbol{t}$ is given by

$$s = i - p \qquad 4.22$$

The initial velocity between the previous two frames can be given by

$$u = \frac{s}{t} \quad 4.23$$

Let us assume the time '*t*' as 1/120 of a second, as the optical tracking is capturing at 120 frames/sec. From the experiments that were done by Sanchez and his team (Sánchez et al., 2014), the maximum acceleration '***a'*** produced by a surgeon cannot exceed 0.8 m/s^2. Therefore, if the displacement '***d***' can be given as:

$$d = ut + at^2 \quad 4.24$$

Therefore, the maximum value 'd' can have per frame is given by:

$$dmax = (i - p) + 0.8\left(\frac{1}{120}\right)^2 = (i - p) + 0.000055 \quad 4.25$$

If d is found to have a value higher than '*dmax'*, the coordinate value of the current position is ignored or if possible, replaced with another reliable reference, till the required displacement per frame is observed.

4.5.4.3 Ultrasound image processing object tracking

The experiment for dynamic tracking is done with the setup described previously. Automated tracking is done by using ultrasound image processing, and the centroids of the catheter cross section as visualized on the Ultrasound image is plotted in Figure 4.36(a). In order to reduce the number of points, a notch size filter for specific blob sizes between 10px and 40px is applied. In Figure 4.36 (b) only blobs of such a size are only considered in the above graph with the output from Optical tracking plane line output.

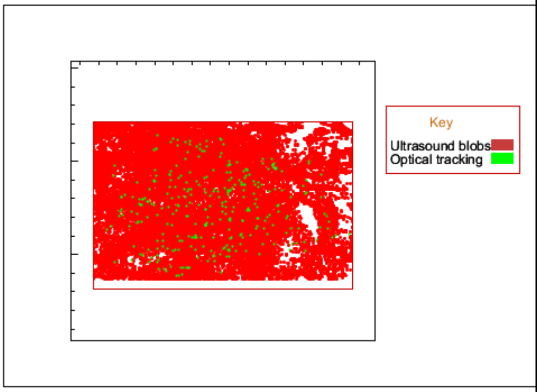

(a) Ultrasound blob tracking output

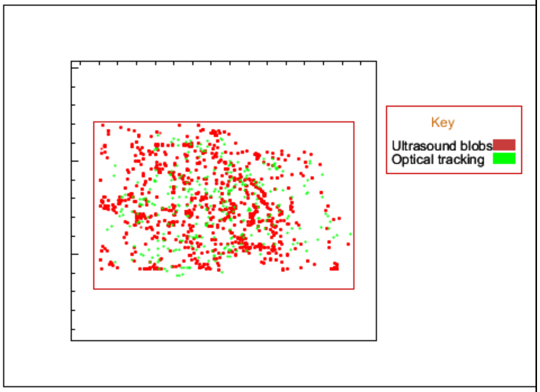

(b) Ultrasound blob tracking and blob size filter

Figure 4-35 Reduction of number of blobs identified with size filter (a) shows image processing output of blob tracking output on the ultrasound, within the region of interest, the maximum and minimum amount of movement (b) shows the ultrasound image processing blob output with blob size filter

Though the number of points has gone down with the size filter, the number of false positive blobs can still exist as a very high percentage. Therefore, to best obtain the least number of points with the highest efficiency, finding the region of interest (ROI) for image processing and tracking the ultrasound objects becomes essential. In the next section, the possibility of usage of optical tracking for reducing the ultrasound errors is discussed.

4.5.4.4 Combined optical and ultrasound tracking

Reduction in the number of false positive blobs in the ultrasound processed image output can be achieved by cross- referencing the respective blobs with the optical tracking output. This is done because optical tracking is more accurate and robust when compared to ultrasound. Figure 4.36 (b) shows a further reduction in the amount of ultrasound blob tracking points to the optical tracking points by 11 mm or 23.925 pixels square block as the region of interest from the blob detection output

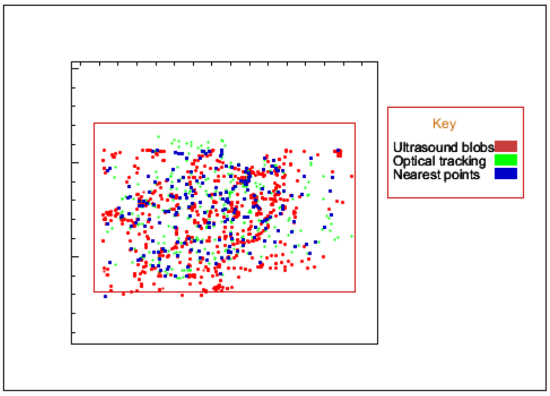	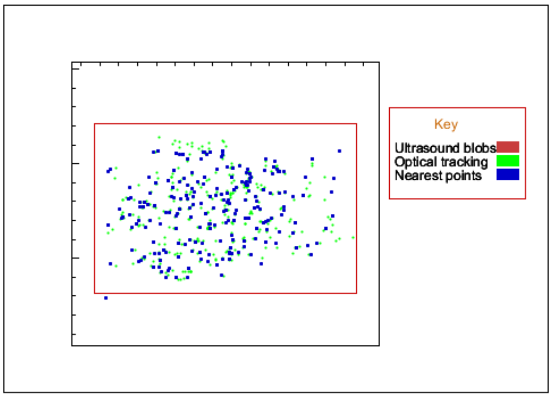
(a)Ultrasound blob tracking output, Optical tracking plane line intersection 2D output and Closest points between optical and ultrasound	(b)Closest points in Ultrasound tracking and optical tracking

Figure 4-36 Reduction of a number of blobs identified using ultrasound image processing by merging Optical tracking output. (a) shows output from optical and ultrasound tracking outputs and the closest points in optical tracking to that of ultrasound (b) Only Optical tracking points close to that of ultrasound points

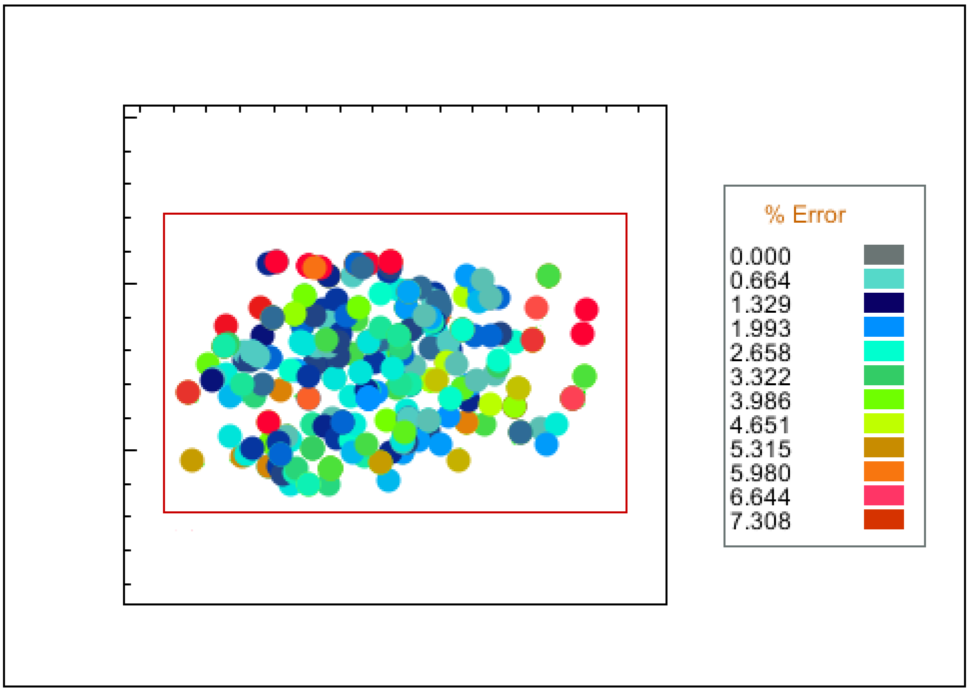

Figure 4-37 Chromatograph of errors with reference to the optical tracking output

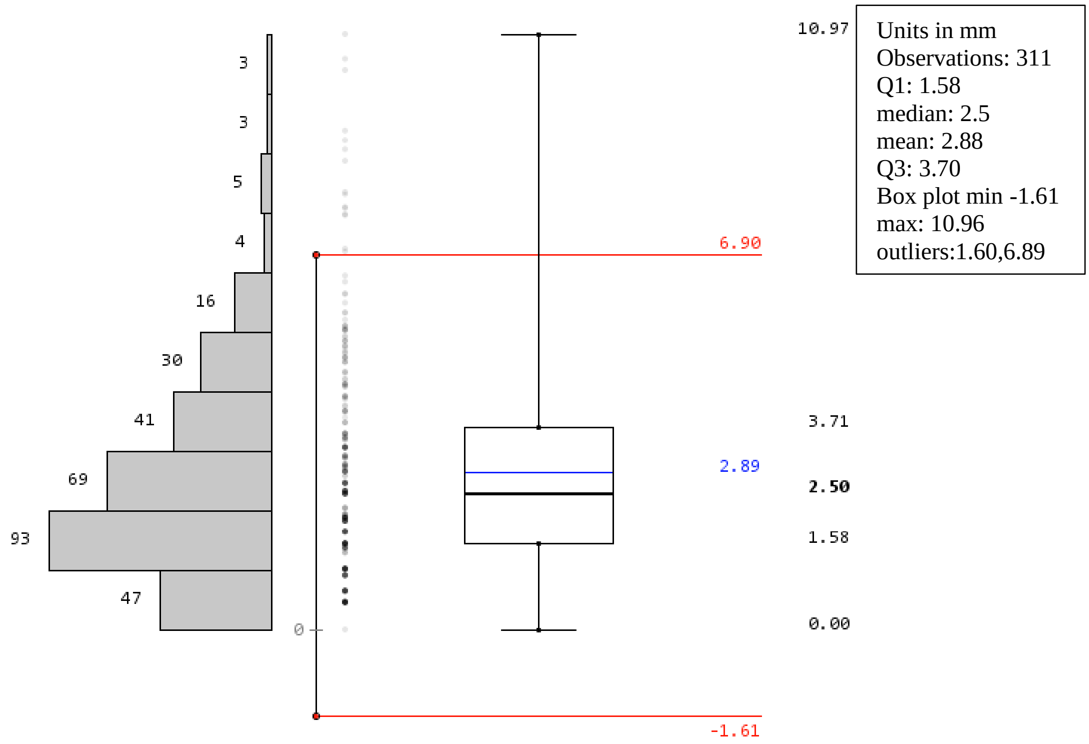

Figure 4-38 Histogram- box plot combination showing results from a combination of u ltrasound and Optical tracking

From Figure 4.37, it can be observed that the distribution of gross errors is more to the periphery of the ultrasound images and less towards the centre, very much similar to that of the manually observed blob centroid errors. Figure 4.38 shows that the mean error is at 2.88 mm which is much lower than that of manual tracking which is at 3.86 mm. However, this method has resulted in outliers because of glitches in optical tracking, due to the marker confusion described in the literature review.

4.6 Discussion

Experiment 1 evaluated the amount of static noise within the ultrasound image while trying to track a static metal object. In Figure 4.30, the optical tracking variations observed are used to indicate that the catheter movement has been under 0.8mm for the most part from 86461 observations and has been static, while the ultrasound blob shows a movement of up to +/- 0.8mm error for every 30 frames, indicative of high static noise. Therefore, ultrasound imaging as a tracking system with simple image processing techniques cannot have sub millimetre accuracy.

Experiment 2 evaluated dynamic movement tracking of manual tracking of the cross section of the metal catheter in the ultrasound plane. The subjects identified all the movements of blobs within the ultrasound images. However, the centres marked, as identified by the sonologists had a mean error of about 3.86mm when compared to optical tracking. Also, it is to be noted that the optical tracking induced overshoots because of markers crossing over and uncertainties of mathematical projection algorithms employed by the optical tracking system. This results in spikes which can be observed in Figure 4.35.

The spikes seen in the optical tracking output due to loss of tracking temporarily can be compensated by finding the velocity of object movement and using it as a time dependant displacement filter. Another method which has been discussed is to combine with the ultrasound blob tracking output. Combined optical tracking with ultrasound tracking output had 2.88 mm mean error which was lower than the manual method of blob tracking. Therefore, optical tracking combined with optical tracking is more accurate in locating objects on the ultrasound frame than manual judgement.

The chromatograms show that irrespective of manual tracking or ultrasound-optical combined tracking, the accuracy of identification was lower at the edges and higher in the centre because of reduced image quality at the peripheries.

4.7 Summary

Ultrasound image resolution and accuracy in a medium can be variable depending on the type of medium and a number of variations of sonic reflection and the material used within the medium. Such effects can be reduced by using hybrid materials but not eliminated. The ultrasound blob tracking results have very less specificity and low sensitivity at high velocities. Complex image processing techniques resulted in high processing times and relied on the processing power of the computer. Irrespective of the processing method used, ultrasound can have random static noise which can compromise on the accuracy of blob tracking.

With optical tracking being used as a reference, the combined tracking accuracy improved. Table 4.1 shows the different things which have been tried and their respective results. Sonologists were able to identify the blobs with 100% accuracy whereas without any filters on the Ultrasound frame, the sensitivity was high, but the specific identification percentage was down to 1.2. When a blob size filter was implemented, 7.729% success of identification was noticed. With plain optical tracking, there was 0.06% of error in identification. This error was brought down when ultrasound image processing with adaptive thresholding for the brightness within the region of interest was used. Using the combined approach, the FPS was about 24 and therefore is acceptable, considering the fact that USG system cannot do more than 30 FPS(25 to 29.97 FPS for NTSC).

Table 4-1 Table of Results from Ultrasound, Optical and manual tracking

Technique	No of frames	Source Live / Recorded	No of blobs	Average Latency(FPS)	% of successful identification
Blob tracking no filters	13870	L	11545	2.491	1.2%
Blob tracking size filter	13870	L	4153	1.446	7.729%
Human tracking	318	Rec slides	318	0.541	100%
Optical tracking	1705908	L/UDP	1705001	~120	99.94%(0.06% outside ROI)
Optical tracking ROI + velocity identification + blob tracking + dynamic thresholding	13870	R/csv	13870	24.1	100%(excluding marker flicker error outliers)

From the observations made in optical and ultrasound tracking combination to obtain the area of interest, the processing time has been found to reduce considerably when compared to complex ultrasound image processing methods. Even in frames where the blobs were not identified, the optical tracking still provided an area of interest, from which the blob centroid can be found by adaptive thresholding techniques on the ultrasound frame. However, in the case of hidden markers or tracking loss in the case of improper infrared reflections or marker confusion, the optical tracking output can be nonsensical, where a velocity filter needs to be applied to ensure that the optical tracking is temporarily cut off and the tracking switches priority to ultrasound tracking output.

4.7.1 Targets set vs achieved

Table 4-2 Comparison of targets set vs targets achieved

Parameter	Human tracking (Set target)	Multimodality tracking (Target achieved)	Outcome
% of successful identification- (Sensitivity & Specificity)	100	100	At par with human tracking capabilities
Tracking accuracy on ultrasound plane	3.86	2.88	Higher accuracy
Average Latency of detection (FPS)	0.541	24.1	Real-time tracking

From Table 4.2, it can be observed that the targets set for the multimodality tracking system have been reached successfully.

4.8 Conclusion

Manual ultrasound, while considered as the most relied method in current forms of ultrasound guided surgeries, through experiment, has been found to be more sensitive and less accurate in terms of estimating the tip position or orientation. When supplemented with optical and ultrasound tracking acting as complementary systems, the overall accuracy of the system in identifying the surgical objects under ultrasound becomes higher. Also, optical tracking can have marker confusions which can be identified and bypassed till the tracking stabilises by merging with ultrasound tracking.

Chapter 5

Design & Development of Robotic Fetoscope

5.1 Introduction

The conventional video fetoscope, (Yao et al., 2014) is a mechano-electrical device consisting of a handle and a stem. The stem usually contains a port and a camera and its lighting(Curtiss, 1976). In scopes which make use of a micro camera at the end, the stem is more of mechanical support. In cases where there are lenses to relay the image(Curtiss, 1976) or in certain other cases such as fibre optic image transfer, the camera is present at the level of the handle. The port can be used for collecting samples, balloon inflation or beaming LASER via a fibre optic unit. The stem diameter in the case of fetal surgery is quite crucial, and under (1, 1.2, 2 mm with just the camera and up to 5 mm with operation port) 3mm diameter is usually desired and hence, does impose several sophistications including limited camera field of view, reduced dexterity.

Though smaller diameter of the stem is generally desired(Huber et al., 2008), the fetoscopes with smaller diameters have poor optical resolution and limited field of view(Macdonald et al., 2005) resulting in reduced usability and loss of orientation(Rauskolb, 1979). The aim of the hardware design is to achieve a balance between the resolution of the system, the weight of the device and to simplify the usage so that the bar for the level of skills and experience required for challenging procedures is lowered.

5.2 Aims

This chapter deals with the design and development of a video fetoscope with communication, actuation and haptic capabilities. The design of the robotic fetoscope is illustrated with rendered images and actual pictures of the construction. The actuators and haptics, on the other hand, are evaluated.

5.2.1 Design targets for robotic fetoscope

Advanced requirements for a smart fetoscope which form the specifications for the novel design of the proposed fetoscope:

a) Multi-modality 6 DoF tracking and navigation support with sub millimetre accuracy
b) Simple visual cue-based Target guidance and trajectory tracking- with LEDs, Visual display and vibrational feedback
c) Automatic needle withdrawal and passive control- Automatic needle overshoot control and withdrawal
d) Vacuum/pressurization pump for air or fluid transmission and pressure measurements – Closed loop barometric and drainage control
e) Automatic LASER focusing guidance & ablation guidance – Active focusing and ablation control
f) Automatic identification of blood vessels and structures for cauterization – image processing-based blood vessel identification
g) Additional port for micro forceps and its electronic actuation – Multiple micro tool options
h) Bi-directional wireless connectivity for all the above – Duplex high-speed communication >5MBPS for video transfer
i) Forceps and manipulation – Manipulation of complex tools
j) Haptic feedback and tactile feedback – Force and proprioceptive feedback
k) Cloud computing/onboard processing – Offloading on-board processing to more powerful computers via cloud and highspeed data communication.

5.3 Methodology

Requirements of a surgeon during ultrasound guided procedures are dictated by the complexity of the procedure being done and the number of constraints to be taken care of. Whereas, in procedures such as the ones done by fetal surgeons, the theory behind the procedures can be relatively simple but, because the number of constraints limiting the dexterity of the surgeon, the complexity of the procedure raises the bar for the skill levels required (Lamata et al., 2008).

Since the device has quite a number of size constraints, the number of features to be added are quite limited. But with the advancement of microelectronics and micro machining techniques most of the above can be achieved. There are quite a few fetal surgical procedures introduced since the 1990s.

5.3.1 Design requirements

The design of surgical instruments entirely depends on the type of procedures done and the surgeon's approach and the planning. As the details of fetal surgeries are described in further detail in the literature review, the equipment required for the procedures are being given in Table 5.1. It can be observed that all procedures have Ultrasound guidance and video camera guidance in common, as surgeons are required to orient themselves according to the images and mental reconstruction of the surgical environment with the knowledge of anatomy. Also, to do the steering can be very demanding and entirely depends on the surgeon's experience and level of skills.

Specialized requirements in these surgical procedures mainly include LASER ablation, RF ablation, drainage, sampling, balloon inflation, needling and stenting. Therefore, a new design of the fetoscope is expected to have them as an integral part while more features can be added to help the surgeon even further.

Table 5-1 Comparison of fetoscope requirements for different surgeries

Procedure	Equipment							
	USG guidance	Video output	Balloon inflation	Needling and stenting	Sampling	Drainage	LASER ablation	RF ablation
CDH	✓	✓	✓	X	X	X	X	X
TTTS	✓	✓	X	X	X	✓	✓	X
CCAM	✓	✓	X	✓	✓	✓	X	X
EPS	✓	✓	X	✓	X	✓	X	X
SCT	✓	✓	X	X	X	X	X	✓
UTO	✓	✓	X	✓	X	✓	X	X
CHD	✓	✓	X	✓	X	X	X	X
TRAP	✓	✓	X	X	X	X	X	✓

Table 5.2 describes the different fetoscopes commercially made for use in fetal surgeries, the main parameters being size, resolution, flexibility and field of view. It can be seen from the table that most devices are either rigid or semi-rigid based on the image transmission technology used (Klaritsch et al., 2009). Also, when a direct camera approach is used, very high resolutions can be achieved, but the fetoscope stem is always rigid in this case because a flexible shaft would cause misalignment of optics. Further, with a decrease in diameter of the fetoscope camera elements, the Field of View and the resolution decreases due to limits in the size of CMOS manufacturing for cameras. It can be observed that though these devices are very small in diameter, which reduces the force perception of the surgeon to a great extent (Lamata et al., 2008), these units do not contain active or passive compensation mechanisms to give a force or tactile feedback. The importance of force feedback in surgeries has been well studied over the years but has been undermined in equipment development and designed (Tholey et al., 2005). It can also be observed that the lighting has mostly been fiber-optic (Kim et al., 2011) but with the advent of low light capable CMOS cameras

and high brightness SMD 0402 and 0201 LEDs, it can be much easier to place the lighting right beside the camera, eliminating the need for optical fiber based lighting (Sazontova et al., 1984).

From the Table 5.1, it can be seen that there are quite a few ultrasound guided procedures which require high levels of practise and dexterity (Lamata et al., 2008). Since the fetoscopes seen in Table5.2 do not offer any help to the surgeons in terms of orientation and guidance, the surgeons are required to rely heavily on ultrasound and video guidance to form a mental image of the orientation. Further, these units do not offer any sensory feedback of force or precise tip control in many cases.

There is a total lack of assistance from the side of the technology used in orientating the surgeons in real time. Hence these procedures are primarily dependant on the efficiency of the surgeons and their intuition. Further, the number of procedures attempted can be significantly increased if the sensory feedback to the surgeons is enhanced. This can be seen in the case orthopaedic and urological procedures, where robotics and navigation have had a complete acceptance. More recently, neurological procedures with robotics, image and navigation guidance have been introduced for intricate procedures.

Table 5-2 Comparison of features and capabilities of different fetoscope

Image Resolution	Dia(mm)	Length(mm)	Transmission	Flexibility	Angle	FOV	Working details	Manufacturer part no
30000	1	200	Fibre	Semi-rigid	0	70	Remote eyepiece	Storz 11510A
30000	3.3	300	Fibre	Semi-rigid	0	70	Remote Eyepiece	11506AAK
30000	1.3	306	Fibre	Semi-rigid	0	90	Remote eyepiece	11540AA
30000	2.0	300	Fibre	Semi-rigid	0	95	Remote eyepiece	11630AA
Direct/external	1.9-2.0	260	Rod lens	Rigid	0	-	Fixed length	26008AA
Direct/external	2.0	260	Rod lens	Rigid	12	-	Fixed length	26008FUA
Direct/external	2.0	260	Rod lens	Rigid	30	-	Fixed length	26008BUA
50000	2.0	270	Fibre	Semi-rigid	0	-	Fixed length	Wolf 8754.401
50000	3.3	300	Fibre	Semi-rigid	30	-	Fixed length	8930.422
50000	3.8	300	Fibre	Semi-rigid	12	-	Fixed length + working channel 1.64mm	8746.401
22.62 lines per mm	3.0	600	Fibre	Flexible	0	60	1 mm channel Deflection 130 to 160 degrees	7331.001

Incidence of premature rupture of membranes is quite common in fetal surgical procedures is of utmost concern to surgeons (Lyerly et al., 2001). Fetoscopes with bigger sizes have the advantages of having more space for instrumentation and cameras with wider field of view. However, the larger fetoscopes are avoided because there is research to suggest that the increase in the size of the fetoscope is somewhat related to the premature rupture of membranes(PROM) as seen in Table 5.3. Therefore, care should be taken so that the size of the fetoscope does not exceed 4 mm. But in general, it can be observed that the overall risk of PROM is very high.

Table 5-3 Rupture rates (%) are those reported ≤37 weeks, or at the time point specified(Beck et al., 2010). ABS, amniotic band syndrome; CO, cord occlusion; FETO, fetoscopic endoluminal tracheal occlusion. References in the last column can be found in the original publication(Beck et al., 2010).

Conditions	No of cases	PROM risk	Diameter of instrument	Reference
MMC	3	67%	3.8mm	(Kohl et al., 2006a)
	4	33%	Three ports, Largest 5.0mm	(Bruner et al., 2000)
LUTO	10	17%	1.3mm smallest	(Welsh et al., 2003)
	13	13%	~2.5mm	(Quintero et al., 1995)
ABS	2	100%	3.3mm	(Soldado 2009)
	2	100%	4.0mm	(Keswani 2003)
	2	50%	2.7mm	(Quintero 1997)
Fetoscopic LASER	4 (TTTS)	75%	5.0mm	(Kohl et al., 2006a)secondary LASER
	6 (TTTS)	33%	3.3mm	(van Schoubroeck et al., 2004) triplets
	175 (TTTS)	28% (<34 weeks)	3.3mm	(Yamamoto and Ville 2005)
	20 (TTTS)	7% (<1 week)	3.3mm	(Crombleholme et al.,2007)
	24 (TTTS)	5% (<28 weeks)	4.0mm	(Change et.al, 2006)
	6 (TRAP)	4%	2.0mm	(Quintero et al., 2006)
		0% (<3 weeks)		
CO	80	38%	2.3 or 3.3mm	(Lewi et al., 2006)
	4	25%	2.7mm	(Ville et al.,1994)
	39	20% (<3 weeks)	3.5mm	(Quintero et al., 2006)
	25	16% (<3 weeks)	3.5mm one or two ports	(Nakata et al., 2004)
	12	8%	3.0mm	(Young et al., 2005)
FETO	11	100%	5.0mm (one or three ports)	(Harrison et al., 2003)
	210	47%	3.0mm	(Jani et al., 2009)
		7% (<3 weeks)		

5.3.1.1 Design targets for robotic fetoscope

Advanced requirements for a smart fetoscope which form the specifications for the novel design of the proposed fetoscope:

l) Multi-modality 6 DoF tracking and navigation support with sub millimetre accuracy
m) Simple visual cue-based Target guidance and trajectory tracking- with LEDs, Visual display and vibrational feedback
n) Automatic needle withdrawal and passive control- Automatic needle overshoot control and withdrawal
o) Vacuum/pressurization pump for air or fluid transmission and pressure measurements – Closed loop barometric and drainage control
p) Automatic LASER focusing guidance & ablation guidance – Active focusing and ablation control
q) Automatic identification of blood vessels and structures for cauterization – image processing-based blood vessel identification
r) Additional port for micro forceps and its electronic actuation – Multiple micro tool options
s) Bi-directional wireless connectivity for all the above – Duplex high-speed communication >5MBPS for video transfer
t) Forceps and manipulation – Manipulation of complex tools
u) Haptic feedback and tactile feedback – Force and proprioceptive feedback
v) Cloud computing/onboard processing – Offloading on-board processing to more powerful computers via cloud and highspeed data communication.

5.3.2 Proposed design of the fetoscope

Based on the requirements of the fetoscope in intra-uterine fetal procedures, as seen in Table 5.1 and technical capabilities are seen in Table 5.2 a new design of a hand held and self-contained fetoscope was designed. Addition of other features described earlier helps the fetoscope achieve more complicated tasks, which can help further the fetal surgical procedures and other such procedures which have very high special constraints.

5.3.3 Fetoscope hardware design proposition

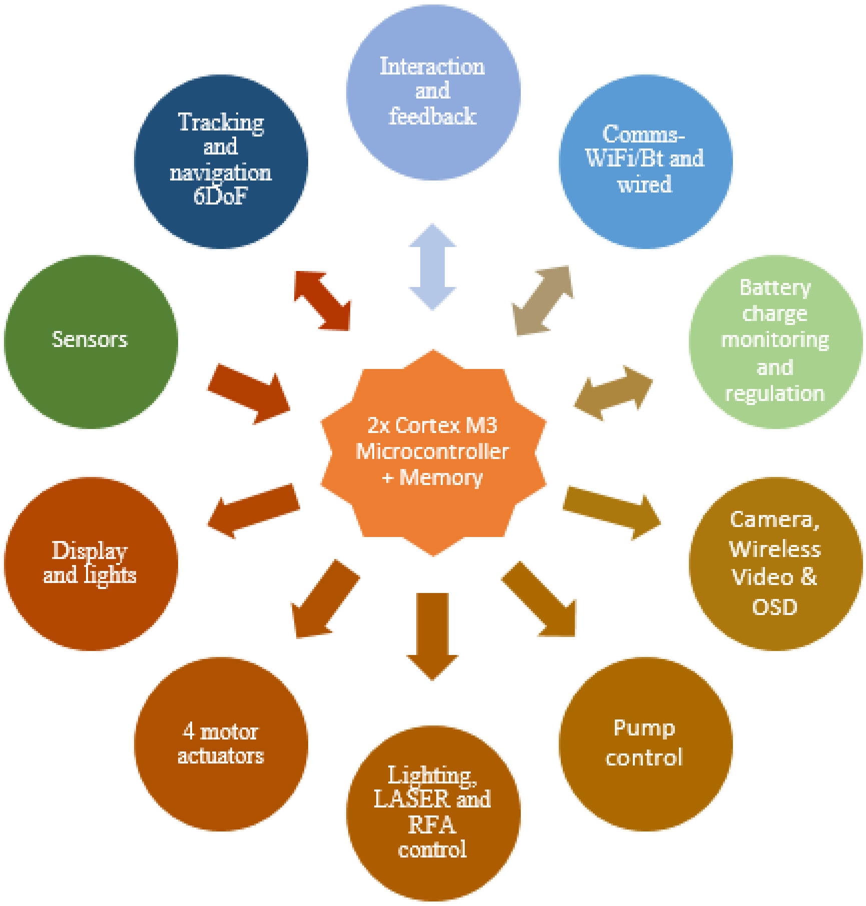

Figure 5-1 Robotic fetoscope electronics overall layout

The diagram of functional blocks being used in the robotic fetoscope is given in Figure 5.1. Two Cortex M3 micro controllers are used, one handling the communications display and also acts as a master and the other controller acts as a slave and communicates the feedback through a serial protocol to the master controller. While one is used for user input, communication, input data processing and display control, the other controller takes care of mechanical, electrical control, on screen display for NTSC video, lighting, sensor input and battery monitoring. The fetoscope unit is powered by a 400mAh Lithium ion battery with inbuilt low voltage cut-off at 3.4 volts and protection for over load beyond 300 mA of current consumption. Further, there is a set of 4 multi-color LEDs which help in gross navigation guidance with the help of visual cues.

User input for powering and frame capture is via buttons and the menu options are capacitive touch enabled. CSR Bluetooth 2.0 is used, but the device also includes serial Wi-Fi communication module based on ESP8266 with UDP protocol implemented. Other relevant parts of the circuitry include 3.3 to 12 V buck boost converter for the pump, lighting and backlight of the detachable LCD for video display, which is optional. The camera, rotary encoders, linear encoder, force transducer signal conditioning circuitry and LED drivers to operate on regulated 3.3V and 2 rotary servos work on unregulated battery output while the third servo which is a custom made linear actuator, also works on a separately regulated 3.3V. The haptics work on 3.7 to 4.2 V battery supply, as the MOSFET double ‘H’ bridge circuitry handles up to 15 V and 1.2A without problems. The another single MOSFET controls the micropump capable of up to 50 kPa pressure.

The interface is handled by an analog joystick in combination with the haptic feedback which includes both impedance and vibrational haptics, applied in the required fashion wherever required. There are buttons for simplified input and also a wireless footswitch for operations such as LASER ablation.

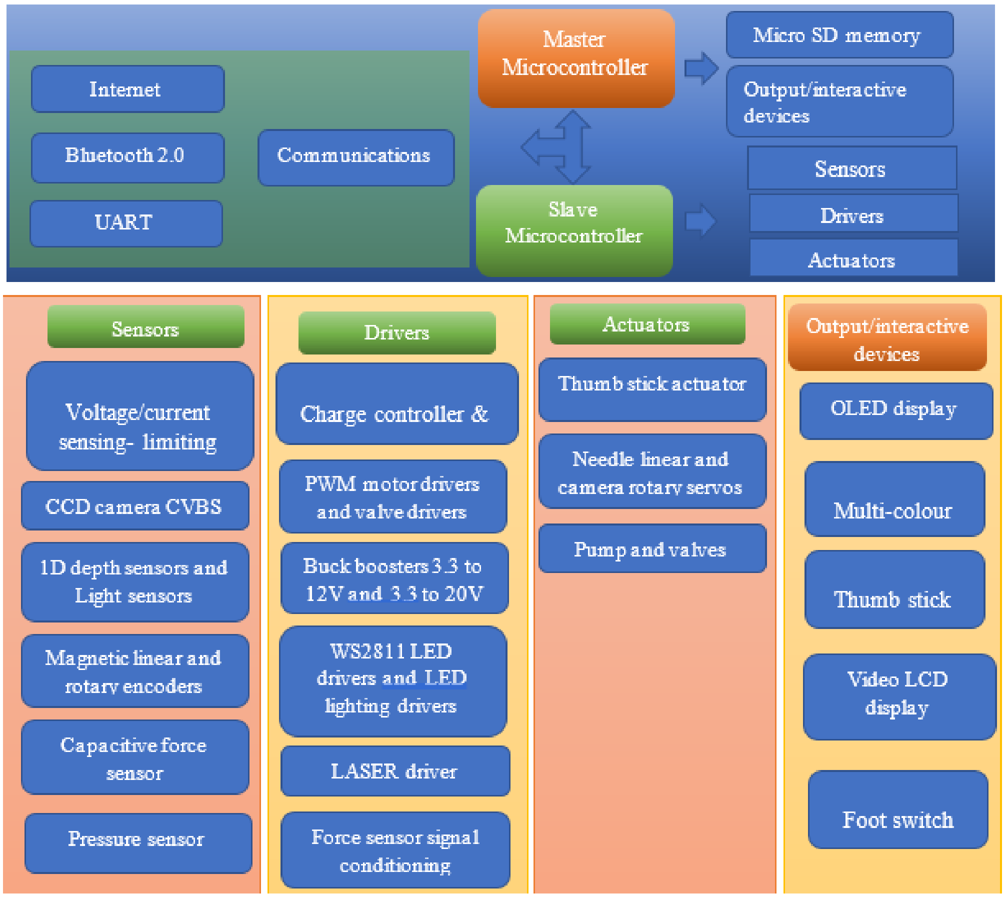

Figure 5-2 Fetoscope electronics – Controllers, sensors, driving elements and display systems

The hardware organisational chart is given in Figure5.2, where most of the important hardware forming the fetoscope construction are outlined.

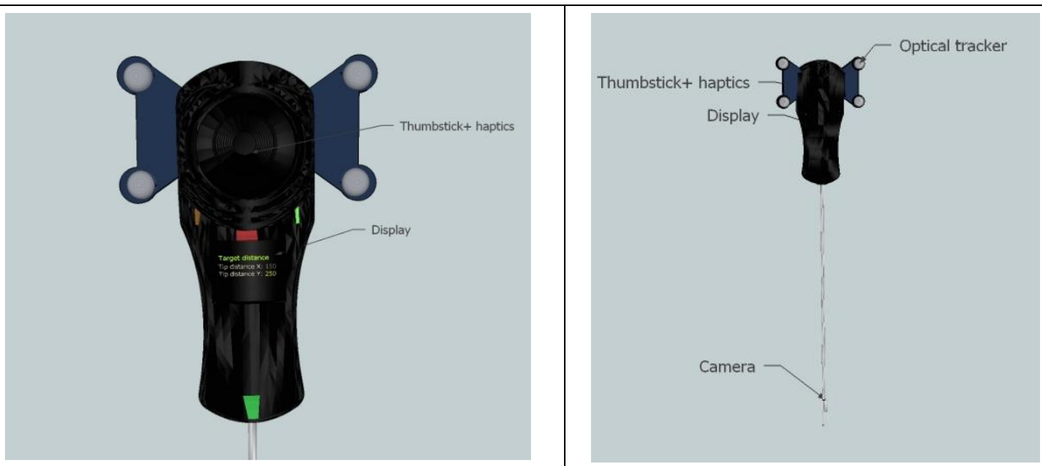

(a) Front rendering

(b) Back rendering

Figure 5-3 Rendered 3D model of the fetoscope from front (a) and behind (b)

Figure 5.3 shows a rendered version of the fetoscope in the front with on OLED display and optical trackers (a) and back (b) with the camera on the fetoscope tip. The fetoscope is designed to be portable and hand held and is required to weigh only a few hundred grams, in order for the surgeon to not experience any feeling of fatigue. Therefore, the design shown in Figure 5.3 is used. Figure 5.4 shows the fetoscope tip with a CMOS camera and metal tube capable of mounting a needle with force transducer.

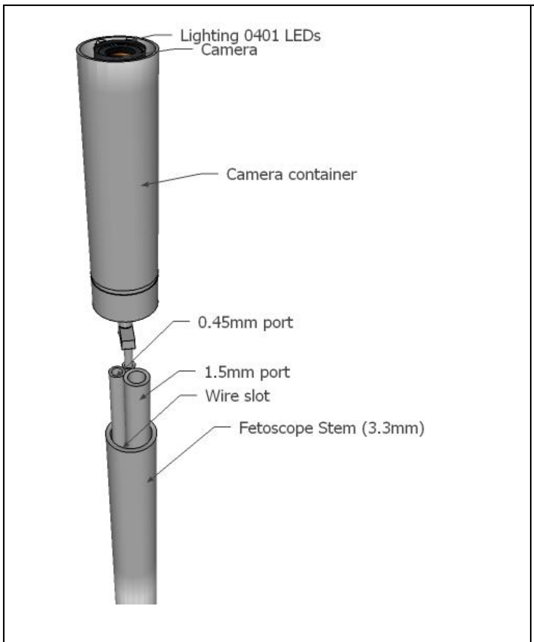

(a) Rendering of the tip with ports

(b) Picture of fetoscope tip with camera

Figure 5-4 Catheter tip of the fetoscope is seen with 3 major ports, wire slots and camera

5.2.2 Description of fetoscope electronics and sensors

Table 5.4 shows the different types of sensors used within the fetoscope device. Based on functionality, the sensors have been classified for simplification. Every sensor used has a specific crucial information which will be discussed below. Also, it should be noted that the most modern sensors have I2C and SPI communication interfaces, while the camera has a simple NTSC output, therefore the microcontroller is not capable of handling the video stream. Hence, for onscreen display purposes, an I2C minim OSD PCB was used, and the output was transmitted using a micro video transmitter. If any of the sensor output freezes over 200mS, the timeout protocol tries to automatically re-initialize, therefore the firmware on the microcontoller is non-blocking. With further development of technology, the sensor data acquisition and processing can be done parallelly, reducing the time for execution of algorithms.

Table 5-4 Sensor classification and application and the dynamic range within which the sensor can be used

Type	Description	Application	Dynamic range
Position encoder	Linear magnetic encoder	Relative linear position	0-20mm
	Magnetometer as Rotary	Relative angular position	0-360 degrees
Distance	1D ToF Distance	Relative distance in mm	0 - 200 mm
Force	Capacitive transducer	Output of forces in N	0 to 20 N
Pressure	MEMS Barometric sensor	Pressure in Pa	0 – 2MPa
Image sensors	CMOS colour	Live Analog Video	300000p NTSC
	CMOS grayscale (digital)	Onboard Blob tracking	320 x 240 pixels

5.3.3.1 Selection of sensors by order of importance:

a) Relative position estimation

The robotic unit primarily relies on optical tracking and ultrasound guidance for orienting itself but is not capable of finding the fulcrum of rotation and translational constraint, which can help determine the kinematics to reach the target, as shown previously. Further, the distance between the tip and the anatomical structures need to be found to be able to focus the LASER beam.

With the advancement of Avalanche photodiodes and the technology for ultrafast switching transistors, companies like ST micro electronics have been able to manufacture Time of Flight of light based ranging devices using Single Photon Avalanche Diode (SPAD) module, which are capable of accurate 1D distance measurements along the Z axis. VL530LX and VL6180X are such sensors made into SMD packages capable of measuring between 3 cm to 2 metres, without having to triangulate using multiple locations. Hence it has been implemented in the fetoscope. The resolution and the accuracy of the

SPAD sensor is 1mm and further details can be found in ST microelectronics datasheet (http://www.st.com/resource/en/datasheet/vl53l0x.pdf).

Using such a 1D sensor, the distance between the base of the fetoscope and the abdomen can be measured. This helps the software set the fulcrum (point of rotation) of the fetoscope stem when inserted into the abdomen.

b) Pressure and temperature

Gel based MEMS barometer MS5837-02BA (https://www.mouser.in/datasheet/2/418/NG_DS_MS5837-02BA01_A-1013620.pdf) measures the pressure in the pipes used for pressurization and vacuuming, to switch off the pump when required. The temperature is measured.

c) Force sensing

Needle force measurement has always been a challenge, and several research teams have adopted a variety of techniques to measure needle forces. Most methods involve usage of sophisticated 6 Axis force transducers at the base, which tends to be rather bulky for the intended application. Teleoperated force sensing would include the effects of impedance while the force is relayed and is very difficult to remove such artefacts, as they vary quite largely with the rate of movement of the needle. Hence, the force sensing transducer had to be custom made for use with the distal end of the actuator, not compromising on the patency of the hole in the hypodermic needle.

The sensor is custom made out of a bifilar coil un- braided 0.1mm parallel bonded polyimide coated magnet wire forming a parallel plate capacitor and coated with a corona doping agent having a high dielectric constant of 4100V/mil of the coat. A bifilar wire length of 12mm was wound to 1.14mm diameter and 0.25mm in thickness, with 0.34mm hole through the centre, keeping the patency intact. The force, in this case, can only be transmitted through capacitive force transducer section to the stainless-steel tube or rod depending on the procedure done, to the surgical environment. The ultrafine copper wires painted with the corona dope to prevent leakage in capacitive charge which can result in an apparent variation of capacitance.

5.3.3.2 Imaging and transmission

One of the primary requirements of the fetoscope is to be able to show a real-time video of the intra-uterine view. The stem of the fetoscope is a major limiting factor because of its diameter, which is expected to be under 3mm. Hence the CCD camera module OV6922, having 300,000 pixels RGB with brightness compensation and of the dimensions 2.1 x 2.3mm. Though the module is of a relatively small size, with the addition of the optics, waterproofing and casing, the size increased to 3.9 mm, as seen in Figure 5.5. The output of this camera is NTSC with a rolling shutter system capable of up to 60 frames per second.

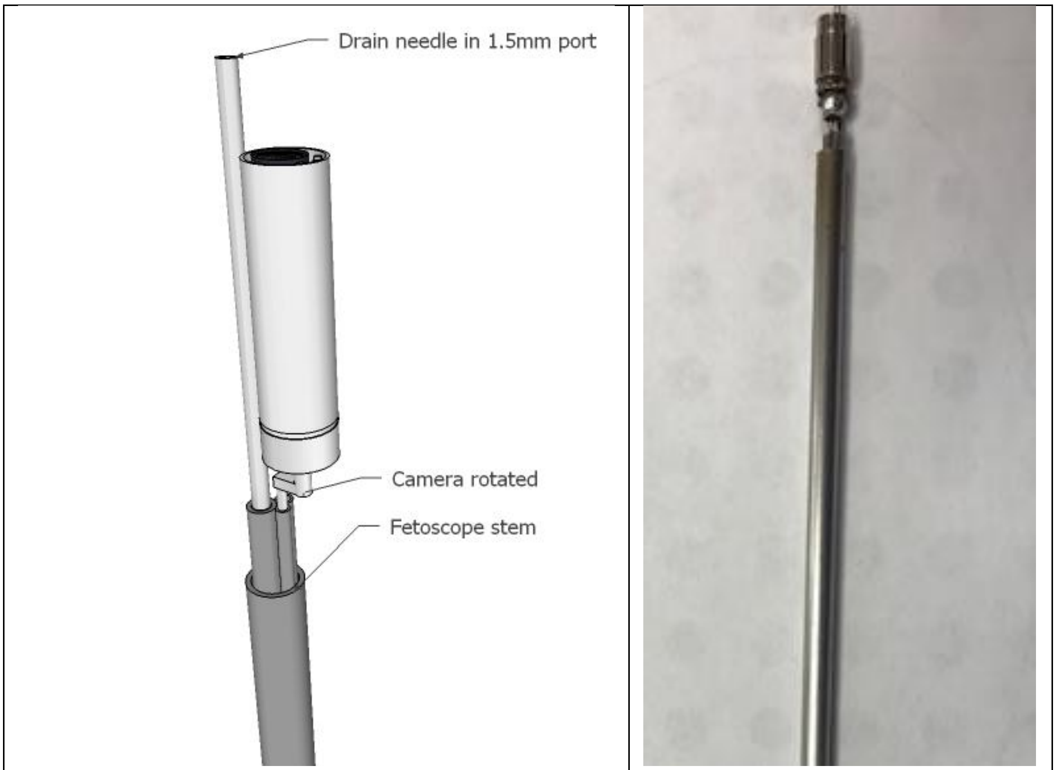

(a) Fetoscope tip rendering with tip and needle | (b) Fetoscope tip with camera

Figure 5-5 Fetoscope with camera and needle rendering is seen in (a) and (b) is a picture of the actual device

Since the camera output is analog, a simple NTSC video transmitter chip working at 2.370GHz is used. The microcontroller can change the frequency of transmission using simple 8 logic states which correspond to specific frequencies on the video transmission module so that multiple video transmission devices can be used at the same time. The ready-made analog transmission unit can be seen in Figure 5.6.

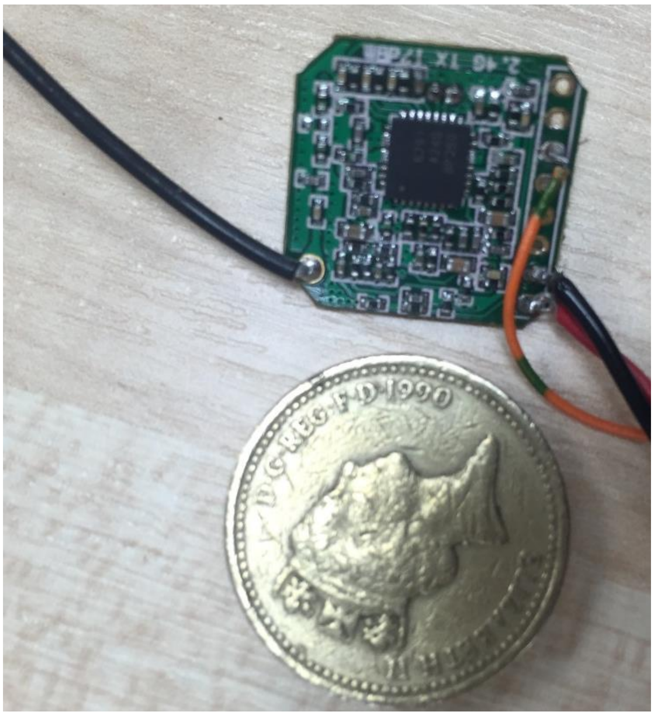

Figure 5-6 Micro analog video transmitter 2.4 GHz

a) Lighting

As the camera module in conventional cases is on the handle, there is a fibre optic relay cable, as described previously and hence a powerful light source is required for illumination. Therefore, fetal surgery uses cold light from Xenon bulbs, which are a source of intense light. Whereas in the case of a low-light sensitive CCD module such as OV6922, the light reflected from the surgical environment passes through the waterproofing glass layer and directly falls on the camera lens, without having to pass through many other materials. Hence a simple on board SMD LED lighting was found bright enough even in the darkest of conditions. The camera with lighting and waterproofing casing is given in Figure 5.7.

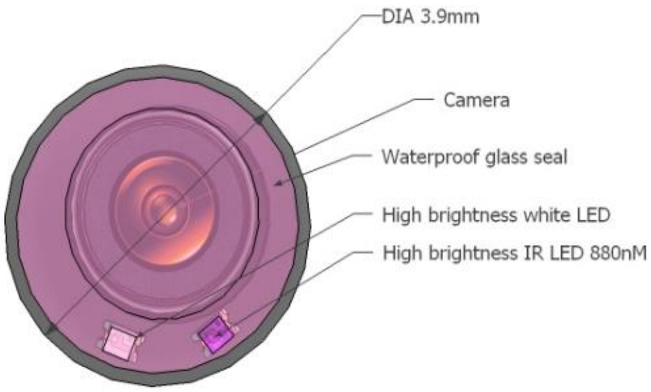

(a) 3D model of micro camera

(b) 3.9mm Micro camera

Figure 5-7 Micro camera with two different types of lighting (IR and warm White) are shown in (a) and (b).

One of the SMD high brightness LEDs is an IR LED of 880 nm wavelength and is included for potential pulse oximetry measurement of tissues and to visualize patency of blood vessels post cauterization.

b) Abdominal insufflation

Carbon-dioxide insufflation of abdomen is quite common for MIS as it provides a clear and almost unaltered view of the surgical field. It is also non-combustible, and the risk of gas embolus is very minimal, as carbon-dioxide is water soluble, but for the same reason, some argue that it may lead to fetal acidosis. Also, gas prevents proper viewing under ultrasound.

Therefore, in the case of most fetal surgeries, warmed Hartmann solution (Klaritsch P and surgery., 2009)warmed by an infusion warmer is used(example Hotline Smith's medical warming unit). There are many sophisticated placental surgeries done under CO2 insufflation, but there have not been any reports of fetal acidosis. Alternatively, nitrous oxide insufflation has been proposed (Klaritsch P and surgery., 2009). Hence, a universal pump capable of pumping both gas and liquids at 2litres per minute has been chosen and incorporated into the fetoscope unit. The direction and rate of the pumping can be switched and depending on the requirements; it can be used for hydro dissection or fluid removal.

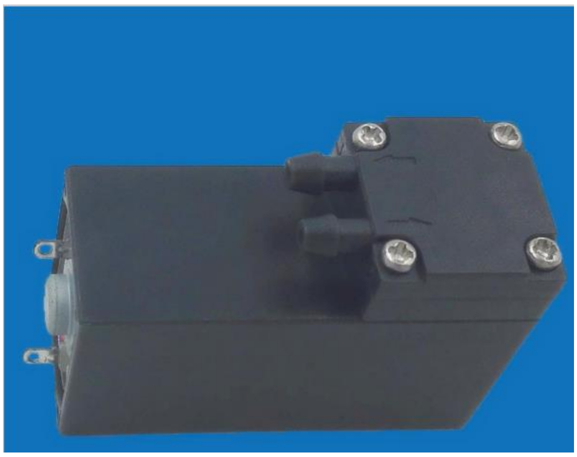

Figure 5-8 Fluid pump with 55kPa capacity at 3V DC and 5 Litres/ minute flow rate

c) Balloon inflation in Fetal surgery

Self -sealing balloon can be attached to the tip of the drain tube and gas, or saline can be pumped in. The membrane micro pump seen in Figure 5.8 which is compatible with both fluids and gases is connected to the major port, internally.

The self- sealing balloon is a balloon unit with a non-return valve at one end which stays open when inserted through a needle and closes once the needle is removed. So, if the balloon is inflated before the needle is removed, the balloon remains inflated. Figure 5.9 shows the rendered version of the fetoscope tip with the balloons at different levels of inflation.

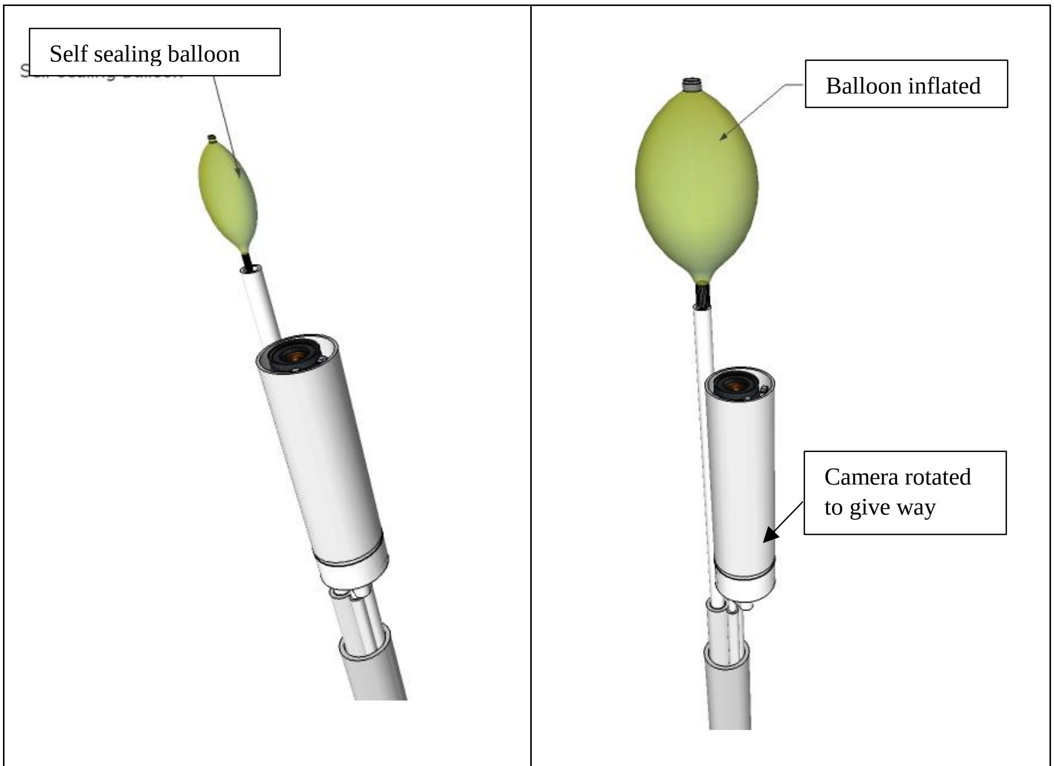

(a) Deflated self- sealing balloon (b) Inflated self-sealing balloon

Figure 5-9 Fetoscope tip with self-sealing balloon which can be detached (a) and (b) show them in different states

(d) Coagulation devices:

LASER coagulation is considered the most effective treatment for TTTS. The aim is to do an ablation of twin – twin anastomoses(Klaritsch P and surgery., 2009) recognizable on the chorionic surface. The diameter normally considered beyond 20 weeks of age ranges between 2.0 to 3.8mm. LASER type used is usually Nd:YAG(Neodymium Yttrium Aluminium Garnet) of 1064 nm wavelength and very high-power requirements from about 50 to 100W, similar to LASERs from Dornier MedTech, Wessling, Medilas Fibertom 8100 and in the case of diode lasers, GaAs(Gallium Arsenide) based 940 nm wavelength at 20 – 60 W power, such as Medilas D Multibeam, Dornier MedTech or Potassium Titanyl Phosphate(KTP 532 nm green LASER) such as the ones from Laserscope 800 series(Klaritsch P and surgery., 2009) and have optimal absorption in the haemoglobin spectrum there by ensuring higher efficiency.

The LASER fibres have about 600 – 800 microns core diameter, but including the plastic sheath, the diameter is roughly about 1 mm and operate as seen in Figure

5.10. Figure 5.10(a) shows the output of an unfocussed fiber coupled LASER and Figure 5.10(b) shows a fiber coupled LASER system with focusing optics. There are variations with focusing elements (built in optics) to enable focusing of the optical energy. Therefore, the major port of the fetoscope has been made to accommodate instruments of up to 1.5mm diameter. LASER ablation is the most efficient at 90 degrees as seen in Figure 5.11. Hence bent LASER probes have been considered but are still under development. The LASER being an optical device produces a beam which disperses beyond a specific distance, and the intensity may become very weak to have any significant effect on the surgical environment. An ideal distance from the tip is about 10 mm(Klaritsch P and surgery., 2009).

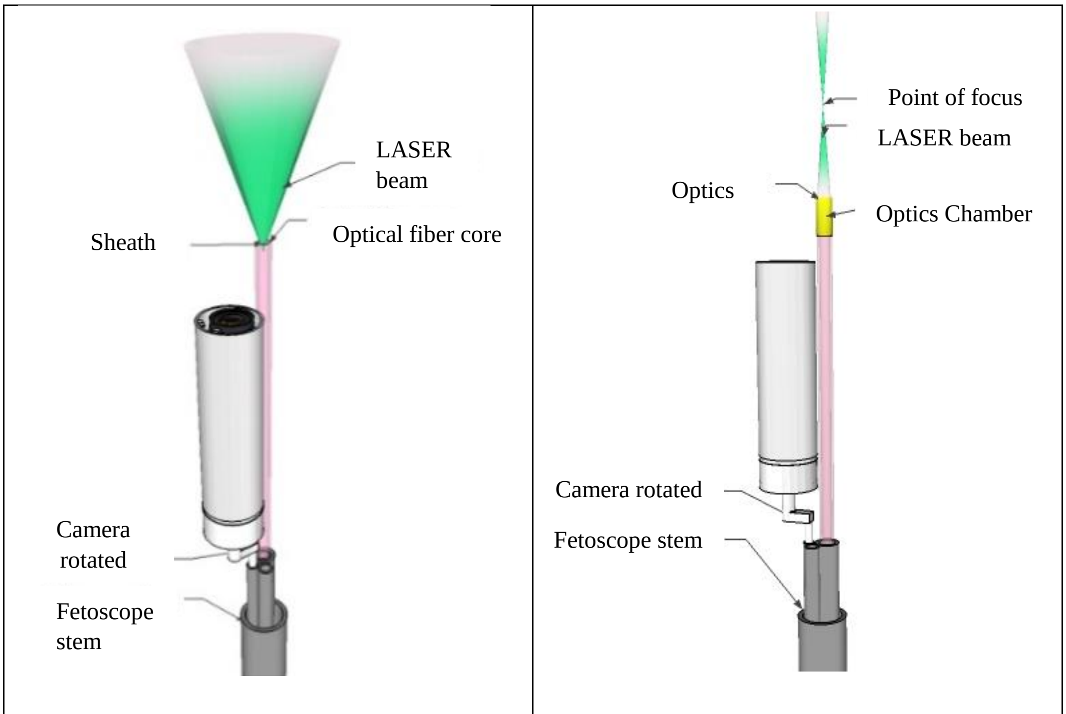

(a) Fetoscope tip with unfocused LASER | (b) Fetoscope tip with LASER focusing

Figure 5-10 Major port of the fetoscope with needle or probes is replaced with fibre-optic LASER for ablation procedures

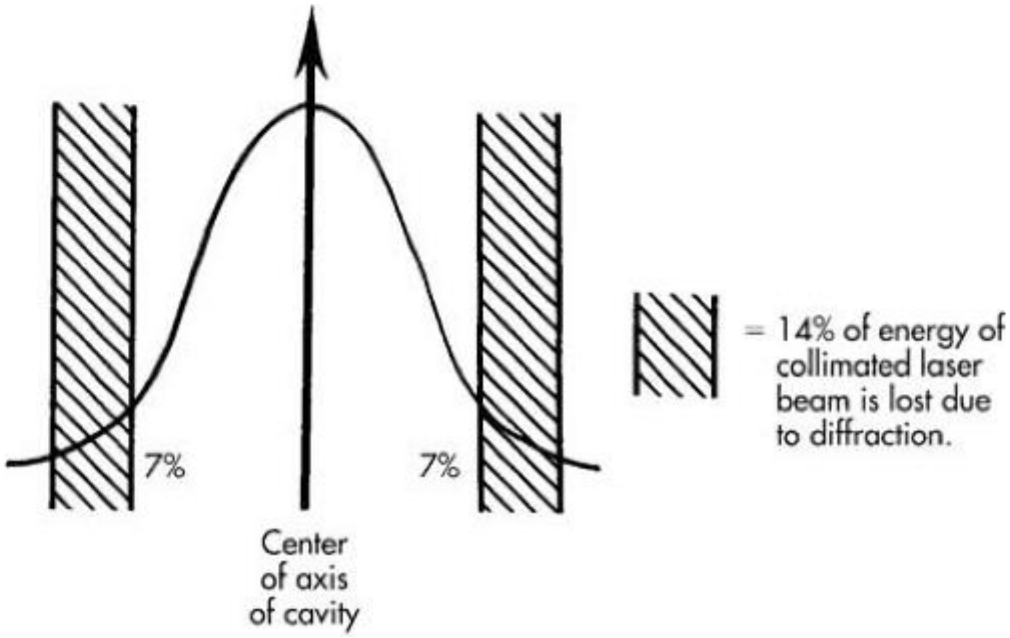

Figure 5-11 Intensity variation of the LASER beam from centre to the peripheries. The quantity (watts) of laser energy interacting per square unit of tissue area (cm^2) is referred to as the power density.

$$Power\ density = \frac{Watts}{\pi\left(\frac{beam\ diameter}{2}\right)^2} = \frac{Total\ power\ (watts)}{Spot\ surface\ area(cm^2)} \quad 5.1$$

(g) Display unit:

The display units in the Robotic fetoscope helps the user obtain visual information of the status of the fetoscope and offer a simple indication to the user about progression towards the target. The micro OLED display gives information about connectivity, target distance and guidance. The multicolour LEDs offer guidance and indicate potential overshoot.

The tracking and kinematics are combined to offer the user very simple visual cues to reach a specific target. Once the target is reached, the user would receive the indication for it. The display also shows information about battery levels and with some work, can also be used for guidance for incision placement. The OLED display used is a SSD 1331 device from Solomon Microsystems uses SPI communication for initialization and control. The multicolour LEDs, on the other hand, use a single wire timing-based communication and are daisy chained to one another.

5.2.3 Ports of the fetoscope

The fetoscope has a total of 3 ports and 2 slots, as seen in Figure 5.12(a). The major port is 1.5mm in inner diameter, and there are two minor ports of each 0.45 mm inner diameter. Depending on the application, the ports can be reconfigured for fibre optics, drainage, forceps or ballooning and cautery. The 3 slots are lacunar. The smallest serves to carry wires from the camera; the bigger hole carries the wires for lighting and the force transducer to the rest of the circuitry. The wires from the force transducer are painted with corona paint to avoid any leak of capacitance. The other bigger slot carries the camera hinge which is formed by a stainless-steel rod attached to the camera and a servo controls the angle of the hinge and also provides a path for the other ports for clear access. Figure 5.12 (b) shows the lateral perspective of the fetoscope stem

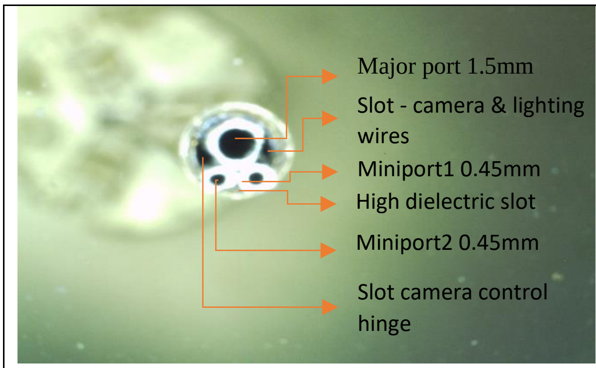

(a) Axial view of the ports of fetoscope stem

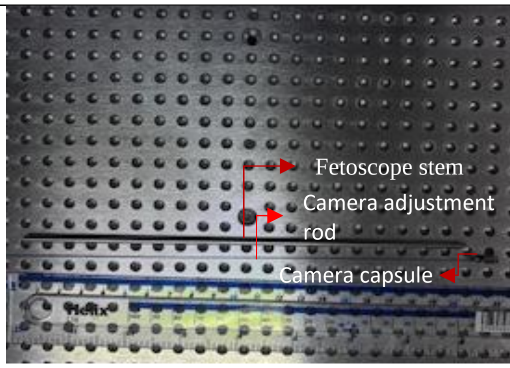

(b) Lateral view of the fetoscope stem, camera rotation wire and camera

Figure 5-12 Fetoscope tip with ports is seen in (a) and turning element for the camera and the camera capsule (b)

The largest port communicates internally with a pump, a flexible tube and an inbuilt LASER source and also communicates externally, so that Fiber optic LASERs, drains, stents or needles can be inserted, or for fluid insufflation and drainage. During normal operation, when the major port is filling the surgical site with fluid, one of the mini port offers a release to the pressure when required. There is one more port which can be used for pulse oximetry of the surface using fibre optics or developed to control forceps using tendons or insertion of suturing material.

5.3.4 User interface and interaction with the surgical environment

The user can have access to a variety of settings including connectivity, safety settings and limits on the force, haptic feedback gain, LASER or RFA operation if required. The hardware made, however, does not contain high power LASERS or RFA unit. However, a simulated 690 nm LASER diode CLASS IIIa is included which can provide an indication of LASER operation, and safety is used for demonstration purposes.

The physical interactions with the surgical environment are translated to the haptic interface on the thumbstick corresponding to the input forces at the tool tip. The surgeon can look at the force status and connection status if required. Also, the fetoscope communicates with the computer the sensor data which has been in real-time at 115.2 Kbps. The computer receives the serial data and the interface shows the received data in real-time.

The Figure 5.13 is representative of the user hardware and software interaction and feedback. The user can interact with the computer software and has complete access to a complete interactive software with visual feedback of the actions performed and surgical planning as discussed in Chapter 6. Settings such as target registration used for guidance of the fetoscope, fetoscope tip registration with the anatomy, calibration and setting the limits of the highest forces, displacement and best tolerance for the orientation of the fetoscope exist within the control panel of the interface which has been developed.

The user can physically interact with the fetoscope hardware using the joystick as an interactive device for the registration process, using switches and the thumbstick. A combination of the footswitch, thumbstick and the inbuilt switch can be used for tip actuation control, LASER or RFA triggering, pump aspiration of fluids, ballooning and can be adapted for many other uses. The joystick interacts with the user by giving the user force and tactile feedback and visual display using the built in OLED display. The camera on the fetoscope transmits the view of the surgical environment in real-time to a display placed externally.

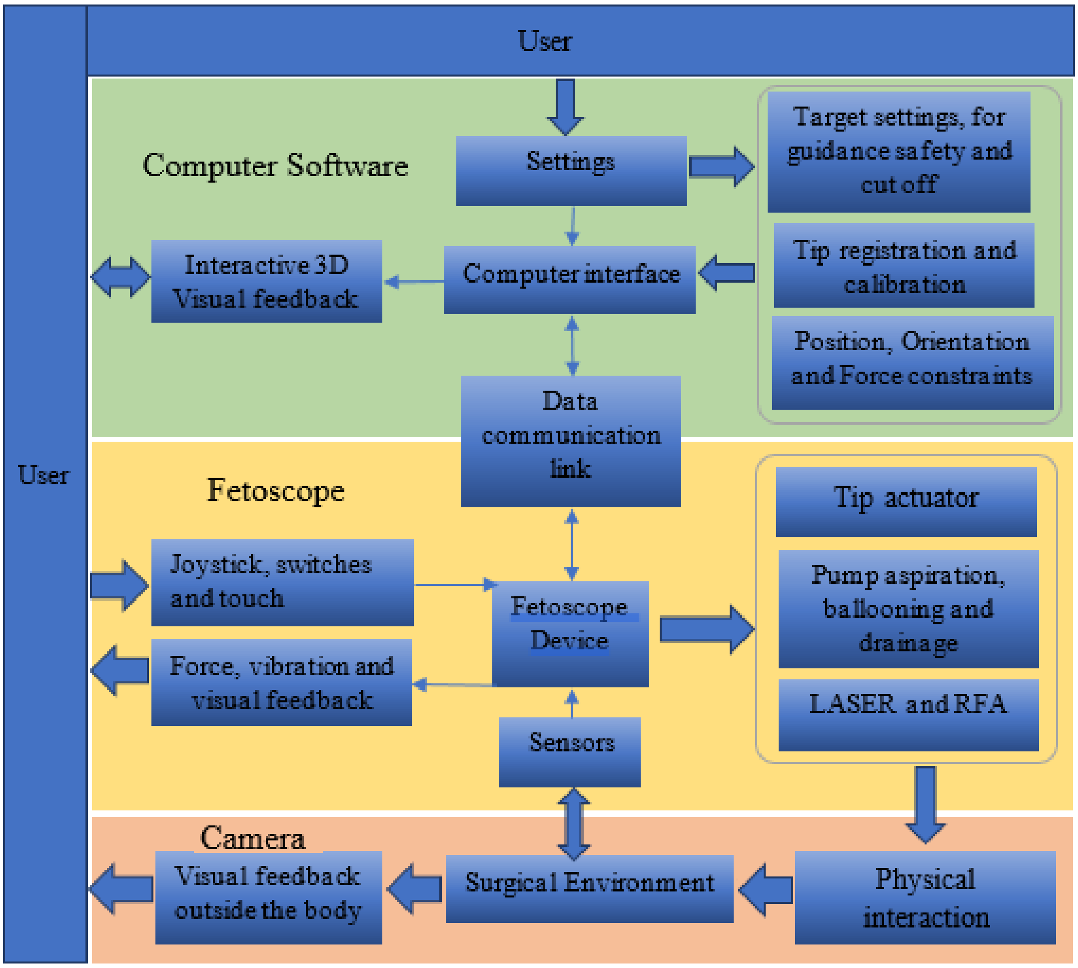

Figure 5-13 Flowchart for user interaction and feedback with the device and the environment

5.3.5 Communications and synchronization

As mentioned earlier in this chapter the primary mode of duplex communication with the user interface is either using Bluetooth 2.0 hardware or WiFi network. The former is preferred because of lower power consumption and offers up to 2 Mbps of over the air data rate. WiFi, on the other hand, has a much higher achievable data rates, but the power consumption can be ten times higher, depending on the quantity of data and range of transmission. Figure 5.14 illustrates the above-stated elements integrated into the fetoscope.

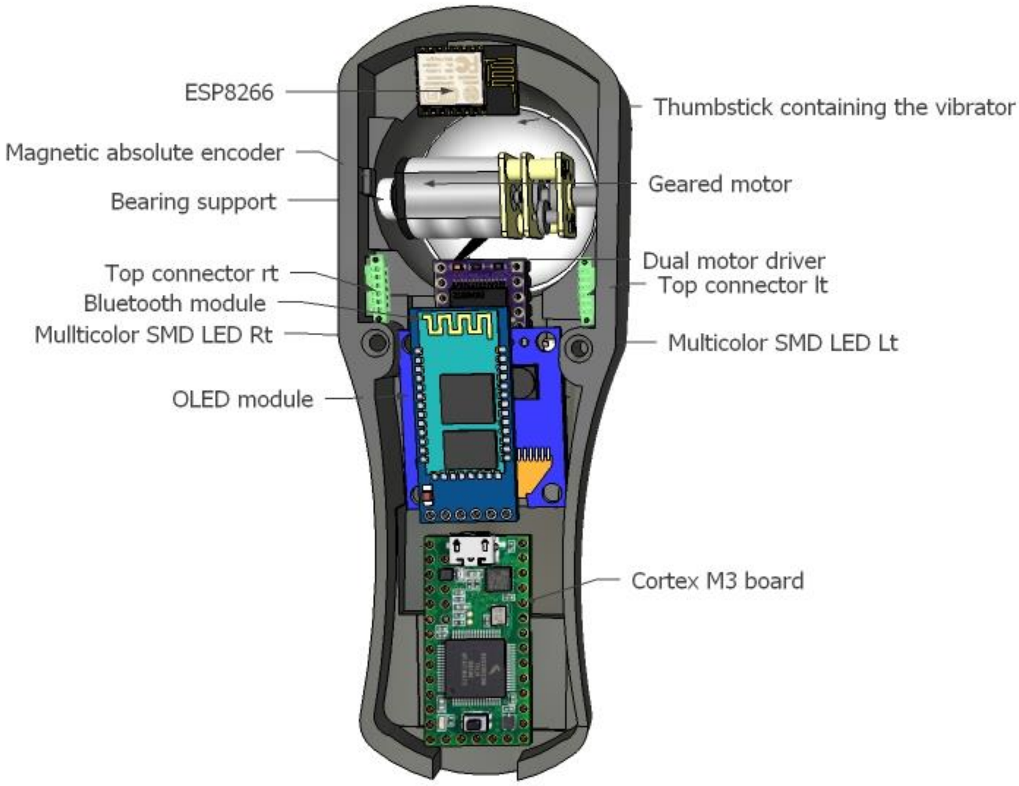

Figure 5-14 Shows bottom view of the top portion of the fetoscope

The primary data from the Fetoscope includes the distance from the body for inverse kinematic calculations, battery information, force data, thumbstick interface, haptics, tip actuation distance. The data to be received into the fetoscope includes the data of the 3-dimensional target point for reaching, target force setting, haptic mode settings.

In Figure 5.14, ESP8266 module is used for WiFi protocol for wireless transmission and HC05 uses Bluetooth 2.0 protocol for data communication. The communication through WiFi is with the modem while the Bluetooth 2.0 communication can be done directly with the computer or with another trans-receiver module. In this case, a HC 06 Bluetooth module was paired with the HC 05 module. The thumbstick base has a motor driven gear-train which is backdrivable and monitored by a single chip magnetic encoder LIS 3 MDL which will be described later in this chapter. A dual motor driver unit comprising of a DRV8825 board from Pololu is used for the geared motor control and a DRV2605 board from Pololu as well is used for vibrational haptic motor control on the joystick. The charging unit is micro USB based and uses a TP4056 charge control module. The unit further has three multicolour LEDs which flash to indicate error or success and an OLED screen which provides a real-time visualization of the set target distance from the tip or from the stem, distance from the body, forces and modes. The top section contains a cortex M3 based chip from Kinetis Freescale microcontrollers. The connectors in the top casing from the processor board can connect to the bottom when the unit is closed.

Wireless communication does more than synchronization of sensor details with the computer. Certain calculations which are better done by the computer are off loaded to the computer. Also, this extends the possibility of over the air firmware updates for the controller, without any physical connections. The bandwidth that WiFi offers is very suitable for digital image streaming, and ESP8266 has 4MB of flash memory, capable of buffering full image frames. For continuous digital image streaming, processing requirements are higher, as image compression becomes a primary requirement. In which case, either a Cortex M4 chip or a suitable FPGA based image compression becomes essential.

5.3.6 Mechanics and control of the Fetoscope

The Fetoscope mechanics consist of an active joystick controller controlling an actuator and feedback forming a mechatronic system. In the initial section, the structure of the joystick controller and its sensor system will be discussed. The next section deals with closed loop control system for the catheter. Figure 5.15 shows all the joystick control elements and the feedback system used to implement the haptic feedback. The actuators primarily include the geared motor at the thumbstick, tip motion servo actuator and the vibrator at the thumbstick. Feedback system involves the aforementioned force transducer, rotary position sensor at the joystick axis of rotation, linear position sensor within the linear servo actuator. The computations and PWM control are done by the microcontroller.

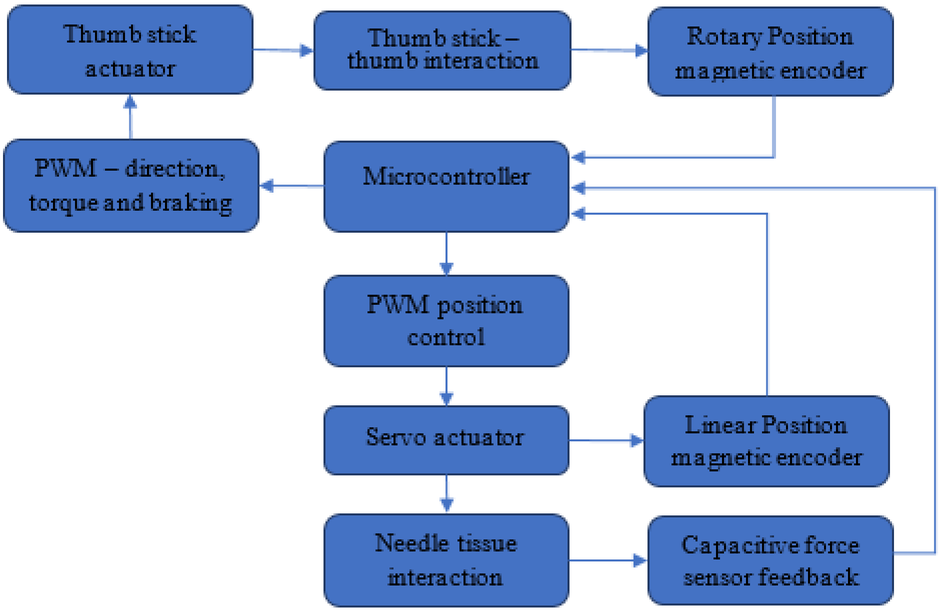

Figure 5-15 Joystick closed loop control elements for enabling haptic feedback

5.3.6.1 Joystick controller with haptic feedback

The fetoscope joystick is a single degree of freedom motorised thumbstick equipped with a magnetic encoder for 10-bit angle feedback and also includes a vibratory feedback for low amplitude forces. The said motor is geared 1:100 is driven by a MOSFET H-Bridge driver chip capable of driving 2 brushed motors with Ultrasonic PWM control up to 100kHz to provide decreased audible hum. The microcontroller can control the direction, rate of movement and torque of the thumbstick based on gain G calculated in the next section. Further, the position feedback is also used to limit the working range of the thumbstick to prevent locking of the joystick. The control elements for this system is described in Figure 5.15. The bottom view of the top half of the fetoscope Figure 5.16 reveals the placement of the motor, its encoder and gear train.

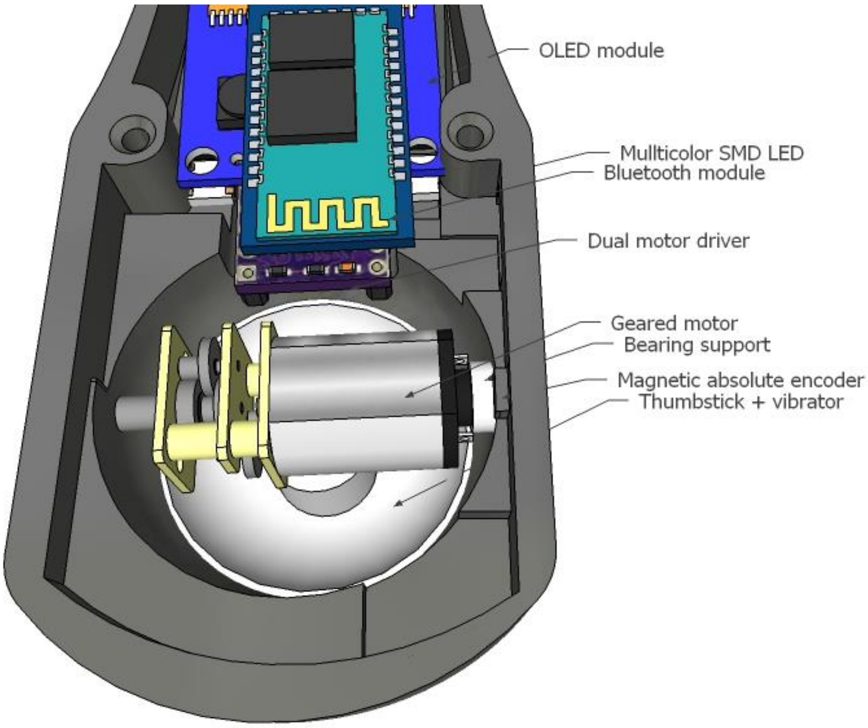

Figure 5-16 Posterior view of the joystick system showing the geared motor, encoder and driving module

The vibratory feedback driver DRV2605 receives I2C communication from a microcontroller and activates a micro-vibrator, PWM modulated with variations in low amplitude forces. These vibrations can be felt by the thumb while using the thumbstick for control of the tip.

The feedback in the joystick is actively enabled by capacitive proximity sensing to save power. Position feedback from the joystick uses an AS5040 sensor with 10 - bit resolution along with a 3000 mG diametrically magnetised Neodymium magnet, to improve the specificity of the magnetic encoder. The encoder output is obtained with SPI communication and is used for controlling the linear actuator position.

5.3.7 Haptics and development and control

One of the major problems in Minimally Invasive Surgeries and Micro Invasive surgeries is a loss of dexterity, precision and force perception as discussed in the literature review. In hand held surgical instruments, among the 6 axes of forces, the vertical axis of the instruments is quite important especially in cases of needle insertion-based procedures. Therefore, when the depth perception is limited, and the vertical axis force is diminished considerably, ultrasound-guided procedures can quite commonly lead to either overshoot within the operating space or posterior wall puncture in the case of blood vessels is quite common. Further, in cases of fetal surgeries, the structures encountered can be quite fragile. Hence a reliable force feedback system is a requirement.

5.3.7.1 Development of closed loop micro actuator

Most RC servos from did not have the required dimensions or torque and delivered an accuracy of +/-3 degrees but use simple PWM control, with 11 to 20 mS pulse width. Such inaccuracy is not acceptable for use in the robotic catheter operation. Further, while a linear actuation was required in most surgeries, most servos provided rotational movement, and the servos which did provide linear movement were either not durable or inaccurate or bulky and hence did not suit the application. Hence a servo with PID control was constructed within the available profile within the fetoscope.

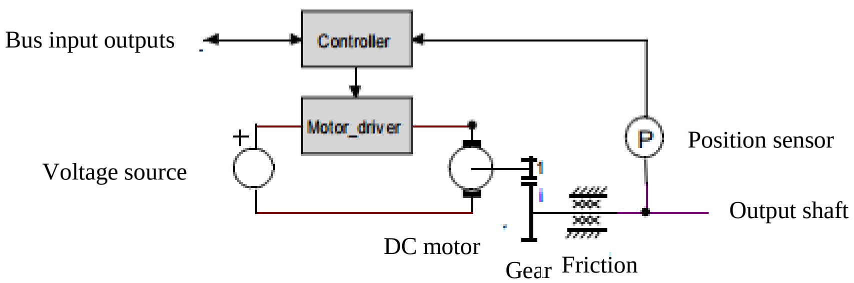

Figure 5-17 Simplified generic servo model for use in fetoscope needle driving application

From Figure 5.17, it can be observed that provided the control algorithm is accurate, and the gear network has a low back-lash, the position sensor is the most crucial part to achieve precise actuation. Most simple RC servos use a potentiometer for feedback and a 10 bit ADC resolution. The reduced accuracy and resolution of feedback appeared to be the main cause of the errors. There are multiple constraints on the size of the encoder, positioning and the available technologies for rotary encoding. An absolute rotary encoder like a potentiometer had to be chosen. Hence the potentiometer connected to the servo output shaft was replaced with a diametrically magnetised magnet and a 3 axis digital magnetometer with 16-bit resolution on each axis.

5.3.7.2 Development of angle encoder for servo

The magnetometer output is initially used to align the sensor with relation to the magnet. The angle of the shaft with respect to the sensor. The earth's magnetic field is 0.6 Gauss (48 A/m) which can produce minimal interference, compared to the 1200 Gauss produced by the used Neodymium magnet. However, the sensor was magnetically shielded using high permeability (μ metal) sheets to minimize the noise due to the earth's magnetic field and stray electromagnetic fields.

The output of the magnetometer is given as x and y in 16-bit values and can have negative values due to 2’s compliment .Hence, the angle of the shaft **θ** is given using the following equations with different combinations of x and y assigned as:

$$\theta = \frac{90 - atan\left(\frac{x}{y}\right) \cdot 180}{\pi}, (y > 0) \tag{5.2}$$

$$\theta = \frac{270 - atan\left(\frac{x}{y}\right) \cdot 180}{\pi}, (y < 0) \tag{5.3}$$

$$\theta(y = 0, x < 0) = 180 \tag{5.4}$$

$$\theta(y = 0, x > 0) = 0 \tag{5.5}$$

Due to the size limitations imposed by high accuracy potentiometers, reduced repeatability and durability issues, simple potentiometers could not be used as angle encoders. Further, in most cases, there is a requirement for absolute position encoding up to 360 degrees and more. Whereas, the smallest available angle encoder at the time of research is AMS 5406 from Austria Microsystems and a few other modules from Avago micro systems which were evaluated but were still were much bigger than the 3mm maximum size required. Hence, AMR compass modules (of size 2x2x0.8 mm) from ST micro electronics – LIS 3 MDL was modified to be used with a 1mm diameter diametrically magnetised magnet, for angle encoding.

5.3.7.3 Magnetic encoder evaluation

A simple experiment was done with the diametric magnet aligned with the axis of a Dynamixel MX-28 servo capable of 0.08 degrees resolution and LIS3 MDL chip set at an offset of 3 mm from the diametric magnet. The angular output for 360 degree continuous rotation is given in Figure 5.18. The relationship between the Dynamixel servo output and the magnetometer output based on Figure 5.18 and Figure 5.19 is found to be repeatable and therefore can be characterized with high accuracy.

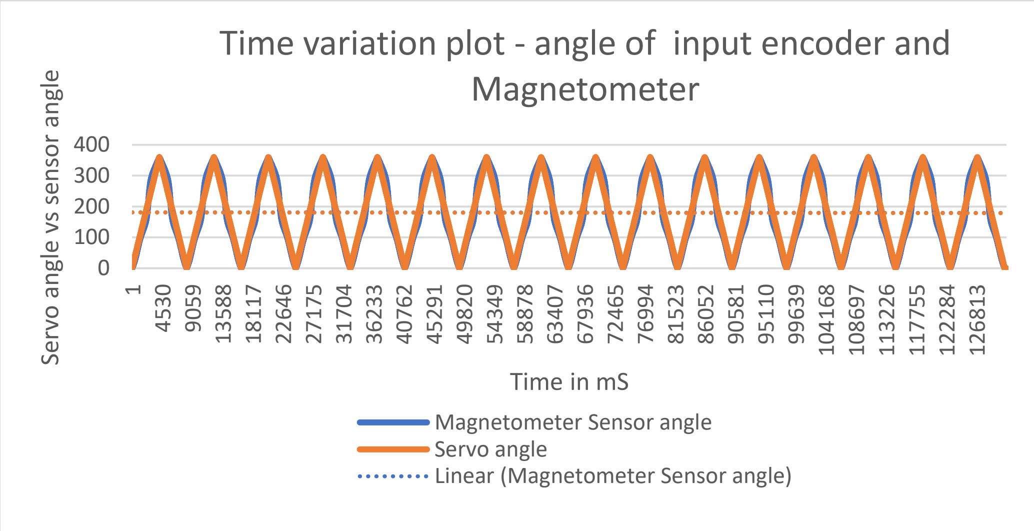

Figure 5-18 Time variation plot of MX 28 servo input vs angle output of the magnetometer

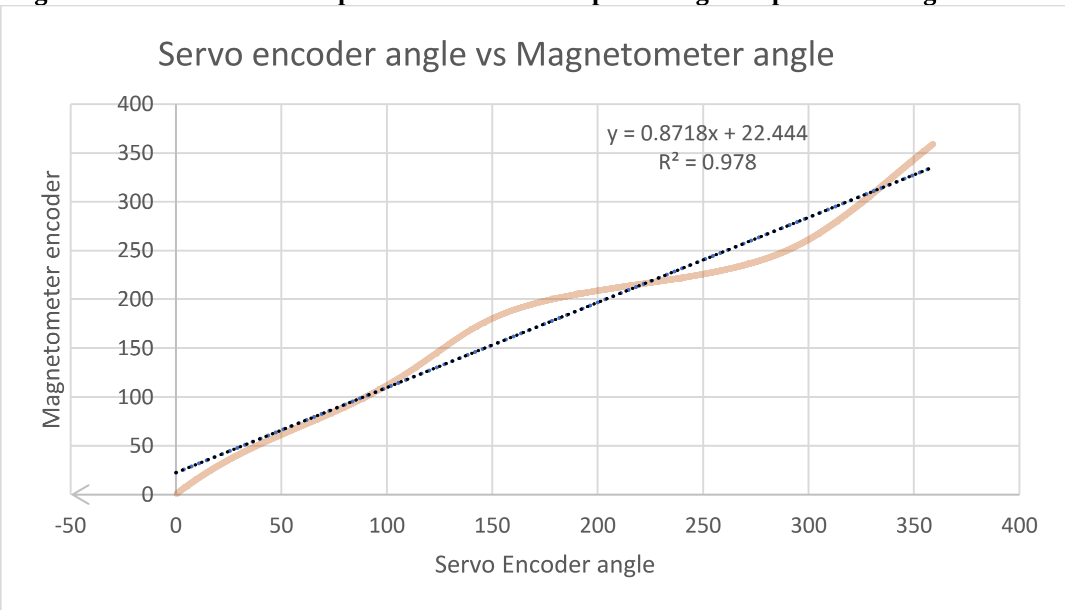

Figure 5-19 Relationship between the MX 28 servo angle and the Magnetometer sensor output

5.3.7.4 PID control of the actuator

PID control combines the three elements P, I and D controls the gain as seen in Figure 5.18 and follows the following set of rules to attain the desired position:

(a) P gain refers to the value of proportional band. P component combats present error

(b) I gain refers to the value of integral action. I component combats the past (cumulative) error

(c) D Gain refers to the value of derivative action. D component combats future error Gains values are in between 0~254. Gains must be tuned together

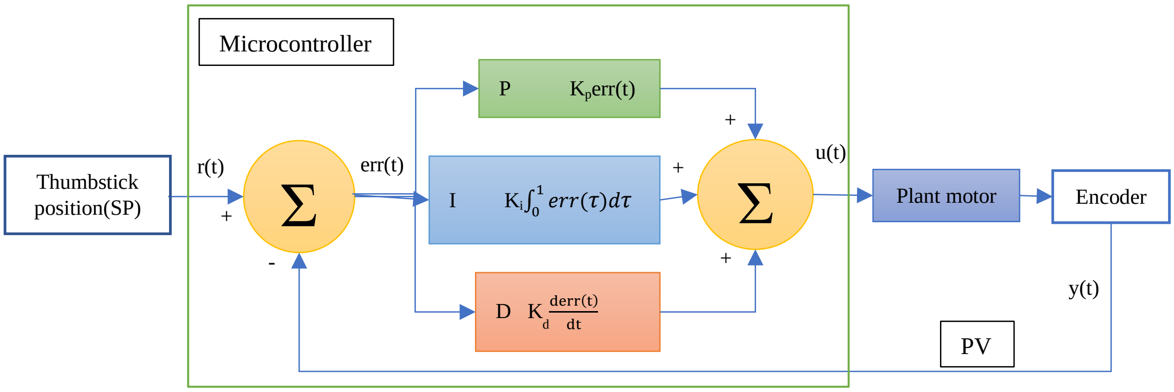

Figure 5-20 Control flow chart used within the custom - made Servo for needle actuation

The flowchart in Figure 5.17 and Figure 5.20 are used for PID control of the servo position. The angle subtended '**θ**' is calculated using the equations 5.6, 5.7, 5.8 and 5.9 and is used for rotational feedback and multiplied by the pitch of the screw to get the linear displacement.

In Figure 5.18, r(t) is the desired process value or the setpoint (SP) and y(t) is the measured process value (PV). Error '*err(t)*', is a difference in actual position, 'y(t)' measured using the encoder and the reference position '*r(t)*' is given as:

$$err(t) = r(t) - y(t) \qquad 5.6$$

PID control output '*u(t)*' can be given as:

$$u(t) = Kp * err(t) + Ki * \int err(t')dt' + Kd * derr(t)/dt \qquad 5.7$$

Torque output as per PID control in torque terms can be derived and represented as

$$\tau = Kp * err(t) + Ki * \int err(\tau)d\tau + Kd * derr(t)/dt \qquad 5.8$$

The voltage for the amplifier can thus be obtained as:

$$Va = \frac{\boldsymbol{\alpha}\left(K_p\, err(t) + K_i \int err(\tau)d\tau + K_d \frac{derr(t)}{dt}\right)}{K} + \beta \qquad 5.9$$

The DC motor has a current consumption 'I' proportional to the motor torque 'τ' at a given voltage 'V' and can be given by:

$$V = \alpha I + \beta \qquad 5.10$$

Where $'\alpha'$ and $'\beta'$ are coefficients determined experimentally. The relationship between torque and current, characterized by a torque constant K can be given

$$\tau = KI \qquad 5.11$$

'V' can also be represented as:

$$V = \alpha\tau/K + \beta \qquad 5.12$$

From the above equations, the control of motor rotation with reference to an input angle and the magnetometer as the feedback can be obtained. The setup with magnetometer, actuator and PID control implemented within the fetoscope is presented in Figure 5.19.

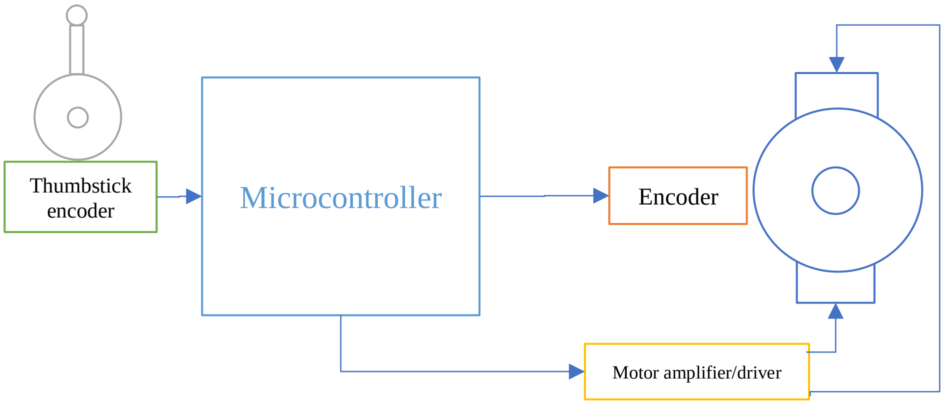

Figure 5-21 Fetoscope with servo actuator implemented

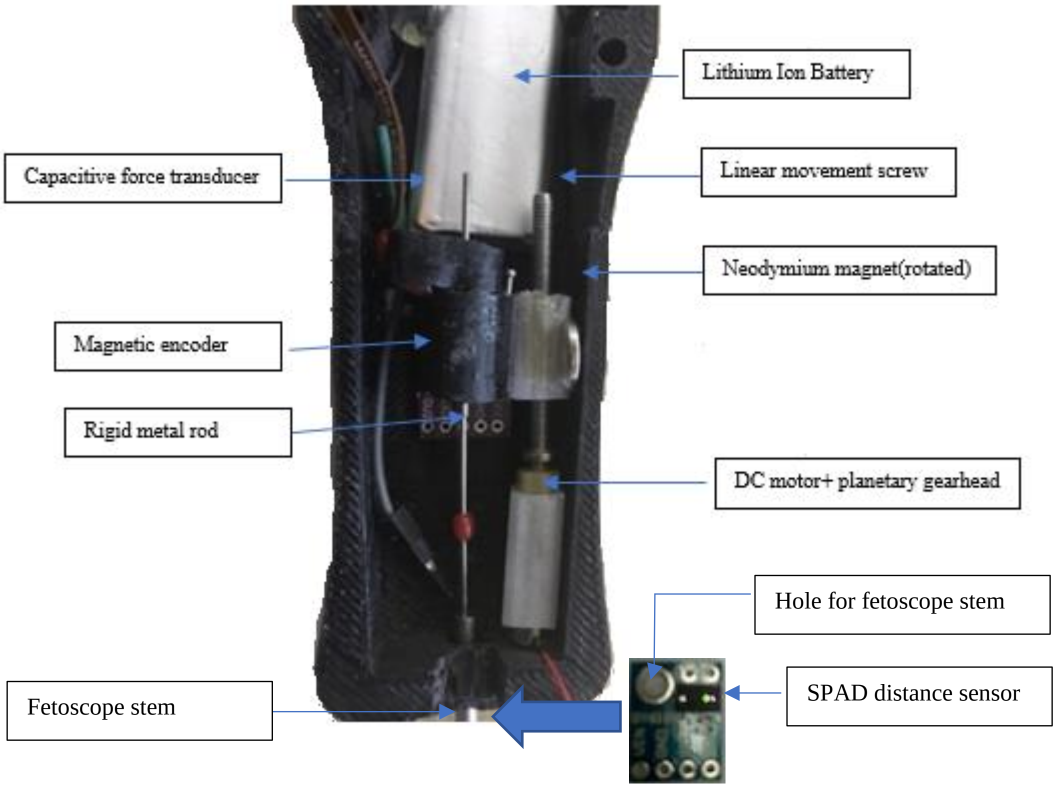

Figure 5-22 Completed servo construction showing the linear actuator and magnetic linear encoder

In Figure 5.21, the simplified schematic of the servo is shown and Figure 5.22 shows the linear servo construction with a geared linear motor and a magnetic encoder. The thumbstrick with a rotary magnetic encoder provides the thumbstick angle input. Figure 5.21 is the output of the PID implemented with the displacement range between 0 and 15mm.

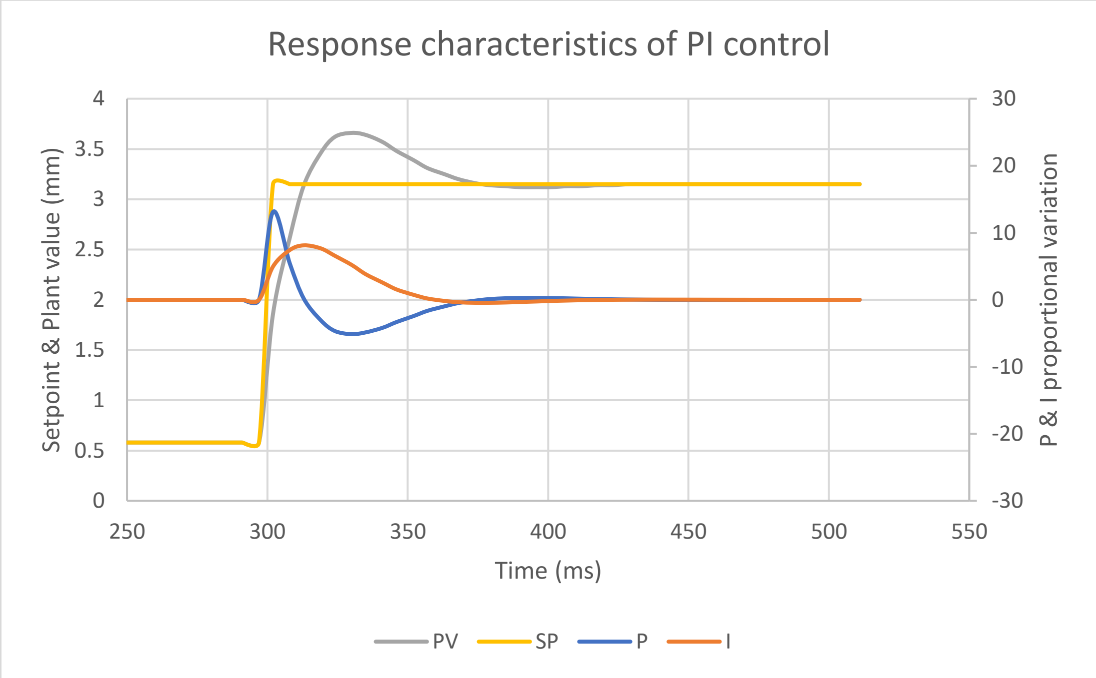

Figure 5-23 PI controller step response in no Load condition showing a settling time of 220 ms

From Figure 5.23 the response of P and I to the setpoint raised from ~0.50mm to ~3.2mm can be observed. Figure 5.23 the settling time of the PI controller can be observed as 220ms under no-load condition. The amount of overshoot does not exceed ~0.5mm, which is well under the resolution of ultrasound imaging itself.

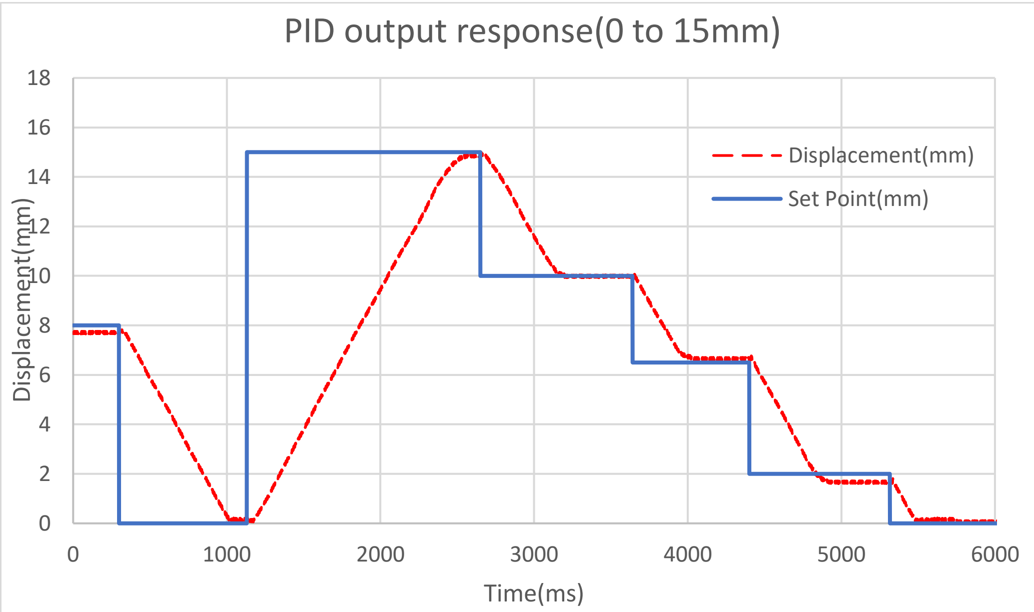

Figure 5-24 PID multi step output response in no Load condition

In Figure 5.24, multi step actuator output response can be seen. It can be observed that the setup requires 1450ms to cover the entire range of motion. Though the actuator can be made much faster, the current speed is kept at 10mm/second in order to avoid mechanical overshoots and the necessity to avoid complex algorithms to correct them(Jeng, 2013).

5.3.7.5 Servo output evaluation

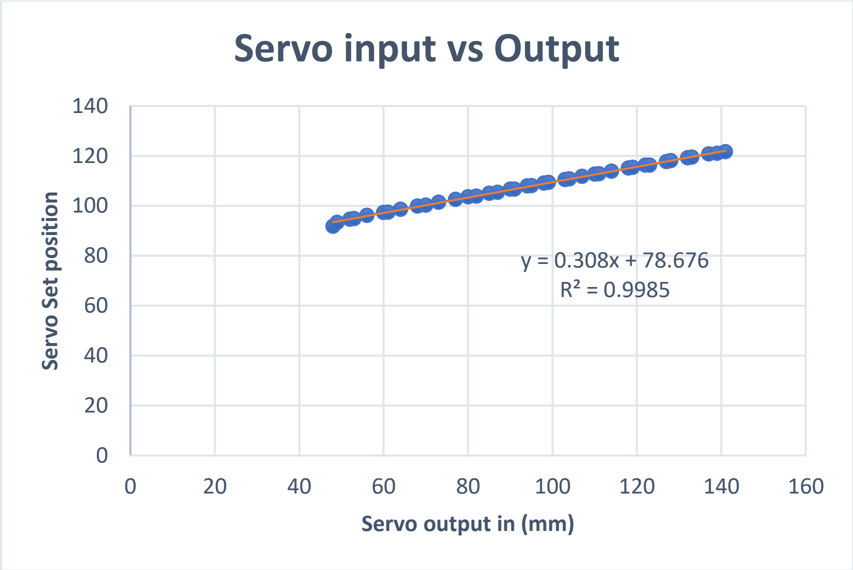

Figure 5-25 Servo output vs measured value (using a digital micrometer) in (mm)

The servo output is a result of the angle encoder, linear motor drive and the PID algorithm combined. The mechanical displacementwas a total of 30 mm which changes with PWM input change, which was kept between 800ms to 2500ms. The mechanical displacement output was tested with digital Vernier callipers for every 50mS increment in PWM timing. The servo output seen in Figure 5.25 shows that the accuracy is well over 99%, and hence further evaluation can be done for sub-millimetre accuracy verification.

5.3.7.6 Capacitive force sensor construction and calibration

Capacitance is a measure of electrostatic energy accumulated between two conductive plates or electrodes, separated by a distance and holding opposite charges.

The value of the capacity of a capacitor – Capacitance, depends on a few factors such as the area of the plates, the distance of separation and the material which sandwiches the system forming the dielectric. By maintaining the charge between the plates constant, the distance between the plates can be obtained by just measuring the voltage across. When a force is applied across a capacitor, and the plates come closer, the voltage changes can be measured as a proportion of the pressure applied.

This simple approach has been routinely used by in the industry for use in pressure vessels robotics and in biomechanics applications. There are many advantages to capacitive sensing when compared to conventional strain gauging methods. Some of them include no requirement of bonding adhesives (self - imposed thermal differential strains), no high levels of amplification required, though signal condition circuitry is essential. Lower amplification results in the lower amount of EMI and RFI which can confuse the sensor output as received by the ADC. Recently, a lot of laparoscopic device research has gone into development of capacitive force transducers(Lee et al., 2016).

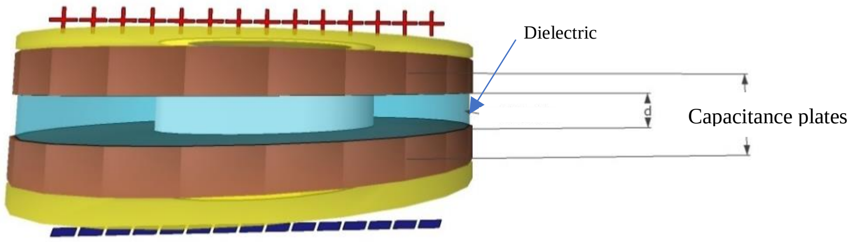

Figure 5-26 Capacitive sensor configuration. 'd' is the distance between the plates, 'A' being the surface area of the parallel plates

In the Figure 5.26, the parallel plate capacitor configuration is illustrated. The relationship of the capacitive sensor with dielectric constant, Area of the plates and the distance between the plates can be given by:

$$C = \mu A/d \qquad 5.12$$

Where,

C = capacitance

μ = dielectric constant of the material

A = area of the plates

d = spacing between the plates

Sensitivity of a capacitance force sensor is equal to the change in capacitance with force ‘*F*’, and displacement input ‘*D*’ can be given as:

$$\frac{\partial C}{\partial F} = \frac{\partial C}{\partial D} \qquad 5.13$$

Deformation of the transducer due to force ‘*F*’, ‘*Z*’ is a function of elastic modulus of the dielectric material ‘*E*’ and permeability of the medium ‘μ ‘ and can be given as:

$$\frac{\partial C}{\partial F} = \frac{\mu}{E * Z} \qquad 5.14$$

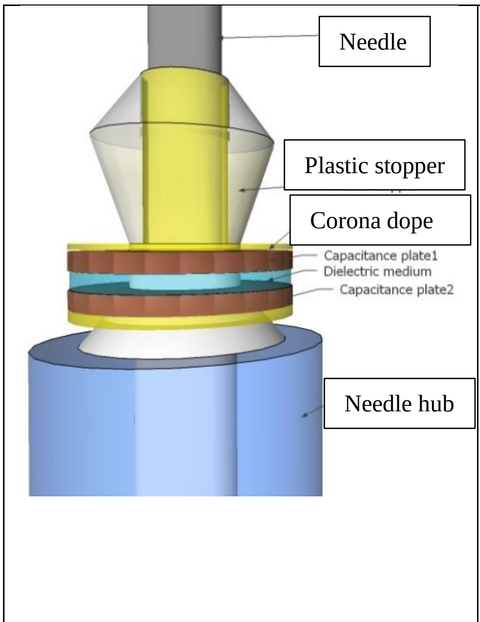

(a) Force transducer rendering	(b) Needle force transducer

Figure 5-27 Capacitive sensor configuration (a) Rendering of the capacitive sensor and (b) Needle force transducer

For accurate force measurements, the material chosen for the dielectric needs to have a low thermal expansion to avoid errors (Lee et al., 2016). The surface area of the plates is of utmost importance, as the lower surface area can result in capacitance values becoming very low and prevention of capacitive leak along the measurement leads becomes difficult. Therefore, the sensor was painted with a protective coat of high dielectric corona dope paint, and the charge amplification had to be kept close and shielded to prevent loss of electrostatic energy. The force transducer was placed behind the needle loading element attached to the actuator, as seen in Figure 5.22 or attached to the tip of the needle as seen in Figure 5.27(a). The relationship between the loading force and the force output observed from the force transducer in mV can be seen in Figure 5.29.

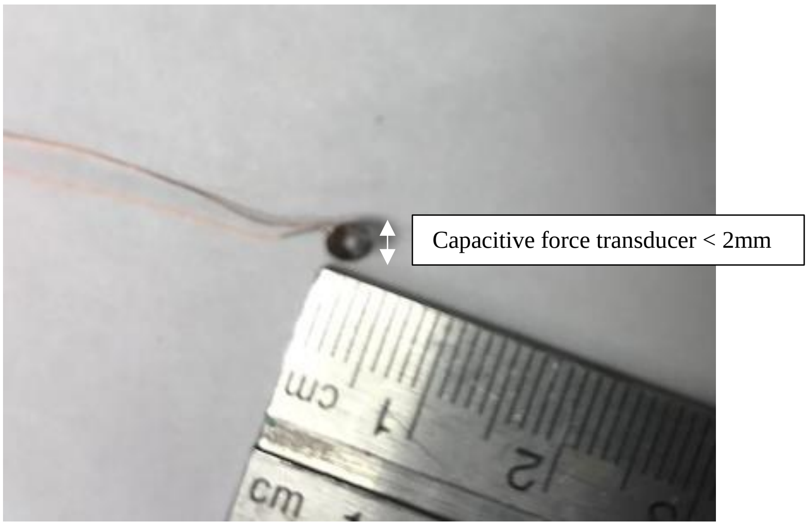

Figure 5-28 Micro-force transducer for measuring axial forces in the needle

It can be observed from Figure 5.28 that the size of the transducer is less than 2mm in size and can easily fit on the needle hub so that the forces can be measured directly. Figure 5.27 (b) shows the micro capacitive force transducer implemented in the base of a needle.

5.3.7.6.a Force transducer evaluation

The capacitive force transducer constructed is loaded with a linear stage and an Optoforce transducer(www.optoforce.com) by vertically loading it.

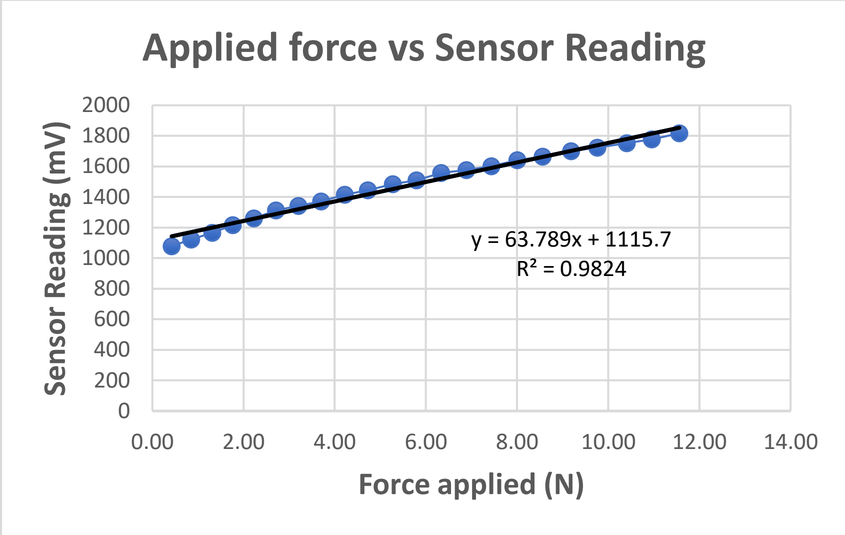

Figure 5-29 Capacitive force sensor calibration applied force vs output

In Figure 5.29, the linearity of the force transducer thus formed is over 98%. It can be further improved with the better construction of the sensor. The range of the sensor from the graph seen in Figure 5.28 can be observed to be between 0.1 to 12N approximately. The observed accuracy of the force transducer is over 98%, and repeatability is consistent over 1000 cycles. It has to be noted that zero drift can be observed over every repetition for every loading and unloading cycles when tested over 1000 cycles and is mainly because of the sensor construction and not a limitation of the capacitance force measurement technology.

5.4 Fetoscope Evaluation

Hardware evaluation of the fetoscope includes evaluation of inter- device communication, sensor interface and mechanical evaluation of the active parts. Other than the sensors which are factory made and have documented data sheets, which can be found in the appendix, the output from the sensors which are specifically made for use with the fetoscope and calibrated are discussed in this section.

5.4.1 Evaluation of sensor outputs and communication

The complete system is verified at the computer interface in the next chapter, where the byte communication and user interface in the next chapter and the whole system are evaluated in the later chapters. Now that the force transducer, the micro servo actuator controlled by the joystick and the displacement encoders have been developed and the implementation of the above have been achieved, the setup can be used to provide haptic feedback using impedance control(Hogan, 1980-August.) at the thumbstick end with just a few additional hardware.

5.4.1.1 Impedance control for fetoscope application

Mechanical impedance is defined as the force response of a system to an imposed motion (Hogan, 1980-August.). Hogan published his work on impedance control in 1985, which marked an important step in robotic control systems. Impedance can be represented as:

$$Z(w) = \frac{F(w)}{\dot{x}(w)} \qquad 5.15$$

Where,

Z(w) is the impedance

F(w) is the force applied

x(w) is the displacement.

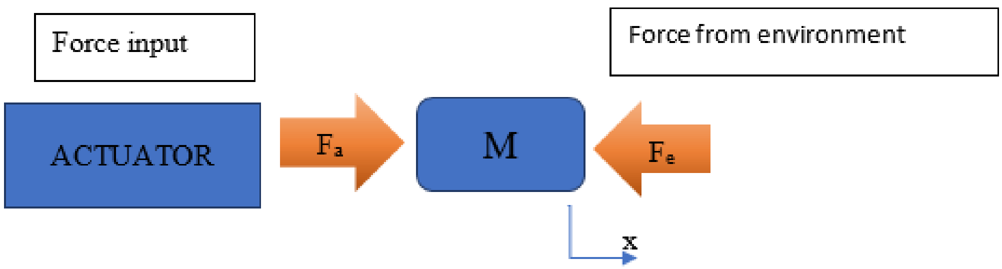

Figure 5-30 Force input from the actuator F_a resulting in a reaction force from the surgical environment F_e

F_a = Force applied by the actuator

F_e = Force applied by the environment

x = Displacement

M = Mass of the moving object

Figure 5.30 suggests that the force feedback from the environment reduces inertia.

$$M\ddot{x} = \sum F = F_a - F_e \tag{5.16}$$

When F_a feedback is not present,

$$M\ddot{x} = -F_e \tag{5.17}$$

From 5.15, 5.16 and 5.17 applied in a proportional feedback controller with gain G, desired force F_d and external force F_e the actuator force F_a is:

$$F_a = G(F_d - F_e) \tag{5.18}$$

$$M\ddot{x} = -(G+1)F_e \tag{5.19}$$

$$F_e = -\frac{M\ddot{x}}{(G+1)} \tag{5.20}$$

From the above, we observe that when the external force F_e is applied, the mass of the system would appear to be reduced by G+1. But in a PI controller,

$$G = k_p + k_i/s \tag{5.21}$$

Where,

k_p= proportional gain

k_i= integral gain

s = unit time

Equations 5.13 to 5.18 are derived directly from the work done by Neville Hogan (Hogan, 1980-August.).

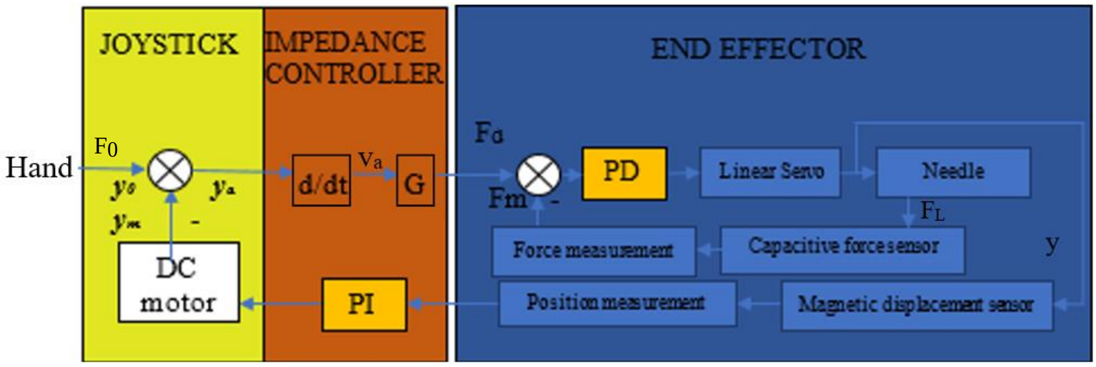

Figure 5-31 Complete control flowchart for measured input force used for mechanical control of the motors used for haptic feedback

In Figure 5.31, the hand interacts with the fetoscope joystick with a force F_0, however only the joystick's position 'y_a' is measured and transformed into assumed force 'F_a' and then the controller drives the servo actuator which moves the mobile tip of the actuator and acts on an external object when it is met. The main objective of this strategy is to control the motor drive at the thumbstick level when the tip of the fetoscope is in contact with the load. The resulted deformation creates an external force 'F_L', in the opposite direction to that of the applied force. The difference between the assumed position 'y_a' and the actual position, which is the position error, is then transformed through a differentiator and an impedance function 'G' into a reference force 'F_a'.

The position error formed between the actual position and assumed position are compared by the operator and as a result, the operator sets the assigned position 'y_0' on the thumbstick by driving the motor drive. The thumbstick therefore exerts a force on the thumb in a direction opposite to the direction of force application when the tip meets an object. The impedance transfer function for the linear joystick can be expressed as follows:

$$G(x) = \frac{Fa(x)}{Va(x)} = M\frac{dx}{dt} + B + C\int_0^t x(t)dt \qquad 5.22$$

Where,

G(s) – Impedance function

Fa(s) – Assumed force function at drive level

Va(s) – Velocity function of the interface at drive level

M – mass of the tip assembly <5 grams

B – friction of the parts within the stem

C – stiffness of the tissue

$$F = Ma + Cv + Kx + \text{friction} + \text{static force} \tag{5.23}$$

Where,

M = mass

a = acceleration

K = Spring constant

x= displacement

C = Coefficient of pure viscous dampening

v = Relative velocity

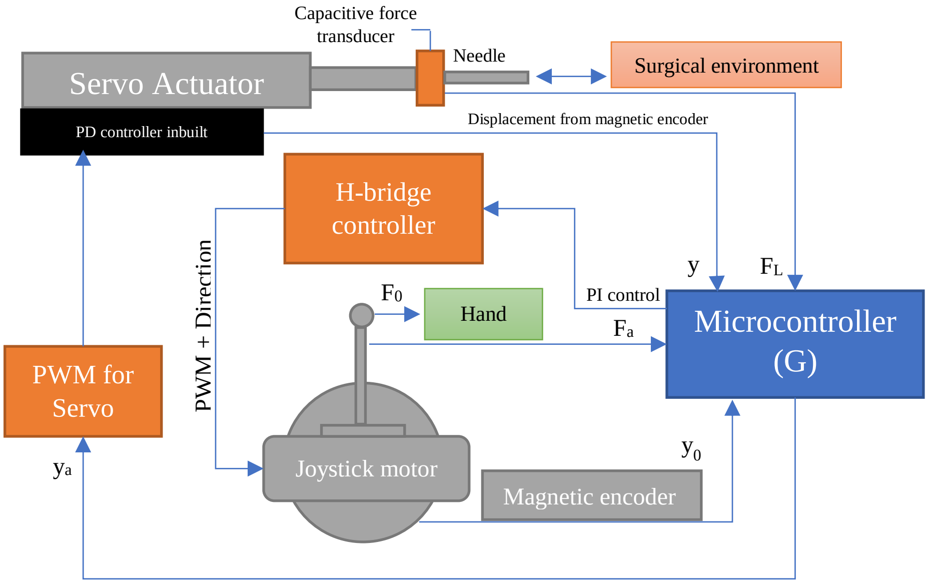

Figure 5-32 Scheme of haptic hardware setup within the fetoscope

The Figure 5.32 shows the design of an impedance controller with motion error in the position domain. The assumed position ‘y_a’ is compared with the real position by the operator and the operator sets the assigned position to the Joystick ‘y_o’ as stated earlier. The linear position measured from the tip gives the position of the Joystick motor driver, which then is driven by the PI control system.

In the haptic impedance control system shown in Figure 5.32, the user moves the joystick attached to a geared DC motor and also a magnetic rotary encoder which gives a digital output as an angle which is converted into displacement units ‘y_a’ and is then transformed to ‘G’ the impedance and then the desired force ‘F_d’ within the microcontroller section. This desired force is initially assumed which then drives the linear servo actuator when fed into the end effector section which carries the needle. When the needle attached to the linear servo end effector comes in contact with an object, based on the force exerted by the object in the opposite direction ‘F_L’, the capacitance force sensor’s capacitance varies thereby giving a value for ‘F_m’. The difference between the assumed position ‘y_a’ and the real one is the position error ‘e’, transformed through a differentiator and an impedance function ‘G’, into the reference force ‘F_a’. This transformed displacement parameter is used to drive the servo using PD loop.

Figure 5-33 Impedance control implemented in the fetoscope

Figure 5.33 shows the physical implementation of the impedance-controlled haptics including the force transducer and signal preconditioning circuitry, servo and rechargeable power source.

5.4.2 Fetoscope communication and user interface

The fetoscope has a joystick interface and a single button interface which communicate wirelessly with the computer and wireless foot switch which operates important functions such as the LASER, RFA or marking 3D positions in the space. Figure 5.34(a) shows the top view of the wireless foot switch and Figure 5.34(b) shows the charging port and the switch for activating the system.

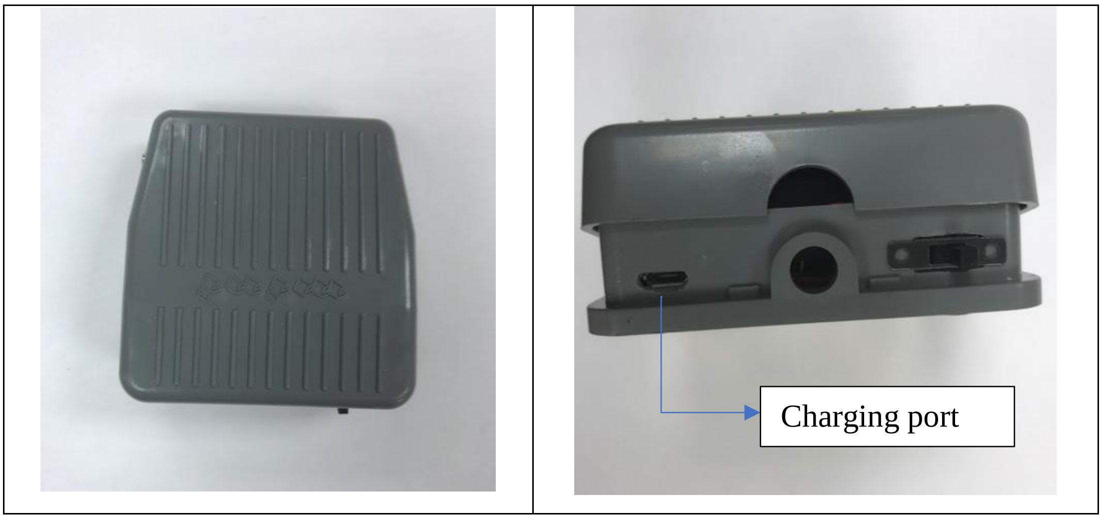

Figure 5-34 Foot switch with wireless capabilities capable of connecting to the fetoscope and the wireless base

Figure 5.35gives the flowchart of wireless operation of the Fetoscope, the footswitch and the computer via Bluetooth and WiFi. This system communicates in real-time with the software interface discussed in the next chapter.

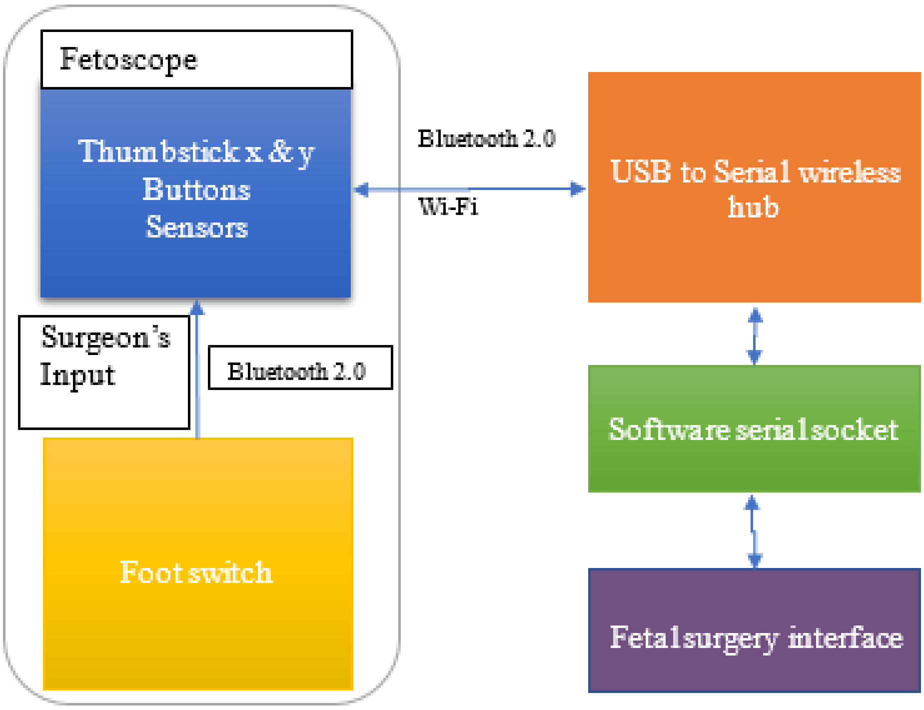

Figure 5-35 Fetoscope communication interface

5.4.3 Evaluation of impedance-controlled haptics

The force transducer and actuator have been evaluated in the previous sections and principle behind impedance control for haptics have been established in the previous chapter. Haptic force feedback can be achieved by combining the elements of force sensing and actuation in the physical setup. These when combined, result in a force feedback at the joystick level when a force is applied to the tip of the needle. The setup is shown in Figure 5.36 (a) with the fetoscope stem mounted on an active linear stage is used for loading the needle while an 'Optoforce' transducer (Burka et al., 2016) does the force feedback measurements as seen in Figure 5.36 (b).

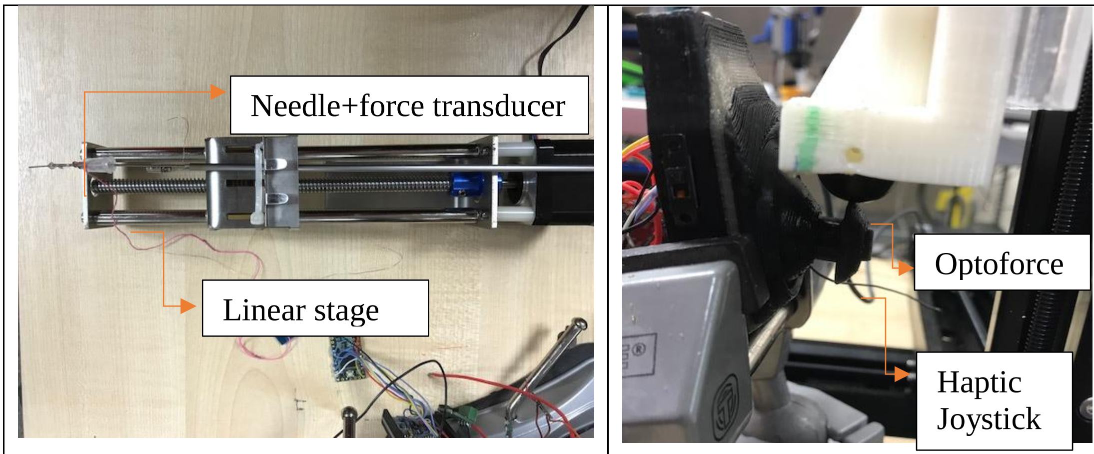

(a) Force transducer at needle tip and linear stage to load the tip on a solid target

(b) Joystick tip force measured using Optoforce transducer while the tip experiences force

Figure 5-36 Setup for evaluating force input using capacitive force transducer and output force at the joystick level

This chapter describes the use of different sensors which were incorporated into the proposed fetoscope design. The basic physical sensors which required evaluation have been characterized and explained. Since haptic feedback system is a combination of the sensing and actuating elements, the evaluation was done using the setup seen in Figure 5.36. In Figure 5.36 (a), a motorised linear stage with a carriage with the fetoscope stem and the force transducer attached to the fetoscope tip is shown. Figure 5.36(b) shows the fetoscope stabilized by clamping and the thumbstick of the fetoscope has been made to come into physical contact of an Optoforce force measurement device.

5.5 Discussion and results

Forces applied at the end of the needle by the linear stage are relayed to the force transducer and the microcontroller which has been calibrated with the force transducer equation produces a proportional output which is then translated into mechanical force and vibratory feedback. Data is collected during the phase of loading and retraction.

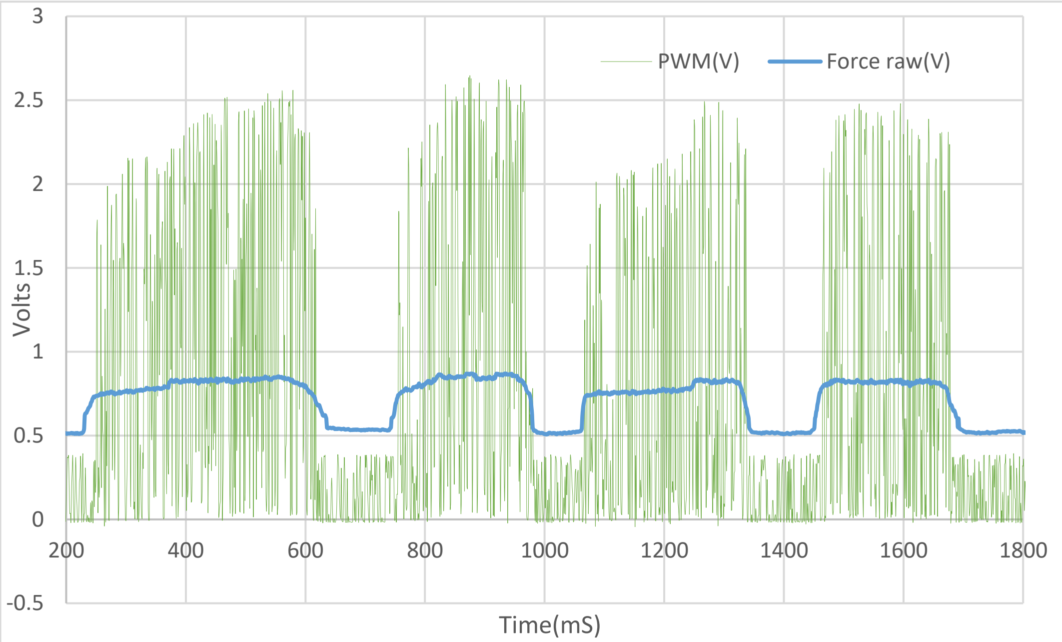

Figure 5-37 Haptics evaluation experiment - Force input vs PWM output

From the graphs in Figure 5.37 and Figure 5.38, the force observed from the capacitive force transducer in electrical units was used to adjust the Gain of the PWM amplifier which was used to supply the Joystick motor. As described earlier, the motor torque is directly proportional to the current, or the PWM applied. The motor PWM starts only after a specific force threshold, as the motor would otherwise consume current but will not be able to perform any actual mechanical work. Whereas dynamic, periodic signals which start beyond a specific lower threshold than the static forces and are significant such as pulsations are given to the haptic vibrator at the thumb level, driven by DDRV2605.

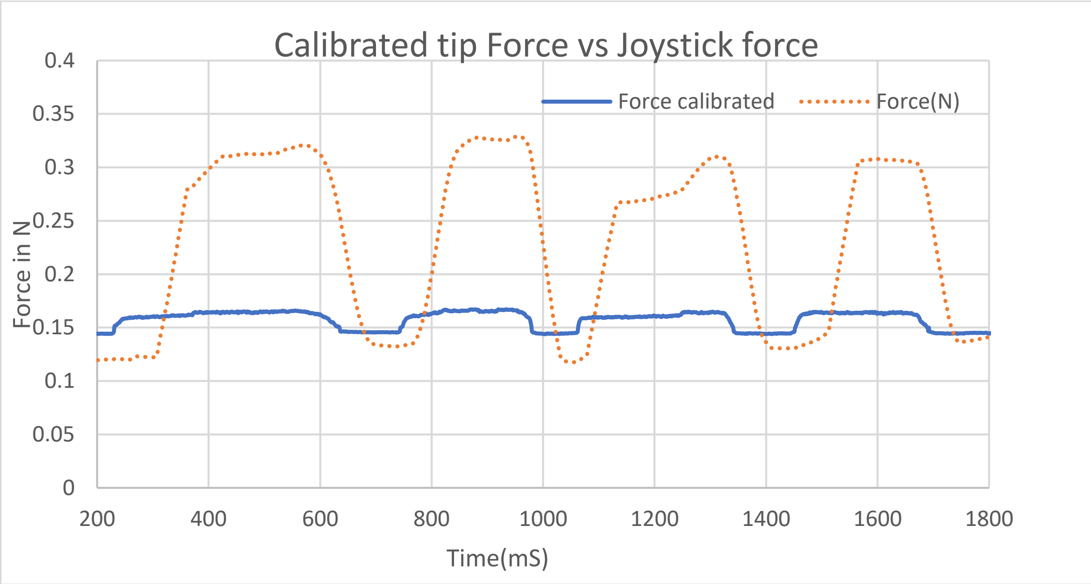

Figure 5-38 Haptics evaluation experiment - Force output at thumb-stick level vs input force

Although the torque, as described earlier corresponds to the PWM applied and the loop in the microcontroller is running at about 1000 cycles per second, there are a few milliseconds of lag which can be seen to persist because of problems such as mechanical characteristics of the gearbox such as friction, backlash. Such issues can be reduced with better manufacturing.

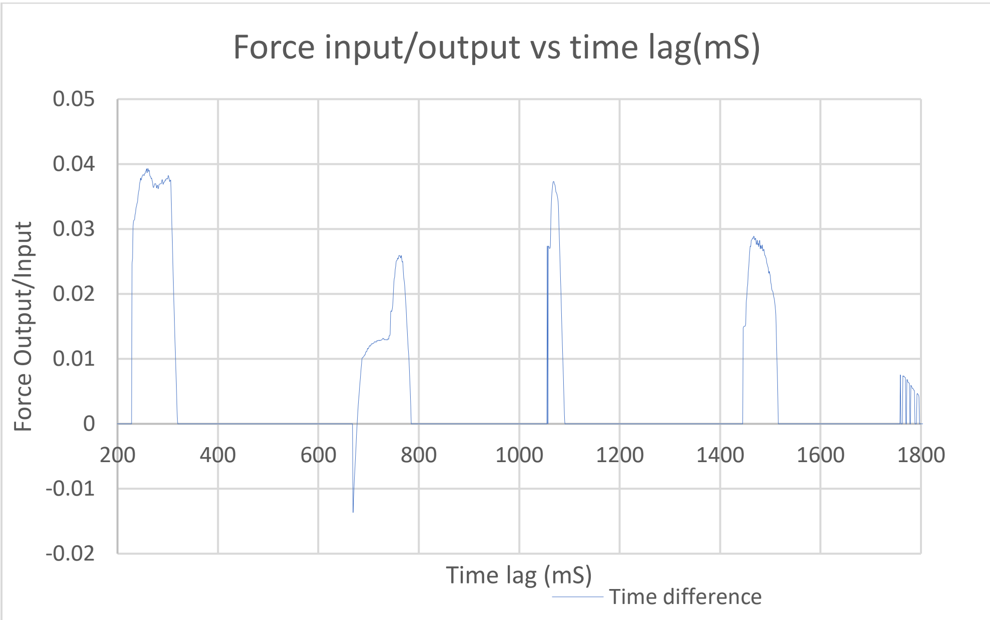

Figure 5-39 Latency of the output vs input showing an average latency of 100 mS to 150mS between the tip force and the force felt at the thumbstick level

Every system has a latency between the time of initiation of action and the time of the observed effect. In Figure 5.39, period between time of force application and the time of force exerted (latency) by the Joystick on the transducer can be seen because of reduced back-drivability due to the friction of the gearbox owing to reduced displacement. Further, the resolution of the forces depended on the resolution of the FDC 1004 capacitance to digital converter, which has a rated sensitivity of 0.5 fF and a dynamic range of 0 to 15 pF. The value of the capacitance of the capacitive sensor, with the application of force varied between 76 to 90 pF, as measured by a capacitance meter.

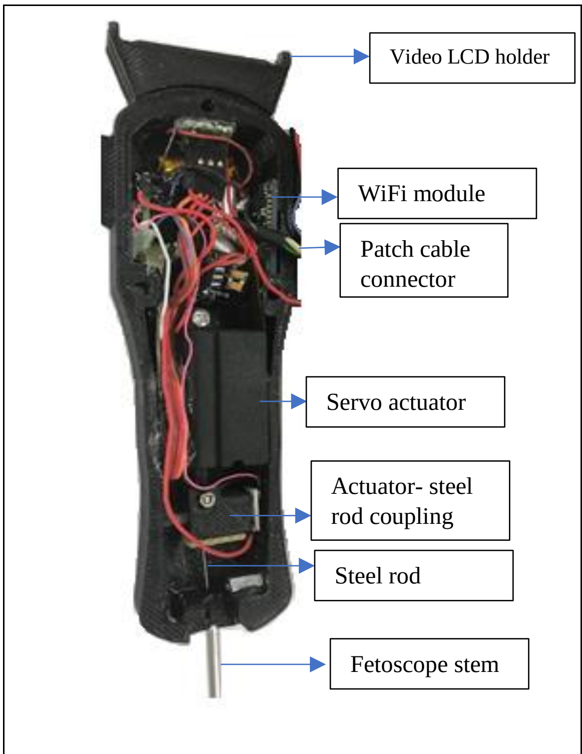

(a) Bottom of the Fetoscope

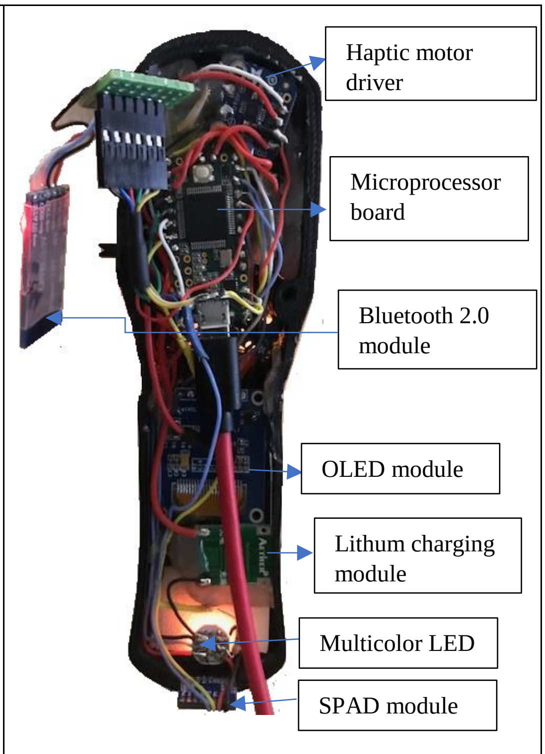

(b) Top of the fetoscope

Figure 5-40 Completed fetoscope construction. Fetoscope with two servo actuators, driver, micro controllers, force transducer & amplifier installed. Thumbstick haptics, Bluetooth module, Wi-Fi module, video transmitter, ToF module and the display units go on the top of the fetoscope. The pump is not installed in this version of the fetoscope.

The fetoscope and most internal elements have been 3D printed, while the other miniature elements such as shaft adapters for actuators were manually machined. Most of the circuitry used have been constructed from modular parts and did not require specific manufacturing. The thumbstick of the joystick has been 3D printed and has been bearing supported. The angle encoder has been installed and aligned to the axis of rotation of the thumbstick spherical base, in order to prevent crashing from the rim of the fetoscope. The base of the fetoscope with some of the proposed elements- sensing, processing, communication, actuation and measurement elements built-in is shown in Figure 5.40(a). The display, interaction and certain other sensors including the ToF, pressure sensor and 6DoF accelerometer/gyroscope are built into the top half of the fetoscope as seen in Figure 5.40(b).

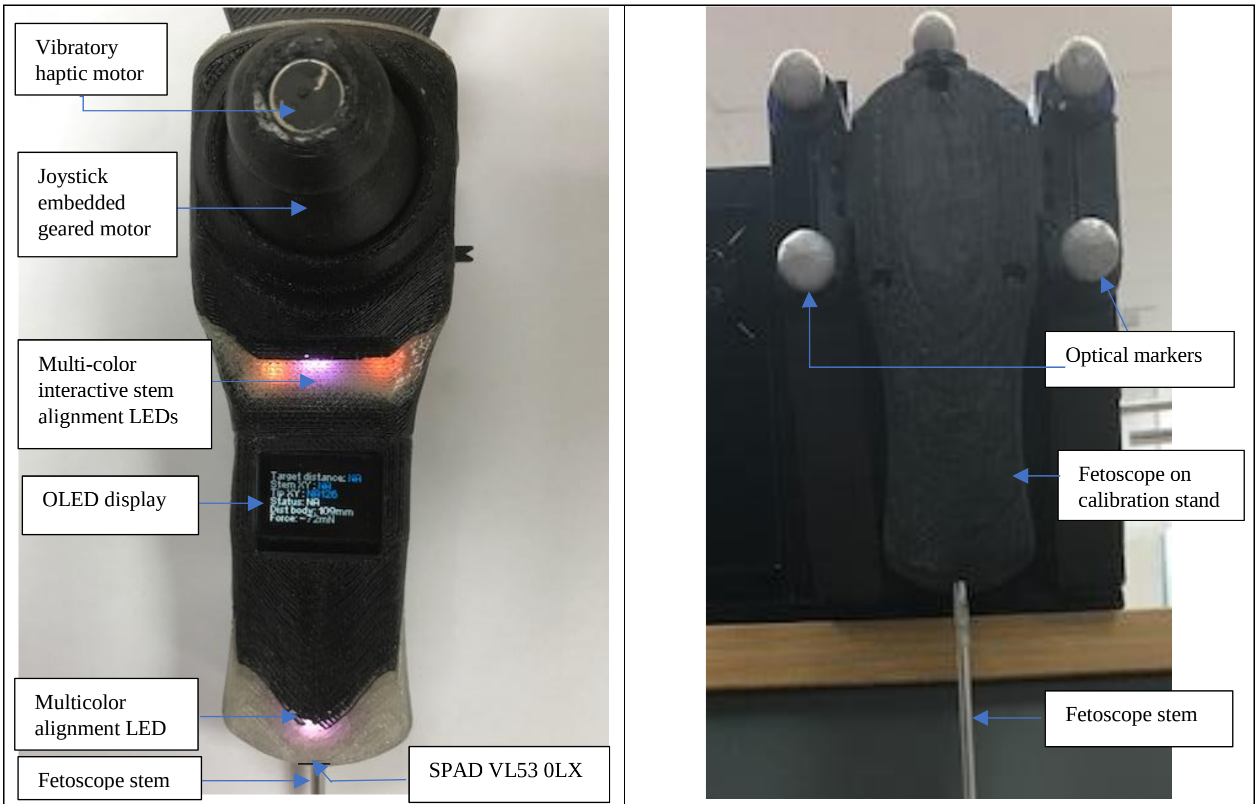

(c) Fetoscope front view

(d) Posterior view of the fetoscope

Figure 5-41 Completed fetoscope with all circuitry and actuators (a) and (b) show the anterior and posterior rendered views and (c) Fetoscope with OLED screen showing the forces and LEDs indicating the reaching status (d) Posterior view of the completed fetoscope with optical trackers

Fully completed fetoscope prototype with optical markers magnetically attached to its posterior can be seen in Figure 5.41(a) and Figure 5.41(b). In Figure 5.41 (a), the anterior part of the fetoscope can be seen with the haptic thumbstick and the OLED display showing real-time position in (mm), force from the capacitive transducer in (mN) and distance from the body information from the ToF distance sensor in millimetres. The magnets on the fetoscope also help attach and align itself on the calibration rig, which also serves as a charging station for the lithium polymer battery inside the fetoscope. This device works in synchronization with the fetoscope interface described in the next chapter to help the surgeons orient themselves, set targets, aid in surgical planning and maintain safety while handling potentially hazardous ablation methods. The fetoscope will be used in the upcoming chapters to demonstrate and evaluate the fetal surgery system, which can also be used for other minimally invasive surgeries.

5.6 Summary

Fetal surgery equipment requirements have been discussed, and the procedural requirements are tabulated. Based on these requirements, a fetoscope design has been proposed. The development of a robotic fetoscope, the rationale behind its development, modelling and evaluation of different sections of the fetoscope are discussed in this chapter. Table 5.5 shows the technical summary of achievements which mainly include the robotic fetoscope with inbuilt hardware.

Table 5-5 Technical summary of the hardware achievements in this section

Hardware	Status	Resolution	Dynamic range
Novel 6DoF tracking integration	Implemented, evaluated	2mm at 2 metres distance	2m
SPAD distance sensor	Implemented, evaluated by ST microelectronics	1mm accuracy	3 cm to 2m
Encoder	Evaluated and implemented	0.08 degrees	0 to 360
Micro actuator	PID implemented and evaluated	0.1mm and accuracy 0.2mm	0 to 30 mm but only 0 to 15mm used
Haptics	Impedance control implemented and evaluated	0.1 N resolution	0 to 12N
LASER	Micro LASER diode implemented	3Mw	Only for demonstration
Display, LEDs	OLED SPI display and multicolour LED guidance implemented	96 x 64 pixels	16 bit color
Camera	NTSC wireless implemented	300000 pixels	Analog color camera
Pump – diaphragm type	Tested but not implemented in the current version	-	40Kpa

The working of the fetoscope along with basic kinematics and the software interface are discussed in the next chapter.

5.6.1 Targets specifications proposed vs specifications achieved

Table 5-6 Proposed target specifications vs target specifications achieved

Proposed solutions	Proposed target specifications	Target specifications attained
Multi-modality 6 DoF tracking and navigation support	Sub millimetre accuracy	2mm accuracy at 2 metres
Simple visual cue-based Target guidance and trajectory tracking	Visual – HD LCD live image, LED indication and vibrational feedback	OLED text indication, LED indication and vibrational feedback
Automatic needle withdrawal and passive control	Closed loop needle withdrawal	Only indication is given no compensation
Vacuum/pressurization pump for air or fluid transmission and pressure measurements	Chamber pressure maintenance and drainage	Pressure measurement implemented but pump control and pump have only been tested and not implemented
Automatic LASER focusing guidance & ablation guidance	Automatic distance measurement to the surgical site/ surface and LASER focussing adjustment	Distance measurement and indication implemented focussing not implemented
Automatic identification of blood vessels and structures for cauterization	Image processing to recognise blood vessel size and automating LASER control	Not implemented
Additional port for micro forceps and its electronic actuation	Multiple port access for surgical instruments	Implemented 1 large port 2 mini ports and 2 more micro ports for wiring
Bi-directional wireless connectivity for all the above	5MBPS Communication interface	Implemented at 115200 baud
Forceps and manipulation	Control over micro forceps	Not implemented
Haptic feedback and tactile feedback	Mechanical and visual feedback	achieved
Cloud computing/onboard processing	Offloading processing power to computer	Achieved and both systems work hand- in hand at 115200 baud

From Table 5.6, it can be seen that most of the important target specifications have already been achieved. Since the technology is not a limitation to the development of such robotic equipment for Minimal Access Surgeries, further research in miniaturisation and design modification can make the product feasible

5.7 Conclusion

A robotic fetoscope has been designed and developed, capable of being tracked in 3D space and obtaining force feedback from the environment. The above features should help surgeons orient and interact with the surgical environment more confidently when combined with an imaging interface system. Most of the target specifications have been achieved. Therefore, further refinement of the attained functionality can result in a viable robotic hand-held equipment with a scope of application far outstretching fetal surgeries.

Chapter 6

Development of Fetal surgery navigation environment and interface

6.1 Introduction

A surgical navigation system consists of a 3D virtual navigation environment registered to real world objects, constraints for interaction, a unified coordinate system for all the elements within the system, an interface control panel and duplex communication protocols. The navigation environment is composed of multiple elements such as ultrasound and optical tracking systems as objects which exist in different local coordinate systems.

In this chapter unification of the different coordinate systems is discussed in detail. The concepts within the environment such as interactive objects within the environment, application of constraints, collision detection methodology, virtual camera orientation calculations and kinematics are discussed. Hardware communication is an integral part of the tracking system and the fetoscope navigation and operation. Therefore, the communication protocols used are discussed in this chapter as well.

6.2 Aims

This chapter focusses on development of surgical navigation interface. Hence, the aims of this chapter include the discussion of the following elements:

a) Unification of coordinate systems
b) Interactive elements and constraints
c) 3D collision detection
d) Virtual camera orientation
e) Communication
f) 2D control panel

The chapter will also aim at demonstrating some of the important capabilities of the navigation system such as:

a) Collision detection for navigation guidance
b) Use of interactive frames and markers for surgery
c) Demonstration of virtual camera automatic orientation

6.3 Methodology

Surgical navigation interface has components of 3D navigation environment which requires a unified coordinate system, followed by objects which can interacted by the user with the help of real-time communication protocols and manipulated using an interactive control panel.

6.3.1 Unification of Coordinate systems

For merging the different systems, both should be integrated into a world coordinate system with a common reference origin. The merging of the different coordinate systems is done by using a common the plane of operation, formed by the table and the instruments used for surgical simulation are mounted with 5 optical markers forming rigid bodies. For ultrasound and the fetoscope, the rigid calibration setup has been described in the earlier chapters. Once placed in the respective holders, the ultrasound probe and the fetoscope can be conveniently declared as separate 6Dof objects with reference to the table's corner as the origin as shown in Figure 6.1. The coordinate system used is described in Figure 6.2 and is similar to the one used by Julia, Christopher et al.(Schwaab et al., 2015a).

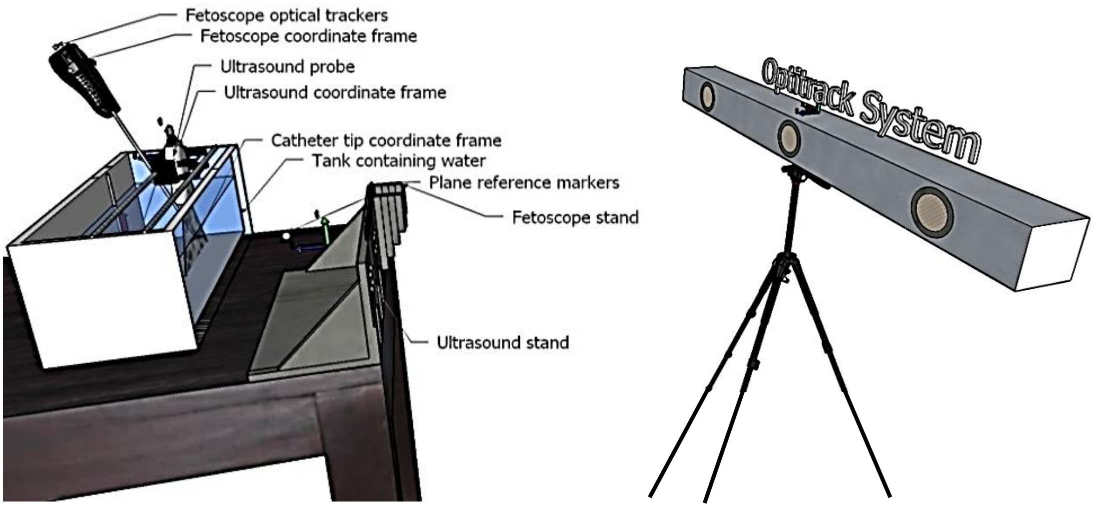

Figure 6-1 Setup used for ultrasound image frame and Optitrack tracking system cross calibration

In the world coordinate system '***W***', which represents the edge of the operating table, given in Figure 6.1, there are four sub coordinate systems, one for the Optical tracking system '$\boldsymbol{O}_{xyz}$', one for the tool body, '$\boldsymbol{To}_{xyz}$', tool tip was given by '$\boldsymbol{Tt}_{xyz}$', can be variable in length and one for the 2D image plane of the ultrasound machine '$\boldsymbol{USi}_{xy}$' and 3D image plane observed by the optical tracking system, '$\boldsymbol{USo}_{xyz}$' . Any point '$\boldsymbol{Pus}_{xy}$' on the ultrasound plane can be given in the world coordinate system '$\boldsymbol{Pw}_{xyz}$' and is represented using the geometric transformation equation given below:

$$Pw = O\ to\ W.USo\ to\ O.USi(Pus)\ to\ USo \qquad 6.1$$

The ultrasound plane in world coordinate system ***'Pw'*** (Schwaab et al., 2015) can be mathematically expanded as a series of transformations:

a) Transformation of Optical tracking system to the world coordinate system
b) Transformation of Ultrasound frame to the Optical tracking system
c) Transformation of the 2Dpoint tracked on the ultrasound frame to the ultrasound frame

The above can be presented as shown in equation 6.2

$$T_{Pw}^{M} = T_{O}^{M} T_{W}^{M} . T_{USo}^{M} T_{O}^{M} . T_{I_{PUS}}^{M} T_{USo}^{M} \quad 6.2$$

Tool tip '***Tw***', concerning the world coordinate system '***W***' can be given using the following geometric transformation equation:

$$Tw = O\ to\ W . To\ to\ O . Tt\ to\ To \quad 6.3$$

The tool tip '***Tw***' can be mathematically expanded as a series of transformations:

a) Transformation of Optical tracking system to the world coordinate system
b) Transformation of tool body to the Optical tracking system
c) Transformation of the tool tip to the Optical tracking system

The above can be presented as shown in equation 6.4

$$T_{Tw}^{M} = T_{O}^{M} T_{W}^{M} . T_{To}^{M} T_{O}^{M} . T_{T_t}^{M} T_{O}^{M} \quad 6.4$$

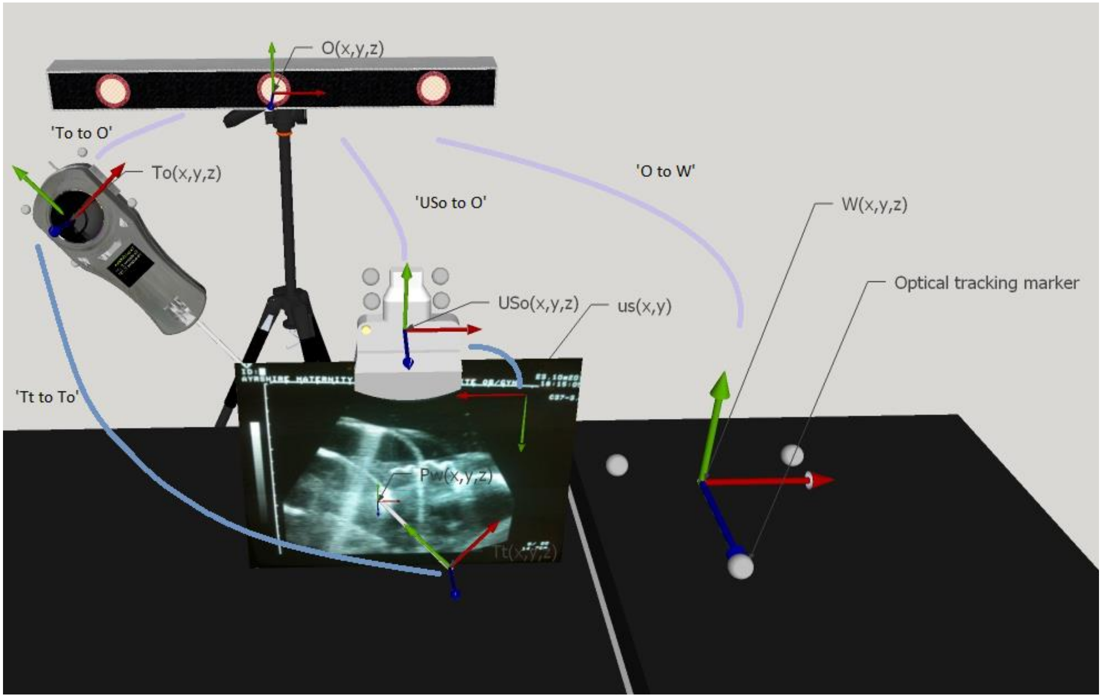

Figure 6-2 Overview of different coordinate systems used in the navigation environment

The coordinate transformation from one system to the other is performed using affine 4x4 transformation matrices in real-time to give us interactions between the tool tip and the ultrasound image plane.The elements described in Figure 6.2 in conjunction the navigation environment,has been used to develop an interactive user interface (Schwaab et al., 2015).

6.3.1.1 Ultrasound to Optical tracking cross calibration and 3D interface development

Cross calibration of different systems requires a common frame of reference. In the cases where the registration is required to be implemented in a virtual environment, interactive and non-interactive software objects are of primary requirement for interaction and simple correlation to real-world positions.

Optical tracking and the 3D navigation environment exist in the same special coordinate system after the zero of the Optical tracking system is mapped to the origin of the navigation interface. However, the ultrasound image is a pixel image and does not exist in the same spatial coordinate system. Hence, the image requires rescaling every point '$up_{[i]}$' in the image frame according to the navigation interface measurements using simple scaling vector sv = (sv_x, sv_y, sv_z). Two methods are adopted to achieve image to measurement scaling. One method is to scale the environment to the scale of the pixel image, and the other is to impose the scale of the Optical tracking – navigation environment to the Ultrasound image frame. The latter is chosen because it has higher least count resolution(>0.1mm) and repeatability than the former(>1.8mm) method.

This can be given by the product of the two elements for the entire pixel frame and can be given as:

$$sv.up = \begin{vmatrix} sv_x & 0 & 0 & 0 \\ 0 & sv_y & 0 & 0 \\ 0 & 0 & sv_z & 0 \\ 0 & 0 & 0 & 1 \end{vmatrix} \cdot \begin{vmatrix} up_x \\ up_y \\ up_z \\ 1 \end{vmatrix} = \begin{vmatrix} sv_x up_x \\ sv_y up_y \\ sv_z up_z \\ 1 \end{vmatrix} \qquad 6.8$$

Ultrasound machines come with an internal calibration and scaling which is very precise, and every medical ultrasound comes with this calibration. This simplifies the cross-calibration process. A graphic element on the screen is chosen along the X direction and using the Ultrasound machine's inbuilt distance measurement methods, two points are marked, and the distance is measured on one hand and the pixel distance, on the other hand, is measured in the 3D interface on the ultrasound frame using the 3D interactive objects with plane constraint in action, using mouse to position them at the same points of distance measurement as seen in Figure 6.3 (a). The same process is repeated in the Y direction, and for diagonal calibration, a circle is created from the Head Circumference measurement interface built into the Ultrasound system, and the diameter is measured across both systems to get the scaling factor, as seen in Figure 6.3 (b).

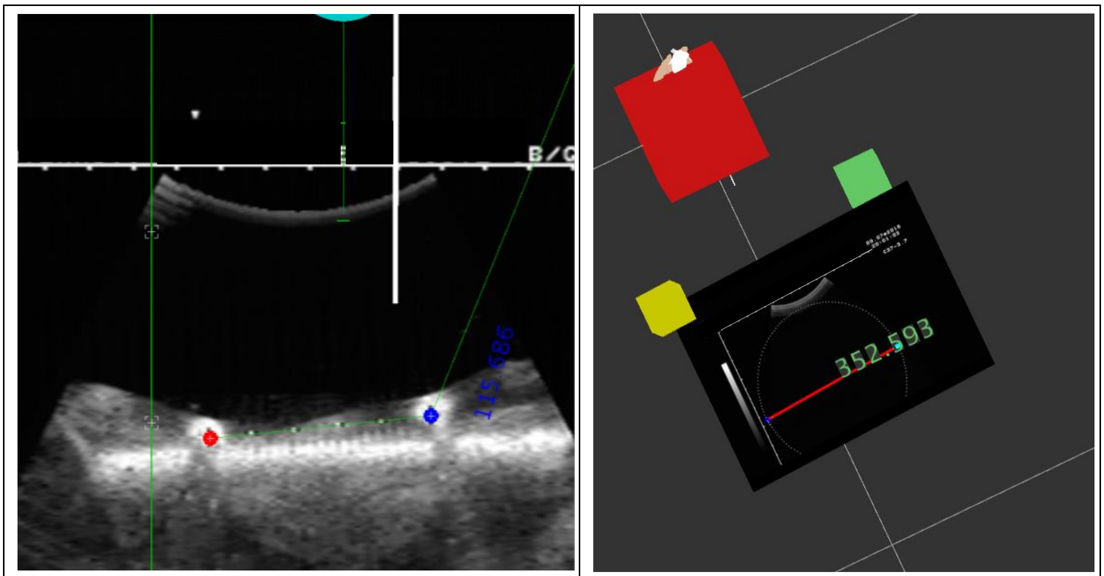

(a) Calibration in comparison with ultrasound line measurement

(b) Calibration against ultrasound circle

Figure 6-3 Ultrasound pixel plane – Navigation interface cross calibration with built in ultrasound functions and 3D navigation interface

6.3.1.2 Ultrasound frame object and features in a unified coordinate system

The ultrasound frame object is capable of holding a live image frame and is capable of 6 DoF movement at the same time. Ultrasound frame object, however, has a 3-dimensional offset to the actual image from the ultrasound, which acts as a translation calibration constant ’$\boldsymbol{Ic}_{xyz}$’. Therefore, cross calibration between the two systems becomes a necessity. This is done by placing an optical marker on the plane and the centre of the ultrasound image. when the object is seen by both the systems, it becomes easy to obtain the 3D reference for the position of the ultrasound plane. The orientation of the plane is found by touching the ultrasound plane using the fetoscope object tip at various points and getting the plane fit equation, as mentioned earlier in the Ultrasound chapter. The rotational calibration obtained using these experiments is '***Iq***', given in the quaternion form (Ken, 1985). Though rotations with Euler angle are possible, it is more processing intensive as it uses multiple floating-point accuracy and may result in Gimbal lock problems, Quaternion rotations were used (Dai, 2015). The image in the world coordinate system '***Iw***', can be given with respect to the translation calibration constant '$\boldsymbol{Ic_{xyz}}$'. Equation 6.6 gives the image in the world coordinate system in a geometrical representation (Schwaab et al., 2015).

$$Iw = O\ to\ W.USo\ to\ O.((USi + Ic).Iq\ )to\ USo \qquad 6.9$$

Equation 6.7 expansion of the ultrasound frame transformation $T_{I_{US}}^{M}$ into its image translation format $t_{I_{US}}^{M}$ and translation calibration $t_{I_C}^{M}$ and the quaternion rotation component I_q.

$$T_{I_{US}}^{M} = \left(T_{USi}^{M} + T_{I_C}^{M}\right).I_q \qquad 6.10$$

Equation 6.10 gives the mathematical representation of the ultrasound image frame with respect to the world coordinate system(Jeffrey Stoll).

The image in the world coordinate system '***Iw'*** can be mathematically expanded as a series of transformations:

a) Transformation of Optical tracking system to the world coordinate system
b) Transformation of Ultrasound frame to the Optical tracking system
c) Transformation of the calibrated 2D ultrasound image frame to the ultrasound frame

The above can be presented as shown in equation 6.11

$$T_{Iw}^{M} = T_{O}^{M}T_{W}^{M}.T_{USo}^{M}T_{O}^{M}.T_{I_{US}}^{M}T_{USo}^{M} \qquad 6.11$$

The actual pictures demonstrating the processes used in ultrasound plane mapping are given in Figure 6.4 and the process is outlined in Chapter 4. Initially the ultrasound probe is optically tracked as seen in Figure 6.4 (a) and registered into the interface with an optical marker placed at the bottom surface of the ultrasound probe as shown in Figure 6.4 (c), marking the start of the image plane. Then the fetoscope is registered as shown in Figure 6.4 (b) and the tip is calibrated. Ultrasound plane calibration is done by intersecting the fetoscope on the virtual ultrasound plane and making sure that the registered fetoscope tip appears on the ultrasound image plane and intersects with the virtual fetoscope on the 3D navigation interface as seen in Figure 6.4 (d). Once the condition of real fetoscope intersection with the ultrasound plane obeys the virtual intersection of the image plane, the objects are considered registered.

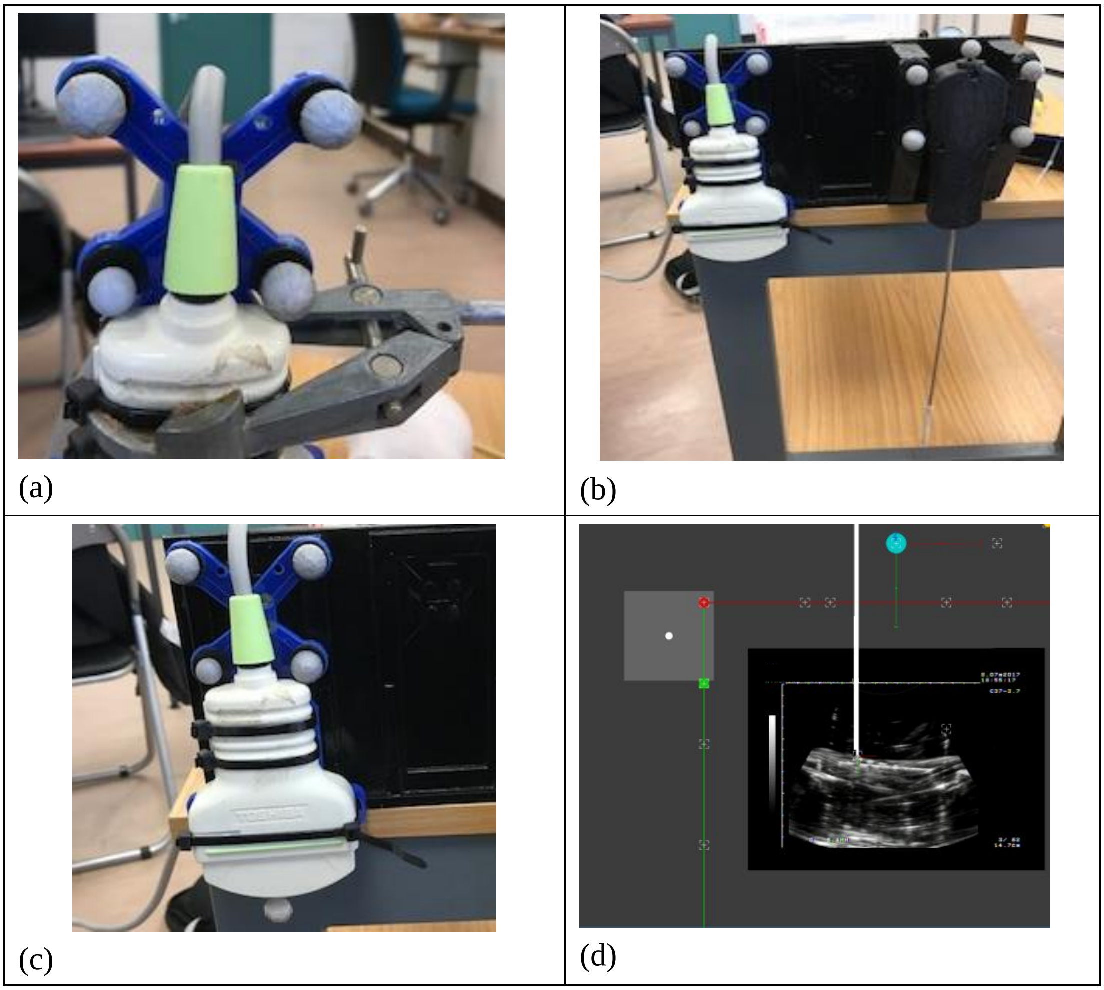

Figure 6-4 Ultrasound probe calibration (a) Ultrasound probe with optical trackers (b) Ultrasound probe & fetoscope on the calibration rig (c) Estimation of plane 3D distance from the Ultrasound frame object -pre-cross calibration (d) Registered image plane in virtual environment

6.3.2 Graphics user interface development

The user interface has a 3D visualization, interaction panel and a 2D control panel, which also has 2D display capabilities of ultrasound images and target setting and monitoring. The interface receives information from the optical tracking system, wireless RF/ WiFi, whichever is required by the user for information exchange.

The interface also helps in calibration, cross calibration and provides a visual guide and can record the surgery in real-time. For achieving the 3D environment, the programming was done in JAVA, and inbuilt OpenGL functions were used. 3D interactive functions were used from Proscene library. Communications were developed using serial and UDP libraries. 2D GUI elements are handled by ControlP5. Beyond this point, every function and calculations were handled by straightforward programming and usage of basic mathematics and projection calculations. Therefore, the environment is flexible and can be extended into any new versions of JAVA, as it is not dependant on any other significant libraries.

6.3.2.1 Development of 3D interactive elements

The 3D user interface primarily makes use of 3D interactive objects and constraints. Inverse kinematics and object environment obtained from sensor perception, when applied to the 3D objects can result in virtual reality guidance which will be described in more detail in this chapter.

6.3.2.2 3D interactive objects

Every 3D interactive object is an object of specific colour, shape, position and orientation, which can be changed by mouse interaction or by manipulating program parameters or using optical tracking coordinate input. In the place of such objects, 3D models and 2D image frames can be called in. Further, these interactive frames in Java can also be constrained to certain translations and rotations in any specific plane and also be used for image manipulation or assigned a local coordinate system with reference to the world coordinate system. The interactive objects can also be chained with constraints for use in simulating inverse kinematics and trajectory estimation.

6.3.2.3 Plane and Axis object constraints

To be able to mark or modify pixels ultrasound planes while the frames are 2 D planes rendered in 3D is very difficult to be manually done. Hence, the creation of plane constraint is used. For example, if there are '*n*' number of 3D interactive objects located on the image plane, for example, the ones are seen in Figure 6.5(a), with the application of a plane constraint, the objects can only move along the surface of the plane and not above or below it, as seen in Figure 6.5(b).

However, a plane in 3D space can have any orientation, and a simple plane constraint cannot work. Therefore, the plane can be declared as an object and the coordinate system of the plane can be rotated using quaternion rotation axis constraint, so that any daughter objects on a specific plane can act as a physical plane constraining the objects to the plane as shown in Figure 6.5(c) and Figure 6.5(d). Such daughter objects will then follow the rules of axis plane constraint on the plane and can be interacted only under such rules, as seen in Figure 6.5(b). Therefore, such interactive objects can be used to selectively manipulate the pixels on the image frame or making measurements between pixels of an image plane with texture from any real-time image source, shown in Figure 6.5(c). Here, the source being ultrasound video, textured on the plane rotated and translated with respect to its optically tracked position and orientation as can be seen in Figure 6.5(d).

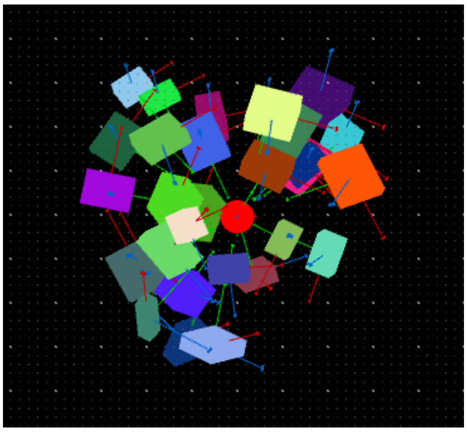

(a) Interactive 3D cube objects are orienting towards one spherical object

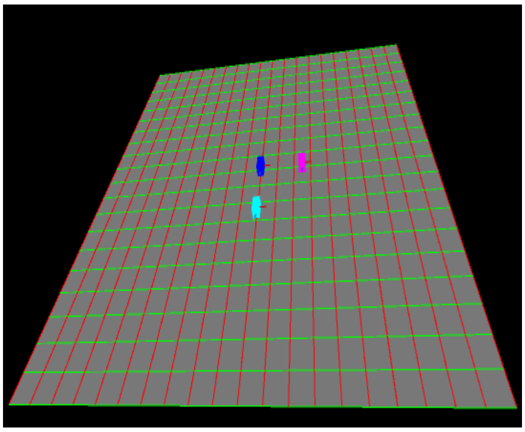

(b) Multiple 3D interactive objects with a plane constraint on a grid

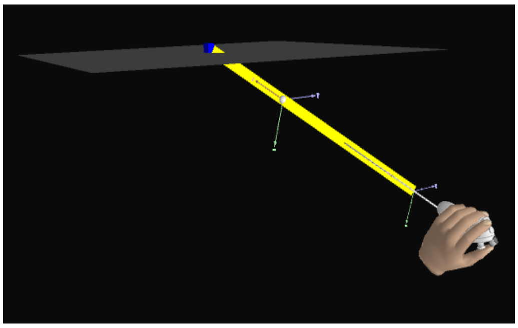

(c) '.Obj' format 3D object with plane constraint interaction

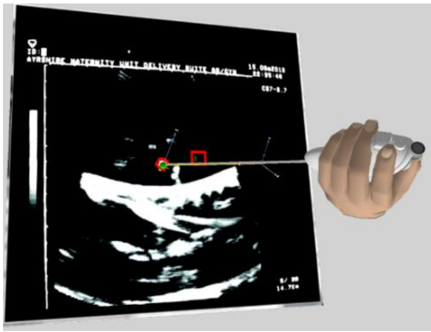

(d) 2D image frame of an ultrasound image with 3D object and plane constraint

Figure 6-5 JAVA objects created for use in the navigation interface.

A plane is described by three points in 3D space. In the case of the ultrasound plane, it is described as a custom pixel frame with linked translation and rotation information obtained from the optical tracking system by UDP communication protocol.

6.3.2.4 Image object, manipulation and image processing

As seen in Figure 6.3 (d), the image can be textured on to the plane and scaled as described in the ultrasound (Chapter 4). Further, the loaded pixel frame can be used for image processing. Area of interest within the ultrasound frame can be dynamically selected using the 3D interactive objects, which can be directly controlled using the mouse or using the 2D control panel. Within the area of interest, the pixels acquired are made binary with a threshold and then the background weight of the pixels 'W_b', mean for background 'μ_b' and variance 'σ_b^2' and the foreground values 'W_f', mean for background 'μ_f' and variance 'σ_f^2', are calculated. The foreground and background variables are then analysed using Otsu's thresholding technique (Otsu, 1979) to choose the threshold to minimize the intraclass variance of the thresholded black and white pixels, using the following equation:

Within Class Variance $$\sigma_w^2 = W_b\sigma_b^2 + \mathrm{W_f}\sigma_\mathrm{f}^2 \qquad 6.12$$

Between Class Variance $$\sigma_b^2 = \sigma^2 - \sigma_\mathrm{w}^2$$

$$\sigma_b^2 = W_b(\mu_b - \mu)^2 + W_f\left(\mu_f - \mu\right)^2$$

$$\sigma_b^2 = W_b W_f\left(\mu_b - \mu_f\right)^2 \qquad 6.13$$

The obtained threshold is used to extract the essential pixels and reduce noise. The location of every single pixel in the frame along with the quaternion rotation is stored in an array and therefore can be displayed as a picture frame array when the user needs and can be used for 3D reconstruction by aligning slices of ultrasound frames in real time. In Figure 6.4(a), a plane ultrasound frame being digitized is seen, which when imported into an OpenGL 3D environment becomes a plane in 3D and is made an interactive object, as can be seen in Figure 6.4(b). With Otsu's thresholding applied as described above, the pixels are extracted and displayed within the 3D environment, as seen in Figure 6.4(c).

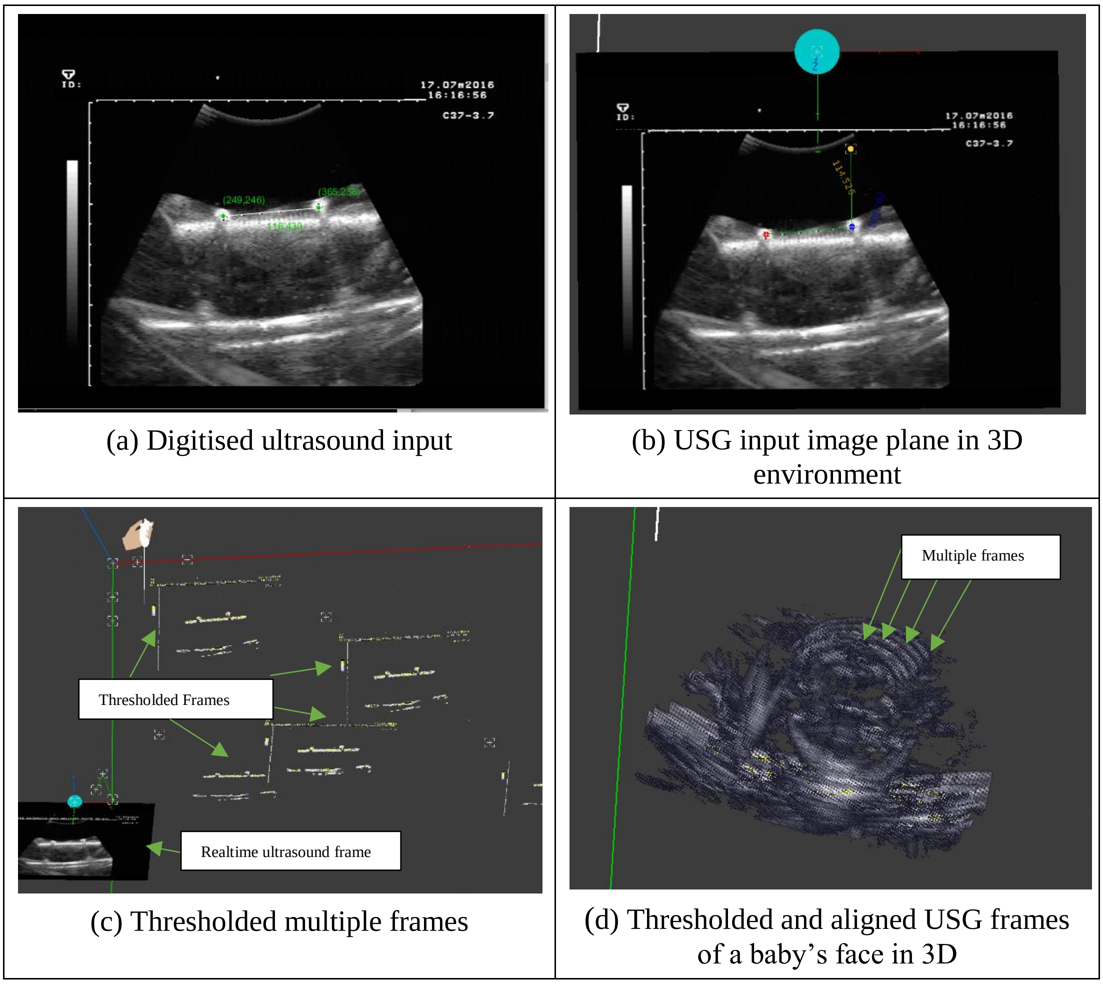

(a) Digitised ultrasound input

(b) USG input image plane in 3D environment

(c) Thresholded multiple frames

(d) Thresholded and aligned USG frames of a baby's face in 3D

Figure 6-6 2D Ultrasound image scaling and 3D Ultrasound plane texturing post scaling

Figure 6.4(d) shows multiple ultrasound frame slices arranged in 3D to form a Computerized Tomogram form of the ultrasound frames of the face of a fetal phantom. The frames were arranged in real-time while the ultrasound probe was optically tracked and when the user chose to capture the frame (Fenster et al., 2011). The acquired point cloud can later be meshed using meshing algorithms and transformed into 3D objects for use in surgery or registration. The interface is capable of capturing multiple 2D frames along with their orientation. Images being made of pixel arrays can be quite processing intensive to display especially multiple frames are recorded or rendered. Image frames by default have 640 x 480 pixels, represented by constant frame size 24-bit array and do not have the flexibility of displaying only the required pixels. For example, in an image with all black pixels, a 640 x 480-pixel frame will still be rendered, making the process very inefficient and time-consuming. Therefore, in order to prevent looping through un-associated pixel locations and making the interface reconfigurable to up sample or down sample pixel numbers per frame on the go, a custom pixel array format consist of pixel (x, y) location, colour array and with start and stop point are encoded to help in frame identification and frame storage within a single object array. Also, while every pixel frame is rendered, every pixel (x, y) location is translated and rotated using quaternions for that specific frame stored in the image linked quaternion array.

6.3.3 Collision detection in 3D virtual environment

One of the major problems faced in a virtual 3D interface is the lack of physical limitations. Unlike the real world where objects can collide and can experience forces which prevent objects from passing through each other, virtual environments lack this capability. Lack of collision detection would mean that 3D objects in a virtual environment can pass through each other seamlessly. Therefore, the surfaces of the 3D objects will need to be monitored for collision. Since any surface can be split into infinite number of points theoretically, monitoring all the points in a 3D mesh though ideal, cannot be practical. Therefore, geometric methods are employed for monitoring and simplifying collision detection.

For example, a fetoscope tip which is a linear object can be within a target cylindrical volume of interest which can lead the subject to reaching a target on the other end of the cylinder. If the subject can be given the guidance to remain within the volume of interest and when the orientation guidance to reach the target is given, reaching the target in a 3D volume can become easier. This process can be simplified as a Line – cylinder intersection. When the axis of the fetoscope, a linear object intersects with the ultrasound plane, a 2-dimensional plane, the intersection can be simplified as Line- Plane intersection.

6.3.3.1 Line–plane and line within cylinder volume detection

The fetoscope in the virtual environment is declared as an object formed by a parent and a child marker with a defined position constraint to always be located at a fixed distance from the parent marker. Therefore, the line joining the two aforesaid points forms the axis of the fetoscope and can be extended as a ray which can be made to intersect with virtual planes or 3D objects, which can mark areas of interest within a real surgery. A plane '**P**' formed by three points A, B, C can be defined by a normal vector '**N**' which can be calculated using the following equation:

$$N = (C - B) \times (A - B) \qquad 6.14$$

Using the normal '**N**' and the ray from the fetoscope axis '**R**', the plane line intersection can be calculated as described in Chapter 4.

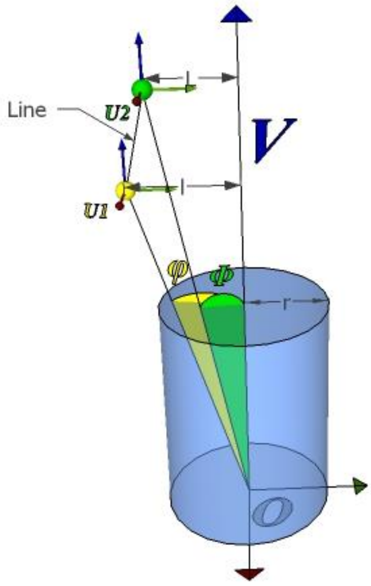

Figure 6-7 Cylinder line intersection. A cylinder of infinite height with radius *'r'*. vectors V(axis of the cylinder) and U1 form a line with length *'l'* and U2, a line *'L'* respectively from the axis.

In cases where needles have to be inserted in a physical cylindrical constrained space without touching other anatomical structures, the cylindrical intersection is of importance. For a given cylinder of radius '***r***', with the axis of the cylinder V and a vector U1 formed between the origin of the cylinder at its base and the axis of the fetoscope, the angle formed between the two vectors is given using the equation:

$$\boldsymbol{\varphi} = \cos^{-1}\left(\frac{\boldsymbol{V}.\boldsymbol{U1}}{|\boldsymbol{V}|.|\boldsymbol{U1}|}\right) \qquad 6.15$$

$$\boldsymbol{\Phi} = \cos^{-1}\left(\frac{\boldsymbol{V}.\boldsymbol{U2}}{|\boldsymbol{V}|.|\boldsymbol{U2}|}\right) \qquad 6.16$$

The distance between the tip and the centre of the cylinder base is 'd' .and the distance between the stem and the centre ***'D'***. Therefore, when the length of the line '***l***' formed between the fetoscope tip and the axis of the cylinder is given by:

$$\boldsymbol{l} = \mathbf{si\,n}(\boldsymbol{\varphi}) \,.\, \boldsymbol{d} \qquad 6.17$$

Length Line of length ***'L'*** formed between the stem and the axis of the cylinder can be given as:

$$\boldsymbol{L} = \ \boldsymbol{sin}(\boldsymbol{\Phi}).\boldsymbol{D} \qquad 6.18$$

When '***l***' is greater than the radius '***r***', the tip point location is outside the cylinder and ***'L'>r*** the stem is away from the cylindrical volume of interest. The above equations were applied to a 3D virtual cylinder and the output obtained can be seen in Figure 6.8 (a) and (b) before and after intersection within the volume of interest of the cylinder.

6.3.4 2D user interface control panel, target setting and guidance capabilities

The control panel is a 2D GUI has an elaborate set of interface buttons and sliders for very specific functionality and fine tuning.

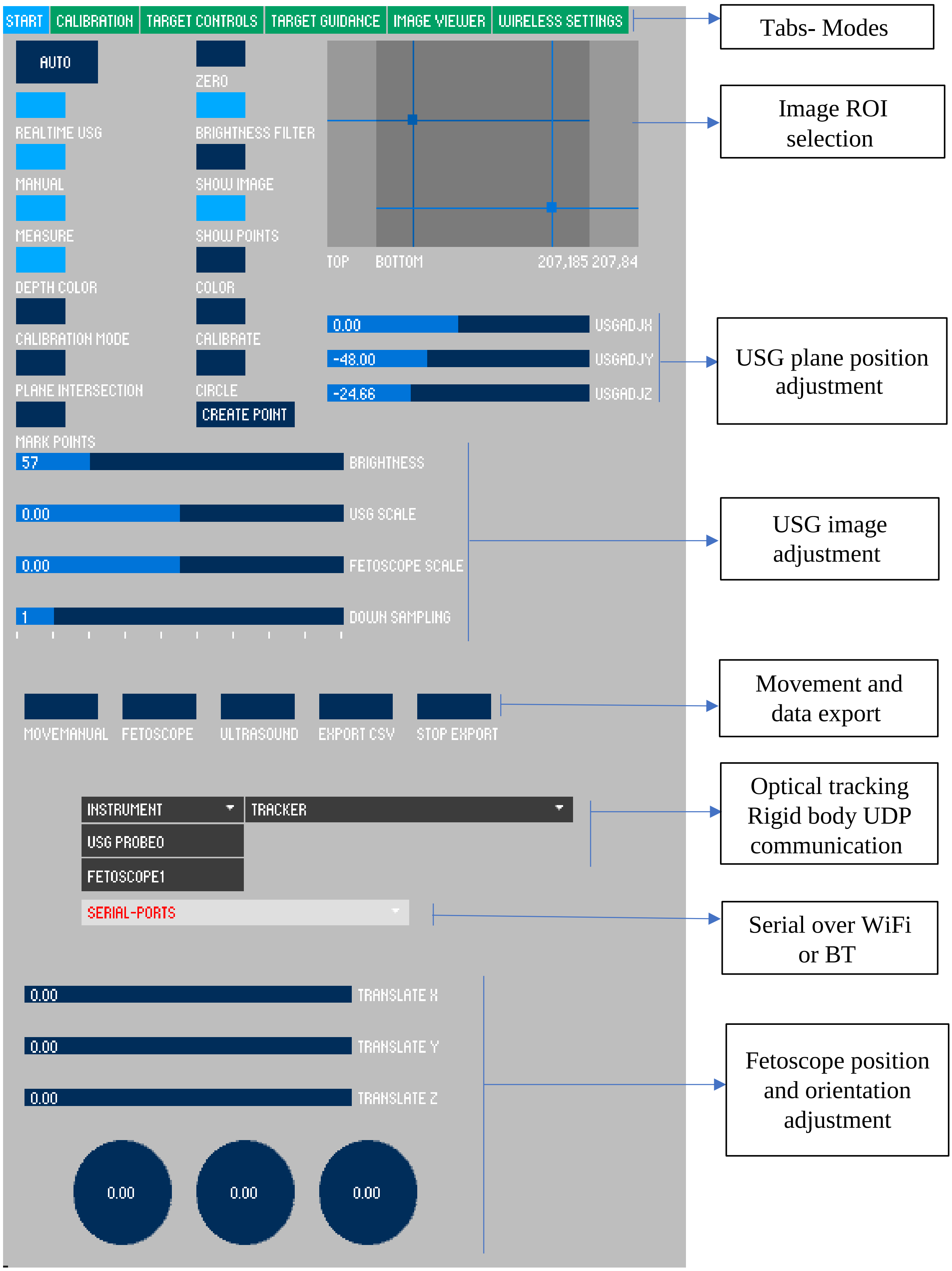

Figure 6-8 Main page of the control panel illustrating the available major settings

Figure 6.8 has the following tabs list the modes available:

1) Main screen buttons:

Button	Function
Auto	Automatic frame capture(JPEG)
Realtime USG	Realtime stream USG image
Manual	Disable UDP instrument tracking
Measure	Measure angle and distances using interactive objects on USG plane
Zero	Zero tip position of fetoscope while needle insertion procedures
Show points	Enable Otsu’s thresholding/ disable pixel image
Show image	Enable pixel image
Brightness filter	Brightness adjustment
Color	Enable color images
Depth color	Enable color mapping of point cloud based on slices of an array images
Calibrate	Calibrate tip position with a temporary marker
Circle	Create circular area of interest
Calibration mode	Enable tip calibration
Plane intersection	Enable ultrasound plane and instrument axis line intersection
Markpoints	Create non-interactive 3D markers at the tip position
Create points	Create multiple non-interactive markers

USG position adjustment panel sliders-

a) X range -200,200

b) Y range -200,200

c) Z range -150,250

Image adjustment panel-

a) Brightness 0,255

b) USG scale -6,6

c) Fetoscope scale -6,6

d) Resolution Down sampling 0 – 10

Translation and orientation adjustments:

Move manual

(a) Fetoscope
(b) Ultrasound

Translate X 0- 1000

Translate Y 0 - 1000

Translate Z 0 – 1000

Pitch 0 - 360

Yaw 0 - 360

Roll 0 - 360

Export functions:

Export, Stop

Dropdown list:

Rigid body list maps to equipment type

Equipment type:

(a) Ultrasound
(b) Fetoscope

Serial Communication:

(a) Bluetooth/WiFi wireless serial for fetoscope
(b) Bluetooth/WiFi wireless serial for Foot switch

2) Calibration

Button	Function
Tip calibrate	Calibration of tip with optical tracking marker
USG calibrate	Calibration of the USG probe with optical marker attached
Plane calibrate	Collect plane calibration points to find the ultrasound frame

3) Target controls

Button/Slider	Function
Target accuracy	Accuracy setting slider 0 – 5mm
Target size	Allowed size of the target sphere
Target VOI	Target cylindrical volume of interest diameter adjustment

4) Target guidance

Display	Function
Needle guidance display	Shows needle 2D position
Needle guidance measurement	Shows distance between the target point in the vessel in mm
Vessel diameter adjustment	Enables adjustment of measured vessel diameter using mouse scroll
Fetoscope visual guidance: Stem guidance Tip guidance	Shows movement of fetoscope towards the target and indicates directions to reach the target using wo radar displays one for the tip and another for the stem

5) Image Viewer

View and scroll images which have been captured using given slider.

6) Wireless settings

Button	Function
WiFi sync	Enable WiFi / BT sync
Activate servo	Real time servo activation with guidance
Reset servo	Reset servo position to zero

The main features of the control panel seen in Figure 6.8 include the following:

1. Frame capture of real-time ultrasound images and display them in the 2D window.
2. The 2D frame window has cross hairs using which area of interest can be decided.
3. Real-time fine tuning for ultrasound calibration, scaling.

4. Brightness filter and resolution control
5. Colour mode selection for the ultrasound depending on the layers or the quantification of grey value.
6. 1 Click calibration for the tip of the tool
7. Options to enable intersection calculations and areas of interest inside every saved frame.
8. Addition of interactive and non-interactive markers, setting constraints.
9. Communication interface for serial UDP socket and Wi-Fi.
10. Dynamic interface for rigid body assignment
11. Manual and automatic translation and rotation modes.
12. Target control and target guidance for surgical planning and trajectory estimation.
13. Over shoot control settings control panel for LASERs and needle operation
14. Output data export settings
15. Surgical equipment monitoring and guidance.
16. Ability to scroll through saved images in 3D and 2D

6.3.5 Duplex communication systems for the navigation environment

Duplex communication is required especially in areas where part of the computation especially that of cameras and sensors are remotely done, as the local processor lacks either the speed, memory or processing power to do complex computations. In the case of multimodality navigation interface, the tracking data is communicated to the interface via UDP communication and the sensor data is communicated to the interface via WiFi or Bluetooth serially. The combined result of tracking and sensor data is then streamed into the robotic fetoscope and can be displayed on the OLED screen on the device or used for physical feedback or control of devices such as LASERs, RFA, needle actuation or joystick control.

6.3.5.1 Optitrack UDP communication protocol

Optitrack optical tracking system has been previously described in detail in the literature review of tracking systems. Therefore, the communication protocol used to establish socket communication with the hardware is discussed in this section. A simple UDP receiving protocol was implemented with JAVA UDP library to acquire the binary data. The binary data is encoded and has a variable index with marker addition. Hence a depacketization client was custom developed in JAVA, which decodes the marker data packets streamed as a multicast from system port 1511 and the command port is 1510. The packet stream format can be seen in Figure 6.9.

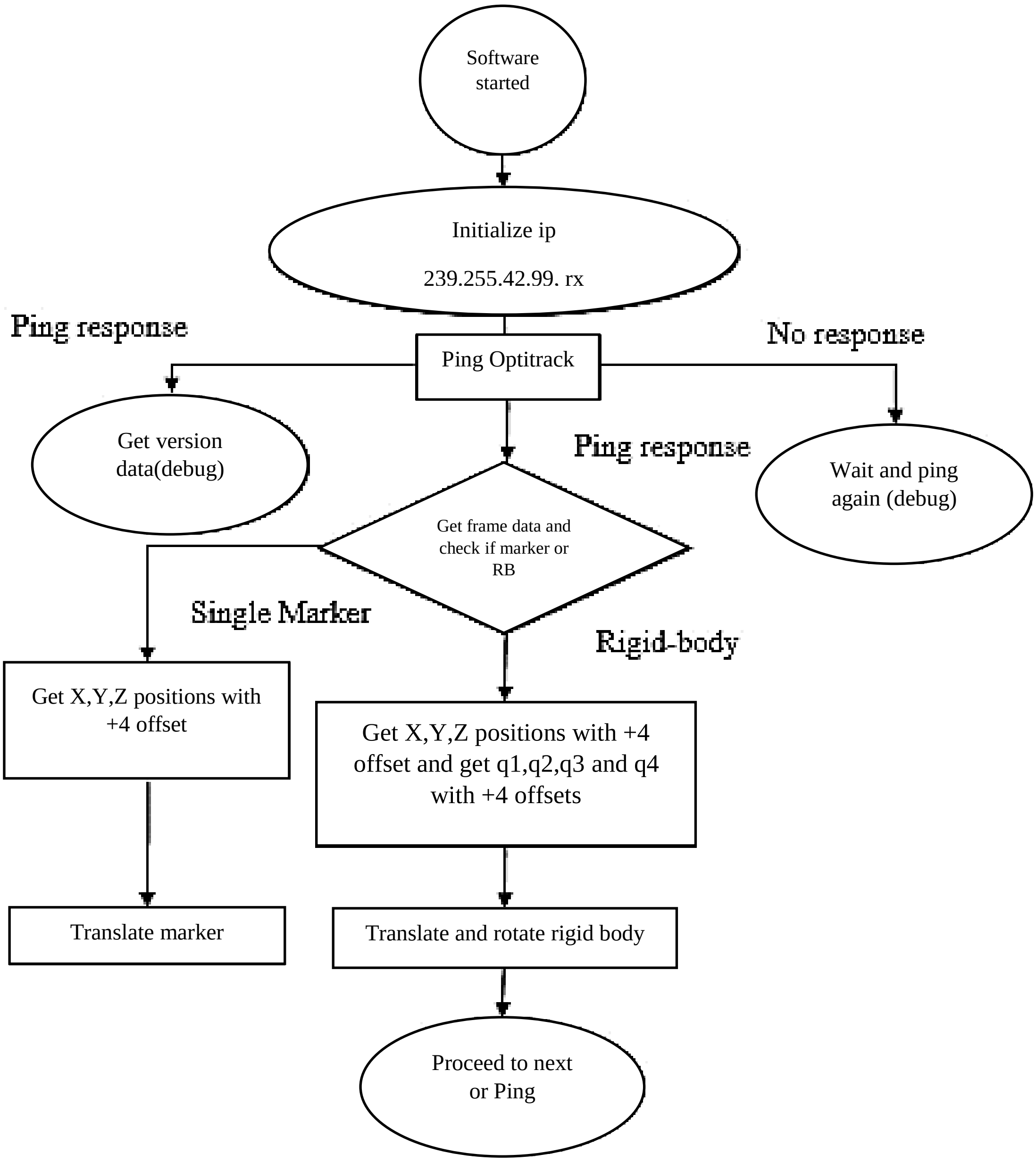

Figure 6-9 Protocol found using experiments to interface with Optitrack UDP stream to unpack the binary bitstream

6.3.5.2 Fetoscope serial communication protocol

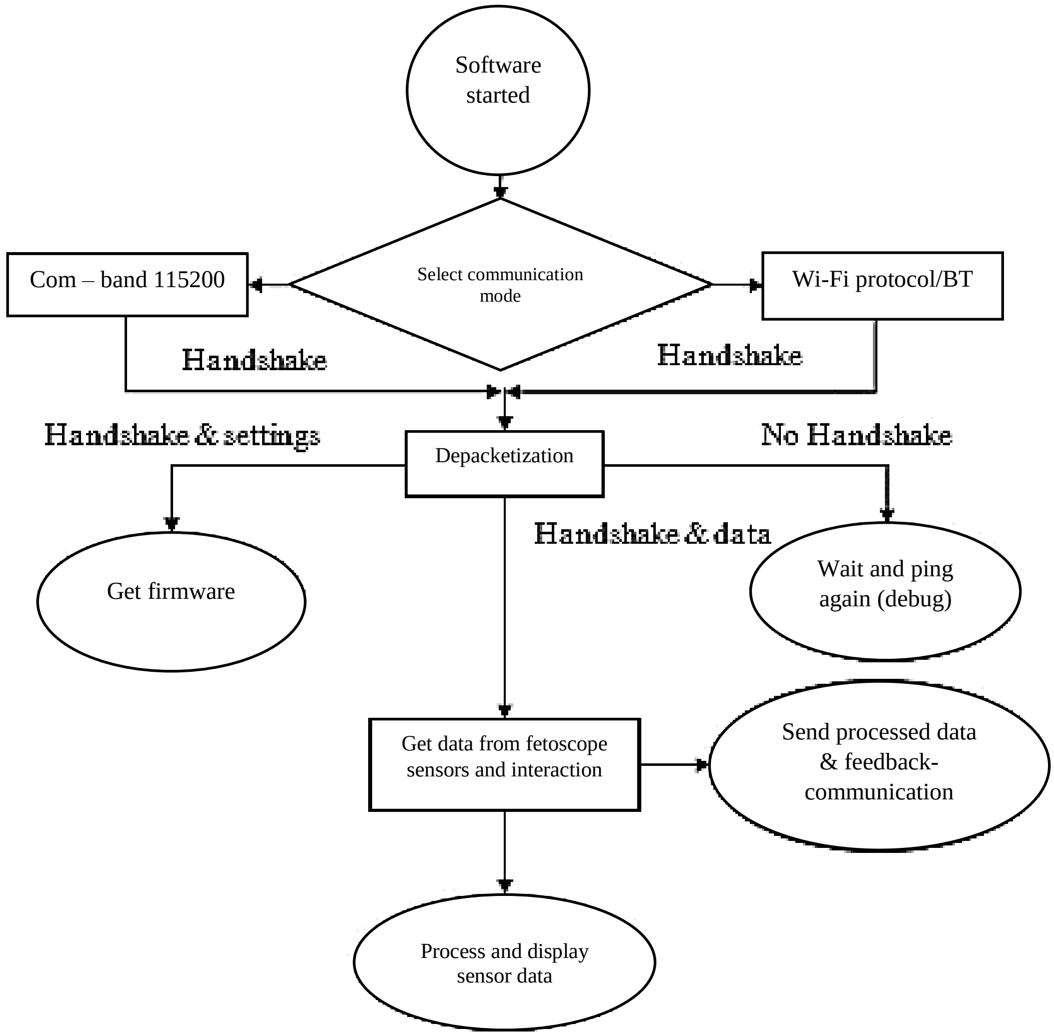

Figure 6-10 Fetoscope hardware interface with Java GUI for duplex data streaming and real-time feedback

In Figure 6.10, the process of hardware software interface is illustrated in the flowchart. Post selection of communication mode, there is a simple binary handshake, followed by the fetoscope hardware sending data from all of its sensors, button interfaces and hardware actuators and these get displayed in the 2D interface and the distance of the fetoscope from the body is monitored real-time from the fetoscope ToF distance sensor. The GUI in return communicates the coordinate data of the fetoscope and its orientation and in target guidance mode, sends the data to help navigate the fetoscope on the OLED display and the multicolour LEDs indicating the status. In fetoscope safety mode, the GUI communicates the on/off and force gain values directly to the fetoscope. Therefore, most hardware elements in the fetoscope other than the pump and actuator can be directly controlled or tuned from the wireless interface.

6.3.6 Automatic Virtual Camera orientation and Smart Navigation

In a 3D virtual environment registered to the real world, for the surgeon to be able to visualize a volume of interest, 3D steering can be confusing and time consuming to bring the view to the required alignment(Zhou, 2009). For example, in the case of the orthopaedic surgeries, the anatomy is first registered into a virtual coordinate system and then the implant needs to be aligned(Zheng and Nolte, 2015). Since the virtual coordinate system is theoretically infinite, a virtual camera with a field of view which shows the surgeon only the area of interest is of utmost necessity. The location and orientation of the virtual camera can be manually or automatically controlled. Manual control of the viewing of the registered points in the patients anatomy can be done though is quite cumbersome. Therefore, automatic virtual camera steering and focus is very important in virtual surgical guidance.

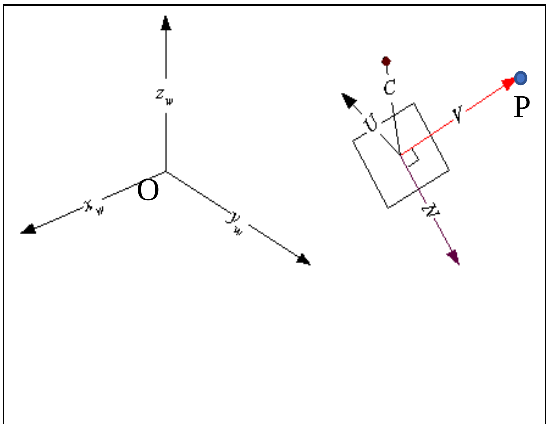

(a) Origin *'O'* of the Virtual world coordinate system and virtual camera *'C'* looking at point *'P'*

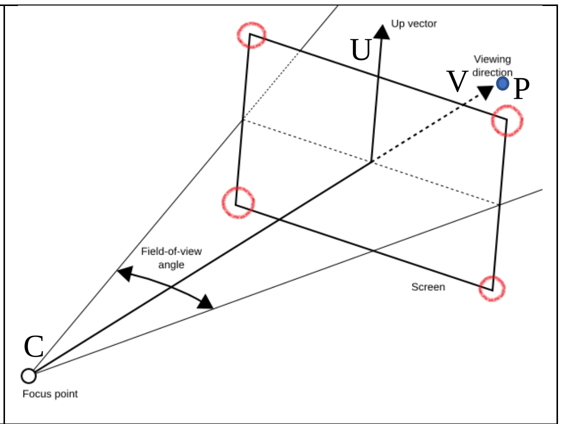

(b) Camera *'C'* with Up vector '*U'* View vector *'V'* and a virtual screen orientation of '*Vq'*

Figure 6-11 Virtual camera within a Virtual coordinate system. The Virtual camera has an image plane and a user defined field of view.

In Figure 6.11, a virtual world coordinate system with origin *'O'* is presented. A virtual camera *'C'* with a view vector *'V'*, up vector *'U'* and quaternion orientation *'Vq'* is present within the world coordinate system.

The camera system has the following characteristics:

- View direction controllable
- Camera up controllable
- No view volume specified
- No view plane window specified
- Perspective projection with viewport as centre of projection

From the Figure 6.11, a virtual camera requires three vectors: Position, View and Up vectors. Let us consider a virtual camera *'C'* with an up vector *'U'* and view vector *'V'*. For steering the virtual camera in the first person perspective mode, only a single view vector needs to be taken into consideration. For steering the camera *'C'* from *'V'* to *'nV'* , initially the view vector needs to be converted into its orientation quaternion *'Vq'*. Using quaternions, the view vector '*V'* can be rotated about an arbitrary axis by first converting it into a quaternion *'Vq'* and then applying the desired rotation quaternion later. This can be done by simply assuming the value of Vq_w as '0' as seen in equation 6.17 initially.

$$Vq_{wxyz} = [0, V_{xyz}] \qquad 6.19$$

Let us assume a case where we have an arbitrary vector *'A'* about which the view vector of *'C'* has to be rotated by an angle *'θ'*. In order to find a rotation quaternion '$Rq_{(x,y,z,w)}$' ,the individual components are required to be found as shown in equations 6.18 to 6.21 as follows:

$$Rq_x = Ax + \sin\left(\frac{\theta}{2}\right) \qquad 6.20$$

$$Rq_y = Ay + \sin\left(\frac{\theta}{2}\right) \qquad 6.21$$

$$Rq_z = Az + \sin\left(\frac{\theta}{2}\right) \qquad 6.22$$

$$Rq_w = \cos\left(\frac{\theta}{2}\right) \qquad 6.23$$

Rq' is the conjugate of Rq

$$Rq'_{x,y,z,w} = Rq_{-x,-y,-z,w} \qquad 6.24$$

With the current orientation *'Vq'* and the above quaternion variables '*Rq*' and '*Rq*'' at hand, the net rotation operation given by the quaternion *'Qw'* for rotation from the current orientation can be given by the following equation:

$$Qw_{wxyz} = [Rq.Vq].Rq' \qquad 6.25$$

In equation 6.23 the multiplication is between quaternions therefore is a subtracted result of the dot product of the matrices from the cross product of the respective matrices.

The new view vector *'nV'* can be given by just using the vector components of *'Qw_{wxyz}'* without the 1st component *'Qw_{w}'*. It can, therefore, be given using the following equation:

$$nV_{xyz} = \left(Qw_x, Qw_y, Qw_z\right) \qquad 6.26$$

6.4 Kinematics of the surgery

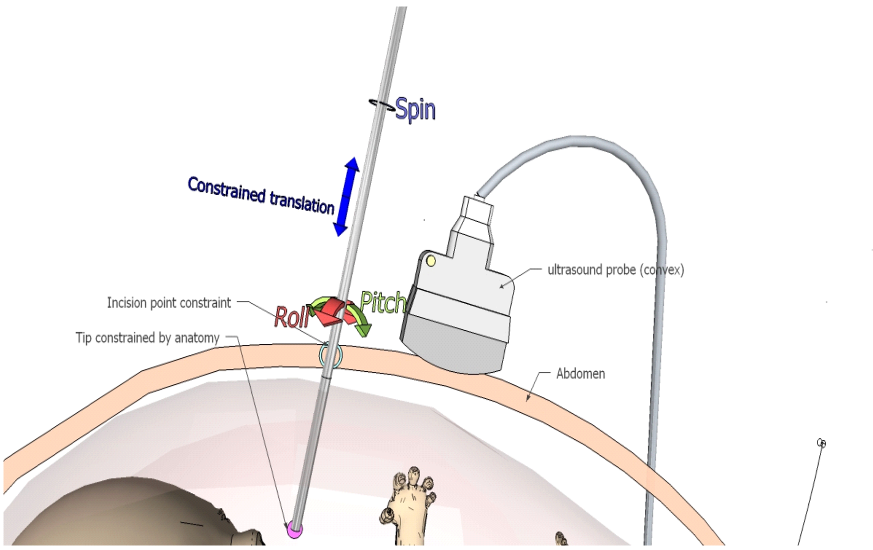

Figure 6-12 Fetal surgery kinematic rendering

The target set to accomplish includes all the above excluding an external 40 to 60W NdYAG CW LASER source, only because of safety and ethical concerns. This will be replaced by a 660 nm diode LASER to demonstrate the required function.

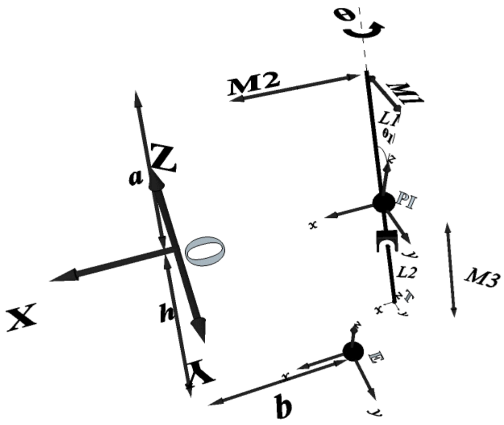

Figure 6-13 Kinematics of the fetoscope in 3D

In a world coordinate system *O*, the catheter with length '*L*' enters the body through '*PI'* and hence it is divided into lengths L1 and L2. Tip location of the catheter is T*(x,y,z)* and the target position E(*x,y,z*). The catheter can undergo rotation about its long axis which is given by '**θ**' and translation along the very same axis, restricted only by the anatomy and the control of the surgeon. 'a' is the length of the fetoscope from the fulcrum point P, outside the body and 'h' is the length of the fetoscope stem inside the body from the fulcrum. 'b' is the distance between the end point and the origin along the X axis, inside the body. For the tip T to reach E, M2 and M1 are displacements along , X and Y directions and M3 is the local vertical distance given using the following equations:

$$M2 = \left(\frac{L1}{L2}\right) \cdot E(y) - T(y) \qquad 6.27$$

$$M1 = \left(\frac{L1}{L2}\right) \cdot E(x) - T(x) \qquad 6.28$$

$$M3 = E(z) - T(z) \qquad 6.29$$

For the above inverse kinematic equations to work efficiently, the point of the incision is required, and the length of the stem of the fetoscope is required to be known at all times. The sensors used, in combination with the optical tracking system enable us to obtain these values for real-time surgical guidance.

6.5 Discussion and Results

By applying the OpenGL 3D environment with interactive and non-interactive object functionality, active dynamic constraints, automatic camera guidance and 2D control panel interface, the fetal surgery target guidance, image acquisition, scaling, calibration and manipulation can be performed.

6.5.1 Image manipulation and 3D frame storage

The interface makes real-time image acquisition and can store multiple 2D frames with their active rotation amounts inclusive of pixel thresholding in the interface, and the area of interest can be selected by using the 2D control panel to include specific sections of the acquired image. Figure 6.14 illustrates the use multiple frame capture, brightness adjustment for pixel extraction and multiple ultrasound static frame objects, which are basically recorded pixels along with their quaternion orientation, thereby forming 3D image frames. Every frame can be translated or located by doing a mouse over or by using the slider to select the frame number of the slide and the translation and rotation parameters on the 2D interface control panel.

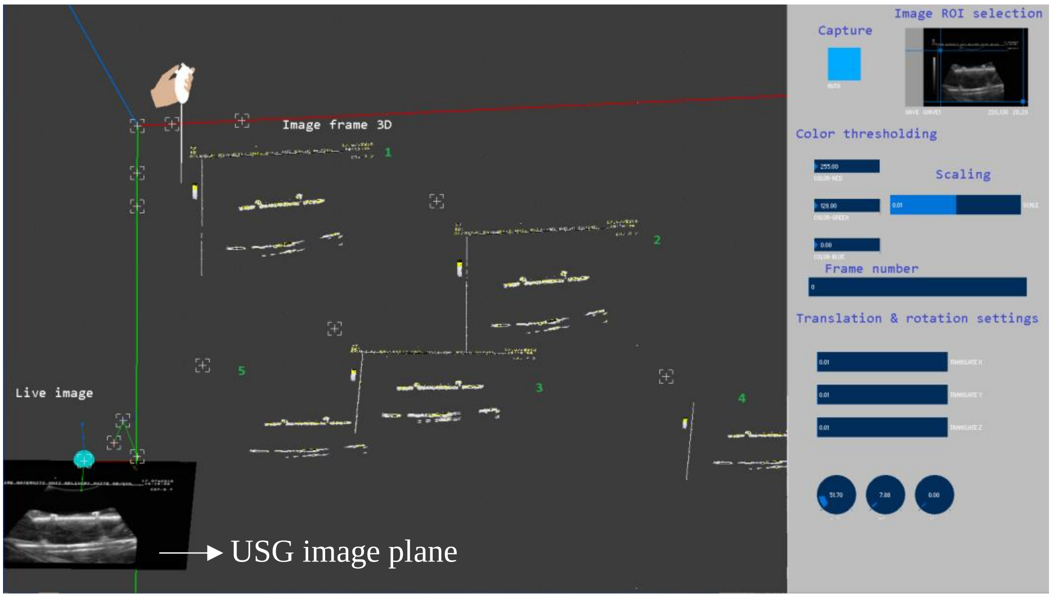

Figure 6-14 Ultrasound live image input and pixel thresholding and multiple 3D frame storage with area of interest selection capability

6.5.2 3D collision detection demonstration

Collision detection between a cylindrical volume and a line has been mathematically described earlier in this chapter. The software application of the line cylinder intersection can be seen in Figure 6.15. A simple interface with a line with 2 interactive spheres capable of being moved in 3D with a mouse and a cylinder with an interactive sphere at the origin of its axis(bottom centre of the cylinder) was developed. In Figure 6.15 (a) a line representing the axis of a fetoscope and an orange transparent cylinder is shown. Once the spherical objects of the line make the line touch or intersect the surface of the cylinder as shown in Figure 6.15 (b), the cylinder automatically changes color in realtime. This demonstrates the working of a collision detection methodology between objects which can be applied later in the fetoscope surgical interface.

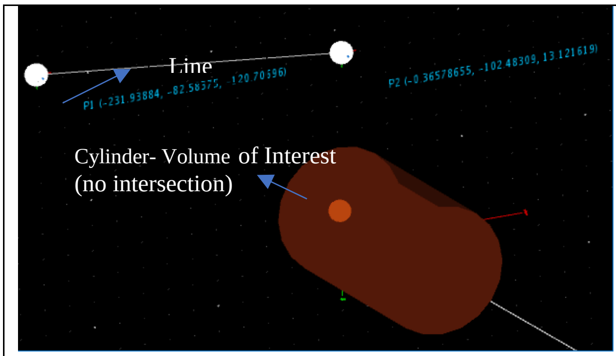

(a) No cylinder line intersection cylinder is orange

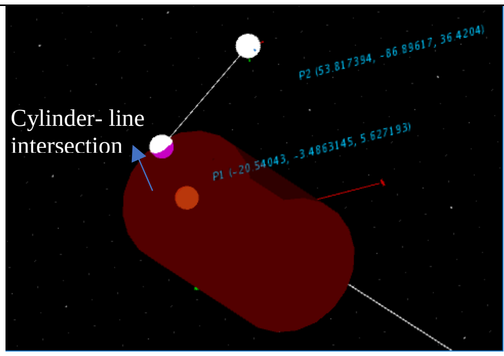

(b) Cylinder line intersection filled transparent red

Figure 6-15 Geometric intersection detection between line and cylindrical volume of interest

6.5.3 Automatic virtual camera steering demonstration

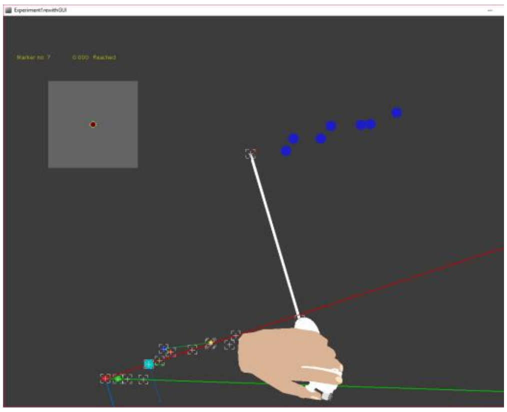	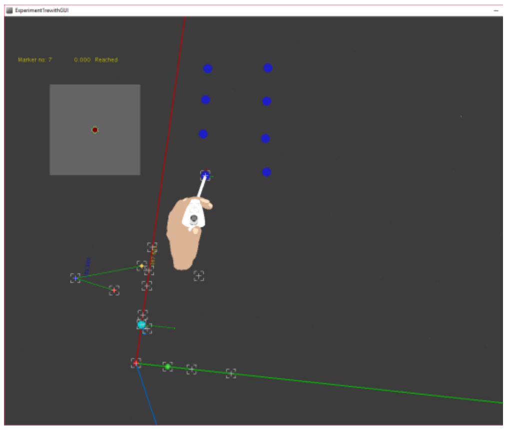
(a) Pre-virtual camera orientation	(b) Post registration completion- automatic virtual camera orientation

Figure 6-16 Virtual camera within the proposed fetal surgery interface pre and post camera orientation

In the fetal surgery navigation interface, after the registration and calibration of the tool and the ultrasound, initially, the camera is set to follow the vector location of the tip of the tool as seen in Figure 6.16 (a) but the orientation is not set. Whereas, once the non-interactive markers are placed, and the required constraints are set, the camera automatically starts following the centroid of the plane or automatically adjusts according to the number of markers placed, so that they are always within the view as seen in Figure 6.16 (b). The orientation vector is given by the average orientation of the elements under the camera, in the opposite direction, which provides the most optimal rotation. Though automatic camera steering is the case, the angle of the camera and its 3D position can also be varied manually, and zooming can be controlled using the mouse from any point within the 3D OpenGL window.

6.5.4 Interactive frames for surgical planning and target guidance:

Guidance to set a target on the image plane in 3D is very difficult in terms of alignment, as it required at least two planes for achieving an accurate position (Zhou, 2009). To achieve this, either multiple 3D perspectives can be given or one 3D perspective for orientation and one 2D calculated position frame with tool tip distance and the handle distance from the axis can be displayed, as described in the ‘cylinder -

line intersections' so that the instrument can be aligned with the axis of the target direction which has been set, as shown in Figure 6.17.

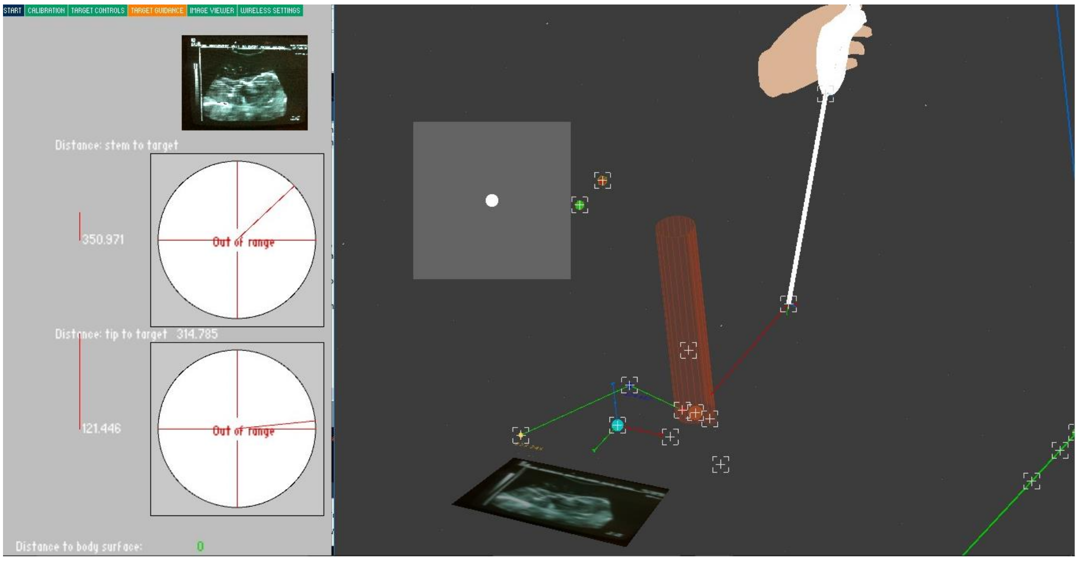

Figure 6-17 USB imaging device real-time image in the 3D navigation environment

It can be seen in Figure6.14 that the 2D control panel shows the image plane of a simple USB 2.0 video input device, in the case of the Ultrasound device, it would be an image digitizer card like EasyCap, and the ultrasound image frame can be loaded directly. The orange marker ball, the target point, corresponds to the centre of the cylinder, which is the volume of interest. Red marker beside the orange marker can be adjusted to control the radius of the volume of interest within the cylinder. These points can be seen to have visual hints in the form of '[+]'. These hints at the centre of the balls provide mouse interactivity. Left click with simultaneous movement helps in translation, while right click with movement enables rotation.

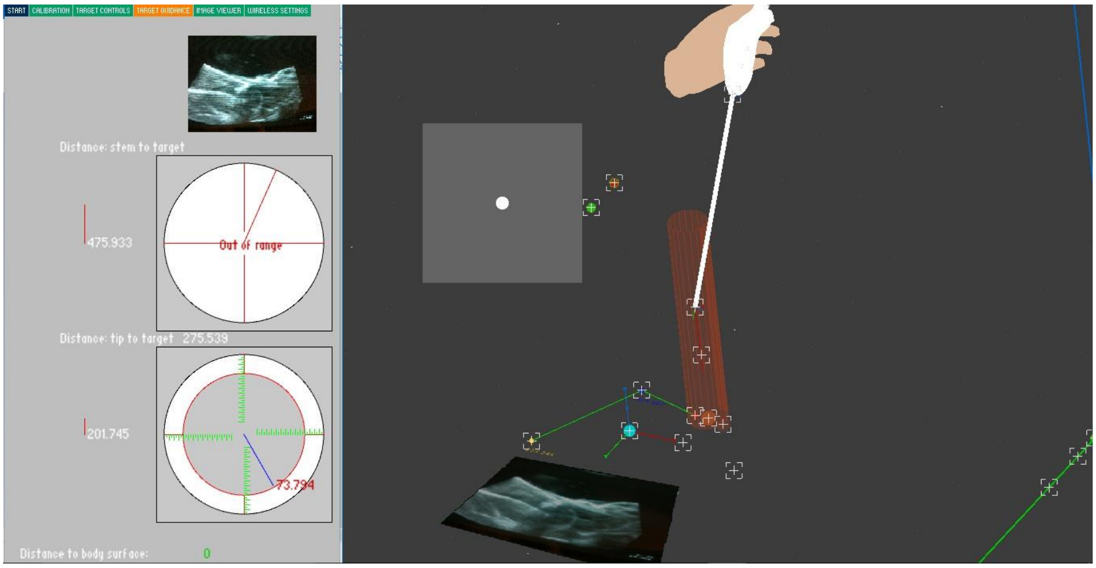

Figure 6-18 Fetoscope tip within the volume of interest, while the rest of the stem is out of the volume and the same, as seen in the 2D control panel

The distance between the target and its directional orientation with respect to the tool(fetoscope) tip can be seen on the 2D control panel, as seen in Figure 6.18. The tip distance in the perpendicular direction to the plane is also monitored in real-time and can be visualised on the 2D interface. In Figure 6.15, it can be seen that the tip alignment is closer to the axis whereas the stem is further away and in Figure 6.18, it can be seen that the stem and the tip are aligned, but the tip has not reached the target. The size of the target monitoring circles is indicative of planar distance in terms of a radius and colour change. The distance between the tip and the target and the stem and the target can be seen in real-time on the 2D panel. When the tip reaches the target, it can be visualised on the 2D panel.

It should also be noted that the fetoscope communicates the distance of the fetoscope stem to the skin of the port of entry. This distance is used to find the kinematics for the guidance of the fetoscope to the target position. The radii of the two circles from the interface are communicated to the fetoscope. The fetoscope, on the other hand, uses this data to turn its LEDs of the specific direction from Red to Amber to Green and then White when the target is reached, as seen in Figure 6.19.

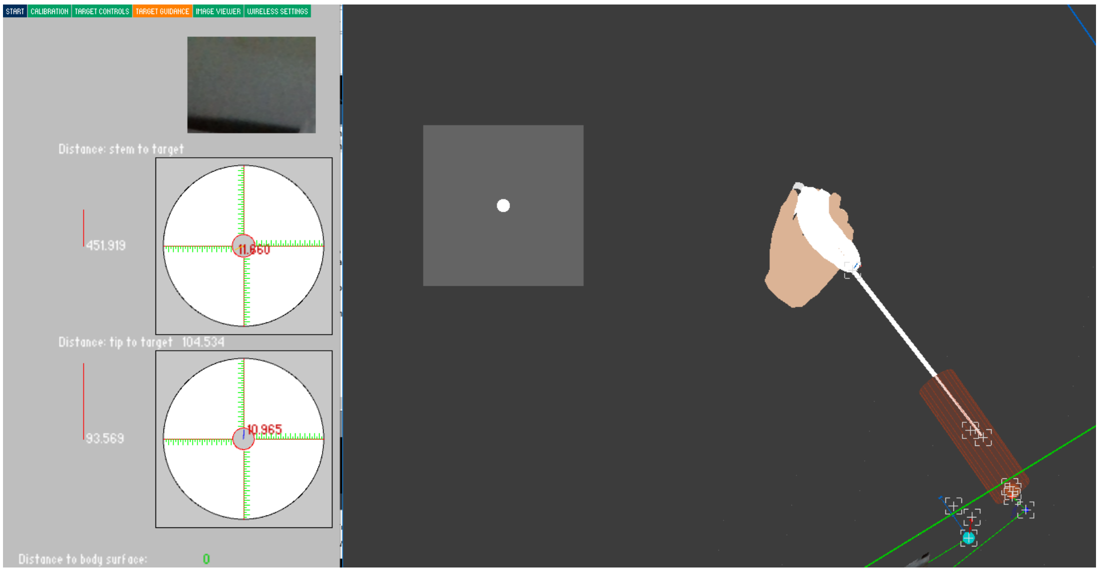

Figure 6-19 Fetoscope tip and stem both are within the volume of interest, but the tip has not reached the target and the tip and stem distance can be seen on the 2D interface

6.5.5 Use of Non-Interactive virtual markers for surgical planning and monitoring

Surface registration is required in almost all navigated surgical procedures. Also, in the procedures where surgical planning or path planning is required, markers will need to be placed and monitored in relation to the surgical tip or anatomical structures, for tracking the path of movement of the non-interactive markers, which do not actually change positions in relation to the surgical equipment and the anatomy. Such markers are used as an ArrayList in JAVA, which can be added or removed on the go. These markers can be selected to obey the rules assigned to a parent interactive marker or to not obey any constraints in certain cases, where they can dictate the terms of interactive markers.

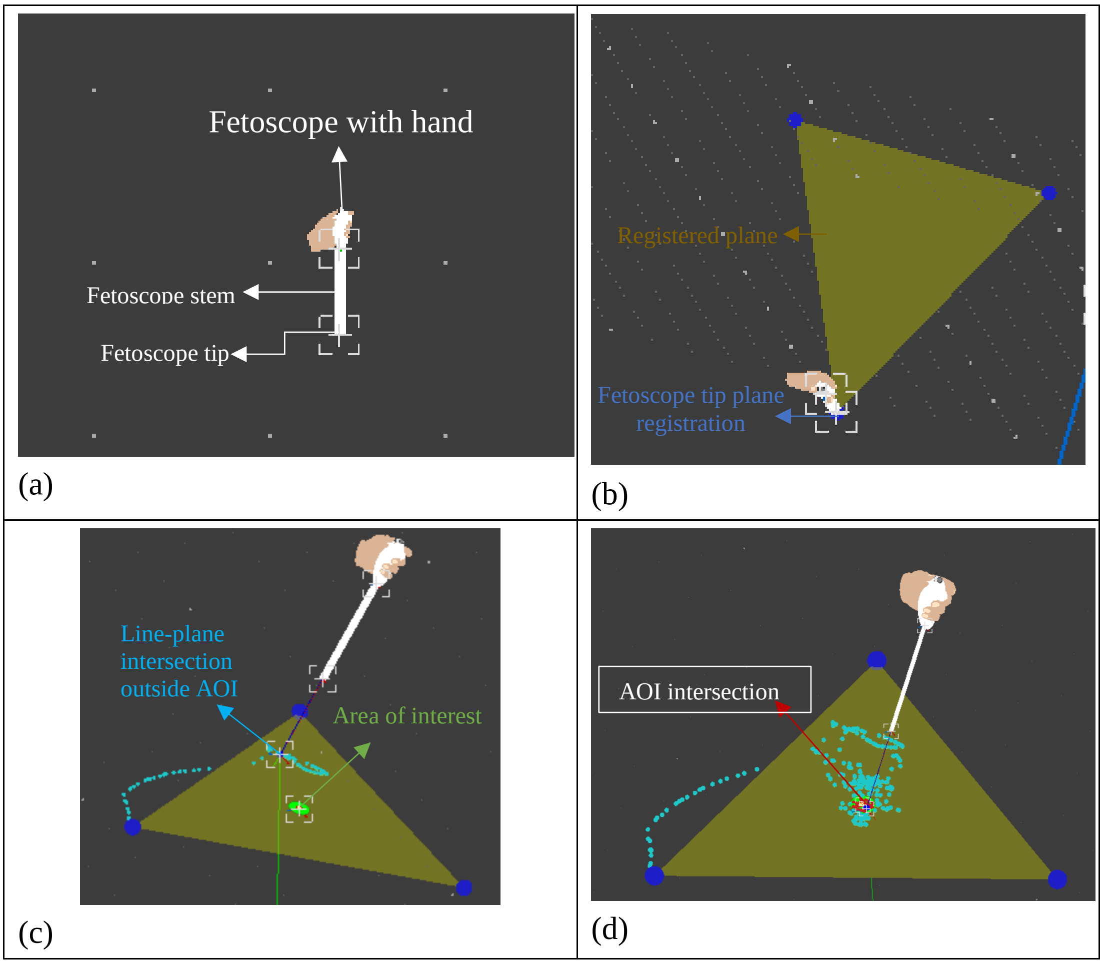

Figure 6-20 Plane -line intersection applied to 3D navigation interface (a) fetoscope with 2 interactive markers, the tip chained to the handle marker (b) Fetoscope tip creates non-interactive blue markers, which form a plane(c) Line plane intersection creates smaller light blue markers (d) Line-plane intersection non-interactive red markers at the circle region of interest

In Figure 6.20 (a), a virtual fetoscope is shown with a calibrated stem and tip with square hints in the form of '[+]'. Figure 6.20 (b), shows the interactive markers in the form of deep blue color which can be formed on registration with the real fetoscope in the surgical environment using the joystick to do a single click – 'One click registration'. Once a plane is formed by way of registering a minimum of 3 markers, plane – line intersection can be calculated in realtime. When the axis of the virtual fetoscope intersects with the plane formed, light blue balls are formed as seen in Figure 6.20 (c). Further, area of interest on this plane can be marked as a green circle as shown in Figure 6.20 (c). When there is a plane- line intersection within the area of interest, red colored non-interactive marker balls are formed as seen in Figure 6.20 (d).

6.6 Summary

The development of fetal surgery navigation system, user interface and calculations have been discussed. The interface developed is demonstrated in this chapter and is used in combination with optical tracking of the fetoscope and the ultrasound probe, ultrasound image processing and communication functions for synchronization with the fetoscope. Software safety settings for active overshoot control can be adapted from line plane and line cylinder intersection bounds explained in this chapter. The 2D control panel is capable of fine tuning the parameters of image processing, tracking, registration, target setting, controls and helps by providing a real-time 2D view of procedures which require depth perspective for accurate manipulation. Table 6.1 shows a gist of the achievements made and their current level of software implementation in the fetal surgery interface.

Further, the inverse kinematics of the surgery has also been discussed, and this understanding can help in automatic target steering and guidance. The user interface thus developed, and its capabilities are used in the future experiments.

Table 6-1 Technical summary of achievements in Chapter 6

Target	Achievement status	Description	Problems solved
3D Ultrasound interactive frames	Implemented	Compressed jpeg files with orientation & position information	Image files do not have 3D information- new image format USG Computerised Tomogram possible
Merging multiple coordinate systems	Implemented	Merging of Optical tracking coordinate system with the world coordinate system, the fetoscope (stem and tip), ultrasound and its plane	Unification of sub coordinate systems under one world coordinate system
1 click registration	Implemented	Pre-calibrated ultrasound image frame can be used to set targets with the fetoscope with 1 click	3D to 2D cross registration takes time
Automatic camera orientation	Implemented	Automatic camera steering according to registered points	Manual camera orientation is cumbersome – Automatic camera steering
Constraints	Line and plane implemented	Object movement constraints	Virtual environment does not obey physical laws without constraints
Volume of interest	Cylindrical volume of interest and area of interest implemented	3D object collision recognition	Virtual 3D space can have objects passing without interacting-Collision detection helps solve this problem
Interface with 2D and 3D interactive controls	Implemented in real-time	Multifeatured interface with communication, registration, calibration, target setting, imaging, tracking and manipulation	Hardware software real-time communication, GUI, interactive display of 2D and 3D environments
Real time 3D guidance	Realtime implementation	Registration, calibration and Collision detection along with GUI for guidance	3D guidance suffers from uncertainties in the depth plane. - Multiplanar registration and 2D and 3D combination guidance
Kinematics	Implemented	Forward kinematics with real-time tracking and body distance measurement	Kinematics with the help of body distance measurement from TOF sensor helps in target guidance

6.7 Conclusion

A multi-faceted navigation interface for use in Minimal Access Fetal Surgeries has been developed with the simplified registration process, communication and safety capabilities built into the system. Once the system settings are done, the interaction requires very less hand interaction.

Chapter 7

Methodology

7.1 Introduction

The aim of the research as discussed in the introduction is to create a surgical system capable of simplifying surgical procedures by using technology, as an extension of surgeon's perception. In the earlier chapters, the development of the fetal surgery system hardware and the interface capabilities were discussed. Further, experiments were performed to prove the functionality of every subsection.

This chapter deals with combining all the subsections of the hardware and the software and evaluation of the entire system to prove that using this system improves the user's perception and reduces the surgical errors.

7.2 Aims and objectives

The primary processes(Beyer-Berjot and Aggarwal, 2013) in an endoscopic surgery include:

1. View images on the imaging modality
2. Understand the environment based on anatomical knowledge
3. Identify the target
4. Orient the surgical instrument
5. Reach the target
6. Manipulate the environment
7. Perceive and verify the change

Based on the above aspects which should be evaluated, this chapter has the following aims:

1) Design and development of phantom for the experiments
2) Design of the experiments

7.3 Materials and Methods

A surgical navigation guidance system in addition to the hardware should help the surgeon reach registered targets with accuracy and repeatability within acceptable limits (sub-millimetre range). Also, the system should not compromise on the effectiveness of the procedure. In other words, the navigation system and the hardware are expected to be an extension of the surgeon, giving the surgeon increased perceptions, dexterity and higher accuracy. Figure 7.1 shows how the system involves the surgeon in interacting with the surgical environment.

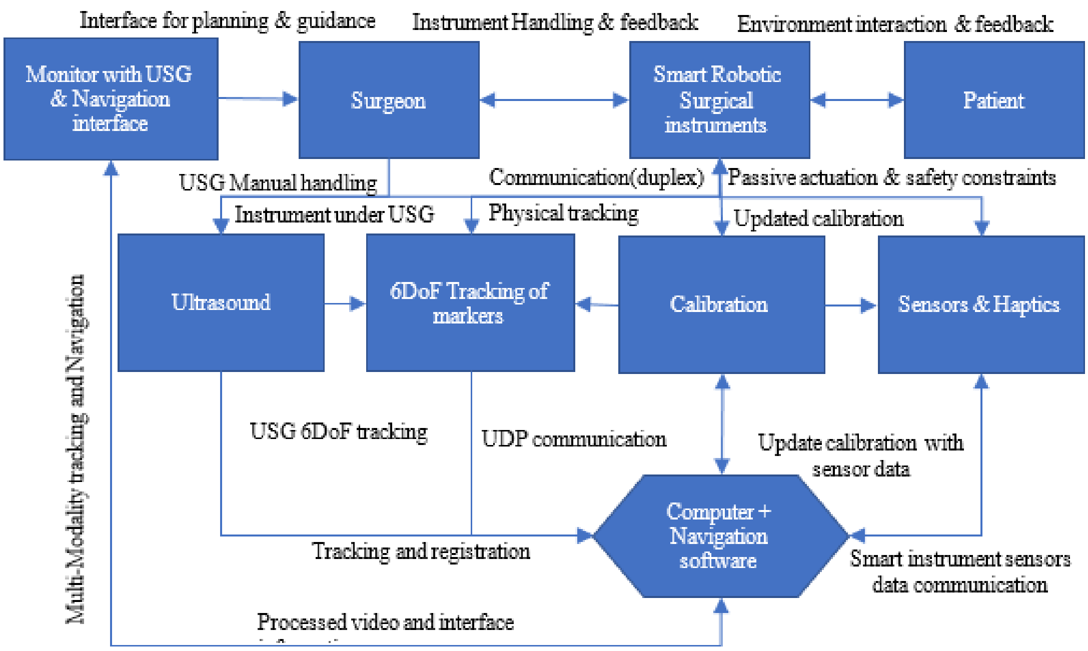

Figure 7-1 Fetal surgical system with Multi-Modality tracking and Navigation flowchart

Experimental setups and phantoms are required to be constructed in order to prove that the system is capable of assisting the surgeon and incresing the efficiency of the surgical process. A set of experiments will be proposed in this chapter which will be able to use the setup to evaluate the claims of higher accuracy, dexterity, confidence and safety.

7.3.1 Experimental setup requirements & Rationale behind the experiments

In a Minimally Invasive Surgery, the efficiency of the procedures not only depend on the surgeon but also the surgical guidance system, which helps to make the process more accurate. Therefore, the parameters in surgery which is to be measured are based on the absolute essentials for guidance in a surgical environment (Zhou, 2009). Based on the above requirements (Beyer-Berjot and Aggarwal, 2013). This chapter will aim at designing experiments and their respective phantoms as shown in Table 7.1.

Table 7-1 Rationale behind the experiments and their respective phantom requirements

S.No.	Parameters to be measured	Aim of the experiments to be designed	Requirements in addition to proposed hardware & software
1.	Visualization, trajectory, confidence	Ability to orient and reach objects with higher confidence and at much lower amount of time	Calibrated USG phantom
2.	Visualization, displacement, confidence, time	High precision of control during needle insertion which could be used for sample collection or procedures	Needle guidance phantom
3.	Visualization, trajectory, Overshoot comparison	Improved safety limits with use of potentially hazardous equipment such as LASERs, RFA or electrocautery.	Plane with a circle traced
4.	Comparison of haptics and their effectiveness	Multimodality haptic feedback – visual + vibrational haptic with high sensitivity to force feedback.	Series of soft materials
5.	Simulation of simple procedure	Simple surgical procedure showing the differences between MMT and normal navigation of the tip, using the type of trajectory and the amount of time used.	Fetal phantom

7.3.2 Phantom development for experiments

For the evaluation of the guidance system in a virtual fetal surgical environment, a fetal phantom and tissue phantoms of different shore hardness's are required to be developed. The manufacturing processes include 3D printing, silicone moulding for the fetal phantom development and dip coating over stainless steel tubes for silicone blood vessel phantoms of different sizes.

The phantoms are held in place under water magnetically, as every phantom has inbuilt magnets which mate with oppositely polarised magnets inside the water tank.

7.3.2.1 Ultrasound phantom development

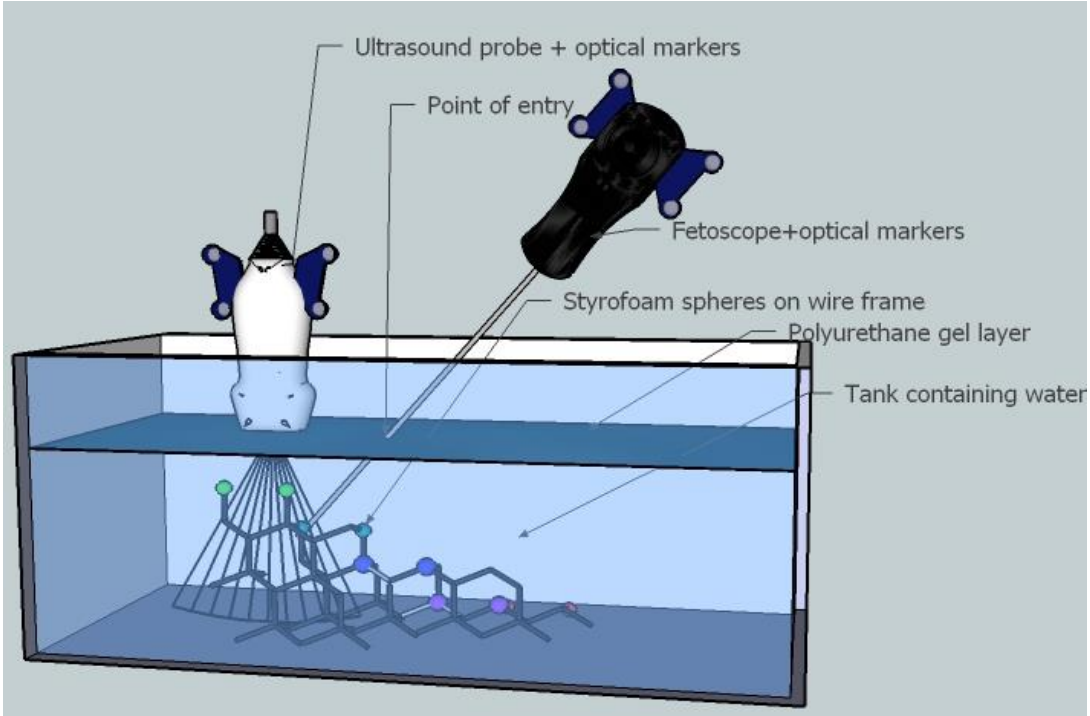

Figure 7-2 Experimental setups to determine subject's reach and repeatability over time with and without the help of the proposed system

Figure 7.2 shows a rendering of the desired setup with a set of pre-calibrated (markers with known positions and geometry) ultrasound visible markers placed in a water tank, an ultrasound probe and the fetoscope which are being optically tracked as mentioned in Chapter 3.

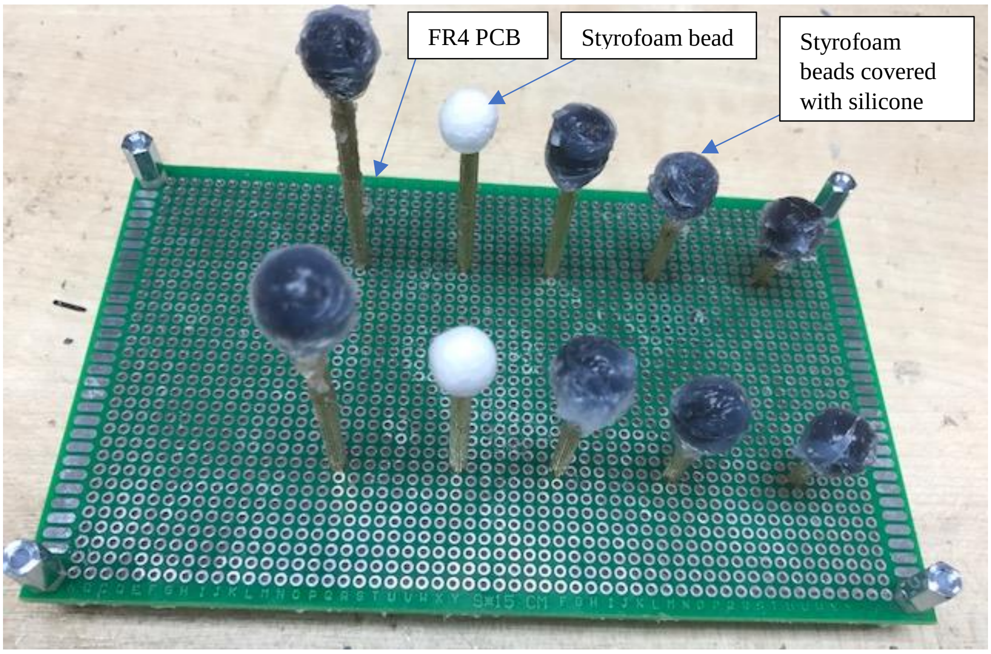

Figure 7-3 Experimental setups to determine subject's reach and repeatability over time with and without the help of the proposed system

Figure 7.3 shows an ultrasound phantom built out of an FR4 material as the base. The separation between every spot on the FR4 board is 2.54mm. Brass inter-locking rods attach with styrofoam beads dip coated with silicone paint so that the beads are visible under ultrasound.

7.3.2.2 Blood vessel phantom

Overshoot of needle either due to ultrasound inaccuracy or due to the surgeon's loss of force perception. Several methods have been postulated for avoiding posterior vessel wall puncture (PVWP). Some of them include using an acute needle angle, reducing the rate of needle insertion and ultrasound-guided in-plane needle guidance(Prada et al., 2014). However, it is not possible to use acute needle angle when the blood vessel or the structure to be penetrated has a high depth. Reducing the rate of insertion and ultrasound guidance in combination has been the most commonly used method to reduce PVWP. However, in the case of narrower blood vessels, ultrasound does not provide enough resolution to give a very clear view(Prada et al., 2014). One possible alternate method to avoid PVWP is to find the diameter of the blood vessel and set the target ideally at the centre of the blood vessel before doing the procedure.

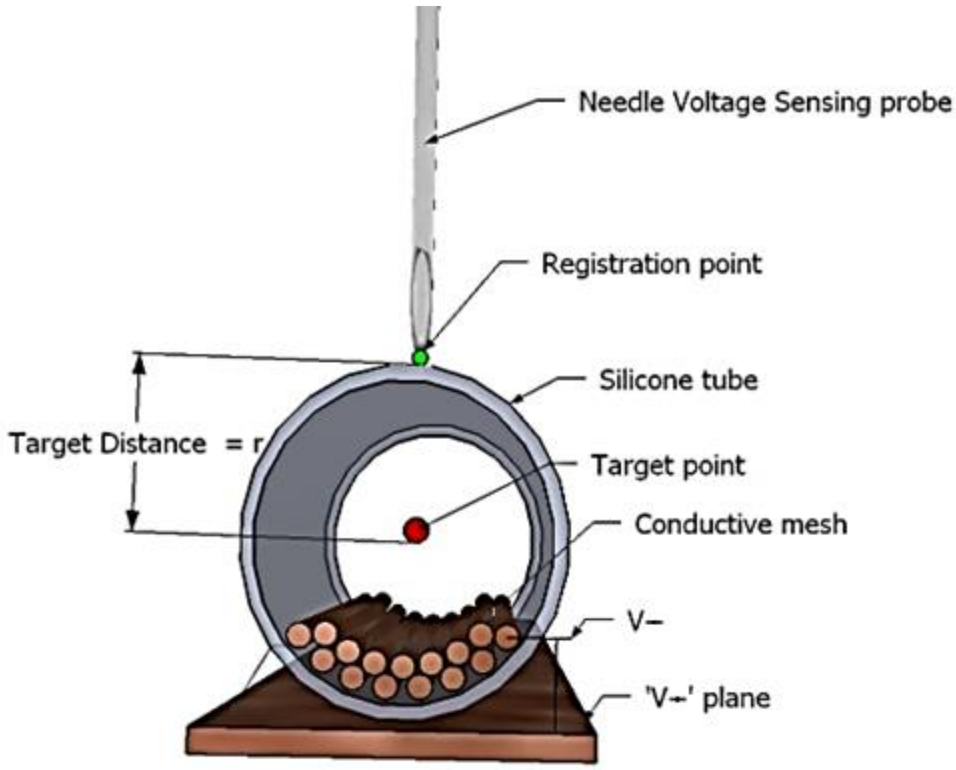

Figure 7-4 Cross sectional view of the blood vessel phantom showing a ground plane, a silicone tube , a wire mesh behind and a conductive copper plane behind it .

To identify a posterior vessel wall puncture under water or blood can prove very difficult because of loss of line of sight, low acoustic visibility if the ultrasound is used. Therefore, an electronic method of contact resistance measurement was used. Let us consider a case as in Figure 7.4, with a schematic shown in Figure 7.5, where an electrically conductive needle which is being monitored for voltage change is introduced into conductive medium like tap water or blood, the potential measured at the needle is not at ground level. Whereas, when the needle tip touches a conductive wires or plane at ground level ‘0V’, the potential drops to 0 and this can be observed by the ADC in a simple microcontroller very quickly.

The microcontroller circuitry samples the ADC0 port at 1000 with a sampling resolution of 12bit samples/second or, in other words, the sensitivity was close to 0.1mV (3.3/4096). The reason why an ADC was used as an input in the place of a digital input is that the tap water used is a conductor and the resistivity is usually more than 200ρ. This can result in false triggering, and therefore, to prevent this problem, an ADC was used. The fetoscope needle before causing a puncture will have to encounter the posterior vessel wall. A Posterior Vessel Wall Contact can be easily measured very reliably using this method.

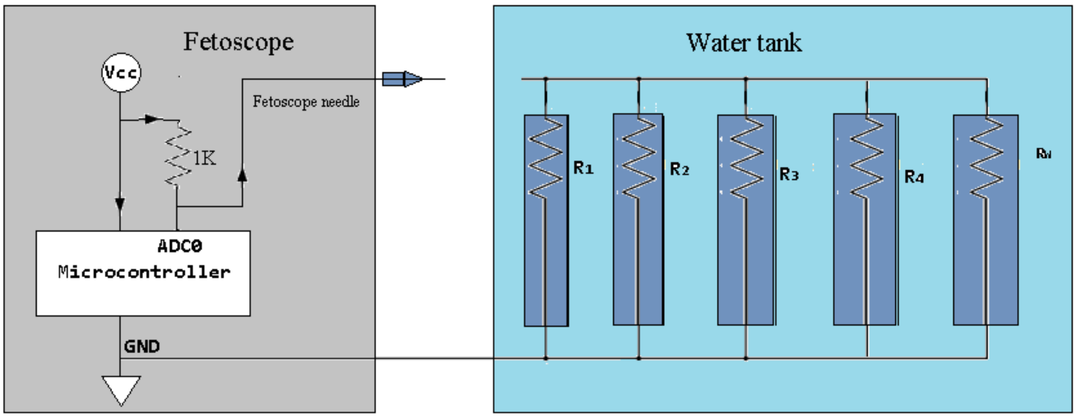

Figure 7-5 Simplified schematic of needle insertion experiment setup. When the Fetoscope needle pierces through the silicone vessel and into the wire mesh, the voltage at the ADC0 drops, and this indicates a posterior vessel wall injury

Figure 7.5 gives the basic schematic of the electronics used to construct the blood vessel phantom. For checking if there is an improvement using the fetal surgery system, a set of blood vessel phantoms of varying diameters are required to be evaluated to find the limits of the system. The phantom has been constructed by using 2, 3, 5 and 6-mm diameter soft silicone tubes 30 – 35 (LIM 6030) Shore A hardness of about 10 (Chueh et al., 2009).

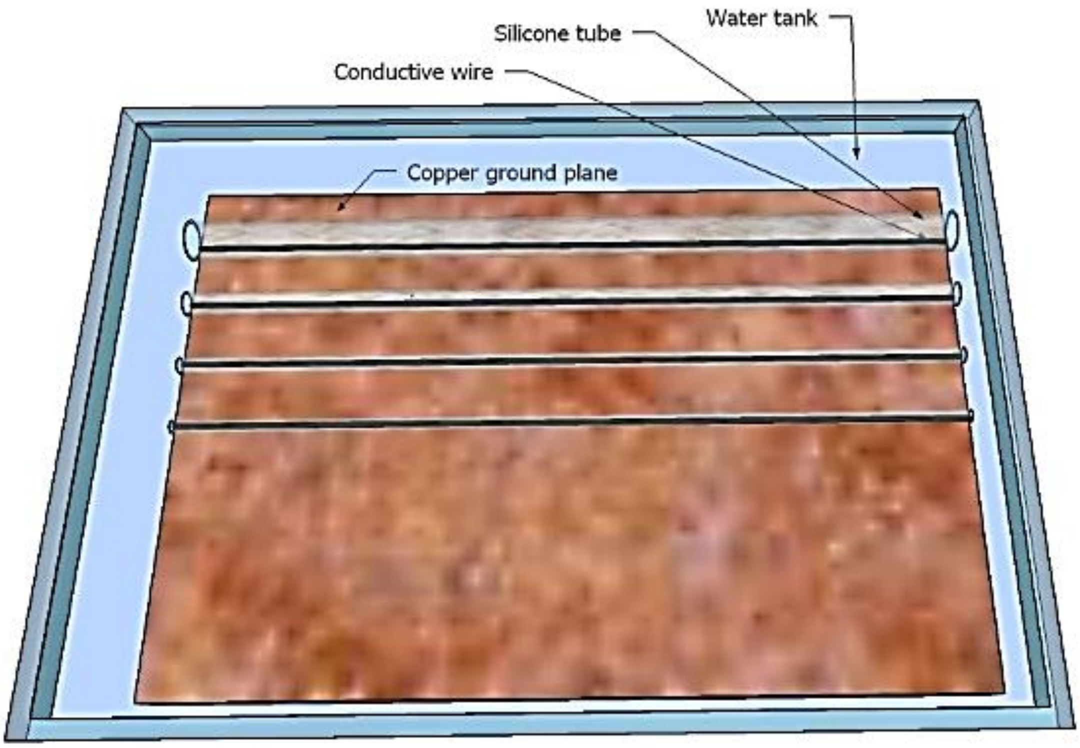

Figure 7-6 A rendering of the phantom showing the parts

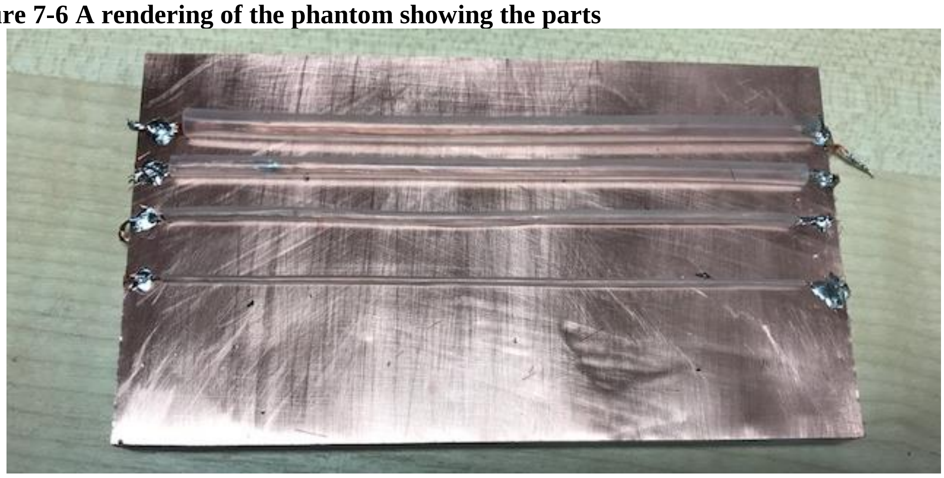

Figure 7-7 Copper plate with silicone tubes and copper mesh inside every silicone tube

The vessels are highly elastic and flexible. Behind the vessels, a pre-strained conductive copper wire bundle layer supported by a conductive metal cladding is used as seen in Figure 7.7 and Figure 7.6 (rendered for more clarity). The plane and the wire bundle are soldered together with pre-straining, and the setup is grounded with the negative terminal of the fetoscope, to have the same reference potential. Doing so also eliminates the accumulation of galvanic potential at the surface of the conductors. One of the ADC pins in the fetoscope is connected internally to the fetoscope needle and is placed at a minor +Ve potential. When the fetoscope tip comes in contact with the conductive layer, it forms an electrical contact. When there is an electrical contact made, the potential measured by the Fetoscope ADC drops to ground level, which is then used to identify posterior vessel wall puncture another method for identification of PVWP is to check for the number of fluid leaks in the tube (Moon et al., 2010). This method is very sensitive and quick. When a contact was made, the data was communicated to the computer which was displayed on the GUI.

Behind the copper clad base seen in Figure 7.6, there are four strong Nickel-plated (avoids corrosion) Neodymium magnets which help stabilize the phantom on the bottom of the water tank, which also contains magnets of opposite polarity, so that the orientation remains the same. If the setup is not stabilized, it can lead to false registration results with the ultrasound and optical tracking.

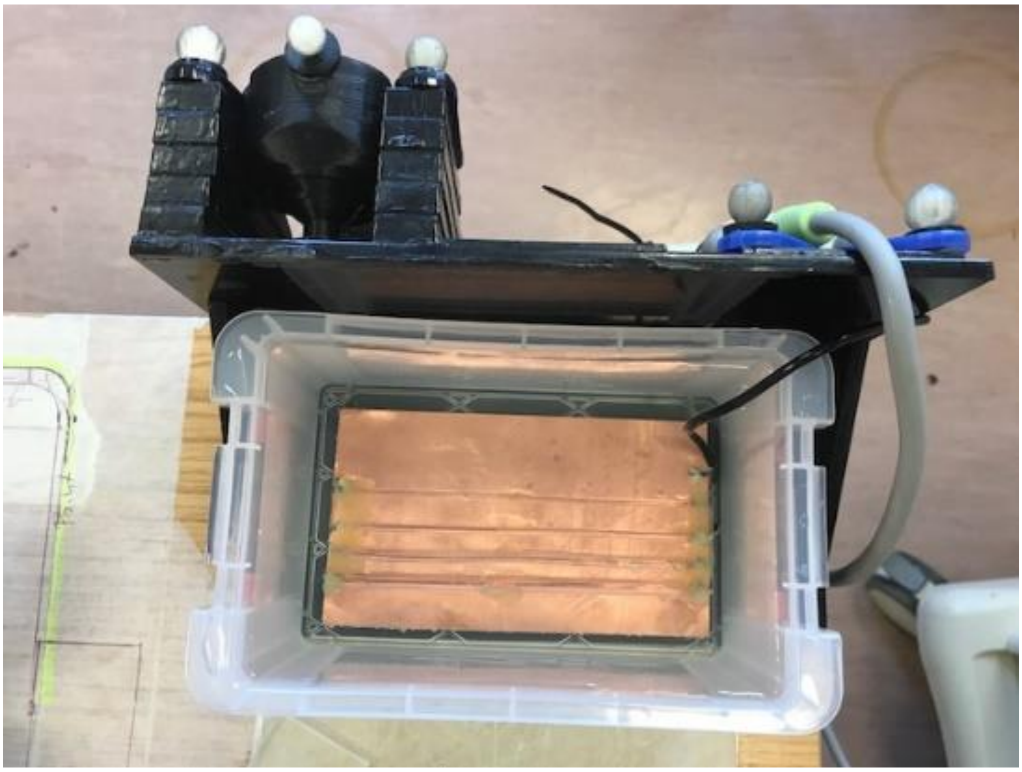

Figure 7-8 Phantom made with silicone tubes and electrical wires for PVWP detection Figure 7.8 shows the water tank with the blood vessel phantom and grounded plane. The entire setup is secured to the table using a set of ‘G – clamps' to reduce errors from the displacement of the setup.

7.3.2.3 Tissue phantom

Six samples of tissue phantoms were made, and every version had a different shore A hardness starting from 5-10(earlobe and soft structures), 10-15(fat), 15-20(muscle), 30- 40(Nose concha), 60-70(Heel), 70-80(Nose cartilage In Figure 7.9(a) image of the blocks of material phantoms with different material samples on the palette can be seen.

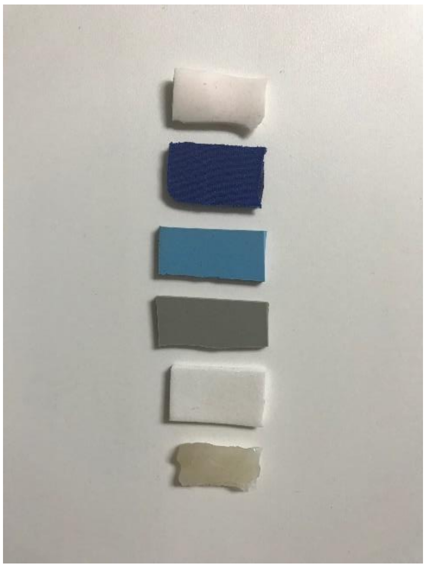

(a) Material samples palette

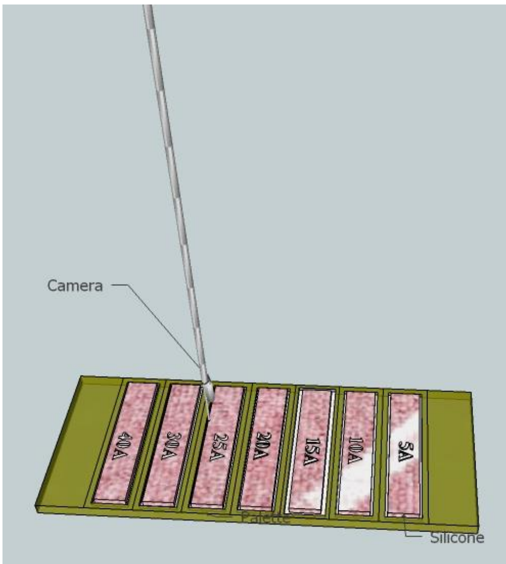

(b) Samples palette being tested by the port top

Figure 7-9 Tissue phantom with different silicone materials of varying hardness's

Table 7.2 shows the observations from the materials shown in Figure 7.9 (a) with hardness like those of tissues, measured using a Shore A Durometer.

Table 7-2 Materials of the samples seen in Figure 7.9 (a) and their hardness when tested by a Durometer

S.No.	Material description	Hardness Shore A
1	Silicone GP	10-15
2	Soft poly urethane	15 – 20
3	EVA blue	20-30
4	EVA grey	30 – 40
5	PLZ (plastazote)	40-50
6	Smooth on silicone	50-60

7.3.2.4 Fetal phantom development

Werner and his group conducted a virtual bronchoscopy on a virtual 3D model (Werner et al., 2011), (Werner et al., 2013). In this section, a similar virtual model of real fetal structures up to the primary bronchi is made for similar but real phantom testing. The fetal phantom is formed in several stages, as the fetus has internal structures which are required to be formed to simulate a simple procedure such as tracheal balloon occlusion.

1. Initially, the 3D model is obtained from an open source MRI image and converted to STL image of a 26 weeks old fetus(Bekiesińska-Figatowska et al., 2017). Skull of the fetus was re-designed as per the dimensions obtained from segmented MRI similar to the process used by Werner and his team (Werner et al., 2014).

2. Trachea, oesophagus, and tongue were 3D modelled based on the information gathered from segmented MRI of the (Szpinda et al., 2012) fetal anatomy(Werner et al., 2011) and (VanKoevering et al., 2015).

3. The sections of external and internal anatomy were 3D printed separately, and plastic welded together.

4. Multiple 3D moulds were made, and the surface finish was initially sanded and then acetone polished.

5. The hollow structures like the trachea were dip coated with platinum cured RTV silicone multiple times to obtain a thickness of at least 1 to 2 mm. Later the 3D printed skull is glued using silicone to the silicone moulded structures. The silicone was left to cure for 24 hours. The result can be seen in Figure 7.10(a).

6. The soft structures are bonded with the 3D printed skull using GP310 RTV silicone as glueing material as seen in Figure 7.10(b).

7. The external facial structures and the body of the fetus were done as two hollow 3D moulds.

8. The internal structures are then covered with the outer structures, and the defects were healed with the same RTV silicone material. The result of which can be seen in Figure 7.10 (d).

9. The neck of the phantom was made with very low shore hardness 10 A silicone so that it can be flexed and manipulated.

 (a)Silicone trachea and oesophagus	 (b)3D printed skull moulded with soft silicone
 (c)Lateral view of composite material phantom	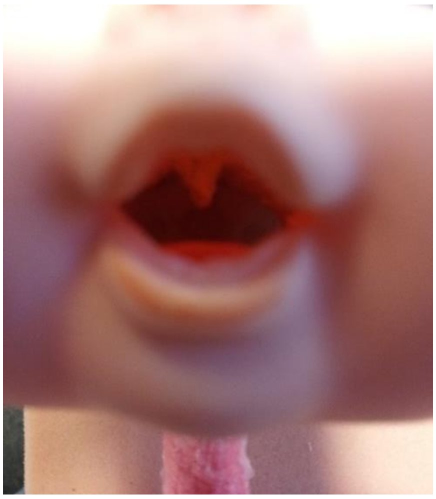 (d) Soft and hard tissue elements embedded inside fetal phantom head

Figure 7-10 Fetal Phantom development (a) Silicone parts, (b) Hard parts moulded with silicone (c) Lateral view composite phantom (d) Completely assembled head

7.4 Experiments and protocols

The effectiveness of the conventional ultrasound guidance can be compared only to having both systems present at the same time so that the control conditions remain the same. The proposed system requires a simple initialisation which was done using the flowchart discussed in the interface section (Chapter 6), and the system auto-calibrates itself as discussed in the earlier chapters (Chapter 3). For all the following experiments, the position and orientation of the water tank used is known in the world coordinate system with the calibration base for the fetoscope as the plane reference origin.

The position of the water tank and the markers under water were fixed. The water tank is set on the table to avoid any accidental movement. Also, the latex used for the water tank and the water tank itself is opaque, and the subjects are not aware of the contents of the tank. Video endoscope usage is considered only for some experiments which simulate the fetal surgery procedures. Whereas, the ultrasound guidance is used in all experiments.

The fetoscope used is the same for all the experiments. The only difference being the active elements of the fetoscope is turned off in the experiments were entirely manual surgical simulation is considered. The forces, movement coordinates, and orientation are constantly monitored during the experiments, and the video is monitored even if not used in some instances.

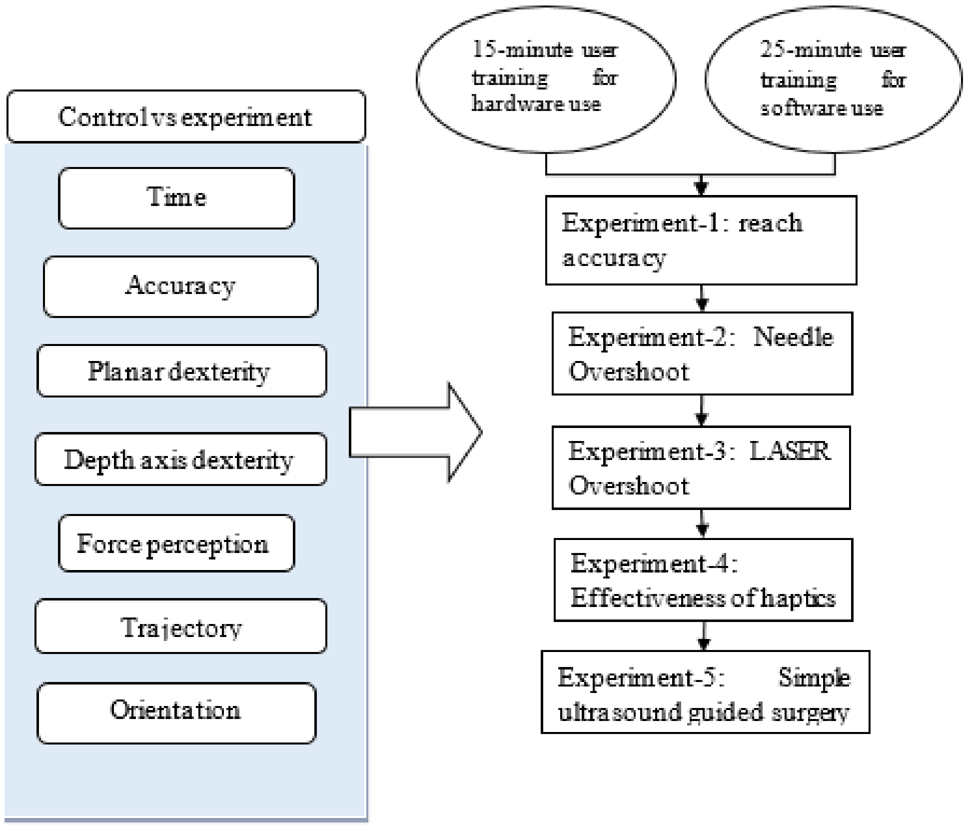

Figure 7-11 Flowchart of experiments and parameters measured

Figure 7.11 shows the general flowchart used for hardware and software training of the subjects for doing the evaluation experiments. In general, all the subjects are given a 15-minute training for hardware use and 25-minute training for the software use. After this training process, the subjects should be able to do the following functions independently:

1.Use of ultrasound to view targets

2.Registration of targets using the fetoscope and the navigation software

3.Ability to use the navigation guidance for reaching objects using the fetoscope.

4.Ability to use fetoscope features such as force feedback, OLED screen reading for checking visual force feedback.

5. Ability to understand use of LASER on the fetoscope and needle insertion functionality

7.4.1 Experiment 1 - Reach and Passive Movement accuracy

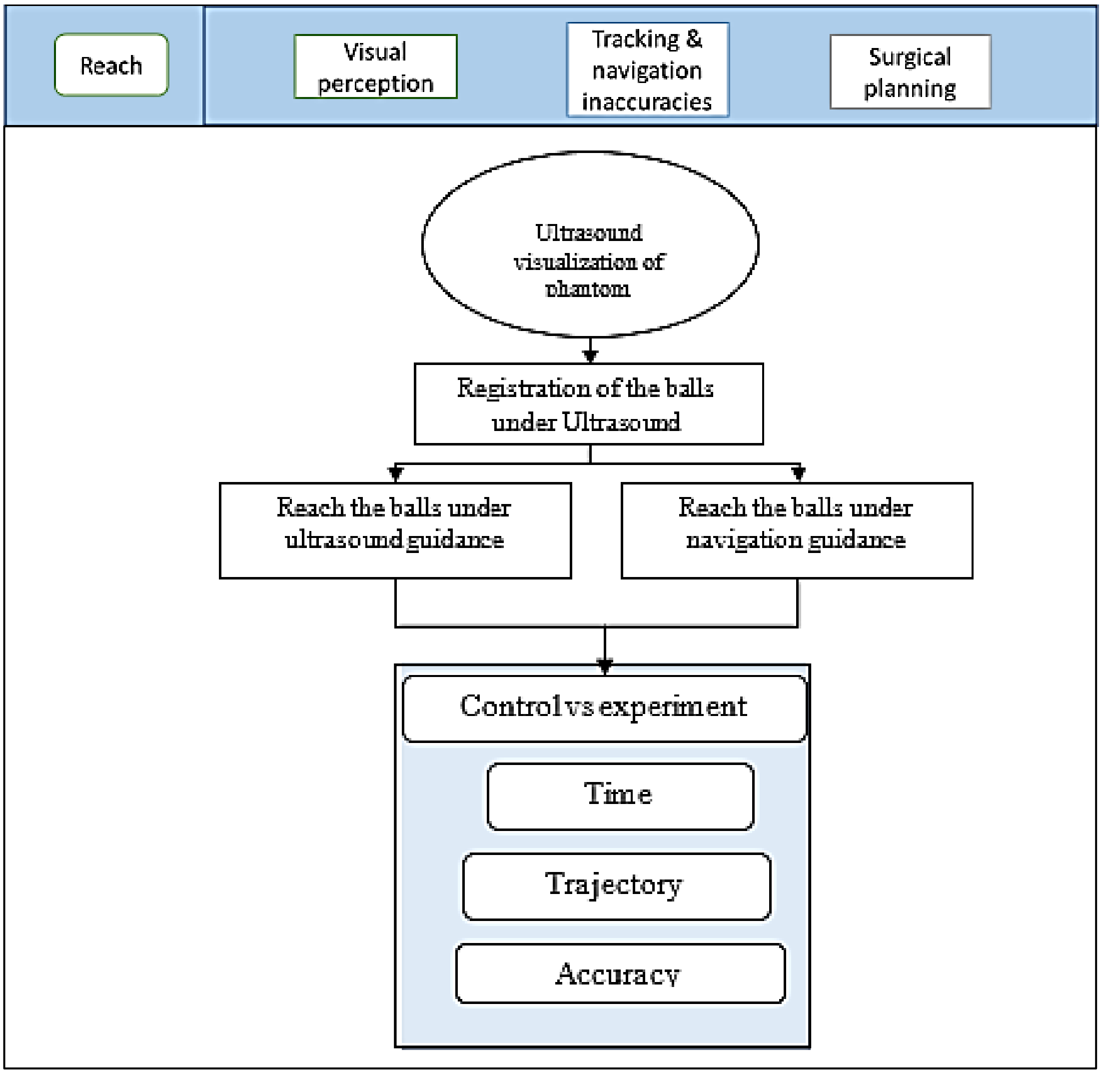

Figure 7-12 Flowchart for Experiment 1 for evaluation of reaching capabilities including time required, trajectory and accuracy

The ultrasound visible phantom which has been constructed as seen in Figure 7.3 is fixed in a known position inside the water tank using positioning magnets underneath. After the initialisation of the interface and hardware registration, the ultrasound visible objects are registered into the interface using the fetoscope manually. After this registration is done, the subjects are asked to follow the protocol shown in Figure 7.12. The subject is first instructed to USG scan the water tank and to find the object located in water with ultrasound guidance while their movements are being optically tracked and recorded.

The latter part of the experiment involves the subjects using the navigation and planning interface. Planning of the required kinematic path and finding the best approach is decided by the subject using the interface. The subjects are then instructed to reach the objects in the virtual environment which had been registered into the interface before the experiments, using the fetoscope by following the path they had planned. The subjects are informed that and any deviation from the registered objects would be considered an error. The subjects would be able to clearly see their movement trajectory in 3D while they do the navigation guided reaching.

The suggestions in the navigation interface for the reach experiment are in the form of visual cues on the fetoscope and are as described in the earlier fetoscope development chapter. Also, the computer display shows the amount of X, Y and Z translation required and indicates any 3- dimensional errors and boundaries to the marked target, provided the target has been registered correctly. The position and orientation data of the tip with respect to the corresponding targets assigned are measured. Once a target is reached, the subjects are informed on the interface that they had reached the specific target and can move to the next target. The rate of movement is tracked during the entire process, and the 3D trajectory is also recorded.

7.4.2 Experiment 2 - Manoeuvring, Dexterity, & Overshoot

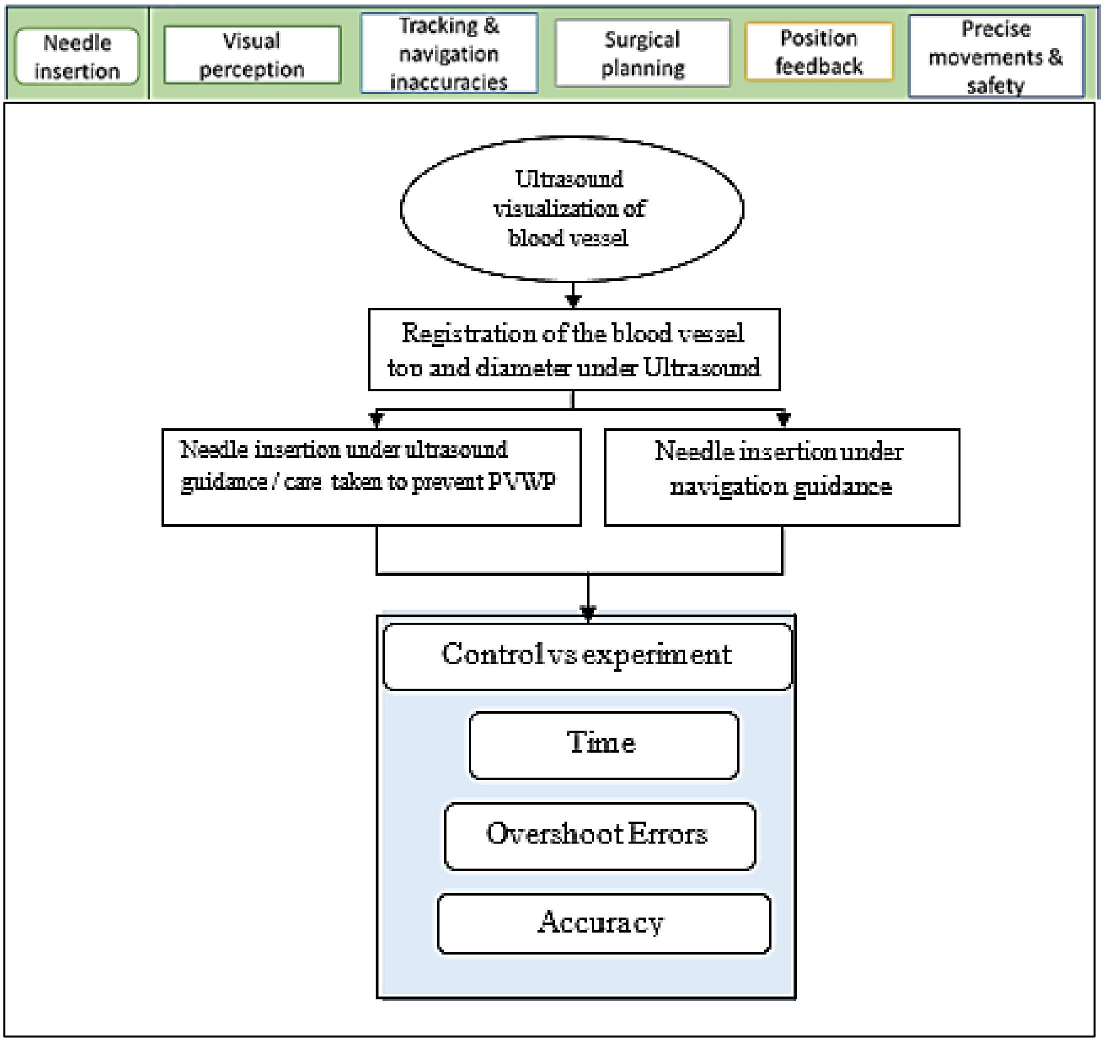

Figure 7-13 Experiments for evaluating Accuracy, Overshoot and Time consumed

Experiment 2 involves testing the needle insertion capability of subjects and how the navigation system helps the subjects improve the needle insertion accuracy. Blood vessel phantom designed and developed as seen in Figure 7.7 is used for this experiment.

As seen in Figure 7.13, the subjects are requested to do needle insertion using the fetoscope under ultrasound guidance, and the posterior vessel wall puncture is monitored by the microcontroller during this process, and the data is sent across to the computer, and a beep can be heard as an indication of PVWP. For the control experiment, the needle is inserted directly into the blood vessel phantom under ultrasound guidance, and the same is repeated 15 times by every subject.

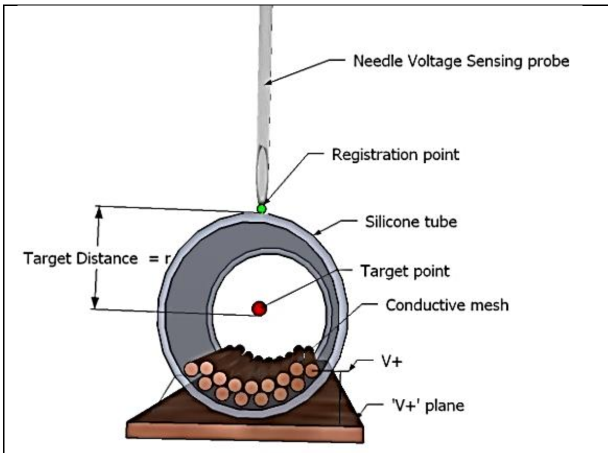

(a)Target set at the centre from the top of the vessel with radius 'r.'

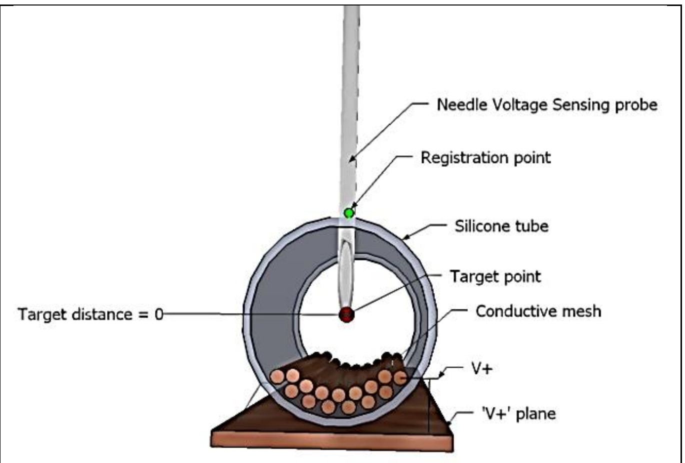

(b)Target reached target distance is zero

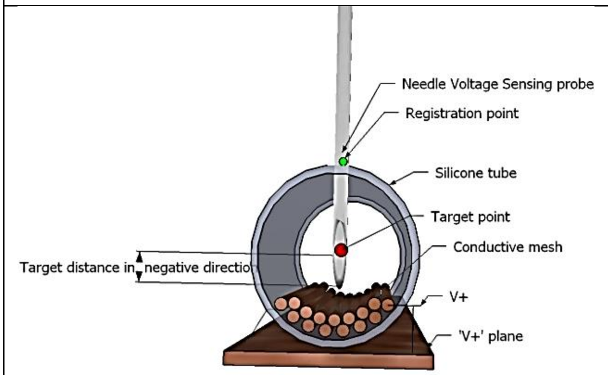

(c)Target past and distance is in negative direction

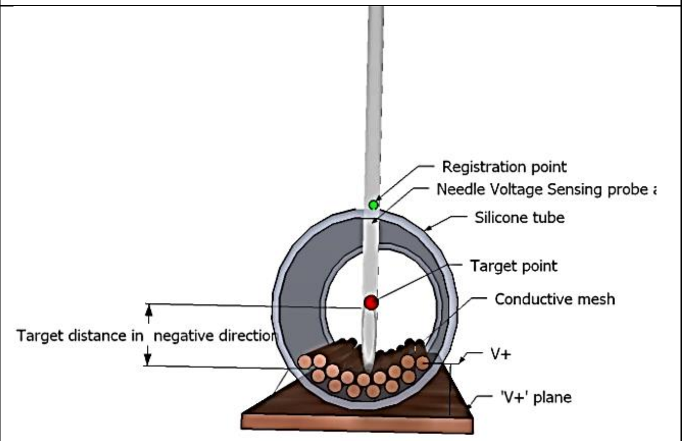

(d)Needle reaches copper mesh, and potential is '+V'.

Figure 7-14 Silicone tube phantoms for needle insertion under ultrasound guidance. When needle reaches the copper mesh, it makes electrical contact, and it signifies posterior wall puncture

For the latter part of the experiment with navigation-based needle guidance, the soft tissue blood vessel phantom is registered to the fetoscope using the process described in the Interface development chapter (Chapter 6), once the top surface of the blood vessel is reached under ultrasound guidance and is registered with 1 click-registration process described in (Chapter 6). After this process, the vessel diameter is measured in ultrasound, and the target is set at the radius as seen in Figure 7.14 (a). Once the needle is inserted further, and past the centre of the vessel as seen in Figure 7.14 (b) and Figure 7.14 (c), when automatic withdrawal is turned on in the interface, the needle withdraws automatically. The instrument indicates that the insertion is complete after the target of insertion is reached by the tip of the tool.

The posterior vessel wall puncture leads to the needle entering the conducting mesh placed on the posterior wall of the silicone tube as seen if Figure 7.14 (d). When the potential drops, the overshoot is recorded. The errors with and without overshoot control, the quantity and the frequency of the errors are noted, the same set of experiments are repeated with the other subjects.

7.4.3 Experiment 3 - Dexterity & automatic LASER safety

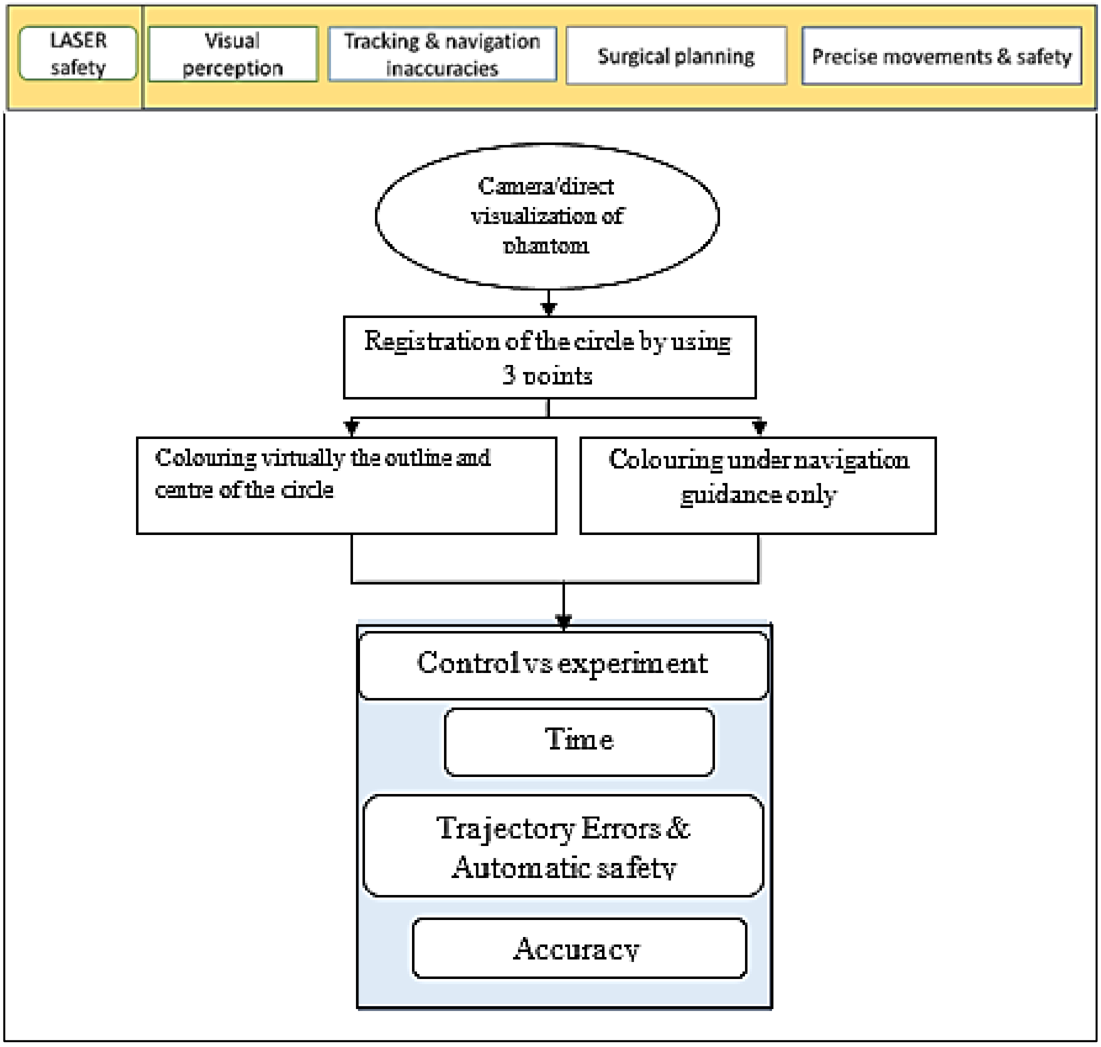

Figure 7-15 Flow chart for Experiment 3 involving measurement of overshoot, LASER Guidance, trajectory and Automatic safety and protection for LASERS

The third experiment is an XY planar variation of the previous experiment. This experiment evaluates the subject's control of lateral movements for use in LASER ablation. Figure 7.15 gives the flowchart of experiment 3. In this experiment, the subjects are instructed to use the Fetoscope to virtually colour a circular area as a raster using the LASER built into the fetoscope under video guidance. The subjects are requested to make close movements to the periphery of the circle.

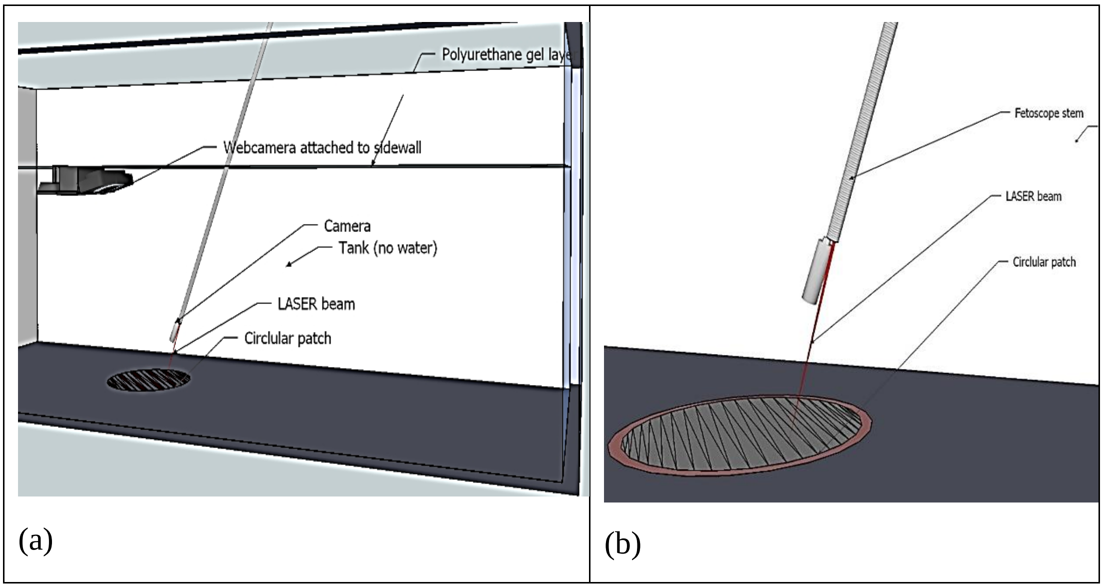

Figure 7-16 Overshoot identification experiment to find out overshoots during simple processes and comparing the effectiveness of the proposed system

For the variation of the planar overshoot experiment, the plane is registered using the fetoscope as described in Chapter 6 Figure 6.20 (b) using interactive markers. The same experiment is repeated with the proposed tracking and navigation system with automatic safety control switched on. The subjects would use the real-time guidance on the navigation guidance as shown in Chapter 6 Figure 6.20 (d). The circle on the tank surface is registered to the optical tracking system, and the area of interest is required to be rastered. The LASER automatically turns off when the beam reaches outside the margin of the circle, and the user is indicated by the LASER status. The subjects are requested to colour as quickly as possible with any random movement in another variation of the experiment.

The number of overshoots, the time required for the procedure and the user's perception of the difficulty of the procedure are considered, and the differences between the experiment and the control are analysed.

7.4.4 Experiment 4 - Force perception and haptic feedback

This experiment investigates the effect of different types of haptic feedback including proportional haptic, thresholded haptic and visual-haptic on force perception as seen in Table 7.3. This experiment utilises the impedance control haptic feedback and OLED force visualization capabilities and actuator control which can be seen in Chapter 5 which deals with the development of the robotic fetoscope.

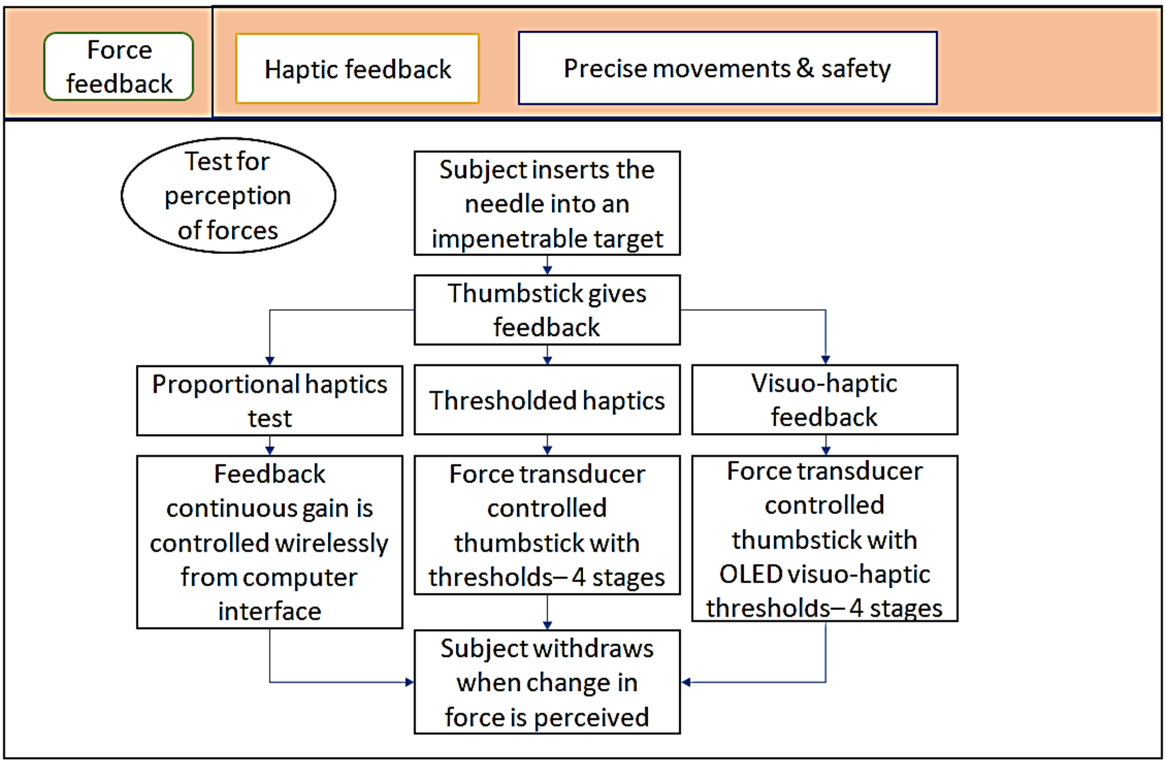

Figure 7-17 Force feedback evaluation experiment process

Figure 7.17 shows the flowchart used for testing the haptic feedback capabilities of the fetoscope device. The subject initially inserts the needle attached to the fetoscope tip into an impenetrable target. While doing the penetration, the subject gets feedback at the thumbstick in the form of force, vibration or visual display or a combination of the above. Whenever the subject perceives a change in the feedback of the force, the subject is required to withdraw. Table 7.3 shows the classification of the type of feedback, the corresponding advantages and disadvantages.

Table 7-3 Classification of the feedback used and comparison

S.No.	Type of feedback	Description	Advantages	Disadvantages
1	Proportional haptics	Haptics proportional to force	Represents true force	Human body is not sensitive to extremes of forces or vibration Memory dependence
2	Thresholded haptics	Plain vibration for set thresholds of force	Represents thresholded force Guaranteed feedback perception	No perception of true force Lack of specificity Requires manual resetting of thresholds
3	Hybrid haptics	OLED visual indication + proportional haptics	Clear quantification of force High sensitivity	Requires surgeon to look at the display

In this experiment attempts to quantify the different feedback perception by the subjects. While in most cases proportional haptic feedback works, with minimal access procedures, the forces encountered are in the order of millinewtons and can have a high dynamic range. To fit this range of force feedback into the fetoscope is possible but can be limited by human sensitivity to the low and the higher end of forces. Force threshold limitation and haptic indication have advantages in this area, as the surgeon can set the instrument to specific force thresholds depending on the type of the tissue encountered. The major problem with this method of haptic feedback is that this feedback is rather binary and needs resetting every-time a different tissue density is encountered.

The third feedback method uses the concept of neural integration(Takahashi and Watt, 2017) of different stimuli to re-enforce the force feedback with visual quantification and the surgeons can expect a specific force. The sensitivity at lower and higher ranges in haptic feedback is much higher as the surgeon knows what to expect.

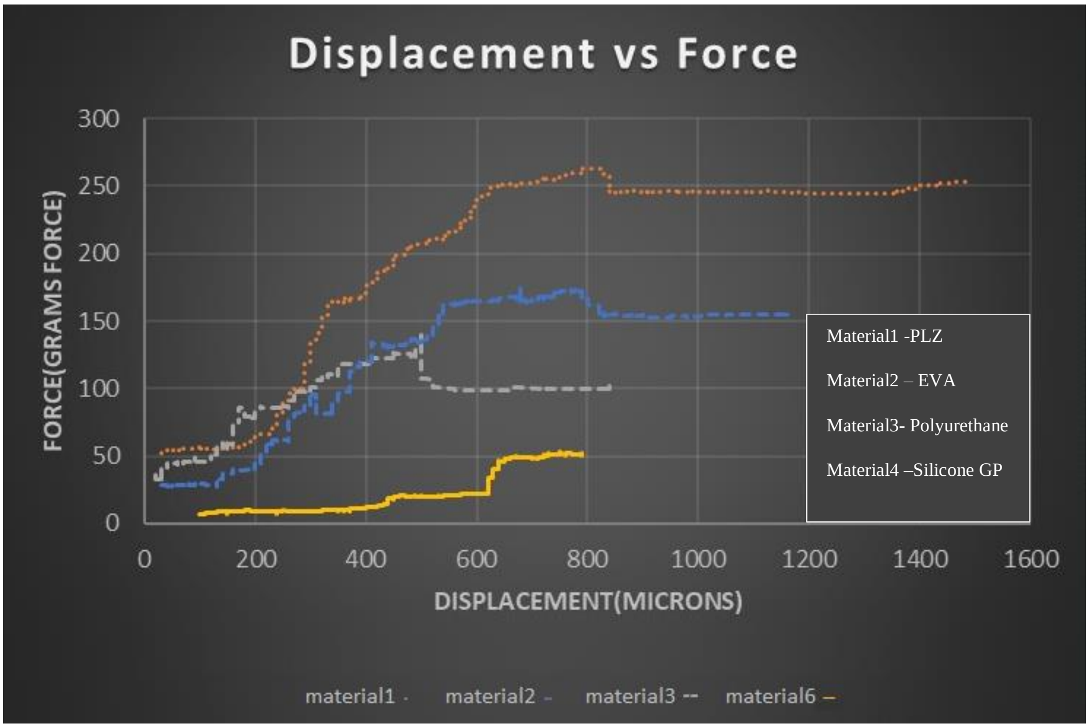

Figure 7-18 Displacement vs force characteristics of difference materials

Characterization of the material as perceived by the fetoscope transducer is first done by fixing the fetoscope to a stand and having the fetoscope automatically actuated, and the displacement of the actuator is compared to the force experienced on the respective material. In Figure 7.18, Plastazote (shore A 30-40), EVA (20-30), Polyurethane (15-20) and Silicone GP (10-15) are the materials tested. Post material characterization, the haptic thresholds are set at 20, 50, 100, 150 and 200-grams force based on the results seen in Figure 7.18. After the threshold setting, the perception experiments are performed using the setup seen in Figure 7.19.

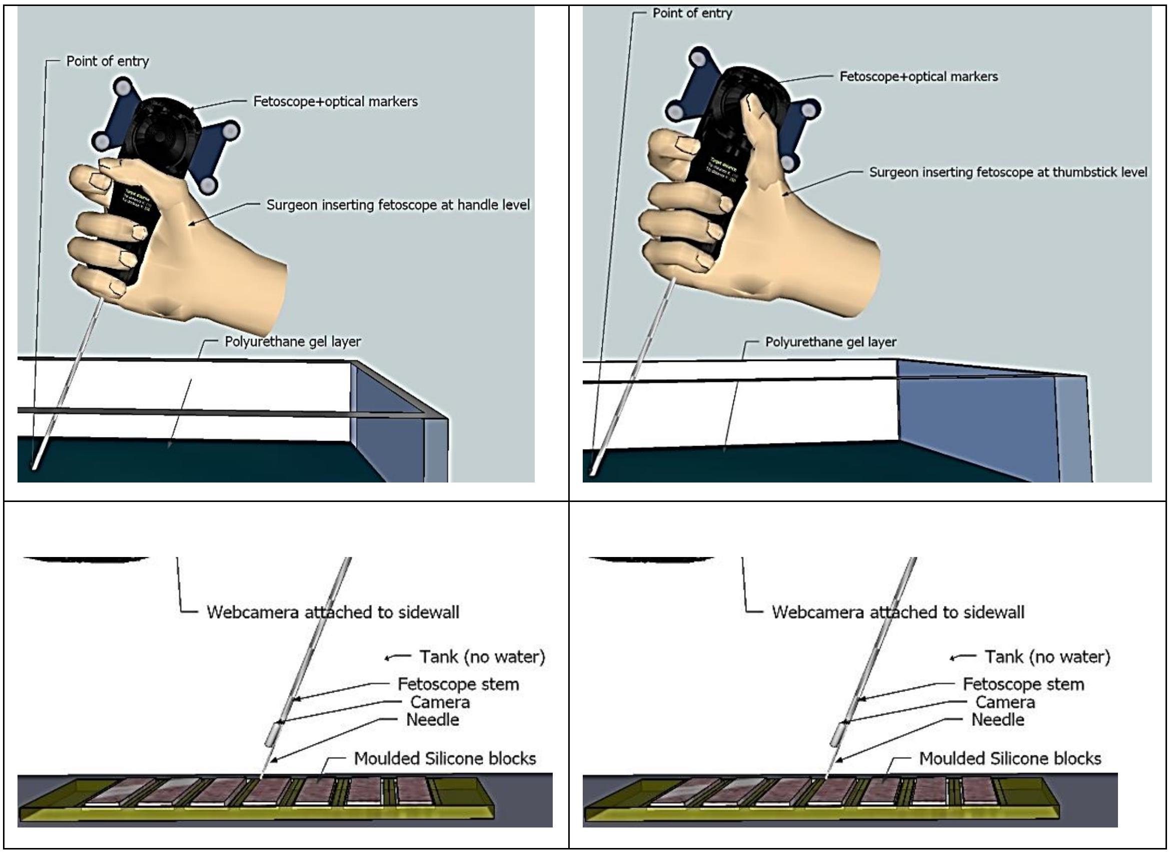

Figure 7-19 Experimental setups for evaluating fetoscope haptics and the subject's perception while using the haptics

7.4.4.1 Proportional haptics experiment

For testing the effects of proportional haptics, the subjects were instructed to attempt to insert the needle till they perceived force feedback and are then required to withdraw. The proportional feedback is switched on in steps of the thresholds set before which it is turned off. The rendered experiment setup is shown in Figure 7.19. As it can be seen the setup is very simple and involves a palette of material samples which were required to be penetrated using the fetoscope needle tip.

7.4.4.2 Thresholded haptics experiment

The second experiment involves indicating to the subject by vibration that they had reached the target force. When indicated the subjects are required to withdraw.

7.4.4.3 Visual haptic feedback

The third variation is done with the subject looking at the OLED display which shows the force and includes proportional/vibrational feedback. The subjects were shown the target force on the screen and were required to reach the force and then withdraw.

7.4.5 Experiment 5 - Fetal phantom balloon inflation

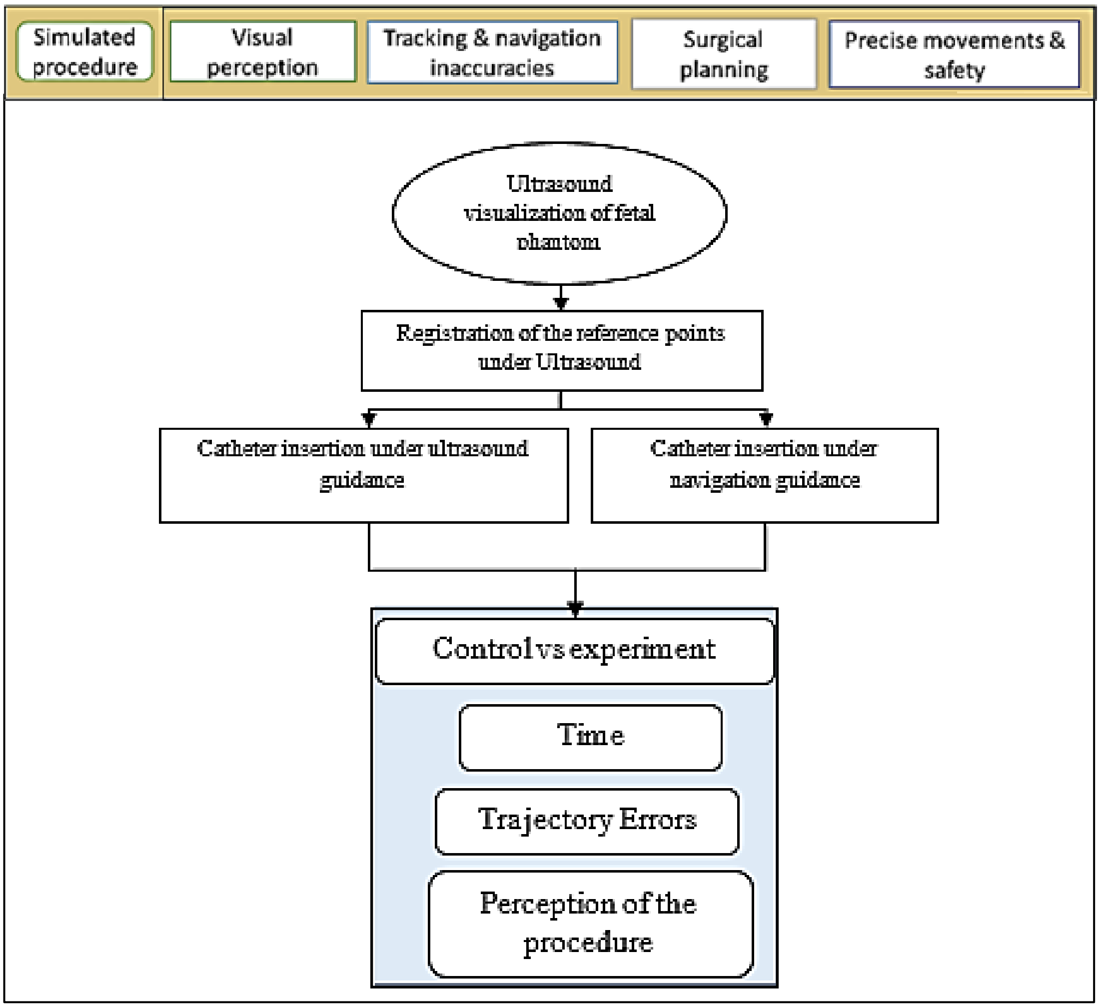

Figure 7-20 Flowchart Experiment 5 for simple surgical procedure demonstration and user perception

Experiment 5 is the final experiment and involves coordination and usage of most of the above components. For this procedure to be performed, the user needs to orient the fetoscope in a specific way to achieve a complete insertion in a trachea of seven centimetres in length (Szpinda et al., 2012), though in the actual surgical procedure, this is not required. The fetal phantom, as shown in Figure 7.20 (a) is placed underwater, and the subjects are requested to perform an ultrasound scan and then requested to simulate balloon inflation at different levels of the trachea, as seen in

Figure 7.20 (b). Initially, the experiment is done under ultrasound guidance, and the subject sets the target. Later, the experiment is repeated with tracking guidance.

Insertion of the tip into the trachea is not easily achievable unless the point of entry on the polyurethane gel, the mouth, and the tracheal orifice are almost in a straight line. In the interface, on the ideal ultrasound frame, the user does marking of the trajectory in 3D. The errors in reaching the target and the time taken are taken into consideration.

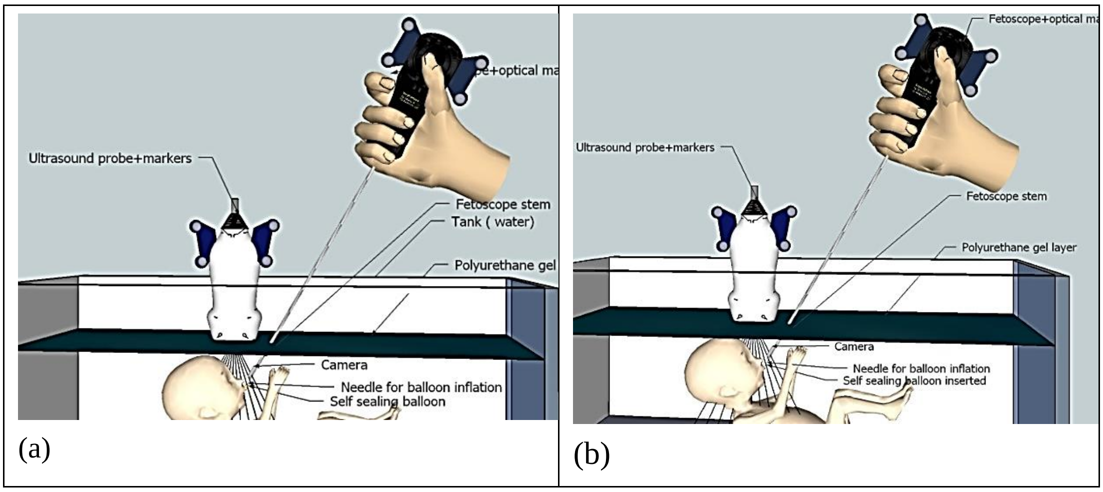

Figure 7-21 Fetal phantom under water setup for fetal balloon inflation experiment. Surgical simulation to assess the confidence of the surgeon and perception and compare it with the conventional ultrasound guided method

7.4.5.1 Operator's confidence and perception

Every robotics guidance system requires feedback for improvisation and effectiveness of control. Since this is entirely subjective, the subjects were requested to briefly report their perception in the surgical environment with every variation in tests and towards the end of the experiment about how the surgical guidance can be improved.

7.5 Summary

Table 7-4 Experiments proposed to evaluate different challenges faced during the surgery

Experiments	Evaluation of the possible challenges faced				
Reach	Visual perception	Tracking & navigation inaccuracies	Surgical planning		
Needle insertion	Visual perception	Tracking & navigation inaccuracies	Surgical planning	Position feedback	Precise movements & safety
LASER safety	Visual perception	Tracking & navigation inaccuracies	Surgical planning		Precise movements & safety
Force feedback	Haptic feedback	Precise movements & safety			
Simulated procedure	Visual perception	Tracking & navigation inaccuracies	Surgical planning		Precise movements & safety

Table 7.4 shows the list of proposed experiments to evaluate the performance of the proposed system with respect to the corresponding challenges faced during fetal surgery procedures.

7.6 Conclusion

A set of experiments have been designed to evaluate the capability of multimodality navigation and tracking system in conjunction with the robotic fetoscope. These experiments are designed with evaluation of the perception of orientation, accuracy of movements, force feedback and also the performance of the subjects along with improvements in dexterity.

Chapter 8

Discussion and Results

8.1 Introduction

The discussion and evaluation of the fetoscope and, the surgical interface design and development have been completed. In the previous chapter, the experiments have been designed for assessment of the solutions proposed for the corresponding problems faced during a surgical process. This chapter discusses the results of tests using the proposed experimental setups in the previous section, after the calibration of every system to the world coordinate system as described in the initial chapters.

In the previous section, the experiments required to evaluate the different aspects of the surgical system were discussed. However, these experiments have their limitations due to the physical constraints set by the hardware, software and the phantom, which need to be found and acknowledged, so that the experiments were done within the constraints set by the system. This chapter also discusses the experiments to find these limitations. The tests were designed to evaluate and compare the operator's accuracy, orientation capability, with and without the assistance of the system.

All experiments done by every subject are consecutive and have been designed to reduce fatigue and loss of concentration. The results obtained during every experiment are mostly real-time, and no error correction or post-processing has been applied to remove any relevant outliers, except the data acquired for calibration and during the idle phase in between the experiments. Estimation of accuracy and dexterity using data comparison between the control and the experimental output were the only data which were post-processed.

8.2 Aims

This chapter aims at discussing the constraints of the surgical system initially and then moves on to discuss the results of the five evaluation experiments of the system described in the previous chapter.

8.2.1.1 Targets for reach experiment

Reach experiment focuses on comparing the ability of the subjects to reach the objects under ultrasound guidance, to using Multimodality navigation guidance. Therefore, the targets set are as follows:

1. Demonstration that the interface can help the subjects navigate
2. Pattern of the strokes – clearer pattern less confusion
3. Proximity to the registered object

8.2.1.2 Targets for needle overshoot experiment

Needle overshoot experiment focuses on comparing the accuracy of the subjects while performing needle insertion into phantom blood vessels under ultrasound guidance, to using Multimodality navigation guidance. Therefore, the targets set are as follows:

1. Demonstration of one-click object registration and sub millimetre guidance
2. Sub millimetre accuracy of needle insertion into the registered phantom
3. Eliminate posterior vessel wall puncture

8.2.1.3 Targets for LASER overshoot experiment

LASER overshoot experiment focuses on comparing the ability of the subjects to colour a circle under visual guidance, to using Multimodality navigation guidance. Therefore, the targets set are as follows:

1. Demonstration of LASER or RFA safety using software and hardware

2. Pattern of the strokes and distribution- indication of confidence
3. Reduce overshoot and have strokes within the area of interest
4. Reduction in time take for the process of colouring

8.2.1.4 Targets for force perception experiment

Reach experiment focuses on evaluating the ability of the subjects to perceive force feedback from phantom objects while using haptic feedback.

1. Demonstration of hardware haptic functionality
2. Evaluating the sensitivity of human hand to different types haptic feedback
3. Proving that visuo-haptic feedback is better than mechanical feedback

8.2.1.5 Targets for fetal phantom simulated procedure

Simulated procedure experiment focuses on comparing the ability of the subjects to reach the objects under ultrasound guidance, to using Multimodality navigation guidance. Therefore, the targets set are as follows:

1. Demonstration of multimodality tracking in a simulated surgical environment
2. Demonstration of target guidance
3. Pattern of the strokes – clearer pattern less confusion
4. Proximity to the registered object

8.3 Investigation of the feasibility of experiment by finding the constraints

Every experimental procedure has its limitations, either imposed by the setup or the subjects. An investigation is performed as a set of minor experiments to quantify these constraints and to find if the main experiments and the controls fall well within these limits. If a physical obstacle would limit the central experiments, the subjects are informed about the specific constraint. If the subject encounters such a constraint, the experiment is then repeated.

8.3.1 Quantification of theoretical hardware constraints

The experiments rely on hardware elements such as optical tracking, ultrasound and robotic fetoscope. Every component used in the hardware has limitations on resolution, size, position, orientation, and line of sight constraints, which will be discussed in further detail below:

8.3.1.1 Constraints for optical tracking

The line of sight problems with optical tracking have been discussed earlier, but there are other problems which are due to the field of view. Therefore, the perimeter of optical tracking is limited to the field of view of the tracking system and the distance from the tracking base. The tracking accuracy increases and errors decrease with a decrease in the distance while the tracking extents reduce as well. Hence most optically navigated robotic surgeries take place in a location which is not more than 2 meters away from the tracking system (Prada et al., 2014). The quantification of maximum and minimum translational extents is done by simple perimetry using the setup shown in Figure 8.1 was performed in the XY plane of the tracking volume. The lab-stand with the optical marker fixed at a specific height was translated to the maximum extent of tracking (till tracking loss happens) and the readings were recorded. The experiment was repeated at different heights of the marker from the table to find the maximum Y-Axis limit.

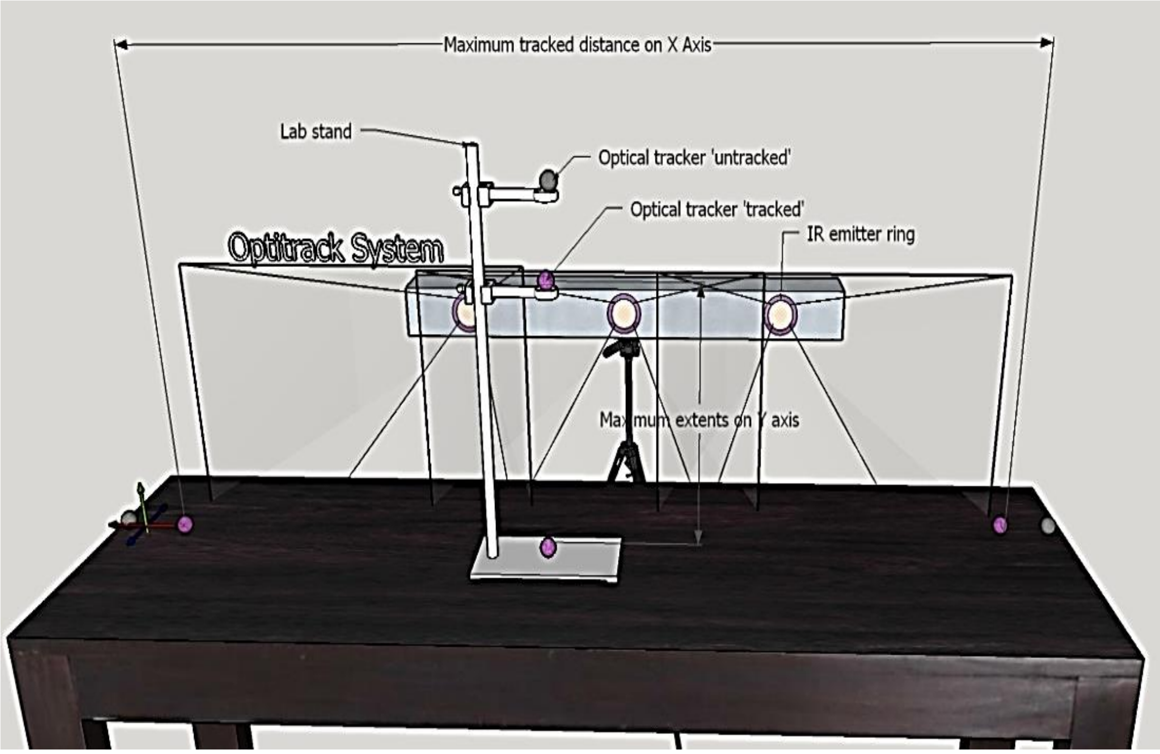

Figure 8-1 Shows the setup used for finding the perimeter of tracking at 2 m distance from the Optical tracking system

From the experiment, the maximum and minimum extents found are presented in the Table 8.1 at 1.745m.

Table 8-1 Perimetry at 1.745m

Direction	Maximum extent(mm)	Minimum extent(mm)
X	727.99	-947.49
Y	592.38	-383.16

8.3.1.1.a Finding rotational limits

Further, the tracking errors of orientation increase with an increase in the tilt of a rigid body along an axis of rotation and beyond a particular angle of rotation, the markers start overriding resulting in complete loss of tracking and position estimation. The theoretical limit given by Natural point for the Optitrack system is 90 degrees, while the practical limit can only be estimated by experiments. For the rotations to be observed in the 'Motive' software from NaturalPoint, 4 to 5 markers are selected in the interface to form a rigid body. Such virtual rigid bodies automatically create a virtual centroid marker and stream across the centroid position and the quaternion rotations about an axis.

Pitch limits estimation setup

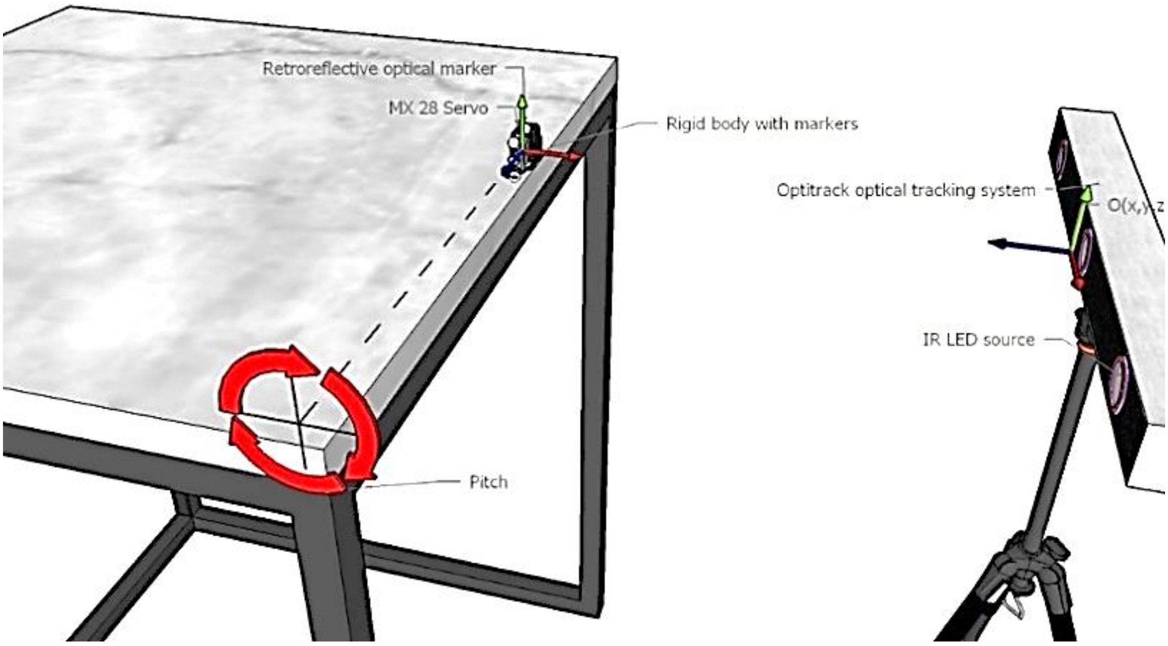

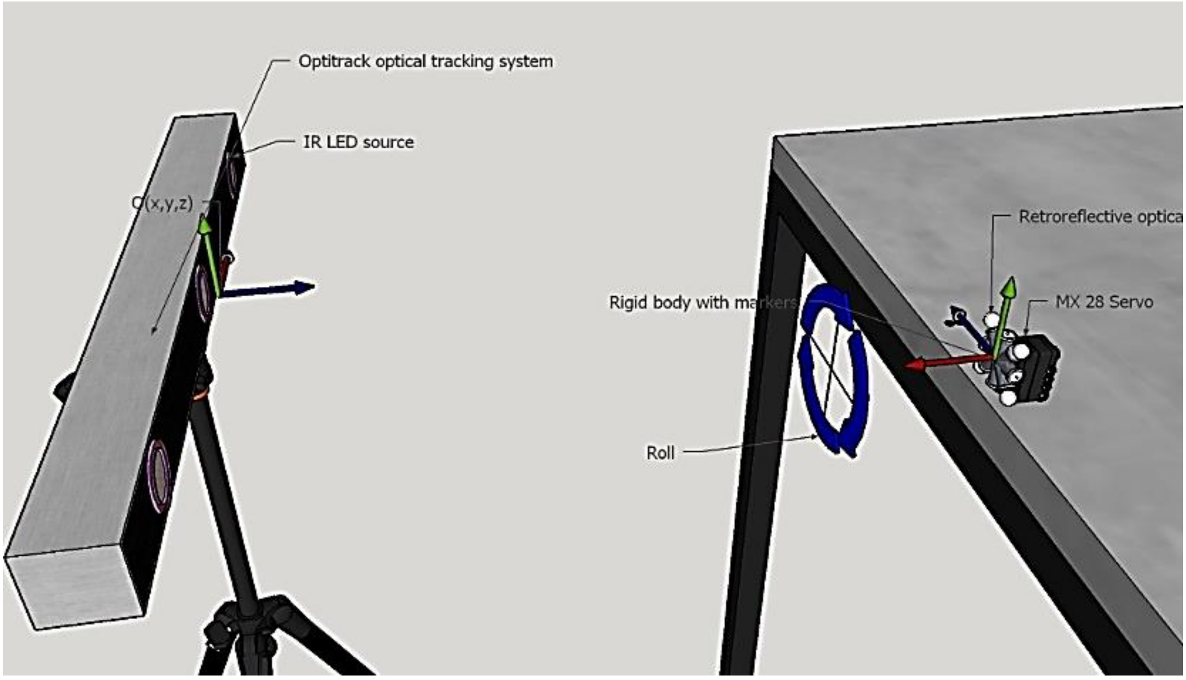

Yaw limits estimation setup

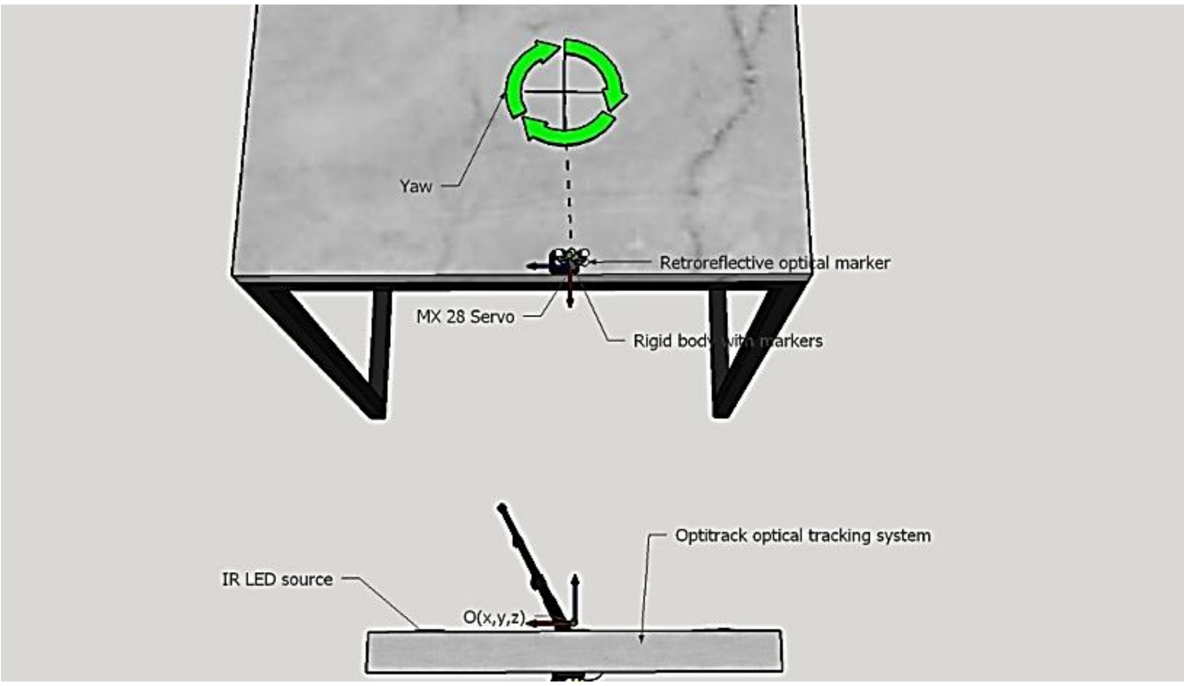

Roll limits estimation setup

Figure 8-2 Rotational limits estimation experiment (a), (b) and (c) shows the setup for pitch, yaw and roll limits estimation

The experimental setup as shown in Figure 8.2 (a), (b) and (c) involves the use of MX-28 servo with a 12-bit absolute rotary encoder with 0.08-degree resolution. The digital servo is controlled serially with a RS 485 interface and commanded to rotate the Optical marker cluster with increments of 0.25 degrees while being tracked by the tracking system. The Optical marker cluster is first rotated in the Pitch direction, and the respective orientations are observed from the Naturalpoint interface, and then the same is repeated with every plane of rotation.

Table 8-2 Range of measurement along the three directions of rotation at 1.745m

Direction	Roll range(degrees)	Pitch range(degrees)	Yaw range(degrees)
Minimum	-109.41	-40.84	-41.87
Maximum	113.90	10.63	8.31

From Table 8.2, the Pitch and Yaw had similar rotation range of about 50 degrees and Roll had a range of about 220 degrees.

8.3.1.1.b Velocity constraint for tracking

The maximum speed which can be reached using the tracking system is entirely dependent on the frame rate of the tracking system. When the speed exceeds the maximum trackable velocity at that specific frame rate, there can be a complete tracking loss or intermittent tracking. Therefore, the maximum limit of velocity had to be determined.

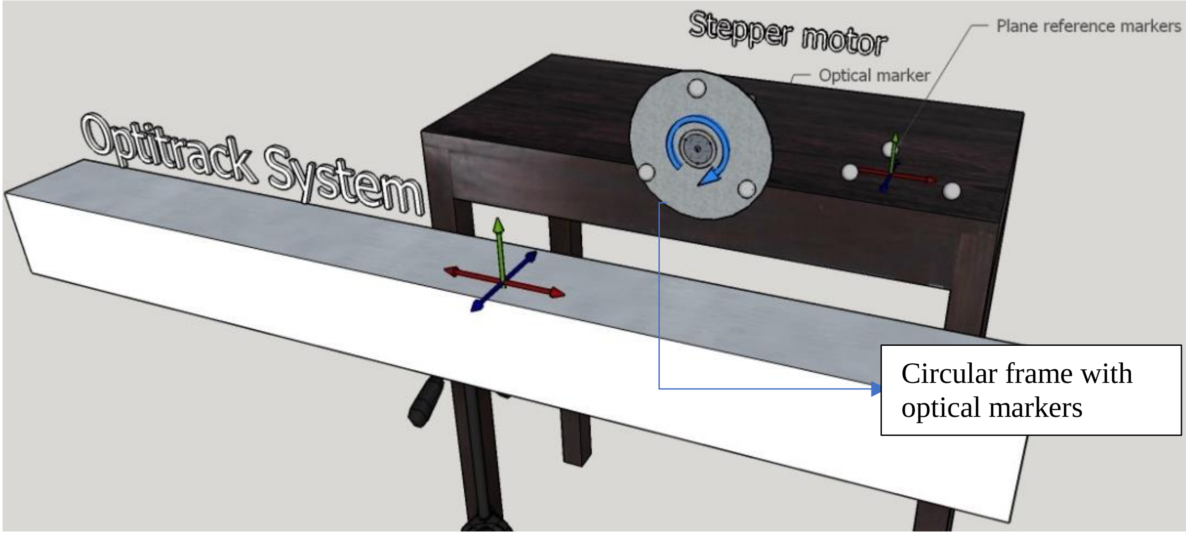

Figure 8-3 Setup for estimation of maximum velocity using the optical tracking system

For the determination of the velocity constraints, the rotating optical marker experiment(Song and Godøy, 2016) is performed to estimate tracking loss. Figure 8.3 Illustrated the setup used to determine the maximum velocity of tracking. Three optical markers were placed on an acrylic disc fitted to a stepper. Since rigid body tracking does not work after 220 degrees of roll, the tracking was done to monitor individual markers. The experiment was repeated, and the maximum velocity was found using the observations to be approximately 727 mm/s at 100 frames /sec approximately. After this velocity, there is a complete loss of tracking. Therefore, if the surgeon's speed of movement exceeds this limit, there can be tracking loss.

8.3.1.2 Dimensional constraints imposed by the stem

The influence of tip size on the procedures has been described in the literature review. Ideally, the smaller the surgical instruments permit access to crevasses and highly confined spaces. However, visibility and orientation constitute a significant concern. In MIS, cameras are required to be able to view the tooltip, and therefore, the camera size and field of view are primary considerations which limit the size of the tooltip. Apart from the size, there are procedural constraints influenced not just by the tip size but also the flexibility of the tip, as the direction of approach is a concern when it comes to complex microsurgeries.

As a rigid tip cannot alter its degrees of freedom as a flexible tip, there are limitations to the approach which can only be solved by a flexible tip. But a rigid tip can be tracked quite readily using optical and mechanical tracking systems while a flexible tip cannot be that easily tracked even with magnetic tracking. The magnetic trackers are highly sensitive to the presence of ferrous materials (Prada et al., 2014) in the surroundings and can easily pick up radio-frequency noise from the wireless communications and active magnetic actuators. Though RF TOF tracking could be used for position estimation in 3D, the resolution achieved so far is a few millimetres and is beyond the scope of coverage of this thesis.

8.3.1.3 Tip size and video visibility constraints of fetal surgery hardware

Tip size is limited to the size of the camera and lighting put together, which amounts to about 3.8 to 3.9 mm. The limitation due to the dimensions leads to a restriction in the smallest spaces the camera can reach, but this restriction can be bypassed with the use of smaller cameras with a similar resolution. For the set of experiments done the tip size forms the primary constraint regarding approach, and only tubes greater than 4mm inner diameter are used for the same reason.

The field of view of the camera used is 60 degrees, but with servo panning, the field of view has been increased to 120 degrees. The lighting primarily used is warm white, but since the IR LED 880 nm is also included, it offers more penetration of the mucous membranes than the visible light spectrum. Though this is the case, the size of the camera restricts entry into smaller structures.

Video interference from RF sources including diathermy and RFA are other limitations regarding using a tip video system. Though the camera is shielded and grounded, the interference from high electromagnetic and static fields is expected.

8.3.1.4 Limitations due to ultrasound propagation

Ultrasound propagation problems through the air and hard substances have been well studied and understood. It is quite well known that ultrasound images may not reveal the true representation of the underlying fetoscope tip to environment interaction, resulting in false observations. Some of the observations can be seen in Figure 8.3, where the proximity leads to differences in visualization and in Figure 8.9(in page 325), where the size of the object leads to confusion.

Since the resolution of the ultrasound images is comparatively lower than those from cameras because of the limiting factors of sound propagation at low frequencies, smaller objects seem to produce more errors regarding size and shape than larger ones. Though this has been the case, it has been taken for granted in most ultrasound-guided procedures as most ultrasound-guided procedures look at structures which are more than 1 mm in size. Figure 8.10 (d) (in page 326) illustrates the missing vessel orifice with narrowing of the vessel diameter.

There is also a variation due to varying densities resulting in the variation of sound velocity. Therefore, the time of reflection is much quicker from a dense object, resulting in differences in the size measured. Silicone and latex were used, as they share properties to that of human tissues are very close to water, regarding sound velocity.

8.3.1.5 Limitations of maximum velocity, force, and latency of the actuators

The maximum measured velocity for the custom-built actuator is approximately 10mm/ sec calculation at 3.6 to 4 volts operation. The latency of the actuators depends on the PWM frequency, processing time and reaction time of the actuator. In this case, lag is a result of the PWM frequency - 50Hz, resulting in a delay of 20ms peak to peak, with a processing time of less than 2ms, along with an actuator reaction time and the velocity above combined. Though the latency cannot be perceived by the user, when used with active moving structures, such as with beating heart surgeries, acceleration requirements are much higher.

The stall force of the actuator is 8 N. Higher forces would mean increased size or higher gear ratios and lower velocity. Hence, to keep the force high enough, without compromising the velocity, the gear system was chosen to suit the requirements in a surgical field (Yamanaka et al., 2015). Though the force transducer is capable of taking up much higher forces, the micro capacitance measurement system has a less dynamic range of capacitance measurement and therefore cannot measure anything beyond an equivalent capacitance generated by the transducer over 20N of the applied force.

8.3.2 Subjects

The fact that there are only a few fetal surgeons around the world has been described earlier(Yao et al., 2014). Because of the limitation of availability of trained medical professionals when it comes to fetal surgery, volunteers had to be trained in simple manoeuvres were utilised to do the tests. The idea behind these experiments being that if subjects with less training can perform the given tasks with the assistance of the system in a shorter period and with lower errors, the system should be able to assist a trained surgeon without question. However, the amount of which it can be helpful to fetal surgeons cannot be quantified, as the available subjects are non-fetal surgeons.

A total of 5 subjects were recruited of with 3 were non-medical postgraduate students, of which 2 were medical doctors with prior ultrasound training, 2 were postdoctoral researchers, and 1 was a lecturer. Every subject was given 30 minutes to complete all the experiments.

8.3.3 Summary

Based on the experiments done to find constraints, the subjects are always suggested to make sure that the rotation of either the fetoscope or the ultrasound probe does not exceed +/- 30 degrees. It is made sure that the fetoscope and the ultrasound probe are always within the tracking volume and the experiments are done well within the tracking volume. Since the maximum velocity of surgeons within MIS environment can be tracked quite reliably with a frame rate of about 30 Hz based on the results obtained from the frame rate estimation experiment, a frame rate of 50 Hz is used for additional reliability and but is not increased any further to avoid overloading the navigation and guidance system.

8.4 Discussion of observations made during experiments

All experiments are guided by automatic 3D camera viewing angle, determined by the position of the ultrasound probe post- registration. Interfaces have developed for every experiment, and the data collection and recording are automated. For needle insertion experiment, the ultrasound probe was fixed using a magnetic base clamp for convenience, while other experiments which require ultrasound guidance, handheld ultrasound guidance was used.

8.4.1 Experiment 1 - Reach

Under ultrasound guidance, the subjects did not have any difficulty finding the dip coated polystyrene balls and marking their presence on the ultrasound frames. These markings form the targets which the subjects were required to reach. However, while locating the balls using the fetoscope tip under Ultrasound guidance, subjects had to coordinate with the ultrasound and the tip movement. During the coordination process, the subjects were required to locate the position of the stem through ultrasound image. However, if the stem is out of the plane, it made the subjects uncertain about the tip position.

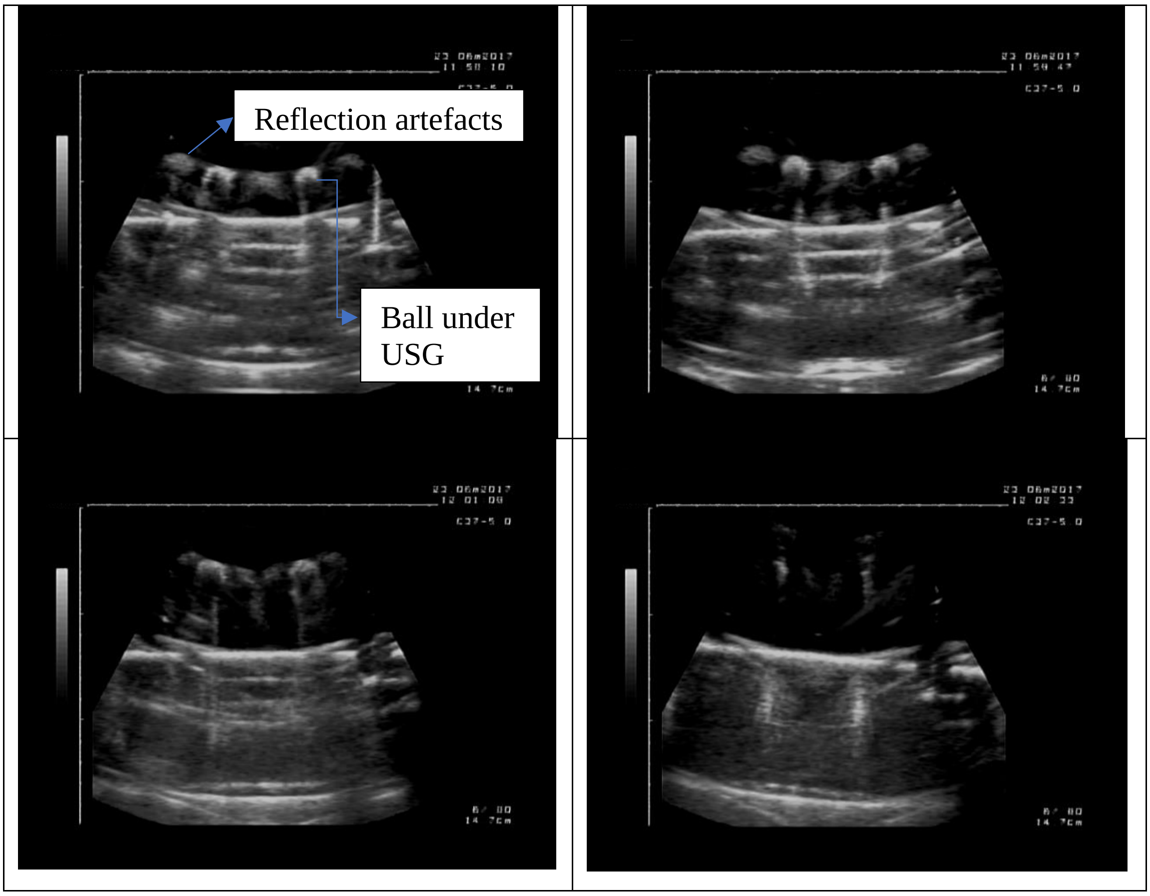

Figure 8-4 Observation of markers under ultrasound examination without fetoscope

In Figure 8.4, the polystyrene balls can be seen in the first row. However, the image of the ball became less clear when the distance between the ball and the ultrasound probe reduced as seen in the second row of Figure 8.4.

The top most surface of the polystyrene balls is touched with the tip of the fetoscope under ultrasound guidance, and registration of the corresponding position is registered using the foot pedal. Optical tracking line of sight is maintained for the entire experiment.

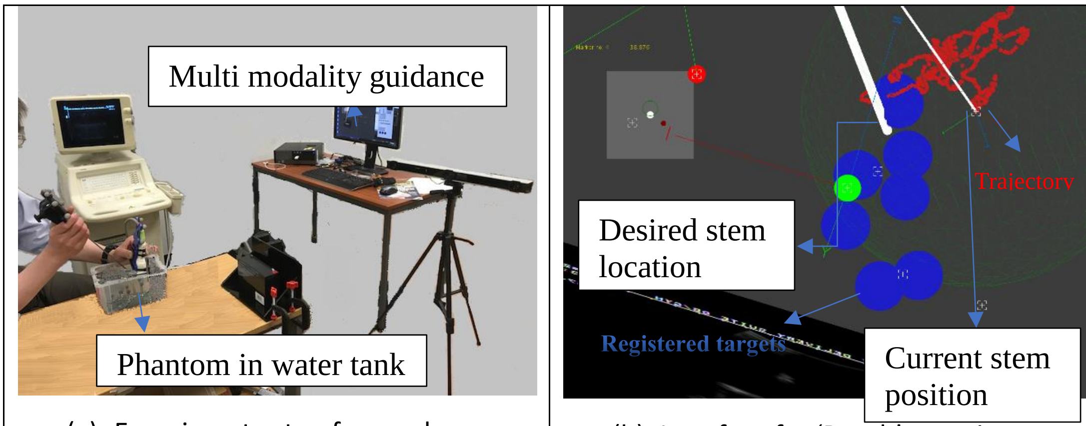

(a) Experiment setup for reach

(b) Interface for 'Reach' experiment

Figure 8-5 Experiment – 1 setup with one subject and assistive navigation user interface. User interface for Experiment -1 Reach

Figure 8.5 (a) shows the experimental setup with one of the subjects. Figure 8.5 (b) is the assistive navigation interface with automated scene camera orientation discussed in the earlier chapters. The blue balls in the interface indicate the registration points, and the red dots show the trajectory of the tracked movements.

8.4.1.1 Results

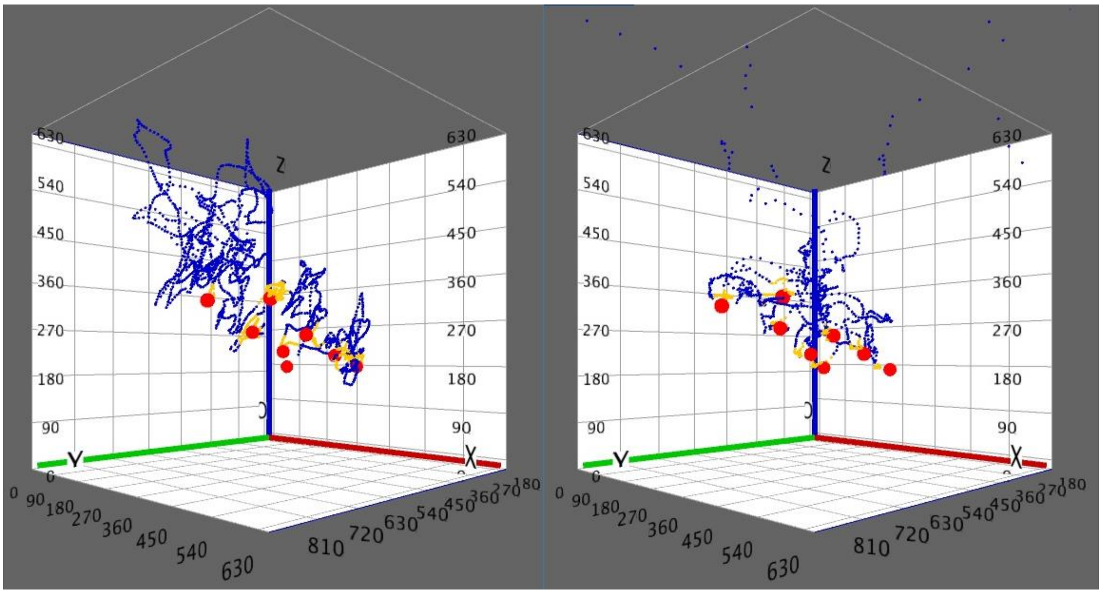

Figure 8-6 Trajectory comparison between navigated and un – navigated methods of reaching. Red balls indicate registered points; yellow markers indicate proximity to the markers and blue points indicate the trajectory(a) The results of using ultrasound navigated version of the surgery (b) The results of using multi-modality navigated surgery

Figure 8.6 (a) and (b) present the average distances between the set positions and the positions reached by the respective subjects using ultrasound. Where 'Red balls' indicate registered positions under ultrasound and 'Blue dots' indicate the trajectory and 'Yellow dots' indicate proximity to the corresponding red ball target. It can be observed that the distance is considerably higher, and the subject had more confusion to reach the target position, shown by the number of yellow dots near the target position when only ultrasound guidance was used. Multimodality tracking, on the other hand, resulted in finer strokes and contributed to lesser confusion, seen as lesser number of yellow dots near the target as seen in Figure 8.6(b).

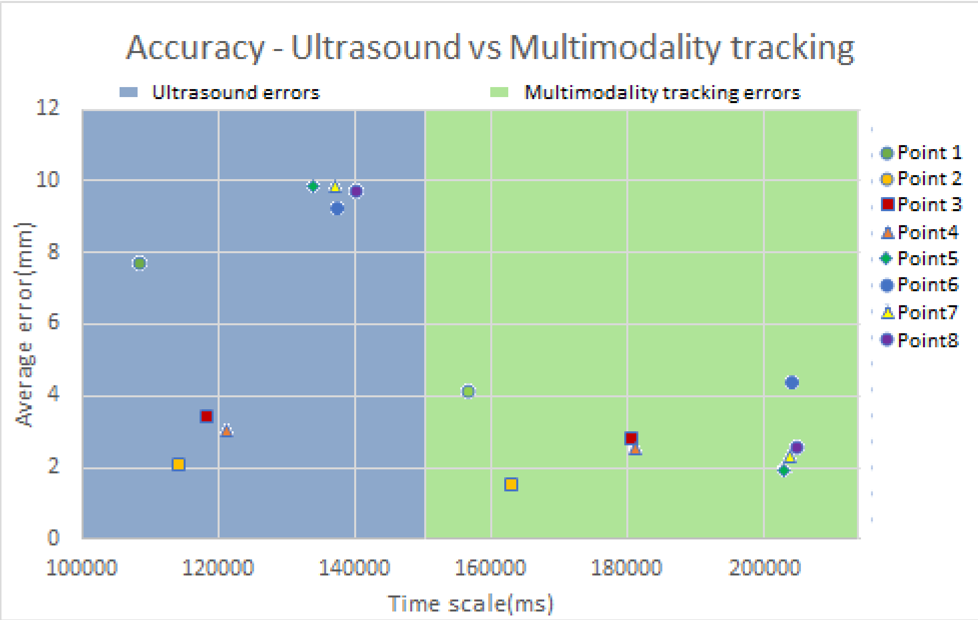

Figure 8-7 Graph distance to target using ultrasound vs distance to target using fetal surgery assistance system

Figure 8.7 shows the corresponding average error distance and time taken to reach ball target. The results of Figure 8.7 suggest that the time taken to reach the Polystyrene ball targets is much higher when the subjects used only ultrasound guidance. On the one hand, it seems to indicate lower effectiveness regarding consumption. Whereas, on the other hand, the proposed tracking system guidance resulted in finer strokes, indicating higher confidence levels and the subjects could concentrate more on getting the position of tip correct.

8.4.1.2 Conclusion

The trajectory of the instrument movement is usually an indication of the confidence of the subjects. When the subjects waver before reaching the target, it shows lack of confidence. From the results, using the ultrasound images only for guidance to find a position, not knowing the tip position related to the ball-target, the subjects tended to waver and even touched different points at times. Whereas, with the proposed tracking system, the users did not fluctuate much and reached the position with relative ease and stability. It can be inferred that the subjects, in general, had a better sense of orientation and had a better perception of the relationship between the tooltip and the target in 3D space. Wavering with a surgical instrument can potentially lead to injuries, especially if the tooltip is either sharp or contains powered actuation. The proposed tracking system may help in reducing such problems.

8.4.2 Experiment 2 - Needle insertion experiment

The subjects were instructed to perform needle insertion under ultrasound guidance. The subjects first mark the top of the blood vessel where the needle is to be inserted one by one. After the procedure is completed, the same experiment is repeated using the proposed needle guidance system with overshoot protection feature enabled.

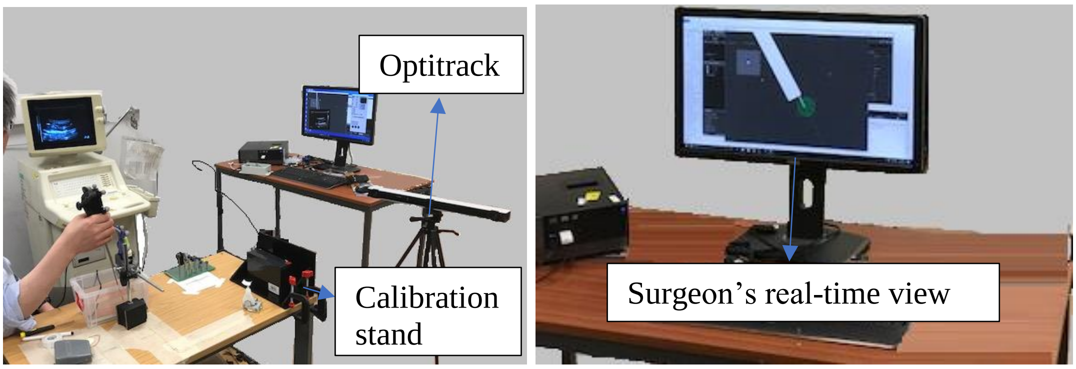

Figure 8-8 Setup for the needle insertion experiment with one subject (left) and user interface (right).

The setup used for needle insertion experiment is shown in Figure 8.8. The ultrasound probe was supported by a magnetic stand, so that the subject can focus more on the experiment, instead of having to concentrate on holding or directing the probe. The subjects were instructed to have the fetoscope optical markers always facing the tracking system.

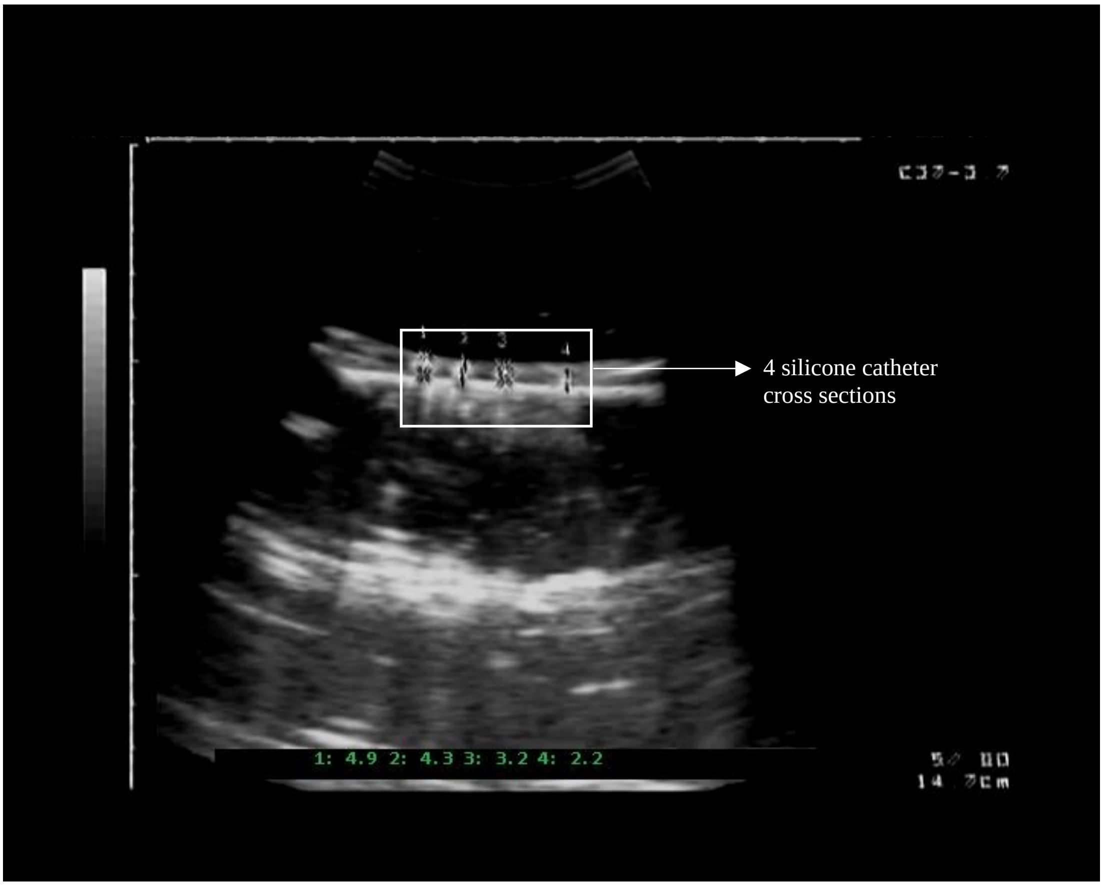

Figure 8-9 Blood vessel phantom under ultrasound. The diameters of 4 vessel phantoms are 4.9,4.3,3.2 and 2.2mm, from left to right respectively.

In Figure 8.9, the measurements of 4 vessel diameters, measured using ultrasound images can be seen. The visibility of the section decreases as the diameters of the vessels decreased. When the diameter is below 4.3mm, the orifice was not visible. Because of the invisibility, the experiment will invariably result in an inability to do the process without puncturing the posterior wall of the vessel. Further, as seen in Figure 8.10, when the metal needle overshadows the vessel phantom, it can create shadows which cover the phantom beneath. Hence, the vessel with 4.3mm diameter was chosen for the experiments. The top surface of the blood vessel phantom is registered using the fetoscope and the foot pedal.

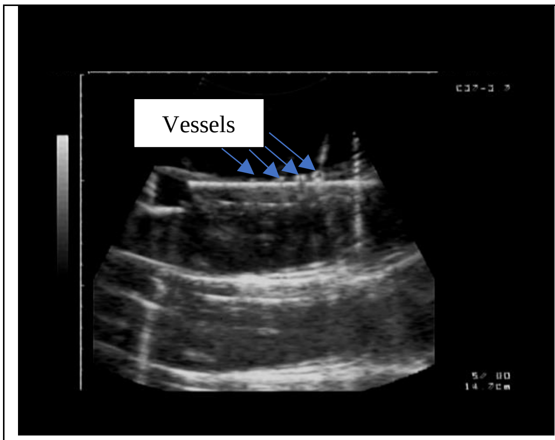

(a) Needle touching vessel with the largest diameter

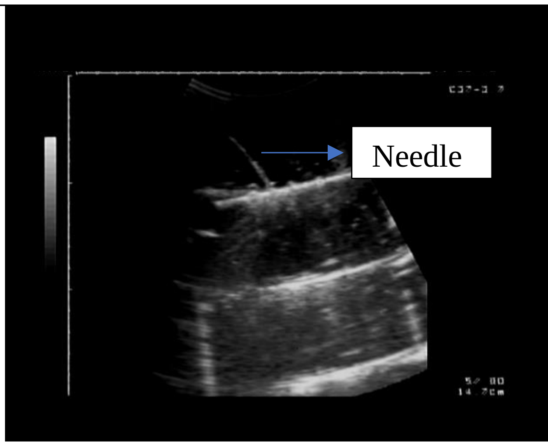

(b) Needle touching vessel with second largest diameter

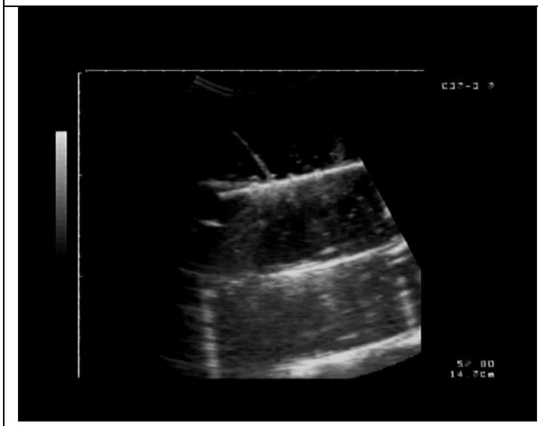

(c) Touching the third largest vessel

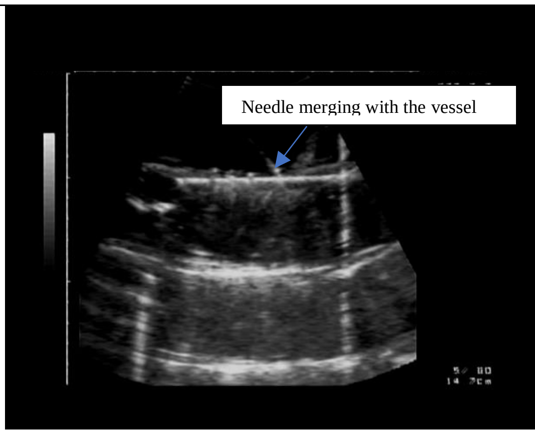

(d) Needle in contact with the smallest diameter vessel

Figure 8-10 Ultrasound visibility comparison for different blood vessel diameters. From figures (a) to (d) shows decreasing visibility with needle-metal shadows

Figure 8.10 gives a comparison of observations of needle creating shadows over the phantom which increased the possibility for the subjects to miss the target. It can also be observed that with reducing vessel diameter, the orifice of the vessel becomes fainter and therefore the needle insertion can no longer be monitored correctly.

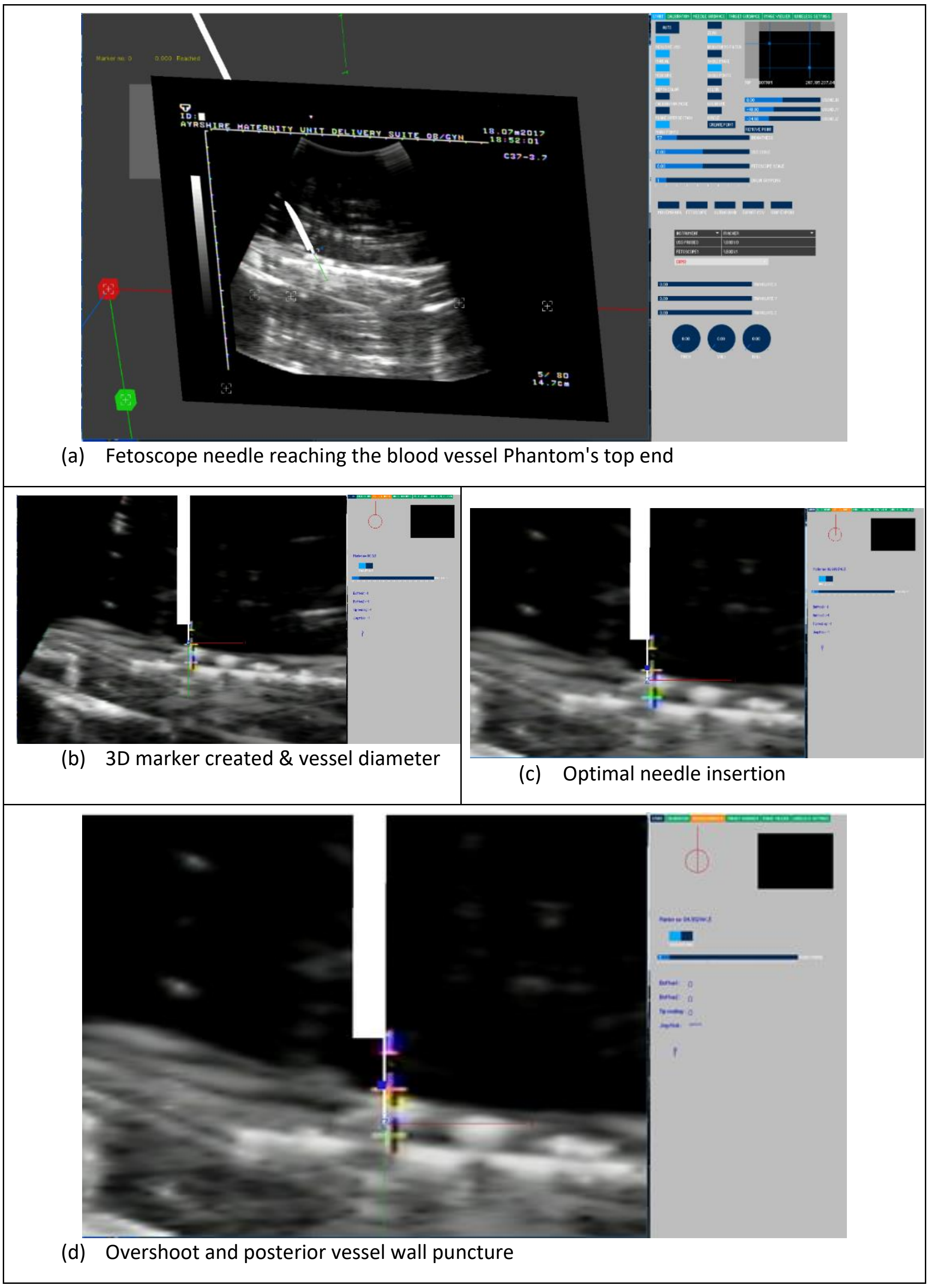

(a) Fetoscope needle reaching the blood vessel Phantom's top end

(b) 3D marker created & vessel diameter

(c) Optimal needle insertion

(d) Overshoot and posterior vessel wall puncture

Figure 8-11 Screenshots showing the fetoscope needle touching the silicone blood vessel phantom (a) Apex of the blood vessel registered (b) Finding vessel diameter and setting target at D/2 (c) needle reaching target (d) Overshoot and posterior vessel wall puncture

Figure 8.11 reveals the process of needle insertion with the help of the navigation system. The process involves initial registration of the top surface of the vessel to be inserted under ultrasound. The diameters of the selected vessel are visualized and noted. The software then maps the 2D position in the ultrasound frame to 3D and uses the vessel diameters to estimate the target point. Any movement further than the centre is highly likely to lead to a posterior vessel wall injury or puncture.

Out of the five subjects, only one subject had no training to back up the procedure. The other four had to be trained extensively on using the Seldinger technique and guided for this procedure before the experiment. Only long axis insertion was used but with a higher angle of incidence than used in the Seldinger's technique. This is the most likely scenario in most of the deeper procedures such as fetal surgery. After the subjects became familiar to the user interface for visualisation and trained with coordination, the experiments were performed.

8.4.2.1 Results

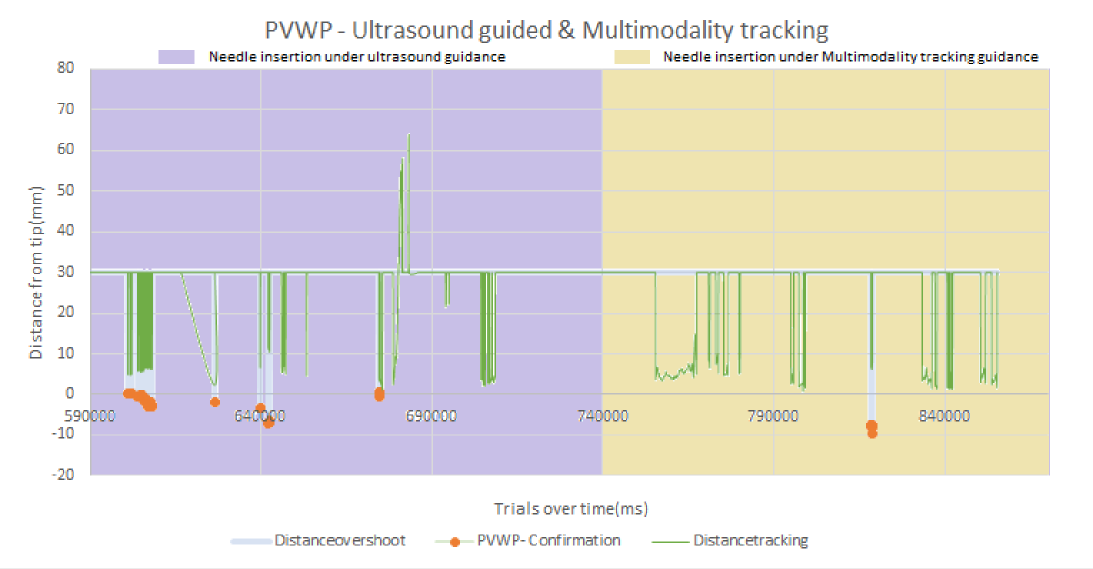

Figure 8-12 PVWP incidence when using the fetoscope without assistance for needling the phantom vessel vs Posterior vessel wall puncture incidence with guidance from the proposed system done by 5 subjects.

Figure 8.12 shows PVWP incidence comparison between ultrasound-guided needle insertion into a blood vessel phantom (left shown in purple colour) and Multi-modality guidance for the same application (right shown in light brick red colour). 'Green line' indicates the displacement of the fetoscope tip below 30 mm distance to the target, while 'Light Blue' line indicates the distance when an overshoot has happened. The 'Orange markers' indicate that the ADC value has dropped close to zero – confirming the incidence of PVWP and accompany the 'Light Blue' line. Comparing the Left-hand side coloured purple to the Right-hand side light brick red, it can be inferred that the posterior vessel wall puncture incidence reduced by using Multi- modality guidance.

8.4.2.2 Conclusion

Each subject performed a total of 20 insertions, resulting in 100 attempts for five subjects. Ten trials for control and ten for the experiment were used consecutively. The order of the experiments was kept the same to deliberately let the subject feel the difference between a navigation-guided insertion and an ultrasound-guided process of insertion. Multi-modality guidance resulted in a significantly lower number of overshoots, although the incidence cannot be eliminated.

8.4.3 Experiment 3 - LASER overshoot protection

Experimental evaluation of LASER overshoot protection and guidance has been discussed in Chapter 7. Figure 8.13(a) shows the subject using the LASER guidance interface with LASER overshoot protection. The subjects were instructed to insert the fetoscope into the tank and trace within the circle and along the outline of a circular phantom. Figure 8.13 (b) shows three blue balls which indicate plane registration points which then form a yellow triangle indicating the plane. Once plane registration is complete, the centre of the circle is registered. After the registration process, a virtual ellipse appears on the plane as seen in Figure 8.13 (b). The centre of the circular phantom is then registered. When moving to the peripheries of the area of interest, the subjects found it difficult to constrain themselves to the circular area of the phantom.

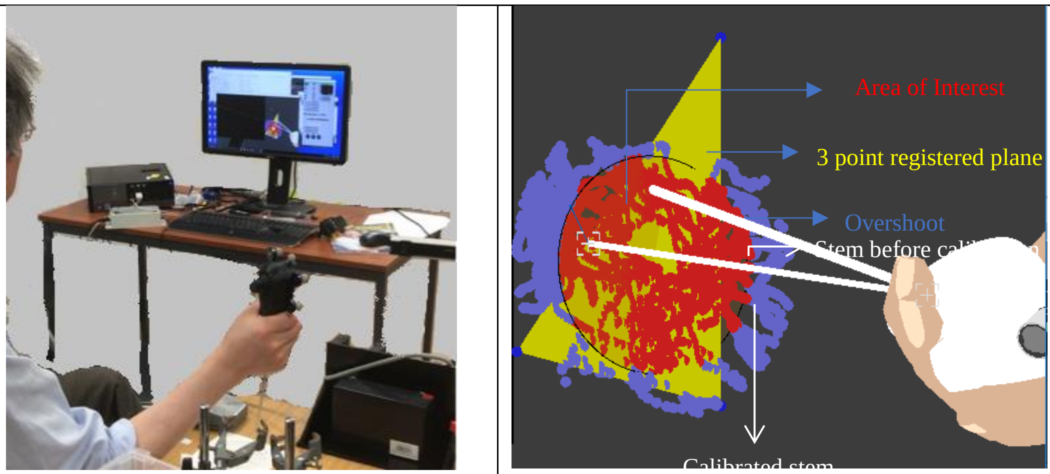

(a) Subject performing the LASER ablation simulation experiment

(b) GUI used for LASER ablation guiding the subject

Figure 8-13 LASER ablation overshoot protection experiment and user interface used for navigation and guidance

The red dots appear when the trajectory from the long axis of the fetoscope tip and the plane meet (Plane-line intersection), provided the Foot switch is pressed simultaneously, and the point of intersection is within the perimeter of the circle. In other words, it is also the point of intersection between the LASER beam and the surface. When the intersection point moves out of the bounds of the circle, the points turned blue, indicating the occurrence of the overshoot. In overshoot protection mode, the Fetoscope automatically turns off the LASER and gives a visual overshoot warning to the user.

8.4.3.1 Results

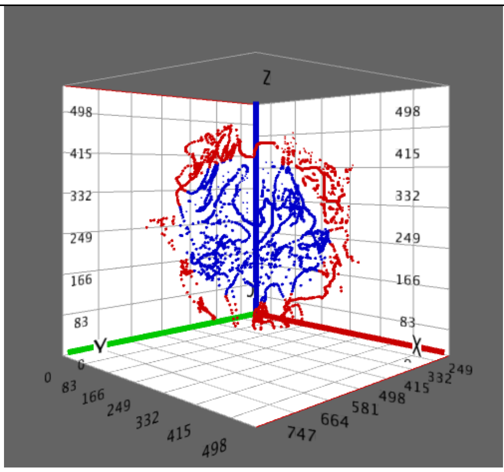

(a) No LASER Safety - Visually guided

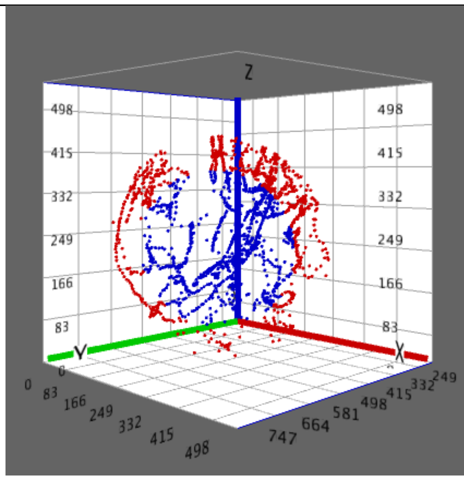

(b) LASER safety - Visually guided

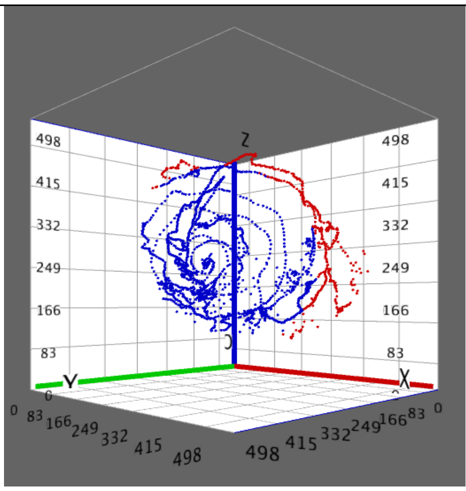

(c) No LASER Safety – Multimodality tracking guided LASER ablation.

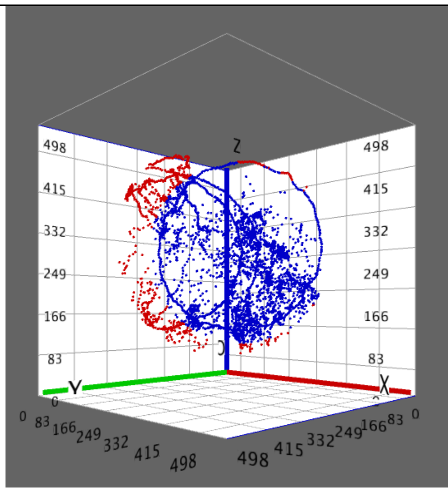

(d) LASER Safety - Multimodality tracking and navigation guided LASER ablation

Figure 8-14 Graph for trajectory (a)and (c) Strokes when LASER safety is turned off (b) and (d) when the LASER safety is turned on.

Figure 8.14 illustrates the trajectory of the subjects during the process of simulated LASER ablation. The subjects were given two options for movement–in spiral and raster forms and were also instructed to switch between the forms when they felt more confident. From the data obtained, the subjects favoured raster pattern movements when the LASER safety was not switched on and resorted to spiral movements when the automatic LASER safety was turned on.

The pattern of strokes in the movement, as seen in Figure 8.14 (b), (c) and (d) appear complete than (a)., This indicates confidence increased and fewer overshoot errors were made. This is because subjects could see the LASER indicator LED on the fetoscope and the beam on the surface to know if the margins are reached.

Observations for overshoot estimation as a result of the procedure can be seen in Table 8.4. The observations suggest that there was considerable overshoot/movement of about 30% when the subjects used plain video guidance which reduced to about 17.2% when using the multimodality navigation system guidance. However, when the automatic overshoot protection was enabled with the proposed Fetal surgery system, there were no errors whatsoever as the LASER automatically turned off, and the number of LASER overshoots was reduced to zero.

Table 8-3 LASER ablation simulation – a comparison between visually guided and multi-modality guided LASER ablation guidance

Subject No	Visual guidance				Multimodality GUI guidance			
	Within AOI	Outside AOI	Observations	% outside	Within AOI	Outside AOI	Observations	% outside
1	850	329	1179	27.905	5012	1222	6234	19.602
2	2878	629	3507	17.935	1556	208	1764	11.791
3	1168	729	1897	38.429	3964	921	4885	18.853
4	2922	163	4185	30.179	1990	484	2474	19.563
5	3130	1747	4877	35.821	5329	1056	6385	16.538

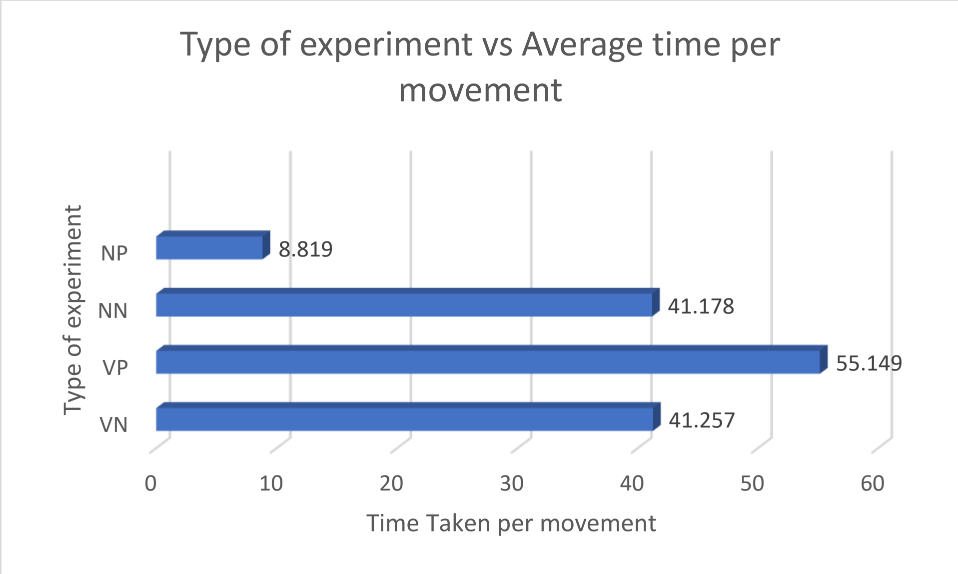

Figure 8-15 Graph showing time taken for the 4 variations of experiments. VN – Visual + No safety, VP – Visual + Safety, NN – Navigated+ No Safety, NP – Navigated + Safety

In Figure 8.15, it is evident that the users took much shorter time per movement when they used the proposed guidance system. This could also suggest that the subjects feel more confident that the system would automatically switch off the LASER when required. Therefore 'NP' Navigated with safety applied has the least time for movements.

8.4.3.2 Conclusion

From the results, it can be inferred that the confidence of the subjects was much higher with a LASER safety system. It also resulted in a higher accuracy and better strokes and required less time for the entire process.

8.4.4 Experiment 4 - Force perception

The loss of tactile sensations and force feedback has been described in the literature review. This set of experiments focus on force perception post training and how haptic feedback can aid force perception. Three variations of haptic feedback are given to the subjects and the subjects are required to withdraw the fetoscope when they perceived that they had reached the target.

8.4.4.1 Types of feedback for haptics

Haptic feedback had been primarily based on force perception. Since force perception can have subject to subject variation and inconsistency regarding quantification, the combination of visual input has been suggested. In this section, the effects of the different types of feedback on force perception are discussed and evaluated with the fetoscope system.

8.4.4.1.a Proportional feedback perception

The first experiment involves giving proportional haptic feedback after the limits of 20, 50, 100, 150 and 200-grams force. The subjects overshot the limit when they did not feel the feedback. Results of this experiment can be seen in Figure 8.16.

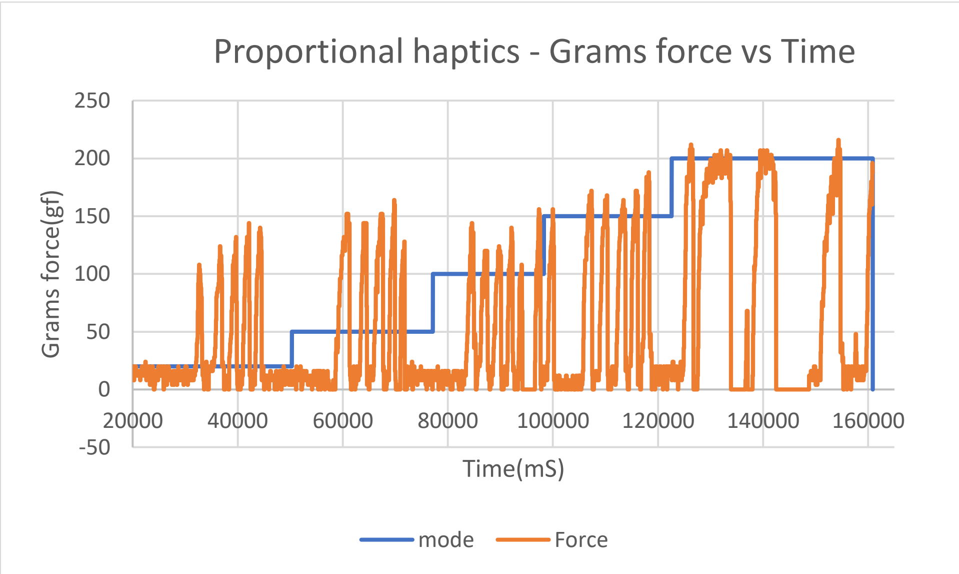

Figure 8-16 Haptic proportional feedback without thresholding

From Figure 8.16, it can be observed that the subjects did not perceive any difference between the force range from 0 to 100 grams force. This loss of feedback can result in several adverse effects in a minimally invasive environment with fragile structures.

8.4.4.1.b Thresholded feedback perception

In the second experiment, the subjects are instructed to pierce the given tissue phantom and are given constant vibrational feedback when they reach the force target. When the vibrational feedback is received, the subjects are instructed to withdraw the fetoscope. In Figure 8.16 the results of this experiment are shown.

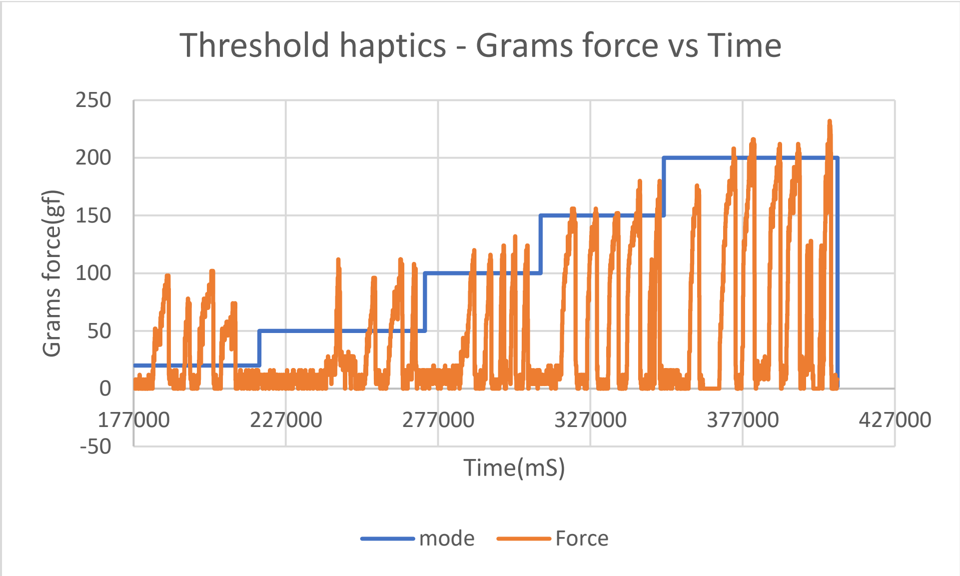

Figure 8-17 Haptic threshold feedback for force control

In Figure 8.17, it can be observed that by the time the subjects reacted to the given vibrational feedback, the force over shot the limits in the lower ranges up to 100 gf. Though this is much better than the case of proportional feedback, in terms of sensitivity, this kind of feedback lacks specificity and quantification.

8.4.4.1.c Visual and haptic combined feedback perception

In the third experiment, the subjects were given visual feedback of the actual force and the target to be reached on the display of the fetoscope and the haptic feedback simultaneously. The subjects were instructed to do the needle insertion process and withdraw when they reached the target force seen on the screen and when they felt the proportional haptic feedback. The results of this experiment can be seen in Figure 8.18.

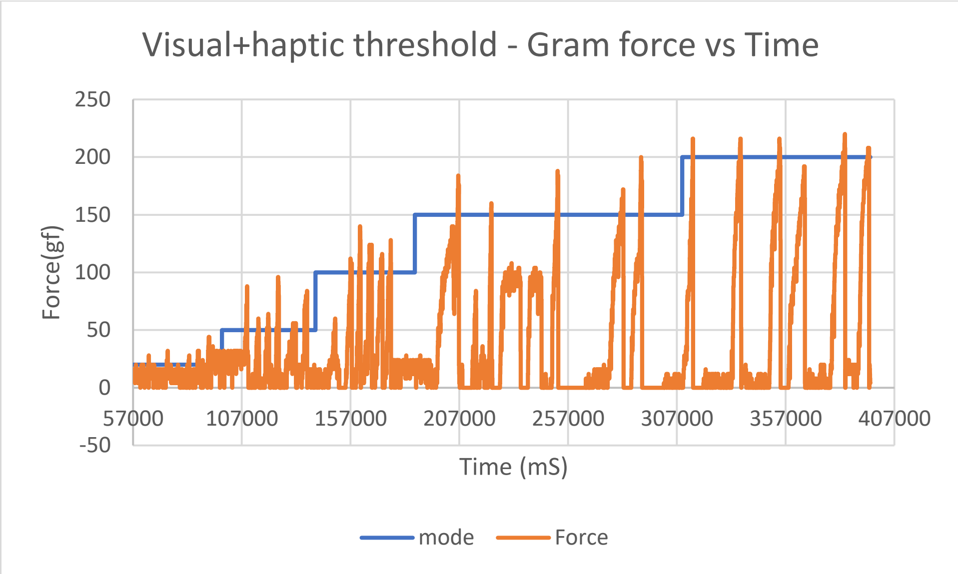

Figure 8-18 Visual and haptic feedback combination output

From Figure 8.18, it is evident that the subjects had a lower incidence of error with combined feedback and were confident at the lower force levels, as very less overshoot is observed.

8.4.4.2 Results

Five subjects repeated the experiments five times for every force range resulting in a total of twenty-five observations per subject. Figure 8.19 compares the errors in perception over the range of forces for the three types of haptic feedback discussed.

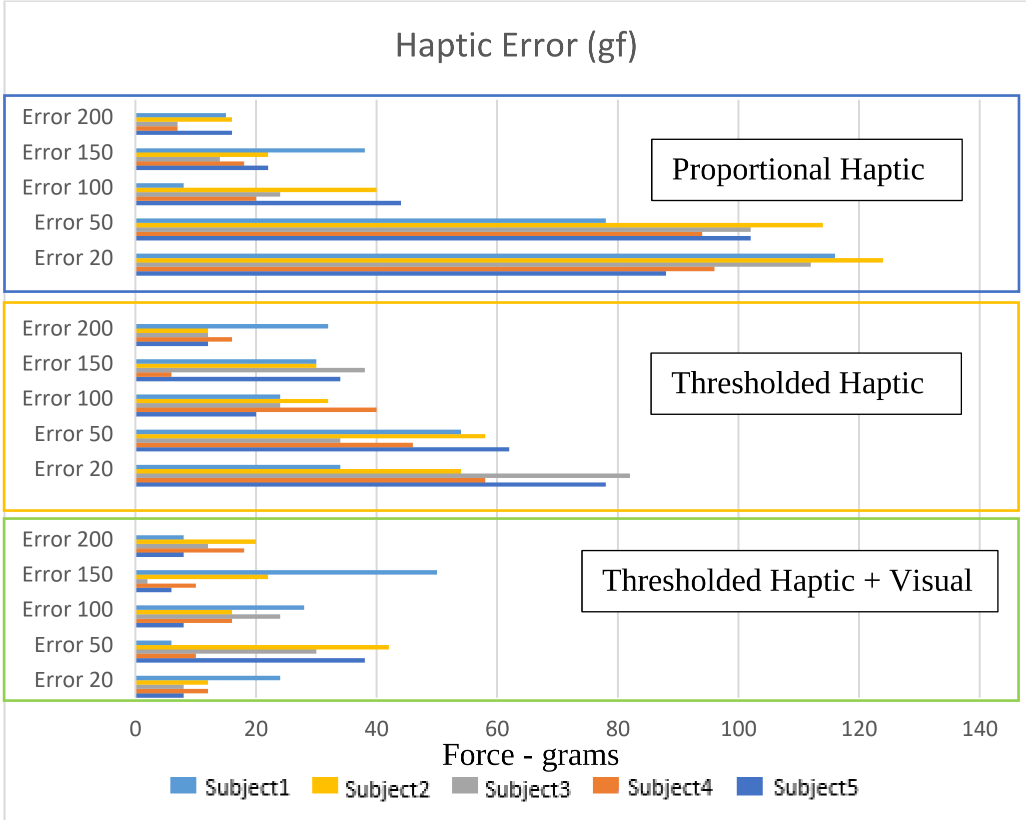

Figure 8-19 Comparison of haptic feedback outputs with five different force ranges

From Figure 8.19, it can be seen that the number of errors reduced in all the ranges of force measurement when visual feedback helped the surgeon quantify and expect the rise in force.

8.4.4.3 Conclusion

Most subjects reported less confidence in the first experiment, where they experienced less to almost no force feedback in the lower ranges of force and hence performed a significant overshoot. In the second experiment, though the subjects were confident about reaching the target, they overshot the target as they did not anticipate the exact incidence of the goal and this resulted in overshoot errors especially in the lower range of forces. Whereas when the subjects were given a quantification of forces visually, combines with the proportional feedback the number of overshoot errors reduced significantly. From the results, it can be inferred that visual input in conjunction with haptic feedback can result in better outcomes of force perception in the environment of Minimal Access Surgeries.

8.4.5 Experiment 5 - Fetal phantom procedure

Experiment 5 focuses on simulating a simple fetal surgical procedure involving the method of reach, and ideal angle of approach. The trajectory of movement adopted for reaching and the time taken to reach the targets can indicate the confidence of the subject during the procedure. The fetoscope insertion into the trachea of the fetal phantom and fetal balloon inflation simulation was done with and without the tracking system guidance. The setup described for this experiment is described in the earlier chapter. Figure 8.20 shows the setup used for this experiment and the subject's orientation to the fetal phantom, ultrasound machine and the navigation guidance in the computer. The subjects were assisted in one click registration within the ultrasound image interface on the computer. Once the required points are registered under ultrasound, the tracheal insertion procedure under ultrasound guidance is compared with the same procedure assisted by the Navigation interface.

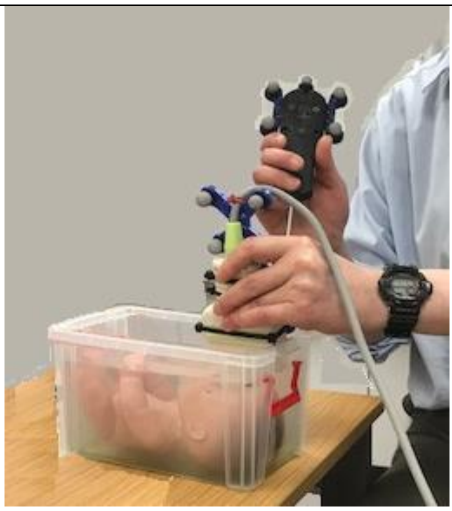

(a) Fetal phantom underwater in view of ultrasound probe

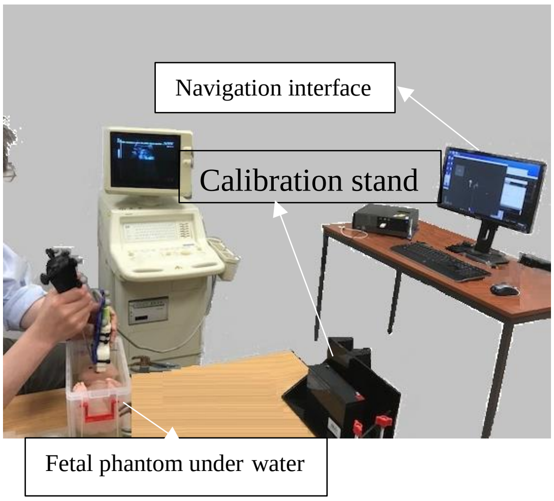

(b) Subject's visualization and screen registration of target

Figure 8-20 Fetal surgery simulation experiment (a) Subjects position and orientation to the phantom (b) Screen visualization of the subject during the experiment

Figure 8.21 shows screenshots of the navigation interface post registration of the target point. It can be seen in Figure 8.21, that the orange transparent cylinder can be directed according to the direction of entry and the required angle on the interactive marker is set. This cylinder serves as the virtual guidance tube within which the fetoscope is to be maintained inside this tube at all times to reach the trachea directly. Any movement outside this volume results in an error indication on the screen, which the user can pick up and correct automatically.

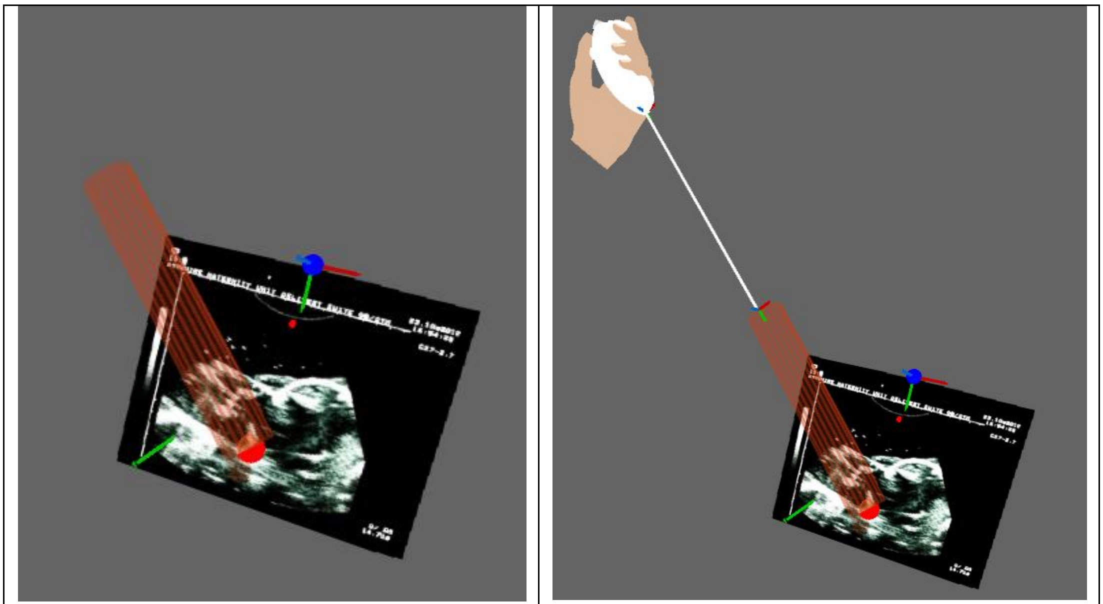

(a) Cylinder volumetric area of interest

(b) Fetoscope entering the volumetric area of Interest

Figure 8-21 Marking volume of interest positioned as a cylinder arising from the point of target

Figure 8.22 illustrates the process of guided Fetoscope usage within the surgical environment and the scenarios of overshoot and overshoot correction guidance. The white circle indicates the cross-section of the cylinder while the dark red dot indicates the cross-section of the tip of the catheter and the green circle represents the distance from the target. In the case of an overshoot, the haptic motor starts vibrating bringing the overshoot to the attention of the subject. None of the subjects experienced an overshoot beyond the set target.

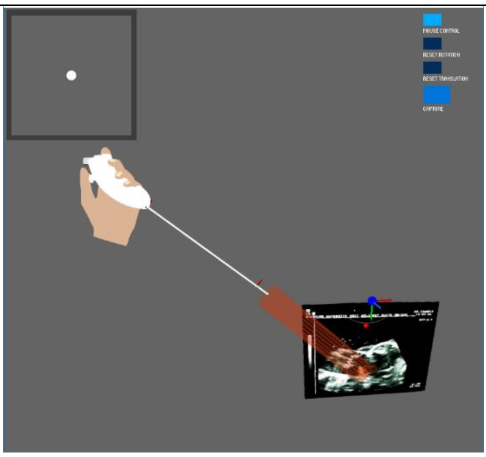

(a) Orienting the Fetoscope

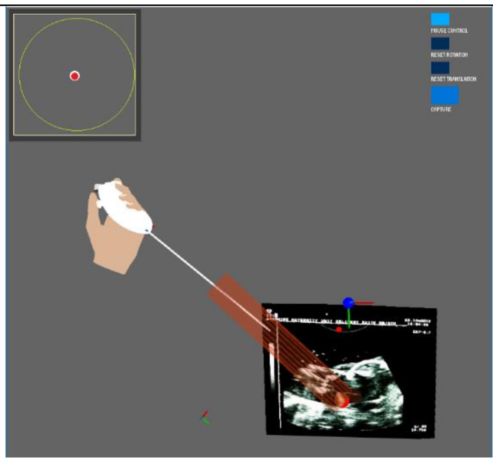

(b) Insertion along the axis of the guidance cylinder

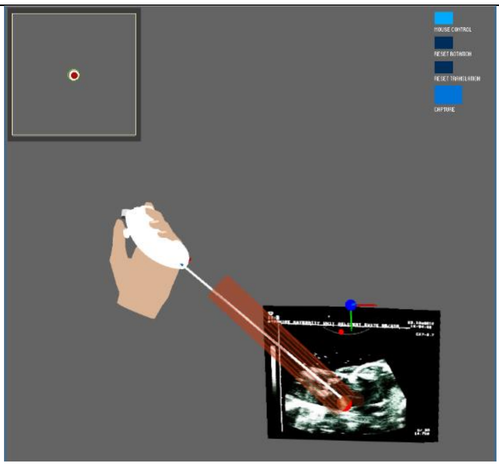

(c) Insertion into the trachea of the fetal phantom

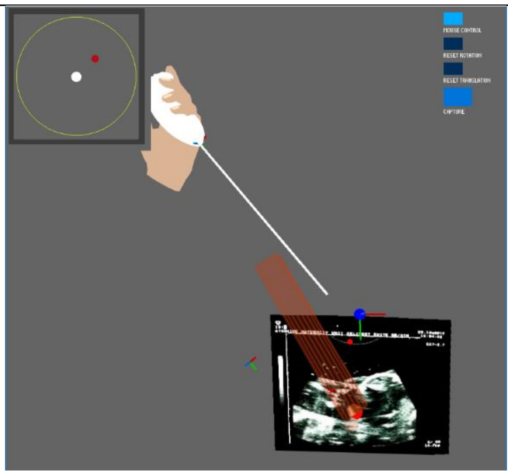

(d) Postero - lateral overshoot

Figure 8-22 Process of Guidance from the user navigation interface Figures (a), (b), (c) and (d) show different scenarios of overshoot as visualized by the interface

While the subject with ultrasound training and experience found the interface and the guidance self - intuitive and relatively straightforward, inexperienced subjects still had orientation problems because of less hand-eye coordination and understanding of mirrored kinematics in terms of endoscopic surgery. But overall, the subjects reported that they had a better 3D orientation with the proposed guidance system.

8.4.5.1 Results

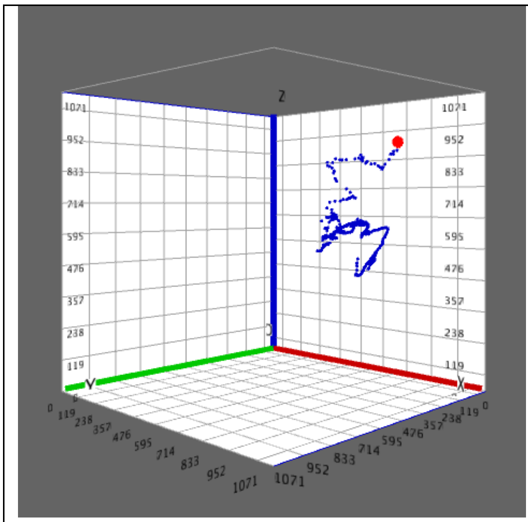

(a) Ultrasound guidance - Trajectory of tip movement (Best case)

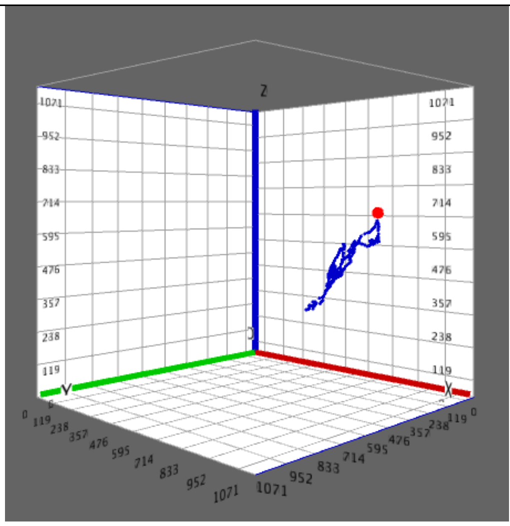

(b) Multimodality navigation guidance – Trajectory of tip movement

Figure 8-23 Trajectory of tip movement during the experiment – a comparison between the two methods

Figure 8.23 compares the movement trajectory accumulated during the best case of ultrasound-guidance assisted simulated surgical procedure and Multimodality assistance. The blue dots represent the movement trajectory, and red dot indicated the point of entry in Figure 8.23(a) and the target point in Figure 8.23(b). The trajectory using only the ultrasound can be seen to have wavering whereas using the proposed system reduced the number of wavering movements of the surgical instrument.

Figure 8.24 shows the results for the time taken to reach the target excluding the registration time when conventional ultrasound techniques are used for reaching the target and when Multimodality navigation guidance is used. The comparison of the two modalities shows that the subjects on an average were 33.6% faster when the subjects used Multimodality tracking when compared to ultrasound guided procedure.

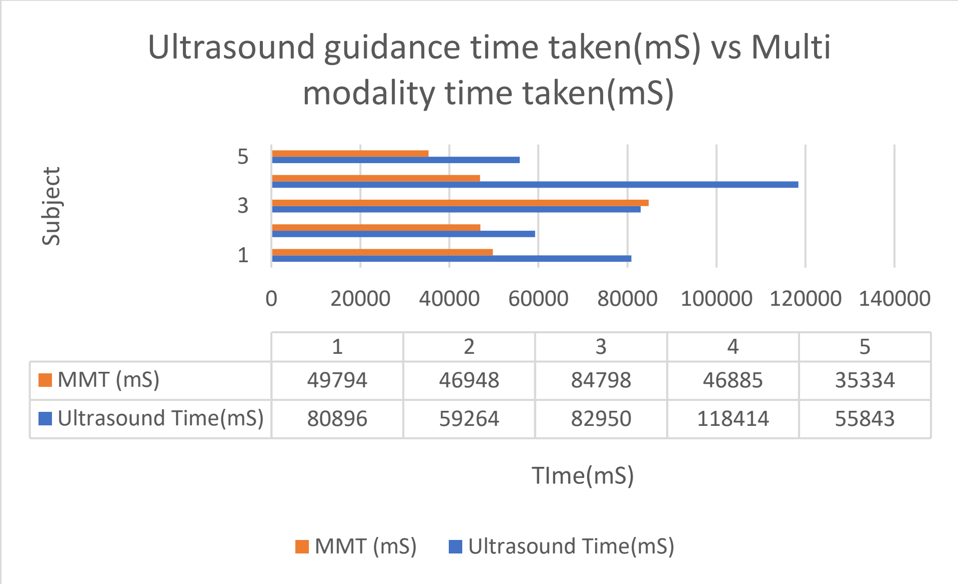

Figure 8-24 Comparison of time taken to reach the target under ultrasound guidance and Multimodality tracking guidance

8.4.5.2 Conclusion

In this experiment, a simple surgical procedure has been simulated on a phantom under ultrasound guidance and Multimodality guidance. The trajectory of movement adopted by the subjects in either of the cases and the time taken have been considered. From the results of the trajectory adopted by subjects when they used Multimodality tracking, the subjects are more confident about the path to the target and the average time taken by the subjects is much lower than when they used only ultrasound tracking. One of the subjects who did not have the complete training took more time than the others, and this explains the impact of training in using the navigation assistance system. Therefore, it is quite evident that the tracking and navigation system has enabled the subjects to perform the procedure. However, more training is expected to improve the results of the time taken.

8.5 Summary

In this chapter, the limitations and the constraints of the fetal surgery system evaluation are initially discussed. Then five experiments have been conducted with five subjects to find the usefulness of the proposed surgical system in minimal access fetal surgeries.

Table 8-4 Proposed target specifications vs target specifications achieved

Experiments	Proposed target specifications	Target specifications attained
Reach experiment	1. Demonstration that the interface can help the subjects navigate 2. Pattern of the strokes – clearer pattern less confusion 3. Proximity to the registered object	1. Navigation guidance and registration have been demonstrated 2.Navigated procedures resulted in clearer strokes than ultrasound guidance. 3. Navigated procedure resulted in higher proximity to registered objects
Needle guidance experiment	1. Demonstration of one-click object registration and sub millimetre guidance 2. Sub-millimetre accuracy of needle insertion into the registered phantom 3. Eliminate posterior vessel wall puncture	1.One-click registration of targets in 3D demonstrated. 2D & 3D submillimetre guidance interface demonstrated. 2.Submillimetre guidance resulted in accurate needle movements 3.Posterior vessel wall under ideal conditions resulted in no PVWP
LASER overshoot experiment	1. Demonstration of LASER or RFA safety using software and hardware 2. Pattern of the strokes and distribution-indication of confidence 3. Reduce overshoot and have strokes within the area of interest 4. Reduction in time take for the process of colouring	1.LASER safety & automatic hardware-software control demonstrated 2. Clearer and bolder strokes used when navigation guidance was used 3.Overshoot percentage dropped from 30% to 17.2% 4.The time taken for the procedure dropped from 55ms per movement to 8 ms
Force perception experiment	1. Demonstration of hardware haptic functionality 2. Evaluating the sensitivity of human hand to different types haptic feedback 3. Proving that visuo-haptic feedback is better than mechanical feedback	1. Hardware haptic functionality demonstrated and evaluated 2. Human hands were not sensitive to forces less than 50gf. 3. Visuo-haptic feedback is has been proven to provide better sensitivity and lower errors of force perception
Simple surgical simulation	1. Demonstration of multimodality tracking in a simulated surgical environment 2. Demonstration of target guidance 3. Pattern of the strokes – clearer pattern less confusion 4. Proximity to the registered object	1. Multimodality tracking use in a simulated surgical environment has been demonstrated 2.Target registration and guidance capabilities has been proven 3. Multimodality navigation guidance resulted in straightforward trajectory while ultrasound guidance showed a lot of fluctuations. 4. Multimodality tracking assistance resulted in higher proximity to the registered target.

From Table 8.5, the following can be summarised:

Experiment 1 demonstrates the effectiveness of the tracking and navigation system in helping the subjects reach the target.

Experiment 2 shows how the subjects can reduce the incidence of overshoots while needle insertion by using the one-click registration method proposed in conjunction with the needle guidance interface.

Experiment 3 shows the capability of the system in reducing the number of overshoots while using methods such as LASER ablation. It also describes the effectiveness and use of automated safety during the process of minimally invasive procedures.

Experiment 4 shows that visual, haptic guidance is more effective than plain haptic force quantification. It also demonstrates lower force ranges in Minimally Invasive Surgeries can benefit from a combined haptic feedback system.

Experiment 5 Illustrates a simple surgical procedure simulation on a phantom. It also shows how the proposed tracking navigation system can help the subject reach the required target with simple navigation planning for approach.

8.6 Conclusion

Five experiments have been performed to evaluate the effectiveness of the proposed multimodality tracking and navigation system along with the robotic fetoscope. The results of these indicate that the system increases the confidence of the surgeon by providing a real-time 6-DoF visualisation. The significantly increased accuracy of reaching target objects is observed using target guidance within the software interface. Combination haptics offers useful force feedback. Therefore, we can conclude that the system provides the surgeon with the necessary perception and assistance to perform intricate procedures even in its current state.

Chapter 9

Conclusion and Future work

A multimodality tracking and navigation system for use in Minimal Access fetal Surgery have been developed, and the effectiveness has been evaluated.

9.1 Contributions

The following are the main contributions of this research:

1. Proposition and demonstration of ultrasound – optical tracking cross calibration process in Chapter 4. This multimodality system is used in all the experiments in later chapters. Further, the extent of manual recognition of surgical instruments under ultrasound has been compared to automatic detection. Also, the automatic centroid detection process has been shown to have a higher accuracy than manual recognition process.

2. Proposition and demonstration of a novel optical tracking system with less crossing over of markers and the least possible number of markers. This proposed novel system is evaluated in Chapter 3.

3. Proposition and demonstration of a novel hand held fetoscope with integrated sensors and haptics and 6 DOF absolute tracking, safety features embedded and haptics feedback. The proposed handheld fetoscope has been explained and evaluated in Chapter 5.

4. Development of multimodality tracking and navigation interface by merging the advantages of the ultrasound with those of Optical tracking. It has successfully demonstrated that it can result in better accuracy and lower the incidence of tracking loss and random positioning during tracking loss.

5. Development of a novel interface platform in Chapter 6. This novel interface platform is used in the experiments of the later chapters. The hardware and software work seamlessly and the communication capabilities and safety features of the software have also been presented in the last few chapters. All the aforementioned effects have been achieved in a real-time environment.

6. Development of a fetal phantom for a demonstration of simple balloon inflation experiment for CDH. Development of experimental setup to estimate accuracy and repeatability of reach, Posterior vessel wall puncture, LASER confinement and Safety in Chapter 7.

7. Evaluation of the experimental results to verify the effectiveness of the proposed system when compared to the usage of plain ultrasound guidance in Chapter 7 and Chapter 8.

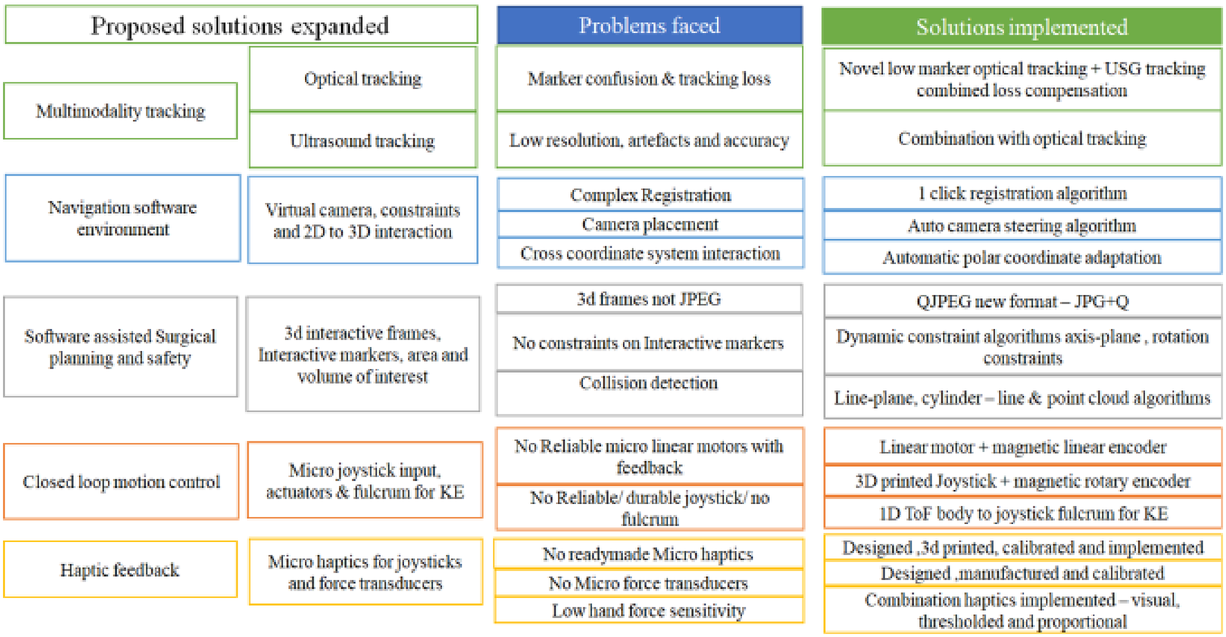

Figure 9-1 Proposed solutions for some problems in instruments used in fetal surgery, problems faced and the solutions that have been implemented so far

9.1.1 Quantification of Software constraints of the interface

The software interface operates in different modes as suggested in the previous chapter. All these modes include the simple real-time 3D rendering of the joystick, the real-time ultrasound plane, mouse handling, communications, and tracking. Table 8.3 lists the observations of software delay limitations.

Table 9-1 Software delay limitations

Parameter	Delay
Average initialization time	≈ 3900 ms
Average time of 3D interaction	≈ 1300 ms
Maximum 3D interaction time	≈1600 ms
Maximum achieved frame rate with no 3D interaction	≈27 / sec
2D screen interaction time	Not noticeable
Communication loss	Startup sync <250 ms
Multiple 3D frame storage/display time lag	+= 25 ms per frame limited to 30 frames
UDP communication + 3Dgraphics rendering	≈200 FPS
Hardware serial + 3D graphics delay 115200 bps	Delay not noticeable

9.2 Limitations

The limitations of the current study are mainly bound to the constraints of time and resources. The following limitations are being acknowledged:

1. **Subjects:**

The inclusion of the recruited subjects was limited by their knowledge and experience of ultrasound handling and at least some level of dexterity and orientation, due to the specific requirements of the experiment. Only 5 subjects were recruited in the study.

2. **Experimental setup:** There are a few limitations due to the currently used technical specifications. But these are not actual limitations of the technology as such.

a) Optical tracking system

The novel optical tracking system designed requires wide field of view and high-resolution cameras and FPGA based processing for optimization. Therefore, this system was presented and evaluated with a certain extent of inaccuracy. The experiments for the surgical navigation were done using Optitrack from Naturalpoint.

b) Phantom environment

The phantoms made for this study may not be an accurate representation of the best materials for biological tissue replacement. Water was used as the ultrasound medium which may not represent a perfect biological environment.

c) Ultrasound system

The ultrasound system used was not a state-of-the-art equipment with inbuilt noise removal algorithms but has a very accurate calibration from Toshiba.

d) Augmented Reality

Though the software virtual camera designed can handle Augmented Reality, it was not implemented in the hardware and therefore has not been discussed.

e) LASER

A 660nm diode LASER of class 2B was used for demonstration of the LASER guidance procedure. In an ideal experiment, fiber coupled LASERs up to 50 Watts should be used for the experiments and the automatic focus adjustment can be done for the focusing elements for best focus at the points of interest.

f) Fetoscope

The fetoscope was designed with all the different elements discussed in Chapter 5 but elements such as the micro camera, micropump, 4" LCD attachment, though completely functional, were removed or inactivated to prevent damage to the physical parts during experiments.

g) Force perception

Proportional haptics were too weak to elicit a response in the lower range and very high intensity was required at higher forces which could theoretically interfere with the procedure.

h) Subjects

Minimal access procedure surgeons are super-specialists at present and are very few. Therefore, only two medical professionals were recruited for the experiments. However, non-medical candidates also reported the effectiveness of the system, the ease of use and confirmed that the interface is self-intuitive.

3.Technology

Most designs have been limited by the technology available, such as the limitation of camera resolution and the availability of highspeed LVDS interface for microcontrollers. Multi-perspective imaging and 360-degree video streaming are achievable but have not been implemented yet because of such limitations.

9.3 Conclusions

A novel multimodality robotic fetal surgery system has been successfully presented in this study. The proposed multimodality surgery system demonstrates several novel points to improve the perception of orientation, enhance the force feedback and prevent errors of overshoot by the combination of the advantages of ultrasound and optical tracking technologies, additional hepatic feedback and safety features. The proposed system is designed for fetal surgeries but can be easily applied to the other types of MIS by minor modifications.

This study, firstly, reviewed the state-of-of-art technologies in Minimal Access Surgeries and identified the current problems. Secondly, potential solutions to the identified problems were proposed and their feasibility and efficacy were evaluated and verified in specific designed experiment before being adapted to the system. The proposed system can be summarised below in terms of its novelties and functionalities.

The proposed solutions to the problems investigated in this study were first evaluated in the experiment. Based on the verified solutions, several components were designed and implemented. The proposed system consists of these components and the effectiveness was evaluated. The different aspects of the fetal surgery system with the solutions incorporated are as follows:

1. A novel optical tracking system with less number of markers and lower interference of crossing over. This system was designed and evaluated.

2. Ultrasound to screen calibration and ultrasound real-time image processing with 'Region of Interest' specified by Optical tracking. The effectiveness of object tracking using ultrasound image processing has been evaluated by comparison to object tracking by 5 sonologists.

3. Optical tracking – Ultrasound tracking 'one-click' registration and cross calibration methodology for rigid body tip tracking. This helps the surgeon save registration time.

4. A hand-held robotic fetoscope unit capable of not only working with the navigation interface seamlessly but also providing multiple forms of communication, storage, interaction, haptics, multiple sensors, display interface and actuation.

5. An enhanced interface for the fetoscope which integrates the capabilities of image capture, tracking and navigation. Several versions of the interface have been developed for experiment evaluation and training purposes.

The goal of the proposed system is to increase the perception of the surgeon in mind. To evaluate its efficacy, five experiments were designed and conducted by 5 subjects. The main parameters used to measure the effectiveness and robustness of the system were orientation, dexterity, accuracy, force perception and confidence. The conclusions of the experiments are summarised as follows:

9.3.1 Experiment 1

The first experiment investigated the perception of orientation and accuracy when the subjects used the system. Results of this experiment showed a cleaner, shorter trajectory with higher accuracy in reaching the target, indicating confidence in orientation without compromising on the accuracy. However, the subjects required more time to complete the task, as they diverted their concentration from getting the 6DoF instrument orientation to the control surface right to reaching their targets as best as they could.

9.3.2 Experiment 2

The second experiment investigated the incidence of vertical overshoot during a simple needle insertion process guided by ultrasound only or combined with navigation guidance. It was found that the number of overshoot errors reduced significantly when the subjects used the navigation guidance.

9.3.3 Experiment 3

Third experiment investigated the occurrence of lateral overshoots and the feasibility of using an automated LASER safety system to prevent such overshoots when using an ablation system for procedures such as Twin to Twin Transfusion Syndrome. The experiment showed a remarkable reduction in overshoot, a cleaner trajectory of movement and automated correction of LASER overshoot errors.

9.3.4 Experiment 4

The fourth experiment evaluated the effectiveness of the robotic fetoscope by providing haptic force feedback. The results indicated that visual feedback combined with proportional haptic feedback have the best outcomes.

9.3.5 Experiment 5

Fifth experiment was designed to simulate a simple surgical environment and a tracheal balloon inflation was to be done by the subjects in future experiments. The trajectory of tip movement was far shorter and the accuracy of reaching the registered target was much higher when the subjects were guided by the navigation interface.

From the conclusions of the above experiments, it provided the evidence and supported that the subjects exhibited a better sense of orientation, dexterity, safety and confidence resulting in better overall outcomes when they used the proposed surgical system. Therefore, a system which can:

- Enhance orientation
- Give force feedback as visual and vibrational haptic,
- Combines accuracy with reaction speed
- Have active safety for instruments.
- Provide sub millimetre guidance, preventing overshoots.

- Include robotic equipment offering precision control of displacement.

has been demonstrated and evaluated.

With further developments, the system should be able to achieve a better feedback and perception to the surgeon and can potentially increase the confidence and accuracy of the surgical procedure performed. This in turn, can open new doors to more complicated procedures which have been limited by the available technology. Such a system should be able to enhance the perception of the surgeon and help the process of Minimal Access Surgical procedures.

At the time of this research and writing the author was not aware of any other system which combines all the features used in MMT for use in minimal access surgeries. Therefore, the author claims novelty in these areas of research.

9.4 Future work

The research study in the development of a fetal surgery system has resulted in a surgical system which provided perception enhancement during the process of surgery. This system can be used as a fundamental framework for development and integration of multiple instruments for use in different surgical applications such as gynaecology, neurology, orthopaedics, urology and many others which require multi-modality image guidance for minimal access procedures. The future works are outlined as follows.

9.4.1 Hardware and software

The elements selected in this research were limited by technical reasons, such as the optical tracking accuracy. Further studies can focus on the improvements in haptic technology and size reduction in fetoscope tips by using smaller cameras. The directions of hardware and software development and application include:

1) **Improvements in tracking technology:**

Non-line of sight tracking with single photon spectroscopy or high speed ToF based GPS and AC Electro Magnetic tracking system require further research and integration into the proposed software.

2) **Augmented reality applications:**

The software developed in this study contains the elements of first person camera view. The software can be further developed and modified for Augmented reality applications with head tracking and head set with VR capabilities.

3) **Mobile platform applications:**

The software is developed in JAVA and can be directly ported into other available mobile platforms. Therefore, absolute 6 DoF tracking can be achieved by just 2 mobile phone cameras. This project has already laid the foundations for the principles of operation, software usage and real-time communication.

4) **Visualisation of the fetal structures in 3D:**

With advancement in camera technology, the micro camera used in this project can be replaced with 'ToF of light' - depth sensing technology. Advanced developments in this area can result in the surgeons being able to see the fetal structures in 3D in real-time. In addition, the fetal structures can also be viewed through the technologies of LASER acoustics or fibreoptic ultrasound; provided, the intensities used do not cause thermal effects on tissues. Alternatively, a development in compact MRI machines could also revolutionise the field of minimal access surgeries. Further studies focused on these fields are desirable.

9.4.2 Experiments

All the major experiments require more sophisticated phantom testing or animal trials before they can be applied to clinical practice.

9.4.3 Subjects

In the next stage of evaluation, experienced fetal surgeons should be recruited as the subjects. The system should also be re-designed and modified to meet their expert requirements.

References

Beck, V., Pexsters, A. and Gucciardo, L. 2010. The use of endoscopy in fetal medicine. Gynecol Surgery.

Bekiesińska-Figatowska, M., Romaniuk-Doroszewska, A., Szkudlińska-Pawlak, S., Duczkowska, A., Mądzik, J., Szopa-Krupińska, M. and Maciejewski, T. M. (2017) 'Diagnostic Imaging of Pregnant Women - The Role of Magnetic Resonance Imaging', *Pol J Radiol*, 82, pp. 220-226.

Beyer-Berjot, L. and Aggarwal, R. (2013) 'Toward technology-supported surgical training: the potential of virtual simulators in laparoscopic surgery', *Scand J Surg*, 102(4), pp. 221-6.

Bruner, J. P., Tulipan, N. B., Richards, W. O., Walsh, W. F., Boehm, F. H. and Vrabcak, E. K. (2000) 'In utero repair of myelomeningocele: a comparison of endoscopy and hysterotomy', *Fetal Diagn Ther*, 15(2), pp. 83-8.

Burka, A., Hu, S., Helgeson, S., Krishnan, S., Gao, Y., Hendricks, L. A., Darrell, T. and Kuchenbecker, K. J. 'Proton: A visuo-haptic data acquisition system for robotic learning of surface properties'. *2016 IEEE International Conference on Multisensor Fusion and Integration for Intelligent Systems (MFI)*, 19-21 Sept. 2016, 58-65.

Cass, D. L. 'Fetal surgery for congenital diaphragmatic hernia: the North American experience'. *Seminars in perinatology*: Elsevier, 104-111.

Cooper, M. A., Hutfless, S., Segev, D. L., Ibrahim, A., Lyu, H. and Makary, M. A. (2014) 'Hospital level under-utilization of minimally invasive surgery in the United States: retrospective review'.

Cruz-Martinez, R., Moreno-Alvarez, O., Garcia, M., Méndez, A., Pineda, H., Cruz-Martinez, M. A., Cruz, M. A. and Martinez-Morales, C. (2015) 'Fetal Endoscopic Tracheal Intubation: A New Fetoscopic Procedure to Ensure Extrauterine Tracheal Permeability in a Case with Congenital Cervical Teratoma', *Fetal Diagn Ther*, 38(2), pp. 154-8.

Curtiss, L. E. (1976) *Comparison of optical performance of selected fetoscope designs. International congress series* Amsterdam: Excerpta Medica ; New York : American Elsevier.

Dai, J. S. (2015) 'Euler–Rodrigues formula variations, quaternion conjugation and intrinsic connections', *Mechanism and Machine Theory,* 92, pp. 144-152.

Deka, D., Dadhwal, V., Gajatheepan, S. B., Singh, A., Sharma, K. A. and Malhotra, N. (2012) 'The art of fetoscopy: a step toward minimally invasive fetal therapy', *J Obstet Gynaecol India,* 62(6), pp. 655-9.

Deprest, J. A., Done, E., Van Mieghem, T. and Gucciardo, L. (2008) 'Fetal surgery for anesthesiologists', *Curr Opin Anaesthesiol,* 21(3), pp. 298-307.

Farmer, D. L. (1998) 'Fetal surgery: a brief review', *Pediatric radiology,* 28(6), pp. 409-413.

Fisk, N. M., Gitau, R., Teixeira, J. M., Giannakoulopoulos, X., Cameron, A. D. and Glover, V. A. (2001) 'Effect of direct fetal opioid analgesia on fetal hormonal and hemodynamic stress response to intrauterine needling', *Anesthesiology,* 95(4), pp. 828-35.

Fowler, S. F., Sydorak, R. M., Albanese, C. T., Farmer, D. L., Harrison, M. R. and Lee, H. (2002) 'Fetal endoscopic surgery: lessons learned and trends reviewed', *J Pediatr Surg,* 37(12), pp. 1700-2.

Gofrit, O. N., Mikahail, A. A., Zorn, K. C., Zagaja, G. P., Steinberg, G. D. and Shalhav, A. L. (2008) 'Surgeons' perceptions and injuries during and after urologic laparoscopic surgery', *Urology,* 71(3), pp. 404-7.

Group, C. O. o. S. T. S. (2004) 'A comparison of laparoscopically assisted and open colectomy for colon cancer', *N Engl J Med,* 350(20), pp. 2050-9.

Ho, C., Tsakonas, E., Tran, K., Cimon, K., Severn, M., Mierzwinski-Urban, M. and Corcos, J. (2012) 'Robot-assisted surgery compared with open surgery and laparoscopic surgery', *CADTH Technology Overviews,* 2(2).

Hogan 1980-August. Mechanical Impedance Control in Assistive Devices and Manipulators. Proceedings of the Joint Automatic Controls Conference.

Hong, J., Dohi, T., Hashizume, M., Konishi, K. and Hata, N. (2004) 'An ultrasound-driven needle-insertion robot for percutaneous cholecystostomy', *Physics in Medicine and Biology,* 49(3), pp. 441.

Howe, R. D. and Matsuoka, Y. (1999) 'Robotics for surgery', *Annual Review of Biomedical Engineering*, 1(1), pp. 211-240.

Huber, A., Baschat, A. A., Bregenzer, T., Diemert, A., Tchirikov, M., Hackelöer, B. J. and Hecher, K. (2008) 'Laser coagulation of placental anastomoses with a 30 degrees fetoscope in severe mid-trimester twin-twin transfusion syndrome with anterior placenta', *Ultrasound Obstet Gynecol*, 31(4), pp. 412-6.

Ken, S. 1985. Animating rotation with quaternion curves. DOI=http://dx.doi.org/10.1145/325334.325242 ed.: Proceedings of the 12th annual conference on Computer graphics and interactive techniques.

Kim, K., Kubota, M., Ohkawa, Y., Shiraishi, T., Kawai, T., Kobayashi, A., Yamashita, H. and Chiba, T. (2011) 'A novel ultralow-illumination endoscope system', *Surg Endosc*, 25(6), pp. 2029-33.

Klaritsch P, A. K., Van Mieghem T, Gucciardo L, Done’ E, Bynens B, Deprest J. Instrumental requirements for minimal invasive fetal and surgery. 2009. Instrumental requirements for minimal invasive

fetal surgery. BJOG.

Klaritsch, P., Albert, K., Van Mieghem, T., Gucciardo, L., Done', E., Bynens, B. and Deprest, J. (2009) 'Instrumental requirements for minimal invasive fetal surgery', *BJOG*, 116(2), pp. 188-97.

Kohl, T., Hering, R., Heep, A., Schaller, C., Meyer, B., Greive, C., Bizjak, G., Buller, T., Van de Vondel, P., Gogarten, W., Bartmann, P., Knopfle, G. and Gembruch, U. (2006) 'Percutaneous fetoscopic patch coverage of spina bifida aperta in the human--early clinical experience and potential', *Fetal Diagn Ther*, 21(2), pp. 185-93.

Koivukangas, T., Katisko, J. P. and Koivukangas, J. P. (2013) 'Technical accuracy of optical and the electromagnetic tracking systems', *Springerplus*, 2(1), pp. 90.

Kwok, K. W. (2012) *Dynamic active constraints for robot assisted minimally invasive surgery [electronic resource]*: Imperial College London (University of London).

Lamata, P., Gomez, E. J., Hernández, F. L., Oltra Pastor, A., Sanchez-Margallo, F. M. and Del Pozo Guerrero, F. (2008) 'Understanding perceptual boundaries in laparoscopic surgery', *IEEE Trans Biomed Eng*, 55(3), pp. 866-73.

Larson, B. J., Longaker, M. T. and Lorenz, H. P. (2010) 'Scarless fetal wound healing: a basic science review', *Plast Reconstr Surg,* 126(4), pp. 1172-80.

Lee, D. H., Kim, U., Gulrez, T., Yoon, W. J., Hannaford, B. and Choi, H. R. (2016) 'A Laparoscopic Grasping Tool With Force Sensing Capability', *IEEE/ASME Transactions on Mechatronics,* 21(1), pp. 130-141.

Liu, L., Oza, S., Hogan, D., Perin, J., Rudan, I., Lawn, J. E., Cousens, S., Mathers, C. and Black, R. E. (2015) 'Global, regional, and national causes of child mortality in 2000-13, with projections to inform post-2015 priorities: an updated systematic analysis', *Lancet,* 385(9966), pp. 430-40.

In the womb (2005) [videorecording]. National Geographic Channel,.

Mezger, U., Jendrewski, C. and Bartels, M. (2013) 'Navigation in surgery', *Langenbeck's Archives of Surgery,* 398(4), pp. 501-514.

Moore, K., Persaud, T. V. N. and Torchia, M. (2015) *The Developing Human10th Edition.* Elsevier.

Padalkar, M. V. and Pleshko, N. (2015) 'Wavelength-dependent penetration depth of near infrared radiation into cartilage', *Analyst,* 140(7), pp. 2093-100.

Pintaric, T. and Kaufmann, H. 'A rigid-body target design methodology for optical pose-tracking systems', *Proceedings of the 2008 ACM symposium on Virtual reality software and technology*, Bordeaux, France. 1450594: ACM, 73-76.

Prada, F., Del Bene, M., Mattei, L., Casali, C., Filippini, A., Legnani, F., Mangraviti, A., Saladino, A., Perin, A., Richetta, C., Vetrano, I., Moiraghi, A., Saini, M. and DiMeco, F. (2014) 'Fusion imaging for intra-operative ultrasound-based navigation in neurosurgery', *J Ultrasound,* 17(3), pp. 243-51.

Quintero, R. A., Hume, R., Smith, C., Johnson, M. P., Cotton, D. B., Romero, R. and Evans, M. I. (1995) 'Percutaneous fetal cystoscopy and endoscopic fulguration of posterior urethral valves', *Am J Obstet Gynecol,* 172(1 Pt 1), pp. 206-9.

Rauskolb, R. (1979) 'Fetoscopy--a new endoscopic approach', *Endoscopy,* 11(2), pp. 107-13.

Sazontova, V. N., Karlina, L. I. u. and Chuprov, P. V. (1984) '[The Am-VS-2 amnioscope with fiber light guide]', *Med Tekh,* (3), pp. 46-7.

Schwaab, J., Kurz, C., Sarti, C., Bongers, A., Schoenahl, F., Bert, C., Debus, J., Parodi, K. and Jenne, J. W. (2015) 'First Steps Toward Ultrasound-Based Motion

Compensation for Imaging and Therapy: Calibration with an Optical System and 4D PET Imaging', *Front Oncol,* 5, pp. 258.

Song, M.-H. and Godøy, R. (2016) *How Fast Is Your Body Motion? Determining a Sufficient Frame Rate for an Optical Motion Tracking System Using Passive Markers.*

Sugano, N. (2003) 'Computer-assisted orthopedic surgery', *Journal of Orthopaedic Science,* 8(3), pp. 442-448.

Szpinda, M., Daroszewski, M., Woźniak, A., Szpinda, A. and Mila-Kierzenkowska, C. (2012) 'Tracheal dimensions in human fetuses: an anatomical, digital and statistical study', *Surg Radiol Anat,* 34(4), pp. 317-23.

Sánchez, A., Rodríguez, O., Sánchez, R., Benítez, G., Pena, R., Salamo, O. and Baez, V. (2014) 'Laparoscopic surgery skills evaluation: analysis based on accelerometers', *JSLS: Journal of the Society of Laparoendoscopic Surgeons,* 18(4).

Thewlis, D. 2011. A COMPARISON OF TWO COMMERCIALLY AVAILABLE MOTION CAPTURE SYSTEMS FOR GAIT

ANALYSIS: HIGH-END VS LOW-COST. *In:* Bishop, C. (ed.). *Congress of the International Society of Biomechanics*.

Tholey, G., Desai, J. P. and Castellanos, A. E. (2005) 'Force feedback plays a significant role in minimally invasive surgery: results and analysis', *Ann Surg,* 241(1), pp. 102-9.

Tsui, C., Klein, R. and Garabrant, M. (2013) 'Minimally invasive surgery: national trends in adoption and future directions for hospital strategy', *Surg Endosc,* 27(7), pp. 2253-7.

Ungi, T., Lasso, A. and Fichtinger, G. (2016) 'Open-source platforms for navigated image-guided interventions', *Med Image Anal,* 33, pp. 181-6.

Welsh, A., Agarwal, S., Kumar, S., Smith, R. P. and Fisk, N. M. (2003) 'Fetal cystoscopy in the management of fetal obstructive uropathy: experience in a single European centre', *Prenat Diagn,* 23(13), pp. 1033-41.

Wiles, A., G. Thompson, D. and Frantz, D. (2004) *Accuracy assessment and interpretation for optical tracking systems.*

Wu, X., Wu, S., Xing, Z. and Jia, X. 2016. A Global Calibration Method for Widely Distributed Cameras Based on Vanishing Features. *Sensors*.

Yamanaka, H., Makiyama, K., Osaka, K., Nagasaka, M., Ogata, M., Yamada, T. and Kubota, Y. (2015) 'Measurement of the Physical Properties during Laparoscopic Surgery Performed on Pigs by Using Forceps with Pressure Sensors', *Adv Urol,* 2015, pp. 495308.

Yao, W., Elangovan, H. and Nicolaides, K. (2014) 'Design of a flexible fetoscopy manipulation system for congenital diaphragmatic hernia', *Med Eng Phys,* 36(1), pp. 32-8.

Yoon, J.-H., Park, J.-S. and Kim, C. (2006) 'Increasing Camera Pose Estimation Accuracy Using Multiple Markers', in Pan, Z., Cheok, A., Haller, M., Lau, R.W.H., Saito, H. & Liang, R. (eds.) *Advances in Artificial Reality and Tele-Existence: 16th International Conference on Artificial Reality and Telexistence, ICAT 2006, Hangzhou, China, November 29 - December 1, 2006. Proceedings*. Berlin, Heidelberg: Springer Berlin Heidelberg, pp. 239-248.

Zhou, M. 2007. Shifts in Force Perception Threshold in Laparoscopic

Surgery with Experience. *In:* Perreault, J. (ed.). Cambridge Health Alliance.

Zhou, T. 2009. Surgical navigation: tool of minimally invasive medical. Chinese University Technology Transfer.

Ziskin, M., Thickman, D., Goldenberg, N., Lapayowker, M. and Becker, J. (1982) 'The comet tail artifact', Journal of Ultrasound in Medicine, 1(1), pp. 1-7.

Adzick, N. S. (2010) 'Open fetal surgery for life-threatening fetal anomalies', Semin Fetal Neonatal Med, 15(1), pp. 1-8.

Adzick, N. S. (2013) 'Prospects for fetal surgery', Early Hum Dev, 89(11), pp. 881-6.

Adzick, N. S., Harrison, M. R., Crombleholme, T. M., Flake, A. W. and Howell, L. J. (1998) 'Fetal lung lesions: management and outcome', Am J Obstet Gynecol, 179(4), pp. 884-9.

Anthony A. Killeen, E. R., David S. Strayer 2006. Developmental and

Genetic Diseases. United States: Philadelphia : Wolters Kluwer Health/Lippincott Williams & Wilkins, c2008.

Beck, V., Pexsters, A. and Gucciardo, L. 2010. The use of endoscopy in fetal medicine. Gynecol Surgery.

Bekiesińska-Figatowska, M., Romaniuk-Doroszewska, A., Szkudlińska-Pawlak, S., Duczkowska, A., Mądzik, J., Szopa-Krupińska, M. and Maciejewski, T. M.

(2017) 'Diagnostic Imaging of Pregnant Women - The Role of Magnetic Resonance Imaging', Pol J Radiol, 82, pp. 220-226.

Belfort, M. A., Whitehead, W. E., Shamshirsaz, A. A., Ruano, R., Cass, D. L. and Olutoye, O. O. (2015) 'Fetoscopic Repair of Meningomyelocele', Obstet Gynecol, 126(4), pp. 881-4.

Beyer-Berjot, L. and Aggarwal, R. (2013) 'Toward technology-supported surgical training: the potential of virtual simulators in laparoscopic surgery', Scand J Surg, 102(4), pp. 221-6.

Bouchard, S., Johnson, M. P., Flake, A. W., Howell, L. J., Myers, L. B., Adzick, N. S. and Crombleholme, T. M. (2002) 'The EXIT procedure: experience and outcome in 31 cases', J Pediatr Surg, 37(3), pp. 418-26.

Brill, A., Torchinsky, A., Carp, H. and Toder, V. (1999) 'The role of apoptosis in normal and abnormal embryonic development', J Assist Reprod Genet, 16(10), pp. 512-9.

Bruner, J. P., Tulipan, N., Paschall, R. L., Boehm, F. H., Walsh, W. F., Silva, S. R., Hernanz-Schulman, M., Lowe, L. H. and Reed, G. W. (1999) 'Fetal surgery for myelomeningocele and the incidence of shunt-dependent hydrocephalus', JAMA, 282(19), pp. 1819-25.

Bruner, J. P., Tulipan, N. B., Richards, W. O., Walsh, W. F., Boehm, F. H. and Vrabcak, E. K. (2000) 'In utero repair of myelomeningocele: a comparison of endoscopy and hysterotomy', Fetal Diagn Ther, 15(2), pp. 83-8.

Burka, A., Hu, S., Helgeson, S., Krishnan, S., Gao, Y., Hendricks, L. A., Darrell, T. and Kuchenbecker, K. J. 'Proton: A visuo-haptic data acquisition system for robotic learning of surface properties'. 2016 IEEE International Conference on Multisensor Fusion and Integration for Intelligent Systems (MFI), 19-21 Sept. 2016, 58-65.

Canfield, M. A., Honein, M. A., Yuskiv, N., Xing, J., Mai, C. T., Collins, J. S., Devine, O., Petrini, J., Ramadhani, T. A., Hobbs, C. A. and Kirby, R. S. (2006) 'National estimates and race/ethnic-specific variation of selected birth defects in the United States, 1999-2001', Birth Defects Res A Clin Mol Teratol, 76(11), pp. 747-56.

Carrera, J. M., Torrents, M., Mortera, C., Cusí, V. and Muñoz, A. (1995) 'Routine prenatal ultrasound screening for fetal abnormalities: 22 years' experience', Ultrasound Obstet Gynecol, 5(3), pp. 174-9.

Cass, D. L. 'Fetal surgery for congenital diaphragmatic hernia: the North American experience'. Seminars in perinatology: Elsevier, 104-111.

Coakley, F. V. (2001) 'Role of magnetic resonance imaging in fetal surgery', Top Magn Reson Imaging, 12(1), pp. 39-51.

Cochrane, D. D., Irwin, B. and Chambers, K. (2001) 'Clinical outcomes that fetal surgery for myelomeningocele needs to achieve', Eur J Pediatr Surg, 11 Suppl 1, pp. S18-20.

Cooper, M. A., Hutfless, S., Segev, D. L., Ibrahim, A., Lyu, H. and Makary, M. A. (2014) 'Hospital level under-utilization of minimally invasive surgery in the United States: retrospective review'.

Cruz-Martinez, R., Moreno-Alvarez, O., Garcia, M., Méndez, A., Pineda, H., Cruz-Martinez, M. A., Cruz, M. A. and Martinez-Morales, C. (2015) 'Fetal Endoscopic Tracheal Intubation: A New Fetoscopic Procedure to Ensure

Extrauterine Tracheal Permeability in a Case with Congenital Cervical Teratoma', Fetal Diagn Ther, 38(2), pp. 154-8.

Curtiss, L. E. (1976) Comparison of optical performance of selected fetoscope designs. International congress series Amsterdam: Excerpta Medica ; New York : American Elsevier.

Dai, J. S. (2015) 'Euler–Rodrigues formula variations, quaternion conjugation and intrinsic connections', Mechanism and Machine Theory, 92, pp. 144-152.

Dane, B., Dane, C., Sivri, D., Kiray, M., Cetin, A. and Yayla, M. (2007) 'Ultrasound screening for fetal major abnormalities at 11-14 weeks', Acta Obstet Gynecol Scand, 86(6), pp. 666-70.

Danzer, E., Sydorak, R. M., Harrison, M. R. and Albanese, C. T. (2003) 'Minimal access fetal surgery', Eur J Obstet Gynecol Reprod Biol, 108(1), pp. 3-13.

Dastgiri, S., Gilmour, W. H. and Stone, D. H. (2003) 'Survival of children born with congenital anomalies', Arch Dis Child, 88(5), pp. 391-4.

Deka, D., Dadhwal, V., Gajatheepan, S. B., Singh, A., Sharma, K. A. and Malhotra, N. (2012) 'The art of fetoscopy: a step toward minimally invasive fetal therapy', J Obstet Gynaecol India, 62(6), pp. 655-9.

Deprest, J., Jani, J., Lewi, L., Ochsenbein-Kölble, N., Cannie, M., Doné, E., Roubliova, X., Van Mieghem, T., Debeer, A., Debuck, F., Sbragia, L., Toelen, J., Devlieger, R., Lewi, P. and Van de Velde, M. (2006) 'Fetoscopic surgery: encouraged by clinical experience and boosted by instrument innovation', Semin Fetal Neonatal Med, 11(6), pp. 398-412.

Deprest, J., Nicolaides, K., Done', E., Lewi, P., Barki, G., Largen, E., DeKoninck, P., Sandaite, I., Ville, Y., Benachi, A., Jani, J., Amat-Roldan, I. and Gratacos, E. (2011) 'Technical aspects of fetal endoscopic tracheal occlusion for congenital diaphragmatic hernia', J Pediatr Surg, 46(1), pp. 22-32.

Deprest, J. A., Done, E., Van Mieghem, T. and Gucciardo, L. (2008) 'Fetal surgery for anesthesiologists', Curr Opin Anaesthesiol, 21(3), pp. 298-307.

Deprest, J. A., Lerut, T. E. and Vandenberghe, K. (1997) 'Operative fetoscopy: new perspective in fetal therapy?', Prenat Diagn, 17(13), pp. 1247-60.

Dolkart, L., Harter, M. and Snyder, M. (2005) 'Four-dimensional ultrasonographic guidance for invasive obstetric procedures', J Ultrasound Med, 24(9), pp. 1261-6.

Farmer, D. L. (1998) 'Fetal surgery: a brief review', Pediatric radiology, 28(6), pp. 409-413.

Fenster, A., Parraga, G. and Bax, J. (2011) 'Three-dimensional ultrasound scanning', Interface Focus, 1(4), pp. 503-19.

Fisk, N. M., Gitau, R., Teixeira, J. M., Giannakoulopoulos, X., Cameron, A. D. and Glover, V. A. (2001) 'Effect of direct fetal opioid analgesia on fetal hormonal and hemodynamic stress response to intrauterine needling', Anesthesiology, 95(4), pp. 828-35.

Flake, A. W. (2001) 'Prenatal intervention: ethical considerations for life-threatening and non-life-threatening anomalies', Semin Pediatr Surg, 10(4), pp. 212-21.

Fowler, S. F., Sydorak, R. M., Albanese, C. T., Farmer, D. L., Harrison, M. R. and Lee, H. (2002) 'Fetal endoscopic surgery: lessons learned and trends reviewed', J Pediatr Surg, 37(12), pp. 1700-2.

Gofrit, O. N., Mikahail, A. A., Zorn, K. C., Zagaja, G. P., Steinberg, G. D. and Shalhav, A. L. (2008) 'Surgeons' perceptions and injuries during and after urologic laparoscopic surgery', Urology, 71(3), pp. 404-7.

Golombeck, K., Ball, R. H., Lee, H., Farrell, J. A., Farmer, D. L., Jacobs, V. R., Rosen, M. A., Filly, R. A. and Harrison, M. R. (2006) 'Maternal morbidity after maternal-fetal surgery', Am J Obstet Gynecol, 194(3), pp. 834-9.

Graya, R., , J. H., Laura Oakleya, , J. J. K., , P. B., and Hollowell, J. 2009. Towards an understanding of variations in infant

mortality rates between different ethnic groups

in England and Wales. Department of Public Health, University of Oxford.

Grivell, R. M., Andersen, C. and Dodd, J. M. (2015) 'Prenatal interventions for congenital diaphragmatic hernia for improving outcomes', Cochrane Database Syst Rev, (11), pp. CD008925.

Group, C. O. o. S. T. S. (2004) 'A comparison of laparoscopically assisted and open colectomy for colon cancer', N Engl J Med, 350(20), pp. 2050-9.

Harrison, M. R., Albanese, C. T., Hawgood, S. B., Farmer, D. L., Farrell, J. A., Sandberg, P. L. and Filly, R. A. (2001) 'Fetoscopic temporary tracheal occlusion by means of detachable balloon for congenital diaphragmatic hernia', Am J Obstet Gynecol, 185(3), pp. 730-3.

Harrison, M. R., Keller, R. L., Hawgood, S. B., Kitterman, J. A., Sandberg, P. L., Farmer, D. L., Lee, H., Filly, R. A., Farrell, J. A. and Albanese, C. T. (2003) 'A randomized trial of fetal endoscopic tracheal occlusion for severe fetal congenital diaphragmatic hernia', N Engl J Med, 349(20), pp. 1916-24.

Hedrick, H. L., Flake, A. W., Crombleholme, T. M., Howell, L. J., Johnson, M. P., Wilson, R. D. and Adzick, N. S. (2004) 'Sacrococcygeal teratoma: prenatal assessment, fetal intervention, and outcome', J Pediatr Surg, 39(3), pp. 430-8; discussion 430-8.

Hinz, S. 'Fast and subpixel precise blob detection and attribution'. IEEE International Conference on Image Processing 2005, 11-14 Sept. 2005, III-457-60.

Hirose, S. and Harrison, M. R. (2003) 'The ex utero intrapartum treatment (EXIT) procedure', Semin Neonatol, 8(3), pp. 207-14.

Ho, C., Tsakonas, E., Tran, K., Cimon, K., Severn, M., Mierzwinski-Urban, M. and Corcos, J. (2012) 'Robot-assisted surgery compared with open surgery and laparoscopic surgery', CADTH Technology Overviews, 2(2).

Hogan 1980-August. Mechanical Impedance Control in Assistive Devices and Manipulators. Proceedings of the Joint Automatic Controls Conference.

Hong, J., Dohi, T., Hashizume, M., Konishi, K. and Hata, N. (2004) 'An ultrasound-driven needle-insertion robot for percutaneous cholecystostomy', Physics in Medicine and Biology, 49(3), pp. 441.

Howe, R. D. and Matsuoka, Y. (1999) 'Robotics for surgery', Annual Review of Biomedical Engineering, 1(1), pp. 211-240.

Huber, A., Baschat, A. A., Bregenzer, T., Diemert, A., Tchirikov, M., Hackelöer, B. J. and Hecher, K. (2008) 'Laser coagulation of placental anastomoses with a 30 degrees fetoscope in severe mid-trimester twin-twin transfusion syndrome with anterior placenta', Ultrasound Obstet Gynecol, 31(4), pp. 412-6.

Ierullo, A. M., Papageorghiou, A. T., Bhide, A., Fratelli, N. and Thilaganathan, B. (2007) 'Severe twin-twin transfusion syndrome: outcome after fetoscopic laser ablation of the placental vascular equator', BJOG, 114(6), pp. 689-93.

Jani, J. C., Nicolaides, K. H., Gratacós, E., Valencia, C. M., Doné, E., Martinez, J. M., Gucciardo, L., Cruz, R. and Deprest, J. A. (2009) 'Severe diaphragmatic hernia treated by fetal endoscopic tracheal occlusion', Ultrasound Obstet Gynecol, 34(3), pp. 304-10.

Jeffrey Stoll, P. D. Passive Markers for Ultrasound Trackingof Surgical Instruments.

Jeng, J.-C. 2013. A one-step tuning method for PID controllers with robustness specification using plant step-response data. In: Tseng, W.-L. (ed.). Chemical Engineering Research and Design.

Johnson, M. P., Gerdes, M., Rintoul, N., Pasquariello, P., Melchionni, J., Sutton, L. N. and Adzick, N. S. (2006) 'Maternal-fetal surgery for myelomeningocele: neurodevelopmental outcomes at 2 years of age', Am J Obstet Gynecol, 194(4), pp. 1145-50; discussion 1150-2.

Kaspers, A. Blob detection. UMC Utrecht: Image Sciences Institute.

Ken, S. 1985. Animating rotation with quaternion curves. DOI=http://dx.doi.org/10.1145/325334.325242 ed.: Proceedings of the 12th annual conference on Computer graphics and interactive techniques.

Keys, R. (1981) 'Cubic convolution interpolation for digital image processing', IEEE Transactions on Acoustics, Speech, and Signal Processing, 29(6), pp. 1153-1160.

Killeen, A. A. 2006. Developmental and

Genetic Diseases. In: Rubin, E. (ed.). United States: Philadelphia : Wolters Kluwer Health/Lippincott Williams & Wilkins, c2008.

Kim, K., Kubota, M., Ohkawa, Y., Shiraishi, T., Kawai, T., Kobayashi, A., Yamashita, H. and Chiba, T. (2011) 'A novel ultralow-illumination endoscope system', Surg Endosc, 25(6), pp. 2029-33.

Klaritsch P, A. K., Van Mieghem T, Gucciardo L, Done' E, Bynens B, Deprest J. Instrumental requirements for minimal invasive fetal and surgery. 2009. Instrumental requirements for minimal invasive

fetal surgery. BJOG.

Klaritsch, P., Albert, K., Van Mieghem, T., Gucciardo, L., Done', E., Bynens, B. and Deprest, J. (2009) 'Instrumental requirements for minimal invasive fetal surgery', BJOG, 116(2), pp. 188-97.

Kline, J. (2012) Handbook of Biomedical Engineering. Elsevier Science.

Kohl, T., Hering, R., Heep, A., Schaller, C., Meyer, B., Greive, C., Bizjak, G., Buller, T., Van de Vondel, P., Gogarten, W., Bartmann, P., Knopfle, G. and Gembruch, U. (2006a) 'Percutaneous fetoscopic patch coverage of spina bifida aperta in the human--early clinical experience and potential', Fetal Diagn Ther, 21(2), pp. 185-93.

Kohl, T., Hering, R., Van de Vondel, P., Tchatcheva, K., Berg, C., Bartmann, P., Heep, A., Franz, A., Müller, A. and Gembruch, U. (2006b) 'Analysis of the stepwise clinical introduction of experimental percutaneous fetoscopic surgical techniques for upcoming minimally invasive fetal cardiac interventions', Surg Endosc, 20(7), pp. 1134-43.

Koivukangas, T., Katisko, J. P. and Koivukangas, J. P. (2013) 'Technical accuracy of optical and the electromagnetic tracking systems', Springerplus, 2(1), pp. 90.

Kurjak, A., Miskovic, B., Andonotopo, W., Stanojevic, M., Azumendi, G. and Vrcic, H. (2007) 'How useful is 3D and 4D ultrasound in perinatal medicine?', J Perinat Med, 35(1), pp. 10-27.

Kwok, K. W. (2012) Dynamic active constraints for robot assisted minimally invasive surgery [electronic resource]: Imperial College London (University of London).

Lally, K. P., Bagolan, P., Hosie, S., Lally, P. A., Stewart, M., Cotten, C. M., Van Meurs, K. P., Alexander, G. and Group, C. D. H. S. (2006) 'Corticosteroids for fetuses with congenital diaphragmatic hernia: can we show benefit?', J Pediatr Surg, 41(4), pp. 668-74; discussion 668-74.

Lamata, P., Gomez, E. J., Hernández, F. L., Oltra Pastor, A., Sanchez-Margallo, F. M. and Del Pozo Guerrero, F. (2008) 'Understanding perceptual boundaries in laparoscopic surgery', IEEE Trans Biomed Eng, 55(3), pp. 866-73.

Langham, M. R., Kays, D. W., Ledbetter, D. J., Frentzen, B., Sanford, L. L. and Richards, D. S. (1996) 'Congenital diaphragmatic hernia. Epidemiology and outcome', Clin Perinatol, 23(4), pp. 671-88.

Larsen, E. C., Christiansen, O. B., Kolte, A. M. and Macklon, N. (2013) 'New insights into mechanisms behind miscarriage', BMC Med, 11, pp. 154.

Larson, B. J., Longaker, M. T. and Lorenz, H. P. (2010) 'Scarless fetal wound healing: a basic science review', Plast Reconstr Surg, 126(4), pp. 1172-80.

Lee, D. H., Kim, U., Gulrez, T., Yoon, W. J., Hannaford, B. and Choi, H. R. (2016) 'A Laparoscopic Grasping Tool With Force Sensing Capability', IEEE/ASME Transactions on Mechatronics, 21(1), pp. 130-141.

Leppig, K. A., Werler, M. M., Cann, C. I., Cook, C. A. and Holmes, L. B. (1987) 'Predictive value of minor anomalies. I. Association with major malformations', J Pediatr, 110(4), pp. 531-7.

Lindeberg, T. (2013) Scale-Space Theory in Computer Vision. Springer US.

Linguraru, M. G., Vasilyev, N. V., Del Nido, P. J. and Howe, R. D. (2007) 'Statistical Segmentation of Surgical Instruments in 3D Ultrasound Images', Ultrasound in medicine & biology, 33(9), pp. 1428-1437.

Liu, L., Oza, S., Hogan, D., Perin, J., Rudan, I., Lawn, J. E., Cousens, S., Mathers, C. and Black, R. E. (2015) 'Global, regional, and national causes of child mortality in 2000-13, with projections to inform post-2015 priorities: an updated systematic analysis', Lancet, 385(9966), pp. 430-40.

Lizzi, F. L. and Feleppa, E. J. 'Image processing and pre-processing for medical ultrasound'. Proceedings 29th Applied Imagery Pattern Recognition Workshop, 2000, 187-192.

Lyerly, A. D., Cefalo, R. C., Socol, M., Fogarty, L. and Sugarman, J. (2001) 'Attitudes of maternal-fetal specialists concerning maternal-fetal surgery', Am J Obstet Gynecol, 185(5), pp. 1052-8.

In the womb (2005) [videorecording]. National Geographic Channel,.

MARDEN, P. M., SMITH, D. W. and MCDONALD, M. J. (1964) 'CONGENITAL ANOMALIES IN THE NEWBORN INFANT, INCLUDING MINOR VARIATIONS. A STUDY OF 4,412 BABIES BY SURFACE EXAMINATION FOR ANOMALIES AND BUCCAL SMEAR FOR SEX CHROMATIN', J Pediatr, 64, pp. 357-71.

Mari, G., Roberts, A., Detti, L., Kovanci, E., Stefos, T., Bahado-Singh, R. O., Deter, R. L. and Fisk, N. M. (2001) 'Perinatal morbidity and mortality rates in severe twin-twin transfusion syndrome: results of the International Amnioreduction Registry', Am J Obstet Gynecol, 185(3), pp. 708-15.

Marwan, A. and Crombleholme, T. M. (2006) 'The EXIT procedure: principles, pitfalls, and progress', Semin Pediatr Surg, 15(2), pp. 107-15.

Metkus, A. P., Filly, R. A., Stringer, M. D., Harrison, M. R. and Adzick, N. S. (1996) 'Sonographic predictors of survival in fetal diaphragmatic hernia', J Pediatr Surg, 31(1), pp. 148-51; discussion 151-2.

Meuli, M., Meuli-Simmen, C., Yingling, C. D., Hutchins, G. M., Timmel, G. B., Harrison, M. R. and Adzick, N. S. (1996) 'In utero repair of experimental myelomeningocele saves neurological function at birth', J Pediatr Surg, 31(3), pp. 397-402.

Mezger, U., Jendrewski, C. and Bartels, M. (2013) 'Navigation in surgery', Langenbeck's Archives of Surgery, 398(4), pp. 501-514.

Milner, R., Kitano, Y., Olutoye, O., Flake, A. W. and Adzick, N. S. (2000) 'Radiofrequency thermal ablation: a potential treatment for hydropic fetuses with a large chest mass', J Pediatr Surg, 35(2), pp. 386-9.

Minor, L. G. and Sklansky, J. (1981) 'The detection and segmentation of blobs in infrared images', IEEE Transactions on Systems, Man, and Cybernetics, 11(3), pp. 194-201.

Moore, K., Persaud, T. V. N. and Torchia, M. (2015) The Developing Human10th Edition. Elsevier.

Morris, R. K., Malin, G. L., Quinlan-Jones, E., Middleton, L. J., Hemming, K., Burke, D., Daniels, J. P., Khan, K. S., Deeks, J. and Kilby, M. D. 'Percutaneous vesicoamniotic shunting versus conservative management for fetal lower urinary tract obstruction (PLUTO): a randomised trial', The Lancet, 382(9903), pp. 1496-1506.

Morris, R. K., Malin, G. L., Quinlan-Jones, E., Middleton, L. J., Hemming, K., Burke, D., Daniels, J. P., Khan, K. S., Deeks, J., Kilby, M. D. and Group, P. v. s. i. L. U. T. O. P. C. (2013) 'Percutaneous vesicoamniotic shunting versus conservative management for fetal lower urinary tract obstruction (PLUTO): a randomised trial', Lancet, 382(9903), pp. 1496-506.

Ng, A. and Swanevelder, J. (2011) 'Resolution in ultrasound imaging', Continuing Education in Anaesthesia Critical Care & Pain, 11(5), pp. 186-192.

Noah, M. M., Norton, M. E., Sandberg, P., Esakoff, T., Farrell, J. and Albanese, C. T. (2002) 'Short-term maternal outcomes that are associated with the EXIT procedure, as compared with cesarean delivery', Am J Obstet Gynecol, 186(4), pp. 773-7.

Oliver, E. R., Coleman, B. G., Goff, D. A., Horii, S. C., Howell, L. J., Rychik, J., Bebbington, M. W. and Johnson, M. P. (2013) 'Twin reversed arterial perfusion sequence: a new method of parabiotic twin mass estimation correlated with pump twin compromise', J Ultrasound Med, 32(12), pp. 2115-23.

Otsu, N. (1979) A Threshold Selection Method from Gray-Level Histograms.

Padalkar, M. V. and Pleshko, N. (2015) 'Wavelength-dependent penetration depth of near infrared radiation into cartilage', Analyst, 140(7), pp. 2093-100.

Paek, B. W., Jennings, R. W., Harrison, M. R., Filly, R. A., Tacy, T. A., Farmer, D. L. and Albanese, C. T. (2001) 'Radiofrequency ablation of human fetal sacrococcygeal teratoma', Am J Obstet Gynecol, 184(3), pp. 503-7.

Pedreira, D. A., Zanon, N., Nishikuni, K., Moreira de Sá, R. A., Acacio, G. L., Chmait, R. H., Kontopoulos, E. V. and Quintero, R. A. (2016) 'Endoscopic surgery for the antenatal treatment of myelomeningocele: the CECAM trial', Am J Obstet Gynecol, 214(1), pp. 111.e1-111.e11.

Peiró, J. L., Carreras, E., Guillén, G., Arévalo, S., Sánchez-Durán, M. A., Higueras, T., Castillo, F., Marhuenda, C., Lloret, J. and Martínez-Ibáñez, V. (2009) 'Therapeutic indications of fetoscopy: a 5-year institutional experience', J Laparoendosc Adv Surg Tech A, 19(2), pp. 229-36.

Pintaric, T. and Kaufmann, H. 'A rigid-body target design methodology for optical pose-tracking systems', Proceedings of the 2008 ACM symposium on Virtual reality software and technology, Bordeaux, France. 1450594: ACM, 73-76.

Prada, F., Del Bene, M., Mattei, L., Casali, C., Filippini, A., Legnani, F., Mangraviti, A., Saladino, A., Perin, A., Richetta, C., Vetrano, I., Moiraghi, A., Saini, M. and DiMeco, F. (2014) 'Fusion imaging for intra-operative ultrasound-based navigation in neurosurgery', J Ultrasound, 17(3), pp. 243-51.

Pratt, R., Deprest, J., Vercauteren, T., Ourselin, S. and David, A. L. (2015) 'Computer-assisted surgical planning and intraoperative guidance in fetal surgery: a systematic review', Prenat Diagn, 35(12), pp. 1159-66.

Press, R. 2008 Mar. Antenatal Care: Routine Care for the Healthy Pregnant Woman. London: RCOG Press.

Pugash, D., Brugger, P. C., Bettelheim, D. and Prayer, D. (2008) 'Prenatal ultrasound and fetal MRI: the comparative value of each modality in prenatal diagnosis', Eur J Radiol, 68(2), pp. 214-26.

Quintero, R. A., Hume, R., Smith, C., Johnson, M. P., Cotton, D. B., Romero, R. and Evans, M. I. (1995) 'Percutaneous fetal cystoscopy and endoscopic fulguration of posterior urethral valves', Am J Obstet Gynecol, 172(1 Pt 1), pp. 206-9.

Rahimian, P. and Kearney, J. (2016) 'Optimal Camera Placement for Motion Capture Systems', IEEE Trans Vis Comput Graph.

Rauskolb, R. (1979) 'Fetoscopy--a new endoscopic approach', Endoscopy, 11(2), pp. 107-13.

RCOG 2010 May. Termination of

Pregnancy for Fetal

Abnormality

in England, Scotland

and Wales. London: RCOG.

Ruano, R., Duarte, S. A., Pimenta, E. J., Takashi, E., da Silva, M. M., Tannuri, U. and Zugaib, M. (2011) 'Comparison between fetal endoscopic tracheal occlusion using a 1.0-mm fetoscope and prenatal expectant management in severe congenital diaphragmatic hernia', Fetal Diagn Ther, 29(1), pp. 64-70.

Ruano, R., Yoshisaki, C. T., da Silva, M. M., Ceccon, M. E., Grasi, M. S., Tannuri, U. and Zugaib, M. (2012) 'A randomized controlled trial of fetal endoscopic tracheal occlusion versus postnatal management of severe isolated congenital diaphragmatic hernia', Ultrasound Obstet Gynecol, 39(1), pp. 20-7.

Rutledge, J. C. (1997) 'Developmental toxicity induced during early stages of mammalian embryogenesis', Mutat Res, 396(1-2), pp. 113-27.

Sazontova, V. N., Karlina, L. I. u. and Chuprov, P. V. (1984) '[The Am-VS-2 amnioscope with fiber light guide]', Med Tekh, (3), pp. 46-7.

Schwaab, J., Kurz, C., Sarti, C., Bongers, A., Schoenahl, F., Bert, C., Debus, J., Parodi, K. and Jenne, J. W. (2015a) 'First Steps Toward Ultrasound-Based Motion Compensation for Imaging and Therapy: Calibration with an Optical System and 4D PET Imaging', Front Oncol, 5, pp. 258.

Schwaab, J., Kurz, C., Sarti, C., Bongers, A., Schoenahl, F., Bert, C., Debus, J., Parodi, K. and Jenne, J. W. (2015b) 'First Steps Toward Ultrasound-Based Motion Compensation for Imaging and Therapy: Calibration with an Optical System and 4D PET Imaging', Frontiers in Oncology, 5(258).

Senat, M. V., Deprest, J., Boulvain, M., Paupe, A., Winer, N. and Ville, Y. (2004) 'Endoscopic laser surgery versus serial amnioreduction for severe twin-to-twin transfusion syndrome', N Engl J Med, 351(2), pp. 136-44.

Song, M.-H. and Godøy, R. (2016) How Fast Is Your Body Motion? Determining a Sufficient Frame Rate for an Optical Motion Tracking System Using Passive Markers.

Stoll, J., Ren, H. and Dupont, P. E. (2012) 'Passive markers for tracking surgical instruments in real-time 3-D ultrasound imaging', IEEE Trans Med Imaging, 31(3), pp. 563-75.

Straňák, Z., Krofta, L., Haak, L. A., Vojtěch, J., Hašlík, L., Rygl, M., Pýcha, K. and Feyereisl, J. (2017) 'Antenatal assessment of liver position, rather than lung-to-head ratio (LHR) or observed/expected LHR, is predictive of outcome in fetuses with isolated left-sided congenital diaphragmatic hernia', J Matern Fetal Neonatal Med, 30(1), pp. 74-78.

Sugano, N. (2003) 'Computer-assisted orthopedic surgery', Journal of Orthopaedic Science, 8(3), pp. 442-448.

Sutton, L. N., Adzick, N. S., Bilaniuk, L. T., Johnson, M. P., Crombleholme, T. M. and Flake, A. W. (1999) 'Improvement in hindbrain herniation demonstrated by serial fetal magnetic resonance imaging following fetal surgery for myelomeningocele', JAMA, 282(19), pp. 1826-31.

Szpinda, M., Daroszewski, M., Woźniak, A., Szpinda, A. and Mila-Kierzenkowska, C. (2012) 'Tracheal dimensions in human fetuses: an anatomical, digital and statistical study', Surg Radiol Anat, 34(4), pp. 317-23.

Sánchez, A., Rodríguez, O., Sánchez, R., Benítez, G., Pena, R., Salamo, O. and Baez, V. (2014) 'Laparoscopic surgery skills evaluation: analysis based on accelerometers', JSLS: Journal of the Society of Laparoendoscopic Surgeons, 18(4).

Takahashi, C. and Watt, S. J. (2017) 'Optimal visual–haptic integration with articulated tools', Experimental Brain Research, 235(5), pp. 1361-1373.

Thewlis, D. 2011. A COMPARISON OF TWO COMMERCIALLY AVAILABLE MOTION CAPTURE SYSTEMS FOR GAIT

ANALYSIS: HIGH-END VS LOW-COST. In: Bishop, C. (ed.). Congress of the International Society of Biomechanics.

Tholey, G., Desai, J. P. and Castellanos, A. E. (2005) 'Force feedback plays a significant role in minimally invasive surgery: results and analysis', Ann Surg, 241(1), pp. 102-9.

Tsui, C., Klein, R. and Garabrant, M. (2013) 'Minimally invasive surgery: national trends in adoption and future directions for hospital strategy', Surg Endosc, 27(7), pp. 2253-7.

Ungi, T., Lasso, A. and Fichtinger, G. (2016) 'Open-source platforms for navigated image-guided interventions', Med Image Anal, 33, pp. 181-6.

VanKoevering, K. K., Morrison, R. J., Prabhu, S. P., Torres, M. F., Mychaliska, G. B., Treadwell, M. C., Hollister, S. J. and Green, G. E. (2015) 'Antenatal Three-Dimensional Printing of Aberrant Facial Anatomy', Pediatrics, 136(5), pp. e1382-5.

Walsh, D. S. and Johnson, M. P. (1999) 'Fetal interventions for obstructive uropathy', Semin Perinatol, 23(6), pp. 484-95.

Welsh, A., Agarwal, S., Kumar, S., Smith, R. P. and Fisk, N. M. (2003) 'Fetal cystoscopy in the management of fetal obstructive uropathy: experience in a single European centre', Prenat Diagn, 23(13), pp. 1033-41.

Werner, H., Dos Santos, J. R., Fontes, R., Daltro, P., Gasparetto, E., Marchiori, E. and Campbell, S. (2011) 'Virtual bronchoscopy in the fetus', Ultrasound Obstet Gynecol, 37(1), pp. 113-5.

Werner, H., Lopes dos Santos, J. R., Fontes, R., Belmonte, S., Daltro, P., Gasparetto, E., Marchiori, E. and Campbell, S. (2013) 'Virtual bronchoscopy for evaluating cervical tumors of the fetus', Ultrasound Obstet Gynecol, 41(1), pp. 90-4.

Werner, H., Rolo, L. C., Araujo Júnior, E. and Dos Santos, J. R. (2014) 'Manufacturing models of fetal malformations built from 3-dimensional ultrasound, magnetic resonance imaging, and computed tomography scan data', Ultrasound Q, 30(1), pp. 69-75.

Wiles, A., G. Thompson, D. and Frantz, D. (2004) Accuracy assessment and interpretation for optical tracking systems.

Wilson, R. D., Johnson, M. P., Crombleholme, T. M., Flake, A. W., Hedrick, H. L., King, M., Howell, L. J. and Adzick, N. S. (2003) 'Chorioamniotic membrane separation following open fetal surgery: pregnancy outcome', Fetal Diagn Ther, 18(5), pp. 314-20.

Wu, X., Wu, S., Xing, Z. and Jia, X. 2016. A Global Calibration Method for Widely Distributed Cameras Based on Vanishing Features. Sensors.

Yagel, S., Cohen, S. M., Shapiro, I. and Valsky, D. V. (2007) '3D and 4D ultrasound in fetal cardiac scanning: a new look at the fetal heart', Ultrasound Obstet Gynecol, 29(1), pp. 81-95.

Yaneza, M. M., Cameron, A., Clement, W. A., Fairgrieve, R., Ledingham, M. A., Morrissey, M. S., Simpson, J., Wynne, D. M. and Kubba, H. (2015) 'An interventional airway delivery service for congenital high airway obstruction', J Laryngol Otol, 129(8), pp. 795-800.

Yao, W., Elangovan, H. and Nicolaides, K. (2014) 'Design of a flexible fetoscopy manipulation system for congenital diaphragmatic hernia', Med Eng Phys, 36(1), pp. 32-8.

Yoon, J.-H., Park, J.-S. and Kim, C. (2006) 'Increasing Camera Pose Estimation Accuracy Using Multiple Markers', in Pan, Z., Cheok, A., Haller, M., Lau, R.W.H., Saito, H. & Liang, R. (eds.) Advances in Artificial Reality and Tele-Existence: 16th International Conference on Artificial Reality and Telexistence, ICAT 2006, Hangzhou, China, November 29 - December 1,

2006. Proceedings. Berlin, Heidelberg: Springer Berlin Heidelberg, pp. 239-248.

Zamora, I. J., Ethun, C. G., Evans, L. M., Olutoye, O. O., Ivey, R. T., Haeri, S., Belfort, M. A., Lee, T. C. and Cass, D. L. (2013) 'Maternal morbidity and reproductive outcomes related to fetal surgery', J Pediatr Surg, 48(5), pp. 951-5.

Zheng, G. and Nolte, L. P. (2015) 'Computer-Assisted Orthopedic Surgery: Current State and Future Perspective', Front Surg, 2, pp. 66.

Zhou, M. 2007. Shifts in Force Perception Threshold in Laparoscopic

Surgery with Experience. In: Perreault, J. (ed.). Cambridge Health Alliance.

Zhou, T. 2009. Surgical navigation: tool of minimally invasive medical. Chinese University Technology Transfer.

Ziskin, M., Thickman, D., Goldenberg, N., Lapayowker, M. and Becker, J. (1982) 'The comet tail artifact', Journal of Ultrasound in Medicine, 1(1), pp. 1-7.